Ajit Kumar Parwani
PL. Ramkumar
Kumar Abhishek
Saurabh Kumar Yadav   *Editors*

Recent Advances in Mechanical Infrastructure

Proceedings of ICRAM 2021

Springer

Lecture Notes in Intelligent Transportation and Infrastructure

The series "Lecture Notes in Intelligent Transportation and Infrastructure" (LNITI) publishes new developments and advances in the various areas of intelligent transportation and infrastructure. The intent is to cover the theory, applications, and perspectives on the state-of-the-art and future developments relevant to topics such as intelligent transportation systems, smart mobility, urban logistics, smart grids, critical infrastructure, smart architecture, smart citizens, intelligent governance, smart architecture and construction design, as well as green and sustainable urban structures. The series contains monographs, conference proceedings, edited volumes, lecture notes and textbooks. Of particular value to both the contributors and the readership are the short publication timeframe and the world-wide distribution, which enable wide and rapid dissemination of high-quality research output.

More information about this series at https://link.springer.com/bookseries/15991

Ajit Kumar Parwani · PL. Ramkumar ·
Kumar Abhishek · Saurabh Kumar Yadav
Editors

Recent Advances in Mechanical Infrastructure

Proceedings of ICRAM 2021

Editors
Ajit Kumar Parwani
Department of Mechanical and Aero-Space
Engineering
Institute of Infrastructure Technology
Research and Management (IITRAM)
Ahmedabad, India

PL. Ramkumar
Department of Mechanical and Aero-Space
Engineering
Institute of Infrastructure Technology
Research and Management (IITRAM)
Ahmedabad, India

Kumar Abhishek
Department of Mechanical and Aero-Space
Engineering
Institute of Infrastructure Technology
Research and Management (IITRAM)
Ahmedabad, India

Saurabh Kumar Yadav
Department of Mechanical and Aero-Space
Engineering
Institute of Infrastructure Technology
Research and Management (IITRAM)
Ahmedabad, India

Organizing committee of ICRAM-2021

Conference Chairs

Dr. Ajit Kumar Parwani, Assistant Professor, Mechanical and Aero-Space Engineering Department, IITRAM

Dr. PL. RamKumar, Assistant Professor, Mechanical and Aero-Space Engineering Department, IITRAM

Dr. Kumar Abhishek, Assistant Professor, Mechanical and Aero-Space Engineering Department, IITRAM

Dr. Saurabh Kumar Yadav, Assistant Professor, Mechanical and Aero-Space Engineering Department, IITRAM

Conveners

Dr. Dileep Kumar Gupta, Assistant Professor, Mechanical and Aero-Space Engineering Department, IITRAM

Dr. Jagat Rath, Assistant Professor, Mechanical and Aero-Space Engineering Department, IITRAM

Registration Committee

Dr. Sumit Tripathi, Assistant Professor, Mechanical and Aero-Space Engineering Department, IITRAM

Dr. Kamlesh Joshi, Assistant Professor, Mechanical and Aero-Space Engineering Department, IITRAM

Preface

This book is brought out to mark the occasion of the 3rd International Conference on Recent Advances in Mechanical Infrastructure (ICRAM-2021) during August 06–08, 2021, organized by the Department of Mechanical and Aero-Space Engineering, IITRAM, Ahmedabad. The purpose of this conference is to provide platform for academicians, researchers and industrial professionals to exchange their views, ideas, experiences and collaborate for expediting progress in the field of thermal, manufacturing, infrastructure planning, design and controls.

The program consists of keynote sessions with eminent speakers and technical paper presentations covering a wide range of topics in mechanical infrastructure. Over hundered manuscripts have been recieved. The recieved manuscripts went through a peer review process. Each manuscript received at least two reviews. Finally, forty manuscripts were selected for presentation in following three different tracks

i   Recent Advances in Thermal Infrastructure
ii Recent Advances in Infrastructure Planning, Design and Control
iii Recent Advances in Manufacturing Infrastructure

The conference organizers would like to thank the delegates who have contributed for the conference proceedings. We would also like to thank our outstanding keynote speakers: Dr. Prabal Talukdar, Professor, IIT Delhi; Dr. Abishek B. Kamaraj, Assistant Professor, Kettering University, USA; Dr. Malti Goel, Founder, Climate Change Research Society, New Delhi; and Dr. Vishesh Ranjan Kar, Associate Dean (R&C), NIT Jamshedpur, India, for sharing their deep insights on future challenges and trends. We would like to thank all the reviewers for their great effort on reviewing the papers submitted to ICRAM-2021.

Special thanks to all the researchers and students who participated in the conference and making this conference a very meaningful and interesting. We are grateful to the management of IITRAM for their help and support in organizing this mega event.

Last but not least, we are thankful for the enormous support of Springer for publishing the proceedings of the 3rd International Conference on Recent Advances in Mechanical Infrastructure (ICRAM-2021).

We hope that this book will motivate many academicians and industrial professionals to specialize in the field of thermal, manufacturing, infrastructure planning, design and controls.

Ahmedabad, India   Ajit Kumar Parwani
                                                                                                        PL. Ramkumar
                                                                                                       Kumar Abhishek
                                                                                              Saurabh Kumar Yadav

Contents

Recent Advances in Infrastructure Planning, Design and Control

About the Editors

Dr. Ajit Kumar Parwani is working as Assistant Professor in the Department of Mechanical Engineering at the Institute of Infrastructure Technology Research and Management (IITRAM), Ahmedabad, India. He has completed his Ph.D. from Indian Institute of Technology (IIT) Delhi, India, in 2013. He has over 15 years of teaching and research experience. His research interests include heat transfer, inverse heat transfer, computational heat transfer, renewable energy, and IC engines. He has published several papers in international journals. He has filed an Indian patent title "Simultaneous reduction of NOx and CO_2 using exhaust gas recirculation and carbon capture." He has conducted several workshops, short-term training programs, and seminars. He is Editor of a book titled "Recent Advances in Mechanical Infrastructure" in the Lecture Notes in Intelligent Transportation and Infrastructure published by Springer Singapore. He has two ongoing research projects funded by SERB-DST, Government of India, and Institute of Plasma Research, Government of India.

Dr. PL. Ramkumar is Assistant Professor in Mechanical Engineering Department at IITRAM, Ahmadabad. He served as Lecturer in the Mechanical Engineering Department at the Birla Institute of Technology and Science, Pilani, KK Birla Goa Campus, Goa, India, for 8 years. He has over 12 years of teaching and research experience. He completed his graduation in mechanical engineering from Madurai Kamaraj University in 2003. He obtained M. E degree in computer-aided design from Anna University, Tamil Nadu, India, in 2008 securing university rank with gold medal. He received his Ph.D. from BITS Pilani in the year 2016. His area of research includes experimental analysis of manufacturing processes, process modeling, computer-aided analysis, and optimization. He has organized various workshops and conferences. He has published good number of research papers in the international journal/conferences of repute. He has written/edited a book titled "Recent Advances in Mechanical Infrastructure" in the Lecture Notes in Intelligent Transportation and Infrastructure published by Springer Singapore. He is Life Member of various prestigious societies which include Institute of Engineers (MIE), Indian Institute of Metals (IIM), and Hong Kong Society of Mechanical Engineers (HKMSE).

Dr. Kumar Abhishek is Assistant Professor in Mechanical Engineering Department at IITRAM, Ahmadabad. He has over 4 years of teaching experience. He received his Ph.D. from NIT Rourkela in the year 2016. His area research includes experimental analysis of manufacturing processes, manufacturing and industrial engineering and decision and information science. He has organized various workshops and conferences. He has published good number of research papers in the international journal/conferences of repute.

Saurabh Kumar Yadav is Assistant Professor in the Department of Mechanical Engineering at the IITRAM, Ahmedabad. He feels that teaching is an art that requires a constant effort for improvement. He consistently conducts research experiments and search for interactive means of classroom instruction. He teaches finite element method at the undergraduate level and dynamic and vibration at both undergraduate and graduate levels.

Recent Advances in Thermal Infrastructure

Performance Analysis of Desiccant Material Prepared by Simple Mixing of Silica Gel and Calcium Chloride

Bhushan C. Behede, Siddharth S. Chakrabarti, and Uday S. Wankhede

Abstract To increase the performance, reliability, and economic feasibility of the desiccant-based dehumidification system, it is required to use good desiccant material in the system. In this research work, five samples of desiccant material are prepared by simple mixing of silica gel granules and calcium chloride by varying percentages of their contribution by weight. To calculate the percentage increase in MRR in five samples, one sample is prepared using stand-alone silica gel as a desiccant. An analysis is done by the gravimetric method to calculate its moisture removal rate (MRR) against the operating conditions of the air in the hot and humid environments. The goal of the current research work is to select the best suitable proportion of silica gel and calcium chloride in the composite desiccant as per as MRR is concerned. Different performance indicators were also determined and discussed in this paper. It is found that there is a 92% increase in the MRR when the sample contains 60% of silica gel and 40% of calcium chloride by weight in the desiccant instead of stand-alone silica gel.

Keywords Desiccant · Dehumidification · Adsorption · Desorption

1 Introduction

Dehumidification is an important process in air-conditioning. Typically, dehumidification can be achieved by removing water vapor present in the air, and to do so, the temperature of the air is reduced well below its dew point temperature. To reduce the temperature, vapor compression refrigeration system (VCRS) is used which consumes electrical energy. Energy-consuming potential is very high for the VCRS systems, and it is increasing day by day; several buildings are adopting air-conditioning devices based on VCRS. We can reduce energy-consuming potential if

B. C. Behede (✉) · S. S. Chakrabarti · U. S. Wankhede
O. P. Jindal University, Chhattisgarh Raigarh 496109, India

B. C. Behede
SVKM's Institute of Technology, Maharashtra Dhule 424001, India

we replace or assist the VCRS system with few other available technologies, which operate on low-grade energy. Desiccant-based dehumidification system is one of them. This system operates on low-grade energy such as waste heat, solar energy. In addition, the operating life of the system is more than the VCRS. Concisely, low energy consumption, low reactivation temperature, and use of low-grade energy for reactivation of desiccant material are the most important advantages and reasons for adopting a desiccant-based dehumidification system instead or along with the VCRS system (Behede et al. 2019) .

Desiccants are porous substances having very fine pores available on their surface. Moisture is trapped in between these pores, and hence, air can be dehumidified without reducing its temperature below dew point temperature. This process is known as adsorption. Moisture can be removed from the desiccant material by exposing it to heat energy; the process is called desorption. After desorption, the desiccant material can be regenerated for further dehumidification. The desiccant is a very important substance in the dehumidification system, as it has to undergo adsorption and desorption continuously during its lifespan. Good desiccant material should possess a high MRR so that size of the system can be reduced. Good desiccant material should also have less regeneration temperature so that energy potential can be minimized. Apart from this, a desiccant material should be easily available in the market at a low cost to increase its adaptability among the industries (Zheng et al. 2014).

Desiccant materials may be solid or liquid, but liquid desiccants are less popular as they are difficult to handle, mostly in the rotary wheel-based dehumidifiers. Desiccants may be physical substances or hygroscopic salt. Physical desiccants are popular as they are easy to handle. Many researchers have studied a variety of physical desiccant materials such as silica gel (Mitra et al. 2015; Lu et al. 2011 Pan and Wang 2018; Lu et al. 2011), activated carbon (Attalla and Sadek 2014; Baiju and Muraleedharan 2014; Banker et al. 2009; El-Sharkawy et al. 2006; Qasem and El-Shaarawi 2015), zeolite (Demir et al. 2008; Zhong 2012), hygroscopic salts (Zhang and Qiu 2007; Nakabayashi et al. 2011; Tso and Chao 2012). Silica gel is one of the very popular desiccant materials as it has less regeneration temperature, good availability, and low cost. However, researchers (Zheng et al. 2014) have identified that physical desiccants have many limitations such as low surface area and volume. This is the main reason behind an increase in the absorption and desorption time. On the other hand, hygroscopic salts are also studied by many researchers and proven to be a good desiccant material as it possesses less adsorption and desorption time (Zheng et al. 2014). Weak structural stability, swelling, and agglomeration are major demerits of the hygroscopic salts, and hence, we cannot rely on hygroscopic salts alone. The idea of mixing physical desiccants with hygroscopic salts becomes popular among researchers as it has shown tremendous improvements against the demerits of both. The authors of the current research have decided to incorporate a mixed form of desiccant which is prepared using a mixing of silica gel and calcium chloride in different proportions. Five different samples were prepared by a simple mixing method and analyzed for their moisture removal rate against the operating conditions of the air in the laboratory. The mixing proportion is pre-decided and varied in all samples to

identify the most suitable proportion of mixing. Results were obtained based on a simple gravimetric analysis technique carried out in the laboratory which is having hot and humid conditions in the nearby vicinity. One sample is prepared of silica gel alone and analyzed in the same manner as that of other samples to compare results.

2   Experimental Facility

Desiccant material is prepared by adding calcium chloride to the silica gel. The experimental facility based on the gravimetric method is thoroughly described in this section. Silica gel is available in the Indian market in a variety of forms. Granules of silica gel (as shown in Fig. 1) are very common and can be easily purchased from the local Indian market.

Crystals of calcium chloride are also purchased from the local Indian market and crushed in the form of small particles as shown in Fig. 2.

Crucible with closable lid (as shown in Fig. 3) is used for keeping the desiccant material in it, and it is good for the heating purpose of the desiccant material. The lid can be easily kept on a crucible and removed from it as per the requirement. A spatula (as shown in Fig. 4) is used for mixing two different types of materials. Skin contact with the desiccant can be avoided by using spatula. An electronic weighing machine is used for measuring the weight of the material. As soon as the desiccant

Fig. 1 Granules of silica gel

Fig. 2 Crushed crystals of calcium chloride

Fig. 3 Crucible with
closable lid

Fig. 4 Spatula

Fig. 5 Muffle furnace

material is prepared, it is kept in the furnace (as shown in Fig. 5) for regeneration. It
is ensured that the moisture, which was present initially in the desiccant, is removed
before experimental analysis.

3 Experimental Methodology

Total six samples of the desiccant were considered for the analysis out of which
CM1–CM5 are prepared by mixing silica gel and calcium chlorides and CM0 is the
sample that contains only silica gel. The method to prepare these samples has been
discussed in Sect. 3.1. Details composition of chemical and physical desiccants was
mentioned below in Table 1 and Fig. 6. The objective is to find out the best possible
composition of mixing which has qualities to be called as a good desiccant.

Table 1 Composition of different desiccant samples

Sample	Total weight (gram)	Weight of silica in the sample (gram)	Weight of calcium chloride in the sample (gram)
CM0	25	25 (100%)	0 (0%)
CM1	25	20 (80%)	5 (20%)
CM2	25	17.5 (70%)	7.5 (30%)
CM3	25	15 (60%)	10 (40%)
CM4	25	10 (40%)	15 (60%)
CM5	25	5 (20%)	80%
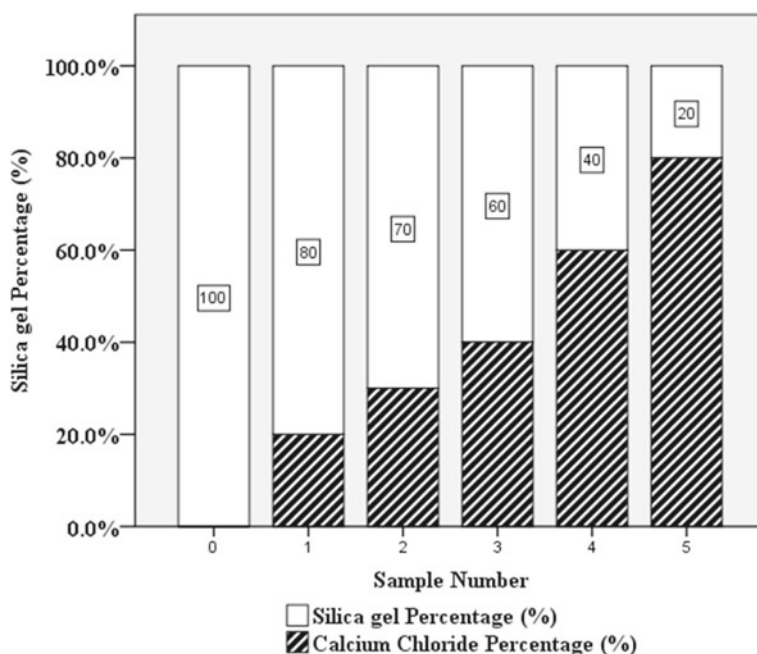
Fig. 6 Configurations of the samples

3.1 Procedure for Making Samples of Desiccant by Mixing Silica Gel and Calcium Chloride

- Put on the hand gloves to avoid physical contact.
- Start EWM and set it at zero after placing the crucible and lid on it.
- Make the samples in the crucible with the composition mentioned in the table.
- To make the samples (Figs. 7, 8, 9, 10 and 11), silica gel granules and calcium chloride crushed crystals are well-mixed in the crucible with the help of a spatula to avoid any physical contact with the desiccant material.

Fig. 7 Sample CM1
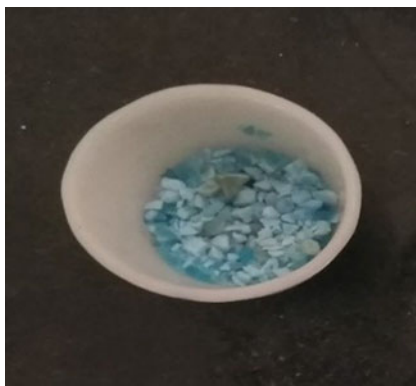
Fig. 8 Sample CM2

Fig. 9 Sample CM3

- Put this sample in the air for 5 min. Make sure that lid of the crucible is open. Meanwhile, prepare the furnace.
- Achieve the temperature of 85–90 °C in the furnace, and keep the crucible with an open lid in the furnace for 5 min.

Fig. 10 Sample CM4

Fig. 11 Sample CM5

- After 5 minutes, carefully take the sample out of the furnace with the tongs. Cover the crucible with the lid to isolate the desiccant from fresh air.
- Measure the weight of the sample on the EWM.
- Note the readings in the observation table.

4   Results and Discussions

Six performance indicators are calculated using the experimentation and formulation mentioned in Table 2. Performance indicators were used to compare the results later.

A good desiccant should have more weight after the adsorption. More the weight of desiccant after the adsorption process shows that the desiccant captures more moisture. Weight after reactivation should be as minimum as possible. More weight after reactivation shows that some quantity of moisture still adheres to the surface of the desiccant. If the difference between the weight of desiccant after adsorption and reactivation is high, then the desiccant is well-accepted in the system. MRR should be high for a good desiccant. MRR can be increased by maximizing the moisture uptake capacity of the desiccant and minimizing the time required for adsorption.

Table 2 Performance indicators and formulation

Sr. no.	Name of the performance indicator	Method of determination	Formulation	Units
	Weight after adsorbing moisture	Experimentation/measured using EWM	–	Gram
	Weight after reactivation of desiccant	Experimentation/measured using EWM	–	Gram
	Weight of moisture removed	Calculated	Weight after reactivation of desiccant—initial weight	Gram
	Weight of the moisture unadsorbed	Calculated	Weight after adsorbing moisture—weight after reactivation of desiccant	Gram
	Material removal rate (MRR)	Calculated	$\frac{\text{Weight of moisture removed}}{\text{Time for adsorption}}$	Gram/s
	% increase in MRR of samples	Calculated	$\left[\frac{\text{MRR of CM}-\text{MRR of Sillica gel}}{\text{MRR of Silica gel}}\right]$	%

4.1 Results

Results were obtained after the experimentation and mentioned in Table 3. Each cycle consists of two processes, adsorption and desorption of desiccant material. Here, cycle time is considered 10 min out of which each process takes 5 min.

Table 3 Table of results (regeneration temperature is kept in the range 85–90 °C)

Sample	Initial weight (g)	Weight after adsorbing moisture (g)	Weight after reactivation of desiccant (g)	Weight of moisture removed = weight after adsorbing moisture (gram) – weight after reactivation of desiccant (g)
CM0	25	31.6	28.9	2.7
CM1	25	31.9	28.7	3.2
CM2	25	32.4	28.3	4.1
CM3	25	33	27.8	5.2
CM4	25	32.1	28.6	3.5
CM5	25	31.6	28.3	3.3

The initial weight of all five samples was kept constant, i.e., 25 g. The weight of the samples was measured after adsorption and reactivation. Performance indicators of desiccant material can be easily calculated by formulation as mentioned in the table, and final values were reflected in the table of results. Discussions based on these results were discussed further in the section below.

4.2 Discussion

Five samples were compared with Sample CM0, and it has been identified that Sample CM3 has the highest quantity of moisture removed. Sample CM3 was prepared by mixing 60% of silica gel granules and 40% of calcium chloride by weight. As shown in Fig. 12, CM3 combination is the best possible as per the moisture removal is concerned compared to other samples because of the following reasons.

1. Thermal stability of the desiccant at 85–90 °C
2. Good structural binding of the silica granules and calcium chloride salt.

Sample CM3 is more thermally stable at a temperature of 85–90 °C because the host material, i.e., silica gel does not get disintegrated. It provides higher strength to the whole structure. On the other side, the MRR for all the five samples of desiccants has been increased than Sample CM0 because of the presence of calcium chloride, which improves the absorption rate. The thermal stability of the Samples CM1 and CM2 is also good, but the moisture removal rate is not much improved because less quantity of calcium chloride is present in those samples. Samples CM4 and CM5 have less MRR because of the higher concentration of calcium chloride. A higher concentration of calcium chloride is responsible for the hygroscopic nature of the whole sample. The sample becomes thermally unstable and difficult to handle. At higher temperatures, the hygroscopic nature of calcium chloride increases and, hence, MRR decreases. From Fig. 13, we can observe the difference in the weight of the samples after adsorption and reactivation. The difference is more for Sample CM3.

Fig. 12 Analysis of moisture removed from the different samples
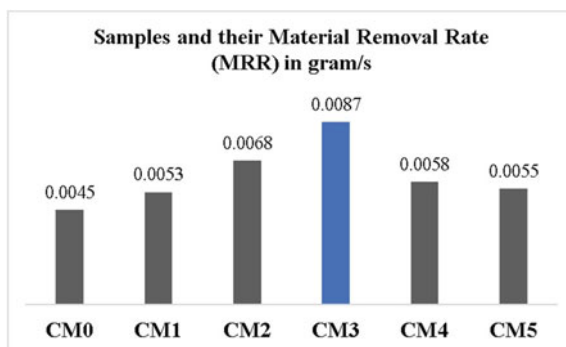
Fig. 13 Initial and final
weights of desiccant
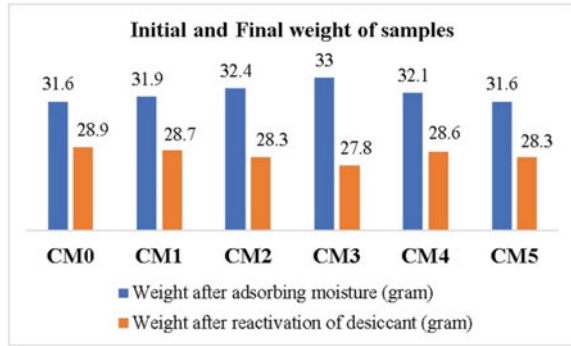
MRR is the most promising performance indicator to compare all the samples, and based on MRR, the trend is plotted as shown in Fig. 14, against the % of calcium chloride in the desiccant material. It has been observed from the bell-shape trend that MRR is maximum for 40% of calcium chloride. As the concentration of calcium chloride is increasing, further, the MRR is decreasing, and it has been confirmed from the experimental results too. This nature of desiccant material gives us the idea of selecting the concentration of calcium chloride and silica gel in the preparation of desiccant. With the concentration of CM3, MRR obtained is 0.0086 g/s, which is almost 92% higher than the MRR obtained with silica alone.

Moisture unadsorbed is the quantity of water vapor trapped into the pores of the composite materials. This performance parameter should be as minimum as possible. The higher the quantity of unadsorbed moisture, the lower is the performance and vice versa. As shown in Fig. 15, moisture unadsorbed is minimum for Sample CM3 that makes it the most suitable mixing composition for desiccant. Sample CM0 has the highest unadsorbed moisture confined into the pores of silica gel granules. The performance of silica gel alone is decreasing, and many researchers tried to reduce

Fig. 14 Trend of material
removal rate (MRR) against
the percentage of calcium
chloride in the mixture of
silica gel and calcium
chloride composite
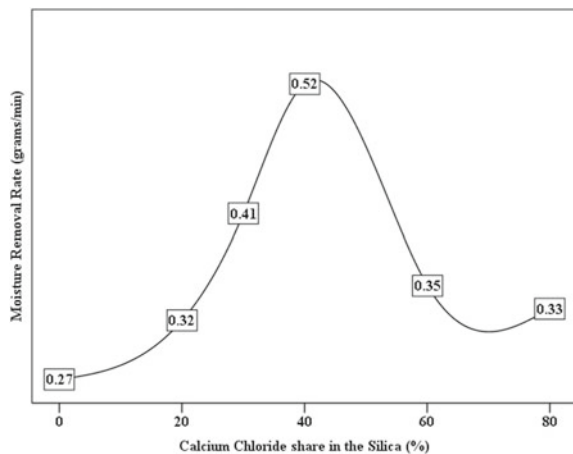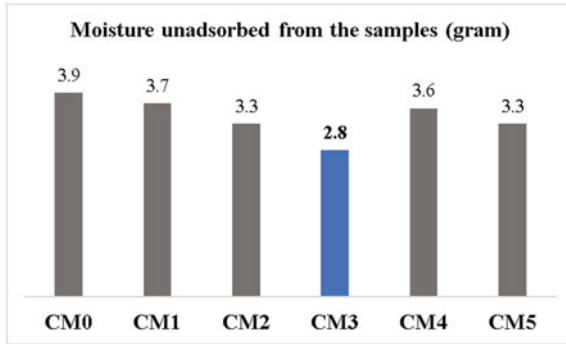
Fig. 15 Moisture unadsorbed from the samples

the amount of unadsorbed moisture from the silica gel by adopting different methods like an increase in heat and mass transfer rates, changing the size, and shape of the silica gel granules.

Briefly, all the samples were arranged in their increasing order of MRR as shown in Fig. 16, and Samples CM2 and CM3 have shown improvement in the MRR by more than 50% compared to the stand-alone silica gel sample. The adsorption and desorption pattern of desiccant material is plotted in Fig. 17. According to the authors, the findings of this research are well-discussed and justified in this section.
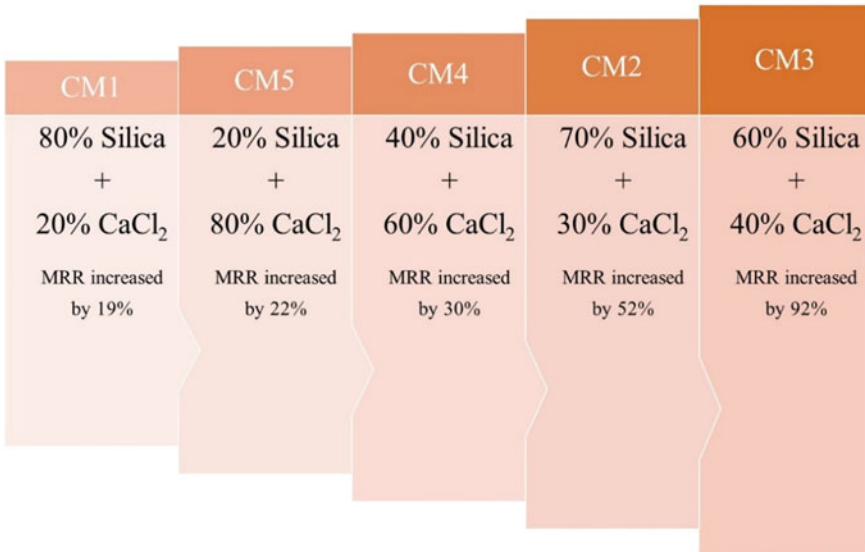
Fig. 16 Samples, composition, and % increase in MRR
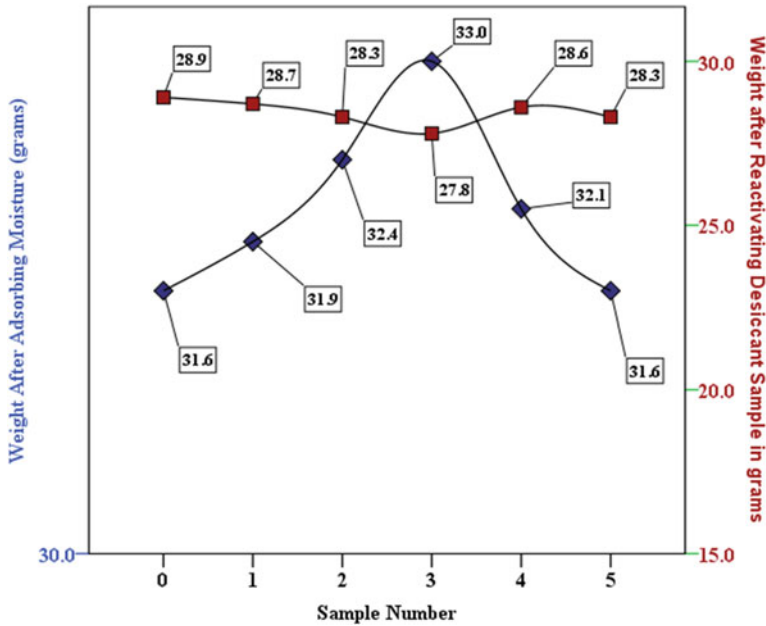
Fig. 17 Adsorption and desorption pattern of desiccant samples

5 Conclusion

In the present work, an attempt has been made by authors to prepare different samples of desiccant material by mixing silica gel and calcium chloride. Different proportions of both the constituents were prepared and tested in an experimental facility for adsorption and desorption of moisture from the air. Five samples of the desiccant material were compared with the stand-alone silica gel desiccant to calculate the increase in MRR.

From the experimentation results, it is clear that the Sample CM3 has the highest MRR than the other samples. The proportion of the Sample CM3, i.e., 60% of silica gel granules and 40% of calcium chloride by weight is proved to be the best proportion of silica gel and calcium chloride in the desiccant material. About 92% hike in the MRR is reported against the stand-alone silica gel desiccant. After Sample CM3, around a 50% increase in the MRR is observed in Sample CM2 which has 70% silica gel and 30% calcium chloride by weight. According to the authors, Samples CM3 and CM2 will be a good choice of desiccant for desiccant-based dehumidification systems situated in a hot and humid environments. The size of the system can be reduced for the same quantity of desiccant material, which is filled with silica gel alone. The reduced size of the system may reduce the high-grade energy consumption in the system and the overall cost of the system as well.

References

Attalla M, Sadek S (2014) Experimental investigation of granular activated carbon/R-134a pair for adsorption cooling system applications (2014):11–20

Baiju V, Muraleedharan C (2014) Experimental analysis on adsorption characteristics of methanol and R134a by activated carbon in adsorption refrigeration system. J Therm Sci Eng Appl 7:1–8. https://doi.org/10.1115/1.4028548.

Banker ND, Prasad M, Dutta P, Srinivasan K (2009) Activated carbon + HFC 134a based two stage thermal compression adsorption refrigeration using low grade thermal energy sources. Appl Therm Eng 29:2257–2264. https://doi.org/10.1016/j.applthermaleng.2008.11.006

Behede BC, Chakrabarti SS, Wankhede US (2019) Review of desiccant based dehumidification system, experimental analysis of desiccant wheel filled with silica-gel granules. In: International conference on advanced mechanical and electrical engineering, Nagpur, pp 1–12

Demir H, Mobedi M, Ülkü S (2008) A review on adsorption heat pump: problems and solutions. Renew Sustain Energy Rev 12:2381–2403. https://doi.org/10.1016/j.rser.2007.06.005

El-Sharkawy II, Kuwahara K, Saha BB, Koyama S, Ng KC (2006) Experimental investigation of activated carbon fibers/ethanol pairs for adsorption cooling system application. Appl Therm Eng 26:859–865. https://doi.org/10.1016/j.applthermaleng.2005.10.010

Lu ZS, Wang RZ, Xia ZZ, Wu QB, Sun YM, Chen ZY (2011) An analysis of the performance of a novel solar silica gel-water adsorption air conditioning. Appl Therm Eng 31:3636–3642. https://doi.org/10.1016/j.applthermaleng.2010.11.024

Lu ZS, Wang RZ, Xia ZZ, Wu QB, Sun YM, Chen ZY (2011) An analysis of the performance of a novel solar silica gel-water adsorption air conditioning. Appl Therm Eng 31:3636–3642. https://doi.org/10.1016/j.applthermaleng.2010.11.024

Mitra S, Kumar P, Srinivasan K, Dutta P (2015) Performance evaluation of a two-stage silica gel + water adsorption based cooling-cum-desalination system. Int J Refrig 58:186–197. https://doi.org/10.1016/j.ijrefrig.2015.06.018

Nakabayashi S, Nagano K, Nakamura M, Togawa J, Kurokawa A (2011) Improvement of water vapor adsorption ability of natural mesoporous material by impregnating with chloride salts for development of a new desiccant filter. Adsorption 17:675–686. https://doi.org/10.1007/s10450-011-9363-1

Pan QW, Wang RZ (2018) Study on operation strategy of a silica gel-water adsorption chiller in solar cooling application. Sol Energy 172:24–31. https://doi.org/10.1016/j.solener.2018.03.062

Qasem NAA, El-Shaarawi MAI (2015) Thermal analysis and modeling study of an activated carbon solar adsorption icemaker: Dhahran case study. Energy Convers Manag 100:310–323. https://doi.org/10.1016/j.enconman.2015.04.054

Tso CY, Chao CYH (2012) Activated carbon, silica-gel and calcium chloride composite adsorbents for energy efficient solar adsorption cooling and dehumidification systems. Int J Refrig 35:1626–1638. https://doi.org/10.1016/j.ijrefrig.2012.05.007

Zhang XJ, Qiu LM (2007) Moisture transport and adsorption on silica gel-calcium chloride composite adsorbents. Energy Convers Manag 48:320–326. https://doi.org/10.1016/j.enconman.2006.04.001

Zheng X, Ge TS, Wang RZ (2014) Recent progress on desiccant materials for solid desiccant cooling systems. Energy 74:280–294. https://doi.org/10.1016/j.energy.2014.07.027

Zhong Y (2012) Size reduction of an engine waste-heat driven air-conditioner for passenger cars and light-duty trucks. Energy Procedia. 14:351–357. https://doi.org/10.1016/j.egypro.2011.12.941

Flow and Thermal Characteristics of Jet Impingement on a Dimple Plate Using Large Eddy Simulation

Ashutosh Narayan Singh and Dushyant Singh

Abstract A round turbulent air jet is impinging on heated plate and is numerically analyzed by large eddy simulation (LES) at the plate to nozzle spacing, $h/D_j = 2$ (where D_j is jet diameter), Reynolds number (Re_j) = 5000, and diameter ratio (D/D_j) = 0.318 (where D is dimple print diameter), and relative depth ($\delta/D_j = 0.3$) (where δ is dimple depth) for concave and convex dimples and is used in the present study, LES, consider sub-grid scale (SGS) model, i.e., Wall Adaptive Local Eddy viscosity (WALE). Averaging in space and time is performed to give information of mean velocity in stagnation and wall jet regions. Various important dynamical stream structures have been visualized from the instantaneous data obtained from LES. The local Nusselt number, mean velocity, and coefficient of pressure are calculated for both configration of dimples. Various flow phenomena such as flow separation and reattachment are represented and their effect on heat transfer phenomenon are explained. Vorticity contours were in good resemblance with experimental results (Terekhov et al., Impingement of an impact jet onto a spherical cavity. Flow structure and heat transfer. Int J Heat Mass Transfer 52:2498–2506, 2009; Kanokjaruvijit and Martinez-botas, Int J Heat Mass Transfer 48:161–170, 2005). Results obtained from WALE sub-grid scale model are in good accordance with experimental results.

Keywords Large eddy simulation (LES) · WALE sub-grid model · Concave · Convex dimple

1 Introduction

Impinging jet has wide industrial applications because of its high rates of convective heat transfer in the target area. The use of impinging jet in industries includes the cooling of gas turbine blades, combustion chamber, dicing on aircraft, tempering of metal and glass, the printing of circuit boards, cooling of microelectronic components, and drying of papers and textiles. There have been attempts to increase the heat

A. N. Singh (✉) · D. Singh
Mechanical Engineering, National Institute of Technology Manipur, Imphal, India

transfer of the precarious components located in the heated sections, such as temperatures reaches 2000 °C, for example, in the internal region of blades and the wall of the combustor. For local heat transfer enhancement, jet impingement is among the most potent methods of heat transfer developed by forming different scales of vortex pairs. Jet impingement cooling with slot nozzle has very exhaustive research during the past year both experimentally and numerically.

Extensive amount of experimental and numerical study focuses on smooth target flat surface of impinging jet. However, few researchers have worked on target convex and concave surfaces. Gau and Chung (1991) experimentally examine slot jet impinging on the concave and convex surfaces, and an observed bunch of counter-rotating vortices was produced near the wall on the stagnation point in convex surface, which amplifies the momentum transit in the flow and enhances the heat transfer process on the impinging wall. The increase of surface curvature can increase the size of the counter-rotating vortices, and in this case study of the concave surface, absence of three-dimensional vortices in the stagnation point were observed. The heat exchanger surface geometry modification is supposed to be an implicit means to control heat transfer and cooling of surfaces; hence, concave and convex dimpled on flat plate altered the flow phenomena and in turn cause augmentation in heat transfer characteristic. A complex unstable flow structure can evolve as a result of vortex formation processes in local flow detachment zones around barriers in the form of cavities/trenches, exhibiting large-scale low-frequency flow pulsations (Dyban et al. 1971), and in such a situation, prediction of heat transfer characteristic is a bit difficult. Effect of Reynolds number significantly affects the pressure distribution and shear stress variation. Kawale and chndermohan (Kawale and Chandermohan 2017) studied the effect of Reynolds number on static pressure and shear stress for cleaning flat soiled surface.

Terekhov et al. (2009) conducted the experimental study with the round jet flowing around the obstacle in the form of single spherical cavity for $Re = (1.2$–$5.8 \times 10^4)$, $D_c/d_j = 5.2$, $H/d_j = 0$–10, $D/D_c = 0$–0.5. At $D/D_c < 0.13$, flow over dimples is comparative similar to a flat plate's flow. In case $D/D_c > 0.26$, formation of large-scale pulsing toroidal vortex in cavity is observed. This vortex results in the formation of a returnable flow of the gas heated up in a cavity and produces hindrance in the heat exchange phenomenon. Kanokjaruvijit and Martinez-Botas (2005), the effect of the crossflow scheme on heat transfer was investigated, and they found that impingement onto dimples is good with the maximum crossflow scheme and larger jet to plate spacing due to the coupled effect of impingement and channel flow.

Xie et al. (2013) experimentally and numerically studied the fluid flow and heat transfer characteristics of a round jet impinging on the single concave dimple on a flat plate for different Reynolds numbers 5000–23,000. The distance between jet nozzle and the plate was fixed and equal to $H/D = 2$ with jet to dimple diameter $Dj/D = 0.318, 0.5, 1.045$ and non-dimensional depth of dimple of $\delta/D = 0.1, 0.2, 0.3$ with the help of combined particle image velocimetry (PIV). Correlative expressions of the local Nusselt number, the Nusselt number at stagnation points, and the average Nusselt number were shown. It can be observed that the depth of dimple significantly

affects pressure distribution and local Nusselt number. At $\delta/D = 0.1$, results obtained are similar to that of flat plate, and as depth increases, local Nusselt number reduces, but the average Nusselt number is more than that of a flat plate. However, in the case of convex dimple, the local Nusselt number is higher in the comparison with a smooth surface on the whole, and the local Nusselt number increases with the protrusion relative depth (Zhang et al. 2013). Azad et al. (2000) conducted studies on variation of heat transfer by impinging jet with array of cylindrical dimpled surface experimentally ($Re_j = 4850$–18,300 and $d/D = 0.5$). The experimental results suggest that the local Nusselt number for the dimpled target surface and the corresponding smooth target surface is about the same. When compared to a smooth surface, the dimpled surface enables better heat to transfer due to the larger surface area.

Van Hout et al. (2018) performed PIV investigation on dimple geometries with spherical, cubic, conical, and triangular-shaped dimples. Majorly, the study investigates the development of secondary vortices and their interaction with the primary vortices that originated in the free jet, as well as the outer shear layer similarities in the wall jet. Experiments were performed at a nozzle to target distance of about 5D for three Reynolds numbers, $Re = 1473$, 6322, and 12,438. It can be observed that none of the dimpled surfaces immensely altered the generation of the secondary vortices by the primary vortices and their successive interaction. Ligrani et al. (2001) observes an flow structure due to dimple depressions on a channel surface with help of smoke wires to visualize the flow and investigated a primary vortex pair which are periodically and continuously sheding from the central portion of each dimple. It was observed that as the distance between nozzle and target surface decreases, the strength of the primary vortex pair is amplified and gives rise to two additional secondary vortex pairs.

Numerical simulations were mostly carried by RANS modeling which foresees the dispersion of mean stream and temperature around dimple due to impinging jet, making it difficult to capture flow structure and eddies and its dissipation around dimple. The capturing of coherent structures can be settled utilizing either direct numerical simulations (DNS) or large eddy simulations (LES). A direct numerical simulations (DNS) gives a lot of data about the tempestuous idea of the flow, and the DNS model additionally turns out to be a significant expensive methodology for higher Reynolds number and complex geometry. As to the best of the authors' knowledge, no study is available in the literature in concern with using LES for simulating jet impingement cooling on dimple plate. Mostly, studies on large eddy simulation for jet impingement are done on flat plate. Shukla and Dewan (2019) performed sub-grid scale LES on a flat plate with a low nozzle to plate spacing and Reynolds number of 20,000 and captured the occurrence of the secondary peak in Nusselt number. They found that LES model predicts well the Nusselt number and overcomes the problems faced by RANS model for over-predicting the Nusselt number especially at the stagnation point.

As previously stated, literature evaluations show that when applied to jet impingement heat transfer, LES is accurate. Furthermore, just a few researches on LES of slot jet impingement heat transfer on a flat plate have been documented, and to the
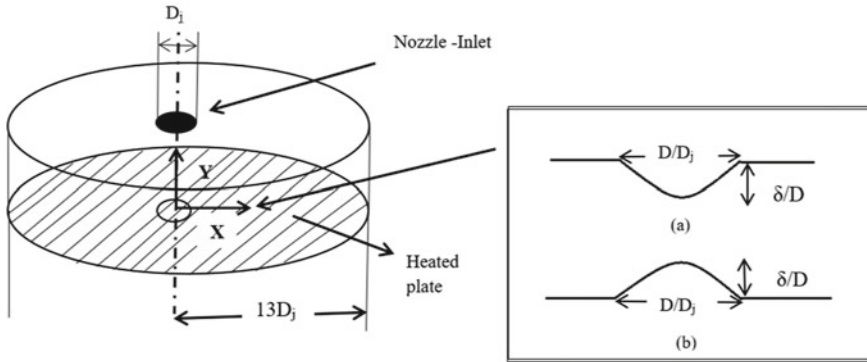
Fig. 1 Pictorial representation of computational domain. **a** Concave. **b** Convex

best of the authors' knowledge, no study on jet impingement on a dimpled plate with LES has been undertaken. WALE, LES, sub-grid model was used in present investigation.

2 Problem Statement

The three-dimensional cylindrical computing domain is depicted in Fig. 1. The inflow at the nozzle inlet is obtained from non-uniform fields derived from RANS simulation of the nozzle channel,which is mapped on the inlet of domain, where nozzle velocity (V) was specified at the inlet based on the value of Reynolds number, $Re_j = V(D_j)/\nu$ (where D_j denotes jet diameter and ν is the kinematic viscosity).

A turbulent intensity of 4% is taken as taken in the experiment of Xie et al. (2009). At the outlet, the outflow conditions were applied. And, outlet was kept at a sufficiently large distance from the nozzle center line ($X/D_j = 13$) to avoid backflow. Reynolds number (Re_j) 5000, nozzle to plate spacing of $h/D_j = 2$, diameter ratio $(D/D_j) = 0.318$, and relative depth ($\delta/D_j = 0.3$), for both concave and convex dimples, are utilized in present study.

3 Governing Equation

The large eddy simulation (LES) method is premised on the theory that larger length scales are sensitive to initial and boundary conditions, whereas smaller length scales are isotropic. The large-scale eddies are resolved, whereas smaller scale eddies are modeled. As a result, unlike DNS, LES requires a coarser grid. A filtering process is being used to distinguish the larger scale from the smaller scale depending on the

given reference scale. It filters out eddies with length scales that are smaller than the filtering grid spacing or width employed in the computations.

Filtering can be thought of as the convolution of a function with a filtering kernel G.

$$\overline{u_i}(\vec{x}) = \int G(\vec{x} - \vec{\xi})u(\vec{\xi})d\vec{\xi} \tag{1}$$

resulting in

$$u_i = \overline{u_i} + u_i' \tag{2}$$

where $\overline{u_i}$ is the resolvable scale part and u_j' is the sub-grid scale part; then, filtering the resulting equation gives the equations of motion for the resolved field:

$$\frac{\partial \overline{u_i}}{\partial t} + \overline{u_j}\frac{\partial \overline{u_i}}{\partial x_j} = -\frac{1}{\rho}\frac{\partial \overline{p}}{\partial x_i} + \frac{\partial}{\partial x_j}\left(v\frac{\partial \overline{u_i}}{\partial x_j}\right) + \frac{1}{\rho}\frac{\partial T_{ij}}{\partial x_j} \tag{3}$$

$$\frac{\partial u_i}{\partial t} + u\frac{\partial u_i}{\partial x_j} = -\frac{1}{\rho}\frac{\partial p}{\partial x_i} + \frac{\partial}{\partial x_j}\left(v\frac{\partial u_i}{\partial x_j}\right) \tag{4}$$

The extra term $\frac{\partial T_{ij}}{\partial x_j}$ arises from the nonlinear advection terms, because of fact that

$$\overline{u_j\frac{\partial u_i}{\partial x_j}} \neq \overline{u_j}\frac{\partial \overline{u_i}}{\partial x_j} \tag{5}$$

$$T_{ij} = \overline{u_i u_j} - \overline{u_i}\,\overline{u_j} \tag{6}$$

the Boussinesq hypothesis, and seeks to calculate (the deviatoric part of) the SGS stress using:

$$T_{ij} - \frac{1}{3}T_{kk}\delta_{ij} = -2\mu_t\overline{S_{ij}} \tag{7}$$

where $\overline{s_{ij}}$ is the rate of strain tensor for the resolved scale defined by

$$\overline{s_{ij}} = \frac{1}{2}\left(\frac{\partial \overline{u_i}}{\partial x_j} + \frac{\partial \overline{u_j}}{\partial x_i}\right) \tag{8}$$

and v_t is the sub-grid scale turbulent viscosity. Replacing into the filtered Naiver-Stokes equations, we then have

$$\frac{\partial \overline{u_i}}{\partial t} + \overline{u_j}\frac{\partial \overline{u_i}}{\partial x_j} = -\frac{1}{\rho}\frac{\partial \overline{p}}{\partial x_i} + \frac{\partial}{\partial x_j}[v + v_t]\frac{\partial \overline{u_i}}{\partial x_j} \tag{9}$$

$$T_{ij} - {}^1\!/\!_3 T_{kk}\delta_{ij} = -2(C_s\Delta)^2\big|\overline{S}\big|\,S_{ij} \tag{10}$$

The eddy viscosity is modeled as

$$\mu_{sgs} = \rho(c_s\Delta)^2\big|\overline{S}\big| \tag{11}$$

where the box width is usually taken to be

$$\Delta = (\text{Volume})^{\frac{1}{3}} \quad \text{and} \quad \overline{S} = \sqrt{2S_{ij}S_{ij}}$$

3.1 Wall Adaptive Local Eddy Viscosity (WALE)

The Wall Adaptive Local Eddy viscosity (WALE) model is an algebraic eddy viscosity model similar to the Smogorinski SGS model, but it has some peculiar features not present in the Smogorinski model, such as taking the rotation rate into account while calculating VSGS. Transitions can be controlled by the WALE model (Nicoud and Ducros 1999). WALE model also returns a zero turbulent viscosity for laminar shear flow, allowing for the proper treatment of laminar zones in domain; i.e., damping is not required for VSGS near the wall

$$\mu_t = \rho\Delta_s^2\frac{(S_{ij}^d S_{ij}^d)^{3/2}}{(S_{ij}S_{ij})^{5/2} + (S_{ij}^d S_{ij}^d)^{5/4}} \tag{12}$$

where

$$\Delta_s = C_w V^{1/3}$$

$$S_{ij}^d = 1/2(\overline{g}_{ij}^2 + \overline{g}_{ji}^2) - 1/3\delta_{ij}\overline{g}_{kk}^2 \tag{13}$$

$$\overline{g}_{ij} = \frac{\partial \overline{u_i}}{\partial x_j}$$

$$\overline{g}_{ij}^2 = \overline{g_{ik}g_{kj}}$$

where $\overline{S_{ij}}$ is the rate of strain tensor for the resolved scale defined by where the constant $C_w = 0.325$.

4 Numerical Strategy

The numerical investigation was conducted using OpenFOAM, an open-source finite volume technique (FVM)-based CFD software. By maintaining density constant, bouyantPimpleFoam, an FVM-based transient solver, was used. The pressure–velocity coupling is controlled by the PIMPLE algorithm, with a collocated grid arrangement. Backward scheme and adjustable time step were used to discretize the temporal derivative. The courant number is kept less than unity to maintain precision. The Gauss linear scheme is used to discretize the gradient and divergence, whereas the Gauss linear corrected method is used to discretize the Laplacian term. For pressure, preconditioned conjugate gradient (PGC) solver is utilized, and for velocity and other properties, smoothSolver is used. Averaging is performed after a steady state is reached. Table 1 shows the thermal fluid properties of air used in the present study. The compressibility effect and temperature dependence on air were disregarded in the present study.

4.1 Boundary Conditions

Nozzle inlet: The inlet is mapped with a fixed velocity inlet condition of non-uniform fields produced from a RANS simulation of the nozzle channel.

TOP: Pressure inlet boundary condition is maintained at the top.

Flat plate (consisting dimple): No-slip boundary condition with a constant heat flux is assumed at the flat plate. And for pressure, Von Neumann bc with value atmospheric is used,and sub-grid scale kinetic energy is zero.

Outlet: The pressure inlet–outlet conditions were applied at the outlet.

4.2 Grid Resolution

Detail of grid size for flat, concave, and convex dimple domains is depicted in Table 2. Near the wall region, $y^+ \sim 1$ at the first grid points and minimum values

Table 1 Properties of air

Property	Value
Density (ρ)	1.225 (kg/m^3)
Kinematic viscosity (ν)	1.5×10^{-5} (m^2/s)
Thermal conductivity(k)	0.025 (W/m–K)
Prandtl number	0.75
Air inlet temperature	300 k

Table 2 Detail description of grid and grid independence study

LES study			No. of nodes in X-direction	No. of nodes in Y-direction	No. of nodes in Z-direction	Total no. of cell	Nu_{st}	y^+
Shape	Re_j	Grid						
Flat	5000	G-1	120	100	120	1.44×10^6	64	1
Concave		G-1	180	120	180	3.88×10^6	52.2	
		G-2	220	140	220	6.77×10^6	54.8	
Convex		G-1	180	120	180	3.88×10^6	78.5	
		G-2	220	140	220	6.77×10	80.2	

of wall distance $\Delta x^+ = 35$ and $\Delta z^+ = 55$ were maintained. A non-uniform mesh was used in the present study, and O-grids were used in order to capture curved surfaces of dimple which can be seen in Fig. 2, and at important locations where flow mechanics were predicted to be complex, the mesh was finer, such as near the wall region, stagnation region, and wall jet regions. The quality of LES mesh was examined with the help of function IQ_v which depends on sub-grid scale viscosity and dynamic viscosity, and its value should lie between 0.8 and 0.99. As shown in Fig. 3, it can be observed that value of IQ_v is within appropriate range. Grid independence study recommends utilization of higher number of grids; i.e., G-2 is used for further studies.
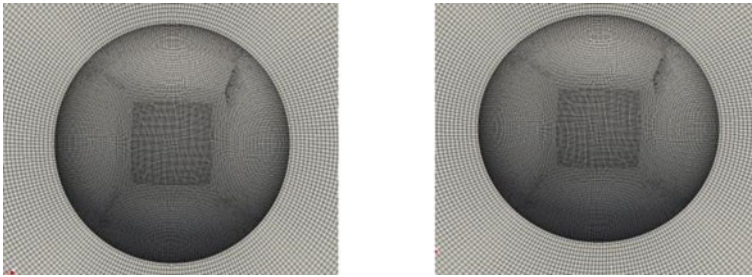
Fig. 2 Representation of computational grid concave (left) and convex (right)
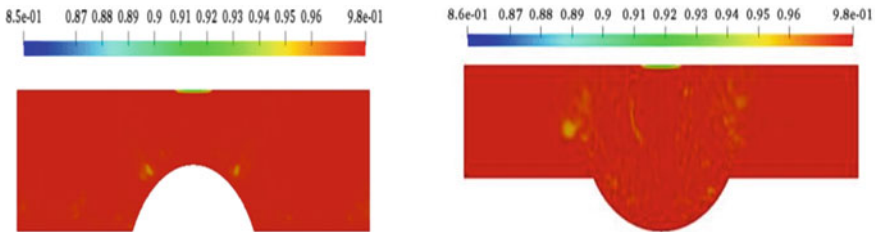
Fig. 3 IQ_v representation of grid concave (left) and convex (right)

5 Results and Discussion

5.1 Numerical Model Validation

Validation study of WALE, LES, sub-grid models for thermal and fluid flow by experimental data (Ashforth-Frost et al. 1997) is performed at $Re_j = 20,000$, $h/D_j = 4$ as shown in Figs. 4 and 5. Figure 6a depicts WALE, LES, sub-grid models performed better in capturing Nusselt number variation when compared with experimental result (Ashforth-Frost et al. 1997). It is observed in Fig. 6a that WALE sub-grid model shows the lowest percentage deviation in stagnation point Nusselt number of about 2% with the experimental results (Shukla and Dewan 2019). Similar trends can be observed in fluid flow characteristics depicted with help of mean velocity variation in Fig. 6b. Figure 6b shows that mean velocity is captured better by WALE, LES, sub-grid models with experimental results of mean velocity at (span-wise) $X/D_j = 1$. However, ability of WALE, LES, sub-grid model is to predict laminar to turbulent transition, flow separation, and near-wall phenomenon. The above validations and advantages lead to the study of dimple in present study with the help of WALE, LES, sub-grid model.

5.2 Flow Field Predictions

Figure 5 represents instantaneous velocity vector at $Re_j = 5,000$ for both convex and concave dimple target surfaces. As the jet enters the quiescent domain, the shear region is formed due to the interaction of jet and quiescent domain which can be seen in Figs. 5a and b. After the jet strike, the curved surface deflection of the jet is depicted with the aid of vector contours. In Fig. 5a rotation of vectors just above the concave surface, a large toroidal vortex is present which mainly affects the mainstream jet and altered many flow and thermal characteristics. As the jet exits the concave surface downstream, i.e., X > 0.23, flow separation can be depicted with reversed velocity vectors. Similarly, in Fig. 5b, on the convex surface at X = 0.014, the region of flow separation can be seen which is due to adverse pressure gradient, and this phenomena affect the thermal phenomenon at that region. At the edge of the concave surface, i.e., at X = 0.023, a recirculation region is formed, which creates a low-pressure region.

Figure 6 represents the variation of coefficient of pressure C_p for various concave, convex, and flat surfaces along with the radial positions (X/D), where $C_P = {2(P_i - P_0)}/{\rho_o U_0^2}$ (U_o and ρ_o are velocity and density at the jet inlet). Parabolic distribution of C_p is observed for all three surfaces, that is, per the observation of Xie et al. (Xíe et al. 2013). As a single jet impinges on a concave surface, flow undergoes acceleration in the radial direction according to the surface profile of dimple. At X/D > 0.4–0.6, acceleration of flow is reduced due to reduction in favorable pressure gradient. Due to the high depth of concave dimple, adverse pressure gradient is
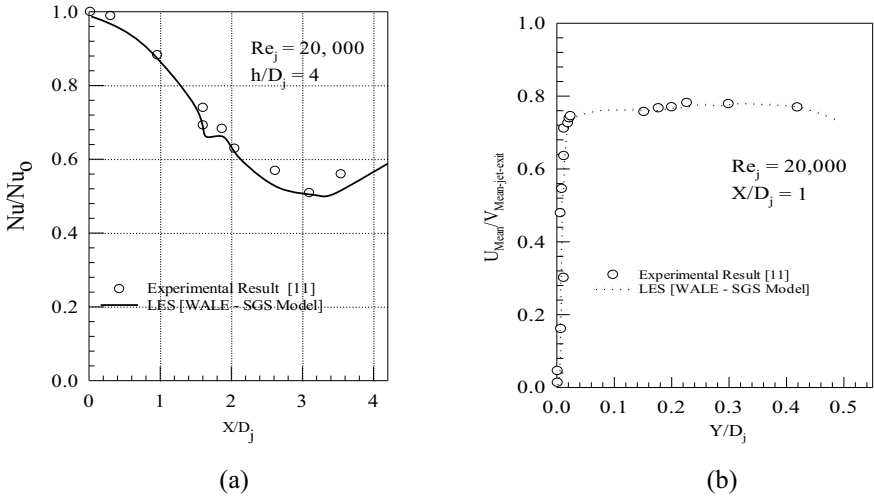
Fig. 4 **a** Comparison of various LES sub-grid models for experimental results (Shukla and Dewan 2019). **b** Comparison of present LES sub-grid model results of mean velocity with experimental data (Shukla and Dewan 2019)

formed at the edge of the dimple which leads to the turning of the stream which leads to a formation of large toroidal vortices. In context to concave dimple, convex dimple also follows the parabolic distribution of coefficient of pressure. Similar to convex dimple, due to curved surface, there is the intense acceleration of jet, but in region $X/D = 0.4$–0.6, due to adverse pressure gradient, deceleration of stream takes place which leads to flow separation after the reattachment flow again starts accelerating slowly. Majorly, δ/Dj ratio governs the extent of adverse pressure gradient in both concave and convex surfaces. In contrast to a curved surface, flat surface shows the lesser acceleration of flow and less adverse pressure gradient and generally follows bell-shaped profile for pressure distribution.

Figure 7 shows a comparison of vorticity obtained from PIV (Xie et al.) and LES performed in the present study obtained by attaining a steady state, for both concave and convex surfaces. In the shear region where the jet interacts with quiescent air, high mixing and high-velocity gradient occurs which leads to higher vorticity. According to Xie et al., PIV is problematic at smaller separation point due to less availability of PIV particles; however, LES does not have any such shortcoming, and higher vorticity can be observed on dimple surface as shown in Fig. 7b. Deflection of jet after striking dimple and exiting dimple can be observed accurately in LES as per results obtained from PIV results. From Fig. 7d, one can observe accurate prediction of large toroidal vortices.
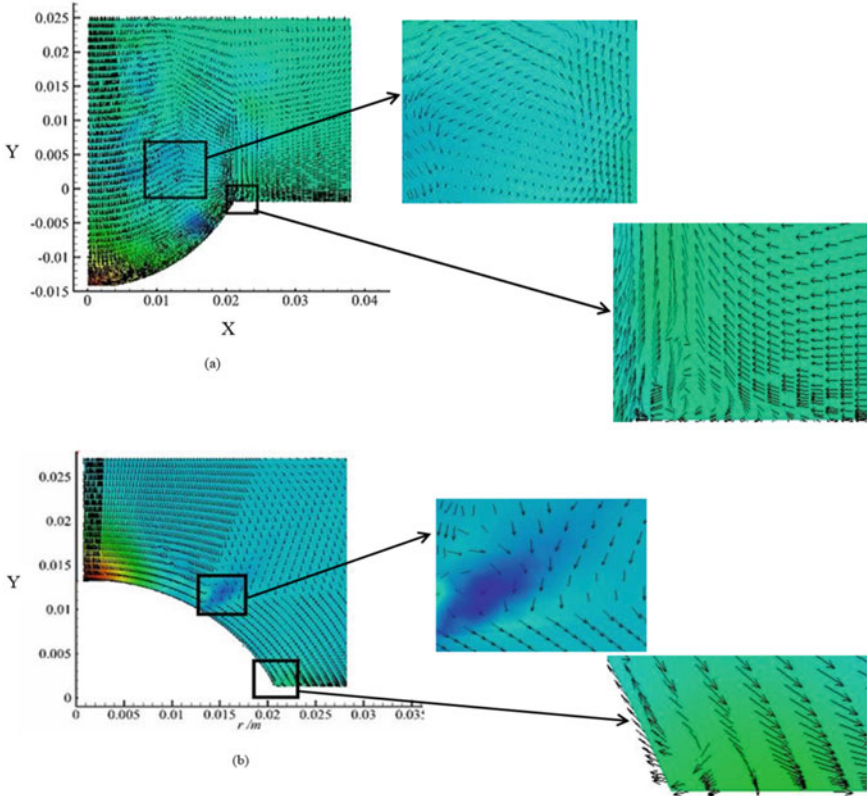
Fig. 5 Instantaneous velocity vector representing various flow regimes in **a** Concave surface. **b** Convex surface

Fig. 6 Distribution of coefficient of pressure (C_p) along radial position (X/D), concave dimple, convex dimple, and flat surface for $Re_j = 5000$, $D/D_j = 0.381$, and $\delta/D_j = 0.3$
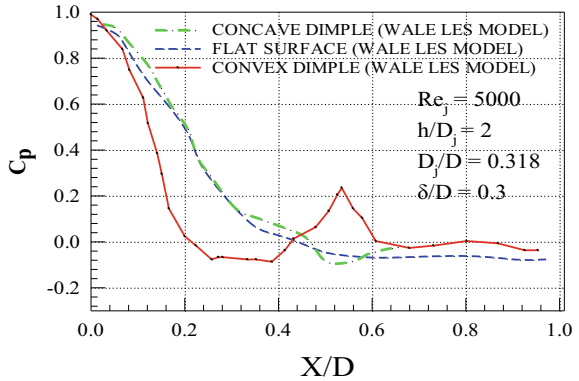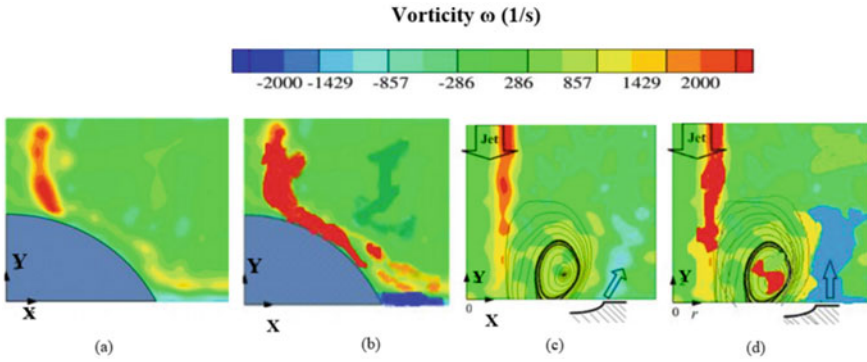
Fig. 7 Vorticity contour on curved surfaces for $Re_j = 5000$, $D/D_j = 0.381$, and $\delta/D_j = 0.3$. **a** Convex (PIV). **b** Convex (LES). **c** Concave (PIV). **d** Concave (LES)

5.3 Thermal Field Prediction

Figure 8 represents stream-wise mean temperature variation on curved surface at different position (X/D) for $Re_j = 5000$, $D/D_j = 0.381$, and $\delta/D_j = 0.3$. It can be observed that non-dimensional temperature is higher at edge of dimple ($X/D = 0.52$); in case of both concave and convex surfaces, this is mainly due to flow separation at this region. It can be noticed from Figs. 8a and b that thermal boundary layer thickness is higher at edge of dimple surface ($X/D = 0.52$) which causes reduction in heat transfer. Thickness of thermal boundary layer increases as we move toward
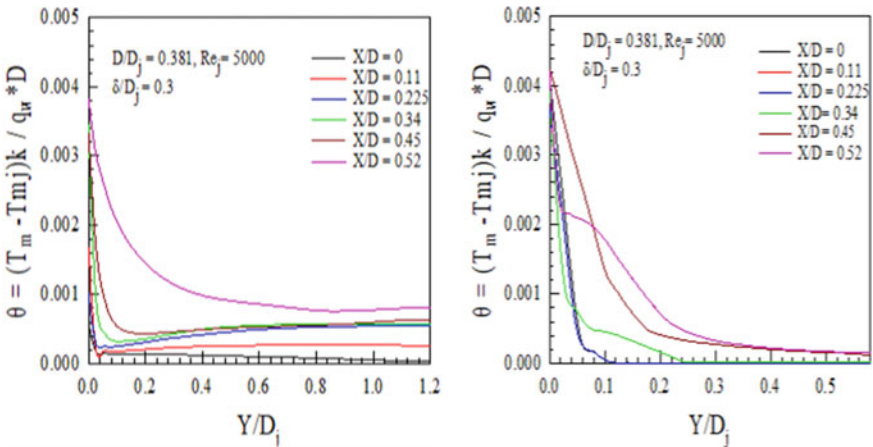
Fig. 8 Stream-wise mean temperature variation on curved surface at different position (r/D) for $Re_j = 5000$, $D/D_j = 0.381$, and $\delta/D_j = 0.3$. **a** Concave. **b** Convex

Fig. 9 Distribution of time averaged local Nusselt number (Nu) (obtained from LES) along radial position (X/D), concave dimple, convex dimple, and flat surface for $Re_j = 5000$, $D/D_j = 0.381$, and $\delta/D_j = 0.3$
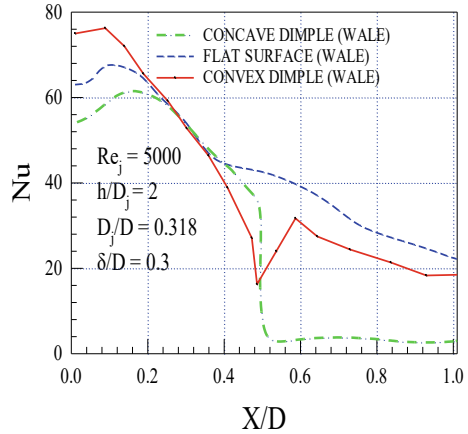
the edge of dimple from the stagnation point, i.e., (*X/D* = 0–0.45), which can be observed from Figs. 8a and b.

Figure 9 shows variation of time averaged local Nusselt number (Nu) along radial position (X/D), concave dimple, convex dimple, and flat surface for $Re_j = 5000$, $D/D_j = 0.381$, and $\delta/D_j = 0.3$. The value of Nusselt number is maximum at stagnation point, and it reduces as *X/D* increases, but a sudden drop in local Nusselt number at *X/D* = 0.52 in convex dimple is observed which is due to separation of the boundary layer at that location due to adverse pressure gradient. However, after reattachment of the boundary layer, the boundary layer becomes thin which causes an increase in Nusselt number after boundary layer separation. In the case of concave dimple, drop in Nusselt number is higher than that of convex dimple due to formation of recirculation region formed because of a large toroidal vortex. And further along, the *X/D* Nusselt number reduces. For flat plate, peak in Nusselt number is captured near the stagnation point and decreases by following bell-curve nature. Convex surface has the highest Nusselt number followed by flat plate and the least in case of the concave surface. But due to increased surface area, overall heat transfer increases in both concave and convex surfaces, diminishing the effect of large toroidal vortices and flow separation.

6 Conclusion

WALE sub-grid scale models were utilized for studying jet impingement on a concave and convex target surfaces at $h/D_j = 2$, Reynolds number (Re_j) 5000, and diameter ratio (D/D_j) = 0.318, and relative depth ($\delta/D_j = 0.3$). The conclusions are as follows:

1. The results obtained from LES of the flow characteristics (vorticity) are close with experimental results obtained from PIV. The flow separation and reattachment are observed in present results.
2. Flow separation and presence of large toroidal vortices are well-explained with the help of the coefficient of pressure (C_p) and its effect on heat transfer.
3. Time averaged Nusselt number for convex dimple is the highest than flat plate and concave dimple except at the edge of dimple surface where flow separation occurs and drop in Nusselt number is observed.
4. At the stagnation point, convex dimple has 25 and 32.5% increment in Nusselt number compared to flat and concave dimpled plates, respectively.

References

Ashforth-Frost S, Jambunathan K, Whitney CF (1997) Velocity and turbulence characteristics of a semiconfined orthogonally impinging slot jet. Experimental Thermal Fluid Sci 14(1):60–67

Azad GS, Huang Y, Han Je-C (2000) Impingement heat transfer on dimpled surfaces using a transient liquid crystal technique. J thermophys Heat Transf 14

Dyban EP, Mazur AI, Epik EY (1971) Flat air jet outflow into a blind pass. J Eng Phys 20(6):1020–1026

Gau C, Chung CM (1991) Surface curvature effect on slotair-jet impingement cooling flow and heat transfer process. ASME J Heat Transf 113

Kanokjaruvijit K, Martinez-Botas RF (2005) Jet impingement on a dimpled surface with different crossflow schemes. Int J Heat Mass Transf 48:161–170

Kawale S, Chandermohan VP (2017) CFD simulation of estimating critical shear stress for cleaning flat soiled surface. Indian Acad Sci 42(12):2137–2145

Ligrani PM, Harrison JL, Mahmmod GI, Hill ML (2001) Flow structure due to dimple depressions on a channel surface. Phys Fluid 13

Nicoud F, Ducros F (1999) Subgrid-scale stress modelling based on the square of the velocity gradient tensor. Flow Turbul Combust 62:183–200

Shukla AK, Dewan A (2019) OpenFOAM based LES of slot jet impingement heat transfer at low nozzle to plate spacing using four SGS models. Heat Mass Transf 2019(55):911–931

Terekhov VI, Kalinina SV, Mshvidobadze YM, Sharov KA (2009) Impingement of an impact jet onto a spherical cavity. Flow structure and heat transfer. Int J Heat Mass Transf 52:2498–2506

van Hout R, Rinskya V, Hershcovichb C, Grobmanb YJ (2018) Outer shear layer characteristics of a radially expanding wall jet on smooth and dimpled surfaces. Int J Heat Fluid Flow72:304–316

Xíe Y, Li P, Lan J, Zhang D (2013) Flow and heat transfer characteristics of single jet impinging on dimpled surface. J Heat Transf 135: 052201–052214

Zhang D, Qu H, Lan J, Chen J, Xie Y (2013) Flow and heat transfer characteristics of single jet impinging on protrusioned surface. Int J Heat Mass Transf 58:18–28

Numerical Investigation and Performance Comparison of Double-Tube Helical Heat Exchanger Incorporating Four-Turn and Six-Turn Models Using Several Nanofluids

Shirish M. Kerur, Anand K. Hosamani, Sanket I. Benni, Shivangouda Annigeri, Tushar Javali, and Prasadkumar Aralikatti

Abstract The study probes the effect of nanofluids in improving heat when used in a blended form. These contain nanoparticles (Ag, TiO$_2$, Al$_2$O$_3$, Cu, Fe, and Au) in volume fraction ranging between 2% and 8%. Three-dimensional numerical simulation has been carried on double-tube helical heat exchanger (on four-turn and six-turn models) using ANSYS Fluent. Three-dimensional governing equations such as mass, momentum and energy equations are solved using SIMPLE algorithm and discretized using finite volume method. The results show that there will be an improvement of heat transfer rate as the nanoparticle volume concentration increases, and from the present study, it is concluded that Au-water nanofluid gives improved results in comparison to other nanoparticles.

Keywords Heat transfer · CFD · Nanofluids · Effectiveness · Double-tube helical heat exchanger

1 Introduction

Investigation was done to check the effect of baffles on helical tube with two concentric tubes one inside another. The simulation was done in counter flow direction of fluids with cold fluid flow rate being maintained with stationary values and varying hot fluid flow rate. They also studied the variation of Nusselt number by changing the thickness of baffle results shows that D/d ratio is inversely proportional to Nusselt number; for steady streamline flow of fluid, the Nusselt number increases, and also for turbulent flow of fluid, Nusselt number increases slightly (Vishnu 2015). Investigators carried out numerical simulation with counter flow of fluids to calculate

S. M. Kerur · A. K. Hosamani · S. I. Benni (✉) · S. Annigeri · T. Javali · P. Aralikatti
Department of Mechanical Engineering, Jain College of Engineering, Belagavi, Karnataka 590014, India

S. M. Kerur
e-mail: smkerur@jainbgm.in

the values of Nusselt number, pressure drop, and friction factor results shows that Nusselt number depends on curvature ratio, and by increasing Reynolds number, the friction factor decreases (Sahoo 2014). Investigators also analyzed the tube-on-tube helical heat exchanger with different nanofluids by maintaining the cold flow rate constant and by varying mass flow rate of hot fluid. Their investigation led them to know that by using CuO and TiO$_2$ nanoparticles dispersed in water can enhance heat transfer, but by increasing the density, the overall heat transfer rate is decreased (Huminic and Huminic 2011). Researchers carried out numerical simulation to improve the heat transfer rate by applying the different boundary conditions and varying the flow direction. They found that the change of boundary conditions on outer wall does not effect on the Nusselt number of inner pipe and also concluded that with increase in flow rate, Nusselt number and heat transfer rate increase (Kanungo 2014). Researchers also carried out numerical simulation using MWCNT/water to enhance the heat transfer. The results show that heat transfer rate and pressure drop are directly proportional to volume concentration of nanoparticles (Mukesh Kumar and Chandrasekar 2019). Numerical simulation has been carried out to identify the values of heat transfer coefficient, pressure drop, and Nusselt number, and further, they compared all the values of a straight pipe. In the results, it is observed that errors are within limits with different mass flow rates (Sunny et al. 2014). To know the variation in Nusselt number by varying Dean number (D/d ratio), they took water as fluid in both pipes with varying velocity of inner pipe and maintaining constant velocity in outer pipe. They concluded that pressure and velocity of inner tube will be always lesser than outer pipe (Naik 2014). Numerical simulation on double-pipe helical heat exchanger was carried out to investigate and study the rate of heat released by hot fluid with laminar flow of fluid and by varying the tubes sizes and flow rates, for counter flow of fluids, and also for parallel flow of fluids. The CFD analysis led them to know that the overall heat transfer rate was directly proportional to Dean number of inner tube (Rennie and Raghavan 2006). Variation in heat transfer rate for flow of fluids in both same and opposite directions by varying the dimensions of pipe. Researchers calculated the values of Nusselt number, temperature, and rate of heat transfer (Q) and concluded that velocity and pressure of inner pipe are lesser than the outer pipe (Mohanty 2013). Researchers have calculated rate of heat released, logarithmic difference in temperature, total coefficient of heat transfer, Nusselt number, Reynolds number, and efficiency. Researchers concluded that flow rate is directly proportional to the coefficient of heat transfer and Nusselt number. And, decrease in flow rate decreases LMTD (Mhaske and Palande 2015). Researchers have used the wavy channel model to simulate using nanofluids to calculate heat transfer rate and concluded that Ag-water nanoparticles give better results compared to other nanofluids (Naik et al. 2021a). Using the double-tube model, investigators simulated for different nanofluids, calculated the enhancement of heat transfer rate, and concluded that they found the heat transfer rate enhanced by using Ag-water nanofluids (Naik et al. 2020, 2021b, c).

2 Model Description

This model is a helical model having two tubes one inside another. Figures 1(a) and 2(a) show the helical heat exchanger model with four turns and six turns, respectively. Figures 1(b) and 2(b) show the meshing done on these models. Specifications of the models are shown in Table 1.

2.1 Boundary Conditions

Boundary conditions are used according to the need of the model. The inlet and outlet conditions are defined as mass flow inlet and pressure outlet. As this is a counter flow with two tubes, there are two inlets and two outlets. The walls are separately specified with respective boundary conditions. No slip condition is considered for each wall. Except the tube walls, each wall is set to zero heat flux condition. The details about initial boundary conditions can be seen in Table 2.

Fig. 1 **a** Four-turn helical heat exchanger model. **b** Four-turn meshed helical model
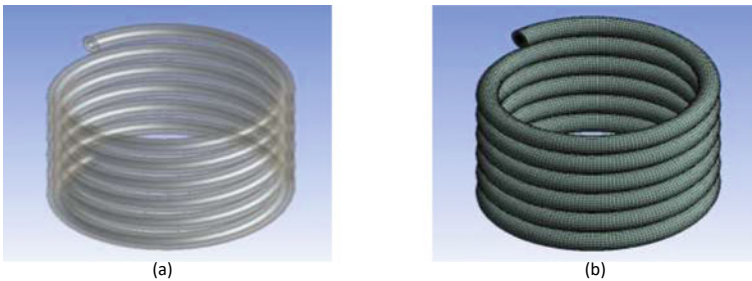
Fig. 2 **a** Six-turn helical heat exchanger model. **b** Six-turn meshed helical model

Table 1 Specifications of helical heat exchanger model

Particulars	Four-turn dimensions (mm)	Six-turn dimensions (mm)
Inner tube inner diameter (di)	10	10
Inner tube outer diameter (do)	12	12
Outer tube inner diameter (Di)	23	23
Outer tube outer diameter (Do)	25	25
Radius of curvature	125	125
Height of helical coil	125	187.5
Number of turns	4 turns	6 turns

Table 2 Boundary conditions

Flow type	Boundary condition type	Mass flow rate (LPH)	Temperature (K)
Cold inlet	Mass flow inlet	480	303
Cold outlet	Pressure outlet	–	–
Hot inlet	Mass flow inlet	120	333
Hot outlet	Pressure outlet	–	–

3 Grid Independent Test

Nine different mesh were tried to evaluate the number of elements essential. To test the grid independence, the grid sizes 38,484, 93,072, 124,386, 165,842, 209,754, 245,838, 318,224, 443,820, and 607,222. It is found that after 607,222 elements, further increase in elements provides <1.5% variation in heat transfer rate which is taken as a criterion for grid independence.

4 Governing Equations

Continuity,

$$div\left(\rho \overrightarrow{V}\right) = 0 \tag{1}$$

Momentum,

$$div\left(\rho \overrightarrow{V} \overrightarrow{V}\right) = -gradp + \nabla \cdot \left(\mu \nabla \overrightarrow{V}\right) + S_m \tag{2}$$

Energy,

$$div\left(\rho \overrightarrow{V} C_P T\right) = div(kgradT) + S_e \tag{3}$$

The viscosity of nanofluid is determined from the Drew and Passman correlation (1999) using the following equation.

$$\mu_{n_f} = \mu_{bf}(1 + 2.5\phi) \tag{4}$$

The density is determined from the Choi correlation (Xuan and Wilfried 2000) using the following equation

$$\rho_{nf} = (1 - \phi)\rho_{bf} + \phi\rho_p \tag{5}$$

The heat capacity is determined from the Xuan and Roetzel correlation (Das et al. 2006) using the following equation

$$\left(C_p\right)_{nf} = \frac{(1 - \phi)(\rho C_p)_{bf} + \phi(\rho C_p)_p}{\rho_{nf}} \tag{6}$$

Thermal conductivity is determined from the Maxwell–Garnett's correlation (1881) using the following equation.

$$\frac{k_{nf}}{k_{bf}} = \frac{k_p + 2k_{bf} + 2\left(k_p - k_{bf}\right)\phi}{k_p + 2k_{bf} - \left(k_p - k_{bf}\right)\phi} \tag{7}$$

Thermal expressions

The LMTD has the form,

$$\Delta T_{LMTD} = \frac{\Delta T_2 - \Delta T_1}{\ln \frac{\Delta T_2}{\Delta T_1}} \tag{8}$$

The heat transfer rate for a cross-flow heat exchanger may be written as,

$$Q = mC_p(Th_o - Th_i) \tag{9}$$

Effectiveness is defined as,

$$E = \frac{C_{\max}(Th_i - Th_o)}{C_{min}(Th_i - Th_i)} \tag{10}$$

Table 3 Thermophysical properties of different nanofluids

Nanoparticle type	ρ (kg/m^3)	Cp (J/kg K)	K (W/m K)
Ag	10,500	234	429
TiO$_2$	4250	686	8.9
Al$_2$O$_3$	3970	765	40
Cu	8933	385	400
Fe	7860	440	80.4
Au	19,320	128	318

The overall hear transfer rate is written as,

$$U = \frac{Q}{\Delta T_{LMTD}} \tag{11}$$

5 Validation

Figure 3 shows the comparison between our study and the study presented by Mhaske and Palande (2015). The graph is plotted between Q_h and hot water flow rate. It can be seen that there is a very close correlation between our study and the earlier study.
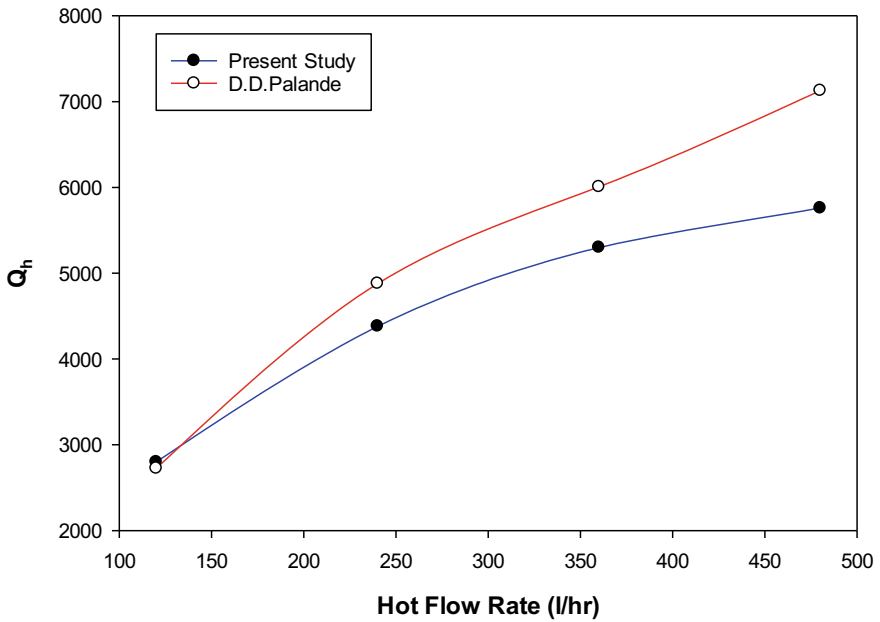
Fig. 3 Comparison between present study and Mhaske and Palande (2015)

It can be observed that the deviation at a few places exists, but it is around 5% which is acceptable. Hence, the work carried out by us and Palande are in close match. This validation is done for water that is used as the working medium. Since our work very closely matches with the earlier work, it concludes that our methodology followed is correct. Hence, we proceeded ahead to carry out similar simulation using nanofluids as the working medium.

6 Results and Discussion

Figure 4a–f show the variation of effectiveness versus hot fluid flow rate with comparison between four-turn and six-turn results for different nanofluids. The effectiveness for 8% of Ag-water nanofluid is increased by 18.99% (four turn) and 19.18% (six turn) as compared to 2% of Ag nanofluid, respectively, 8% of TiO_2-water nanofluid is increased by 3.03% (four turn) and 7.50% (six turn) as compared to 2% of TiO_2 nanofluid, respectively, 8% of Al_2O_3-water nanofluid is increased by 11.17% (four turn) and 11.52% (six turn) as compared to 2% of Al_2O_3 nanofluid, respectively, 8% of Cu-water nanofluid is increased by 19.76% (four turn) and 19.82% (six turn) as compared to 2% of Cu nanofluid, respectively, 8% of Fe-water nanofluid is increased by 15.18% (four turn) and 16.26% (six turn) as compared to 2% of Fe nanofluid, respectively, and 8% of Au-water nanofluid is increased by 32.16% (four turn) and 33.91% (six turn) as compared to 2% of Au nanofluid.

Figure 5a–f show the variation of LMTD versus hot fluid flow rate with comparison between four-turn and six-turn results for different nanofluids. The LMTD for 8% of Ag-water nanofluid is decreased by 12.13% (four turn) and 14.80% (six turn) as compared to 2% of Ag nanofluid, respectively, 8% of TiO_2-water nanofluid is decreased by 1.50% (four turn) and 4.35% (six turn) as compared to 2% of TiO_2 nanofluid, respectively, 8% of Al_2O_3-water nanofluid is increased by 5.66% (four turn) and 6.97% (six turn) as compared to 2% of Al_2O_3 nanofluid, respectively, 8% of Cu-water nanofluid is decreased by 10.49% (four turn) and 12.76% (six turn) as compared to 2% of Cu nanofluid, respectively, 8% of Fe-water nanofluid is decreased by 9.48% (four turn) and 11.60% (six turn) as compared to 2% of Fe nanofluid, respectively, and 8% of Au-water nanofluid is decreased by 18.56% (four turn) and 21.23% (six turn) as compared to 2% of Au nanofluid.

Figure 6a–f show the variation of heat transfer rate (Q_h) versus hot fluid flow rate with comparison between four-turn and six-turn results for different nanofluids. The heat transfer rate for 8% of Ag-water nanofluid is increased by 22.24% (four turn) and 23.03% (six turn) as compared to 2% of Ag nanofluid, respectively, 8% of TiO_2-water nanofluid is increased by 3.05% (four turn) and 6.24% (six turn) as compared to 2% of TiO_2 nanofluid, respectively, 8% of Al_2O_3-water nanofluid is increased by 11.09% (four turn) and 11.37% (six turn) as compared to 2% of Al_2O_3 nanofluid, respectively, 8% of Cu-water nanofluid is increased by 19.41% (four turn) and 20.21% (six turn) as compared to 2% of Cu nanofluid, respectively, 8% of Fe-water nanofluid is increased by 17.67% (four turn) and 18.83% (six turn) as compared
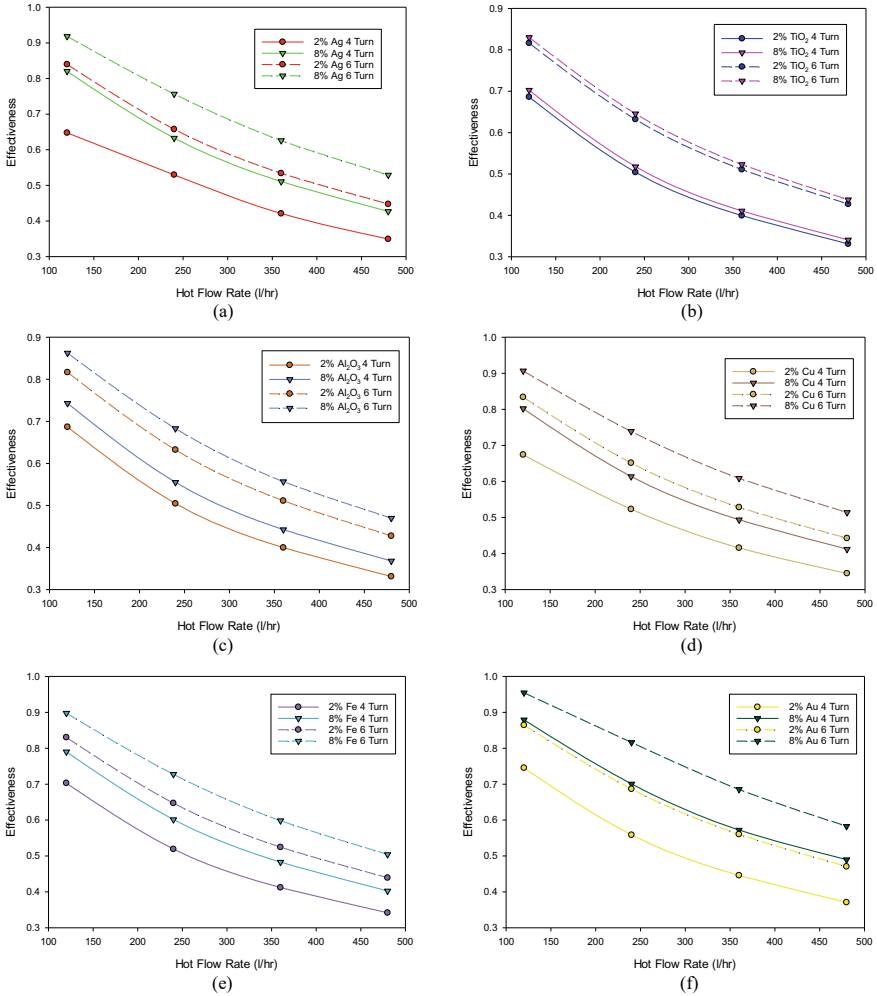
Fig. 4 **a** Effect of silver–water nanofluid on effectiveness. **b** Effect of titanium oxide–water nanofluid on effectiveness. **c** Effect of aluminum oxide–water nanofluid on effectiveness. **d** Effect of copper-water nanofluid on effectiveness. **e** Effect of iron-water nanofluid on effectiveness. **f** Effect of gold-water nanofluid on effectiveness

to 2% of Fe nanofluid, respectively, and 8% of Au-water nanofluid is increased by 32.32% (four turn) and 34.91% (six turn) as compared to 2% of Au nanofluid.

Figure 7a–f show the variation of overall heat transfer rate (U) versus hot fluid flow rate with comparison between four-turn and six-turn results for different nanofluids. The overall heat transfer rate for 8% of Ag-water nanofluid is increased by 39.11% (four turn) and 39.33% (six turn) as compared to 2% of Ag nanofluid, respectively, 8% of TiO_2-water nanofluid is increased by 3.78% (four turn) and 11.08% (six turn) as compared to 2% of TiO_2 nanofluid, respectively, 8% of Al_2O_3-water nanofluid
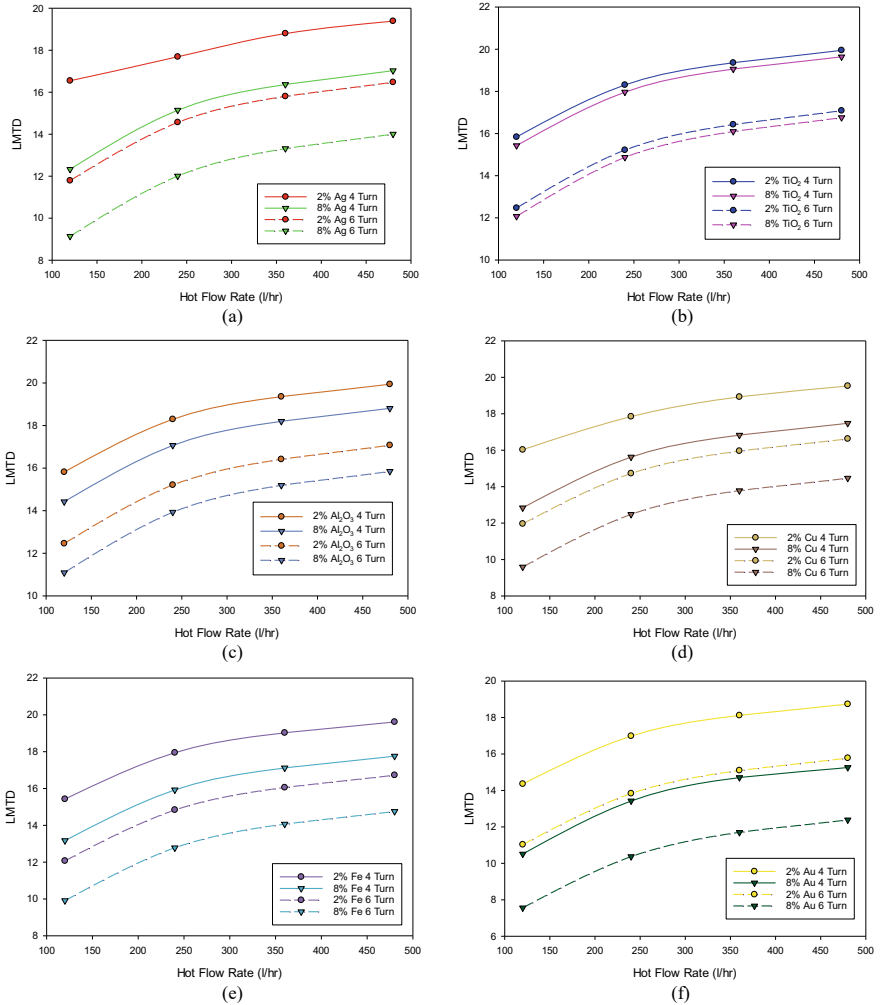
Fig. 5 **a** Effect of silver–water nanofluid on LMTD. **b** Effect of titanium oxide–water nanofluid on LMTD. **c** Effect of aluminum oxide–water nanofluid on LMTD. **d** Effect of copper–water nanofluid on LMTD. **e** Effect of iron-water nanofluid on LMTD. **f** Effect of titanium oxide–water nanofluid on LMTD

is increased by 17.76% (four turn) and 19.86% (six turn) as compared to 2% of Al_2O_3 nanofluid, respectively, 8% of Cu-water nanofluid is increased by 33.42% (four turn) and 43.23% (six turn) as compared to 2% of Cu nanofluid, respectively, 8% of Fe-water nanofluid is increased by 30.00% (four turn) and 39.93% (six turn) as compared to 2% of Fe nanofluid, respectively, and 8% of Au-water nanofluid is increased by 62.49% (four turn) and 67.44% (six turn) as compared to 2% of Au nanofluid.
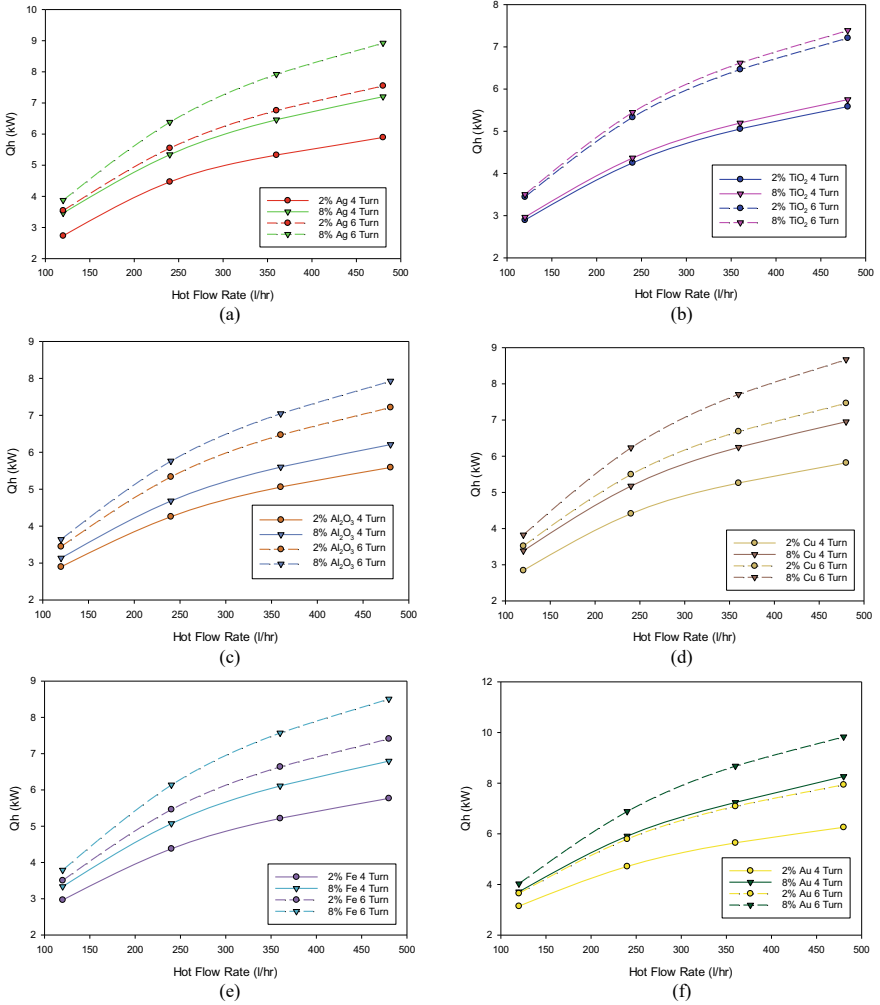
Fig. 6 **a** Effect of silver–water nanofluid on heat transfer rate. **b** Effect of titanium oxide–water nanofluid on heat transfer rate. **c** Effect of aluminum oxide–water nanofluid on heat transfer rate. **d** Effect of titanium oxide–water nanofluid on heat transfer rate. **e** Effect of iron–water nanofluid on heat transfer rate. **f** Effect of gold-water nanofluid on heat transfer rate

Figure 8a–d show the percentage comparison between four-turn and six-turn values of effectiveness, LMTD, heat transfer rate (Q_h), and overall heat transfer rate (U), having the increase in percentage of six-turn values compared to four-turn values shown in Table 4.
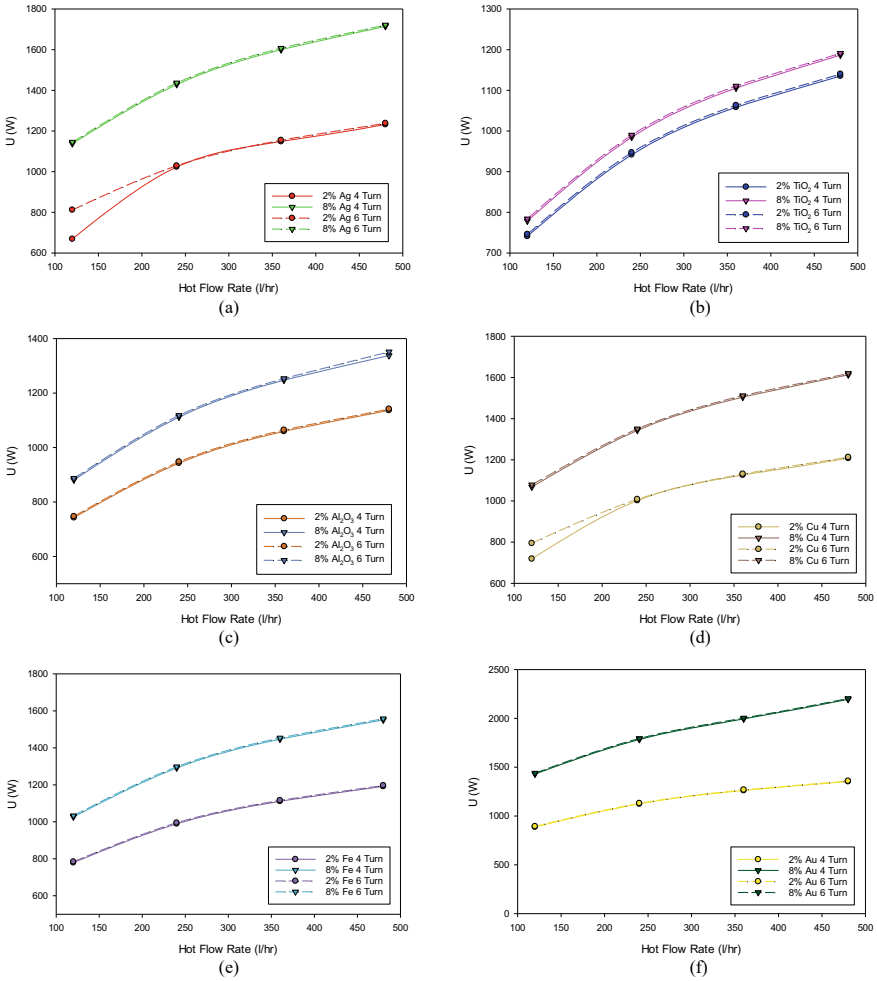
Fig. 7 **a** Effect of silver–water nanofluid on overall heat transfer rate. **b** Effect of titanium oxide–water nanofluid on overall heat transfer rate. **c** Effect of aluminum oxide–water nanofluid on overall heat transfer rate. **d** Effect of copper–water nanofluid on overall heat transfer rate. **e** Effect of iron–water nanofluid on overall heat transfer rate. **f** Effect of gold-water nanofluid on overall heat transfer rate

7 Conclusion

Numerical simulation on a four-turn and six-turn double-tube type helical heat exchanger was performed using ANSYS Fluent software to understand and predict the impact of various nanofluids on the heat transfer characteristics. Based on the results, it can be concluded that increasing the volume concentration of nanoparticles from 2 to 8% improves the heat transfer rate as well as effectiveness. Particularly,
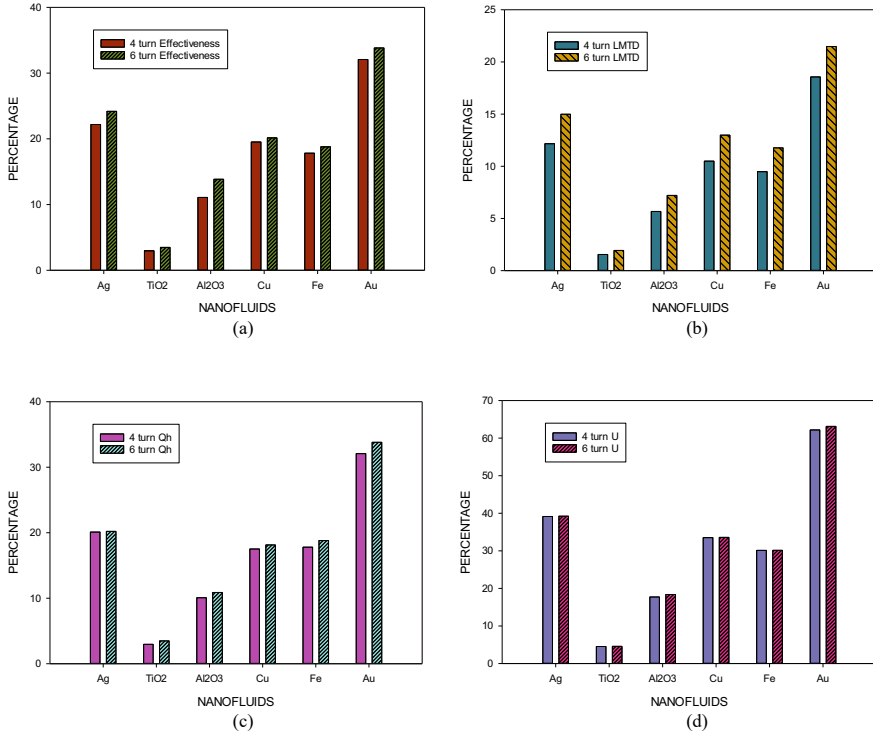
Fig. 8 **a** Percentage comparison of effectiveness. **b** Percentage comparison of LMTD. **c** Percentage comparison of heat transfer rate (Q_h). **d** Percentage comparison of overall heat transfer rate (U)

Table 4 Results

Nanofluid	Type	LMTD (%)	Effectiveness (%)	Q_h (%)	U (%)
Ag	Four turn	12.17	22.19	22.11	39.14
	Six turn	14.99	24.19	22.21	39.22
TiO$_2$	Four turn	1.55	2.96	2.95	4.54
	Six turn	1.93	3.48	3.48	4.58
Al$_2$O$_3$	Four turn	5.67	11.08	10.07	17.71
	Six turn	7.20	13.85	10.87	18.38
Cu	Four turn	10.49	19.52	17.52	33.53
	Six turn	12.99	20.14	18.14	33.58
Fe	Four turn	9.48	17.82	17.80	30.13
	Six turn	11.77	18.78	18.80	30.14
Au	Four turn	18.57	32.07	32.09	62.19
	Six turn	21.48	33.83	33.81	63.13

gold nanoparticles in water yield better results in comparison to other nanoparticles. It can also be observed from the table and concluded that all the parameters tested for improve with the increase in number of turns from four turns to six turns.

References

Drew DA, Passman SL (1999) Theory of multicomponent fluids. Springer

Das SK, Choi SUS, Patel EH (2006) Heat transfer in nanofluids—a review. Heat Transfer Eng 27(10):3–19

Huminic G, Huminic A (2011) Heat transfer characteristics in double tube helical heat exchangers using nanofluids. Int J Heat Mass Transf 54:4280–4287

Kanungo S (2014) Numerical analysis to optimize the heat transfer rate of tube-in-tube helical coil heat exchanger

Maxwell JC (1881) Treatise on electricity and magnetism, 2nd edn. Clarendon Press, Oxford University, UK

Mhaske GB, Palande DD (2015) Experimental investigation of tube in tube helical coil heat exchanger. Int J Inform Futuristic Res (IJIFR) 2:4437–4448

Mohanty SR (2013) CFD analysis of heat transfer in a helical coil heat exchanger using fluent

Mukesh Kumar PC, Chandrasekar AM (2019) CFD analysis on heat and flow characteristics of double helically coiled tube heat exchanger handling MWCNT/Water nanofluids. Heliyon 5:E02030

Naik LR (2014) Optimization of Nusselt number in a helical coil heat exchanger with constant heat flux boundary condition using fluent

Naik B, Soudagar MEM, Thomas M, Dasurkar K, Alloli O, Hossain F, Alloli M (2020) Numerical investigation of double pipe heat exchanger with different nanofluids. IOP Conf Ser: Earth Environ Sci 573:012030

Naik B, Hosmani AK, Kerur SM, Pattanashetti JS, Ratan V, Bhushan C (2021a) Numerical investigation of wavy channel using several nanofluids. IOP Conf Ser: Mater Sci Eng 1065:012007

Naik B, Hosamani AK, Kerur SM, Jadhav CC, Benni S, Annigeri S, Javali T, Aralikatti P (2021b) Numerical investigation of double tube helical heat exchanger using several nanofluids, In: 3rd international conference on advances in mechanical engineering and nanotechnology, material today proceeding. Elsevier

Naik B, Thomas M, Hosmani SBMAK, Alloli O, Dasurkar K, Alloli M (2021c) Performance analysis of double pipe using different nanofluids. In: 3rd international conference on recent advances in mechanical infrastructure. Lecture notes in intelligent transportation and infrastructure. Springer

Rennie TJ, Raghavan VGS (2006) Numerical studies of a double-pipe helical heat exchanger. Appl Therm Eng 26:1266–1273

Sahoo L (2014) CFD analysis of heat transfer in a helical coil heat exchanger with constant wall heat transfer coefficient

Sunny SP, Mhaske SD, Parikh YB (2014) Numerical simulation of a tube in tube helical coiled heat exchanger using CFD. Int J Appl Eng Res 9:5209–5220. ISSN 0973-4562

Vishnu M (2015) Numerical simulation of helical coil tube in tube heat exchanger with baffles

Xuan Y, Wilfried R (2000) Conceptions for heat transfer correlation of nanofluids. Int J Heat Mass Transf 43(19): 3701–3707

Passive Cooling and Human Thermal Comfort: A Case Study

Kiran Shende and Neeraj Agrawal

Abstract In the present scenario with the rise in ambient temperature globally due to greenhouse gas emissions, cooling is one of the major concerns in residential and commercial buildings. Passive cooling techniques are one of the innovatory practices and technologies that, through natural means, provide buildings with comfortable environment. An in-house case study is carried out on passive cooling employing cool roof concept of radiative cooling, namely the application of THERMOROOF paint. A maximum drop of 2.2 °C in indoor room temperature was observed which eventually reduce the radiation heat gain by the occupants. Steady-state human thermal comfort is also modeled. The net heart transfer is found to be 53.2% higher in painted room in comparison to unpainted room due to reduction in painted room temperature.

Keywords Passive cooling · THERMOROOF paint · Thermal comfort · Heat transfer analysis

1 Introduction

Cooling the space is to lowering the temperature than that of surrounding temperature by transferring energy from a space or from the air, to space. In recent years, in order to attain the required human thermal comfort, temperature, humidity, air circulation and air purity within a space are regulated by air conditioning systems. The paucity of conventional energy sources and the escalation of energy prices has led to re-visit of the overall design methods and applications of air conditioning systems and the creation of new techniques and processes in order to obtain natural means of achieving the comfort conditions in buildings (Geetha and Velraj 2012).

The world's second-most populous nation is India with 17.6% of world's population and is expected to surpass China's population by 2022. There is a strong interrelation between energy consumption, economic growth and demographic rise. After

K. Shende · N. Agrawal (✉)
Department of Mechanical Engineering, Dr. B. A. Technological University, Lonere, India

China, USA and Russia, in 2011 India became the fourth largest energy-consuming country (Panchabikesan et al. 2017).

In a building, the energy consumption is mainly due to presence of appliances used for human requirement and comfort, and electricity consumption mainly depends on the construction type and the installed energy consuming devices. Buildings account for around 40% of the world's annual energy usage worldwide mostly used for lighting, heating, cooling and air conditioning. India's annual per capita electricity consumption has increased from 631.4 kWh in 2006 to 1010 kWh in 2015, and annual electrical consumption is forecast to raise from 650 kWh in 2012 to 2750 kWh by 2050, resulting in a substantial rise in consumption of energy in the building sector (Panchabikesan et al. 2017).

Fast installation of air conditioning systems resulted exponential rise in greenhouse gas (GHG) emissions associated with the construction sector. The total energy consumed by the air conditioning units has increased steadily from 2006 to 2011 in the range of 2308–5099 GWh and is projected to raise by 2030 to 50 TWh/y. India is one of the six biggest GHG nations in 2013, emitting 5.7% of the world's total GHG emissions. It is anticipated that emissions would reach 4.9 billion tons of CO_2e during 2030–2031 with a per capita GHG emissions of 3.4 t of CO_2e. A recent study on energy assessment predicted that due to the increase in usage of HVAC systems, the CO_2 emissions would leapfrog from 205 $MtCO_2$ in 2005 to 613 $MtCO_2$ in 2020 (Panchabikesan et al. 2017).

2   Passive Cooling: Reflective Roof Strategy

Passive cooling strategy is one of the eco-sustainable approaches to naturally cool the buildings. Passive cooling relates to any technology or design features that are implemented to decrease the temperature of buildings interior with nil or low power consumption. This also eliminates the need for mechanical cooling with decreased energy consumption rates and environmental harms such as greenhouse gas emissions. Passive cooling methods are also strongly related to occupant thermal comfort.

High solar absorptance of the building material is the indicator of high solar gains through the opaque envelope components in summer. Cool roof paints exhibit high solar reflectance, which reduces the solar gains during daytime, and high emittances, which helps the buildings to radiate away the incident heat. Reflective cool paints include several product categories, and their performance on buildings depends on several parameters like climate, building use, construction geometry and insulation.

The majority of the light from sun is in visible range; the idea of the reflective rooftop works with surface properties as a reflector of imperceptible short- and long-wave electromagnetic radiation and as an excellent IR radiation emitter of heat, unlike dark or hot rooftops that absorb enormous amount of solar energy.

The key factors related to the rooftop temperature are identified with the properties of the material surface, as appeared in Fig. 1.

Fig. 1 Phenomenon of incident rays on roof surfaces (Al-Obaidi et al. 2014)
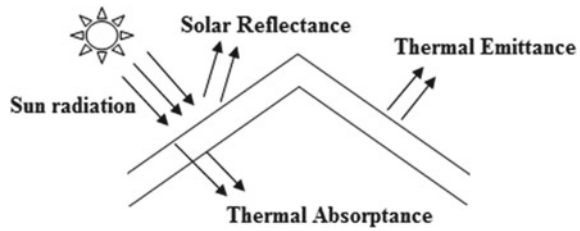
1. **Solar Reflectance or Albedo**: This factor relates to solar energy reflection after it comes into contact with the material surface.
2. **Thermal Emittance**: This feature relates to the radiation heat emission of a particular object in the form of an infrared or thermal radiation and relates to the efficiency of a surface to cool itself.

Geetha and Velraj (2012) have presented a clear framework of passive cooling technologies involving all the preventive measures against overheating of the buildings. Al-Obaidi et al. (2014) evaluated the application of reflective and radiative methodologies in roofing structures to improve environmental sinks for heat dissipation. Heat gain of the roof, which represents 70% of the overall heat gain, is a major concern and should be lowered in order to passively cool the buildings (Al-Obaidi et al. 2014).

Akbari et al. (1996) stated the standard in-lab methods for determining the solar reflectance index (SRI) based on solar reflectance and thermal emittance for non-metallic surfaces. It is demonstrated that the steady-state temperature (SST) of a surface under the sun is emphatically associated with the solar reflectance and infrared emittance of the surface. Pisello (2017) has studied the current literature on the growth of cool coatings and their genuine applications. Ganguly et al. (2016) conducted a comparative assessment of three types of reflective cool paints and even cool black paints to assess potential and constraints of cool paints. The impacts of applying reflective paint to a standard bare rooftop were analyzed mainly by monitoring the decrease of rooftop surface temperature at various case study locations which eventually reduce the cooling loads. Santamouris et al. (2007) explored the capability of all the more encouraging new advancements in the field of passive cooling, similar to the cool reflective coatings to improve outdoor and indoor circumstances of households in warm areas of the planet. De Masi et al. (2018) suggested experimental characterization of a white acrylic paint and its in-field aging effect by evaluating solar reflectance at the beginning and after one year from the application of paint; the suggested paint was contrasted with a commercially used cool roof product and a polished aluminum varnish. Data elaboration leads to interesting findings; first of all, acrylic paint in-field efficiency is similar to cool product and better than aluminum paint. Aging, however, is quicker with a decrease in in-field solar reflectance of around 20–25%.

Uemoto et al. (2010) explored the thermal execution of cool acrylic paints containing infrared reflective pigments. Results showed that the cool colored paint

formulations made impressively higher NIR reflectance than comparable colored paints which the surface temperatures were over 10 °C below those of ordinary paints when exposed to IR radiation. Their research demonstrates that cool paints improve thermal comfort within houses, which can decrease the cost of air conditioning. Kolokotroni et al. (2018) conducted a case study of Jamaica's single-story buildings. Monitoring was performed before and after the installation of a cool paint on the roof; on days with an average solar radiation intensity of 420 W/m^2 and an ambient air temperature of 28 °C, internal ceiling surface temperature is reduced by an average of 6.8 °C and internal air temperature by 2.3 °C.

The aim of this paper is to investigate the effect on indoor air temperature and eventually assess the human thermal comfort inside the room by applying highly reflective Thermo paints on rooftop of the selected building space.

3 Experimental Methodology

A specific room located in top floor in University Guest House, *Lonere (MH), India* was selected for experimentation. The room roof is of sloped type with surface area 24 m^2. The adjacent unpainted room having same surface area with same site rotation and orientation as that of painted room was selected for comparison purpose. The THERMOROOF XT paint is selected for experimentation. The two main properties taken into account while selecting the paint are its solar reflectivity (SRI) and thermal emittance. The average values of solar reflectance and thermal emittance are 0.92 and 0.90 for the selected THERMOROOF paint which is quiet high as compared to conventional white-colored paints. Therefore, its selection for experimentation makes a valid point for saving air conditioning energy cost and reducing carbon footprints. The technical specification of the selected paint specified by manufacturer is as shown in Table 1.

Table 1 Technical specification of THERMOROOF XT paint (Harind Chemicals and Pharmaceuticals 2021)

Properties	Unit	Standard	Values
Color	–	ASTM D 1544	White
pH value	–	ASTM D 1293	6–8
Functional cure	Hrs	ASTM D 1640	24 h
Solar reflectance	%	ASTM E 1549	0.90–0.94
Thermal emittance	–	ASTM C 1371	0.88–0.92
Solar Reflective Index (SRI)	–	ASTM E1980	104–110
Dry film thickness	μm	–	50–60 μ in 2 coats
Recommended dilution	%	–	5–20

(a) Unpainted Roof   (b) Painted Roof

Fig. 2 Unpainted and painted roof configuration

Surface of the roof was cleaned thoroughly to make it free from laitance, dust and dirt. A total of 300 ml of water is mixed with one liter of paint for dilution which helps to increase its fluidity. Before starting the paint application, it was ensured that the concrete roof surface should be moist/water wash and also avoid puddling/ponding of water on surface to be insulated. The first coat was applied on the cleaned and washed roof surface during non-sunny hours. After a gap of 1–2 h, second coat was applied. After completion of full coating, it was allowed to cure for 24 h. The Fig. 2a and b show unpainted and painted roof configuration, respectively.

For the measurement of surface temperature, Testo-made non-contact-type IR Thermometer 830-T1 having IR accuracy and resolution of ± 1.5 °C and 0.1 °C, respectively, was used. For onsite measurement of average roof surface temperature, a matrix was marked on roof surfaces. The room indoor air temperature and wet bulb temperature were measured by regular ordinary thermometer and sling psychrometer, respectively.

4   Results and Discussion

The roof surface temperature and indoor room temperature including ceiling temperature were recorded entire day. The measurement was done on April 28, 2019, when the ambient temperature reaches its peak of 45 °C at 2 P.M. The results obtained for temperature variation on 28th April for both painted and unpainted room are plotted with time.

4.1 Daily Variation of Room Temperatures

Effect on Average Roof Surface Temperature

Figure 3 shows variation of average roof surface temperature with time. It is observed that the roof surface temperature was significantly reduced with painted surface. However, the maximum reduction in surface temperature was observed at 2 P.M. of the order of 14.5 °C. The surface temperature with unpainted roof was observed as 56.4 °C at 2 P.M., whereas it was only 40.5 °C with painted surface. The maximum decrease in roof surface temperature was found to be 28.2% at 2 P.M in comparison to unpainted roof.

Effect on Indoor Room Temperature

Figure 4 shows variation of indoor room temperature in a chosen day. Decrease in roof surface temperature leads to reduction in ceiling temperature which eventually decreases room temperature and enhances thermal comfort.

An average reduction of 1.1 °C of room DBT was observed compared to unpainted room. However, the reduction in room temperature was found as 1.7 °C at 2 P.M which is almost 4.4% compared to unpainted roof room.

Fig. 3 Variation of average roof surface temperature with time
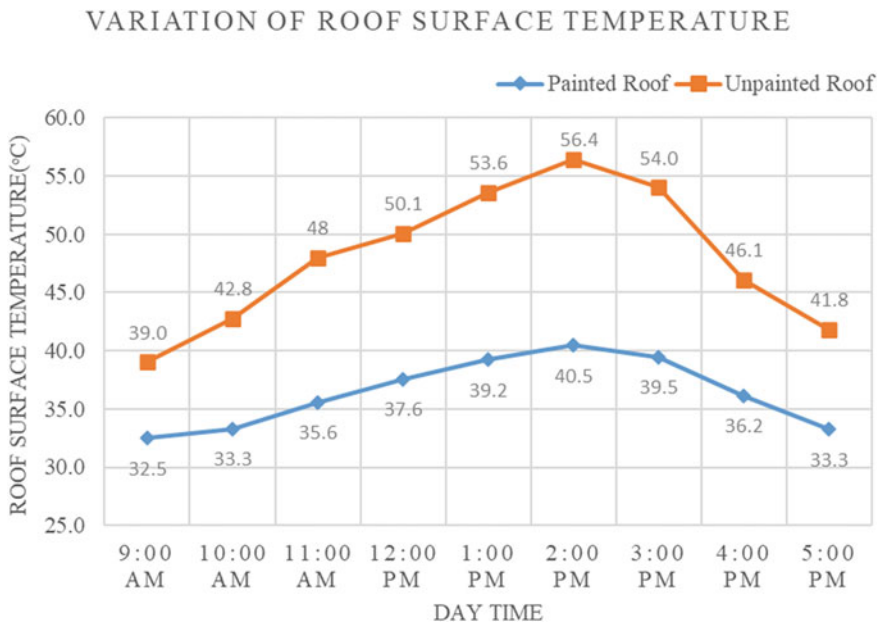
VARIATION OF INDOOR ROOM TEMPERATURE
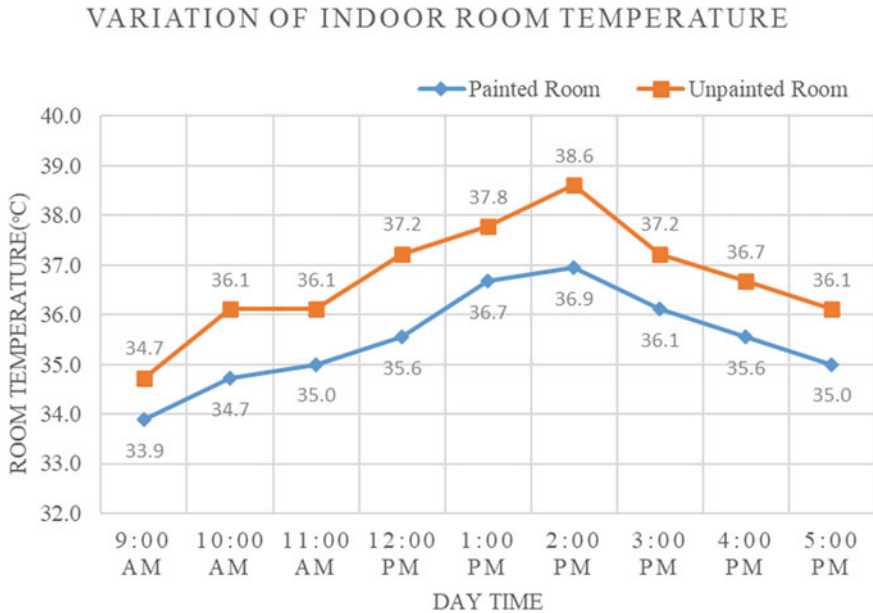
Fig. 4 Variation of indoor room temperature with time

4.2 Monthly Variation of Room Temperatures

The continuous monitoring of roof surface temperature and room indoor temperature at a specific time of 2:30 P.M was recorded for one month. This specific time was selected based on maximum solar insolation. The results obtained for monthly temperature variation for both painted and unpainted room configurations taking ambient temperature as reference are discussed briefly.

Monthly Variation of Average Roof Surface Temperature

Figure 5 shows monthly variation of average roof surface temperature. The unpainted roof surface temperature was well above the ambient temperature throughout the month with the maximum and minimum temperatures as 55.6 and 51 °C, respectively. The surface temperature of painted roof was well below the ambient temperature except for 26th and 27th April where it goes above ambient temperature by 0.7 °C and 2.8 °C, respectively.

Monthly Variation of Indoor Room Temperature

Figure 6 shows monthly variation of indoor room temperature. Reduction in room temperature of the order of 2.0 °C was observed throughout the month except 27th April where drop is only 0.6 °C. It was found that the painted room is maximum 2.2 °C cooler than the unpainted room on 2nd, 22nd and 26th of April which comes out 6.4% compared to unpainted room temperature.
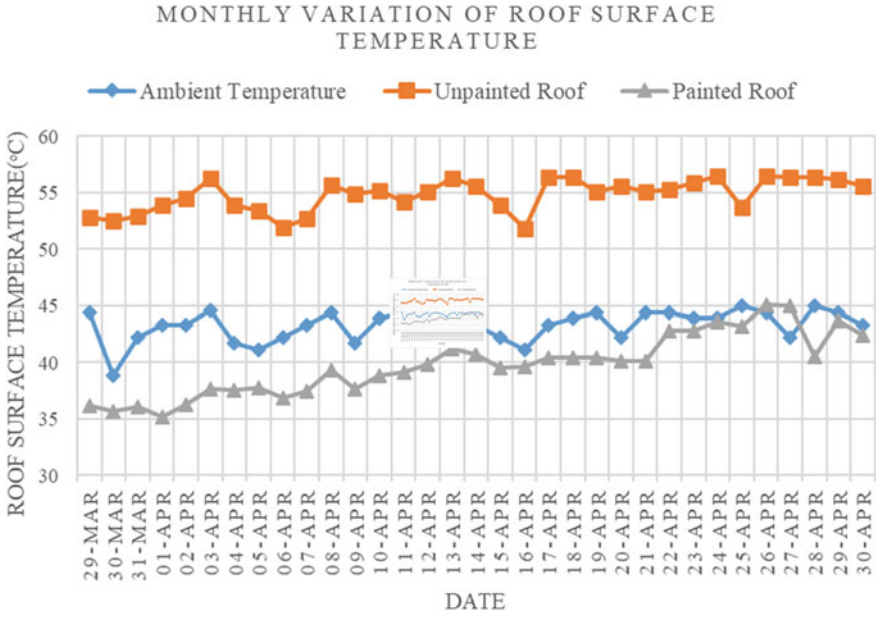
Fig. 5 Monthly variation of average roof surface temperature
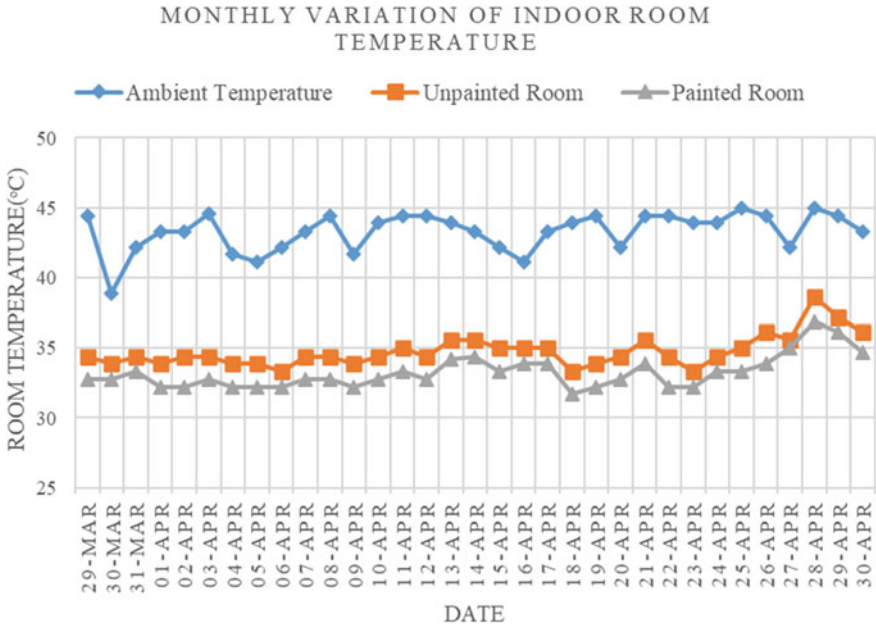
Fig. 6 Monthly variation of indoor room temperature

5 Human Thermal Comfort and Mean Radiant Temperature

Human body primarily rejects the heat from the body surface. Using environmental variables surrounding the body, a stable energy balance on the human body is created. Steady-state Fanger's human body thermal comfort model is presented as

$$\dot{Q}_M = \pm\dot{Q}_{\text{Skin}} \pm \dot{Q}_{\text{Respiration}} = (\dot{Q}_C \pm \dot{Q}_R \pm \dot{Q}_E)_{\text{Skin}} + (\pm\dot{Q}_C \pm \dot{Q}_E)_{\text{Respiration}} \tag{1}$$

where $\dot{Q}_M$ is the net rate of heat produced through metabolism, Q_{Skin} is the heat loss (+) or gain (−) through the skin, and $Q_{\text{Respiration}}$ is the net heat loss (+) or gain (−) due to respiration. The subscript C designates convection, R radiation and E evaporation. The signs are significant, as the heat transfers may be to or from the body.

Fanger identifies six environmental parameters that affect human thermal comfort: air dry-bulb temperature, air velocity, air humidity content, mean radiant temperature, activity level and clothing. The first three are environmental parameters which are directly measured, while activity level and clothing are defined parameters. However, the mean radiant temperature is relatively difficult to measure. It is defined as the uniform temperature of an imaginary enclosure within which the radiant heat transfer from the human body equals the radiant heat transfer within the actual environment. The enclosure of uniform temperature is assumed to be a blackbody (Kuehn et al. 1998).

The mean radiant temperature can be computed when the surface temperature of all surrounding surfaces is known and the angle factor between the person and each surface is known. The surface temperature can be measured using conventional temperature-measuring instruments or can be computed using heat transfer principles. The angle factors between a person and surrounding vertical or horizontal rectangular surfaces were determined by Fanger by plotting angle factor between a seated person and vertical or horizontal surfaces. These angle factors between a person, P, and a rectangular surface, j, can be computed using the following correlation (Kuehn et al. 1998):

$$F_{P-j} \approx \frac{1}{4\pi}\left[\frac{X}{\sqrt{1+X^2}}\tan^{-1}\left(\frac{Y}{\sqrt{1+X^2}}\right) + \frac{Y}{\sqrt{1+Y^2}}\tan^{-1}\left(\frac{X}{\sqrt{1+Y^2}}\right)\right] \tag{2}$$

where $X = a/1.8c$, $Y = b/1.8c$ and a, b and c are dimensions as per room configurations shown in Fig. 7.

The mean radiant temperature can then be computed from,

$$\overline{T_r} = \left(\sum_{j=1}^{N} F_{P-j} T_j^4\right)^{\frac{1}{4}} \tag{3}$$
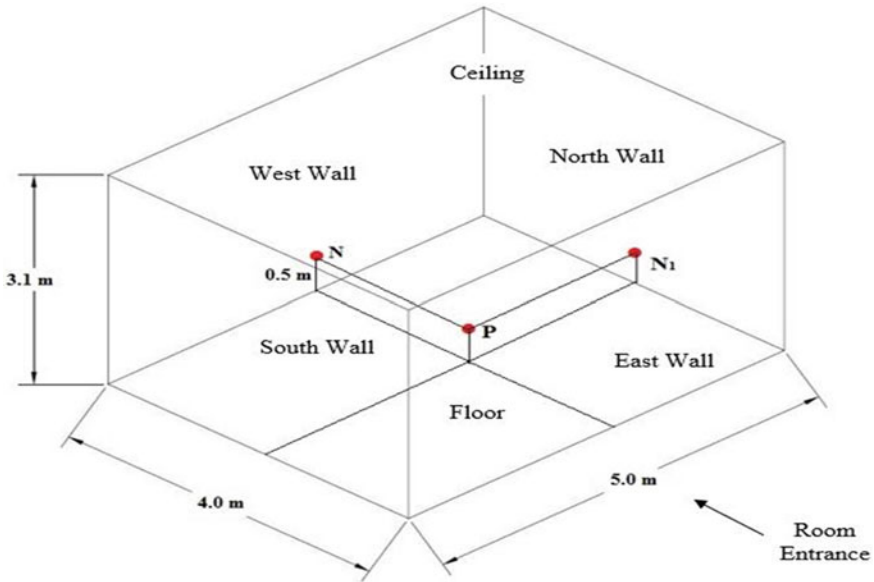
Fig. 7 Schematic drawing of the room

where T_j is the absolute temperature of surface j and $\overline{T_r}$ is the absolute mean radiant temperature.

The same room where experiments are carried out is modeled for thermal comfort analysis taking into considerations effect of radiative, convective and evaporative heat losses (Kuehn et al. 1998). The room dimensions are 5 m long, 4 m wide and 3.1 m high. Consider a person P is seated idle 0.5 m above the floor in the center of an empty room as shown in Fig. 7.

The surface temperature of all four walls of the room and the floor was measured on peak day of April which is found out to be 32 °C, and the temperature of painted ceiling was estimated to be 29 °C.

The following assumptions were made in the heat transfer analysis (Kuehn et al. 1998):

1. Considering unclothed human body as a cylinder with diameter of 0.3 m and length of 1.75 m with DuBois surface area equals to 1.8 m^2 seated quiet 0.5 m above the floor in the center of an empty room.
2. The metabolic heat-generation rate is taken as 1 met which is equal to 58.2 W/m^2.
3. Respiratory heat transfer is neglected, and convective and radiative skin surface areas are set equals, i.e., $A_{sk} = A_R$.
4. The time-averaged normal skin temperature, t_{sk}, in a neutral comfort state was taken as 33.7 °C, and the temperature of the body, t_b was 36.8 °C.
5. The linearized radiative heat transfer coefficient, h_R, is given the value of 4.7 W/m^2 °C by ASHRAE. This value should suffice for normal non-metallic clothing for which emissivity in the infrared spectrum is near 1.0.

6. The average convective coefficient h_C over a body is a function of the position of the person and the relative air-velocity direction and magnitude. The correlation given by Mitchell for a seated person in SI units is,

$$h_c = 8.3 \ V^{0.6} \ \mathrm{W}/\mathrm{m}^{2\,°C} \quad (0.2 \le V \le 4.0) \tag{4}$$

where V is the relative air velocity in the room which is equal to 0.2 m/s for both room configurations. Therefore, the value of computed h_C is equivalent to 3.160 W/m² °C.

7. The mass-transfer coefficient for water vapor, h_E^v, can be evaluated from the convective heat transfer coefficient by using the Lewis relation,

$$h_E^v = \frac{h_C}{L_e c_{pa}} \tag{5}$$

In most of the application, the Lewis number can be set equals to 0.895. Therefore, calculated mass-transfer coefficient for water vapor, h_E^v, will be 3.5132 kg$_a$/m²kJ.

8. The wetted skin surface area is usually given as a fraction of the total skin area, $w = \frac{A_w}{A_{sk}}$. The value for w varies from about 0.06 for normal skin moisture loss to about 0.5 for comfortable conditions, therefore taking average of skin wettedness fraction approximately as 0.3.

The surface of the room can be split into two parts; those at 32 °C and those at 29 °C as shown in Fig. 7. The Eq. (4) can be written as,

$$\overline{T_r} = \left(F_{P-32} T_{32}^4 + F_{P-29} T_{29}^4 \right)^{\frac{1}{4}} \tag{6}$$

The angle factor was computed above and to the right (or left) of point N. The angle factor from the person to the rectangular wall can be determined by drawing a line perpendicular to the wall that intersects point P. This line passes through the wall 0.5 m above the floor and 2.5 m from the end wall and is shown in Fig. 7 as point N. For the combined wall area above and to the right of point N, the value for c equals to the length of the line that passes between P and N. Accordingly, the values of a, b and c in the Eq. (3) are as 2.5 m, 2.6 m and 2 m, respectively, and the angle factor is estimated to be equal to 0.0479. Further, to account for both right and left sides of the wall, the angle factor is 0.096 for the entire wall which is twice the estimated value. Therefore, angle factor, F_{P-32} for all 4 walls and floor which is at 32 °C (F_{P-32}) is computed to be 0.48. The angle factor for ceiling which is at 29 °C (F_{P-29}) can be determined by subtracting the angle factor for the walls and the floor from 1.0 and is computed to be equal to 0.52. Now the mean radiant temperature can be computed from Eq. (6) and is equal to 303.60 K = 30.5 °C. In the similar manner, the mean radiant temperature for unpainted room is calculated with ceiling

Table 2 Comparison of heat transfer rates

Sr. no.	Mode of heat transfer	HT rate (W) painted room	HT rate (W) unpainted room
1	Convection	11.376	2.2752
2	Radiation	27.072	**−4.230**
3	Evaporation	81.850	80.439
4	Net heat transfer	120.3	78.5

temperature of 36.2 °C. The computed mean radiant temperature was found out to be 307.4 K = 34.2 °C.

5.1 Determination of Heat Transfer Rates

A skin temperature of 33.7 °C and dew-point temperature of 21.5 °C, the values of $W_{s,sk}$, $W = W_{s,21.5°C}$ and $h_{fg,sk}$ were computed to be 0.03406 kg_w/kg_a, 0.016245 kg_w/kg_a and 2421.79 kJ/kg_w respectively (Kuehn et al. 1998).

The heat transfer rate with the skin of an unclothed body is calculated neglecting the respiratory heat transfer, and setting the convective and radiative skin surface areas equal, using the experimentally measured DBT and WBT as 31.7 °C and 24.4 °C, respectively and estimated mean radiant temperature as 30.5 °C.

Similarly, the heat transfer rates are also calculated for unpainted room configuration using the values as:

The computed mean radiant temperature = 34.2 °C
Measured dry-bulb temperature = 33.3 °C
Measured wet-bulb temperature = 25 °C
The dew-point temperature computed as per DBT and WBT is 21.8 °C.

Table 2 summarizes the comparison between heat transfer rates of both painted and unpainted room configurations.

It can be seen that heat loss by evaporation is almost same in both the cases which quite obvious and expected; however, heat loss by convection is significantly higher, almost 80% in painted surface. Further, the most remarkable difference is that there is heat gain at the rate of 4.23 W by radiation in the unpainted room as the value is negative. The net heart transfer is 53.2% higher in painted room in comparison to unpainted room which makes person thermally comfortable in painted room.

6 Conclusion

Passive cooling technique with reflective painted roof using THERMOROOF paint is done in a chosen room. The study demonstrates that there is appreciable drop in average roof surface temperature after THERMOROOF paint, in the range from 28 to 35% on daily and monthly basis, respectively. This leads to reduction in room temperature by 2.2 °C.

Steady-state human thermal comfort analysis considering single occupant was also carried taking into account the convective, radiative and evaporative heat transfer. Heat gain at the rate of 4.23 W by radiation in the unpainted room is observed. The net heart transfer is 53.2% higher in painted room in comparison to unpainted room which makes person thermally comfortable in painted room.

References

Akbari H, Levinson R, Berdahl P (1996) ASTM standards for measuring solar reflectance and infrared emittance of construction materials and comparing their steady-state surface temperatures. ACEEE Summer Study Energy Efficiency Build 1:1–9

Al-Obaidi KM, Ismail M, Abdul Rahman AM (2014) Passive cooling techniques through reflective and radiative roofs in tropical houses in Southeast Asia: a literature review. Front Architect Res 3:283–297

De Masi RF, Ruggiero S, Vanoli GP (2018) Acrylic white paint of industrial sector for cool roofing application: experimental investigation of summer behavior and aging problem under Mediterranean climate. Sol Energy 169:468–487

Ganguly A, Chowdhury D, Neogi S (2016) Performance of building roofs on energy efficiency—a review. Energy Procedia 90:200–208

Geetha NB, Velraj R (2012) Passive cooling methods for energy efficient buildings with and without thermal energy storage—a review. Energy Educ Sci Technol Part A: Energy Sci Res 29:913–946

Harind Chemicals and Pharmaceuticals, no. 22 (2021)

Kolokotroni M, Shittu E, Ramowski L, Mollard A, Rowe K, Wilson E, Filho J, Novieto D (2018) Cool roofs: high tech low cost solution for energy efficiency and thermal comfort in low rise low income houses in high solar radiation countries. Energy Build 176:58–70

Kuehn T, Ramsey J, Threlkeld J (1998) Thermal environmental engineering, 3rd edn. Prentice-Hall, Inc., pp 332–346

Panchabikesan K, Vellaisamy K, Ramalingam V (2017) Passive cooling potential in buildings under various climatic conditions in India. Renew Sustain Energy Rev 78:1236–1252

Pisello AL (2017) State of the art on the development of cool coatings for buildings and cities. Sol Energy 44:660–680

Santamouris M, Pavlou K, Synnefa A, Niachou K, Kolokotsa D (2007) Recent progress on passive cooling techniques advanced technological developments to improve survivability level in low-income households. Energy Build 39:859–866

Uemoto KL, Sato NMN, John VM (2010) Estimating thermal performance of cool colored paints. Energy Build 42:17–22

Strain-Engineered Electronic and Thermoelectric Properties of Two-Dimensional SnGe

Hardik L. Kagdada, Vaishali Sharma, Ajit Kumar Parwani, and Dheeraj K. Singh

Abstract The electronic structure and thermoelectric transport of novel two-dimensional SnGe along with compressive and tensile strain (up to 3%) were investigated using density functional theory (DFT) calculations and electronic Boltzmann transport equations. At 0% strain, 0.23 eV direct band gap is obtained. For the tensile strain, a direct bandgap of SnGe is conserved. However, in the case of compressive strain, direct-to-indirect bandgap and semiconducting to metallic transition are observed. The change in electronic nature affected the thermoelectric properties of 2D SnGe. The semiconducting nature of the SnGe monolayer for tensile strain shows high Seebeck coefficients. At the high temperature of 600 K, the highest value power factor of 72.91×10^9 W/mK^{2}s is achieved for 2% tensile strain. Present calculation suggests a promising pathway for SnGe-based thermoelectric materials for heat energy utilization.

Keywords Thermoelectric · Heat energy harvesting · Two-dimensional materials · Electronic properties

H. L. Kagdada · D. K. Singh (✉)
Department of Basic Sciences, Institute of Infrastructure Technology Research and Management (IITRAM), Ahmedabad 380026, India

H. L. Kagdada
e-mail: hardik.kagdada.19pp@iitram.ac.in

V. Sharma
Department of Physics, Indian Institute of Technology Bombay, Mumbai 400076, India

A. K. Parwani
Department of Mechanical and Aero-Space Engineering, Institute of Infrastructure Technology Research and Management (IITRAM), Ahmedabad 380026, India

1 Introduction

Thermoelectric materials have attained a tremendous development in applications like waste heat harvesting, Peltier refrigeration, radio-isotope thermoelectric power generation, etc. ascribed to their direct heat residual conversion to electrical energy ability arising from industries (Harman et al. 2002; Toberer 2008; Qurashi 2014; Poehler 2016). Thermoelectric materials grasped their attention toward several car companies like BMW (LaGrandeur et al. 2006), Honda (Mori et al. 2011), Ford (Hussain et al. 2009) for heat energy utilization. The efficiency of thermoelectric materials is measured through a dimensionless quantity, namely the figure of merit (ZT), which is given by the equation: $ZT = \frac{S^2 \sigma T}{\kappa}$, where S, σ and κ denote Seebeck coefficient, electrical and thermal conductivity, respectively. The quantity $S^2 \sigma$ and κ is known as the power factor and total thermal conductivity. κ consists of the contribution from lattice structure and electronic part. However, from the perspective of potential utilization of thermoelectric materials, the major concern for the research society is to improve thermoelectric efficiency through the heat conversion process of various developed thermoelectric materials. In recent years, significant attention has been dedicated to the two-dimensional group-IV materials due to their extraordinary physical properties with potential applications in various fields (Pan et al. 2011; Wang and Ding 2016; Suzuki 2010; Yu et al. 2015; Wang et al. 2015; Zhao et al. 2016; Zhang et al. 2015). Among them, chalcogenides based on tin (Sn) presents better thermoelectric properties with efficiency in the range of 0.5–2.5 at higher temperatures (Zhao et al. 2016). The two-dimensional SnGe comprises a low-buckled structure similar to silicene and germanene (Wang and Ding 2016; Zhou et al. 2013; Sahin et al. 2009), with a gapped Dirac-like band structure (Wang and Ding 2016; Sante et al. 2015). To modulate thermoelectric properties, it is noticed that strain engineering presents an effective way. Up to now, the thermal transport properties of two-dimensional SnGe are rarely studied. Concerning the flexible structure of SnGe along with considerable bandgap and high average atomic mass, it is probable to possess better thermoelectric performances.

It is noticed that efficiency measured through the ZT is not the solely concerned variable for real-world utilization, the output power is undeniably significant as equal as the efficiency (Liu et al. 2015). On the other hand, the output power is further essential for free and limitless heat sources like solar heat, industrial waste heat, automobiles (Liu et al. 2015) etc. The parameters electrical conductivity and Seebeck coefficient can be altered freely in nanomaterials through adjusting the density of states (DOS), which further improves the output power or power factor (PF). Motivated with these facts, the present study focuses on the electronic and transport properties of two-dimensional SnGe in the framework of first-principle-based DFT calculations. To explore the modification of the aforementioned properties, SnGe with both compressive and tensile strain up to 3% is further investigated.

2 Computational Methodology

Density functional theory (DFT) has been utilized to calculate the total energy and electronic properties of the two-dimensional SnGe. The exchange and correlation functional have been considered in the vicinity of the generalized gradient approximation (GGA) (Perdew et al. 1996). Ionic minimization converged through Broyden–Fletcher–Goldfarb–Shanno (BFGS) method, with energy convergence criteria of 10^{-4} Ry (Giannozzi et al. 2009, Head et al. 1985). The Brillouin zone (BZ) has been mapped using Monkhorst–Pack k-mesh with a grid of $13 \times 13 \times 1$. The Kohn–Sham equation was solved under the convergence threshold of 10^{-8} Ry for electronic minimization. Semi-empirical Boltzmann transport equations were utilized to obtain the electronic part of thermoelectric coefficients, which were illustrated in the BOLTZTRAP distribution (Madsen et al. 2006).

3 Results and Discussion

3.1 Structural Analysis

The structure of SnGe monolayer, where the unit cell contains two atoms in the hexagonal structure, is presented in Fig. 1a. The monolayer SnGe exhibits the buckled structure having 0.81 Å buckling height, while the bond length between Sn and Ge atoms, is 2.61 Å, which is in the range of previously reported monolayer SiGe (Sharma et al. 2019). Further, mechanical strain (compressive and tensile) is applied up to 3% on the unit cell of monolayer SnGe. Figure 1b shows the bond length of Sn-Ge, as a function of applied strain.
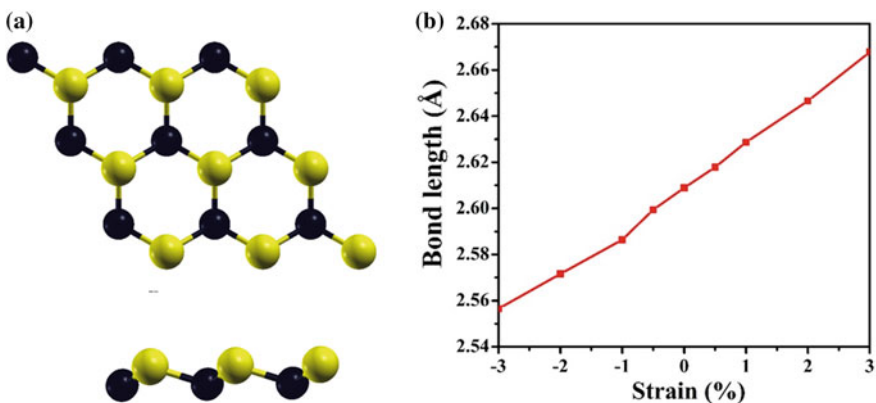
Fig. 1 a 2×2 supercell presentation of monolayer SnGe. Yellow- and black-colored spheres represent the Ge and Sn atoms; **b** bond length between Sn and Ge as a function of applied strain. Positive and negative values on the x-axis determined the tensile and compressive strain, respectively

Along the plane of the unit cell, the compressive strain results in the stretching of the bond between Sn and Ge, while compressive strain results in the reduction of bond length. Such reduction of bond length from their equilibrium geometry might have an impact on electronic properties such as bandgap. Therefore, it is important to understand the electronic properties of monolayer SnGe with applied mechanical strain. Practically, the two-dimensional materials are fabricated on substrates, which causes the lattice mismatching and generates the strain in the material, which further influences the properties of materials.

3.2 Electronic and Thermoelectric Properties

The fundamental physical quantities like the nature of the bandgap, electronic transitions, charge carrier mass, mobility, etc. can be understood from the energy band diagram. Figures 2 and 3 present the strain-induced electronic band structure for monolayer SnGe. Here, 3% compressive and tensile strains along the plane of the monolayer have been applied. At the 0% strain, i.e., equilibrium geometry, the bandgap for monolayer SnGe is 0.23 eV, while a similar group of material, SiGe monolayer, exhibits the metallic nature (Sharma et al. 2019). Further, the band edges are located at the high symmetry point **K**, which suggests the direct nature of the bandgap.

For the tensile strain up to 3%, it should be noted that the energy levels of valence band maximum (VBM) and conduction band minima (CBM) are slightly increasing and preserved the direct nature bandgap. Moreover, as shown in Fig. 2, no band closing is observed for applied tensile strain. However, in the case of compressive strain (see Fig. 3), the two important bandgap transitions were observed: (i) direct-to-indirect bandgap transition and (ii) the transition from semiconducting state to metallic nature. Here, it is noticed that increasing the compressive strain up to 3% results in the faster increase of the energy of the valence band at the zone center (Γ) than the **K**. Simultaneously, the energy of the conduction band at the **K** point of the BZ decreases with increasing the strain and crosses the Fermi energy, which depicts the metallic nature at 3% compressive strain. This shows semiconducting to metallic transition. Further, VBM shifted at the Γ point under the compressive strain, which results in a mismatch of the VBM and CBM (at Γ and **K**, respectively), which illustrates the indirect bandgap nature (Fig. 3). Similar nature of bands was also observed for other materials such as Bismuth-based 2D materials under the applied strain (Pillai et al. 2018). Modification in the electronic bands and bandgap results in the far tuning of thermoelectric coefficients.

Therefore, in the present work, we have calculated the electronic transport coefficients and presented them in Fig. 4 with applied strain. Here, due to metallic nature at 3% compressive strain, the Seebeck coefficient is very low in the whole studied temperature range, while for the tensile strain it maximizes up to -250.39 μV/K. The semiconducting nature of the monolayer SnGe for tensile strain exhibits the
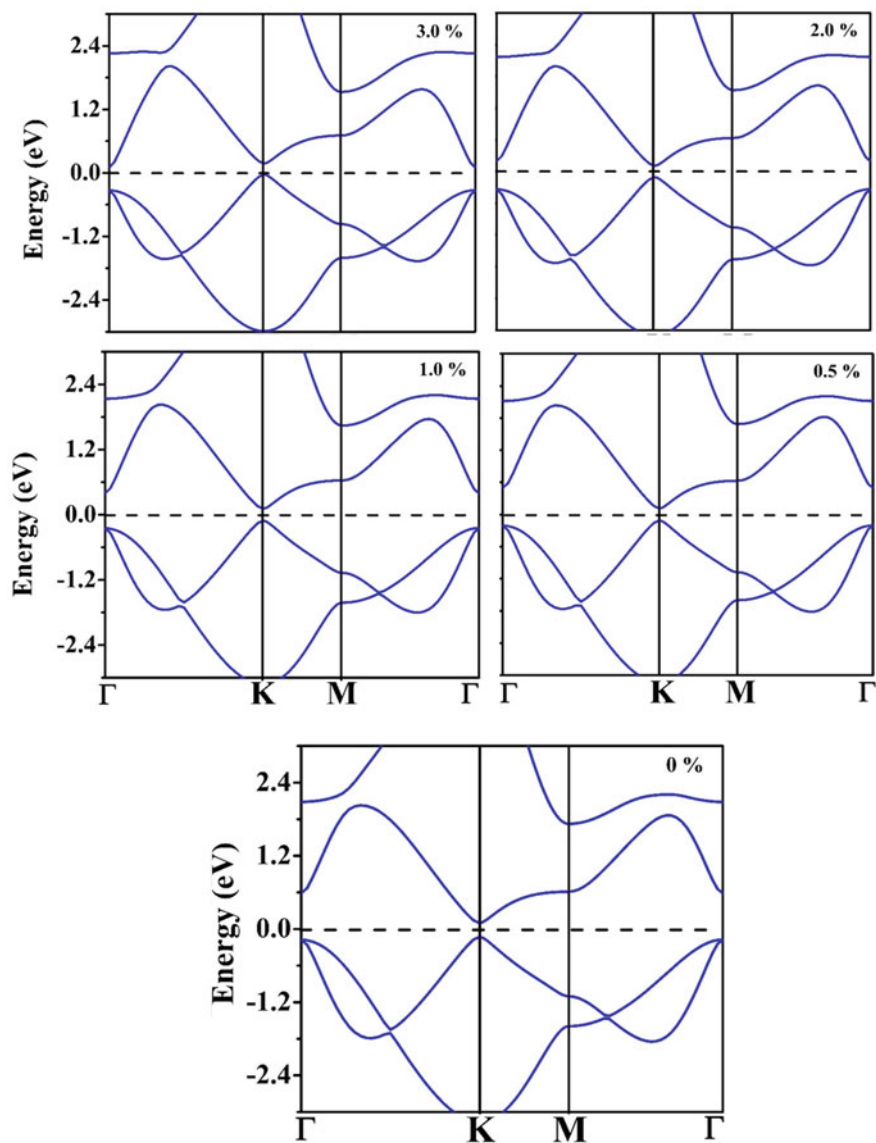
Fig. 2 Tensile strain-induced electronic band structure of monolayer SnGe up to 3.0%. The dashed line presents the Fermi level. The lower panel shows the band structure for 0% strain
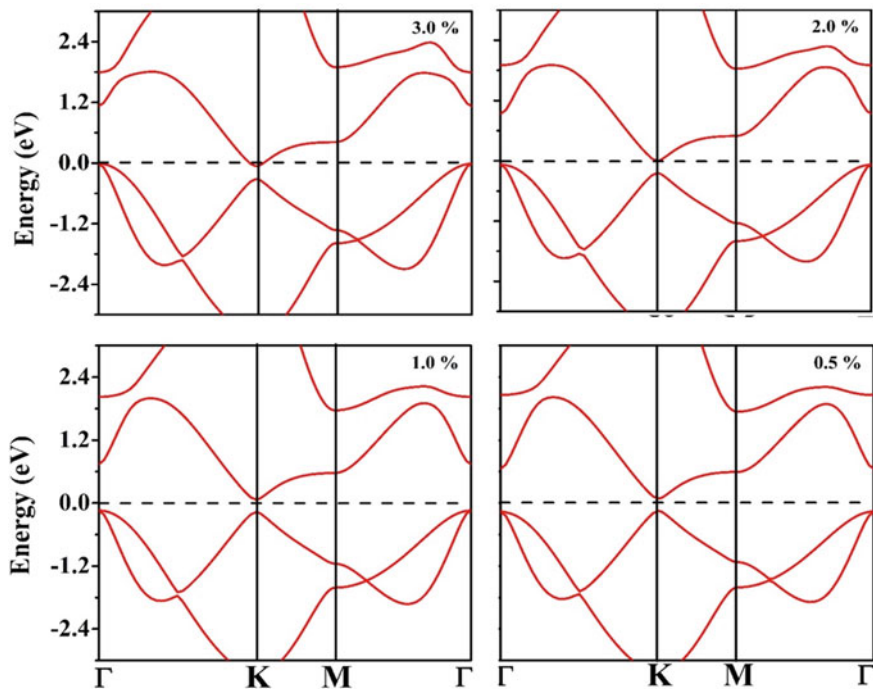
Fig. 3 Electronic band structure of monolayer SnGe for compressive strain up to 3.0%. Fermi level is denoted by dashed lines

large value of Seebeck coefficients. Moreover, the negative value the S in the mono-layer SnGe reveals the majority charge transfer by the electrons. We calculated the electrical conductivity (σ/τ) and the thermoelectric power factor ($S^2\sigma/\tau$), in terms of the relaxation time (τ), which is the limitation of the solution of the Boltzmann transport equation. Due to its metallic nature, the electrical conductivity is higher for 3% compressive strain and increases constantly with the temperature. While for other applied strains, the electrical conductivity first decreases and then increases with the temperature, which confirms the semiconducting nature of monolayer SnGe. Further, the obtained electrical conductivity for equilibrium geometry and other applied strain is in the range for good thermoelectric material, due to highly dispersive bands at the VBM and CBM, which results in the smaller value of effective mass and leads to the faster movements of charge carriers. The power factor is not only important for the increment in thermoelectric figure of merit but also leads to the significant contribution in output power of thermoelectric devices such as converting the solar heat energy to electricity (Kim et al. 2017). Therefore, the temperature and applied strain are important parameters to understand the nature of the thermoelectric power factor (Fig. 4). For the equilibrium geometry, the calculated power factor is higher than the applied strain, while it almost vanishes for the 3% compressive strain. The highest value of power factor 72.91 $\times$ 10^9 W/mK^{2}s, at 600 K is obtained for
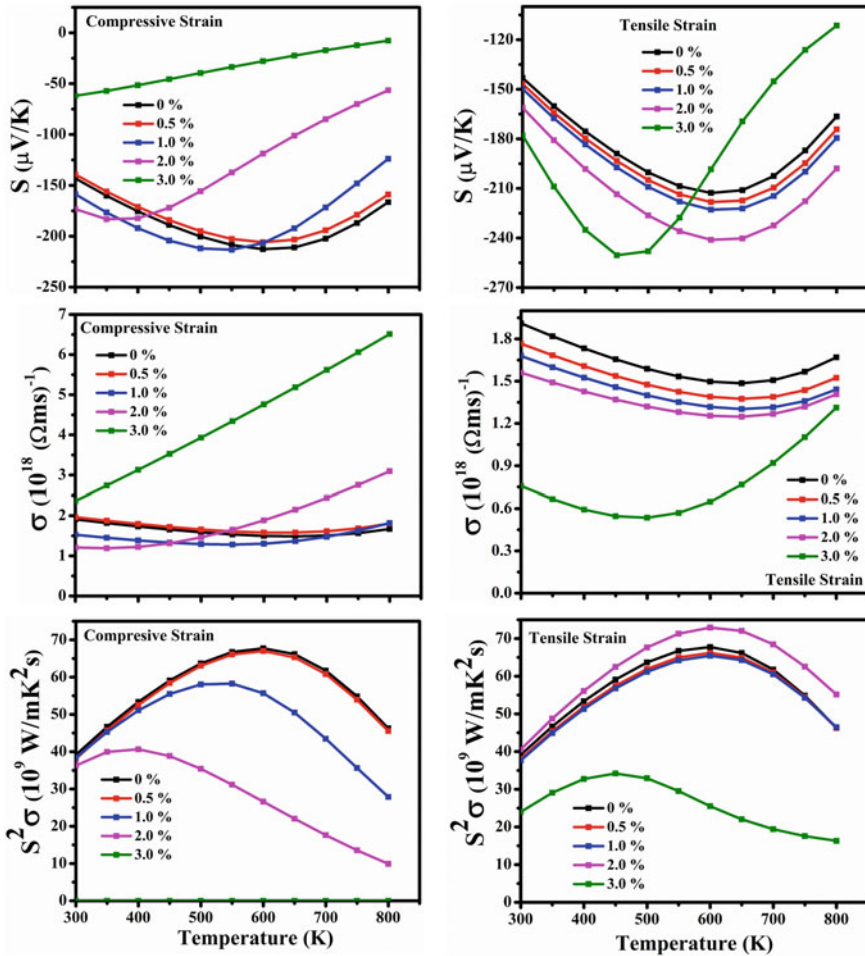
Fig. 4 Thermoelectric parameters: Seebeck coefficient (S) (upper row), electrical conductivity (σ/τ) (middle row) and thermoelectric power factor ($S^2\sigma/\tau$) (lower row) for compressive (left column) and tensile strain (right column)

2% tensile strain. However, at the room temperature, all the applied strain exhibits similar values, which is due to the similar bandgap, except for the 3% compressive and tensile strain. Such a large value of power factor for tensile strain is due to the larger S, which is originated from the bandgap of monolayer SnGe. Therefore, the present work depicts that the monolayer of SnGe might be capable of the waste heat conversion, and the application of mechanical strain further reveals the tuning of electronic and thermoelectric properties. Additionally, the applied strain on such monolayer results in the desired range of properties for heat energy utilization such as in the car, or heavy machinery.

4 Conclusions

We have analyzed the structural properties, electronic bands and thermoelectric transport coefficients of monolayer SnGe by utilizing the DFT calculations. The electronic and thermoelectric parameters are tuned through the applied mechanical strain. For compressive strain up to 3%, the monolayer SnGe shows the closing of the band gap and reveals the metallic nature. However, for the tensile strain, no bandgap closing is observed. The compressive strain reveals the direct to indirect bandgap transition in monolayer SnGe. Thermoelectric analysis with the applied mechanical strain reveals the highest value of magnitude of Seebeck coefficient (250.39 μV/K) for tensile strain, which further results in the larger value of thermoelectric power factor. The present study suggests the engineering of the thermoelectric coefficients of monolayer SnGe to be a potential candidate for heat energy harvesting from industries and complex engines.

References

Giannozzi P, Baroni S, Bonini N, Calandra M, Car R, Cavazzoni C, Ceresoli D, Chiarotti GL, Cococcioni M et al (2009) Quantum ESPRESSO: a modular and open-source software project for quantum simulations of materials. J Phys Condens Matt 21:395502

Harman TC, Taylor PJ, Walsh MP, LaForge BE (2002) Quantum dot super lattice thermoelectric materials and devices. Science 297:2229–2232

Head JD, Zener MC (1985) A Broyden—Fletcher—Goldfarb—Shanno optimization procedure for molecular geometries. Chem Phys Lett 122:264–270

Hussain QE, Brigham DR, Maranville CW (2009) Thermoelectric exhaust heat recovery for hybrid vehicles. SAE Int J Engines 2:1132–1142

Kim H, Anasori B, Gogotsi Y, Alshareef HN (2017) Thermoelectric properties of two-dimensional molybdenum-based MXenes. Chem Mater 29:6472–6479

LaGrandeur J, Crane D, Hung S, Mazar B, Eder A (2006) International conference on thermoelectrics 343

Liu W, Kim HS, Chen S, Jie Q, Lv B, Yao ML, Ren ZS, Opeil CP, Wilson S, Chu CW, Ren ZF (2015) n-type thermoelectric material $Mg_2Sn_{0.75}Ge_{0.25}$ for high power generation. Proc Natl Acad Sci USA 112:3269–3274

Madsen GKH, Singh DJ (2006) Boltztrap. A code for calculating band-structure dependent quantities. Comput Phys Commun 175:67–71

Mori M, Yamagami T, Sorazawa M, Miyabe T, Takahashi S, Haraguchi T (2011) Simulation of fuel economy effectiveness of exhaust heat recovery system using thermoelectric generator in a series hybrid. SAE Int J Mater Manuf 4:1268–1276

Pan L, Liu HJ, Wen YW, Tan XJ, Lv HY, Shi J, Tang XF (2011) First-principles study of monolayer and bilayer honeycomb structures of group-IV elements and their binary compounds. Phys Lett A 375:614

Perdew JP, Burke K, Ernzerhof M (1996) Generalized gradient approximation made simple. Phys Rev Lett 77:3865

Pillai SB, Dabhi SD, Narayan S, Jha PK (2018) Strain effect on electronic and lattice dynamical behavior of two dimensional Bi, BiAs and BiSb. AIP Conf Proc 1942:090022

Poehler TO (2016) Innovative thermoelectric materials: polymer. world scientific, nanostructure and composite thermoelectrics

Qurashi A (2014) Metal chalcogenide nanostructures for renewable energy applications. Wiley

Sahin H, Cahangirov S, Topsakal M, Bekaroglu E, Akturk E, Senger RT, Ciraci S (2009) Monolayer honeycomb structures of group-IV elements and III-V binary compounds: first-principles calculations. Phys Rev B 80:155453

Sante DD, Stroppa A, Barone P, Whangbo M-H, Picozzi S (2015) Emergence of ferroelectricity and spin-valley properties in two-dimensional honeycomb binary compounds. Phys Rev B 91:161401

Sharma V, Kagdada HL, Jha PK, Śpiewak P, Kurzydłowski KJ (2019) Halogenation of SiGe monolayer: robust change in electronic and thermal transports. Phys Chem Chem Phys 21:19488–19498

Suzuki T, Yokomizo Y (2010) Energy bands of atomic monolayers of various materials: possibility of energy gap engineering. Phys E 42:2820–2825

Toberer ES, Snyder GJ (2008) Complex thermoelectric materials. Nat Mater 7:105–114

Wang FQ, Zhang S, Yu J, Wang Q (2015) Thermoelectric properties of single-layered SnSe sheet. Nanoscale 7:15962–15970

Wang Y, Ding Y (2016) Electronic structure and topological features of tin-based binary nanosheets and their hydrogenated/fluorinated derivatives: a first-principles study. Appl Surf Sci 382:1–9

Yu WZ, Yan JA, Gao SP (2015) Band gap characters and ferromagnetic/antiferromagnetic coupling in group-IV monolayers tuned by chemical species and hydrogen adsorption configurations. Nanoscale Res Lett 10:351

Zhang S, Zhou J, Wang Q, Chen X, Kawazoe Y, Jena P (2015) Penta-graphene: a new carbon allotrope. Proc Natl Acad Sci USA 112:2372–2377

Zhao L-D, Tan G, Hao S, He J, Pei Y, Chi H et al (2016) Ultrahigh power factor and thermoelectric performance in hole-doped single-crystal SnSe. Science 351:141–144

Zhao T, Zhang S, Guo Y, Wang Q (2016) TiC_2: a new two-dimensional sheet beyond MXenes. Nanoscale 8:233–245

Zhou H, Zhao M, Zhang X, Dong W, Wang X, Bu H, Wang A (2013) First-principles prediction of a new dirac-fermion material: silicon germanide monolayer. J Phys Condens Matter 25:395501

Techno-Economic Assessment of IGCC Power Plant Retrofitted with Chemical Looping Combustion for Carbon Capture

Pulkit Kumar and Ajit Kumar Parwani

Abstract Chemical looping combustion (CLC) is the most promising technology for decreasing power plant carbon dioxide (CO_2) emissions. Due to the high expense of implementing this technology on a broad scale, it is still in the development stage. This study analyzes the cost and performance of power plants retrofitted with CLC using an integrated environmental control model (IECM). It was discovered that increasing the air and fuel reactor temperatures enhanced net plant efficiency by 11.3% and 12.93%, respectively. Additionally, it was also found that the gasifier used to convert coal to syngas incurred significant operational and maintenance costs. Increases in the temperature of the gasifier resulted in a 1.6% decrease in total plant efficiency, resulting in a 3.2\$/MWh increase in energy costs. As a result, it is recommended that it must be changed or modified to enhance the plant's efficiency.

Keywords Economic assessment · IGCC · IECM · CLC

1 Introduction

The increasing percentage of anthropogenic carbon dioxide (CO_2) emissions, as well as its evident consequences such as climate change and global warming, makes it necessary for researchers to build a reliable clean technology. Fossil fuel-burning power plants, industries, transportation, and agriculture are all substantial sources of CO_2 emissions (IPCC 2014). CO_2 emissions from coal-fired power stations are the highest among these sources (Global energy and CO2 status report 2019). To reduce the cost of CO_2 separation, a number of novel or enhanced CO_2 capture systems have been developed or are being built to remove CO_2 from the stream of combustion gases from power plants. Solvent absorption, solid adsorption, gas–solid looping processes, and membrane selective transport are all used in such systems to separate chemical and physical gases. The end goal is the same in all cases: to produce a filtered stream of high-pressure CO_2 that can be transported and stored

P. Kumar · A. K. Parwani (✉)
Institute of Infrastructure Technology, Research And Management, Ahmedabad, India
e-mail: ajitkumar.parwani@iitram.ac.in

permanently at a lower cost than present technology. Chemical looping combustion (CLC) is an energy-efficient process that uses an air and fuel reactor to extract CO_2 from flue gas (Richter and Knoche 1983; Ishida et al. 1987). The air reactor oxidizes a metal (also known as an oxygen carrier) to metal oxide, which then reduces to metal in the fuel reactor, releasing oxygen for combustion. This reduced metal is then delivered to an air reactor, where it will be used as an oxygen carrier for the fuel reactor once again. This is a relatively new concept in the form of simple condensation that can directly extract pure CO_2. CLC additionally minimizes NOx production since coal combustion occurs in a fuel reactor with just oxygen (Jin et al. 1998). Various researchers are working on CLC to improve its technical development and maturity (Hossain and Lasa 2008). Although a technical understanding of CLC technology is critical, it is also critical to comprehend the system's economics to make it practicable on a broad scale. The economic analysis provides an estimate of the capital, operational, and CO_2 capture costs using CLC technology. There is an economic analysis of various carbon capture systems in the literature (Cormos and Cormos 2017), but it is limited for CLC. Olaleye and Wang (2014) conducted an economic analysis of a 50 MWth power plant using a humid air turbine (HAT) for a CLC system. Their research, on the other hand, focused on estimating the payback time. According to their findings, the CLC-HAT plant had a payback period of about 6 years, which was shorter than the payback period of typical power plants of equal capacity. In their analysis, the cost of energy (COE) and the cost of CO_2 collection were not estimated. Lyngfelt and Leckner (2015) conducted cost assessment research for a coal-fired CLC plant using heat and mass balance in order to assess key costs for the plant. They calculated the price of the oxygen carrier, the cost of employing a pump to fluidize the beds, and the cost of compressing CO_2 into liquid. They came to the conclusion that capturing CO_2 for a CLC power plant costs between 16 and 26 Euros per ton. Porrazzo et al. (2016) compared the Levelized COE with the CLC technique for carbon capture in a power plant using post-combustion carbon capture. They calculated using the ASPEN plus modeling tool, taking into account the cost of fuel and the lifetime of the oxygen carrier. They concluded that a power station using CLC technology for carbon capture had a lower Levelized COE than a power plant using amines as an absorbent.

The preceding literature addresses the economics of the CLC power plant based on parameter analysis. However, no economic analysis of CO_2 capture for a power plant operating on an Integrated Gasification Combined Cycle (IGCC) retrofitted with CLC has been carried out. High-pressure gasifiers are used in IGCC power plants to convert coal into synthetic gas, primarily hydrogen and carbon monoxide. The economic study of the IGCC power plant retrofitted with CLC was performed in this paper. The Integrated Environmental Control Model (IECM) was used to determine the effect of air reactor, fuel reactor, and gasifier temperature on efficiency and COE.

2 Methodology

The IECM developed by Carnegie Mellon University, USA (version 11.4), is used to simulate a CLC retrofitted IGCC power plant (Integrated Environmental Control Model (IECM) 2014). IECM models CCS-equipped pulverized coal (PC), natural gas combined cycle (NGCC), and IGCC plants. The IECM can do systematic calculations of the performance, emissions, and cost of power generation from a fossil-fueled power plant retrofitted with various carbon capture devices.

Table 1 provides details on the power plants under consideration for this investigation. The gross electrical output of the power station is 206.6 MWg with a capacity factor of 75%. Gross electrical output displays the generators' gross power output without supplementary power consumption, while the capacity factor indicates the corresponding percentage of full load in one year. Coal is considered a low-sulfur coal costing 75 $/ ton. The CLC is utilized for the carbon capture of which Table 2 shows technical specifications. Nickel oxide (NiO) is chosen as an OC. These metal oxides are usually paired with an inert substance that acts as porous support for a greater surface reaction area. Inert material also serves as a binder to increase mechanical strength and attrition resistance. Aluminum oxide (Al_2O_3) is employed as an inert material because NiO and Al_2O_3 solid particles have good fluidization and high

Table 1 Assumed parameters for power plant (Porrazzo et al. 2016)

Gross electrical output (MWg)	206.6
Capacity factor (%)	75
Ambient air temperature (dry bulb average) (°C)	28
Ambient air pressure (bar)	1
Relative humidity (average) (%)	54.9
Plant life (in years)	30
Coal cost ($/ton)	75
Internal electricity price ($/MWh)	38.2
Land use cost ($/acre)	3000

Table 2 Assumed parameters for CLC

Metal oxide (MeO) Type	NiO
Inert support material	Al_2O_3
Air reactor temperature (°C)	900
Superficial gas inlet velocity (m/sec)	7.004304 m/s
Residence time of solids (seconds) in air reactor	5
Fuel reactor temperature (°C)	900
Combustion efficiency (%)	99.54
Residence time of solids (seconds) in the fuel reactor	60

thermal stability at a low cost (Ishida et al. 2002; Zhao et al. 2008; Mattisson et al. 2006; Readman et al. 2006). Initially, the air and fuel reactor temperature considered is 900 °C. The velocity of the superficial gas input is 7.004304 m/s and is determined by dividing the volume flow rate of the solid particles by the reactor cross section.

3 Results

All of the factors considered in the preceding section were fed into the simulation as input conditions. The simulation findings were primarily focused on the components used for CLC.

Table 3 shows the power consumption by various auxiliary components of the power plant implemented with CLC. Power consumption is maximum for the air compressor, air separation unit and CLC unit. The air compressor itself consumes 75.25% of the total power required. CLC unit utilizes only 7.8% of the total energy consumed for reducing the emission by 90% almost which is better than other technology of carbon capture.

Figure 1 illustrates the contribution of various components of the power plant toward operation and maintenance costs. The gasifier area has the highest maintenance cost at 42%, followed by the air separation unit at 27%, CO_2 capture at 24%, and sulfur control at 7%. Due to the gasifier's significant contribution and the fact that it requires pure oxygen to convert carbon to syngas, which is an energy-intensive process, the study should focus on decreasing this energy. Additionally, gasifier analysis will assist in reducing the overall operating costs of the plant equipped with CLC. As a result, the effect of adjusting the gasifier temperature on efficiency and cost of power has been determined and displayed in Figs. 2 and 3.

The result shows a decrement in the overall efficiency of the plant by almost 1.6% with an increment in gasifier temperature by 100 °C. Whereas increasing the temperature of the gasifier also caused an increase in the cost of electricity by 3.2$/MWh.

Table 3 Power consumption by various components in a CLC plant

Components of power plant	Consumption of power in MW
Air compressor	228.4
Losses in the turbine shaft	3.050
Miscellaneous power block	5.819
Air separation unit	34.23
Gasifier	3.374
Sulfur capture	2.258
CLC unit	23.96
Cooling tower	2.428
Total power consumed	**303.519**
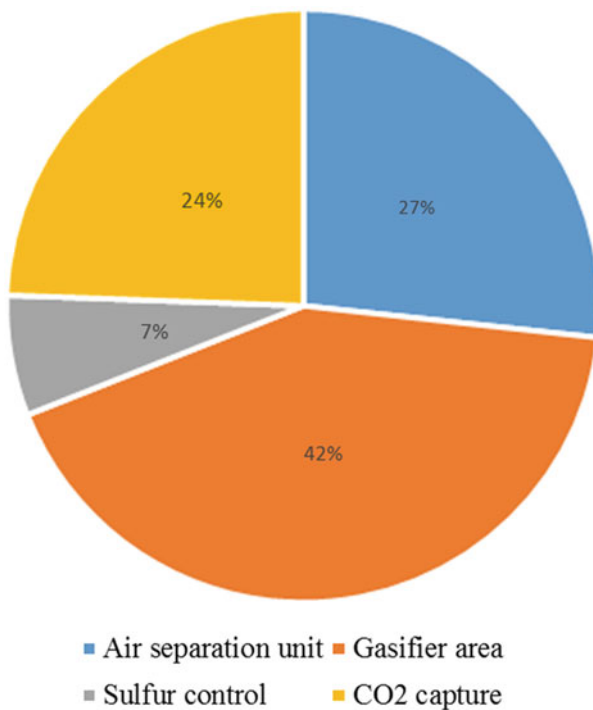
Fig. 1 Cost distribution by different components of the plant
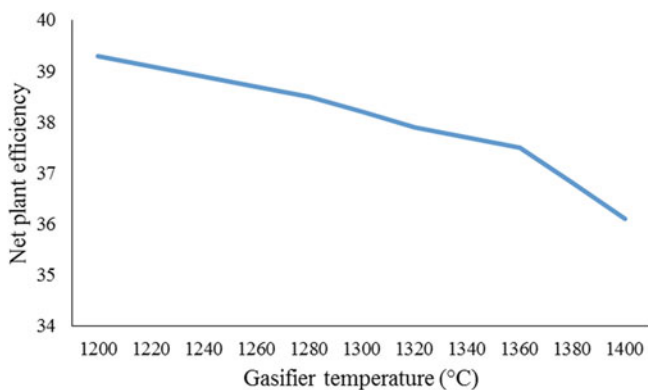
Fig. 2 Effect of gasifier temperature on the efficiency of the plant
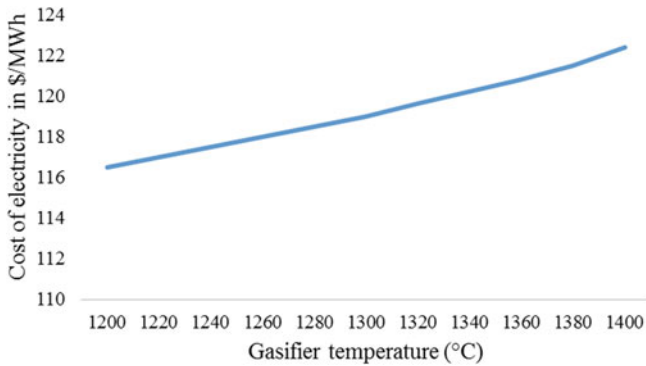
Fig. 3 Change in cost of electricity with gasifier temperature

Therefore, the optimum temperature is needed to design a gasifier where the cost of electricity should not increase by increasing efficiency.

Contribution in operation and maintenance cost of CO_2 capture unit is also significant. As a result, the efficiency and revenue generated by modifying the air reactor and fuel reactor temperatures have been evaluated and are depicted in Figs. 4, 5, 6, and 7. Figure 4 indicates that the plant efficiency rises by 11.3% as the air reactor temperature changes from 900 to 1200 °C. As efficiency is increased, the total revenue required drops by 58.1$/MWh, as illustrated in Fig. 5. This concludes that the air reactor should be operated at a higher temperature of working range.

Figures 6 and 7 show the change in net plant efficiency and total revenue required by increasing the fuel reactor temperature. In this case, also, efficiency increases by 12.93% and total revenue required decreases by 32$/MWh with an increase in fuel reactor temperature from 900 to 1200 °C. Therefore, the fuel reactor should be operated at a higher temperature. However, the effect of the residence time of solids in the air and fuel reactor is neglected.
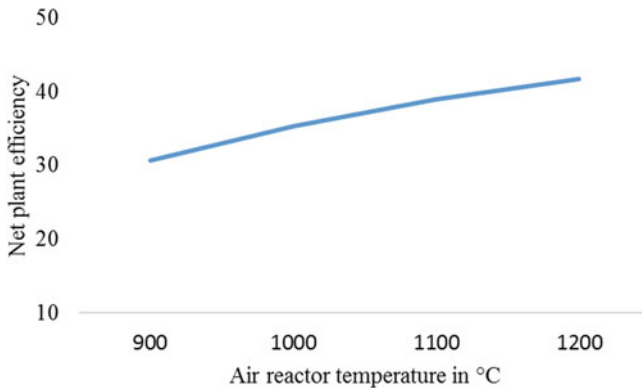
Fig. 4 Effect of air reactor temperature on net plant efficiency
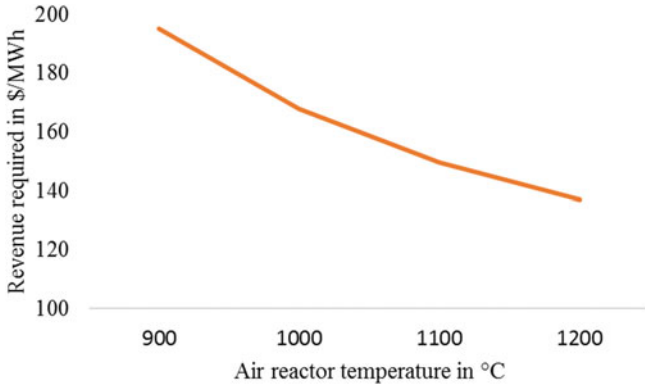
Fig. 5 Effect of air reactor temperature on total revenue required
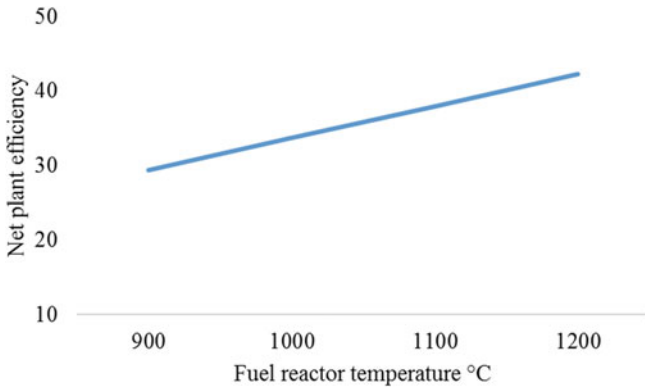
Fig. 6 Effect of fuel reactor temperature on net plant efficiency
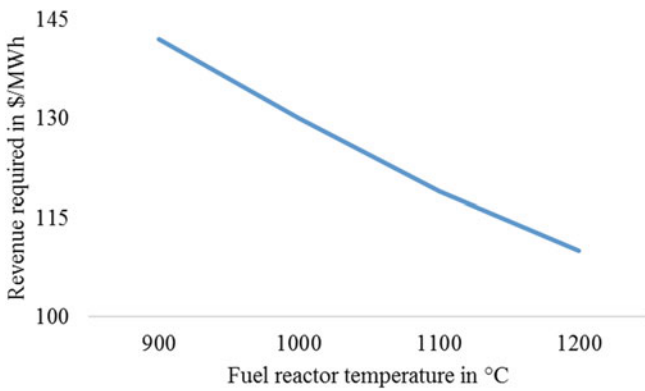
Fig. 7 Effect of fuel reactor temperature on total revenue required

4 Conclusion

Economics analysis of IGCC power plant retrofitted with CLC has been performed using the IECM. The attention has been placed on those components of the power plant that contribute significantly to CLC. The gasifier, air reactor, and fuel reactor were found to have a significant effect on capital cost and COE. As a result, this paper examined the effect of gasifier temperature, air reactor temperature, and fuel reactor temperature on efficiency and COE. The following are the simulation's findings:

1. The CLC unit utilizes 7.8% of the energy required, resulting in a nearly 90% reduction in CO_2 emissions.
2. Increasing the temperature of the gasifier by 100 °C reduced total plant efficiency by 1.6%. This results in a 3.2 $/MWh rise in COE.
3. The overall plant efficiency rose by 11.3% when the air reactor temperature was increased from 900 to 1200 °C. This benefit is also reflected in the required total revenue, which falls by 58.1$/MWh.
4. Reduction of 32$/MWh in total revenue required was also observed by increasing the fuel reactor temperature from 900 to 1200 °C. Overall plant efficiency also increased by 12.93%.

References

Cormos AM, Cormos CC (2017) Techno-economic evaluations of post-combustion CO_2 capture from sub-and super-critical circulated fluidised bed combustion (CFBC) power plants. Appl Therm Eng 127:106–115

Global energy and CO2 status report (2019) https://www.iea.org/reports/global-energy-co2-status-report-2019/emissions (last Accessed 10 May 2021)

Hossain MM, de Lasa HI (2008) Chemical-looping combustion (CLC) inherent CO_2 separations—a review. Chem Eng Sci 63(11):4433–4451

Integrated Environmental Control Model (IECM), Version 8.0; Carnegie Mellon University: Pittsburgh (2012). http://www.cmu. edu/epp/iecm/index.html (Accessed June 2014)

IPCC (2014). Climate change 2014: mitigation of climate change. contribution of working group iii to the fifth assessment report of the intergovernmental panel on climate change Cambridge University Press, Cambridge

Ishida M, Zheng D, Akehata T (1987) Evaluation of a chemical-looping-combustion power-generation system by graphic energy analysis. Energy 12:147–154

Ishida M, Yamamoto M, Ohba T (2002) Experimental results of chemical-looping combustion with NiO/NiAl2O4 particle circulation at 1200°C. Energy Conv Manag 43(9):1469–1478

Jin H, Okamoto T, Ishida M (1998) Development of a novel chemical-looping combustion: synthesis of a looping material with a double metal oxide of CoONiO. Energy Fuels 12(6):1272–1277

Lyngfelt A, Leckner B (2015) A 1000 MWth boiler for chemicallooping combustion of solid fuels-discussion of design and costs. Appl Energy 157:475–487

Mattisson T, Johansson M, Lyngfelt A (2006) The use of NiO as an oxygen carrier in chemical-looping combustion. Fuel 85(5):736–747

Olaleye AK, Wang M (2014) Techno-economic analysis of chemical looping combustion with humid air turbine power cycle. Fuel 124:221–231

Porrazzo R, White G, Ocone R (2016) Techno-economic investigation of a chemical looping combustion based power plant. Faraday Discuss 192:437–457

Readman JE, Olafsen A, Smith JB, Blom R (2006) Chemical looping combustion using $NiO/NiAl_2O_4$: mechanisms and kinetics of reduction-oxidation (Red-Ox) reactions from in situ powder X-ray diffraction and thermogravimetry experiments. Energy Fuels 20(4):1382–1387

Richter H, Knoche KF (1983) Reversibility of combustion processes, efficiency and costing, second law analysis of processes. ACS Symp Ser 235:71–85

Zhao H, Liu L, Wang B, Xu D, Jiang L, Zheng C (2008) Sol-gel-derived NiO/NiAl2O4 oxygen carriers for chemical-looping combustion by coal char. Energy Fuels 22(2):898–905

Design and Development of a Novel Technique for the Maintenance of a Gas Turbine–A Case Study

M. B. Kiran

Abstract Gas turbine is a practical prime mover. Gas turbine assembly consists of compressor, combustion system, power turbine, and integral equipment. Gas turbines are being used in many industry sectors—oil and natural gas, marine, industrial mechanical drives, aerospace, etc. Availability of gas turbine means that the gas turbine should be available whenever its service is required. In order to increase the turbine's availability or uptime, maintenance is done. Thus, maintenance would help in extending the useful service life of a gas turbine. Existing maintenance methods such as preventive and breakdown have many limitations. This has made researchers and practitioners to look for new techniques for maintaining a gas turbine. In this context, reliability-centered maintenance (RCM) assumes special significance. The objective of RCM is to bring down the total maintenance cost. In RCM approach, critical components of a gas turbine are identified, and appropriate maintenance policies are recommended. In the current research work, a novel technique based on RCM is being developed for the maintenance of a gas turbine. MATLAB software is employed for performing analytical network process (ANP) computation, which is required, for identifying the critical components. RCM would help in enhancing gas turbine's availability and will also help in achieving safety of the operators and reliability of the gas turbine. In this context, the current research assumes special significance. The proposed method of maintenance is novel in that it overcomes many of the limitations of the existing approaches. Research findings presented in this paper are going to help academicians, practitioners, and researchers.

Keywords Gas turbine · Maintenance policy selection · Availability · Reliability · Reliability-centered maintenance · FMEA · ANP

M. B. Kiran (✉)
Department of Mechanical Engineering, School of Technology, Pandit Deendayal Energy University, Gandhinagar, Gujarat, India
e-mail: MB.Kiran@sot.pdpu.ac.in

1 Introduction

Today for meeting the customer's expectations, the availability of machines is very much essential. When a gas turbine goes down, it would result in power shut down. This would cause major inconvenience for the customers. If a gas turbine becomes unavailable, then there will be downtime and associated waiting time for its customers. That is, the customer will have to wait for till the gas turbine becomes operational. Amount of waiting time is estimated by the severity of the problem faced by the gas turbine. In this scenario, there will be idle time of the gas turbine and the operator as well. For example, in a manufacturing company, when a gas turbine comes non-functional, it may impact other machines down the manufacturing line. Thus, when a gas turbine becomes non-operational, it would result in affecting the productivity of the manufacturing line. This would result in customer dissatisfaction, and companies will lose its reputation. This clearly shows the significance of properly maintaining a gas turbine. Thus, the productivity of a manufacturing line depends on the availability of gas turbines. For increasing the turbine's availability, selection of a right maintenance policy is very much essential. Selection of right maintenance policy will bring down the maintenance cost of the gas turbine. Additionally, selecting right type of maintenance for a given machine will bring down the workplace-related accidents, and this will enhance employee well-being and comfort level. When a machine becomes available, it would help a machine tool operator in meeting his production targets. Thus, it will make the operator happy and enhance his productivity.

Maintenance can be classified based on time and (Ben et al. 2016; Shayesteh et al. 2018). There is a huge need for reducing the maintenance cost of machines in general and gas turbine in particular. Not much work has been reported in literature, about the economical maintenance of a gas turbine. This has motivated the author in focusing on maintenance of gas turbine. The research findings provide guidelines for selecting maintenance policies for gas turbines.

2 Literature Survey

Aerospace companies have had problems with the conventional maintenance methods, and this has led to the research the emergence of RCM in 1950.

Barlow et al. (1975) and Birnbaum (1969) proposed a technique of identifying components which are significant to a machine. Significant or critical components, when fail, become impossible to meet customer's expectations (Jeyamala et al. 2013). Saaty (1996) has designed a new method called analytic network process (ANP). This method was useful in identifying the critical components. ANP has been employed by many researchers as a decision-making tool (Dorri 2014; Sadeghi and Manesh 2015; Tajadod et al. 2011). A new method was proposed by Moslemi et al. (2017). This technique was used to determine the preventive maintenance schedule for an equipment.

Hamzeh et al. (2015) and Marton et al. (2016) have explored techniques of addressing the maintenance-related problems of an aging distribution system. They have studied in detail of the aging process and its effects on equipment maintenance.

Carnero et al. (2017) have explored electric power systems and proposed right methods for addressing their maintenance problems. Silvestri et al. (2012) have explored a manufacturing industry and designed and developed a maintenance framework for enhancing worker's safety. Wang et al. (2001) have proposed a new technique for evaluating the reliability of a CNC machine in economical manner. Carot et al. (2000) in their study had used non-repairable parts and performed sensitivity analysis for assessing the relative prominence of different parts of a complex network. To overcome the drawbacks of RCM (Alrifaey et al. 2019; Zhou et al. 2016; Liu et al. 2019; Carmignani 2009; Crocker and Kumar 2000; Campbell et al. 2016), a novel method is proposed for selecting the maintenance policy for a gas turbine. Thus, it is evident that RCM technique was not explored for the maintenance of gas turbines. In this context, the current research work becomes very significant. The research outputs are very much useful for both academicians and practitioners in pursuing further research.

3 Methodology

The current research work uses the steps described in the following paragraphs.

3.1 System Selection

In the current research, a gas turbine used in oil and gas processing plant is considered as a case study (power generation 600 MW). Gas turbine (Fig. 1) assembly consists of compressor, combustion system, power turbine, generator, and integral equipment (e.g., fuel, oil, and electrical subsystems) are considered as a system.
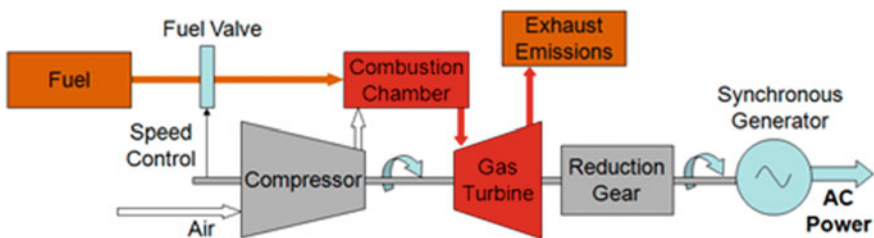
Fig. 1 Gas turbine-based electric power generation

3.2 Analytical Network Process (ANP)

When multiple alternatives exist in a decision, weights can be assigned to each of the alternatives using analytical network process (ANP). That is, ANP would help in classification. Thus, ANP would help in recognizing the critical components. The method was designed by Saaty (1996) in the 1970s. Analytical network process has to follow principles—given problem is set-up in a hierarchical manner, and by paired comparison, relative weights are determined, logical consistency through measurements. MATLAB software is used for making calculations related to ANP process. The technique helps in calculating the weights for different alternatives. The technique makes use of expert's experience in quantifying weights of various decisions through pairwise comparisons. After conducting interviews with experts and based on their feedback, the following criteria clusters are identified: (1) cost: A component is considered critical if it has higher maintenance cost in comparison to other components, (2) complexity: An assembly with large number of components with high failure rates is considered more critical, (3) maintainability: An assembly with large downtime is considered more critical than others, (4) safety: It is important to consider the safety aspect while identifying components which are critical to the functioning of a module, and (5) reliability: It shows the extent to which the equipment is dependable. A more dependable equipment will ensure meeting of the customer expectation in a safe and sustainable way.

ANP consists of the following steps.

Step 1: to calculate the relative importance of each of the five elements—cost, complexity, maintainability, reliability, and safety.

Step 2: computing the relative importance of the components specified.

Step 3: construction of super-matrix that is constructed based on factors and its elements derived from the pairwise comparison.

Step 4: in this step, super-matrix computed in the previous step is multiplied by the priority of the factors.

Step 5: to calculate the inconsistency of the pairwise comparison matrix

$$Compatibility\ Index(CI) = \frac{\lambda max - n}{n - 1} \qquad (1)$$

In Eq. (1), n represents the matrix aspect; the numerator shows the extent of incompatibility existing in the matrix (Birnbaum 1969).

Ratio of compatibility is calculated by using Eq. (2)

$$CR = \frac{CI}{RI} \qquad (2)$$

If CR < = 00.1, matrix is said to be compatible.

Step 6: to calculate the weight of the super-matrix by using the following equation.

$$Aw = \lambda_{max} W \tag{3}$$

where A is the matrix of the paired-comparison, λmax is the maximum eigen value, and W is the eigen vector.

Step 7: normalize the matrix.

Step 8: to calculate the weights of final limit matrix (W).

$$WL = Wr^{2k+1} \tag{4}$$

4 Results and Discussions

The objective of performing the current research is to figure out right maintenance policy for different components of gas turbine used in an electricity generation in oil and gas company. The main problem here is that there are multiple components in a gas turbine, and the company has a maintenance budget. It was not possible to maintain all the components of a gas turbine company within the allocated budget. The company was looking for ways to improve service by maintenance without exceeding maintenance budget. In this context, the present research work assumes special significance.

Current research work uses analytical network process, and steps are described in previous section (Sect. 3, of this paper). For performing the analytical network process, MATLAB software is used. The results of the ANP are given in Tables 1, 2, and 3.

Table 1 shows the criteria-wise pairwise comparison to goal. The table shows the relative importance of the different criteria with respect to each other. In Table 1, G1–G5 are the different criteria identified by experts (G1: cost; G2: maintainability;

Table 1 Pairwise criteria matrix

Goal	G1	G2	G3	G4	G5	Mean	Goal
G1	1	5	0.77	1.25	2.5	2.104	0.226
G2	0.2	1	0.25	1.67	1.43	0.91	0.145
G3	1.3	4	1	2.5	1.25	2.01	0.256
G4	0.8	0.6	0.4	1	1.47	0.85	0.145
G5	0.4	0.7	0.8	0.68	1	0.72	0.228
Total						6.594	1

Table 2 ANP super-matrix (criteria/alternatives)

	Goal	G1	G2	G3	G4	G5	PSM	CBM	PM
Goal	0	0	0	0	0	0	0	0	0
G1	0.226	0	0	0	0	0	0.26	0.25	0.24
G2	0.145	0	0	0	0	0	0.146	0.148	0.145
G3	0.256	0	0	0	0	0	0.156	0.246	0.258
G4	0.144	0	0	0	0	0	0.148	0.146	0.134
G5	0.228	0	0	0	0	0	0.248	0.127	0.235
PSM	0.3	0	0	0	0	0	0.3	0.3	0.3
CBM	0.4	0	0	0	0	0	0.4	0.4	0.4
PM	0.2	0	0	0	0	0	0.2	0.2	0.2

Table 3 Weights—super-matrix (W)

	Goal	G1	G2	G3	G4	G5	PSM	CBM	PM
Goal	0	0	0	0	0	0	0	0	0
G1	0	0.226	0.226	0.226	0.226	0.226	0	0	0
G2	0	0.24	0.24	0.24	0.24	0.24	0	0	0
G3	0	0.34	0.34	0.34	0.34	0.34	0	0	0
G4	0	0.04	0.04	0.04	0.04	0.04	0	0	0
G5	0	0.12	0.12	0.12	0.12	0.12	0	0	0
PSM	0.3	0	0	0	0	0	0.3	0.3	0.3
CBM	0.4	0	0	0	0	0	0.4	0.4	0.4
PM	0.2	0	0	0	0	0	0.2	0.2	0.2

G3: complexity; G4: reliability; G5: safety). Experts selected are seniors working in different departments of the oil and gas company. Five experts are chosen for the current research work. Information is obtained from experts by conducting interviews.

Inconsistency ratio was determined, and compatibility was ensured. Similarly, pairwise criteria matrix steps give the other columns of the super-matrix (Eq. 3). Table 2 shows the super-matrix for criteria and alternatives. This is obtained by using Eq. (3). All these calculations were done using MATLAB software. After prioritization of criteria and alternatives, decision tree was implemented to select the maintenance policy for the different failure modes. Table 4 shows the failure modes, its ranking, and the maintenance policy. Failure modes with top ranking will attract condition-based maintenance. As, these failure modes would result in severe ill-effects.

Table 4 Selection of maintenance policies

Failure mode	Rank	Type of maintenance policy
Temperature transmitter	5	CBM
Transmitter and other control valves	6	PSM
Heater	7	PSM
Control system	9	CM
Control panel	10	CM
Fire detector	1	CBM
Vibration and displacement transmitter	2	CBM
Purging controller	3	CBM
Bearing transmitter	4	CBM
Blowdown valves	8	PSM

5 Conclusion

Maintenance (conditional maintenance/scheduled preventive mainte-nance/preventive maintenance) helps in extending the useful life of the machine tools in a manufacturing company. In the present research work, a gas turbine-based electricity generator in an oil and gas company is considered as a case study. An effort is made to apply the analytical hierarchy process for selecting the appropriate policy for maintaining the different components of a gas turbine.

Enhancing the availability will ensure meeting customer orders. A gas turbine consisted of different components. In the oil and gas company (case study), budget of maintenance was limited. Thus, it was not possible to focus on all the components of gas turbine for enhancing the availability of the gas turbine. In this context, critical components had to be identified for reducing the maintenance cost.

Analytical network process (ANP) makes it possible to assign weights to multiple alternatives. Thus, it helps in selecting or classifying alternatives. The technique helps in calculating the weights for different decisions. The technique makes use of expert's experience in quantifying weights of various decisions through pairwise comparisons. After conducting interviews with experts and based on their feedback, the following criteria clusters are identified: (1) cost cluster: A component is consid-ered critical if it has higher maintenance cost in comparison to other components; (2) complexity cluster: A machine with large number of components with high failure rates is considered more critical; (3) maintainability cluster: A machine with large downtime is considered more critical than others; and (4) safety cluster: It is impor-tant to consider the safety aspect while identifying components which are critical to the functioning of a module; (5) reliability: It measures the extent of dependability of equipment. Having a more dependable equipment would ensure meeting customer expectations in safe and sustainable way.

Pairwise comparisons have showed the relative importance of each component with respect other components. Overall importance and the criticality analysis showed that certain components—fire detector, vibration and displacement transmitter, purging controller, bearing and its transmitter, and temperature transmitter—are critical for the effective functioning of the gas turbine. As these components are critical and since the availability of the gas turbine depends on these components, condition-based maintenance policy is preferred. Certain components, e.g., transmitter and control valve had scored less criticality rating. Thus, transmitter and control valve are not considered as a critical component of the gas turbine, and preventive maintenance is preferred. For certain components, control system and control panel, because they are not critical, corrective maintenance (CM) policy is preferred. The current research work showed that not all components require same type of maintenance policies. Thus, by focusing only on critical components of gas turbine, there will be a reduction of total maintenance cost.

References

Alrifaey M, Sai Hong T, Supeni EE, As'arry A, Ang CK (2019) Identification and prioritization of risk factors in an electrical generator based on the hybrid FMEA framework. Energies, 12:649

Barlow RE, Proschan F (1975) Statistical theory of reliability and life testing probability models to begin with. Technometrics 72:304

Ben A, Mabrouk Chelbi A, Radhoui M (2016) Optimal Imperfect Preventive Maintenance Policy for Equipment Leased during Successive Periods 54:5095–5110

Birnbaum ZW (1969) On the importance of different components in a multicomponent system. Multivariate Anal 2:581–592

Campbell JD, Jardine AKS, McGlynn J (2016) Asset management excellence: optimizing equipment life-cycle decisions, 2nd edn. CRC Press, New York

Carmignani G (2009) An integrated structural framework to cost-based FMECA: the priority-cost FMECA. Reliab Eng Syst Saf 94:861–871

Carnero MC, Gomez A (2017) Maintenance strategy selection in electric power distribution systems. Energy 129:255–272

Carot V, Sanz J (2000) Criticality and sensitivity analysis of the components of a system. Reliab Eng Syst Saf 68:147–152

Crocker J, Kumar UD (2000) Age-related maintenance versus reliability cantered maintenance: a case study on aero-engines. Reliab Eng Syst Saf 67:113–118

Dorri M (2014) Proposing a model for the selection of repair and maintenance strategy for its systems with the help of dematel and anp fuzzy. Kuwait Chapter, Arabian J Business Manag Rev 3:202–218

Hamzeh M, Vahidi B, Askarian-Abyaneh H (2015) Reliability evaluation of distribution transformers with high penetration of distributed generation. Int J Electrical Power Energy Syst 73:163–169

Jeyamala D, Balamurugan S, Jalila A, Nathan K (2013) Fault-prone components identification for real-time complex systems based on criticality analysis. Int J Comput Commun Inform J 3:17–23

Liu H-C, Liu L, Liu N (2019) Risk evaluation approaches in failure mode and effects analysis: a literature review. Expert Syst Appl 40:828–838

Marton I, Martorell P, Mullor RS, Anchez AI, Martorell S (2016) Optimisation of test, and maintenance of ageing components consisting of multiple items and addressing effectiveness. Reliab Eng Syst Saf 153:151–158

Moslemi N, Kazemi M, Abedi SM, Khatibzadeh-Azad H, Jafarian M (2017) Maintenance scheduling of transmission systems considering coordinated outages., IEEE Syst J 1–11

Saaty T (1996) Decision making with dependence and feedback: the analytic network process, vol 370. RWS Publications

Sadeghi A, Manesh RA (2012) The application of fuzzy group analytic network process to selection of best maintenance strategy- a case study in Mobarakeh steel company. In: 6th Asian conference on environment-behavior studies, Iran University of Science and Technology, Tehran, Iran, vol 62, pp 1378–1383

Shayesteh E, Yu J, Hilber P (2018) Maintenance optimization of power systems with renewable energy sources integrated. Energy 149:577–586

Silvestri A, De Felice F, Petrillo A (2012) Multi-criteria risk analysis to improve safety in manufacturing systems. Int J Prod Res 50:4806–4821

Tajadod M, Ghasemi E, Bazargan HA (2011) Combined method based on fuzzy analytical network process and fuzzy data envelopment analysis for maintenance strategy selection. In: Proceedings of International Conference on Advanced Electrical Electronics Engineering (ICAEE 2011), pp 179–183

Wang Y, Yam RCM, Zuo MJ, Tse PA (2001) Comprehensive reliability allocation method for design of CNC lathes. Reliab Eng Syst Saf 72:247–252

Zhou D, Zhang H, Li Y-G, Weng SA (2016) Dynamic reliability-centered maintenance analysis method for natural gas compressor station based on diagnostic and prognostic technology. J Eng Gas Turbines Power 138:061601

A Review on Recent Advances in Pulsating Heat Pipes

Kamlesh Parmar, Ajit Kumar Parwani, and Sumit Tripathi

Abstract Thermal management has a big impact on how long electronic gadgets last and how well they work. With the ever-increasing number of closely packed electronic devices, heat transport concerns in such devices are becoming increasingly common. Pulsating heat pipes (PHPs) are newly developed devices in which two-phase heat transfer occurs. The most favorable advantage of PHPs over conventional heat pipes is that the PHP does not have wick structure through which condensate returns for heating purpose. Many researchers have analyzed and performed studies on pertinent design of PHPs, but due to thermodynamics and hydrodynamics combined effect, the working mechanism of PHP is exceptionally multifaceted. Further, the use of nano-fluids has attained significant attention over the last few decades because of higher heat transfer capabilities. Researchers have suggested hybrid nano-fluids for power applications where more heating is required; however, this mechanism has not been completely explored. The present review explores the current research trends in PHPs in terms of its main features and working parameters based on experimental and numerical analysis as well as multiphase modeling.

Keywords Pulsating heat pipe · Two-phase flow · Nano-fluids

K. Parmar (✉) · A. K. Parwani · S. Tripathi
Institute of Infrastructure, Technology, Research and Management, Ahmedabad, India
e-mail: kamlesh.parmar.20pm@iitram.ac.in

A. K. Parwani
e-mail: ajitkumar.parwani@iitram.ac.in

S. Tripathi
e-mail: sumittripathi@iitram.ac.in

K. Parmar
Parul University, Vadodara, India

Nomenclature

D	Diameter, m
Eo	Eotvos number
Bo	Bond number
R	Thermal resistance, K/W
N	Number of turns

Greek letters

ρ density	Kg/m^3
σ surface tension	N/m

Subscripts

h	Hydraulic
crit	Critical
l	Liquid
g	Vapor

1 Introduction

Thermal management has significant role in the performance of electronic devices (Aubin et al. 2019). Heat transfer queries in electronic systems considerably increase with the growing world of closely packed electronic devices. For cooling such electronic systems and devices, an operative thermal management explanation is needed (Kim and Kim 2020). Effective heat transfer is one of the most considerable challenges in the cooling of such electronic systems (Han et al. 2016), and with an increase in the heat flux of such devices, the need of a novel heat pipe increases continuously (Noh and Kim 2019). For fulfilling this demand of thermal management of electronics devices, the new type of heat pipes was invented by Akachi (1990) in 1990, which is known as the pulsating heat pipes (PHPs). PHPs have higher thermal performance and do not have wick structure. So, PHPs are the most promising alternative of conventional heat pipes for thermal management (Noh and Kim 2019). Due to this advantage, PHPs have vast areas of pertinent applications such as solar energy, avionic and space, waste heat recovery, cooling of power/microelectronic components and renewable energy applications (Han et al. 2016). As per channel arrangement, PHPs have two main types: closed-loop PHP (CLPHP), in which a

meandering channel forms a closed loop; and closed-end PHP (CEPHP), in which both meandering ends are not connected to each other (Kim and Kim 2020). A PHP is principally a non-equilibrium-type heat transfer appliance, which is operated by multifaceted arrangement of different types of two-phase flow uncertainty (Khandekar 2004). PHPs have distinct advantages in electronics cooling. The structure of PHP is simple and economical due to its small diameter and wick-less structure. The heat transfer capability of PHP is exceptional which can reach many times to that of copper. The size of PHP can be too small which is its most favorable feature, and the channel of PHP is also more flexible (Han et al. 2016). The key features of PHPs are noiseless operation, low cost, trustworthy and simple design.

The PHP is made of capillary dimensions with many turns that may have open-loop and closed-loop structures. One side of a PHP has an evaporator in which heat is received, and on the other side the heat is dissipated in a condenser, and there is a section in between the evaporator and condenser, which is known as an adiabatic section as shown in Fig. 1 (Khandekar 2004). A conventional PHP is a serpentine tube of small size, the tube is first evacuated and then half of it is filled with working fluid. Because of the natural process, a form of vapor/liquid bubbles and plugs disseminates into capillary tube. Initial plug or bubble distribution does not depend on any external factor. By oscillating the liquid–vapor systems, the evaporative end transfers heat to the other end (condenser). The liquid plugs and vapor bubbles are conveyed in the tube because of oscillating effects inside the system. PHP device does not require external mechanical power, and the dynamic pressure pulsations are driven totally by thermal effects (Khandekar 2004).

By referring pertinent literatures, it has been observed that the heat transfer analysis of the PHPs is classified into three groups. First group includes various geometric
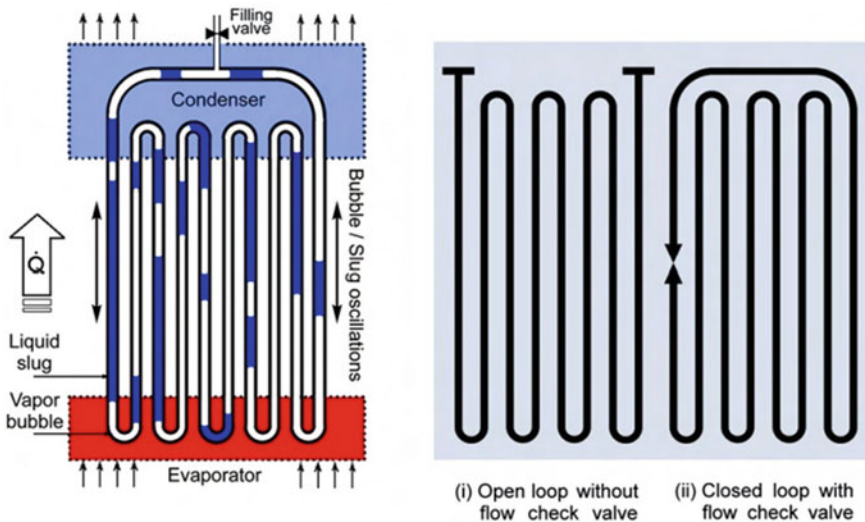
Fig. 1 Diagram of a pulsating heat pipe (Khandekar 2004)

working parameters like internal diameter, cross-sectional design, channel feature, multiple of turns, length of evaporator zone and condenser zone. Second group includes physical properties of working fluids like viscosity, surface tension, thermal conductivity and specific heat. The third group includes operational parameters like thermal flux, pulsation indications, charge ratio, inclination angle and gravity (Han et al. 2016). The present work reviews recent research trends on PHPs with experimental analysis, numerical analysis, multiphase modeling for heat transfer using various working fluids and parameters.

2 Experimental Analysis

Kim and Kim (2020) estimated and compared influence of the flow behavior between closed-loop and closed-end PHPs through a thermal performance. They used microelectromechanical systems (MEMS) techniques to develop PHPs of ten turns using silicon material. The flow behavior in the PHPs had been visualized using a fixed silicon wafer protected by Pyrex glass. As working fluids, the researchers employed ethanol and R-134a. When a diameter ratio $D_h/D_{h, \text{crit}} < 0.5$ was considered, the closed-loop PHP (CLPHP) performed slightly poor than a closed-end PHP (CEPHP). When a diameter ratio $D_h/D_{h, \text{crit}} = 0.29$ was used and PHP was filled with ethanol, CLPHP indicated 20% lower maximum heat flux and 33% higher thermal resistance than CEPHP. When a diameter ratio $D_h/D_{h, \text{crit}} > 0.5$ was considered, the CEPHP performed inferior to CLPHP. When a diameter ratio $D_h/D_{h, \text{crit}} > 0.69$ was considered and PHP was filled using R-134a, CEPHP indicates 117% lower maximum heat flux and 72% higher thermal resistance than CLPHP (Kim and Kim 2020).

Khandekar (2004) estimated thermo-hydrodynamics of CLPHP. The setups were designed for flow visualization including videography and infrared thermography. The device was designed for self-driven pulsation action and improved experiments for the specified heat using filling ratio range from 20 to 80%. Mathematical modeling of the device operations had also been accomplished by applying via semi-empirical modeling and modeling by artificial neural network. The Eotvos number criteria, i.e., Eo $\simeq 4$, for surface tension adiabatic slug flow, only provided a tentative design rule for internal diameter of a CLPHP. The author presented a tentative criterion, i.e., bond number, Bo ≤ 2 (Khandekar 2004). Bond number is defined as:

$$\text{Bo} = \sqrt{\text{Eo}} = \sqrt{\frac{g(\rho_l - \rho_g)}{\sigma}} D \tag{1}$$

Czajkowski et al. (2020) performed experiments on a larger-scale PHP. They considered various working parameters such as high heat load (up to 2 kW), various lengths of adiabatic section and different filling ratios. They used acetone, ethanol and water as working fluids. For water, the lowermost thermal resistance was achieved nearer 0.05 °C/W. They considered different length of adiabatic section around 500 mm, 750 mm and 1000 mm for a filling ratio of 25%, 50% and 75%, respectively.

The filling ratio of about 75% was considered as an optimum value for water. A filling ratio of about 75% established a steady performance for all ranges of different heat loads (Czajkowski et al. 2020).

Baitule et al. (2013) performed on CLPHP using different filling ratios from 0 to 100% in steps of 20%. They considered a two-turn CLPHP and used pertinent fluids such as ethanol, acetone, methanol and water. Material of evaporator and condenser sections was taken as copper capillary tube. The outer and inner diameters of capillary tube were 3 mm and 2 mm, respectively. They achieved optimal outcome of PHP at inlet ratio of 60%. The resistances from thermal side had the results of $R_{acetone} < R_{methanol} < R_{ethanol} < R_{water}$ up to 48 W. However, for acetone, the thermal resistance increased somewhat higher than 48 W (Baitule 2013).

Yang et al. (2009) estimated and performed an experimental analysis of two-flat-plate CLPHPs in the thermal spreader structure. The optimum filling ratio of 50% to 60% was found for heat orientations of horizontal and top using ethanol as working fluid, but the condition of bottom heat alignment was more difficult. Mostly, the heat load increased the performance because pumping action was generated by using the main source of input heat load (Yang et al. 2009).

Mohammad et al. (2014) performed the PHP experimentally by twisting a copper tube. For various working fluids, they achieved acceptable and constant thermal performance by using different inclination angles from 22.5° to 90°. When a magnetic field was not available, then the most favorable charging ratio was 55% for ferro-fluid and distilled water. However, when a magnetic field was present, the most favorable charging ratio was 70% for ferro-fluid (Mohammadi et al. 2014).

Nano-fluids

Zufar et al. (2020) established an experimental setup of PHP with four turns of copper tube using hybrid nano-fluids. They also produced a numerical analysis of same setup using 0.1% weight concentration of Al_2O_3–CuO, SiO_2–CuO hybrid nano-fluid and water, and compared with experiment results. They considered a heating power and filling ratio as 10 to 100 W and 50 to 60%, respectively. They found that pulsation started early, and minor heating power required for hybrid nano-fluids than water comparatively for all filling ratio experienced. They suggested hybrid nano-fluids for power applications where more heating was required. Due to higher viscosity and thermal conductivity, highest thermal resistance was presented by Al_2O_3–CuO, then secondary are water and SiO_2–CuO hybrid nano-fluid for all filling ratios. For four-turn PHP using hybrid nano-fluids, optimum filling ratio was established as 60% (Zufar et al. 2020).

Xu et al. (2020) established an experiment investigation of two phase heat transfer of PHP system using mixture of working fluids such as graphene nano-fluid, ethanol–water blend and surfactant aqueous solutions. Exfoliated graphene in liquid phase was distributed in 40% water–ethanol blend to create nano-fluids of graphene with outstanding constancy. Thermal resistance nearer to 25.16% could be reduced by using graphene nano-fluids. Few layer graphene nano-fluids (FLG) had better heat transfer than LPEG nano-fluids. For application of larger industries, FLG was more costly to heat transfer systems, and 30% by volume ethanol–water blend showed the

most favorable thermal operation between water deionized (DI) water, ethanol and ethanol–water blend from 20 to 77 volume percentage. The heat transfer operation could be increased considerably by using graphene nano-fluids. Graphene nano-fluids had a stability issue for thermal operation which was dangerous. This stability issue could be solved by alternation of graphene nano-sheet surface (Xu et al. 2020).

Chen et al. (2020) established investigational analysis on a PHP with the use of TiO_2 having nano-fluids for Li-ion battery in electric vehicles. They observed that the Li-ion battery executes well for the range of temperature form 20 to 50 °C, and a battery can be discharged at higher efficiency of heat transfer of PHPs for discharge rate of 1C and 1.5C (Chen and Li 2020).

Xing et al. (2017) established and performed a thermal operation of vertical closed PHP, in which they used water and hydroxylated multiwalled nano-tubes (MWNTs) nano-fluids. Nano-particles were suspended in the main fluid, i.e., known nano-fluids. Below 0.3% of weight concentration, PHP with MWNTs nano-fluids revealed higher heat transfer than water. A thermal resistance of MWNTs nano-fluid was reduced to 34% compared to pure water for 0.1% of weight with 100 W of input power (Xing et al. 2017).

3 Numerical Analysis and Multiphase Modeling

Aubin et al. (2019) modeled numerical simulations of CLPHPs. For solving a two-phase flow, single-phase models were used by developing 1-D simulation code. They assumed that liquid and vapor plugs did not interrelate at the boundary (Aubin et al. 2019).

Noh et al. (2019) conducted a thermal optimization using numerical approach. In this model, thermal relation was considered and simulated conjugate mode of heat transfer between pulsating liquid or vapor plugs and a solid wall. They mathematically established ideal amount of turns and channel diameter for the given space. The merit number was mathematically established to be D^2N for ideal amount of turns for given space. When the proposed merit number used in design of PHP turns into maximum, thermal performance was optimized (Noh and Kim 2019).

Gupta et al. (2017) studied two-phase flow by developing a computational model for CLPHP and also envisage its thermal performance. Multiphase modeling was developed by using FLUENT through volume of fluid (VOF) model. An influence of surface tension was found by considering continuum surface force (CSF). Bubble generation and pulsation phenomena which included in the process of CLPHP envisaged using unsteady model of simulation (Parwani and Gupta 2017).

Nano-fluids

Xu et al. (2019) analyzed flat-plate PHP (FP-PHP) with microchannel structure and used silver nano-fluid as working fluid. They used FLUENT for simulation and thermal performance using three-dimensional model in condenser section. For silver nano-fluids, the optimal volume fraction was 1%, which increased heat transfer

efficiency of a FP-PHP. Because of this reason, patterns of flow involved bubble, slug, annular and column flows. Thermal resistance was considerably decreased, and a FP-PHP cycle also steadied up to 120 W of heating power.

Jafarmadar et al. (2016) numerically analyzed a flow through PHP using pertinent nano-fluids such as Al_2O_3, CuO, silver and pure water. Equal rate of entropy generation was found by using Al_2O_3 and CuO nano-fluids, and the Ag nano-fluids had lag in pulsation and bubble formation resulting in higher entropy generation rate. The minimum entropy generation and proper thermal process could be optimized from 0.5 to 1 vol. % of nano-fluids.

4   Conclusions

The key facts and challenges observed for PHPs are presented by reviewing the available literature. Many researchers have considered the influence of use of wick materials on the yield of heat transfer and capillary action for relevant pulsating heat pipes. However, due to partially known mechanism of PHPs, the test of micrometres and sub-millimeter ranges of PHPs are not thoroughly explored. The limitations of heat transfer characteristics on number of turns in PHP, the lifecycle test of a PHP, effects of fluid mixtures and non-condensable gases also need further investigations. Researchers have used FLUENT for simulation and thermal performance from 3D models because of the instability of the nano-fluids in thermal analysis of experimental observations. One key factor for improving the heat transfer process is settlement of nano-particles in the evaporator. Many researchers analyzed and performed on pertinent design of PHPs but due to thermodynamics and hydrodynamics combined effect between liquid plugs and vapor slugs, the working mechanism of PHP is not fully understood. Currently, there are no consistent tools or design techniques for pulsing heat pipes as heat exchangers in research. After reviewing the current advances of pulsating heat pipes, the present work concludes that there is a wide range of possibility to amend the heat transfer efficiency and pulsating effects of the PHPs to fully understand its working mechanism and its dependency on design, thermal performance, fluid and flow characteristics.

References

Akachi H (1990) Structure of heat pipe, United State Patent, no. 19, 1990

Aubin P, D'Entremont B, Cataldo F, Marcinichen JB, Amalfi RL, Thome JR (2019) Numerical simulations of pulsating heat pipes, part 1: modeling. In: 2019 18th IEEE intersociety conference on thermal and thermomechanical phenomena in electronic systems (ITherm), pp 232–242, 2019

Baitule DA (2013) Experimental analysis of closed loop pulsating heat pipe with variable filling. Int J Mech Eng Robot Res 2(3)

Chen M, Li J (2020) Nanofluid-based pulsating heat pipe for thermal management of lithium-ion batteries for electric vehicles. J Energy Storage 32

Czajkowski C, Nowak AI, Błasiak P, Ochman A, Pietrowicz S (2020) Experimental study on a large scale pulsating heat pipe operating at high heat loads, different adiabatic lengths and various filling ratios of acetone, ethanol, and water. Appl Thermal Eng 165:114534. https://doi.org/10.1016/j.applthermaleng.2019.114534

Han X, Wang X, Zheng H, Xu X, Chen G (2016) Review of the development of pulsating heat pipe for heat dissipation. Renew Sustain Energy Rev 59:692–709. https://doi.org/10.1016/j.rser.2015.12.350

Jafarmadar S, Azizinia N, Razmara N, Mobadersani F (2016) Thermal analysis and entropy generation of pulsating heat pipes using nanofluids. Appl Therm Eng 103:356–364

Khandekar S (2004) Thermo- hydrodynamics of closed loop pulsating heat pipe. Universitaet Stuttgart, Germany

Kim W, Kim SJ (2020) Effect of a flow behavior on the thermal performance of closed-loop and closed-end pulsating heat pipes. Int J Heat Mass Trans 149:119251

Mohammadi M, Mohammadi M, Ghahremani AR, Shafii MB, Mohammadi N (2014) Experimental investigation of thermal resistance of a ferrofluidic closed-loop pulsating heat pipe. Heat Transfer Eng 35(1):25–33

Noh HY, Kim SJ (2020) Numerical simulation of pulsating heat pipes: parametric investigation and thermal optimization. Energy Convers Manag 203:112237

Parwani A, Gupta A (2017) CFD modeling for thermal performance of closed loop pulsating heat pipe in bottom heated mode, pp 46–50

Xing M, Yu J, Wang R (2017) Performance of a vertical closed pulsating heat pipe with hydroxylated MWNTs nanofluid. Int J Heat Mass Transf 112:81–88

Xu H, Zhang P, Yan L, Xu D, Ma W, Wang L (2019) Thermal characteristic and analysis of microchannel structure flat plate pulsating heat pipe with silver nanofluid. IEEE Access 7:51724–51734

Xu Y, Xue Y, Qi H, Cai W (2020) Experimental study on heat transfer performance of pulsating heat pipes with hybrid working fluids. Int J Heat Mass Trans 157

Yang H, Khandekar S, Groll M (2009) Performance characteristics of pulsating heat pipes as integral thermal spreaders. Int J Therm Sci 48(4):815–824. https://doi.org/10.1016/j.ijthermalsci.2008.05.017

Zufar M, Gunnasegaran P, Kumar HM, Ng KC (2020) Numerical and experimental investigations of hybrid nanofluids on pulsating heat pipe performance. Int J Heat Mass Trans 146

Experimental Investigation of Solar Panel Integrated with Mirror Reflector and Cooling

Krunal Patel and Dileep Kumar Gupta

Abstract The paper presents an experimental investigation of solar panel integrated with mirror reflected and cooling. The performance of the PV module decreases at the peak hours of sunlight, due to the loss of energy in the form of heat as the temperature of the module increases. Therefore, the cooling of the solar panel may increase the overall performance of the PV module. An attempt has made to improve the performance of the solar PV module by integrating mirror reflector and cooling of the panel. Subsequently, a comparatively analysis has been presented among three conditions, i.e., simple solar panel, solar panel with cooling, and solar panel with mirror reflector and cooling. The results show significant improvement using the proposed cooling system along with the mirror reflector.

1 Introduction

In the present scenario, energy crises is one of the worldwide challenges due to the limited source of fossil fuel available. Therefore, the scientific community had worked a lot to find alternative sources of energy. Solar energy for power generation has gained more attraction nowadays, due to its long life, and the huge amount of solar radiation is available at free of cost. Fortunately, the availability of solar irradiation in India is significantly higher than in other countries; hence, there is a huge possibility to use solar energy for power generation. The solar PV module is one of the viable and most accepted technologies for solar power; however, the lower efficiency of the module became a major concern. There are several works including modifications in PV cells, method of cooling, and tracking systems which enhance the radiation and have been carried out by various researchers. The development stages for the performance improvement of the PV module have been summarized below.

Arshad et al. (2014) discuss the practical approach to improve solar panel efficiency using reflector mirrors and cooling. The experimental results specify considerable improvement in overall output. It was reported that the efficiency of the system

K. Patel · D. K. Gupta (✉)
Institute of Infrastructure Technology Research And Management, Ahmedabad, India

© The Author(s), under exclusive license to Springer Nature Singapore Pte Ltd. 2022
A. K. Parwani et al. (eds.), *Recent Advances in Mechanical Infrastructure*,
Lecture Notes in Intelligent Transportation and Infrastructure,
https://doi.org/10.1007/978-981-16-7660-4_9

improved up to 32% and 52% respectively, using a reflector without and with a cooling mechanism. Ceylan et al. (2014) studied different PV/T systems for the cooling of the PV module, using a spiral cooling heat exchanger. It was found from the experimental result that efficiency improved from 10% to 13% using the cooling system. It has also been recommended there should be an addition of module and collector to PV/T, connected parallel to each other, and collectors are connected in series. So that the cooling water inlet temperature can be maintained the same for all module. Alam et al. (2016) presented a comparative study on solar panel integrating with mirror reflection, cooling system, and associated tracking system. It was concluded that the reflecting mirror and cooling simultaneously improve the output of the panel significantly. Subsequently, additional improvement was observed using the tracking system. The average improvement has been observed up to 60%.

Cazzaniga et al. (2018) have performed an experimental investigation on photovoltaic with floated installation, for enhancing the performance in terms of efficiency and cost-effectiveness. The system also had additional features, i.e., cooling with tracking and concentration. It was found that the efficiency of the system significantly improved with the tracking and cooling effect. The possibility to use the floating structure on water has been explored. Idoko et al. (2018) presented an experimental investigation on two 250 W solar panels, mounted on 37 heights to achieve air cooling as well as water cooling. It was found that the power output increased by 10% and efficiency improved by 3%.

Salem et al. (2019) presented an experimental investigation of a PV module with a cooling system. A compound cooling using water and Al2O3/PCM mixture with nanoparticles were used for cooling. It was reported that the Al2O3 nanoparticles make the compound technique (Al2O3/PCM mixture þ water) better than the cooling with 100% water. Awan (2019) analyzed the impact of shading on the rooftop PV systems and the cooling load on the building. There was three-test approach opted for PV configurations, i.e., zero tilt angle, monthly adjusted tilt angle, and PV configuration with a dual-axis sun-tracking system. It was found that the system performance improved by 8.7% and 6.7% economically using monthly tilt and dual-axis tracking arrangements, respectively.

Kasim et al (2019) presented an experimental study on a polycrystalline solar module with the V-Trough concentrator, with two optical reflectors. The output power was measured using a PVR module that tilted 30° from the horizontal plane. It was found that the average power gains up to 91% than the reference module. The tracking system used in the system also reduces the area of installation and cost. The result was promised to good feature for PV projects in Iraq. Jahagirdar et al. (2019) have presented a study on the effect of temperature on the performance of the solar panel. The different way to maintain the surface temperature of solar panel has been discussed. The experiment has been presented on PV panel with cooling system, and it was reported that there was a significant improvement in the efficiency and net output using the cooling system in solar panel.

Cotfas et al. (2019) presented a review on the various method developed the increase the efficiency of the PV panels. The main focus is on cooling, tracking, and boosting the solar radiations. It was found that there is a significant effect of the panel temperature and performance can be increased by cooling the panel. On other hand, increasing the falling radiation also increases the performance of the PV panel; however, more cooling is required for the same. These enhancements also lead to complexity in the system, operating feasibility, and increased cost. Sheikh et al. (2020) presented an experimental investigation on a photovoltaic (PV) system with a forced water cooling system in a 395 W solar panel. It was concluded that the power output enhanced up to 14.29% at 1000 W/m2 (irradiance) and 35 °C ambient temperature. The power required for the water supply was just 8.5 W, and total electric power improved by 9.58%. It is observed in the literature that the majority of the work is focused on either cooling of the panel or in the mirror reflector; however, limited study was available in the combined analysis. In this work, an attempt has been made to experiment with combined analysis as well as compare the performance of the same.

2　Experimental Analysis

The experimental setup has been fabricated using a 20 W polycrystalline solar panel and two same sizes of simple mirror reflectors. The cooling of the panel has been done by spraying water over the panel surface. The tracking and cooling of the panel have been done manually, and the temperature of the solar panel has been reduced to 303 K during cooling. The mirror has been placing both sides of the panel with an angle of 60º from the ground level. The actual photo of the experimental setup is shown in Fig. 1. The detail of the solar panel is given in Table 1.

Fig. 1 Experimental setup

Table 1 Specifications of the solar panel

Size of the panel	450*350*22 (L*W*H) mm
Rated efficiency	16.5%
Type of cell	Polycrystalline
Maximum power (Pmax)	20 Wp
Maximum power voltage (Vmp)	19.25 v
Maximum power current (Imp)	1.04 A
Short-circuit current (Isc)	1.11 A
Open-circuit voltage (Voc)	22.5 V
Maximum system voltage	600 V

3 Results and Discussion

The experiment has been performed in typical Ahmedabad conditions, in December; the test results have been recorded for 15 days in three sets of operating, i.e., simple solar panel, solar panel with cooling, solar panel with two mirrors and cooling. In all the sets of the experiment, the tracking has done manually and reading has taken with no load conditions.

Figure 2 depicts the variation of the irradiation measured between 9 am to 5 am for all three conditions, i.e., simple panel, panel with cooling, and cooling and mirror reflectors, separately. It has been observed that there is minor variation in the irradiations, due to the variation in weather conditions in a particular daytime. This data has been further used to calculate the overall efficiency of the panel.

Figure 3 depicts the variation of voltage with time for all three arrangements of the simple panel with cooling and mirror reflectors. It has been observed that the voltage output has significant improvement because of cooling. However, there is small deviation observed between the system with only cooling and cooling with reflectors.
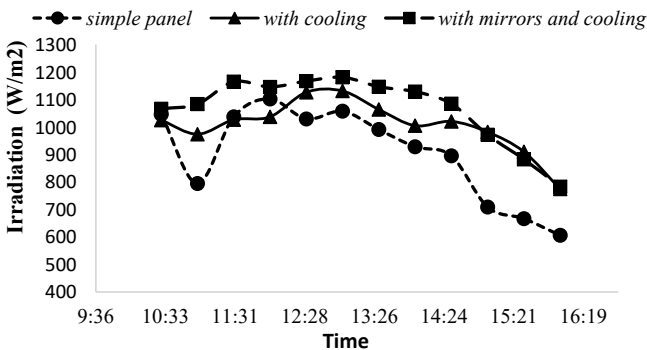
Fig. 2 Measured irradiation with time
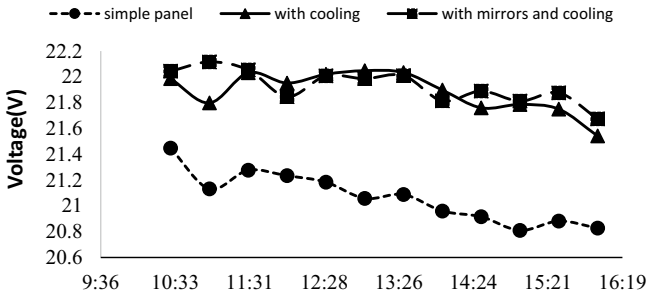
Fig. 3 Measured voltage with time
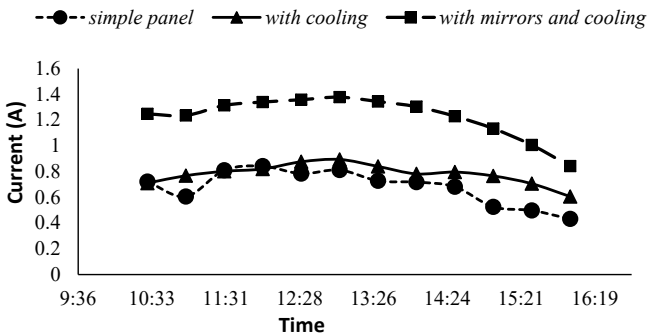
Fig. 4 Measured current with time

Similarly, Fig. 4 depicts the variation of current with time for all three arrangements of the simple panel with cooling and mirror reflectors. It has been observed that the current output has significant improvement because of mirror reflectors in the solar panel. However, there is small deviation observed between the system with only cooling and a simple panel without cooling.

Figure 5 indicated power output calculated using well-known equation, Power = Voltage x Current. It shows the cumulative effect of the variation of voltage and current (as shown in Figs. 3 and 4). It can be seen that the power output significantly improves using a mirror reflector with the cooling arrangement.

Finally, Fig. 6 shows the variation of the efficiency with time using the equation output/input. It has been calculated using the previous data from Figs. 3, 4 and 5.

It has observed from the above results that using mirror reflectors and cooling arrangement, the efficiency increases throughout the investigations. There is an improvement observed using only cooling without mirrors in the panel. The detailed measured and calculated data has been shown in Tables 2, 3, and 4 for the simple panel, panel with cooling, and panel with reflector and cooling, respectively. It can be seen from Table 2 that the power output varies from 9 W to 17.8 W and efficiency ranges from 9.41% to 10.52% in a day of the experiment.
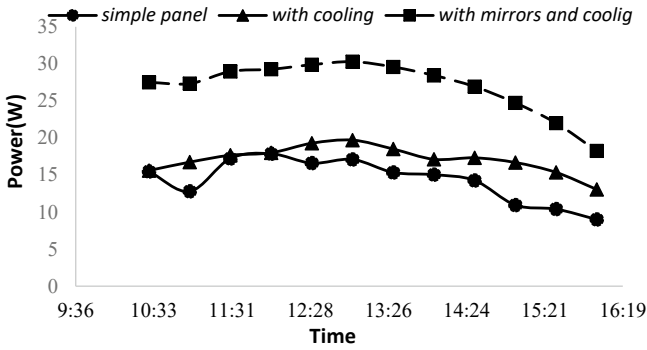
Fig. 5 Power output with time
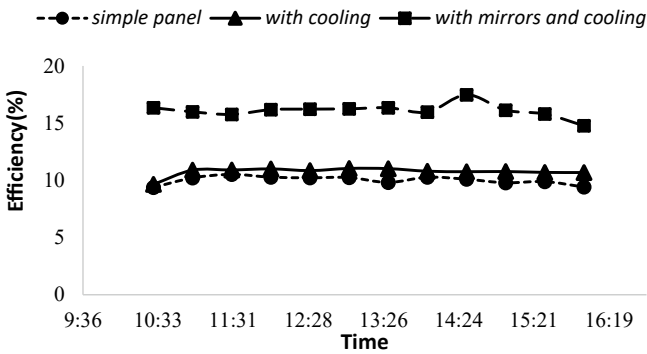
Fig. 6 Efficiency with time

Table 2 Simple solar panel

Time	Voltage (V)	Current (A)	Power (W)	Irradiation (W/m$_2$)	Efficiency (%)
10:30	21.448	0.722	15.485	1048	9.38
11:00	21.132	0.606	12.8	795.6	10.21
11:30	21.276	0.81	17.233	1039.2	10.52
12:00	21.234	0.842	17.879	1104.4	10.278
12:30	21.184	0.784	16.608	1031.2	10.225
13:00	21.058	0.812	17.1	1059.6	10.246
13:30	21.088	0.728	15.352	992.8	9.817
14:00	20.96	0.718	15.049	930	10.274
14:30	20.916	0.682	14.264	897	10.096
15:00	20.81	0.526	10.946	710	9.788
15:30	20.882	0.498	10.4	667.6	9.89
16:00	20.828	0.432	9	606.8	9.417

Table 3 Solar panel with cooling

Time	Voltage (V)	Current (A)	Power (W)	Irradiation (W/m^2)	Efficiency (%)
10:30	21.986	0.71	15.61	1027.2	9.648
11:00	21.798	0.768	16.74	975.8	10.892
11:30	22.032	0.802	17.67	1028.6	10.907
12:00	21.952	0.82	18	1039	11
12:30	22.02	0.876	19.29	1128.6	10.852
13:00	22.048	0.894	19.71	1133.4	11.041
13:30	22.034	0.84	18.508	1066	11.023
14:00	21.898	0.782	17.124	1006.8	10.798
14:30	21.76	0.796	17.32	1022.4	10.755
15:00	21.786	0.766	16.688	983.8	10.77
15:30	21.75	0.706	15.355	911.6	10.694
16:00	21.542	0.606	13.054	775.8	10.683

Table 4 Solar panel with mirrors and cooling

Time	Voltage (V)	Current (A)	Power (W)	Irradiation (W/m$_2$)	Efficiency (%)
10:30	22.044	1.248	27.51	1068.4	16.348
11:00	22.116	1.236	27.335	1085.6	15.987
11:30	22.054	1.314	28.978	1167.4	15.76
12:00	21.846	1.34	29.273	1148.2	16.18
12:30	22.008	1.358	29.886	1169.4	16.226
13:00	21.986	1.378	30.297	1183.4	16.25
13:30	22.01	1.344	29.581	1148.8	16.348
14:00	21.814	1.304	28.445	1131	15.968
14:30	21.89	1.23	26.924	1087	17.478
15:00	21.812	1.134	24.734	973.4	16.133
15:30	21.876	1.006	22.007	884.2	15.802
16:00	21.674	0.842	18.249	784.2	14.775

Similarly, Table 3 shows the detailed data for solar panel with cooling, where the power output varies from 15.61 W to 19.71 W and efficiency ranges from 9.71% to 11% in a day of the experiment. It can also be observed that the power output has significant variation but a minor improvement in efficiency.

Table 4 shows the performance of the panel with mirror reflector as well as the cooling arrangements. It shows a significant improvement in power as well as efficiency. The power output ranges from 18.24 W to 30.29 W, and efficiency varies from 14.77% to 17.478%.

Finally, Table 5 indicates the summary of the overall performance of the panel and its comparison by integrating mirror reflector and cooling arrangements. It is found

Table 5 Comparative analysis for power output and efficiency improvement

Time	Power increases		Efficiency improvement	
	Cooling	Mirrors and cooling	Cooling	Mirrors and cooling
10:30	0.807	77.65	2.857	74.28
11:00	30.78	113.55	6.68	56.58
11:30	2.536	68.15	3.679	49.8
12:00	0.677	63.72	7.025	57.42
12:30	16.15	79.95	6.132	58.69
13:00	15.26	77.17	7.76	58.6
13:30	20.56	92.68	12.28	66.53
14:00	13.79	89.01	5.1	55.42
14:30	21.42	88.75	6.527	73.12
15:00	52.45	125.96	10.03	64.82
15:30	47.64	111.6	8.13	59.77
16:00	45.04	102.77	13.44	56.9

that the maximum improvement in power is 52% and 126% using only cooling, cooling with mirror, respectively. Subsequently, efficiency increases up to 10% and 74.28% using only cooling, cooling with mirror, respectively.

4 Conclusion

Experimental analysis on PV panel has been carried out with two different arrangements, i.e., cooling and mirror reflector with cooling. It has been concluded from the results that there is a significant improvement in the performance using the mirrors and cooling arrangements. The power output can be improved up to 52% and 126% using only cooling, cooling with mirror, respectively. Subsequently, efficiency increases up to 10% and 74.28% using only cooling, cooling with mirror, respectively.

References

Alam SMS, Rahman AM (2016) Performance comparison of mirror reflected solar panel with tracking and cooling. In: 2016 4th international conference on the development in the in renewable energy technology (ICDRET) (pp 1–4). IEEE

Arshad R, TariqS, Niaz MU, Jamil M (2014) Improvement in solar panel efficiency using solar concentration by simple mirrors and by cooling. In: 2014 international conference on robotics and emerging allied technologies in engineering (iCREATE) (pp 292–295). IEEE

Awan AB (2019) Optimization and techno-economic assessment of rooftop photovoltaic system. J Renew Sustain Energy 11(3):033501

Cazzaniga R, Cicu M, Rosa-Clot M, Rosa-Clot P, Tina GM, VenturaC (2018) Floating photovoltaic plants: Performance analysis and design solutions. Renew Sustain Energy Rev 81:1730–1741

Ceylan I, Gürel AE, Demircan H, Aksu B (2014) Cooling of a photovoltaic module with temperature controlled solar collector. Energy Build 72:96–101

Cotfas DT, Cotfas PA (2019) Multiconcept methods to enhance photovoltaic system efficiency. Int J Photoenergy

Idoko L, Anaya-Lara O, McDonald A (2018) Enhancing PV modules efficiency and power output using multi-concept cooling technique. Energy Reports 4:357–369

Jahagirdar G, Khot P, Joshi SH (2019) Improving efficiency of solar panel using simple cooling system. Int Res J Eng Technol (IRJET) **6**(6)

Kasim NK, Atwan AF, Oleiwi FM, Hameed JS (2019) Study the performance of V-Trough PV solar system with two axis tracking. In: AIP conference proceedings (Vol 2144, No 1, p 030008). AIP Publishing LLC

Salem MR, Elsayed MM, Abd-Elaziz AA, Elshazly KM (2019) Performance enhancement of the photovoltaic cells using Al2O3/PCM mixture and/or water cooling-techniques. Renew Energy 138:876–890

Sheikh YA, Butt AD, Paracha KN, Awan AB, Bhatti AR, Zubair M (2020) An improved cooling system design to enhance energy efficiency of floating photovoltaic systems. J Renew Sustain Energy 12(5):053502

Investigation of Thermophysical Properties of Synthesized N-Hexacosane-Encapsulated Titania Phase Change Material for Enhanced Thermal Storage Application

Sakshum Khanna, Sagar Paneliya, Priyanka Marathey, Khilan Shah, Parth Prajapati, Rakesh Chaudhari, and Jay Vora

Abstract Herein, we developed a simple and versatile method to fabricate N-Hexacosane-encapsulated Titania phase change composite (TPCM) using a sol-gel technique (hydrolysis and polycondensation of Titania precursor). In the composite structure, the phase change material, i.e., N-Hexacosane, was used as a core material, with Titania acting as the shell. The morphology, chemical structure, crystalloid and structural phases of as-prepared TPCM were determined using field-emission scanning electron microscopy (FESEM), Fourier transformation infrared (FTIR) spectroscopy, Raman profile and X-ray diffraction (XRD) measurements. The results revealed the development of TPCM composite material with size ranging from 150 ± 50 nm. Also, the diffractogram profile, Raman and IR spectra confirmed the formation of TPCM composite by revealing the characteristic peaks of both N-Hexacosane and Titania in the composite. The thermophysical properties of the composite were determined using a differential scanning calorimeter (DSC) and thermogravimetric analyzer (TGA). Simulations were also performed for investigating the thermal change within the TPCM composite for numerous thermal cycles, which showed excellent composite stability. TPCM behavior studied using DSC curves resulted in liquefaction and solidification of the PCM at 54.02 °C and 52.08 °C with a latent heat of 142.09 J/g and 127.37 J/g, respectively. The thermogravimetric curves revealed that on increasing Titania content in the composite the overall thermal stability increases. The fabrication of such TPCM composite with such high thermal stability makes it a potential candidate for thermal storage application.

Keywords Titania · N-Hexacosane · Latent heat · COMSOL

S. Khanna (✉) · S. Paneliya · P. Marathey · K. Shah
Department of Solar Energy, Pandit Deendayal Energy University, Gandhinagar, Gujarat, India

P. Prajapati · R. Chaudhari · J. Vora
Department of Mechanical Engineering, Pandit Deendayal Energy University, Gandhinagar, Gujarat, India

1   Introduction

In the modern scenario, there has been a rapid increase in the demand for energy due to the exponential growth of population worldwide, leading to an energy crisis. Thermal energy can be considered one solution for such a crisis as it can absorb the heat and store it more efficiently for secondary use. The thermal energy can be categorized based on the temperature ranges, latent (LHS) and sensible heat storage (SHS). The LHS system has the edge over the SHS systems, as it can have energy density even at a lower cost (Agyenim et al. 2010; Paneliya et al. 2020). The properties of phase change materials (PCM's) like higher latent heat storage capacity, low vapor pressure, consistent melting/freezing, nontoxicity, ease of availability and high thermal stability have proven to be more effective as compared to other thermal storage materials. Till now, various phase change materials like paraffin, fatty acids, salt hydrates and alkanes have been examined for numerous applications like greenhouses gas temperature (Najjar and Hasan 2008), energy conservation (Usadadia et al. 2021), solar thermal systems (Lad et al. 2021) and heat management of electronics (Jaworski 2012). Among all, N-Hexacosane has been extensively used as an organic phase change material because of its high latent heat storage capacity with chemical and thermal stability. The utilization of various phase change material for thermal storage systems is limited due to their low thermal conductivity and leakage problem during the phase transitions. To overcome these downsides, encapsulation can be considered as one of the primary techniques, which has been comprehensively utilized in the past (Su et al. 2012; Singh et al. 2020). This technique enables control of the expansion and contraction phenomenon throughout the solid–liquid (S-L) phase transition process and improves heat transfer efficiency without much lower latent heat storage (Hawlader et al. 2003).

Till now, various organic and inorganic shell methods have been incorporated by the research fraternity for the encapsulation of PCM like interfacial or in situ polymerization, spray drying (Teixeira et al. 2004) and sol-gel method (Paneliya et al. 2021). In an organic process, urea or melamine-formaldehyde resins have been utilized as a covering polymer for various PCMs (Sarier and Onder 2007). However, the major drawbacks associated with them are high flammability, low thermal conductivity, toxicity and poor thermal stability under temperature conditions. To overcome drawbacks as mentioned earlier, researchers have used aluminum oxide, silica and other inorganic materials for encapsulating organic PCMs (Pan et al. 2012).

In 2006, Zhang et al. (2006) synthesized paraffin and expanded graphite (EG) PCM composite with enhanced thermal conductivity, large storage capacity and no liquid leakage problem during phase transition. Also, Li et al. (2012) developed paraffin/SiO2/EG composite by simple sol-gel technique. SiO_2 was used as a supporting material, whereas EG was incorporated to enhance the thermal conductivity of the composite system. The result revealed an enhancement in the thermal conductivity of about 94.7% higher than pure PCM. Similarly, in 2013 Xu et al. (2013) and Mehrali et al. (2013) synthesized paraffin wax with diatomite and PA@GO PCM composite, respectively. The results showed good thermal storage capacity

and chemical stability. Furthermore, the thermal conductivity was observed to be enhanced by three times that of PCM. Recently, Guan et al. (2015) synthesized paraffin wax/expanded vermiculite stable PCM composite, where expanded vermiculite was used as supporting material. The results showed an enhancement in the overall thermal conductivity of the PCM with high stability. These techniques, as mentioned earlier, confirm that the incorporation of inorganic supporting materials increases the thermal conductivity and stability and prevents the leakage of pure PCM.

Till now, very few studies have been carried out with Titania as inorganic supporting material for encapsulating the PCMs. Herein, we report a simple method to encapsulate N-Hexacosane PCM with Titania using an emulsion interfacial hydrolysis and polycondensation process of titanium (IV) isopropoxide. The as-prepared Titania/N-Hexacosane PCM materials improved thermal storage stability, indicating that the prepared encapsulated material can be exploited for thermal energy storage.

2 Experimental Section

2.1 Material, Method and Instrumentation

Please The industrial-grade N-Hexacosane phase change material with a melting temperature of about 54–58 °C, titanium (IV) isopropoxide (TTIP), ammonia (NH_3) and ethyl alcohol (99.9%) were obtained from Sigma Aldrich (India). The used reagents were analytical grade and were used without any purification. Morphological analysis was carried out under field-emission scanning electron microscopy (FE-SEM) operated at 5 keV. In contrast, the structural and chemical analysis was carried out using Raman spectroscopy (Laser 532 nm), X-ray diffraction ($\lambda = 1.54$ Å) and Fourier transform IR spectroscopy. The thermophysical properties like the phase transition temperature, latent heat, stability were analyzed using differential scanning calorimeter (heating rate of 2 °C/min) and thermogravimetric analysis with a heating rate of 10 °C/min from 27 °C (R.T.) to 600 °C in ambient conditions.

2.2 Synthesis of Titania/N-Hexacosane PCM Composite

Titania-encapsulated N-Hexacosane composite (TPCM) was synthesized by mixing N-Hexacosane (2 g) with ethanol (50 mL) in a flask (500 mL) and stirred for 15 min at 70 °C. As the solution turns transparent, a mixture of titanium (IV) isopropoxide (TTIP) (Ti $(OCH (CH_3)_2)_4$), ethanol and water (1:3:50) was added to the solution. Subsequently, a few drops of ammonia were added to the solution to balance the mixture's pH.

Table 1 Titania precursor content in N-Hexacosane composite

S. No	Material	Precursor (wt%)	N-Hexacosane (wt%)
1.	N-Hexacosane	NA	100
2.	TPCM1	3	97
3.	TPCM2	5	95
4.	TPCM3	7	93

The stirring continued for a few hours, and after some time, the transparency changed to a turbid solution at 70 °C. Various weight proportions of the N-Hexacosane and TTIP were used to synthesize Titania-encapsulated N-Hexacosane, as mentioned in Table 1. The final product was obtained by using centrifuge system at 8000 rpm for 10 min and washed with DI water and ethanol numerous times to remove unwanted residue. Different N-Hexacosane-encapsulated Titania composites were obtained after grinding and calcination in a muffle furnace at 150 °C for 6 h and were denoted TPCM1, TPCM2 and TPCM3. A yield around ~68% was obtained as a resultant composite during the experimentation. For comparison, pure anatase material was prepared using the same process without the presence of PCM.

3   Results and Discussion

3.1   *Morphological, Structural and Chemical Study of TPCM Composite*

The morphological study of TPCM composites was carried out under FESEM imaging. Figure 1a–c illustrates FESEM micrographs of different TPCM variants prepared by changing the precursor concentration. The morphological results reveal that the Titania significantly influence the morphology and homogenous size (150
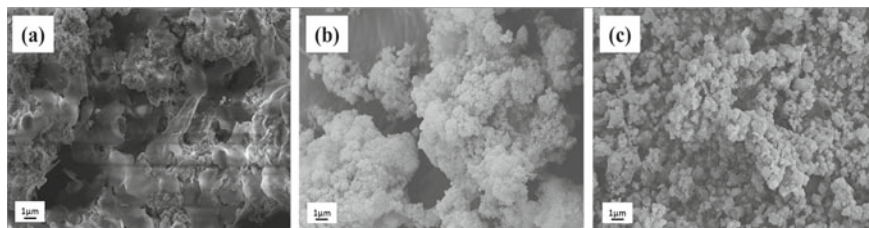
Fig. 1 FESEM images of encapsulated N-Hexacosane with Titania shell (**a**) TPCM1, (**b**) TPCM2 and (c) TPCM3, respectively
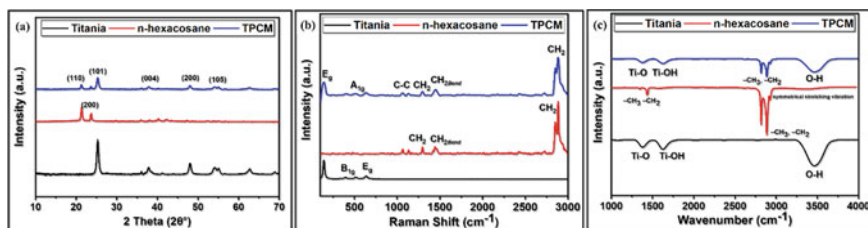
Fig. 2 XRD pattern of the N-Hexacosane, Titania and TPCM composite

± 50 nm) for TPCM1, TPCM2 and TPCM3. The high Titania content composites suggest higher shell encapsulation of N-Hexacosane, precluding PCM leakage during the phase transition temperature as observed under scanning microscope.

The XRD pattern of the N-Hexacosane, Titania, and TPCM composite is shown in Fig. 2a. The diffraction profile of N-Hexacosane shows distinct peaks at $2\theta = 21.27°$ and $23.75°$, corresponding to (110) and (200) crystal planes with a d spacing of 4.2 Å and 3.7 Å respectively (JCPDS No. 40-1995) (Khanna et al. 2020). The XRD spectrum of Titania indicates the formation of pure anatase phase with tetragonal crystal structure and characteristic sharp peaks at $2\theta = 25.3°$, $38.5°$, $48°$, $54.1°$, corresponding to (101), (004), (200) and (105) crystal planes. The diffractogram of the TPCM composite shows diffraction peaks corresponding to both crystalline anatase Titania and N-Hexacosane. Figure 2b shows the Raman shift of the N-Hexacosane, Titania, and TPCM composite. The characteristic Raman peaks of pure N-Hexacosane were observed at $\nu = 1460, 1296, 1058$ and 1150 cm^{-1}, indicating carbon–carbon stretching and CH$_2$ and CH$_3$ deformation (Khanna et al. 2020). In addition, peak at $\nu = 151, 409, 515$ and 633 cm^{-1} is attributed to E$_g$, B$_{1g}$, A$_{1g}$ and E$_g$ vibrational modes of Titania (anatase phase), respectively (Khanna et al. 2021). The Raman profile of the TPCM composite exhibits both characteristic peaks of N-Hexacosane and Titania, supporting the XRD results. The absence of additional peaks confirms the physical attachment between the materials and no occurrence of chemical reaction.

In addition, FT-IR spectroscopy was used out to study and determine the presence of inorganic and organic compositions for N-Hexacosane, Titania and TPCM, as shown in Fig. 2c. Three distinct absorption bands of Titania were observed, i.e., first prominent peak at 1384 cm^{-1}, the second around 1631 cm^{-1} and last a broad peak at 3490 cm^{-1}, indicating to Ti–O, Ti–OH and stretching vibration of the hydroxyl group O-H in Titania, respectively (Khanna et al. 2021). Similarly, the peaks of pure N-Hexacosane at 1471, 2848 and 2916 cm^{-1} indicate the deformation vibration of –CH$_3$, –CH$_2$, rocking vibration CH$_2$ group and symmetrical stretching vibration of –CH$_3$, –CH$_2$ group, respectively (Abazović et al. 2006). Further, the FTIR spectrum of TPCM shows all the individual characteristic peak of PCM (N-Hexacosane) and Titania at 796, 1384, 1470, 1631, 2848, 2916 and 3490 cm^{-1}(Chaudhari et al. 2021; Khanna et al. 2021). Hence, no significant new peak was observed in the TPCM

spectrum, thus confirming that Titania encapsulates PCM has a physical interaction and no chemical interaction between the N-Hexacosane and Titania material.

3.2 Simulation of Encapsulated Titania/N-Hexacosane PCM Composite

The encapsulation of various phase change material by an inorganic shell is mainly due to the unique properties of the shell material, which they provide in terms of thermal behavior and stability (Jurkowska and Szczygieł 2016). Thus, the composite structures of Titania/N-Hexacosane were simulated in order to identify the thermal strain at the TPCM interface by using COMSOL 4.4 under laminar flow. The result obtained for volumetric strain under a thermal expansion and contraction of N-Hexacosane was around 2.11% and 0.76% at temperature values of 57.71 °C and 49.51 °C, respectively, using the below equations:

$$\frac{\Delta V}{V} = \exp\left[\alpha_v\left(T_f - T_i\right)\right] - 1 \tag{1}$$

whereas T_i *and* T_f stand for the initial and final temperatures of N-Hexacosane material, ΔV is the change in the volume due to the surface stress (no significant effect on thermophysical properties) and αv is the thermal expansion coefficient. The COMSOL simulations were performed within 300 to 340 K temperature for S–S (solid–solid) and S–L (solid–liquid) phase transitions of N-Hexacosane. Figure 3a–f shows different stages of change in temperature inside the core and supporting material for TPCM during the charging process. Similarly, Fig. 3g–l shows various stages of cooling during the discharging process, where the N-Hexacosane core was used as a heat source. A lower volumetric strain was observed at the Titania/N-Hexacosane interface during the discharging process, making it a potential material to be used in thermal storage systems. The strain calculated at the interface of Titania/N-Hexacosane suggests that the material is highly durable for multiple
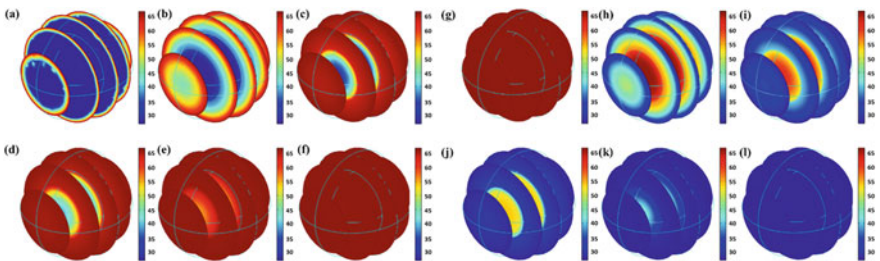
Fig. 3 COMSOL simulation of N-Hexacosane core material with Titania supporting matrix of size 150 nm (Dia.) during liquefaction (a-f) and solidification processes (g-l)
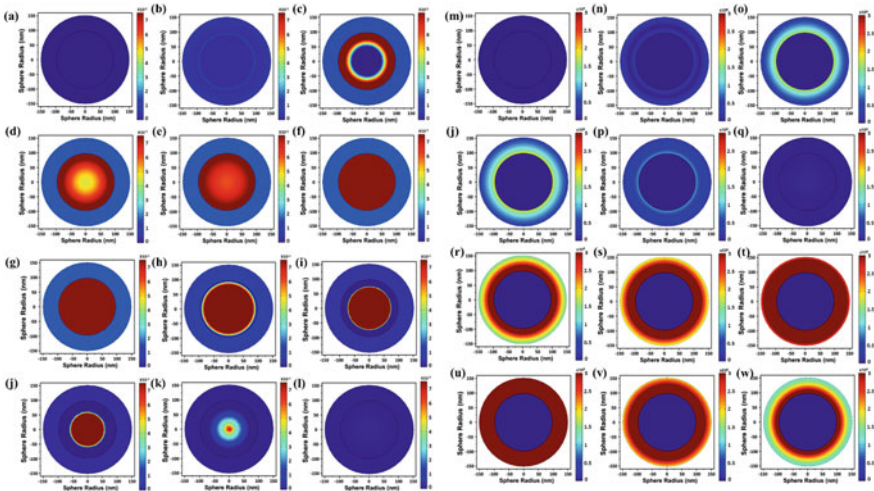
Fig. 4 COMSOL simulation for (**a-l**) stress and (m-w) strain in TPCM composite during liquefaction and solidification processes

cycles of charging and discharging. Volumetric stress and strain for a whole cycle of charging and discharging for a TPCM composite with a desired shell thickness are shown in Fig. 4 (a-l) and (m-w), respectively. The result indicates the improved thermal stability of the composite over multiple thermal cycles.

3.3 Thermal Analysis

The latent heat and phase transition temperatures of N-Hexacosane PCM, TPCM1, TPCM2 and TPCM3 were examined under differential scanning calorimeter (DSC). The DSC measurement consisting of charging (liquefaction) and discharging (solidification) curves for pure PCM, TPCM1, TPCM2 and TPCM3 composites is illustrated in Fig. 5a, b. Two distinct peaks were observed at lower and higher temperatures indicating S–S and S–L phase transition with small and large heat flows. The phase transition temperature for S–S transition remains quite similar. In contrast, a small deviation in S–L transitions temperature was observed compared to pure PCM (N-Hexacosane) with major peaks at 38.78 °C for S–S and 56.71 °C S–L transitions. Before charging or liquefaction stage, the S–S phase transformation is persuaded, altering the ordered phases to disordered phases (Sarı and Karaipekli 2009).

The difference between discharging or cooling onset temperature and a peak temperature of the TPCM composites is relatively lower than N-Hexacosane, suggesting that the super-cooling degree of the composite's material is lesser than that of PCM, which can be due to the Titania shell (Song et al. 2010). Further, the
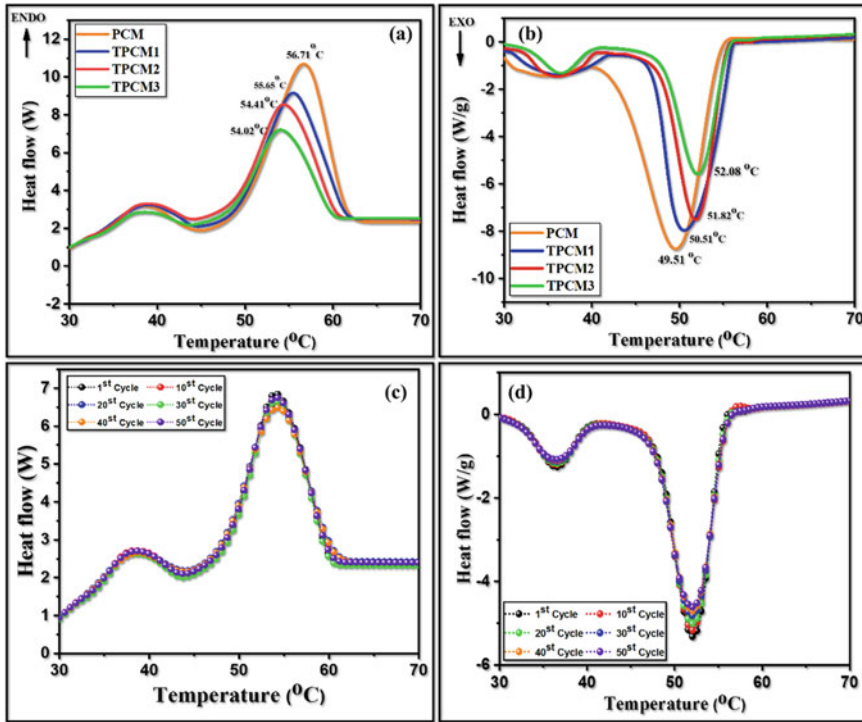
Fig. 5 (**a**) Liquefaction and (**b**) solidifying differential scanning calorimeter curves of the N-Hexacosane, TPCM1, TPCM2 and TPCM3 nanocomposites and (**c**, **d**) stability profile of 50 thermal cycle of TPCM composite during the process

latent heat values of pure PCM (N-Hexacosane) and TPCM were determined using the phase transition temperature and were used as an experimental input in COMSOL simulation. The latent heat and phase transition temperature of pure PCM, TPCM1, TPCM2 and TPCM3 are shown in Table 2. The results indicate that the TPCM composites have slightly lower thermal storage capacity and high thermal stability than N-Hexacosane PCM. Also, the stability of the composite was investigated for 50

Table 2 Latent heat and phase transition temperature of as-prepared TPCM composites during thermal cycle process

Samples	Liquefaction		Solidification	
	Temp. (°C)	ΔH_l (J/g)	Temp (°C)	ΔH_s (J/g)
PCM	56.71	187.4	49.51	176.34
TPCM1	55.65	164.09	50.51	157.49
TPCM2	54.41	158.67	51.82	138.93
TPCM3	54.02	142.09	52.08	127.37
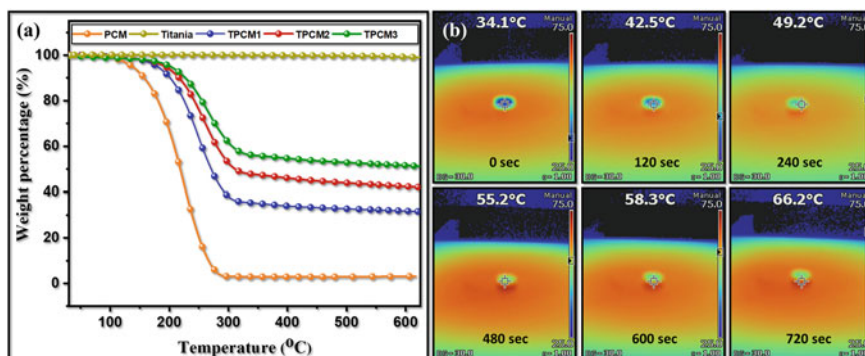
Fig. 6 (**a**) TGA profile and (**b**) IR imaging of N-Hexacosane and TPCM composites

thermal cycles, as shown in Fig. 5c, d. The results revealed that the TPCM composite is highly thermal stable with 10% degradation in the latent heat after 50 thermal cycles.

3.4 Thermal Stability and IR Imaging TPCM Composites

Further, thermal stability and weight% loss of Titania, N-Hexacosane and TPCM were investigated using thermographic measurements, as shown in Fig. 6a. The stability study was carried out within the temperature range of PCM, i.e., room temperature (RT 27 °C) to 600 °C. A slight dehydration was observed in the stable (Titania) material at a temperature below 200 °C and nearly 2% loss at elevated temperatures. This confirms the choice of Titania as a shell or supporting material to organic PCM due to its high stability at elevated temperatures. Whereas the N-Hexacosane material showed initial weight loss below 200° C and nearly 98% weight loss at elevated temperature of 350 °C, hence restricting the operational temperature for the TPCM below 350 °C.

Thermogravimetric examination of TPCM composite for their weight loss can directly be correlated to the encapsulation of PCM with Titania shell. The different TPCM composite shows 5%, 3% and 2% weight loss below 250 °C for TPCM1, TPCM2 and TPCM3, respectively. The residual weight at the elevated temperature (350°C) of TPCM was observed to be 65%, 53% and 44% for TPCM1, TPCM2 and TPCM3, respectively. In addition, a shift in the onset temperature was observed for the TPCM composite, which was greater than pure PCM. The temperature at which the maximum weight loss of TPCM composite occurred was nearly 20 °C more than that of N-Hexacosane, which indicate that the covering of Titania to the core material improves the overall stability of organic PCM. Further, the effect of Titania with respect to a temperature change, infrared (IR) thermal imaging was carried out for various TPCM composites, as shown in Fig. 6b. The surface temperature

distributions of the N-Hexacosane and TPCM composites were recorded every 120 s, and the surface temperatures were observed. All the TPCM composites showed quicker heat absorption than the N-Hexacosane at every moment, indicating better temperature and time regulating ability during the heating process. The average temperature TPCM attained after 720 s was 66.2 °C which was 15 °C higher than pure N-Hexacosane, indicating better heat absorption and transfer within the composite.

4   Conclusion

We report a scalable method to synthesize Titania/N-Hexacosane phase change material composite. The organic N-Hexacosane phase change material was used as the core material for heat storage with Titania as a supporting matrix and shield to the core PCM. The morphological, chemical and structural investigation confirms the formation of Titania/encapsulated N-Hexacosane PCM composite (TPCM). The protective layer of Titania over the core enables better thermal stability and prevents the leakage of organic phase change material, even if heated above the liquefaction temperature of the organic material. The TPCM composites were able to maintain its phase effectively with liquefaction and solidification at 54.02 °C and 52.08 °C, respectively. The as-prepared TPCM composite exhibited decent latent heat storage capability during the phase transition process, i.e., 142.09 J/g (liquefaction) and 127.37 J/g (solidification), respectively and high thermal stability. The overall results indicate that the composite has a potential to be used as a thermal energy storage material in large-scale application.

References

Abazović ND, Čomor MI, Dramićanin MD, Jovanović DJ, Ahrenkiel SP, Nedeljković JM (2006) Photoluminescence of anatase and rutile TiO$_2$ particles. J Phys Chem B 110(50):25366–25370

Agyenim F, Hewitt N, Eames P, Smyth M (2010) A review of materials, heat transfer and phase change problem formulation for latent heat thermal energy storage systems (LHTESS). Renew Sustain Energy Rev 14(2):615–628

Chaudhari R, Vora J, Lacalle LN, Khanna S, Patel VK, Ayesta I (2012) Parametric optimization and effect of nano-graphene mixed dielectric fluid on performance of wire electrical discharge machining process of Ni55. 8Ti Shape Memory Alloy Materi 10

Guan W-M, Li J-H, Qian T-T, Wang X, Deng Y (2015) Preparation of paraffin/expanded vermiculite with enhanced thermal conductivity by implanting network carbon in vermiculite layers. Chem Eng J 277:56–63

Hawlader M, Uddin M, Khin MM (2003) Microencapsulated PCM thermal-energy storage system. Appl Energy 74(1–2):195–202

Jaworski M (2012) Thermal performance of heat spreader for electronics cooling with incorporated phase change material. Appl Thermal Eng 35:212–219

Jurkowska M, Szczygieł I (2016) Review on properties of microencapsulated phase change materials slurries (mPCMS). Appl Thermal Eng 98:365–373

Khanna S, Marathey P, Paneliya S, Chaudhari R, Vora J (2012) Fabrication of rutile–TiO$_2$ nanowire on shape memory alloy: a potential material for energy storage application. Mater Today: Proc

Khanna S, Paneliya S, Hinshu H, Singh AP, Bhatt N, Barik B, Mishra R, Motiani R (2020) Incorporation of Anatase-TiO$_2$ in cement to enhance the self-cleaning and mechanical properties: a systematic study. Mater Today: Proc

Khanna S, Marathey P, Patel R, Paneliya S, Chaudhari R, Vora J, Ray A, Banerjee R, Mukhopadhyay I (2021) Unravelling camphor mediated synthesis of TiO$_2$ nanorods over shape memory alloy for efficient energy harvesting. Appl Surface Sci 541:148489

Khanna S, Marathey P, Vanpariya A, Paneliya S, Mukhopadhyay I (2021) In-situ preparation of Titania/graphene nanocomposite via a facile sol-gel strategy: a promising anodic material for Li-ion Batteries. Mater Lett 29:130143

Lad M, Usadadia N, Paneliya S, Khanna S, Bhavsar V, Mukhopadhyay I, Joshi D, Ray A (2021) A systematic investigation on evaporation, condensation and production of sustainable water from novel-designed tubular solar still. Proceedings of the 7th international conference on advances in energy research, Springer, pp 1121–1130

Li M, Wu Z, Tan J (2012) Properties of form-stable paraffin/silicon dioxide/expanded graphite phase change composites prepared by sol–gel method. Appl Energy 92:456–461

Mehrali M, Latibari ST, Mehrali M, Mahlia TMI, Metselaar HSC (2013) Preparation and properties of highly conductive palmitic acid/graphene oxide composites as thermal energy storage materials. Energy 58:628–634

Najjar A, Hasan A (2008) Modeling of greenhouse with PCM energy storage. Energy Conver Manag 49(11):3338–3342

Pan L, Tao Q, Zhang S, Wang S, Zhang J, Wang S, Wang Z, Zhang Z (2012) Preparation, characterization and thermal properties of micro-encapsulated phase change materials. Solar Energy Mater Solar Cells 98:66–70

Paneliya S, Khanna S, Patel U, Prajapati P, Mukhopadhyay I (2020) Systematic investigation on fluid flow and heat transfer characteristic of a tube equipped with variable pitch twisted tape. Int J Thermofluids 1:100005

Paneliya S, Khanna S, Singh AP, Patel YK, Vanpariya A, Makani NH, Banerjee R, Mukhopadhyay I (2021) Core shell paraffin/silica nanocomposite: a promising phase change material for thermal energy storage. Renew. Energy 167:591–599

Sarı A, Karaipekli A (2009) Preparation, thermal properties and thermal reliability of palmitic acid/expanded graphite composite as form-stable PCM for thermal energy storage. Solar Energy Mater Solar Cells 93(5):571–576

Sarier N, Onder E (2007) The manufacture of microencapsulated phase change materials suitable for the design of thermally enhanced fabrics. Thermochimica Acta 452(2):149–160

Singh AP, Khanna S, Paneliya S, Hinsu H, Patel Y, Mehta B (2020) Preparation and characterization of solid-state neopentyl glycol/expanded graphite micro composite for thermal energy storage applications. Materi Today: Proc

Song G, Ma S, Tang G, Yin Z, Wang X (2010) Preparation and characterization of flame retardant form-stable phase change materials composed by EPDM, paraffin and nano magnesium hydroxide. Energy 35(5):2179–2183

Su J-F, Wang X-Y, Wang S-B, Zhao Y-H, Huang Z (2012) Fabrication and properties of microencapsulated-paraffin/gypsum-matrix building materials for thermal energy storage. Energy Conver Manag 55:101–107

Teixeira MI, Andrade LR, Farina M, Rocha-Leão MHM (2004) Characterization of short chain fatty acid microcapsules produced by spray drying. Mater Sci Eng C 24(5):653–658

Usadadia N, Lad M, Paneliya S, Khanna S, Ray A, Mukhopadhyay I (2021) Novel Design of PV integrated solar still for cogeration of power and sustainable water using PVT technology. Proceedings of the 7th international conference on advances in energy research, Springer, pp 1131–1143

Xu B, Li Z (2013) Paraffin/diatomite composite phase change material incorporated cement-based composite for thermal energy storage. Appl. Energy 105:229–237

Zhang Z, Fang X (2006) Study on paraffin/expanded graphite composite phase change thermal energy storage material. Energy Conver Manag 47(3):303–310

Recent Advances in Infrastructure Planning, Design and Control

Design of Bluetooth-Controlled Floor Cleaning Robot

Unmesh Gorade, Din Bandhu, Soni Kumari, Jagat Rath, and Kumar Abhishek

Abstract Floor cleaning is one of the most useful and hygienic practices done at all houses as well as workplaces to keep them neat and clean by removing the stains, dirt, litter, and obstructions on the floor. The process of floor cleaning not only cleans the floors but also makes them look beautiful. Although it is an essential practice, it is hectic and time consuming too. To overcome this problem, the floor cleaning robot was introduced into the market. The first-floor cleaning robot was introduced in the market by a company named iRobot in 2002 followed by other competitive players. These robots, equipped with various types of tools and features, are technologically advanced that makes them more attractive and effective in their operations. In this paper, the making and the working process of a Bluetooth-controlled floor cleaning robot are discussed. The key purpose of this work is cost cutting and introducing the floor cleaning robot at affordable rates in the market. The design consists of different components, namely Arduino, L293D motor driver board, DC motors, Bluetooth module, and water pump. The design also consists of other structural components to form the robot that can clean the floor on the commands given from a smartphone application. This robot serves the cleaning purpose effectively and efficiently, hence reducing the labor force as well as fulfilling the motto of cost cutting.

Keywords Floor cleaning · Robots · Bluetooth · Robotic cleaning · Design · Robotic design

U. Gorade · D. Bandhu · J. Rath · K. Abhishek (✉)
Department of Mechanical and Aero-Space Engineering, Institute of Infrastructure, Technology, Research and Management (IITRAM), Ahmedabad, India

S. Kumari
Department of Mechanical Engineering, GLA University, Mathura, India

121

1 Introduction

Due to their usefulness in aiding people in floor cleaning activities at residences, resorts, workplaces, restaurants, industries, distribution centers, institutions, hospitals, and other locations, robotic cleaners have garnered a lot of interest in robotics research. These cleaning robots can function manually, semi-automatically, or entirely autonomously (Asafa et al. 2018; Khan et al. 2013; Ong et al. 2020; Bordoloi et al. 2017). It is a smartphone-controlled robot that cleanses the floors of any home by spinning mops positioned at the robot's front. A floor cleaning robot is a compact robotic system that eliminates human error and provides cleaning activity with much more efficiency. The specifications like Bluetooth-controlled, dry or wet cleaning, etc., correspond to some of the expected behavior that is programmed into the robot.

1.1 Historical Development

A robot cleaner is an electronically programmable electronic instrument that utilizes a vacuumed cleaner component to cleanse a particular surface. Some companies have recently released devices that can sweep over jagged corners and edges, whereas others have added functions like UV sterilizing and liquid cleaning. Here is the list of some available products in the market (Prassler et al. 2000; Kim et al. 2019; Ilyas et al. 2018):

iRobot

iRobot unveiled its first robotic vacuum cleaning product in 2002 named Roomba. It immediately becomes a huge market sensation and its demand increased immediately, and due to this, the company launched the series of robots which are shown in Table 1.

Table 1 iRobot's variant for floor cleaning

iRobot		
(a) Roomba	(b) Scooba	(c) Braava
• Launch year: 2002 • Manufacturer: iRobot (American) • Type of use: dry vacuum • Technology: IR, RF, and auto-charging mechanism • Price: $500	• Launch year: 2005 • Manufacturer: iRobot (American) • Type of use: wet washing of floor • Technology: IR with virtual wall accessories • Price: $500	• Launch year: 2006 • Manufacturer: iRobot, KITECH, Sony • Type of use: floor moping for hard surfaces/dry clean • Technology: IR with virtual wall accessories for industrial cleaning • Price: $700

Table 2 Robotic cleaner developed by NEATO Robotics

Neato XV-11
• Launch year: 2010
• Manufacturer: NEATO Robots XV series (California)/China
• Type of use: vacuum cleaning
• Technology: Laser range finder technology, simultaneous localization and mapping (SLAM), and auto-charging
• Price: $399

Table 3 Robotic cleaner developed by Dyson

EYE-360
• Launch Year: 2016
• Manufacturer: Dyson (UK)
• Type of use: vacuum cleaning
• Technology: It uses a 360° panoramic vision camera to monitor its environment in real time and a turbo brush for efficient cleaning along with an auto-charging mechanism (benchmark in history of cleaning robots)
• Price: $1000 (approx)

After that, several countries have started manufacturing robotic cleaners. China also jumped into this market with "NEATO Robotics" having more reliable technology and advanced features. Table 2 lists the variants of robotic cleaners developed by NEATO Robotics.

Similarly, Dyson launched a robot name EYE-360 that employs a unique path tracking technique than NEATO and iRobot's competing robotic devices. Table 3 lists a brief detail about this robotic cleaner.

Some of these robots are autonomous, some are manual, and some are hybrid. It means that they can be controlled either manually through remote control or autonomously. Some robots are having waste containers for storing the waste and some having a fluid tank for storing the cleaning fluid. IR sensor mechanism is used for autonomous motion, and GUI is used for manual controlled robots. The movement of certain autonomous cleaning robots can be regulated by infrared sensors data utilizing an inertial navigation approach; however, it may also be configured with a magnetization unit for computed paths and rotations (Adithya n.d.; Rubio et al. 2019; Jain and Singh Rawat 2017).

This section provides a quick overview of the Bluetooth-controlled floor cleaning robot and its specifications to assist humans and make their life easy. Besides this, the historical development in the robotic sector has also been discussed along with some companies and their manufactured robots to get some more clarity about this industry.

2 Materials and Methods

The system is developed by using various components like Arduino, DC motors, L293D motor driver board, 12 V water pump, Bluetooth Module, etc. The block diagram of the intended model is shown in Fig. 1. The 12 V lead-acid rechargeable battery is used for the operation purpose of this robot. A separate 5 V input is given through Arduino via breadboard to the components like Bluetooth module and motor driver board. TIP31C transistor is used for the switching purpose of the motor and pump. The employed components are described as follows.

2.1 Microcontroller—Arduino Mega 2560

The Arduino Mega is a microcontroller board based on the ATmega2560. It features 54 digital input/output pins (with 15 of them being PWM outputs), 16 analog inputs, 4 UARTs (hardware series ports), a 16 MHz crystal oscillator, a USB connection, ICSP header, a power connector, and a reset button. To get begun, it must be linked to
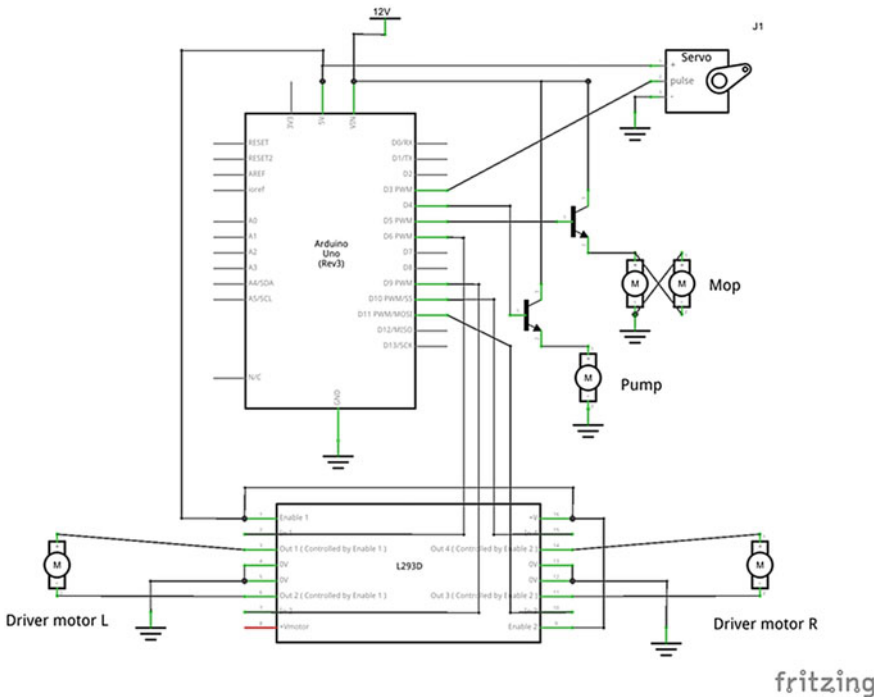
Fig. 1 Block diagram of the intended model

Fig. 2 Arduino Mega 2560
microcontroller
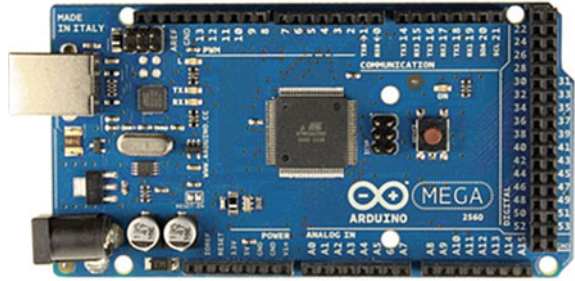
a computer by USB connection or an AC to DC converter, or it must be inextricably linked to rechargeable batteries. Figure 2 displays the structure of the microcontroller.

2.2 L293D Motor Driver Board

The L293D motor driver board makes it very safe and simple to regulate the velocity and movement of two DC motors using a single IC. Its motor voltage ranges between 4.5 and 36 volts, with a full-load motor current of 600 milliamperes. Its maximum peak motor current is 1.2A. It requires a supply voltage between 4.5 V and 7 V. The IC operates on the half H-bridge concept. H-bridge is a configuration that allows the user to access motors both clockwise and counterclockwise. Figure 3 depicts the L293D motor driver board along with its interface circuit with DC motor.

2.3 Bluetooth Module (HC-05)

The Bluetooth module is implemented to govern the robot by communicating with it through cell phone or mobile. It takes the information from the phone and sends it to the robot. It is an Arduino Bluetooth serial module. It works between the operating voltage of 4 V-6 V and an operating current of 30 mA. Its range is a radius of 100 m. Frequency-hopping spread spectrum (FHSS) is used in it. It has three modes of operation: master, slave, and master/slave. The Bluetooth module utilized in this design is shown in Fig. 4.

2.4 DC Motor

A direct current motor (DC motor) is an electrical motor that transforms electrical energy into mechanical energy and is powered by a direct current (DC). In it, supply
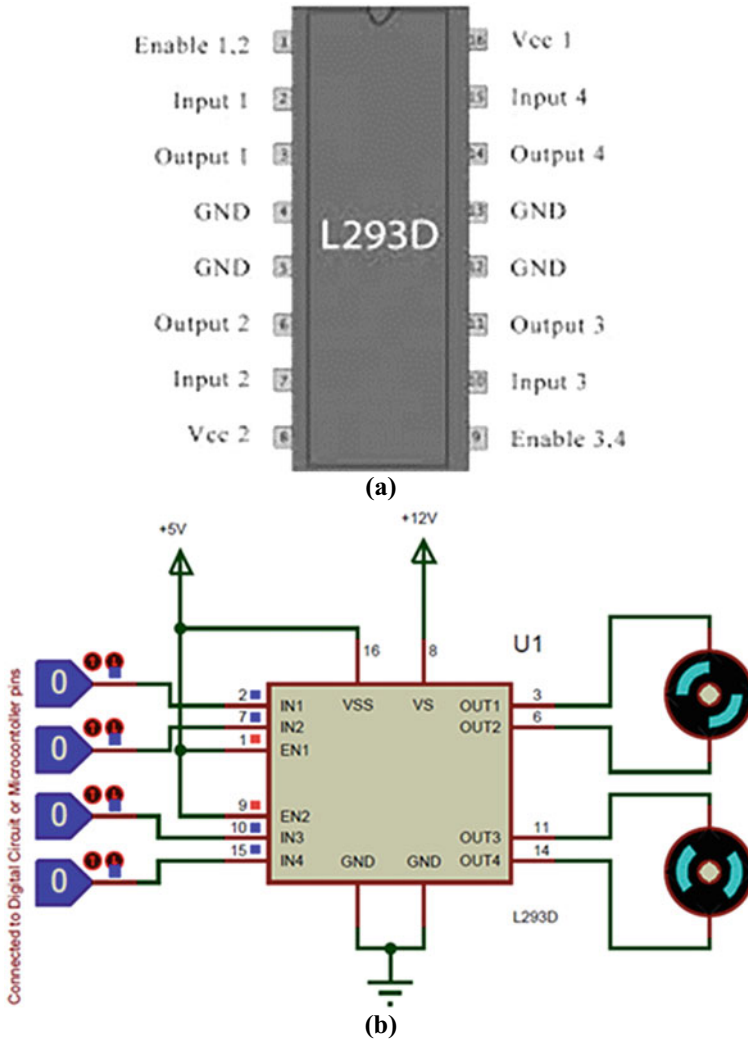
Fig. 3 L293D motor driver board: **a** pin configuration and **b** interface circuit with DC motor

voltage and current are given to the input port, and we get torque and speed as an output at the output port. DC motor employed in this design is shown in Fig. 5.

2.5 BO Motor

Battery operation (BO) motor is a type of DC motor which also converts electrical energy into mechanical energy. It is a single-shaft plastic geared motor with high

Fig. 4 Design of the
Bluetooth module (HC-05)
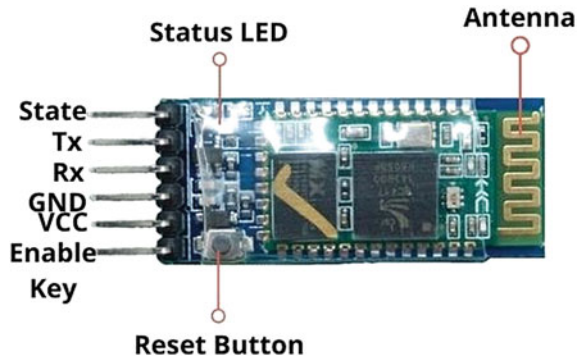
Fig. 5 Design of DC motor

torque and rpm at low running voltages. The robot's design is optimal because of its tiny shaft and matched wheels. It is ideal for in-circuit use due to its lightweight and installation slots on the casing. Its operating voltage range is 2 V–12 V with an output RPM of 150. Figure 6 depicts the BO motor.

2.6 Breadboard

A breadboard is a solderless device used for prototyping electronics and testing circuit designs. Several electronic components in circuit boards can indeed be interlinked by putting their leads or ends into slots and connecting them with cables wherever necessary. The two side sets of slots are horizontally linked and divided in the midway, whereas the rest slots are vertically linked. Figure 7 depicts a breadboard.

Fig. 6 Design of BO motor
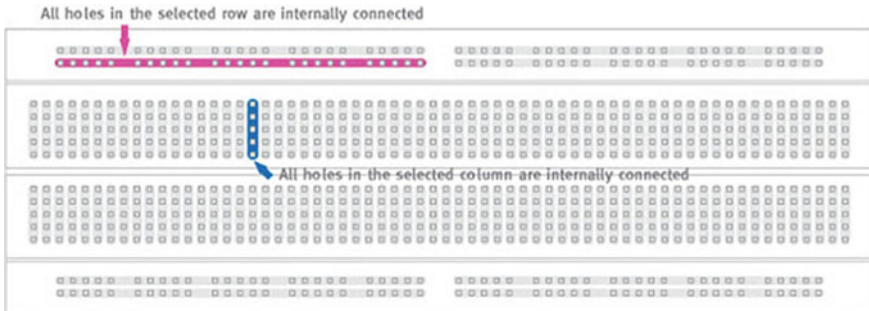
Fig. 7 Design of the breadboard

2.7 Water Pump (6–12 V DC Mini Aquarium)

It is an ideal non-submersible pump for a variety of liquid movement applications. When properly driven, it can withstand hot fluids up to 80 °C, draw water down the pipe from up to 2 m, and pump water upward for up to 3 m. It requires a voltage between 6–12 V DC and 0.5–0.7A current. Its maximum flow rate is 1–3 L/min. The design of the water pump is shown in Fig. 8.

2.8 TIP31C Transistor

TIP31C is an NPN transistor with an emitter, base, and collector. The emitter is normally connected to the ground and collector to load. The base is normally used

Fig. 8 Design of the water pump

Fig. 9 Design of the transistor
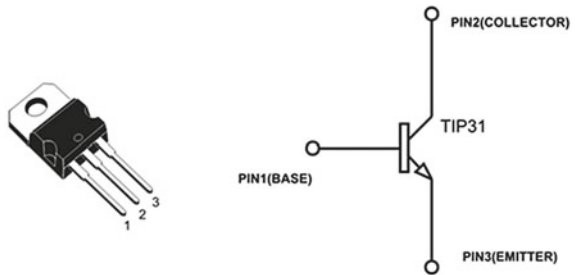
as a trigger to turn on the transistor. Its maximum operating temperature is 150 °C. The transistor design is shown in Fig. 9.

3 Application Software

Generally, the Java language is used to develop an Android app. One does not need to have a knowledge of Java language for this app as it is available on Google's play store by the name of "Bluetooth Serial Controller". It can also be developed using MIT App Inventor by anyone. Users may customize the button's description, action, visibility, and recurrence in this software. It allows users to save up to five distinct configurations. The software's URL may be found here: https://play.google.com/store/apps/details?id=nextprototypes.BTSerialController&hl=en_IN&gl=US.

This app communicates with the robot (as shown in Fig. 11) via a Bluetooth module. The module has a particular MAC address which is selected by the app to connect to the module. The user interface of this application software is shown in Fig. 10.
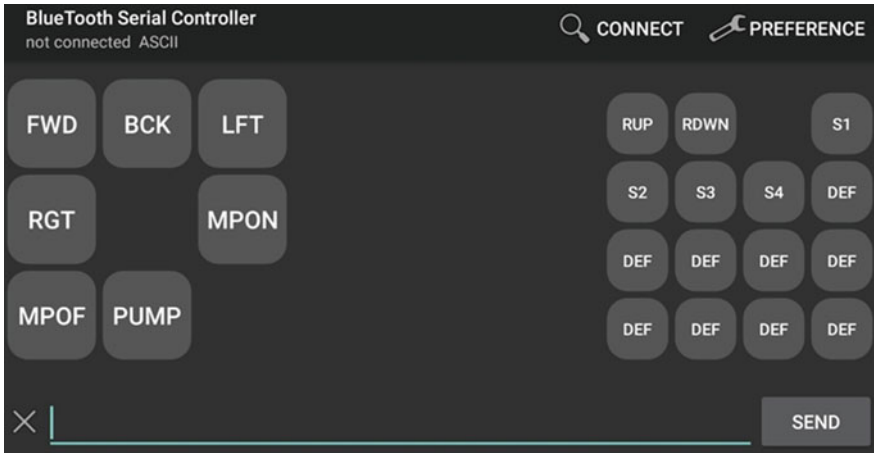
Fig. 10 User interface of the software
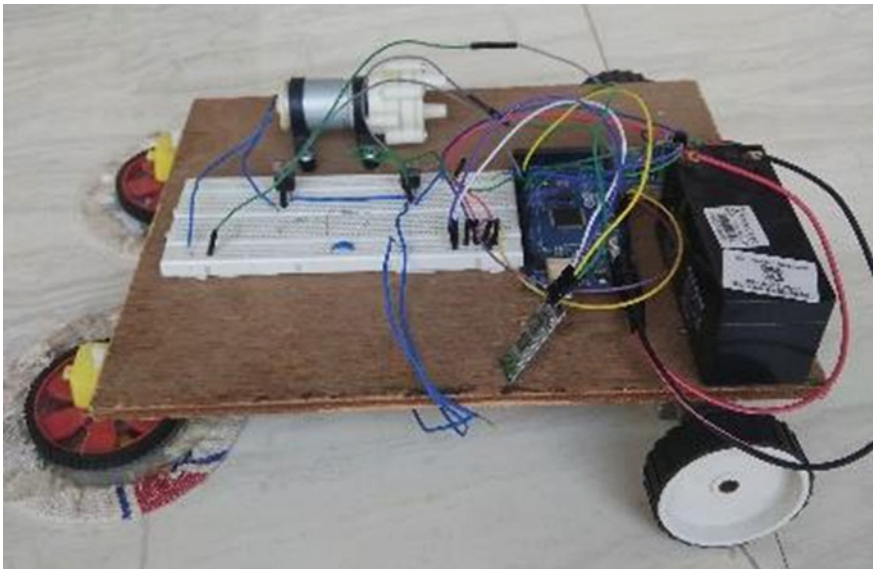
Fig. 11 Model of Bluetooth-controlled floor cleaning robot

4 Conclusions

A Bluetooth-controlled floor cleaning robot can be developed using an Arduino board, DC motors, Bluetooth module, and other electronic components at a very affordable price. It is easy to use and can be used over a small cleaning area. The intended design can easily fulfill the said purpose by helping and assisting at the

workplace to get the best results by reducing manpower and time consumption. The future scope of this project is to make it fully autonomous using ultrasonic/IR sensors, dry cleaning mechanisms, battery monitoring, etc.

References

Adithya PS, Tejas R, Sai Varun V, Prashanth BN, Design and development of automatic cleaning and mopping robot. https://doi.org/10.1088/1757-899X/577/1/012126

Asafa TB, Afonja TM, Olaniyan EA, Alade HO (2018) Development of a vacuum cleaner robot. Alexandria Eng J 57:2911–2920. https://doi.org/10.1016/j.aej.2018.07.005

Bordoloi AK, Islam F, Zaman J, Phukan N, Kakoty NM (2017) A floor cleaning robot for domestic environments. In: ACM international conference proceeding series. association for computing machinery. https://doi.org/10.1145/3132446.3134883

Ilyas M, Yuyao S, Mohan RE, Devarassu M, Kalimuthu M (2018) Design of sTetro: A modular, reconfigurable, and autonomous staircase cleaning robot. J Sens 2018. https://doi.org/10.1155/2018/8190802

Jain M, Singh Rawat P, Morbale J (2017) Automatic floor cleaner. Int Res J Eng Technol

Khan MR, Huq NML, Billah MM, Ahmmad SM (2013) Design and development of mopping robot-'HotBot'. In: IOP conference series: materials science and engineering, p 012008. IOP Publishing (2013). https://doi.org/10.1088/1757-899X/53/1/012008

Kim J, Mishra AK, Limosani R, Scafuro M, Cauli N, Santos-Victor J, Mazzolai B, Cavallo F (2019) Control strategies for cleaning robots in domestic applications: a comprehensive review. Int J Adv Robot Syst 16. https://doi.org/10.1177/1729881419857432

Ong RJ, Azir KNFK (2020) Low cost autonomous robot cleaner using mapping algorithm based on internet of things (IoT). In: IOP conference series: materials science and engineering, p 012071. Institute of Physics Publishing. https://doi.org/10.1088/1757-899X/767/1/012071

Prassler E, Ritter A, Schaeffer C, FioriniP (2000) A short history of cleaning robots. Auton Robots 9:211–226. https://doi.org/10.1023/A:1008974515925

Rubio F, Valero F, Llopis-Albert C (2019) A review of mobile robots: concepts, methods, theoretical framework, and applications. https://us.sagepub.com/en-us/nam/, https://doi.org/10.1177/1729881419839596

Detection of Sensor Fault in a DC Microgrid Using Supertwisting Observer

Daijiry Narzary, Subrat Kumar Swain, Jagat Rath, and Kalyana C. Veluvolu

Abstract The detection of sensor faults in a direct current (DC) microgrid is essential to provide a safe and uninterrupted supply of power. The fault detection techniques in the DC microgrid should involve immediate sensor fault detections to protect the system from adverse effects. To address this issue, in this paper, a fault detection technique is designed which addresses the scenario where the interconnected distributed generation units (DGUs) are affected by sensor faults in a DC microgrid. Multiplicative faults in the grid-connected voltage and current sensors are considered. A model-based multiple sliding mode observers (HOSM) are designed to estimate the states of the DGUs, and faulty sensors are detected based on the generated residuals. The stability of the overall microgrid system can be achieved by designing a hierarchical controller which ensures uniform current sharing among all the DGUs. The validation of the proposed method is supported through extensive MATLAB simulations for various arrangements of the DC microgrid subjected to numerous known and unknown disturbances. A common threshold is selected from the multiple simulations for sensor fault detection.

Keywords Sensor faults · Fault detection · DC microgrid · DGUs · HOSM observer · LMI · Renewable energy

1 Introduction

In recent years, the DC microgrid is emerging as an efficient choice for providing the required energy demand. It consists of distributed generation units (DGUs), energy storage systems like batteries and compressed air storage systems, with

D. Narzary · S. K. Swain · K. C. Veluvolu (✉)
School of Electronics Engineering, Kyungpook National University, Daegu, South Korea
e-mail: veluvolu@ee.knu.ac.kr

J. Rath
Institute of Infrastructure Technology Research and Management,
Ahmedabad 380026, Gujarat, India

different loads (Meng et al. 2015). The operation of a DC microgrid (Yang et al. 2011; Elsayed et al. 2015) in the grid-connected and islanded mode is feasible according to the situation requirement. It provides more advantages than AC microgrids like easy availability of DC energy sources and inverters, improved energy efficiency, maximum energy consumption, interfacing of batteries, and better power quality and reliability. They are efficiently used in charging electric cars, trains, ships, and also in the space (Beheshtaein et al. 2019). However, the integration of DGUs into the communication network can pose some challenges in the protection and control of the system. Hence, an effective and intelligent protection scheme should be designed to reduce the faults in the main grid and the microgrid. Detecting a fault sooner is quite essential for an overall monitoring system. During faults, the microgrid should be isolated from the main grid immediately to protect the loads, lines, and microgrid. The protection of the overall system by considering possible sensor faults in the DC microgrids and detecting them is extensively studied in Wang et al. (2020), Sharma et al. (2010). The DC microgrid is prone to different faults like actuator fault, component fault, any fault due to interconnection, which is explained in Kumar et al. (2017), Beheshtaein et al. (2019).

The use of sensor networks has increased in recent years, and it has gained much research attention. The data of the sensor faults should be carefully collected to detect the sensor fault conditions accurately. The faults in the sensor can occur due to short circuits, broken sensors, and even due to low power and calibration errors. However, the poor quality of sensor data can cause software faults. The sensor fault detection methods can be categorized as rule-based, estimation, time-series analysis, and learning-based methods (Gao et al. 2015). To prevent the system from loss of any network information, the sensor faults should be detected promptly. The existing work on sensor faults detection techniques is mainly based on additive faults, and multiplicative sensor faults are less considered. In Bansal and Sodhi (2018), sensor fault detections in a grid-connected or islanded mode DC microgrid are discussed using model-based and data-driven-based fault detection. A state observer is used in the model-based fault detection (Poon et al. 2016) to generate the residuals, and a fault is detected based on the threshold selected. A model-based methodology for fault detection is used in switching power converters in Gao et al. (2015) to detect random sensors and components faults. However, the variation of load and parameters values may trigger a false alarm and results in inaccurate fault detection. Hence, to address this issue, observers based on H_∞/H_- (Poon et al. 2017) criteria are designed. The use of this methodology balances the robustness of the residual and sensitivity from the faults to the generated residual in the presence of disturbances. A linear parameter varying extended state observer is used for the detection of fault and diagnosis in Asadi et al. (2020). These observers use linear matrix inequality(LMI) computation of the H_2/H_∞ norm minimization to deal with the noise and external disturbances. However, this technique depends on the frequency domain and less information is available about its stability condition.

In Yan et al. (2017), sliding mode techniques are used for estimating the states of the inverter in the presence of three types of communication delays. In Mola et al. (2020), a distributed observer is designed for various types of fault detection in a DC

microgrid. In Shao et al. (2013), a first-order sliding mode observer (SMO)-based fault detection is used in a modular multilevel converter for locating the fault in a switching device. In Lan et al. (2018), a fault-tolerant controller based on adaptive SMO is designed to estimate the pitch system states and eliminate actuator faults in a wind turbine system. Similarly, in Veluvolu and Soh (2011), the authors have used a multiple SMO for the estimation of state and unknown input for a class of multi-input multi-output (MIMO) nonlinear systems. However, the effect of chattering in the first-order SMO can be eliminated by using a higher-order SMO based on STA as discussed in Kommuri et al. (2016). The HOSMO has important features like high accuracy and robustness with respect to the change in internal and external disturbances. An integral disturbance observer is designed with a super twisting SMC to suppress both matched and unmatched uncertainties in a DC microgrid as shown in Kumar et al. (2020).

Based on the works as mentioned earlier, it is inspired to design two HOSM observers for generating the residuals and detect the sensor faults in the presence of noises and delays in a DC microgrid. In the DGUs of the DC microgrid, the output voltage and current are estimated by using STA-based HOSM observers. A threshold is selected for the faulty sensors in the presence of noise and unknown loads for detecting the sensor faults. Numerous simulations are conducted for the sensor fault detections based on critical and non-critical loads. A multiplicative sensor fault is considered in the sensors for various DGUs. The changes in the generated residuals of the voltage and current sensors are observed, and a common threshold is finally selected for the DGUs. The paper is organized as follows: The problem is formulated and discussed in Sect. 2. Section 3 provides an overview of the modeling of HOSM observers and detection of the faulty sensors. The simulation results are presented and discussed in Sect. 4. Finally, the conclusion of the paper is done in Sect. 5.

2 Problem Statement

A typical DC microgrid with n interconnected DGUs can be modeled as shown in Fig. 1. The communication network among all the DGU s in a DC microgrid can be represented by a graph, $G = (\upsilon, \kappa)$. The DGUs are represented by nodes $\upsilon = 1, ... p$ and the power lines can be represented by edges, $\kappa \subseteq \upsilon \times \upsilon$. Applying Kirchoff's voltage and current law, the dynamic model of DGU-i is

$$\frac{dV_i}{dt} = \frac{1}{C_{pi}}(I_i(t) - I_{li}(t)) + \sum_{j \in n_i} \frac{1}{C_{pi} R_{ij}}(V_j(t) - V_i(t)) \tag{1}$$

$$\frac{dI_i}{dt} = \frac{1}{L_{pi}}V_{pi}(t) - \frac{R_{pi}}{L_{pi}}I_i(t) - \frac{1}{L_{pi}}V_i(t), i = 1, 2, ... n. \tag{2}$$

where $V_i(t)$ and $I_i(t)$ are the capacitor voltage and output current of the DGU, respectively. The input command to the buck converter is $V_{pi}(t)$. C_{pi}, L_{pi}, R_{pi} are

Fig. 1 Considered DC
microgrid with 3 DGUs
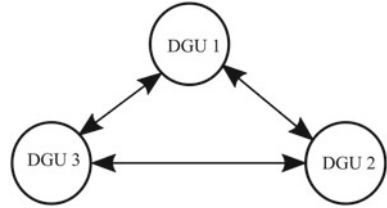
the constants denoting the capacitor, inductance and resistance of the filter. R_{ij} and I_{li} denote the impedance's of the power lines interconnecting between the DGU-i and DGU-j. The system states are denoted by $V_i(t)$, $I_i(t)$. The capacitor voltage at the point of common coupling can be represented by V_j, where $j \subseteq n_i$. The conductance matrix of power lines is denoted by $\frac{1}{R_{ij}}$ and $T = [t_{ij}]$ denotes the adjacency matrix. In this case, bidirectional communication in between the DGUs is considered (i.e., $t_{ij} = t_{ji}$). When a communication exists in between the networks, $t_{ij} = 1$, otherwsie it is zero.

Thus, we can represent the state space equation of the system DG_i as follows:

$$\dot{Z}_i(t) = \beta_{ii} Z_i(t) + \sum_{j \in N_i} \beta_{ij} Z_j + \Lambda_i U_i(t) + \chi_i \omega_i(t) + \beta_{di} \zeta_i(t) \tag{3}$$

$$H_i(t) = O_i Z_i(t) + \Delta_{d_i}(t) \zeta_i(t) \tag{4}$$

Defining $Z_i = [V_i, I_i]^T$ as the states, $U_i(t) = V_{ni}(t)$ and $\omega_i(t) = I_{li}(t)$ as the inputs, $H_i(t)$ is the output with Z_i as measurable states and $\zeta_i(t)$ as unknown disturbance. where

$$\beta_{ii} = \begin{bmatrix} \sum_{j \in n_i} -\frac{1}{R_{ij} C_{pi}} & \frac{1}{C_{pi}} \\ -\frac{1}{L_{pi}} & -\frac{R_{pi}}{L_{pi}} \end{bmatrix}, \beta_{ij} = \begin{bmatrix} \frac{1}{R_{ij} C_{pi}} & 0 \\ 0 & 0 \end{bmatrix}, \Lambda_i = \begin{bmatrix} 0 \\ \frac{1}{L_{pi}} \end{bmatrix}, \chi_i = \begin{bmatrix} \frac{1}{C_{pi}} \\ 0 \end{bmatrix}, \beta_{di} = \begin{bmatrix} 0.1 \\ 0 \end{bmatrix}, \Delta_{di} = \begin{bmatrix} 0.1 \\ 0.1 \end{bmatrix},$$

A decentralized state feedback primary controller is designed to regularize the voltage at each PCC and ensures stability of the grid. The dynamics of the primary voltage controller is (Fig. 2)

$$\begin{aligned} \dot{\theta}_i(t) &= \epsilon_i(t) + e_i(t) \\ &= V_{ri}(t) - V_i(t) + e_i(t) \\ &= V_{ri}(t) - E_i O_i Z_i(t) + e_i(t) \end{aligned} \tag{5}$$

where $V_{ri}(t)$ is the voltage used as reference and $e_i(t) \in R$ is the input of the secondary controller. The state feedback controller can be written as $U_i(t) = \varrho_i Z'_i(t)$, where $Z'_{ii}(t) = [Z_i^T, e_i(t)]^T$ and $(\beta'_{ii} + \Lambda_i K_i)$ is always Hurwitz. The state matrix can be represented as $\beta'_{ii} = \begin{bmatrix} \beta_{ii} & 0 \\ -E_i & 0 \end{bmatrix}$ and E_i is the identity matrix.
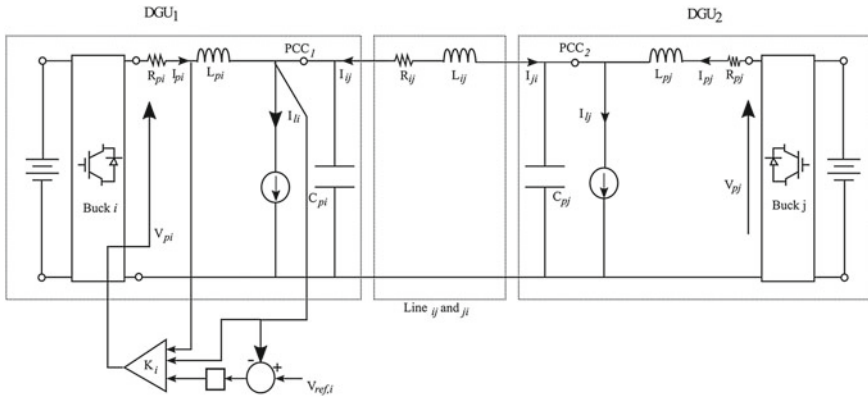
Fig. 2 Electrical structure of interconnected DGUs in a DC microgrid

And ϱ_i is designed using the linear matrix inequality (LMI) (Boyd et al. 1994). On account of proportional current sharing among the DGUs, the loads can be supplied without any interruption. Hence, the load is proportionally shared among all the other DGUs in the microgrid at the steady-state condition. An equation of the secondary controller for the DGU-i is designed as follows:

$$\dot{e}_i(t) = -W_{I,i} \sum_{j \in n_i} a_{ij} \left(\frac{I_i(t)}{I_i{}^s} - \frac{I_j(t)}{I_j{}^s} \right) \tag{6}$$

where $W_{I,i}$ denotes the integral coefficient of the DGU-i. The stability of the secondary controller can be proved similar to Tucci et al. (2015).

The main objective of this paper is to design a super twisting algorithm(STA) based on HOSM observers for the estimation of current and voltage for system (1)–(2) for fault detection. Separate HOSM observers are designed for each DGUi for the estimation of current and voltage. A threshold is selected based on the load conditions and interconnection of DGUs in different scenarios. In this work, sensor fault is detected in the presence of multiplicative sensor faults. A hierarchical controller is designed to maintain stability and ensure uniform current distribution between the interconnected DGUs.

3 Modeling of STA-based HOSM Observer and Detection of Sensor Faults

To enhance the robustness of the proposed method, an STA-based proposed observer (Rinaldi et al. 2019) is incorporated to estimate the voltage and the current in each DGUs. The unknown voltage can be estimated from the current dynamics by using the following HOSM observer design:

$$\frac{d\hat{I}_i(t)}{dt} = \frac{1}{L_{pi}}V_{pi}(t) - \frac{R_{pi}}{L_{pi}}\hat{I}_i(t) - \frac{1}{L_{pi}}\alpha_i(e_{vi})) \tag{7}$$

where $\alpha_i(t)$ is the robust term of the super twisting (STA) (Chalanga et al. 2016). Let $e_{vi}(t) = \hat{I}_i(t) - I_i(t)$, represent the observer error.

The robust terms of the STA (Moreno and Osorio 2012) can be designed as

$$\alpha_i(e_{vi}) = -\kappa_{i1}|e_{vi}|^{\frac{1}{2}}sign(e_{vi}) - \kappa_{i2}\int_0^t sign(e_{vi})d\tau - \kappa_{i3}e_{vi} \tag{8}$$

where κ_{i1}, κ_{i2}, and κ_{i3} are the STA gains. The error dynamics of the SMO can be modeled as:

$$\dot{e}_{vi} = -\frac{R_{pi}}{L_{pi}}e_{vi} + \frac{1}{L_{pi}}\alpha_i(e_{vi}) + \frac{1}{L_{pi}}V_i = \chi_i + \frac{1}{L_{pi}}\alpha_i(e_{vi}) \tag{9}$$

where $\chi_i = \chi_{i1}(e_{vi}) + \chi_{i2}$ denotes the higher-order perturbation terms. Hence, the boundedness of the estimated voltage can be assumed as $||\chi_{i1}|| \le \Delta_{i1}||e_{vi}||$ and $||\dot{\chi}_{i2}|| \le \Delta_{i2}$, where Δ_{i1} and Δ_{i2} denote the positive bounds of the perturbation terms. The error convergence of the sliding surface in finite time, i.e., e_{vi} to the origin, can be proved similar to Chalanga et al. (2016). The STA gains k_{i1}, k_{i2}, and k_{i3} can be designed according to Rath et al. (2014). The voltage reconstruction of the ith DGU can be written as:

$$\hat{V}_i = k_{i2}\int_0^t sign(e_{vi})dt \tag{10}$$

Similarly, the current dynamics of the HOSM Observer can be designed according to the following equations:

$$\frac{d\hat{V}_i(t)}{dt} = \frac{1}{C_{pi}}(I_i(t) - I_{li}(t)) + \frac{1}{C_{pi}R_{ij}}V_j(t) - \frac{1}{C_{pi}R_{ij}}\alpha_{vi}(e_{ci})) \tag{11}$$

where $\alpha_{vi}(e_{ci})$ is the robust term of the STA. The sliding surface of the current can be defined as $e_{ci}(t) = \hat{V}_i(t) - V_i(t)$ and its error dynamics can be governed as:

$$\dot{e}_{ci} = -\frac{1}{C_{pi}}s_{ci} - \frac{1}{C_{pi}R_{ij}}\alpha(e_{ci}) + \frac{1}{L_{pi}}V_i = \gamma_i + \frac{1}{C_{pi}R_{ij}}\omega(e_{ci}) \tag{12}$$

The block diagram of the proposed observers for fault detection is designed and depicted as shown in Fig. 3. The various sensor faults in the DGUs are considered as multiplicative faults and modeled as follows:
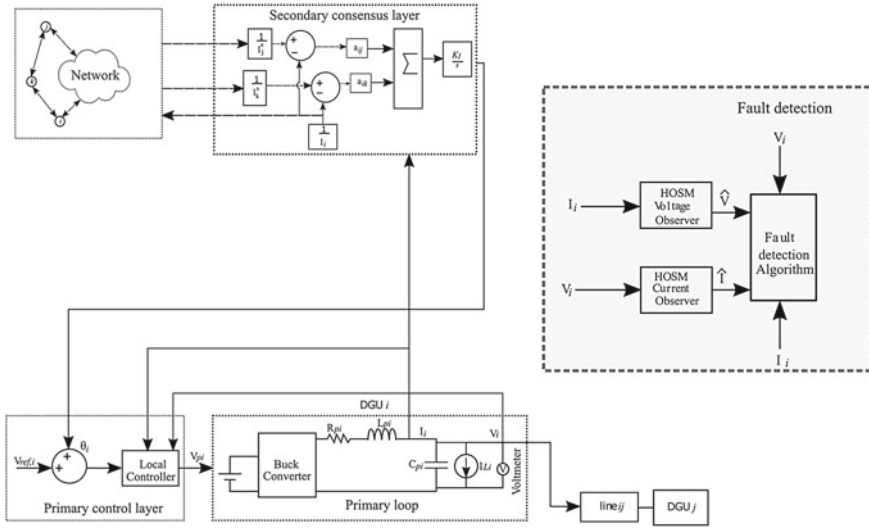
Fig. 3 Functional block diagram of the DGU-i

$$F_{i,1}^{\text{faulty}}(t) = V_i(t)(1 + \gamma_i^v) \tag{13}$$

$$F_{i,2}^{\text{faulty}}(t) = I_i(t)(1 + \gamma_i^i) \tag{14}$$

where $-1 < \gamma_i^v, \gamma_i^i \le 0$. Based on this model, the voltage and current residuals are selected for fault detections. At the instant of sensor faults, the generated residual is compared with the selected thresholds, and an alarm is set to trigger the immediate occurrence of faults. The fault detection residuals, R_{Thi}, can be formed as follows:

$$R_{Thi}(t) = |r_i(t)|, i = 1, 2...., n \tag{15}$$

where the voltage and current sensor residuals can be evaluated as $r_i = \hat{V}_i - V_i$ or $\hat{I}_i - I_i$, respectively.

4 Simulation Results and Discussions

In this section, extensive simulation results for sensor fault detections in a DC microgrid are presented to illustrate the robustness and efficiency of the HOSM observers. The electrical and line parameters specifications of the 3 DGUs are considered similar to Mola et al. (2020) and shown in Tables 1 and 2. A band-limited white noise

Table 1 Parameters of the electrical circuit in each DGUs

DGUs	$R_p(\omega)$	$C_p(mF)$	$L_p(mH)$
DGU 1	0.21	2.1	1.7
DGU 2	0.3	1.9	2.0
DGU 3	0.1	1.7	2.2

Table 2 Specification of the electrical line parameters of the DGUs

DGUs interconnection	$R_{ij}(\omega)$	$L_{ij}(\mu H)$
(1,2)	0.06	2.3
(1,3)	0.07	2.1
(2,3)	0.04	1

Fig. 4 Voltage of each DGU at each PCC
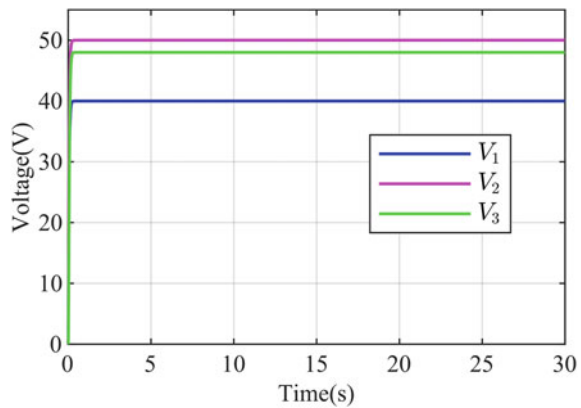
of 0.6 dB is considered in the DC microgrid to prove the robustness of the proposed methodology. The voltages of the primary controller in each DGU are shown in Fig. 4.

Every DGU is subjected to multiplicative voltage and current sensor faults in the presence of an unknown load. The HOSM observers generate the residuals from the estimated and faulty states of the sensors. To prove the robustness of this method, random noise of 1–5% is considered in the sensors. When there is a fault in the voltage sensor, the current sensors also get affected. The generated residuals lie above the threshold at the instant of DGUs sensor faults. After undergoing multiple simulations in the presence of random noise and delay in the DGUs, a common threshold is considered. As shown in Fig. 5a, a voltage sensor fault is considered in the DGU1 at t = 15s. The voltage residual lies below the threshold before the fault, and it crosses the threshold after the fault has occurred as DGU1 is interconnected to DGU2 and DGU3, the generated residuals of the respective voltage and current sensor changes. However, the residuals of DGU2 and DGU3 lie below the threshold
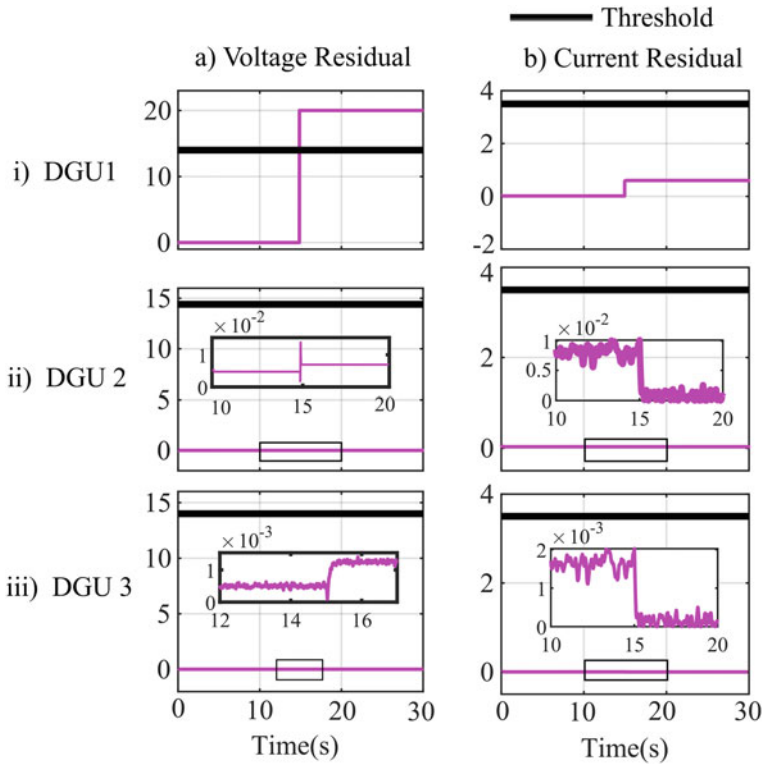
Fig. 5 **a** Voltage and **b** current residuals of the DGUs for fault detection in voltage sensor of DGU1 at t = 15s

as shown in Fig. 5a (ii), (iii), respectively. Similarly, at the instant of current sensor faults at t = 20s as demonstrated in Fig. 6b (i), the respective residual lies above the threshold. At the instants of fault occurrence, a fault detection algorithm is used to detect the faults. The residual of the voltage sensor also gets affected, which can be seen in Fig. 6a (i). However, the voltage sensor residual at the instant of the current sensor fault lies below the threshold. The effect of the multiplicative current sensor fault in the DGU1 is seen in the residuals of DGU2 and DGU3 as shown in Fig. 6 (ii) and (iii), respectively.

In this paper, we have also considered a delay between the local primary controller and the Buck converter. A 3 samples delay is considered in the voltage sensor of the DGU3, as shown in Fig. 7a. The estimated voltage tracks the actual voltage and is insensitive to delay. The delay in the voltage sensor causes a change in the residual of the current sensor of DGU3. As DGU3 is interconnected to DGU1 and DGU2, the estimated error corresponding to the HOSM observer-based output voltage and current is minimum after a certain delay. If there is an increase in delay, the stability of the system gets distorted, and the fault detection will be delayed. As shown in
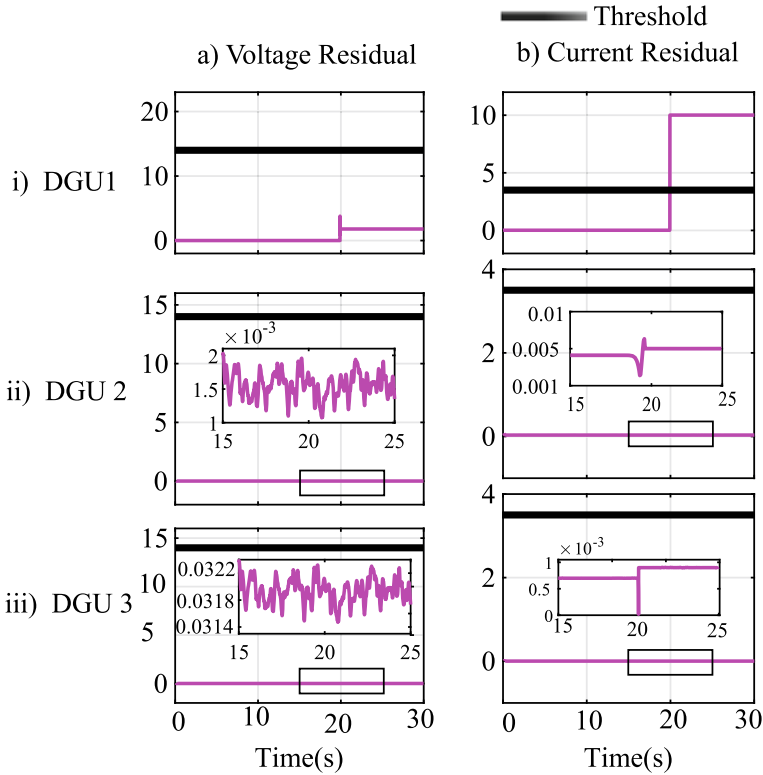
Fig. 6 **a** Voltage and **b** Current residuals of the DGUs for fault detection in current sensor of DGU1 at t = 20 s

Fig. 7a, (i) the faulty voltage sensor is detected at t = 15.03s after a delay of three samples. A load change of 10% is also considered in the DGUs. This shows a change in the RMSE % of 0.58%, 0.091%, 0.0032% in DGU1-DGU3, respectively, from its nominal value. The residuals generated by the HOSM observer can detect the faults in the presence of the said load. However, when the load is increased to 25%, the RMSE values are 1.501, 1.88, 1.5351%. In this case, there will be a huge deviation in the errors of the estimated sensors, and the sensor faults will fail to be detected with the selected threshold.

5 Conclusions

In this paperwork, an STA based on a higher-order observer is employed for the sensor fault detections scheme in the DGUs. The multiple HOSM observers are designed to detect the sensor faults in the respective DGUs. To achieve this objective,
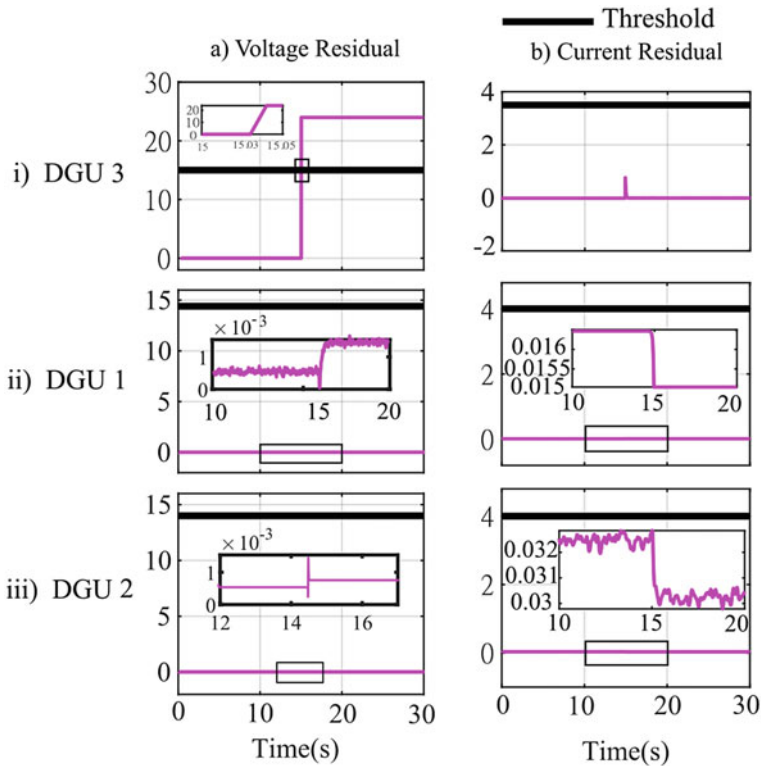
Fig. 7 Residuals of the HOSM observer in the presence of delay and a voltage sensor fault in DGU3 at t = 15 s. **a** HOSM-based residuals of the voltage sensor; **b** HOSM-based residuals of the current sensor

multiple simulations are performed, and a common threshold is selected based on the residuals generated from the HOSM observers. The effectiveness and robustness of the proposed method are achieved by simulating the system in the presence of different loads, noise, and delay.

References

Asadi S, Vafamand N, Moallem M, Dragičevič T (2020) Fault reconstruction of islanded nonlinear dc microgrids: an lpv-based sliding mode observer approach. IEEE J Emerging Select Topics Power Electron

Bansal Y, Sodhi R (2018) Microgrid fault detection methods: reviews, issues and future trends. In: IEEE innovative smart grid technologies-Asia (ISGT Asia) 2018, pp 401–406

Beheshtaein S, Cuzner RM, Forouzesh M, Savaghebi M, Guerrero JM (2019) Dc microgrid protection: a comprehensive review. IEEE J Emerging Select Topics Power Electron

Boyd S, El Ghaoui L, Feron E, Balakrishnan V (1994) Linear matrix inequalities in system and control theory. SIAM

Chalanga A, Kamal S, Fridman LM, Bandyopadhyay B, Moreno JA (2016) Implementation of super-twisting control: Super-twisting and higher order sliding-mode observer-based approaches. IEEE Trans Industr Electron 63(6):3677–3685

Elsayed AT, Mohamed AA, Mohammed OA (2015) Dc microgrids and distribution systems: an overview. Electric Power Syst Res 119:407–417

Gao Z, Cecati C, Ding SX (2015) A survey of fault diagnosis and fault-tolerant techniques-part i: fault diagnosis with model-based and signal-based approaches. IEEE Trans Industr Electron 62(6):3757–3767

Gao Z, Cecati C, Ding SX (2015) A survey of fault diagnosis and fault-tolerant techniques-part ii: fault diagnosis with knowledge-based and hybrid/active approaches. IEEE Trans Industr Electron 62(6):3768–3774

Kommuri SK, Defoort M, Karimi HR, Veluvolu KC (2016) A robust observer-based sensor fault-tolerant control for pmsm in electric vehicles. IEEE Trans Industr Electron 63(12):7671–7681

Kumar V, Mohanty SR, Kumar S (2020) Event trigger super twisting sliding mode control for dc micro grid with matched/unmatched disturbance observer. IEEE Trans Smart Grid 11(5):3837–3849

Kumar D, Zare F, Ghosh A (2017) Dc microgrid technology: system architectures, ac grid interfaces, grounding schemes, power quality, communication networks, applications, and standardizations aspects. IEEE Access 5:12230–12256

Lan J, Patton RJ, Zhu X (2018) Fault-tolerant wind turbine pitch control using adaptive sliding mode estimation. Renewable Energy 116:219–231

Meng L, Dragicevic T, Vasquez JC, Guerrero JM (2015) Tertiary and secondary control levels for efficiency optimization and system damping in droop controlled dc-dc converters. IEEE Transactions on Smart Grid 6(6):2615–2626

Mola M, Afshar A, Meskin N, Karrari M (2020) Distributed fast fault detection in dc microgrids. IEEE Syst J

Moreno JA, Osorio M (2012) Strict lyapunov functions for the super-twisting algorithm. IEEE Trans Autom Control 57(4):1035–1040

Poon J, Jain P, Konstantakopoulos IC, Spanos C, Panda SK, Sanders SR (2016) Model-based fault detection and identification for switching power converters. IEEE Trans Power Electron 32(2):1419–1430

Poon J, Jain P, Konstantakopoulos IC, Spanos C, Panda SK, Sanders SR (2017) Model-based fault detection and identification for switching power converters. IEEE Trans Power Electron 32(2):1419–1430

Rath JJ, Veluvolu KC, Defoort M, Soh YC (2014) Higher-order sliding mode observer for estimation of tyre friction in ground vehicles. IET Control Theory Appl 8(6):399–408

Rinaldi G, Menon PP, Edwards C, Ferrara A (2019) Higher order sliding mode observers in power grids with traditional and renewable sources. IEEE Control Syst Lett 4(1):223–228

Shao S, Wheeler PW, Clare JC, Watson AJ (2013) Fault detection for modular multilevel converters based on sliding mode observer. IEEE Trans Power Electron 28(11):4867–4872

Sharma AB, Golubchik L, Govindan R (2010) Sensor faults: detection methods and prevalence in real-world datasets. ACM Trans Sens Netw (TOSN) 6(3):1–39

Tucci M, Riverso S, Vasquez JC, Guerrero JM, Ferrari-Trecate G (2015) Voltage control of dc islanded microgrids: a decentralized scalable approach. In: 2015 54th IEEE conference on decision and control (CDC). IEEE, pp 3149–3154

Veluvolu K, Soh Y (2011) Multiple sliding mode observers and unknown input estimations for lipschitz nonlinear systems. Int J Robust Nonlinear Control 21(11):1322–1340

Wang T, Liang L, Gurumurthy SK, Ponci F, Monti A, Yang Z, De Doncker RW (2020) Model-based fault detection and isolation in dc microgrids using optimal observers. IEEE J Emerging Select Topics Power Electron

Yan H, Zhou X, Zhang H, Yang F, Wu Z-G (2017) A novel sliding mode estimation for microgrid control with communication time delays. IEEE Trans Smart Grid 10(2):1509–1520

Yang J, Fletcher JE, O'Reilly J (2011) Short-circuit and ground fault analyses and location in vsc-based dc network cables. IEEE Trans Industr Electron 59(10):3827–3837

Computer Vision-Guided Human–Robot Collaboration for Industry 4.0: A Review

Jaimin G. Pandya and Nirav P. Maniar

Abstract Instead of robot replacing the human in industrial workplaces, human–robot collaboration (HRC) focuses on collaborative working of human and robot in the shared workspace. Robots can provide accurate, repetitive and fast working, but it does not have flexibility and adaptability like humans. In human–robot collaboration (HRC), robots are programmed to make decisions about its motions and operations for the specific given task. Therefore in human–robot collaboration, robots are often needed to change their motions and operations to collaborate with humans. But, robots in the industries are pre-programmed with rigid codes and cannot support human–robot collaboration. Hence, computer vision-guided systems can be used for human–robot collaborations. In this paper, an overview of computer vision-guided human–robot collaborative for Industry 4.0 has been given, and it also highlights future research directions. In this paper, various aspects of computer vision-guided human–robot collaboration, such as introduction, gesture recognition, computer vision as a sensor technology, and human safety have been reviewed.

Keywords Human–robot collaboration · Computer vision · Industry 4.0

1 Introduction

Robots can provide accurate, repetitive and fast working, but it does not have flexibility and adaptability like humans. Hence, human–robot collaboration (HRC) is a recent trend of robotics research to include capabilities of human and robot both in the industry (Wang et al. 2019). In manufacturing industry, human–robot collaboration (HRC) focuses on working of human and robot simultaneously in the workspace (Wang et al. 2017).

J. G. Pandya (✉)
Gujarat Technological University, Ahmedabad, India

N. P. Maniar
VVP Engineering College, Rajkot, India

2 Human–Robot Collaboration (HRC)

In different scenarios like coexistence, cooperation, interaction and collaboration, relationships of the humans and robots are different. It can be evaluated based on the following criteria (Wang et al. 2019):

- Workspace: Working area.
- Contact: Direct physical contact with each other.
- Working task: Same operation towards the same working objective.
- Resources: Available equipment and machines.
- Simultaneous process: Working on same time but different tasks.
- Sequential process: No overlapping of task, one by one task.

Based on above criteria, different human–robot relationships can be defined as follows (Wang et al. 2020) (Table 1):

In Fig. 1, possible cases and roles of human–robot collaboration have been given. Human–robot collaborative system should have following characteristic:

- It should follow safety standards and operational regulations
- Flexibility and adaptability for specific functions

Table 1 Different kinds of (human–robot relationship Wang et al. 2020)

	Coexistence	Interaction	Cooperation	Collaboration
Shared workspace		Yes	Yes	Yes
Shared contact		Yes		Yes
Shared working task		Yes		Yes
Shared resource			Yes	Yes
Shared simultaneous process	Yes		Yes	Yes
Shared sequential process		Yes	Yes	
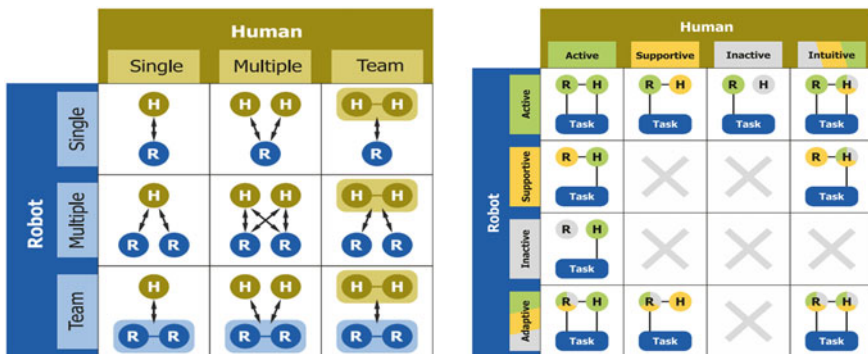
Fig. 1 Possible cases and roles in human–robot collaborations (Wang et al. 2020)

- Potential of improvement in productivity and product quality
- Support, assistance and collaboration with human in hazardous, tedious, non-ergonomic and repetitive tasks.

3 Gesture Recognition in Human–Robot Collaboration (HRC)

In manufacturing with robots, robots in the industries are pre-programmed with rigid codes, and reprogramming is a challenging task as it is tedious and time consuming (Liu et al. 2018). Although by programming with demonstration, reprogramming of robots for a different task has been made easy. Rigid code-based robotic control cannot support human–robot collaboration. To solve this problem, intuitive programming with communication channels like gesture, poster, voice, and haptic can be used to implement in human–robot collaboration.

As shown in Fig. 2, gesture recognition for human–robot collaboration can consist of sensor data collection, gesture identification, gesture tracking, gesture classification and gesture mapping (Liu and Wang 2018).

There are three types of gesture that can be used as a communication channel as follows:
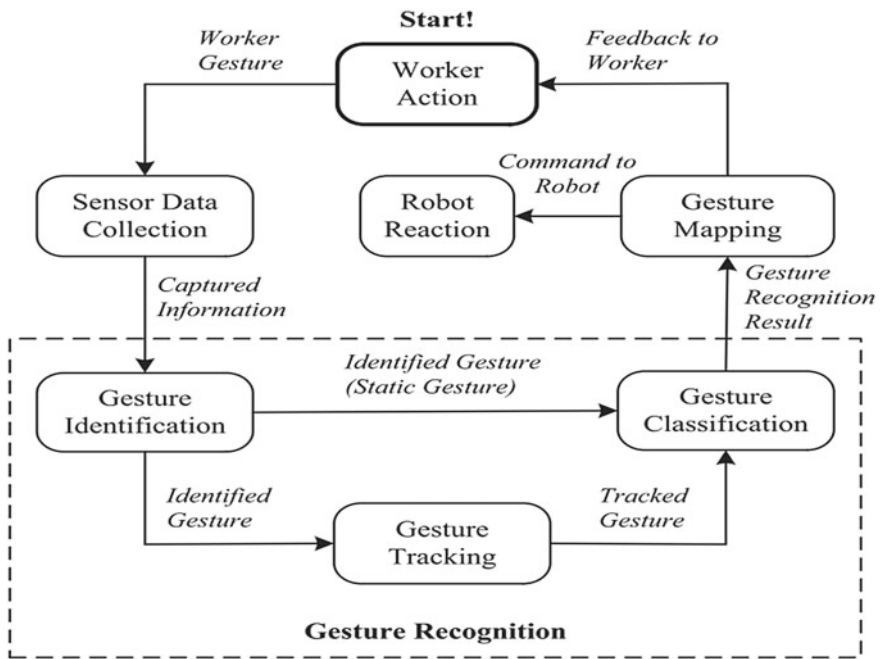
Fig. 2 Model for human–robot collaboration (Liu and Wang 2018)
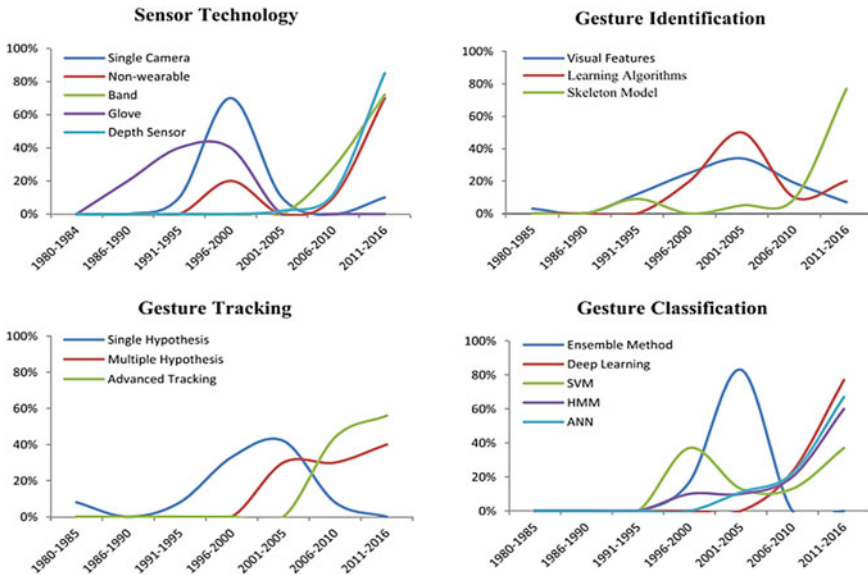
Fig. 3 Past work and future trends in gesture recognition (Liu and Wang 2018)

- Head and face gesture
- Hand and arm gesture
- Full body gesture.

Hongyi Liu and Lihui Wang have reviewed gesture recognition for human–robot collaboration and identified research trend as follows (Liu and Wang 2018) (Fig. 3).

4 Computer Vision as a Sensor Technology in Human–Robot Collaboration

To implement human–robot collaboration, proper communication channel must be implemented. Computer vision-based communication channels can be applied effectively for the same (Liu and Wang 2018). For gesture recognition, sensor data collection needs to be done. As shown in Fig. 4, various sensors can be used for the same (Liu and Wang 2018).

In image-based sensor, single camera and depth camera are widely used in recent gesture recognition research. Depth camera will also give depth information along with RGB data. The depth and visual information provided by the depth sensor (like Kinect sensor) can be used in object tracking and recognition, human activity analysis, hand gesture analysis and indoor sematic segmentation for human–robot collaboration (Papadopoulos et al. 2014; Pham et al. 2016). Fig. 5 shows basic structure and working of depth sensors like Kinect (Han et al. 2013).
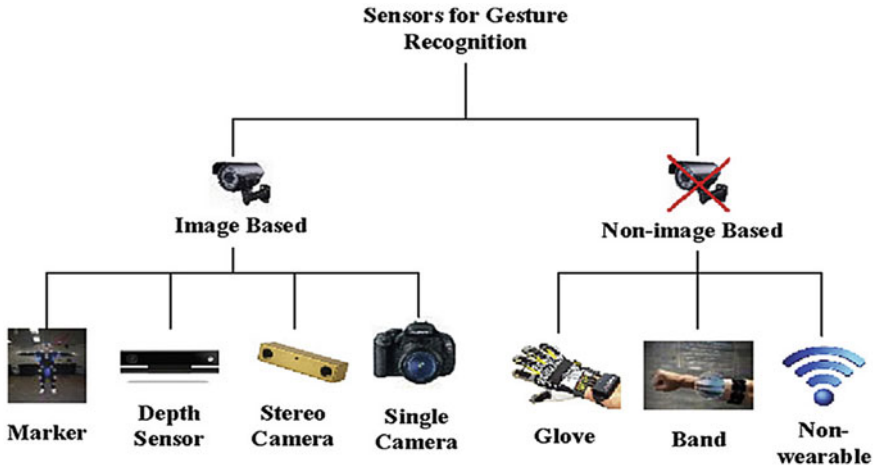
Fig. 4 Different type of sensors for gesture recognition (Liu and Wang 2018)
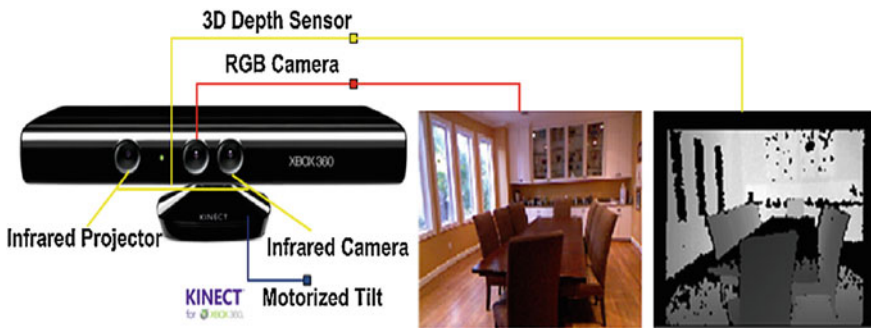
Fig. 5 Basic structure and working of depth sensors like Kinect (Han et al. 2013)

For effective human–robot collaboration, human gesture should be correctly understood by robot and so human gesture should be interpreted mathematically (Nakamura 2018). In HRC system, mathematical modelling of sequence of human operations and motions is very important.

Liu H. has modelled sequence of human motion in assembly line using existing motion recognition techniques and applied hidden Markov model (HMM) to predict human motion by generating a motion transition probability matrix (Liu and Wang 2017). Example of task-level representation in an assembly line for a case study is shown in Fig. 6.

Liu H has also applied recurrent neural network (RNN) to predict human motion by generating a motion transition probability matrix (Zhang et al. 2020). Overview of RNN for motion prediction in human–robot collaboration (HRC) is shown in Fig. 7.
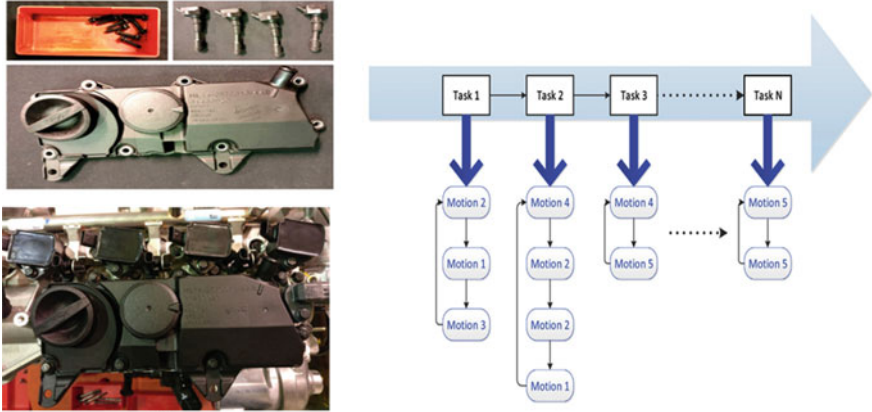
Fig. 6 Example of task-level representation in an assembly line (Liu and Wang 2017)
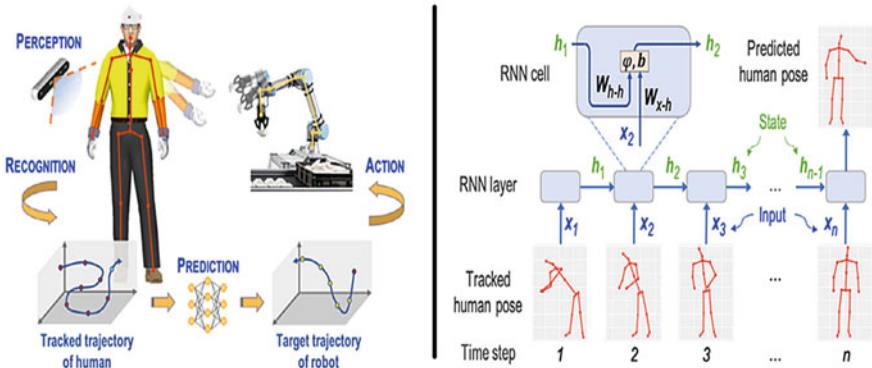
Fig. 7 Overview of RNN for motion prediction (Zhang et al. 2020)

Mainprice and Berenson (2013) proposed framework based on early prediction of the human's motion. These generate a prediction of human workspace occupancy by computing the swept volume of learned human motion trajectories. This framework is based on generation of a prediction of human workspace occupancy by calculating the swept volume of learned human motion trajectories (Mainprice and Berenson 2013). In Fig. 8, human workspace occupancy has been explained by example.

In recent years, multimodal approach has also been widely investigated. This approach is multidisciplinary including fields like artificial intelligence (AI), image processing, automation control, sensor networks and path planning (Liu et al. 2018). For human–robot collaboration, multimodal programming by deep learning approach has been explained in Fig. 9.

(a) Goal 1 (b) t = 1 (c) t = 13 (d) t = 14

(e) Goal 2 (f) t = 1 (g) t = 4 (h) t = 5
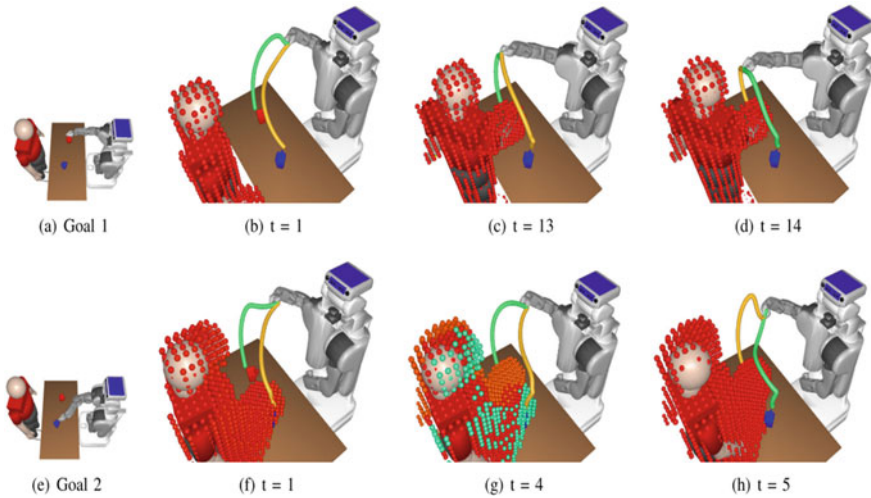
Fig. 8 Example of human occupancy in human–robot collaboration (Mainprice and Berenson 2013)
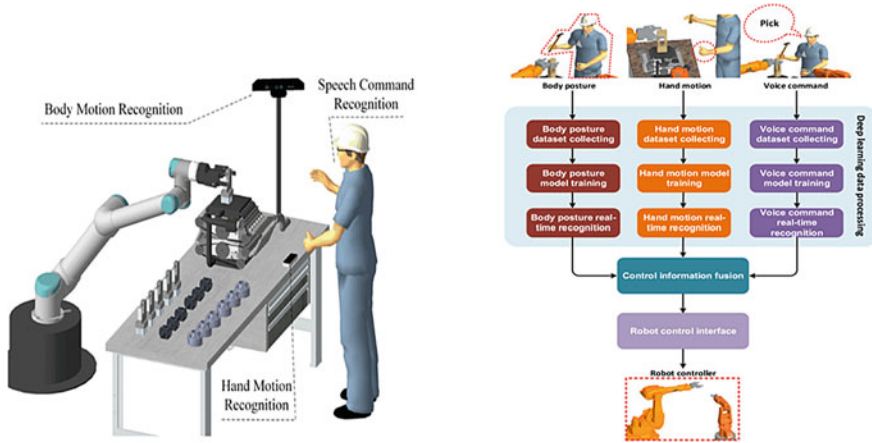
Fig. 9 Multimodal conceptual framework for (human–robot collaboration Liu et al. 2018)

5 Human Safety in Human–Robot Collaboration (HRC)

In implementing human–robot collaboration (HRC) for industry, the most important characteristic of HRC is human safety. The seven elements of the collision events are pre-collision, detection, isolation, identification, classification, reaction and collision avoidance (Haddadin et al. 2017). Possible causes of collision can be categorized into three categories as shown in Fig. 10.
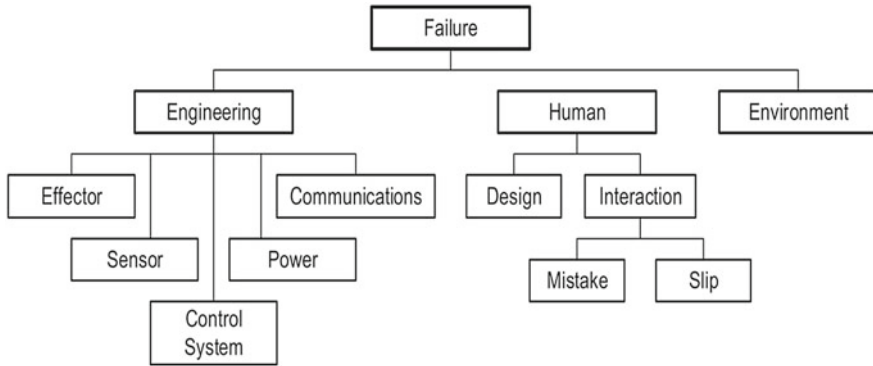
Fig. 10 Possible causes of collision (Haddadin et al. 2017)

In computer vision-based human–robot collaboration (HRC), some research like Schmidt implements a depth camera-based method for collision detection (Mohammed et al. 2017).

Depth camera (like a Kinect sensor) can be used to calculate relative distance for collision detection as shown in Fig. 11.
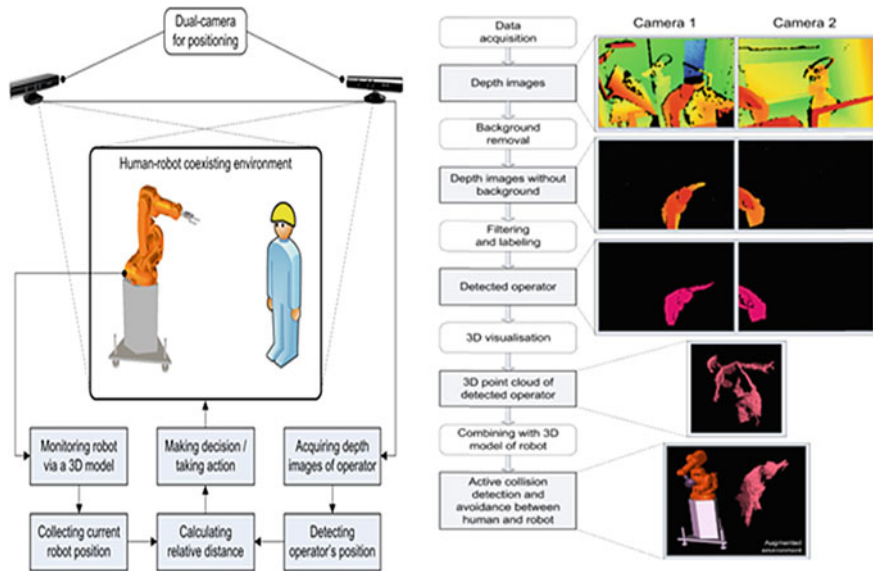
Fig. 11 Depth camera-based collision avoidance system (Mohammed et al. 2017)

6 Conclusion

This paper explains research in computer vision-guided human–robot collaboration for Industry 4.0 in brief. After introducing the human–robot collaboration, different types of human–robot relationship and roles have been explained. In the second section of the paper, gesture recognition in human–robot collaboration has been studied as the most important element of human–robot collaboration systems. In the third section of the paper, sensor data collection needs to be done, and computer vision-based gesture recognition has been identified as the best suitable method. In the fourth section of the paper, recent research in computer vision-based human–robot collaboration has also been reviewed. In the fifth section of the paper, human safety for human–robot collaboration has been reviewed.

References

Haddadin S, De Luca A, Albu-Schäffer A (2017) Robot collisions: a survey on detection, isolation, and identification. IEEE Trans Rob 33(6):1292–1312

Han J, Shao L, Xu D, Shotton J (2013) Enhanced computer vision with microsoft kinect sensor: a review. IEEE Trans Cybern 43(5):1318–1334

Liu H, Fang T, Zhou T, Wang L (2018) Towards robust human-robot collaborative manufacturing: multimodal fusion. IEEE Access 6:74762–74771

Liu H, Wang L (2017) Human motion prediction for human-robot collaboration. J Manuf Syst 44:287–294

Liu H, Wang L (2018) Gesture recognition for human-robot collaboration: a review. Int J Ind Ergon 68:355–367

Mainprice J, Berenson D (2013) Human-robot collaborative manipulation planning using early prediction of human motion. In 2013 IEEE/RSJ international conference on intelligent robots and systems. IEEE, pp 299–306

Mohammed A, Schmidt B, Wang L (2017) Active collision avoidance for human–robot collaboration driven by vision sensors. Int J Comput Integr Manuf 30(9):970–980

Nakamura Y (2018) Classification of multi-class daily human motion using discriminative body parts and sentence descriptions

Papadopoulos GT, Axenopoulos A, Daras P (2014) Real-time skeleton-tracking-based human action recognition using kinect data. In: International conference on multimedia modeling. Springer, Cham, pp 473–483

Pham TTD, Nguyen HT, Lee S, Won CS (2016) Moving object detection with Kinect v2. In: 2016 IEEE international conference on consumer electronics-Asia (ICCE-Asia). IEEE, pp 1–4

Wang L, Gao R, Váncza J, Krüger J, Wang XV, Makris S, Chryssolouris G (2019) Symbiotic human-robot collaborative assembly. CIRP Ann 68(2):701–726

Wang XV, Kemény Z, Váncza J, Wang L (2017) Human–robot collaborative assembly in cyber-physical production: Classification framework and implementation. CIRP Ann 66(1):5–8

Wang L, Liu S, Liu H, Wang XV (2020) Overview of human-robot collaboration in manufacturing. In Proceedings of 5th international conference on the industry 4.0 model for advanced manufacturing. Springer, Cham, pp 15–58

Zhang J, Liu H, Chang Q, Wang L, Gao RX (2020) Recurrent neural network for motion trajectory prediction in human-robot collaborative assembly. CIRP Annals

Design and Fabrication of Mini Woodworking Lathe Machine

Param Jogidas, Din Bandhu, Soni Kumari, and Kumar Abhishek

Abstract The lathe is the one among all and the foremost versatile machine. It is commonly referred to as the mother of all other machines. The most important function of a lathe is to get rid of a portion of the metal from employment to offer it the specified shape and size. In this paper, the main aim is to develop a functional wood lathe machine for small-scale industries along with the purpose of easy to carry from one place to another place. In order to achieve the aim, different possible design solutions and concepts were analyzed as well as well considered under the synthesis of a portable wood lathe machine. In this analysis, the components of the portable lathe machine dimensions were decided based on load and stress calculation and their compatibility was analyzed. The dimensions of the components of the portable lathe machine were determined based on load and stress calculations, and their compatibility was examined in this study. The equipment and materials for creating the wood lathe machine were obtained from the manufacturing workshop. Finally, the lathe's components were put together and the assembled lathe was undergone for a run–test. This model was examined by looking at real behavior that was anticipated using the model information. It was the first attempt to build a mini lathe (150 mm in length) for the precision turning of tiny components. Interactive processes were used to guarantee that optimum performance was achieved. To evaluate the manufacturing cost of a prototype, the material, labor, and overhead expenses were calculated. When compared to other manual machining processes, it was discovered during the run–test that the portable mini wood lathe machine performs well. It can conduct a variety of operations and can machine a bigger number of projects in the same amount of time that a carpenter can perform those operations manually. Its fabrication is simple, and the materials necessary for construction are readily available, so anybody may manufacture it for their usage. Machining using a mini lathe saves time and money since it is dependable, energy-efficient, and simple to maintain.

P. Jogidas · D. Bandhu · K. Abhishek (✉)
Department of Mechanical & Aero-Space Engineering, Institute of Infrastructure, Technology, Research and Management (IITRAM), Ahmedabad, India

S. Kumari
Department of Mechanical Engineering, GLA University, Mathura, India

157

1 Introduction

A lathe turns a cylindrical workpiece along its axis and removes material to shape it into the desired shape, whether for woodworking or metalworking. The cutting tools on a woodworking lathe are normally handheld against support and pushed in and out and back and forth over the surface of the work by hand to make a table leg shape. The cutting tools on metalworking lathes are held tightly in a tool holder positioned on a moveable platform called the carriage. The tool is pushed in and out using handwheels, and back and forth using either a handwheel or the lathe's power. As a result, materials are frequently far removed from the workpiece and subjected to extremely fine supervision in order to provide precision-made forms. Dimensional accuracies of one-tenth of a millimeter or one–one-thousandth of an inch (0.001") are common. The vast majority of work produced on a lathe is cylindrical owing to the lathe's intrinsic rotating nature. Despite this, the lathe is a very flexible machine capable of producing a wide range of things that are mostly employed as parts of mechanical systems. One of the most versatile and commonly used machine tools on the globe is the lathe. It is often referred to as "the mother of all machines." A lathe's primary role is to remove metal from the workpiece in order to give it the desired form and size. The workpiece is held firmly and rigidly within the chuck or between centers on the lathe machine, and then, it is turned against a single-point cutting tool, which eliminates metal from the workpiece in the form of chips. An engine lathe is the most basic and straightforward type of lathe. Its name is derived from the early lathes, which were powered by engines. Apart from the turning process mentioned above, lathes are frequently used for various tasks such as drilling, reaming, boring, taper turning, knurling, screw thread cutting, grinding, and so on. Lathes come in a variety of sizes and styles, ranging from small lathes for precise work to huge lathes for turning huge steel shafts. All types of lathes, including speed lathes, center lathes or engine lathes, bench lathes, tool room lathes, capstan lathes, turret lathes, and automated lathes, operate and perform in the same way (Gupta et al. 2009; Moriwaki 2008; Harten and Derks 1975; Keith 1962; Woodbury 1963; Kumari et al. 2020; Mohan et al. 2016).

All these lathe machines are cumbersome and fixed at a particular place. Even for a small piece of work, the user has to visit the workshop for performing the operations. In such cases, operating a big machine is tedious. Also, the valuable time of the user gets wasted. To eliminate such problems, an attempt has been made to construct a mini lathe with the objectives of portability, adaptability, and accessibility.

Fig. 1 Working principle of a lathe
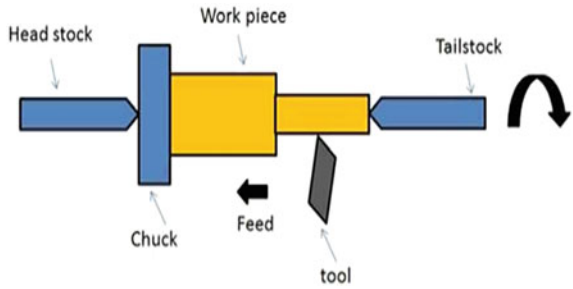
1.1 Construction and Working of Lathe

A lathe is a machine that holds the workpiece between two rigid and strong supports known as centers, or in a rotating chuck or faceplate. The tool is gripped and maintained tightly in a tool post that feeds against the rotating work. The tool is fed either parallel or at right angles to the axis of the work in traditional cutting processes. Figure 1 depicts the working principle of the lathe. Table 1 lists the important constructing elements of a lathe (Kalpakjian and Schmid 2010; Lizarralde et al. 2009; Virasak 2021; Niranjan Kumar 2019).

1.2 Operations Performed on a Lathe

The engine lathe is an accurate and versatile machine that can execute a wide range of tasks. Table 2 shows the many operations that may be done on a lathe machine.

2 Materials and Methods

The equipment operates with the assistance of a drill machine that rotates the workpiece. The drill machine is the primary unit of the portable mini wood lathe machine and is located at the headstock. The tool is supported on the tool post, and the workpiece is coupled between a fixed headstock and a moving tailstock. A human must hold the tool on the tool post since it is a manual type of lathe machine. On it, many operations may be accomplished by operating the drill machine. The design of a portable woodworking lathe machine is discussed as follows:

Table 1 Essential elements of a lathe (Kalpakjian and Schmid 2010)

Elements	Description
Bed	The bed, on which the lathe's working elements are situated, is a large and sturdy component made by casting. It supports the workpiece by carrying the headstock and tailstock and serves as a foundation for the carriage assembly, which moves the tool
Legs	The machine's whole weight is carried by the legs, which are firmly fastened to the floor by foundation bolts
Headstock	The drive pulleys, rear gears, headstock spindle, live center, and feed reverse gear are all housed in the headstock, which is fastened on the left-hand side of the bed. The headstock spindle is a hollow cylindrical shaft that drives the work holding devices from the motor
Gearbox	The quick-change gearbox is located underneath the headstock and has a range of gears of varying sizes
Carriage	The carriage is located between the headstock and tailstock, and its purpose is to support, guide, and feed the tool against the work while it is being used. The following are the most critical components of a carriage: • The saddle is an H-shaped casting installed on the lathe's highest axis. Cross-slide, compound rest, and gear post are all supported by it • The cross-slide is located on the topmost of the saddle and provides the tool with a mounted or motorized cross-movement • The compound rest is installed on the top of the cross-slide and serves to support the tool post and, as a result, the tool • The tool post is attached to the compound rest and tightly clamps the cutter or tool holder at the proper height in relation to the work centerline • The gears, clutches, and levers needed to control the carriage or cross-slide are housed in the apron, which is attached to the saddle. When the half-nut engages the leadscrew, the feed rod's automated feed action is interrupted
Tailstock	The tailstock is a moveable casting on the bed's ways opposite the headstock. Between the centers, the tailstock may move along the bed to accommodate varying lengths of the workpiece. The tailstock may be locked in any position with the use of a tailstock clamp. To carry the dead center and hence the tapered shank tools like reamers and drills, the tailstock spindle has an indoor taper

Table 2 List of operations that may be done on a lathe (Kalpakjian and Schmid 2010)

Possible operations performed on a lathe are	Plain turning, step turning, taper turning, facing, parting, drilling, reaming, boring, knurling, grooving, threading, forming, chamfering, filing, and polishing

2.1 Compact Design

The term "compact design" refers to a wooden lathe's ideal dimension, which is determined by the size of the workpiece. Here, the dimension of the proposed wooden is 35 × 8 in (889 × 204 mm). Table 3 gives a detailed description of the dimensions of the intended wooden lathe machine.

Table 3 Dimensional specification of the proposed wooden lathe machine

Specification	Size	Unit
Length	889	mm
Width	204	mm
Height	210	mm
Weight	23	kg
Maximum stroke	130	mm

2.2 Modular Design

Modular design separates a system into smaller sections known as modules, which may be built, updated, replaced, or swapped with other modules or across other systems independently. This prototype was created in the form of many distinct modules that can be simply joined to construct a wooden lathe.

Moreover, each module of this wooden lathe can be frequently replaced by another. These modules can be powered up, scaled up, and customized to serve a different system on a regular basis.

2.3 Small-Scale Resolution

Equation 1 was used to calculate the resolution of the smallest movement for this wooden lathe design.

$$R_m = DR \times TR \times CR \tag{1}$$

where R_m = Resolution of the machine/machine precision (mm)

DR = Resolution of the drill/drill precision (rad)
TR = Transmission ratio (rad/rad)
CR = Converter ratio (mm/rad)

These parameters and their specifications are listed in Table 4.

The working resolution of the proposed wooden lathe machine can be obtained by entering the specification data in Eq. 1.

Table 4 Small-scale resolution parameters with their specifications

Parameter	Specification
Drill resolution (DR)	2π rad/30
Transmission resolution (TR)	1/4
Converter resolution (CR)	10 mm/2 radπ

$$R_m = \left(\frac{2\pi\, rad}{30}\right) \times \left(\frac{1}{4}\right) \times \left(\frac{10\,\text{mm}}{2\pi\, rad}\right) \tag{2}$$

$$R_m = 0.083\,\text{mm} \tag{3}$$

It illustrates that the suggested wooden lathe machine's working resolution may reach 0.083 mm.

2.4 Three-Dimensional Design of the Lathe

Figure 2 depicts the three-dimensional design of the proposed lathe.

2.5 Step-By-Step Fabrication of Mini Woodworking Lathe

The construction of a mini lathe is simple and inexpensive. Wooden materials (such as plywood and woodblocks), drilling machines, bearings, nuts, bolts, Fevicol, and other items are used in fabrication. The motor is replaced with a drilling machine in the design, which eliminates the need for a belt drive system while simultaneously producing high torque. The bed, headstock, tailstock, chuck, and carriage are the key elements of a mini lathe machine. This section details the fabrication of the proposed lathe machine. Table 5 lists the materials used in the fabrication of the lathe's elements.

Step 1: Cutting of plywood and wooden blocks

The first step is to cut the plywood sections to the correct measurements. The lathe is made out of two different pieces of plywood with thicknesses of 12 and 19 mm. A 12 mm plywood sheet was utilized for the bottom section. In addition, the wooden blocks (1.25 × 1.50 in) are chopped into 35-in and 8-in lengths, respectively. The prepared plywood and wooden blocks utilized in this design are shown in Fig. 3.

Step 2: Base Preparation

As illustrated in Fig. 4, the lathe's base was constructed by assembling the prepared plywood and wooden pieces. To accomplish so, a ½-in slot with a 10-in length was cut into the plywood, and the assembly was completed using mechanical fasteners.

Step 3: Making support for drill machine/Headstock part

The headstock must now be prepared. A drilling machine with a capacity of 13 mm was employed for this. To begin, structural support (platform) for the drill machine was constructed using plywood at an acceptable height, as illustrated in Fig. 5a. The drill machine was then placed on the prepared platform and clamped in place (Fig. 5b). As indicated in Fig. 5b, a clamping force was applied to the drill machine

(a)

(b)
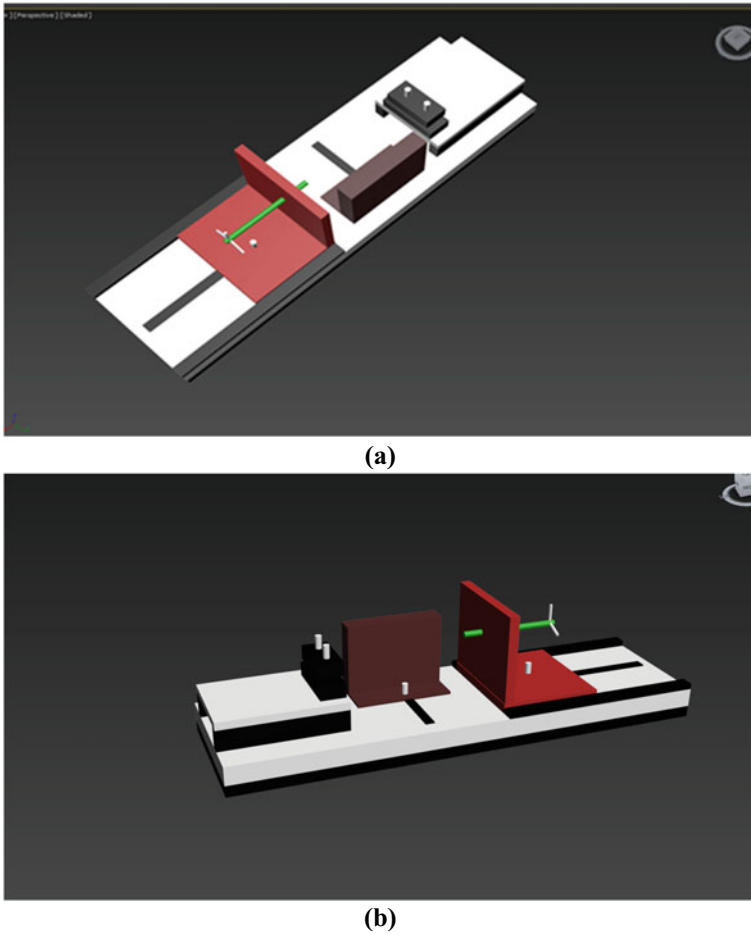
Fig. 2 Three-dimensional sketch of the proposed portable woodworking lathe: **a** top view and **b** front view

using a wooden clamp and mechanical fasteners. This wooden clamp is positioned in such a manner that it allows users to attach and detach the drill machine.

Step 4: Making tailstock as a movable part

Thereafter, tailstock was prepared. As indicated in Fig. 6a, two wooden strips were linked at 90° and connected with the other pieces of the tailstock. Then, this assembled section was placed on the prepared slot (in step 2) and tightened properly using a ½-in bolt of 2-in length from the bottom end as shown in Fig. 6b.

Table 5 Dimensional specification of the proposed wooden lathe machine

Lathe's element	Materials used to make the lathe's element
Base part	• 12 mm plywood sheet (35 × 11 in) • 1.25 × 1.50 × 35 in wooden blocks (2 nos.) • 1.25 × 1.50 × 8 in wooden blocks (2 nos.) • Screws
Drill support	• Drill machine • 12 mm plywood (8.5 × 10 in) • 12 mm plywood (3.5 × 10 in), 2 nos • Wooden blocks ¾-in thickness (5-in length) • 2 nos., 5/16-in bolts (4-in length) with fly nuts and washers
Movable part/tailstock	• 2 nos., 5/16-in bolts (4-in length) with fly nuts and washers • 2 nos., 1-in wooden strips (14-in length) • 3 nos., 19 mm plywood pieces (9 × 5 in) • ½ in bolt (8-in length) with nut • ½ in bolt (2-in length) with fly nut and washer
Tool support/tool rest part	• 3 nos.—plywood pieces • 3/8-in bolt (2-in length) with fly nut and washer • 22 gauge metal sheet (6 × 4 in) • Chisel

Fig. 3 Plywood and wooden blocks used in making a mini lathe

Fig. 4 Base preparation for the proposed lathe design
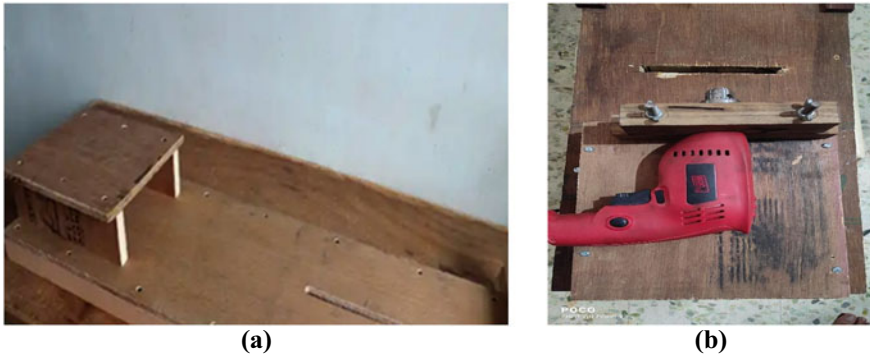
Fig. 5 Preparation of headstock: **a** support structure (platform) for the placement of drill machine and **b** clamped drill machine as the headstock

Fig. 6 Preparation of tailstock: **a** assemblage of tailstock components and **b** placement of the tailstock on the prepared slot

Step 5: Preparation of Tool Support/Tool Rest

The preparation of tool support is the final phase. Assembly was done for all the elements of the tool support as shown in Fig. 7a. Thereafter, this assembled component was attached to the main assembly of the mini lathe by means of bolt and fly nut as shown in Fig. 7b. The depth adjustment can be made by moving the tool rest portion in and out through the fly nut and bolt. Also, a 22-gauge steel sheet was attached on the top of the tool rest part for better performance.

Consequently, the mini woodworking lathe is prepared as shown in Fig. 8.

3 Advantages and Applications

This section discusses various advantages and applications of the designed mini woodworking lathe.
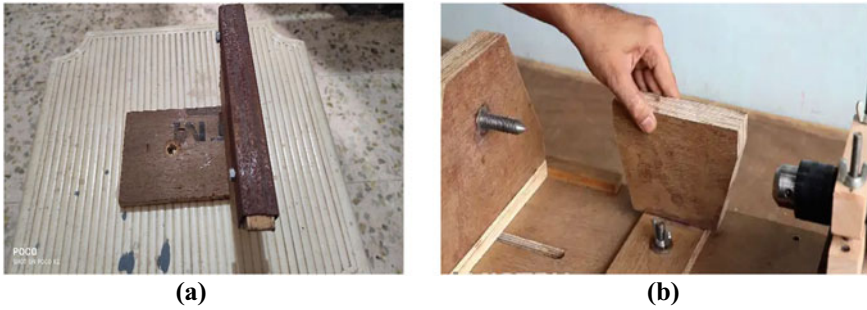
Fig. 7 Preparation of tool support: **a** assemblage of tool rest components and **b** attaching the tool support assembly to the mainframe of the mini lathe

Fig. 8 Mini woodworking lathe
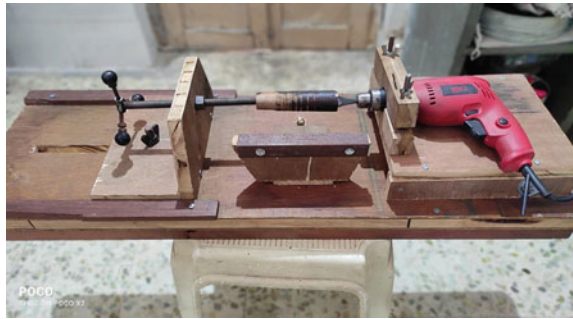
3.1 Advantages of Mini Woodworking Lathe

The designed lathe is prepared on the principle of cost-cutting, hence making this machine economical in daily-purpose applications. It is also simple and compact in design which makes the machine easy in handling. The machine's small shape and lightweight are beneficial attributes that allow it to be moved easily from one area to another. It almost requires no maintenance as well as has a low initial cost and operating cost.

3.2 Applications of Mini Woodworking Lathe

The designed lathe can easily machine woods and plastics. It can also be useful for the roadside key makers and other small shop mechanics to perform day-to-day tasks.

4 Conclusions and Future Scope

The design and fabrication of a miniature woodworking lathe have been successfully done. This lathe has advantages over conventional manual machining methods in terms of adaptability, portability, and cost-cutting. It can accomplish a wide range of tasks and machine a greater number of projects in the same amount of time as a carpenter can accomplish those tasks manually. Its construction is easy, and the materials required are easily available, so anybody may make it for their use. Because it is trustworthy, energy-efficient, and easy to maintain, machining using a micro-lathe saves time and money.

The scope of this effort will expand in the future to include performance improvements. The following modifications can be made to improve the performance of the designed mini lathe machine:

- A moveable carriage based on the rack and pinion system can be used instead of a fixed tool post.
- The machine's size may be adjusted to meet the user's needs.
- Instead of a drill machine, a high-powered motor can be employed.

References

Gupta HN, Gupta RC, Mittal A (2009) Manufacturing processes

Harten GA, Derks PM (1975) A new ergonomically improved lathe. Appl Ergon 6:155–157. https://doi.org/10.1016/0003-6870(75)90005-8

Kalpakjian S, Schmid SR (2010) Manufacturing engineering and techonology

Keith L (1962) The design, construction and evaluation of a wood turning lathe duplicating attachment

Kumari S, Bandhu D, Kumar A, Yadav RK, Vivekananda K (2020) Application of utility function approach aggregated with imperialist competitive algorithm for optimization of turning parameters of AISI D2 steel. Presented at the. https://doi.org/10.1007/978-981-32-9971-9_6

Lizarralde R, Azkarate A, Zelaieta O (2009) New developments in lathes and turning centres. In: Machine tools for high performance machining. Springer London, pp 261–278. https://doi.org/10.1007/978-1-84800-380-4_7

Mohan M D, Shaikshavali G, Goud EV (2016) Optimization of the machining parameters in turning En 9 steel using taguchi method. In: National conference on technological advancements in mechanical engineering, 22–23 July 2016 at University College of Engineering Kakinada (A) JNTUK Kakinada A.P. India, pp 65–68

Moriwaki T (2008) Multi-functional machine tool. CIRP Ann. Manuf. Technol. 57:736–749. https://doi.org/10.1016/j.cirp.2008.09.004

Niranjan Kumar H (2019) To model and fabrication of portable wood lathe machine

Virasak L (2021) Chapter 2: lathe machine

Woodbury RS (1963) The origins of the lathe 208:132–143. https://doi.org/10.2307/24936538

Implementation of Kaizen in Industries and Its Challenges

Mudit M. Saxena

Abstract Kaizen is the process of continuous improvement. It is a Japanese idea for continuous improvement in a firm, (Kai-Change, Zen-Good). For successful Kaizen program in a firm, the sound Kaizen approach and appropriate techniques implementation are necessary. Many case studies have shown that the majority of the companies have put into practice Kaizen effectively and found enhanced performance. Some firms could not implement Kaizen since there was short right facts about Kaizen. Firms ought to be competitive to the rivals since they appreciably support to the economy of our country. If continuous improvement tactic is applied, improvement is definite. Some factors are considered in this study contributing to the right Kaizen execution. It also considered its challenges among a range of size of firms. The factors which are successful in Kaizen accomplishment are clear corporate strategy, better idea exchange amid the higher management and the workforce, the Kaizen champion presence in the firm, superior workforce empowerment and knowledge management. The challenges in implementing Kaizen may be lacking to inspire workforce, resistance to change and ambiguity. This paper enlightens the contributing factors for successful accomplishment implementation of Kaizen and threats in its implementation. It is expected that for the firms formulating their Kaizen strategies this study can be helpful.

Keywords Seven QC tools · Poka-yoke · Five why technique · Kaizen · 5 s · Seven wastes · PDCA cycle

1 Introduction

Manufacturing companies across the globe are affected in recent times. Strong rivalry is one great challenge faced by the manufacturers. Manufacturers require to take a step to make sure that they survive and be competitive in the market. Competitiveness of many companies is improved by applying the concept of Kaizen. (Teece 2007). The

M. M. Saxena (✉)
Indus University, Ahmedabad, India
e-mail: muditsaxena.me@indusuni.ac.in

basis of Kaizen viewpoint is that a consistent improvement is required continuously. Hence, to respond to this increased global competitiveness, the firms have to initiate and sustain the upgrading incessantly for decreasing wastages.

Kaizen viewpoints

1. Kaizen improves the processes, thereby delivering better result for the organization.
2. It uses correct data to improve, hence it improves accuracy.
3. Kaizen eradicates the issues and problems from the root.
4. It encourages workforce to give their ideas and managers act on them to improve process.
5. Elimination of inefficient processes hence increases efficiency.
6. All the people in the organization are involved and responsible for development.

2 Implementation of Kaizen in an Organization

To do enhancements in terms of quality, costs, flexibility (Bessant et al, 1994) (Bessant 2000) and also productivity (Choi et al. 1997), Kaizen is necessary. Kaizen ponders on three areas of improvement: *Muda* (waste), *Mura* (discrepancy) and *Muri* (strain) (Imai 1986). As per Imami (1986) the tools that are used to implement Kaizen are total quality control (TQC), total productive maintenance (TPM), quality improvement, zero defect (ZD), automation, Kanban, just-in-time (JIT), quality control circle and the system of suggestion.

To put into practice Kaizen, firms will adopt the plan-do-check-action cycle (Fig. 1) to resolve unit-functional and cross-functional both the problems in their actions (Imai 1986).

Areas of improvement are identified that require upgrading during the planning phase. Once problem areas are identified, the next step is the Kaizen implementation. Five Whys technique or value stream mapping (VSM) technique is used to implement Kaizen.

3 Five Whys Technique

Problem Statement: In grinding, machine belt in the main transmission drive cracked (Fig. 2).

Further the value stream mapping comprises flowcharts making of the steps, activities or process engrossed. That is how, the non-value activities (waste) can be identified by workers that is happening in that process and attempts to discover the methods to get rid. To work collectively on the project, employees' cross-functional groups of are employed.

Steps involved in creating a value stream map (Fig. 3).

Fig. 1 Plan-do-check-act

Fig. 2 Five why example

Fig. 3 Value stream map
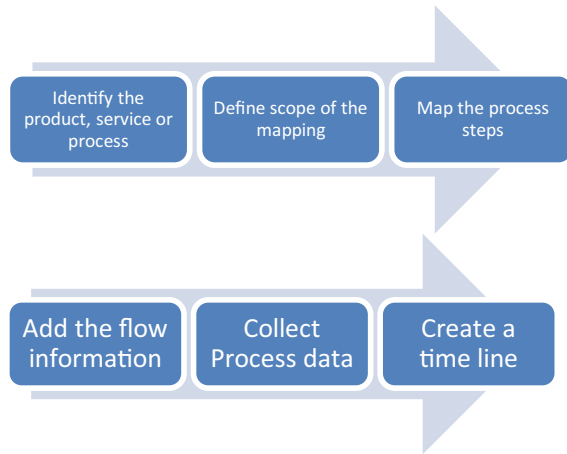
The next step after necessary data is gathered, to analyze and assess, is put to achieve a rational goal. Areas to concentrate may depend on the identified problem areas like the scrap rate, level of product quality, amount of space used, total distance traveled in making the product, work-in-process quantity or people employed in a specific job. The team will attempt after modest brainstorming sessions to find alternatives to get better the existing problem. Finest options are chosen by the team and their implementation on the shop floor.

Plan-do-check-action cycle is the third phase to carry out a feedback on the activities of Kaizen to observe if the action gives any satisfactory result for the concerned problem. Their attainment is recorded on scorecard and shows it to the higher people of management and also to others so that it is assessable to everybody. To assess all of the achievement and observe is the last phase if corrective action to standardize the Kaizen actions can be taken to related process inside the firm.

4 The 5 S Approach

It is a pre-arranged plan to put into practice workplace arrangement and standardization. 5S represents methods for visual workplace maintaining: 1. Sort, 2. Sustain, 3. Straighten, 4. Shine and 5. Sustain.

5 Poka-Yoke

Zero defect is achieved by poka-yoke. It is one among numerous mechanisms of Shingo's zero quality control (ZQC) system, and its objective is to eradicate substandard product output. Poka-yoke concept of quality management is given by a production engineer at Matsushita named Shigeo Shingo to human errors avoidance from happening in the production line.

6 Seven QC Tools

Seven QC tools are also known as seven basic tools and quality management tools. These statistical and graphical methods are employed to analyze and answer problems related to work effectively. These seven quality tools have been extensively applied by a lot of firms for product and process enhancements and to resolve significant quality trouble.

Seven QC tools:

1. Check sheet
2. Fishbone diagram
3. Histogram
4. Pareto chart
5. Control chart
6. Scatter diagram
7. Stratification

7 Seven Wastes

Taiichi Ohno has defined it. Waste is something that utilizes resources without adding any *value* to altering the goods or service.

The seven wastes in production systems are as follows:

1. Transportation
2. Inventory
3. Motion
4. Waiting
5. Over-processing
6. Over-production
7. Defects

8 Steps to Implement Kaizen

1. Involve
2. Discover problems
3. Chalk out solutions
4. Implement
5. Inspect
6. Standardize
7. Repeat

1. Employees' Involvement: Employees' involvement is quite significant for analyzing the issues and problems which requires improvement
2. Finding Problems/Process Analysis: It is analyzed why the issues and problems are arising
3. Think Solution: All the ideas of all the people are taken into consideration. Best idea is chosen
4. Implement: The selected idea is implemented, and action is taken on it
5. Check/Analyze: The resulting change after implementation is analyzed
6. Standardize: If results are better/optimal, the new process is standardized
7. Repeat: Cycle of Kaizen is repeated.

9 Factors Contributing Implementation of Successful Kaizen

Previous studies have identified some firms have got success in Kaizen accomplishment. As shown by Hiam (2003) that firm which has used an average working culture will be having low understanding between workers and the top management on the requirement to produce productive views. It is very important to having a better system of improvement suggestion that persuades effectual communication between workers and the top management. The improvement suggestion system to contribute their improvement ideas based on the experience they have gained throughout their daily working life will encourage the employees (Womack and Jones 2003). Hence, the workforce is expected to develop a better way to make the process more efficient. The success of the Japanese suggestion system has enabled the Japanese firms to improve customer satisfaction, improve productivity index, achieve world-class standard, improve employee job satisfaction and perk up company returns.

Top management commitment is the second factor. It can contribute to Kaizen success in having a transparent management strategy, goals and policies that can awaken Kaizen culture in the firm (Imai 1986). Methodology of Kaizen through top management commitment guided by the Deming PDCA cycle can be employed like a technique in resolving interdepartmental matters involving different activities in a firm.

The third causative factor toward successful implementation of Kaizen is the presence of a quality Kaizen champion in a company. A Kaizen champion with good individual perceptive in accomplishing Kaizen and a high own desire and obligation to escort the incessant development activities can be a significant change agent in an organization (Bateman and Rich 2003). Also, knowledge management and effective communication are vital issues that a Kaizen champion ought to have in for successful Kaizen implementation according to Nonaka and Takeuchi (1995), Pagell (2004). Operation managers having such skills are most appropriate Kaizen champion to guide the alters at the level of shop floor. The role of a Kaizen champion role as the relation between the higher management and the workers is very significant particularly at the time of the transform. The Kaizen champion should work as a motivator to the group under his direction. As per Bateman and Rich (2003), the existence of a dominant Kaizen champion is further obvious particularly inside a small firm.

Organization structure is another significant factor that will put effect on Kaizen accomplishment outcome. As per an observation organization with horizontal structure that uses informal association and combined membership with an elevated degree of independence, self-discipline and sincerity will be successful in comparison with a bureaucratic firm (Watanabe 2011). Participation of management, right setting of goals and gauging, the existence of a person in-charge of continuous improvement, dynamic employees' involvement, resources' availability, presence of multi-departmental teams and comprehensible structure of organization are amid the issues causative to the achievement of Kaizen accomplishment. Quality circles and multi-divisional group working jointly to put into practice Kaizen are also being a catalyst toward Kaizen accomplishment. As per Bessant (2000), Womack and Jones (2003), Liker and Hoseus (2008) studies show that employee's empowerment is extremely significant to the success of implementation of Kaizen. By workforce empowerment, more people will be engaged energetically in the process of problem solving, and it can also augment the feeling of responsibilities for the correct solution finding.

According to the case study done on SME, Puvanasvaran et al. (2010) suggested that owing a correct thinking and a strong participation of management are considerable factors in making certainty to success of implementation of Kaizen. A correct attitude is put forward that workers ought to have a "can do attitude" toward Kaizen implementation. Further, the administration in the firm should also support and sustain the people process-oriented effort toward the development completed by their workforce.

10 Challenges in Implementing Kaizen

Yet a lot of firms comprehend the requirement to put into practice Kaizen at their firm, not all firms are victorious with the accomplishment. Its cause is that, since Kaizen activities management is not at all an easy task (Pullin 2005; Garcia-Sabater and Marin-Garcia 2011) in a study identified, Kaizen challenges are the opposition

to change particularly amid older people and misunderstanding on the continuous improvement concept. The study by Bateman and Rich (2003), Bessant (2000); Dale et al. (1997), Jorgensen et al. (2003); Kaye and Anderson (1999) too supported the prior work conducted.

In a study amid the US manufacturers, it is indicated that merely 11% firms doing continuous improvements have well thought-out their plans to be winning (Mendelbaum 2006). According to Robinson and Schroeder (2004) few firms were unsuccessful to inspire their workers to partaking in the Kaizen activities because of the absence of monitory benefits, be short of suitable guidance for the workers and extended delays in obtaining the processed suggestions. As per Imai, 1986 management ought to build up an incentive system that would distinguish the workers' and managers' effort to make certain Kaizen success firms which want to bring in Kaizen and should also take additional precaution before initiating Kaizen. As per Hiam (2003), it is due to the fact that firms likely to build up a tactical way that is deficient in a good understanding between the higher management and the workers.

According to Kiernan, 1996, Pullin (2005), amid additional challenges in implementing Kaizen in their firm faced by the management was to administer the incessant enhancement itself. Deficient of resources to run the activities, little focus due to pressure of business and deficiency of understanding the need to change is also Kaizen implementation challenges. Administrators do not know what to do to change their cultures or how to deal with challenging and demanding nature of Kaizen and be unsuccessful to encourage the workforce that they need to change (Bateman and Rich 2003).

11   Conclusions

The study reveals an inner view into a number of chosen factors in making sure Kaizen a successful implementation. The review reveals that issues like gap of communication between the management and workers, right strategy, the requirement of a person who can head the Kaizen implementation in a firm, owing excellent knowledge and give workforce with sufficient empowerment are significant to make certain winning implementation of Kaizen. Challenges faced by the organization in implementing Kaizen, on the other hand, include issues like be short of ability to administer the incessant development itself, the opposition to changes and be short of inspiration amid the workforce due to the absence of incentive schemes.

References

Bateman N, Rich N (2003) Companies perceptions of inhibitors and enablers for process improvement activities. Int J Oper Prod Manag 23(2):185–199

Bessant J (2000) Creating and maintaining high involvement innovation. Paper presented at Seminar on Kaizen from Understanding to Action, Institute of Electrical Engineers, London

Choi TY, Rungtusanatham M, Kim JS (1997) Continuous improvement on the shop floor: lessons from small to midsize firms. Bus Horiz 40(6):45–50

Dale BG, Boaden RJ, Wilcox M, McQuater RE (1997) Sustaining total quality management: what are the key issues? TQM Mag 9(5):372–380

Garcia-Sabater JJ, Marin-Garcia JA (2011) Can we still talk about continuous improvement? Rethinking enablers and inhibitors for successful

Hiam A (2003) Motivational management: Inspiring your people for maximum performance. New York: American Management Association. Hill, T. (1991). Manufacturing Strategy, 2nd edn. Macmillan, Basingstoke

Imai M (1986) Kaizen: the key to Japan's competitive Success. McGraw-Hill, New York

Jorgensen F, Boer H, Gertsen F (2003) Jump-starting continuous Improvement through self-assessment. Int J Oper Prod Manag 23(10):1260–1278

Kaye M, Anderson R (1999) Continuous improvement: the ten essential criteria. Int J Quality Reliab Manag 16(5):485–509

Liker JK, Hoseus M (2008) Toyota culture: The heart and soul of the toyota way. McGraw-Hill Professional Publishing, New York

Mendelbaum G (2006) Keep your eye on the ball. APICS Magazine

Nonaka I, Takeuchi H (1995) The knowledge-creating company: How Japanese companies create the dynamic of innovation. Oxford University Press, New York

Pagell M (2004) Understanding the factors that enable and inhibit integration of operations, purchasing and logistics. J Op Manag 22(5):459–487

Pullin J (2005) Room for improvement. Prof Eng 18(15):38–138

Puvanasvaran AP, Kerk ST, Ismail AR (2010) A case study of kaizen implementation in SMI. In: Proceeding of national conference on mechanical engineering research and postgraduate studies (2nd NCMER 2010), Pekan, Kuantan, Malaysia, pp 374–392

Robinson AG, Schroeder DM (2004) Ideas are free: how the idea revolution is liberating people and transforming organizations. Berrett-Koehler Publishers, USA

Teece DJ (2007) Explicating dynamic capabilities: the nature and micro-foundations of (sustainable) enterprise performance. Strateg Manag J 28(11):1319–1350

Watanabe RM (2011) Getting ready for Kaizen: organization and knowledge management enablers. J Inf Knowl Manag Syst 41(4):428–445

Womack J, Jones D (2003) Lean thinking: banish waste and create wealth in your corporation. New York: Simon & Schuster. Womack J, Jones D, Roos D (2007) The machine that changed the world published. New York: Simon & Schuster.

Review on How IIoT Has Revolutionized Greenhouse, Manufacturing and Medical Industries

Visheshgiri Goswami, Priyanka Jadav, and Sneh K. Soni

Abstract The transformation of the physical world into digital in terms of industries has made everything connected. Evolution of technologies has created different terms and concepts. IIoT is one of the major concepts in not only manufacturing industries but industries like agro-based or medical. Over the period of time, IIoT and IoT have been used interchangeably although they are two very different concepts. When IoT is applied in manufacturing, it is known as 'Industrial Internet of Things.' This technology is a combination of different technologies like M2M communication, machine learning, big data, sensor data and automation those already existed in industries. IIoT deals with industrial applications (manufacturing), large-scale networks, while IoT deals with general applications (consumer usage), small-scale networks. IIoT or Industry 4.0 aims at interconnectivity, automation, real-time data. There are a number of benefits, but at the same time one cannot neglect all the challenges that are faced. This paper gives an overview of what is meant by IIoT and its related concepts, Industry 4.0, and also tries to analyze the benefits, challenges faced, its applications, smart manufacturing and its successful implementations and a look into how it has and is continuously contributing to different industries like manufacturing, greenhouse industry and medical industry.

Keywords IIoT · Manufacturing · Industry 4.0 · Smart manufacturing · Greenhouse and medical industry

V. Goswami · P. Jadav · S. K. Soni (✉)
Institute of Technology, Nirma University, Ahmedabad, India

V. Goswami
e-mail: 18bic021@nirmauni.ac.in

P. Jadav
e-mail: 18bic025@nirmauni.ac.in

1 Introduction

There have been four industrial revolutions taken place which have helped in improving the process and products. IIoT helps in improving the efficiency in terms of productivity. IIoT enables the coordination and communication of data and data analytics between a large number of connected industrial systems, and it acts as a catalyst to improve the industrial performance. Cloud computing, encryption, ubiquitous data, big data analytics and smart machines are all characteristics of the IIoT (Li et al. 2017). The Industrial Internet of Things (IIoT) is used in a variety of industries, including manufacturing, transportation and utilities (Lu et al. 2020). The Industrial Internet of Things is primarily used in manufacturing processes, distribution, asset management and maintenance, as well as field service. Automation systems, such as supervisory control and data acquisition (SCADA), distributed control system (DCS), programmable logic controller (PLC) and manufacturing execution systems (MES), are used by many manufacturers (Boyes 2018) for the processes of managing and controlling the motors and robots. Connected factory applications, vehicle and asset monitoring, air quality management, access control (security), smart measurement of radiation gases and liquid levels, and risk measurement are all benefits of the IIoT for manufacturing companies.

2 Background

Figure 1 shows the changes industries have gone through over a period of time. Industry 4.0 is referred to as the fourth major industrial revolution that took place. It tries to revolutionize the ways the entire manufacturing processes would operate and grow.
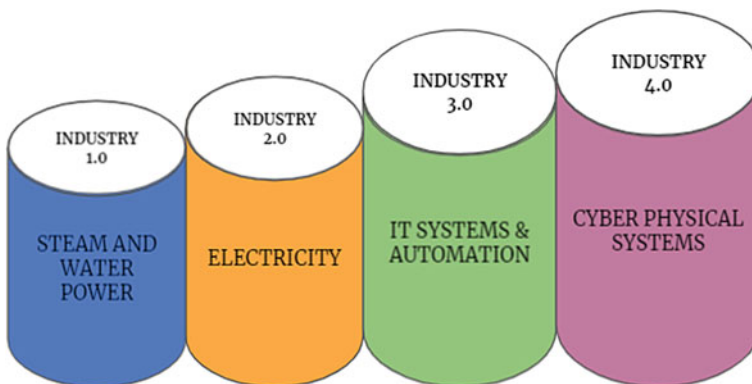
Fig. 1 Industrial revolution over the years

The First Industrial Revolution (Late 1700s and Early 1800s)

A major turning point because it developed new machines and technologies which could change matter into steam. It essentially evolved human labor conducted manually into human labor performed using steam power (Desoutter Industrial Tool 2021; Simio Blog 2021). Further massive improvements such as the steamship and the steam-powered locomotive, which enabled people and goods to travel long distances in less time, took place. It is also seen that from here that all the industrial culture shifts to equally prioritizing quality, efficiency and sale.

The Second Industrial Revolution (Early Twentieth Century) (AKA Technological Revolution)

It introduced assembly line production and the use of electricity in industries. Here, electricity was also being used as a primary source of power (Desoutter Industrial Tool 2021). Electrical machines were more cost-effective to run and maintain. Henry Ford introduced the idea of an assembly line, and the first assembly line was installed (Simio Blog 2021) which further streamlined the mass manufacturing process. It increased efficiency and helped industries become more mobile.

The Third Industrial Revolution (Late 1950s) (AKA Digital Revolution)

A big step forward, when computers and automation dominated the manufacturing landscape. During this transition period, more and more robots were used in processes to perform tasks that were previously performed by humans (Simio Blog 2021). Slowly and gradually, manufacturers began to incorporate computer and computer-based technologies into the manufacturing. This revolution majorly emphasized the growth of digital technology and automation software (Desoutter Industrial Tool 2021). More automated devices, such as programmable logic controllers (PLCs), were added to the assembly line to perform human tasks. Despite the presence of automated systems, they still needed human input and intervention.

The Fourth Industrial Revolution or Industry 4.0

The 'Smart Machine' era. It emphasizes on digital technology and has set new goals and developed new levels of interconnectivity, Industrial Internet of Things (IIoT), cyber-physical system, cloud computing (Lu et al. 2020). It has also expanded 'smart manufacturing.' It aims at producing high-quality products and has an adaptability to quickly changing conditions. Industry 4.0 is a broad term and a new trend in manufacturing (and related industries) that is focused on the convergence of technologies that allow ecosystems of intelligent, autonomous and decentralized factories, as well as automated products and services (Boyes et al. 2018). Industry 4.0 has introduced 'smart factory' (Desoutter Industrial Tool 2021). Products and production methods become networked and can 'communicate,' allowing for new production methods, value creation and real-time optimization. The capabilities needed for smart factories are created by cyber-physical systems.

2.1 Cyber-Physical Systems

CPSs are smart systems that involve engineered communicating networks of physical and computational components and are a key element in the implementation of Industry 4.0 concepts. Cyber-physical systems are characterized by large numbers of tightly integrated heterogeneous components in a network, which may expand and contract dynamically. Cyber-physical systems are common and are becoming ubiquitous (Antsaklis 2014; Sanislav and Miclea 2012). CPS has a lot of potential to enable creative applications and has an impact on a variety of economic sectors (ISA Interchange 2021) around the world. From a manufacturing perspective, CPS is an Internet-enabled physical entity (Boyes et al. 2018). According to the NSF, advances in cyber-physical system research have the potential to transform our world by creating systems that respond faster (e.g., autonomous collision avoidance), more precisely (e.g., robotic surgery and nano-tolerance manufacturing) and work in dangerous or inaccessible environments (e.g., autonomous systems for search and rescue, firefighting and exploration). There are four interactions between the physical and cyber spaces. CPS can be described as operating in a decentralized, structured and unstructured communication (Cronin et al. 2019). CPSs are not traditional embedded systems; instead, they have characteristics of: cyber capabilities in every physical component; networked at multiple and extreme scale; dynamically reconfiguring; high degrees of automation; control loops must close; and operation must be dependable and certified in some cases (Antsaklis 2014).

CPS has a number of benefits: safe and efficient. They allow individuals to collaborate to create complex systems with new capabilities (Sanislav and Miclea 2012). Areas where this technology can be used are: critical infrastructure control, safe and efficient transportation, alternative energy, environmental control, medical devices and integrated systems, social networking, gaming.

2.2 Industrial Automation and Control Systems

IACS defines different types of control systems and related instrumentation, such as the instruments, systems, networks and controls that are used to run and/or automate industrial processes (Boyes et al. 2018). IACS products are mostly based on common embedded system architectures and are used in a variety of devices, including routers and cable modems.

2.3 Supervisory Control and Data Acquisition

For high-level process supervisory management, supervisory control system architecture includes computers, networked data communications and graphical user
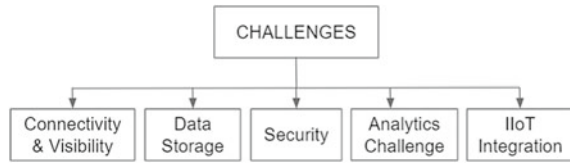
interfaces (GUI), as well as other peripheral devices such as programmable logic controllers (PLCs) and discrete proportional–integral–derivative (PID) controllers to communicate with process plant or machinery (Boyes et al. 2018). The use of SCADA has been considered also for management and operations of project-driven process in construction.

3 Challenges in Real-Time Implementation of IIoT

Due to the rapid transformation of the physical world into the digital world (Jaidka et al. 2020), the users and devices are subjected to stay constantly connected to each other. Most of the manufacturers want their companies to inculcate IoT in their business for growth and development and to get used to the latest technology. This leads to challenges and opportunities for companies and their users. Figure 2 gives a macro-understanding of challenges faced by industries; for instance, the lack of connectivity is at the root of the crucial IIoT implementation issues. To boost production, it is critical to track machines in real time and ensure they are working at their best. Increased visibility and deeper insights into the machine's health are also important for detecting abnormalities and resolving problems before they arise. Since IIoT machines are attached to a variety of modules, synchronization may be difficult due to Internet outages (Arumugam 2019), power outages and human/technical errors. This would cause connected devices to be disconnected from the network, disrupting the entire manufacturing process and potentially costing millions of bucks in damages. Data security is a major concern considering real-time implementation of IIoT technology.

4 Benefits of IIoT in Manufacturing Industries

Despite all the challenges faced by IIoT in manufacturing, there are more benefits as listed in Figure 3. Industrial Internet of Things (IIoT) is the use of 'connected smart devices' to track, automate and forecast various industrial processes and outcomes. These innovations range from improved worker safety through factory floor control systems to the predictive maintenance capabilities that are currently revolutionizing the fleet management industry (Arumugam 2019). The widespread adoption
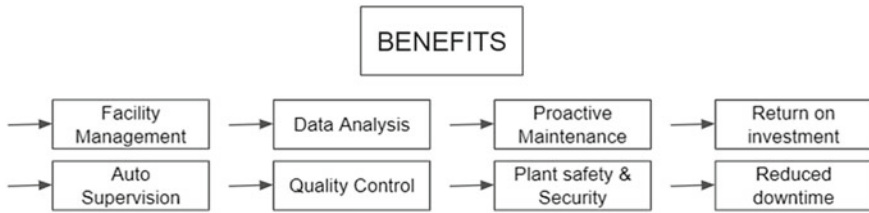
Fig. 3 Benefits of IIoT in manufacturing

of such systems improves the efficiency of producers, supply chains and warehouse managers. Data-driven observations enhance performance in the IIoT.

5 Needed Infrastructure

Despite a number of challenges and benefits related to IIoT in manufacturing, one thing it can guarantee is that in the near future without IIOT, it would be much more difficult to increase efficiency and profit. So, there exists an infrastructure for IIoT so that it can be established in a system of any industry. So as per ARC advisory group (Arumugam 2019), there exist four key parts to establish an infrastructure of IIoT in any particular manufacturing industries:

- **Intelligent assets**: These intelligent assets are a combination of the components such as controllers, sensors, edge devices which are hardware which is for controlling data flow at the boundary between two networks as well as application software and security components (Arumugam 2019). Here, each of these assets can connect to the Internet, has knowledge built in and can be used for analytics. They gather information and distribute it across the supply chain.
- **A data communication infrastructure**: The Internet and other network technology are needed for assets in an IIoT system to communicate with cloud infrastructures (Arumugam 2019) that are often used to install IIoT applications. Cloud storage involves collecting, handling and processing data over the Internet rather than on a single local server.
- **Software**: The data obtained by your appliances and computers is analyzed by IoT software. It also serves as a user interface for interacting with the IIoT framework (Arumugam 2019). People can make smarter decisions and work better with the help of technology. Manufacturers profit from cloud-based computing over presuppose solutions in a variety of ways. These benefits include a lower overall cost of ownership, increased durability, increased speed and reduced maintenance costs.
- **People**: We know that people are a critical but frequently underestimated component of every IIoT scheme. People communicate with the system by making decisions based on the data and interpretation provided by the IIoT components as a

whole. People will become more linked to plant machinery, computers, networks and other employees with better data and more effective analytics software. As a consequence, quantitative decision-making will become the standard.

6 Applications

6.1 Smart Greenhouse

In smart greenhouse agriculture, the IoT plays a critical role. As in this, a system is created for monitoring the crop field with the use of sensors (light, humidity, temperature, soil moisture, etc.) and automating the irrigation system in IoT-based smart greenhouse farming (Behrtech 2021). Owners can keep an eye on their fields from anywhere. When compared to traditional greenhouse farming, IoT-based smart greenhouse farming is extremely efficient. Greenhouse farming is a technique for increasing the output of vegetables, fruits and other crops. Greenhouses employ either manual intervention or a proportional control method to regulate environmental factors smart.

- **Maintain Appropriate Climate conditions**: Farmers may collect varied sets of data using IoT devices. Throughout the greenhouse, they give real-time data on important climatic parameters (Behrtech 2021) such as temperature, humidity, light exposure and carbon dioxide. This information drives changes and settings to keep the favorable conditions for plant development while also increasing energy efficiency.
- **Improved Irrigation and Fertilization system**: IoT-based greenhouses allow farmers to keep track of their crop status in addition to environmental indicators (Behrtech 2021). This means that irrigation and fertilization are matched to the real demands of farmed plants, resulting in higher yields. Sprinkler and spraying systems may be turned on automatically based on this information to meet real-time crop demands with minimal user involvement.
- **Prevent Disease Outbreaks by Containing Infection**: Crop infection (Behrtech 2021) is a chronic farming problem, causing major damage on crop yields. Data on greenhouse, weather and soil parameters, combined with machine learning, offers significant insights on insect and fungus threats. Farmers may utilize this data to apply treatments exactly when they are needed, guaranteeing a healthy crop at the lowest possible chemical expense.
- **Enhance Safety and Prevent Robbers**: Greenhouses with high-value crops are a popular target for robbers. Many growers do not have an adequate security system (Behrtech 2021) in place since standard monitoring networks with CCTVs are costly to build. IoT sensors in smart greenhouses provide a cost-effective infrastructure for monitoring door status and detecting suspect activity in this context. When they are linked to an automatic alarm system, they may immediately alert growers if a security concern occurs.

Case Study: A New Outlook for Greenhouse Using IIoT

The global farming industry has come under significant pressure as a result of climate change, dwindling resources and rising population. In this strain, only the combination of a greenhouse (it comes with a controlled environment specially built for vegetation to be cultivated inside) and IIoT is more prevalent in agriculture than ever before. Combination of both is also called smart greenhouse. It used different types of sensors so as to measure temperature, mixture, humidity, PH, light level and CO_2 concentration, which are connected to actuators such as fan, bulb, sprinkler and many others so as to adjust the climate inside (Touhami et al. 2020). These both are being operated by controller which works on the set of defined rules. Smart greenhouses automatically sense and deliver information whole time on the surroundings and also of the crop. Table 1 lists the equipment and apparatus required for different parameters.

As for each different parameter like if the temperature is being changed in the greenhouse system, then the sensor will sense it and the signal will be send to microcontroller (Touhami et al. 2020) as shown in Figure 4, from where with respect to the set point the actuator which is fan will be on, and for the case of pH w.r.t. to set point the motor pump with solution of alkaline or acid will be sprayed; then if there is change in moisture and humidity, then water pump and exhaust pump will be turned on, respectively. With the change in CO_2 concentration we with concern with the data which is with sync with the gas consumption of our crops then CO_2 gas cylinder or exhaust fan in many case can be on and for controlling the light we have light level sensor which will detect if the light level is sufficient and if is changed with respect to the setpoint then the bulb will be turned on. (Figure 5 represents a selfmade setup.) So, this is how a whole greenhouse system with the combination of IIoT (Behrtech 2021) can have heft of benefits and the improvements with this IIoT system being installed are:

- **Overall cost and time are reduced**: Here, there is no extra labor cost, and as it is 24/7 surveillance, there is no requirement to spend extra money on other resources and time is saved to look after the whole system.

Table 1 Sensors and actuators used in setup

Parameter	Sensor	Actuator
Humidity	DHT11	Exhaust fan
Temperature	DS18b20,WS-9160U-IT	Fan and sprinkler
Soil moisture	EC-5	Water pump
pH sensor	HI 99,121 pH meter kit	Motor pump (acidic or alkaline solution)
light level	Light-dependent resistor (LDR) or SQ-110 sensor	Bulb
CO_2 sensor	Carbon dioxide detector gas analyzer, WRF04 CO_2 sensor	Exhaust fan or CO_2 gas cylinder

Fig. 4 Block diagram of working
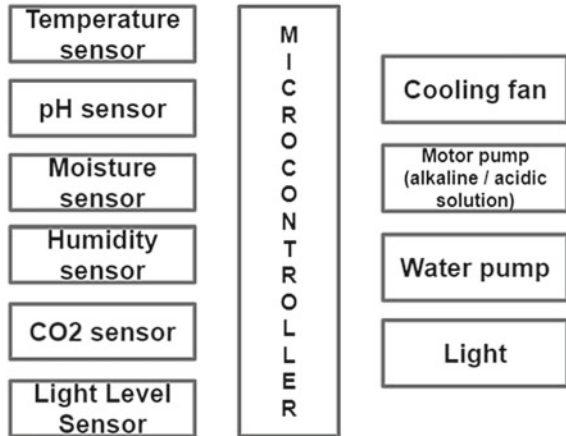
Fig. 5 Structural view of greenhouse

- **Human error**: The whole system is controller operated, so there is no need for human intervention and chance of error is also reduced.
- **Increased production**: As there is near to ideal conditions for farming, there is increased production.
- **Quality**: Overall quality of the crop is increased.

6.2 IIoT in Manufacturing Industries

As it is seen that manufacturing industries have close to uncountable plants and with such a large and heavy business, it comes with different troubles. Their main problem was lack of real-time access into process data, which was causing quality

problems. Even so, they were not able to determine the energy consumption of both systems and appliances. Paper logbooks were used to record the information. Even if the data from the PLC/SCADA was open, it was only accessible to the operators. It was impossible for the team to make some real-time operation interactions; as a result of this, they were having trouble with a real-time alert system for constructive and predictive process control (Tulip 2021). The efficiency optimization, energy expenditure, quality improvement, batch-level traceability and many others were all concerns for these types of industries. So, they need to come up with a solution as it would be a major problem. So, they analyze key benefits by introducing IIoT in the manufacturing process. So by using IIoT in the plant through the required locations, they installed different systems of IIoT within their old plants so as to improve productivity, CBM, quality and energy (Altizon 2021). The teams collected data from PLC/SCADA and created a multi-tenant cloud manufacturing data pool. They have used a variety of real-time analytics and dashboarding modules. It was seen as a major improvement in different areas as given below:

- **Correct performance measurements**: A connected shop floor aids data availability and accuracy, allowing the plant operations staff to take corrective decisions in real time.
- **Digital dashboards**: Digital dashboards provide plant managers real-time insights into key KPIs in productivity, quality, maintenance and energy.
- **Automated Bookings**: Integrate IoT with ERP via IT/OT to automatically book production, allowing for better visibility and inventory unblocking.
- **Energy**: The development team should analyze energy consumption through all operations to keep costs under control.
- **Process deviation warnings**: With constant tracking of vital process parameters, operators receive alerts to respond on any process deviation.
- **Batch traceability**: Production teams can easily respond to problems by following a component or substance back into the supply chain to find the source of the problem.
- **Quality**: Using statistical and machine learning methods, perform root cause analysis of parameters that control process quality.

Case Study: Transformation of Lean Six Sigma Approach for Global Supply Chain Management Using Industry 4.0 and IIoT

Frontrunners in the manufacturing industry have already begun to integrate IoT into production and the supply chain (Jayaram 2016). It is one of the new and established technologies in the industry. As we know in any industry supply chain (Jayaram 2016) (management of the network of resources and activities which are physically situated far from one another) for this purpose lean six sigma approach(Quality control methods which removes unnecessary processes and remove defects in the product which can benefit an enterprise from reducing the costs and less wastage of resources is being used from for quite a time). Here in this approach with Lean Six Sigma, they use IIoT and Industry 4.0 which will make the supply chain of the whole process fully autonomous with steps as seen from the below given figure. In

the proposed model, global supply chain can follow this with support for IIoT and Industry 4.0 whose steps are given:

- **Connectivity-** It is the fundamental infrastructure for connecting the production and supply chain in a network to make it within reach from anywhere.
- **Visualization-** It is the development of graphs and live data visualization. It is possible after the supply chain is fixed in a network and forward data regarding the operations of the machines.
- **Optimization-** It increases the efficiency of processes by the support of visualization and making decisions that help in the optimization in the working of the enterprise. Also here at supply chain level, it can minimize costs and resource consumption so as an increase in the overall efficiency.
- **Autonomy-** Here for the automation of the IIoT systems that can operate the supply chain operations itself, it also oversees the enterprise, predicts events and also takes actions itself.

Manufacturing is unquestionably the best industry for demonstrating the IIoT full potential. Companies may utilize IoT sensors to reconstruct old processes from the bottom-up, monitor equipment quality and staff productivity remotely, manage supply chains remotely and identify future difficulties well in advance. So by implementing IIoT, they will be able to overcome the problems which their organization faced. IIoT backed system in more advanced models is installed till date so that one organization could stay ahead from the other competitors.

6.3   IIoT in Health Care

In the healthcare industry, IIoT has ushered in a new era of increased possibilities, with regular medical equipment now able to acquire and exchange critical data (Control Automation 2021), giving healthcare professionals and medical practitioners more insight into symptoms and treatment trends when connected to the Internet. Furthermore, the IIoT has significantly reduced healthcare professionals' duties.

- **Early Maintenance and Utilization of Resources**
  The Industrial Internet of Things (IIoT) can help manufacturers mitigate some of the hazards, for instance, FDA restrictions on sterilizing techniques for medical connectors in manufacturing environments. If there are errors in equipment maintenance, it could result in product flaws or much harmful illness or injuries, even the most compliant corporation could suffer recalls, reputational harm and government fines (MPO 2021).
- **Remote, On-Demand Manufacturing**
  One of the most important Industrial Internet of Things technologies is 3D printing. For various reasons, connected industrial printers represent a key development in medical device manufacturing. Faster prototyping is one of them.

Depending on their level of communication with the greater IIoT, 3D printers' capabilities may be expanded further (MPO 2021). Patients will most likely acquire unique medical equipment and perhaps custom-printed drugs at their local pharmacy in the near future.

- **Ensuring Safety of Equipment and of Personnel**
  Sensors and other data loggers can be used as part of an IIoT system in the medical manufacturing industry to keep workers and workplaces safe. For example (MPO 2021), a company used the Internet of Things to collect data on staff posture, speed, process bottlenecks, air quality and other factors in 11 different industrial environments and processes. This aided the facility owner in creating a new atmosphere in which employees can do their duties without fear of injury or fatigue, and automated systems may work alongside them even more safely.
- **Improvement in Accountability and Transparency**
  Even though the IIoT is powerful on its own, adding blockchain to the mix will boost device and medical connector manufacturing even more. The IIoT gathers and distributes data that is accurate, up to date and as tamperproof as possible, because of blockchain. Any risk-averse industry, including connectors and medical devices, needs complete and unfalsifiable documents demonstrating a product's provenance including the procedures used to acquire, harvest, construct, assemble or ship it to end users.

Case Study: Coping up COVID-19 with IIoT and Smart Hospital

As a whole pandemic outbreak, it is seen that healthcare industries (NCBI 2021) have now more emphasis on IIoT-based facilities as the ability to seamlessly handle the outbreak will require more technology support and also the increase in quarantine facilities is making it impossible for health workers (MPO 2021) to handle the situation. So to tackle this situation, IIoT gives its answer as it can be done by:

- **IIoT-based smart hospital**: IoT with real-time location service (NCBI 2021) may be used to treat the COVID-19 patient to its full potential. Various medical equipment and devices may be used for monitoring in the IoT domain. It can also be used to monitor and regulate hospital environment parameters such as temperature and humidity. IoT applications are aiming to create a smart bed (NCBI 2021) that can adjust its height to meet the needs of COVID-19 patients. This intelligent bed can change the pressure and support for the patient automatically.
- **Data handling**: The smart hospital may use the data on the patient's ongoing difficulties to provide all information with a complete digitization (NCBI 2021) of the system, thus reducing the patient's waiting time. It also analyzes the procedure and the patient's records. COVID-19 patient data would be sent, effectively stored and analyzed via IoT devices, allowing for improved treatment in the future. Raise awareness about the virus's origins. As the right information to be provided to a healthcare worker, including their location, time stamp and database, it will be helpful in understanding the patient's requirements.
- **Monitoring and alerting**: It analyzes the COVID-19 patient's arrival and keeps track of the condition of support facilities (NCBI 2021). This technology alarms

the human for COVID-19 illness with real-time tracking in life-threatening situations. It alerts individuals via connected devices in a timely manner. Report and accurately provide an opinion on the state of human health. Provide real-time alerting, on-time treatment and improved monitoring, such as notifying doctors in the event of a drop in oxygen levels.

- **Medical apparatus and Medication**: The major use of this technology is to remind patients to take their medications. It informs the patient to take in the required time when there are missing doses. Check the glucose level and flow (NCBI 2021) according to the patient's needs. Adjust the insulin dosage automatically to keep it within a healthy range. It keeps track of the COVID-19 patient's medicine, as well as his or her protein and food consumption.
- **Assist in remote quarantine facilities**: IoT can assist patients who are far away from hospitals at either home or quarantine centers (NCBI 2021) in contacting doctors via smart mobile phone applications. It will be helpful in the examination of a COVID-19 patient and the determination of the infection's source. As a result, patient care will improve and hospital digitization will grow.

7 Conclusion

This paper is focusing on how the Industrial Internet of Things (IIoT) is a rapidly evolving technology that will radically transform the way businesses operate. Since IIoT will occupy every sector in the future, it is critical that we consider IIoT technology, its applications in all the industries and how to overcome the challenges with new technology. It was seen with the case study that how different types of industries from agriculture to manufacturing are going to cope with IIoT.

It is also seen that IIoT is the product of the combination of many existing technologies, and it is now being used in combination with big data, sensor data and cloud computing to minimize manual overhead in a cost-effective way. But still how to overcome the problem of privacy and security will be a heck of a task for the professional so as to have optimal amount of efficiency.

References

Altizon https://altizon.com/case-studies/. Accessed 23 July 2021

Antsaklis P (2014) Goals and challenges in cyber-physical systems research editorial of the editor in chief. IEEE Xplore

Arumugam SK (2019) An industrial IOT in engineering and manufacturing industries-benefits and challenges. Int J Mech Product Eng Res Dev (IJMPERD)

Behrtech https://behrtech.com/blog/4-benefits-of-smart-greenhouses-and-how-to-get-started/. Accessed 21 July 2021

Boyes H, Hallaq B, Cunningham J, Watson T (2018) The industrial internet of things (IIoT): an analysis framework. Comput Indust 101:1–12

Control Automation https://control.com/technical-articles/growing-iiot-capabilities-in-the-health care-and-medical-industries/. Accessed 21 July 2021

Cronin C, Conway A, Walsh J (2019) Flexible manufacturing systems using IIoT in the automotive sector. Proced Manuf

Desoutter Industrial Tool https://www.desouttertools.com/industry-4-0/news/503/industrial-revolu tion-from-industry-1-0-to-industry-4-0. Accessed 17 July 2021

ISA Interchange https://blog.isa.org/cyber-physical-systems-the-core-of-industry-4.0. Accessed 01 Aug 2021

Jaidka H, Sharma N, Singh R (2020) Evolution of IoT to IIoT: applications & challenges. In: Proceedings of the international conference on innovative computing & communications (ICICC)

Jayaram A (2016) Lean six sigma approach for global supply chain management using industry 4.0 and IIoT. In: 2nd International conference on contemporary computing and informatics (IC3I)

Li JQ, Yu FR, Deng G, Luo C, Ming Z, Yan Q (2017) Industrial Internet, F.: A survey on the enabling technologies, applications, and challenges. IEEE Commun Surv Tutor

Lu Y, Witherell P, Jones A (2020) Standard connections for IIoT empowered smart manufacturing. Manuf Lett

MPO https://www.mpo-mag.com/contents/view_online-exclusives/2020-09-02/4-ways-the-iiot-improves-medical-manufacturing/. Accessed 24 July 2021

NCBI https://www.ncbi.nlm.nih.gov/pmc/articles/PMC7897999/. Accessed 21 July 2021

Sanislav T, Miclea L (2012) Cyber-physical systems - concept, challenges and research areas. Research Gate

Simio Blog https://www.simio.com/blog/2018/09/05/evolution-industrial-ages-industry-1-0-4-0/. Accessed 21 July 2021

Touhami A, Benahmed K, Parra L, Bounaama L, Lloret J (2020) An intelligent monitoring of greenhouse using wireless sensor networks. Smart Struct Syst

Tulip https://tulip.co/ebooks/iiot-for-manufacturers/. Accessed 07 Aug 2021

Fracture Analysis of Crack Positioned Perpendicular to the Poling Direction in Piezoelectric Material Using XFEM

Srinivasu Chadaram and Saurabh Kumar Yadav

Abstract In this paper, the fracture analysis of the penny-shaped crack positioned perpendicular to the poling direction is presented in detail. The path independent J integral is used for the evaluation of the stress intensity factors (SIFs) and electric displacement intensity factor (EDIF), which defines the singularities near the crack front. Depending on the J integral, the relationship between interaction integral and the fracture parameters is established through Irwin matrix ($\mathbf{Y}$) by appropriately choosing the auxiliary functions. The extended finite element method (XFEM) is utilized to solve the crack problem, which enriches the standard FE approximation with the additional functions with the given coupled boundary conditions. The code is validated with the available literature for different crack radius, applied load conditions are presented, and it shows good accuracy. Further in the numerical example, the effect of the crack position on the fracture parameters in the poling direction is studied.

Keywords Fracture · Crack · J Integral · SIFs · EDIF · Irwin matrix · XFEM

1 Introduction

In the recent years, the application of piezoelectric components is rapidly enhanced with the evolution of the science and technology, which are subjected to enormous changes in the service requirements continuously (Rao and Rahman 2003). However, it includes certain defects like cracks, inclusions and voids that arise during the manufacturing process. These defects are severe problem in the piezoelectric materials, as these materials are brittle in nature and lead to sudden failure. It is known that the stress and electric field near the crackfront produce singular fields which affect the crack enhancement and failure of the component under electromechanical loading.

Rao and Rahman (2003) proposed the new interaction integral for the fracture analysis of the functionally graded orthotropic material. Rao and Kuna (2008) presented

S. Chadaram (✉) · S. K. Yadav
Department of Mechanical and Aero-space Engineering, Institute of Infrastructure, H Technology, Research and Management (IITRAM), Ahmadabad, India

the domain form of the interaction integral for the analysis of the crack tip fracture parameters in the functionally graded piezoelectric materials (FGM's). Lin et al. (2003), Li and Lee (2004) derived the exact solution for penny-shaped crack using Hankel transform under mode I loading condition. Shang et al. (2003) analyzed the three-dimensional cracks in piezoelectric structures using the finite element (FE) techniques under coupled mechanical and electric loads, Enderlein et al. (2005) analyzed the stationary in piezoelectric structures under dynamic-coupled electromechanical loading using FE techniques, and Qin and Noda (2004) obtained general solution to the similar cracks using green's function by boundary element methods (BEM). Sanz et al. (2005) presented the boundary element method (BEM) for the three-dimensional fracture analysis of the piezoelectric materials. The approach is based on the Deeg's fundamental solutions and the extended displacement boundary integral equation. Qin et al. (2007) analyzed the three-dimensional planar cracks using the hypersingular integral equation method in piezo domain subjected to coupled body forces. Solis et al. (2009) studied the cracked piezoelectric solids using the boundary element approach. This procedure is executed based on the extended displacement and the extended traction integral equations for the discontinuity.

Béchet et al. (2009) modeled the cracks using the extended finite element methods (XFEM) and proposed the new additional functions ahead of crack front that is defined to estimate fracture parameters. Zamani and Eslami (2010) implemented the XFEM for the dynamic fracture study of the stationary crack under the thermal and mechanical shocks. Nguyen-Vinh et al. (2012) adopted time implicit β-Newmark integration scheme for the dynamic fracture analysis of piezoelectric material using XFEM. Hattori et al. (2012) analyzed the fracture parameters using the interaction integral, and the novel crack tip enrichment functions for XFEM are derived by using the Stroh formalism. Sharma et al. (2013) studied the influence of bimaterial interface crack on the fracture parameters using XFEM, and Li et al. (2014) evaluated the two-dimensional dynamic SIFs and EDIF for the interface cracks in bimaterials using the extended scale boundary finite element method (SBFEM). Fan et al. (2014) obtained the analytical solution for the isotropic three-dimensional piezoelectric solid with penny-shaped crack using extended displacement discontinuity method. Pramod et al. (2018) developed the scaled boundary finite element methods for the analysis of the FGPMs with semi-analytical technique to study the fracture parameters. Yadav (2020) evaluated the three-dimensional fracture parameters of piezoelectric materials using interaction integral by XFEM.

In the paper, the authors extended the case study (Yadav 2020, Chadaram and Yadav 2020, Chadaram Yadav nd) of three-dimensional fracture study of piezoelectric material using the interaction integral. In the analysis, the crack is placed in the transverse plane and perpendicular to the poling direction. The mechanical and electric displacement intensity factors are then obtained and validated. Numerical example under impermeable boundary condition is investigated with finite crack position in poling direction and variable coupled electromechanical loading. The accuracy and the exactness of the obtained results are verified with the available analytical solution in the literature (Lin et al. 2003). The paper is arranged as follows.

The introduction is followed by governing equation, XFEM for piezoelectric materials, computation of the fracture parameters, and validation and some conclusions drawn from the present work are presented in the last section.

2 Governing Equations

The symmetric stress tensor and the electric displacement, respectively, are related combined linear Lagrange symmetric strain tensor ε_{kl} and electric field vector E_k through the direct and indirect linear piezoelectric constitutive equations (Yadav 2020) as depicted in Fig. 1.

$$s_{ij} = C^E_{ijkl}\varepsilon_{kl} - e_{kij}E_k \tag{1}$$

$$D_k = e_{ikl}\varepsilon_{kl} + k^{\varepsilon}_{ik}E_k \tag{2}$$

Fig. 1 Piezoelectric domain with boundary conditions
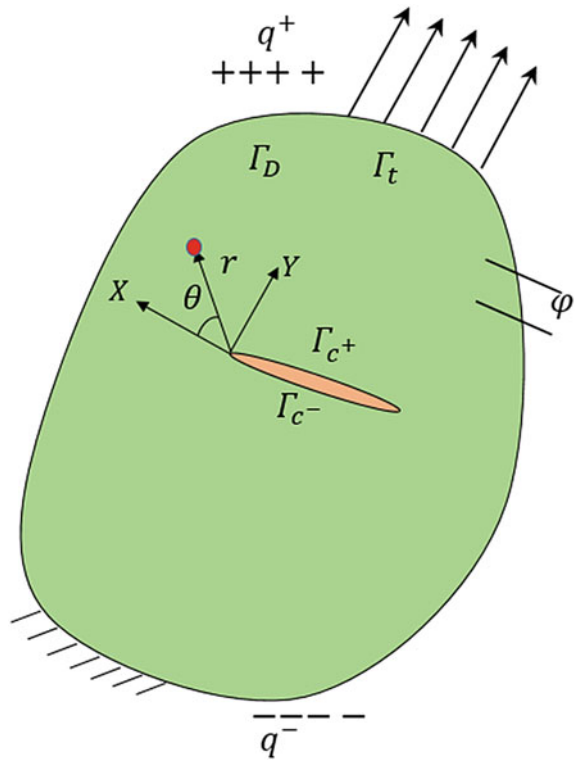
$$\varepsilon_{ij} = \frac{1}{2}\big(u_{i,j} + u_{j,i}\big); \; E_k = -\varphi_{,k}) \tag{3}$$

Boundary conditions

$$s_{ij}n_k = t_j^0 \, on \, \Gamma_t; \; D_k n_k = \Omega^0 on \Gamma_D \tag{4}$$

$$u_k = u_k^0; \; \varphi = \varphi^0 on \Gamma_\varphi \tag{5}$$

3   XFEM for Piezoelectric Materials

The XFEM is developed based on the standard FE workspace with some additional enrichment functions that span the discontinuities and the singularity fields with an optimal accuracy (Yadav 2020).

$$u^h(x) = \sum_{i \epsilon S_s} \tilde{S}_i(x)u_i(x) + \sum_{j \epsilon S_s} \tilde{S}_j(x)[h(f(x))]a_j + \sum_{k \epsilon S_{CF}}^{k=4} \tilde{S}_j(x) \sum_\gamma \big[A_\gamma(x)\big] b_k^\gamma \tag{6}$$

$$\varphi^h(x) = \sum_{i \epsilon S_s} \tilde{S}(x)\varphi_i(x) + \sum_{j \epsilon S_h} \tilde{S}_i(x)[h(f(x))]c_j + \sum_{k \epsilon S_{CF}}^{k-=4} \tilde{S}_k(x) \sum_\gamma \big[A_\gamma(x)\big] d_k^\gamma \tag{7}$$

4   Computation of Fracture Parameters

The fracture parameters are computed through the domain form of $\boldsymbol{J}$ integral or interaction integral given in Eqs. 8–11.

$$J = \int_A \left(s_{ij}\frac{\partial u_i}{\partial x_i} + D_j\frac{\partial \varphi}{\partial x_i} - \overline{P}\delta_{1j} \right)\frac{\partial q}{\partial x_j}dA + \int_A \frac{\partial}{\partial x_j}\left(s_{ij}\frac{\partial u_i}{\partial x_i} + D_j\frac{\partial \varphi}{\partial x_i} - \overline{P}\delta_{ij} \right)qdA \tag{8}$$

$$M^{(1,2)} = \int_A \left(s_{ij}^1\frac{\partial u_i^2}{\partial x_1} + D_j^1\frac{\partial \varphi^2}{\partial x_1} + s_{ij}^2\frac{\partial u_i^1}{\partial x_i} + D_j^2\frac{\partial \varphi^1}{\partial x_1} - \overline{P}^{(1,2)} \right)\frac{\partial q}{\partial x_j}d\Gamma \tag{9}$$

$$\overline{P}^{(1,2)} = \frac{1}{2}\big(s_{ij}^2\varepsilon_{ij}^1 + s_{ij}^1\varepsilon_{ij}^2 - D_j^1 E_j^2 - D_j^2 E_j^1\big) \tag{10}$$

$$\begin{pmatrix} M^{(1,I)} \\ M^{(1,II)} \\ M^{(1,III)} \\ M^{(1,IV)} \end{pmatrix} = Y \begin{pmatrix} K_I^1 \\ K_{II}^1 \\ K_{III}^1 \\ K_{IV}^1 \end{pmatrix} \tag{11}$$

5 Validation

5.1 Penny-Shaped Crack with Variable Stress Field

To check the accuracy and the validation of the XFEM approach, the benchmark problem, penny-shaped crack is considered as shown in Fig. 2. In the previous study, the validation is presented with constant load with variable mesh size (Yadav 2020), but in this present analysis, a case study is presented with variable applied stress for mode I and mode IV as shown in Figs. 3 and 4. It is assumed homogeneous and linear piezoelectric domain with the following
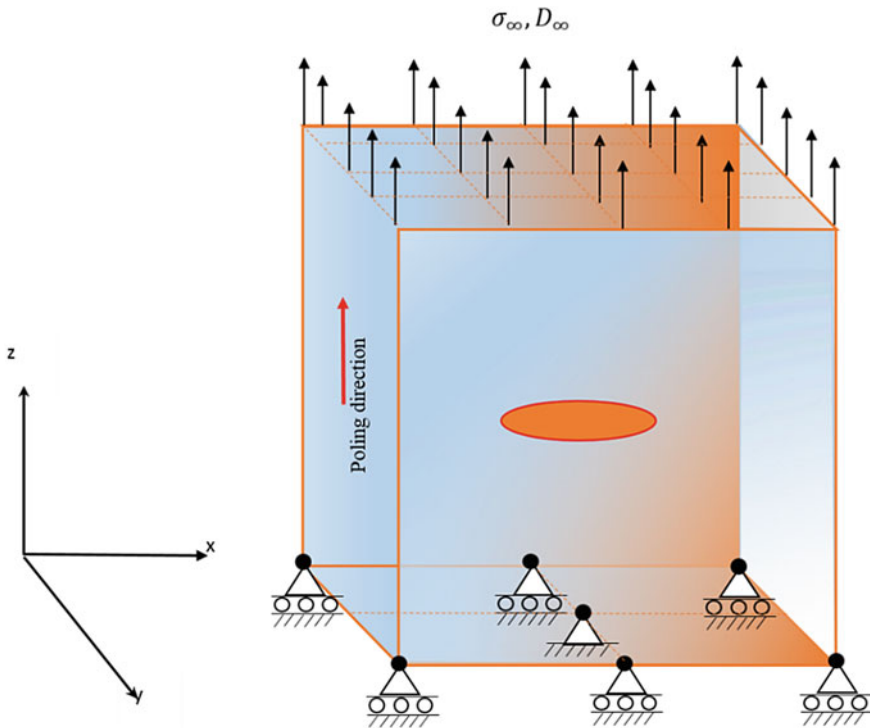
Fig. 2 Penny-shaped crack with loading in poling direction
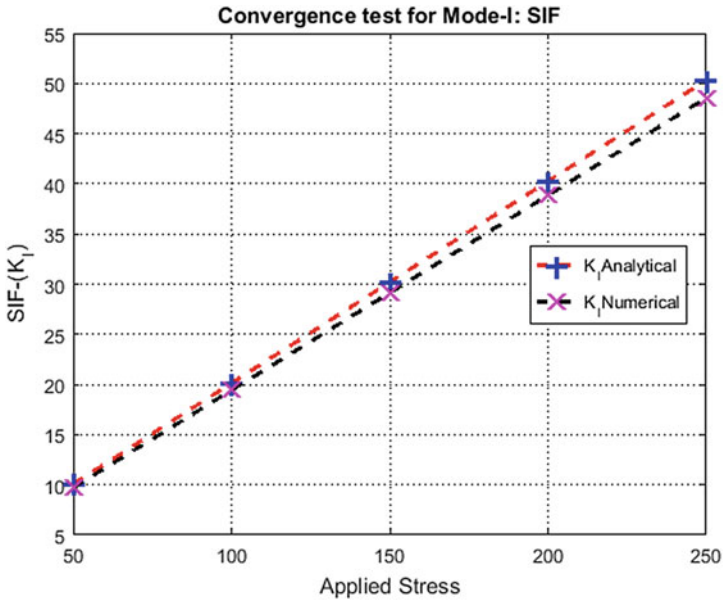
Fig. 3 Mode I validation with variable applied stress
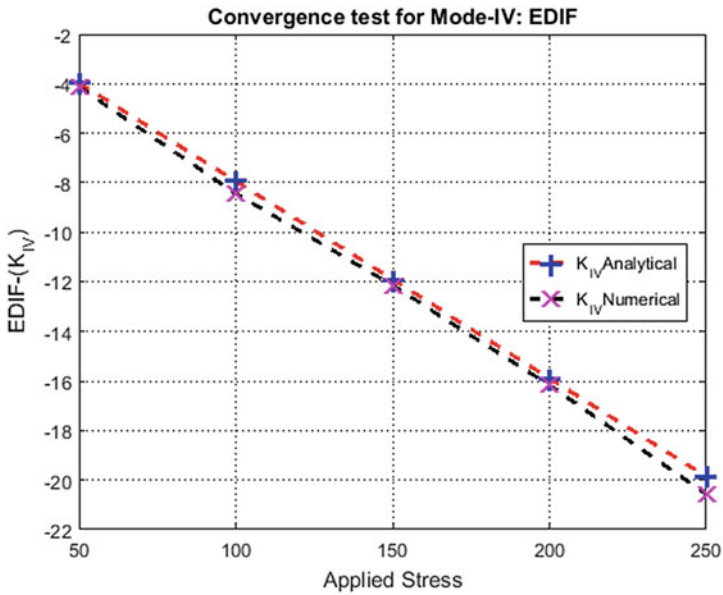
Fig. 4 Mode IV validation with variable applied stress

material parameters:$C_{11} = 139Gpa$; $C_{12} = 77.8Gpa$; $C_{13} = 74.3Gpa$; $C_{33} = 113Gpa$; $C_{44} = 25.6Gpa$; $e_{13} = -6.98C/m^2$; $e_{33} = 13.8C/m^2$; $e_{15} = 13.4C/m^2$; $\kappa_{11} = 6.00C/(GVm)$; $\kappa_{11} = 5.47C/(GVm)$. The analytical expressions for comparison of stress intensity factor (mode I) and electric displacement intensity factor (mode IV) are given by Lin et al. (2003), Yadav (2020) as follows:

$$K_I = \frac{2}{\pi}\sigma_\infty \sqrt{R} \tag{12}$$

$$K_D = \left(\frac{1}{F}\sum_1^3 h_j d_j\right) K_I \tag{13}$$

5.2 Effect of Intensity Factors with the Offset of Crack in Poling Direction

In the following case study, a symmetric penny-shaped crack is presented with the electromechanical-coupled far-field boundary conditions. The domain is subjected to constant stress field and electric field displacement with the variable crack position in the poling direction as shown in Fig. 2. The variation of the fracture parameters is plotted in Figs. 5 and 6. It is observed from Figs. 5 and 6 that the stress intensity
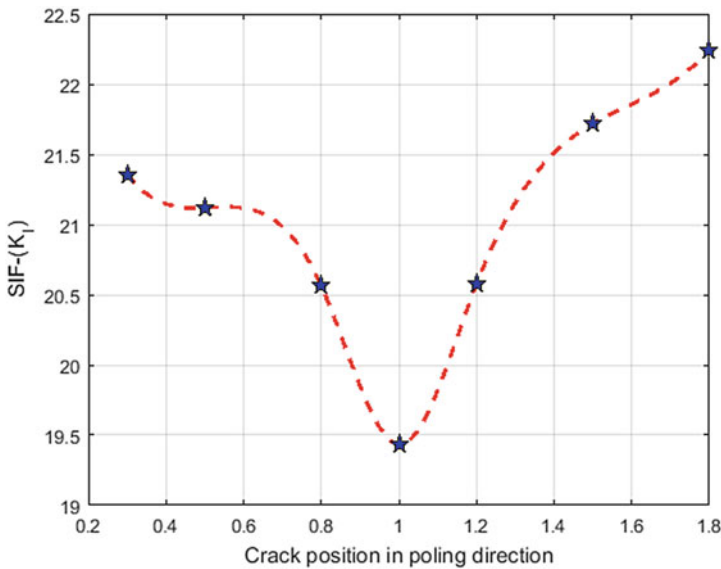
Fig. 5 Effect of crack position in poling direction on K_I
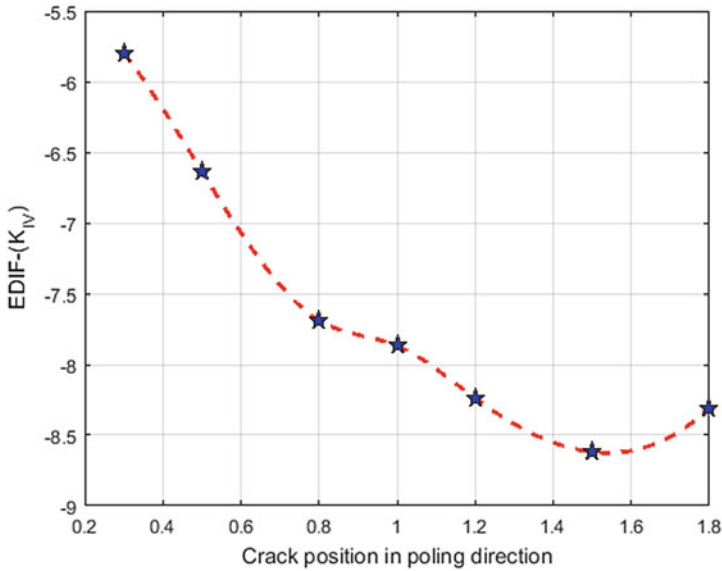
Fig. 6 Effect of crack position in poling direction on K_{IV}

factor (SIF) away from mean position is almost symmetric, and electric displacement intensity factor (EDIF) is found increasing with negative sign with the crack position offset from 0.5 to 1 below the crack and 1–1.5 above the crack.

6 Conclusions

In this paper, the fracture analysis of the penny-shaped crack positioned perpendicular to the poling direction is presented using XFEM approach. The path independent J integral is used for the evaluation of the stress intensity factors (SIFs) and electric displacement intensity factor (EDIF), which defines the singularities near the crack front. The accuracy of the present method is verified with analytical solution, which shows good agreement as shown in Figs. 3 and 4. Further the offset position of the crack is investigated under constant-coupled electromechanical loading. It is observed that the stress intensity factor (mode I) is almost symmetric and electric displacement intensity factor (mode IV) is increasing with negative sign.

References

Béchet E, Scherzer M, Kuna M (2009) Application of the X-FEM to the fracture of piezoelectric materials. Int J Numer Meth Eng 77(11):1535–1565

Chadaram S, Yadav SK (2020) Identification of cracks length by XFEM and machine learning algorithm. In: Recent advances in mechanical infrastructure. Springer, pp 265–272

Chadaram S, Yadav SK (nd) Evaluation of stress intensity factors (SIF) for elliptical crack in piezoelectric material (PZT-4H) using XFEM. Indian Society Of Theoretical and Applied Mechanics

Enderlein M, Ricoeur A, Kuna M (2005) Finite element techniques for dynamic crack analysis in piezoelectrics. Int J Fract 134(3–4):191–208

Fan C, Guo Z, Dang H, Zhao M (2014) Extended displacement discontinuity method for nonlinear analysis of penny-shaped cracks in three-dimensional piezoelectric media. J Eng Anal Bound Elem 38:8–16

Hattori G, Rojas-Díaz R, Sáez A, Sukumar N, García-Sánchez F (2012) New anisotropic crack-tip enrichment functions for the extended finite element method. J Comput Mech 50(5):591–601

Li X-F, Lee KY (2004) Three-dimensional electroelastic analysis of a piezoelectric material with a penny-shaped dielectric crack. J Appl Mech 71(6):866–878

Li C, Song C, Man H, Ooi ET, Gao W (2014) 2D dynamic analysis of cracks and interface cracks in piezoelectric composites using the SBFEM. Int J Solids Structu 51(11–12):2096–2108

Lin S, Narita F, Shindo Y (2003) Electroelastic analysis of a penny-shaped crack in a piezoelectric ceramic under mode I loading. J Mech Res Commun 30(4):371–386

Nguyen-Vinh H et al (2012) Extended finite element method for dynamic fracture of piezo-electric materials. J Eng Fract Mech 92:19–31

Pramod A, Ooi ET, Song C, Natarajan S (2018) Numerical estimation of stress intensity factors in cracked functionally graded piezoelectric materials–a scaled boundary finite element approach. J Compos Struct 206:301–312

Qin T, Noda N-A (2004) Application of hypersingular integral equation method to a three-dimensional crack in piezoelectric materials. JSME Int J Ser A Solid Mech Mater Eng 47(2):173–180

Qin T, Yu Y, Noda N (2007) Finite-part integral and boundary element method to solve three-dimensional crack problems in piezoelectric materials. Int J Solids Struct 44(14–15):4770–4783

Rao B, Kuna M (2008) Interaction integrals for fracture analysis of functionally graded piezoelectric materials. Int J Solids Struct 45(20):5237–5257

Rao B, Rahman S (2003) An interaction integral method for analysis of cracks in orthotropic functionally graded materials. J Comput Mech 32(1):40–51

Sanz J, Ariza M, Dominguez J (2005) Three-dimensional BEM for piezoelectric fracture analysis. J Eng Anal Bound Elem 29(6):586–596

Shang F, Kuna M, Abendroth M (2003) Finite element analyses of three-dimensional crack problems in piezoelectric structures. J Eng Fract Mech 70(2):143–160

Sharma K, Bui TQ, Zhang C, Bhargava R (2013) Analysis of a subinterface crack in piezoelectric bimaterials with the extended finite element method. J Eng Fract Mech 104:114–139

Solis M, Sanz J, Ariza M, Domínguez J (2009) Analysis of cracked piezoelectric solids by a mixed three-dimensional BE approach. J Eng Anal Bound Elem 33(3):271–282

Yadav SK (2020) A XFEM approach for the three-dimensional cracks in piezoelectric material using interaction integral. J Eng Fract Mech 239:107322

Zamani A, Eslami MR (2010) Implementation of the extended finite element method for dynamic thermoelastic fracture initiation. Int J Solids Struct 47(10):1392–1404

FE Analysis and Optimization of Excavator Bucket Teeth

Smriti Sahay and S. K. Srivastava

Abstract Excavator machines, also called earth removers, are extensively seen in agriculture and construction, industries, mining works, and for trenching purposes. During the process of excavation, the unknown resistive forces act by the earth surfaces to the bucket tooth which is transformed to the other parts of the bucket. The increase magnitude of the resistive forces affects the parts of the machine and causes effective failure in the excavation process. The present work deals with the finite element analysis (FEA) as a tool for the static as well as fatigue analysis of excavator bucket and shape optimization of bucket teeth for three different design profiles. Three different types of teeth shape, namely standard teeth, chisel teeth, and flat penetrator teeth, are designed. It is observed that the bucket with standard teeth experiences minimum equivalent stress with the highest safety factor.

Keywords Excavator machines · FEA · Optimization · Fatigue analysis

1 Introduction

With an increase in globalization and advancement in technologies, various modifications have been done in design aspects. These modifications are done either to obtain high durability or to increase the reliability of the existing machines. The researchers are always looking for minimum operational costs and try to reduce the likelihood of frequent failures of the machines. Excavator machines are considered to play a significant role in agricultural, earthmoving, and mining industries. The element of this machine consists of a bucket. Buckets are considered as the elements which are in direct contact with the excavated machines. The contact of the corners, teeth, and cutting edge of the bucket causes wear that limits the life of the bucket after certain period.

The present work aims at the FE analysis for the static as well fatigue analysis of the bucket that suggests the useful life and damage along with the stresses and

S. Sahay (✉) · S. K. Srivastava
Department of Mechanical Engineering, Madan Mohan Malaviya University of Technology, Gorakhpur, U.P., India

total deformation in the bucket teeth. Several research works have been carried out in the excavation operation for designing the teeth involving optimization techniques. Sarkar et al. (2015) performed the static analysis to check the stress, total deformation, and directional deformation in the bucket. It was observed that stress level near to bush region as well as teeth area was high; hence, they were prone to failure. Suryo et al. (2017) considered the rake angle effect to find the stress distribution on bucket teeth during the excavation process. The results showed that the materials used were in safe limits and had a large potential for experiencing failure as well. Patel and Prajapati (2012) performed the static and dynamic analysis of backhoe. The kinematics, differential motion, mechanism were applied for the development of generalized breakout and digging force model.

Comparative wear tests were conducted on hard-facing teeth and regular teeth by Singla et al. (2014). It was found that there was weight loss on regular tooth after the field testing due to abrasive wear. The H33 CR material is depicted negligible wear resistance. Tiwari et al. (2020) carried out the transient analysis of bucket to find the failure locations. The bucket design parameters were modified, and it was found that modified bucket gives the best result when tested for more than 200 h. Hadi et al. (2018) designed a trapezoidal bucket for the analysis of maximum strain at the top position of the bucket and maximum deformation at the tooth end of the entire bucket body.

With the increasing rate profile of industry growth of earth removing machines, it is very important to assure through the high performance of construction machineries, maximum reliability, durability, and strength with lightweight and minimum cost by keeping safe design under all adverse loading conditions. In the present work, FEA is used to determine the maximum stress distribution, total deformation, and the number of life cycle of the bucket with the safety factor which indicates that design is safe.

2 Digging Force

According to SAE J1179, the bucket digging force (F_b) Fig. 1 is defined as the maximum force of teeth which is produced by the bucket cylinder in tangential direction at bucket tooth. It is expressed as (SAE 1990).

$$F_b = \frac{Bucket\ Cylinder\ Force \cdot A \cdot C}{R_1 \cdot B} = \frac{p \cdot \left(\frac{\pi}{4}\right) \cdot D_{B.}^2 A \cdot C}{R_1 \cdot B} \tag{1}$$

where bucket cylinder force = Working pressure × End area of bucket cylinder.

For working pressure, $p = 15.7$ MPa, $D_B = 40$ mm, distance between boom and arm fixed point, $A = 627$ mm, distance between arm end and cylinder end fixed point, $C = 260.7$ mm, distance between bucket end to the tip of teeth of bucket, $R_1 = 923.7$ mm and $B = 360$ mm, the bucket digging force, $F_b = 9.754$ KN.

Fig. 1 Force produced by bucket cylinder (F_b)
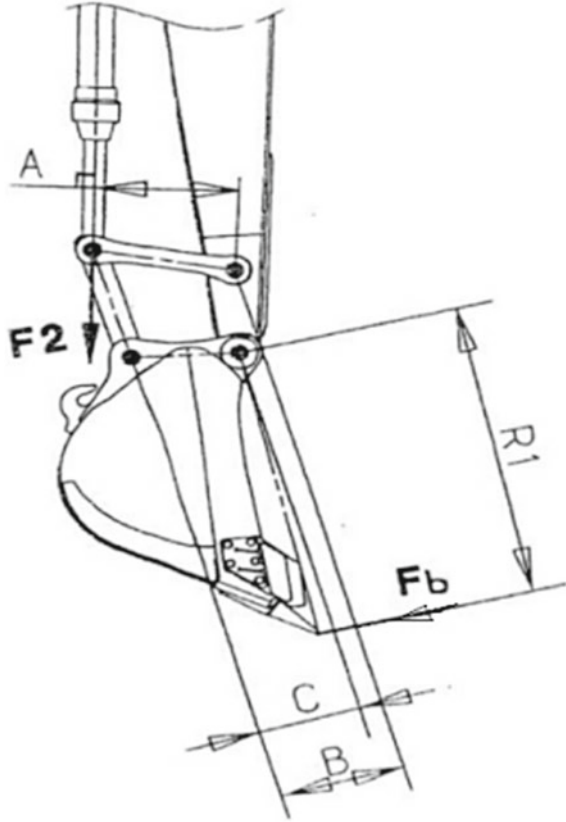
The maximum tooth force produced by the arm cylinder (Fs) Fig. 2 is the digging force generated by arm cylinder in the tangential direction at bucket tooth position where force of bucket teeth gets maximized due to the bucket cylinder. It is given by

$$F_s = \frac{Arm\ Cylinder\ Force \cdot A \cdot C}{R_1 \cdot B} = \frac{p \cdot \left(\frac{\pi}{4}\right) \cdot D_A^2 \cdot R_3}{R_2} \tag{2}$$

For $D_A = D_B = 40$ mm, $R_3 = 430$ mm, $R_2 = 1868.4$ mm,

The maximum tooth force, $Fs = 4.53$ KN,

Here, F_b is more than Fs; therefore, this is taken for the static analysis of bucket tooth. For three-bucket teeth, the total force applied on each teeth end will be 9754/3 = 3252 N.

For this, bucket digging force due to bucket cylinder, $F_b = 9754.8$ N and digging force due to arm cylinder, $Fs = 4538.2$ N.

Fig. 2 Force due to arm
cylinder (Fs)
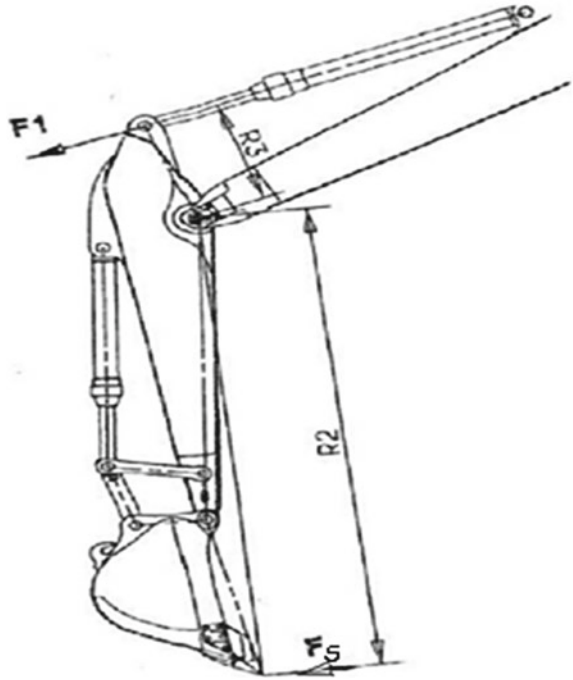
2.1 Material Properties

The Hardo $\times$ 400 is an abrasion-resistant steel. It increases service life while maintaining good processability and toughness. The following property of material is considered (https://ssworks.in/wear-abrasion-resistant-steel 2021):

Density $=$ 8000 kg/m^3, Ultimate tensile strength $=$ 1250 MPa, Yield tensile strength $=$ 1000 MPa, Modulus of Elasticity $=$ 190 GPa.

3 Finite Element Analysis

The 3D model with given dimensions of excavator bucket is developed in Creo Fig. 3a and b, and FE structural and fatigue analysis is carried out in ANSYS software. The static structural analysis is used to determine displacements, stresses, strains, and forces in structures or components caused by loads under static loading conditions. However, the fatigue analysis is used to predict component's life and safety factor provided by it.

Meshing is the first stage for analysis which creates nodes and elements. It influences the accuracy, convergence, and speed of the simulation. In the present analysis,
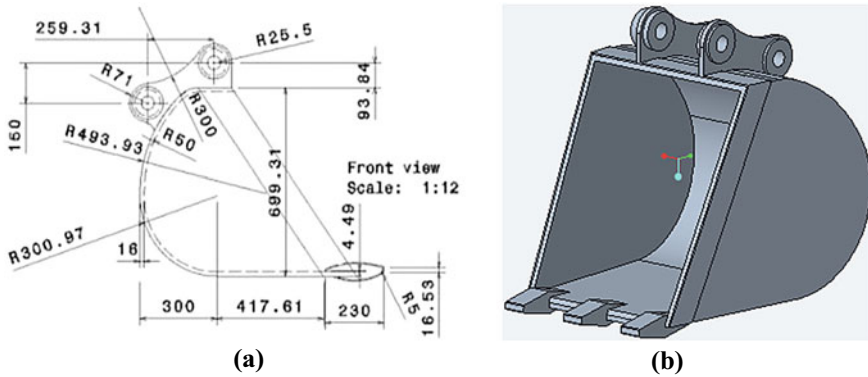
Fig. 3 **a** 2D sketch and **b** 3D model of bucket

total number of elements and nodes are taken as 885,541 and 1,516,703, respectively, with an element size of 3.8 mm.

The following boundary conditions, as shown in Fig. 4, are used for FE analysis.

i. Displacement in X-, Y-, and Z-directions are restrained at all nodes at the top of the excavator under the two shell parts which are hinged to the bucket at the top.

ii. Bucket teeth force is applied at each tooth end in Y-direction.

The static structural FE analysis is carried out after applying the boundary conditions. It is observed that the total deformation is found to be 2.37 mm (Fig. 5) which is higher at the bucket teeth region. For fatigue life, the maximum number of life cycle applied is 2000 cycles, but the component can withstand minimum 1163.9 number of cycles, thus indicating its infinite life.
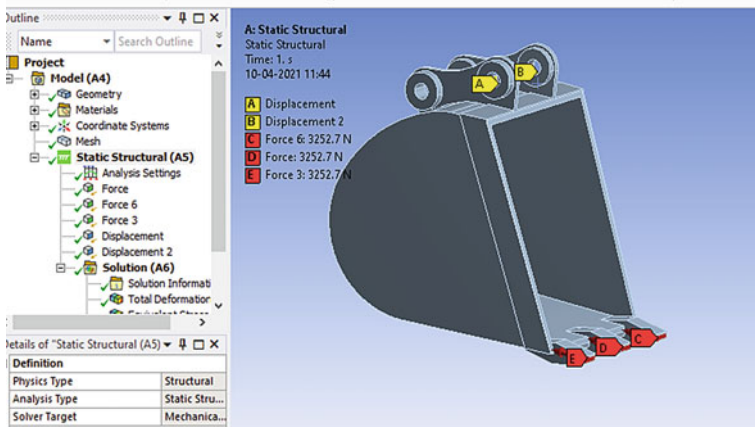
Fig. 4 Boundary conditions and forces
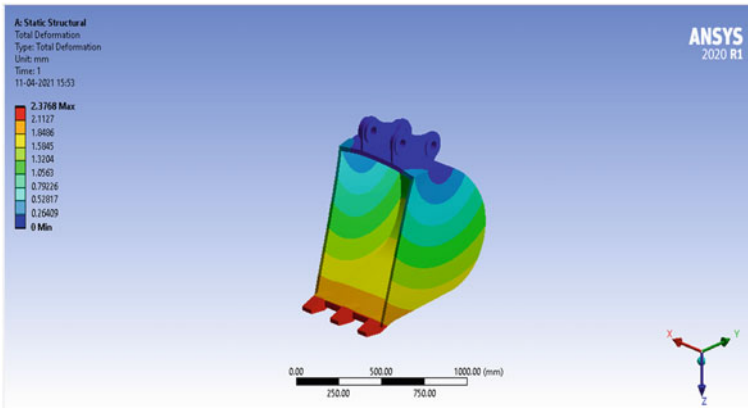
Fig. 5 Total deformation

Table 1 FE results for existing bucket teeth

Parameters	Hardo × 400
Equivalent stress	263.42 MPa
Strain	0.0015
Total deformation	2.49 mm
Life factor	2000
Safety factor	0.94
Damage	1E6

For fatigue safety factor, the magnitude less than 1 indicates failure before the designed life is reached. In the present case, the fatigue safety factor of 0.94 (which is less than 1) indicates that the design is not safe (Table 1).

3.1 Optimization Process

The FE result of existing model shows that the design of bucket is not safe; therefore, there is need to optimize the model for the sufficient life and safe design. The optimization is carried out for different types of teeth profile of bucket using chamfer, extrude and round operations, keeping overall weight of the bucket constant. Three types of bucket teeth are optimized based on the finite element analysis results.

Standard teeth

This type of teeth Fig. 6a is used for multi-purpose, general duty, and good choice for most daily basic applications.

(a)   **(b)**   **(c)**
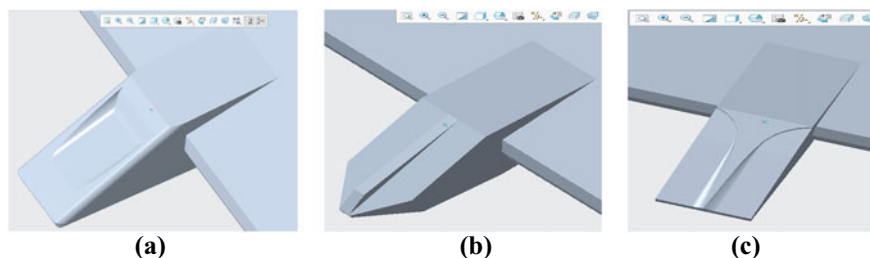
Fig. 6 3D model of **a** standard teeth **b** chisel teeth, and **c** flat penetrator teeth

Table 2 FE results for different bucket teeth profiles

Parameters	Standard teeth	Chisel teeth	Flat penetrator teeth
Equivalent stress (MPa)	222.9	330.5	230.6
Strain (mm/mm)	0.0013	0.0016	0.0014
Total deformation (mm)	2.67	2.71	2.69
Life factor	2000	2000	2000
Safety factor	2.92	1.97	2.82
Damage	5E5	5E5	5E5

Chisel teeth

It is best used for rock and hard ground purposes and sometimes may also have poor penetration in hard ground Fig. 6b.

Flat penetrator teeth

The flat penetrator teeth Fig. 6c is used for digging action for medium-to-hard ground condition. It is commonly used on clay media.

Table 2 shows the FE results for three different types of bucket teeth profiles. It can be concluded that the excavator bucket with standard teeth is best as far as the equivalent stress and safety factor are considered.

4 Conclusions

It is concluded that existing model of excavator bucket is not safe and suitable; therefore, optimization process is carried out by designing three types of bucket teeth such as standard teeth, chisel teeth, and flat penetrator teeth. The bucket with

standard teeth shows maximum safety among all types of teeth profiles. The life cycle of optimized models shows that bucket can have more than 2000 life cycles, hence more reliable as compared to the existing model.

References

https://ssworks.in/wear-abrasion-resistant-steel. Last Accessed 08 April 2021

Hadi S, Andika RM, Chamid K (2018) Design and analysis of trapezoidal bucket excavator for backhoe. SHS Web Conf 49:02001

Patel BP, Prajapati JM (2012) Evaluation of bucket capacity, digging force calculations and static force analysis of mini hydraulic backhoe. Mach Des 4(1):59–66

SAE INTERNATIONALS, SAE J1179: hydraulic, excavator and backhoe digging forces, 400 commonwealth drive. Warrendale, PA, p 1

Sarkar M, Shaw RK, Ghosh SK (2015) Numerical analysis of stresses in mine excavator bucket. J Min Sci 51:309–313

Singla S, Kang AS, Grewal JS, Cheema GS (2014) Wear behavior of weld overlays on excavator bucket teeth. Procedia Mater Sci 5:256–266

Suryo SH, Bayuseno AP, Jamari J, Wahyudi AI (2017) Analysis of rake angle effect to stress distribution on excavator bucket teeth using finite element method. Civil Eng J 3(12)

Tiwari A, Rajput J, Chaudhari A, Dixit V, Kumar P (2020) Fatigue analysis and design optimization of excavator bucket using FEA. Int J Res Eng Sci Manag 3

A Novel Technique for the Surface Texture Inspection of Electrical Discharge Machined Surfaces Using Vision System

M. B. Kiran

Abstract Evaluation of surface roughness has gained importance mainly because it would help in predicting the functionality of the product. Contact-based roughness measurement techniques provide accurate measurements. These techniques are slow, and they are suitable for sampling inspection. To overcome these techniques, non-contact techniques came into being. Information that they furnish is not enough, for the full characterization of the surface. Also, many of these techniques find it difficult to evaluate roughness of products having complicated geometries. In this scenario, the proposed technique assumes special significance. The method uses vision system for surface roughness assessment. The method is non-contact type. High measuring speeds are possible. The method finds application in 100% inspection of machined surfaces such as molds and dies.

Keywords Surface roughness measurement · Non-contact inspection · Texture assessment · Texture evaluation · EDM inspection

1 Introduction

Surface texture is composed of three components—roughness, waviness, and form error. Roughness is a type of surface irregularity having small wavelengths. Waviness is a type of irregularity having medium wavelength, and form error is also a type of surface irregularity having the largest wavelength.

Surface texture measurement helps in the functionality assessment of product. Contact techniques make use of a stylus of diamond for traversing the surface to be inspected, while making texture measurement. These instruments provide very accurate readings, and they are considered as standard for measurement. These techniques are contacted in nature, and they are used in sampling inspection of surfaces. To overcome some of these drawbacks of contact techniques, non-contact techniques were

M. B. Kiran (✉)
Department of Mechanical Engineering, School of Technology, Pandit Deendayal Energy University, Gandhinagar, Gujarat, India
e-mail: MB.Kiran@sot.pdpu.ac.in

proposed by researchers. Non-contact methods are fast in measurement. Information that they furnish is not enough, for the full characterization of the surface. Also, these methods are restricted to work in laboratory environments. But nowadays, the thrust is toward 100% inspection. This clearly shows that there is a strong requirement for non-contact-based techniques which can be used in industrial scenarios.

The aim of the current research work is to design and develop a novel surface roughness measurement method for measuring components made out of electric discharge machining (EDM).

2   Literature Survey

Several researchers have been working for many decades and have proposed methods for surface texture measurement, listed in Table 1.

Haralick et al. (1973) defined the texture features—contrast (C), correlation (CR), cluster prominence (CP), dissimilarity (D), energy (E), entropy (EP), homogeneity (H), maximum probability (MP), sum entropy (SE), difference variance (DV), difference entropy (DE), inverse difference moment normalized (ID-M), and inverse difference normalized (ID-N) as follows. In Equations from (1) to (13), P (I, j) means the element of co-occurrence matrix (GLCM) (Haralick et al. 1973).

$$C = \sum_{n=0}^{G-1} n^2 \left\{ \sum_{i=1}^{G} \sum_{j=1}^{G} P(i, j) \right\}, |i - j| = n \tag{1}$$

$$CR = \sum_{i=0}^{G-1} \sum_{j=0}^{G-1} \frac{\{i X j\} X P(i, j) - \{\mu_x X \mu_y\}}{\sigma_x X \sigma_y} \tag{2}$$

$$CP = \sum_{i=0}^{G-1} \sum_{j=0}^{G-1} \{i + j - \mu_x - \mu_y\}^4 X P(i, j) \tag{3}$$

$$D = \sum_{i=0}^{G-1} \sum_{J=0}^{G-1} P(i, j)|i - j| \tag{4}$$

$$E = \sum_{i=0}^{G-1} \sum_{J=0}^{G-1} \{P^2(i, j)\} \tag{5}$$

$$EP = -\sum_{i=0}^{G-1} \sum_{J=0}^{G-1} P(i, j) X log(P(i, j)) \tag{6}$$

Table 1 Survey of surface roughness measuring methods

Method	Authors	Description
Optical-taper section method	Nelson (1969)	In this technique, the test surface is cut at angle θ and then the test surface is examined by using a microscope. The method gives a very accurate result Peak to valley height can be measured by this technique
Optical-light section method	Kayser (1943), Way (1969), Shaw and Pecklenik (1963)	In this technique, a beam of light passing through a slit is made to illuminate the test surface at 45^0. The surface is viewed at 45^0 by a microscope. The image is then analyzed. If the image is straight, then the surface is smooth. Any deviation from the straight line is a measure of roughness
Optical-gloss measurement	Elmendorf and Vaughan (1958), Halling (1954), Westberg (1967), Vashist and Radhakrishnan (1974)	The degree of reflectivity of posts is measured as a measure of roughness
Optical-diffraction measurement	Dainty (1975), Asakura and Fuji (1974), Parry (1975), Leger et al. (1975)	Speckle is helpful for measuring surface finish
Optical-direct fourier transformation	Ribbens and Lazik (1968), Anderson (1969), Nagata et al. (1973), Thwaite (1979)	The PSD of the photographic film is used for determining the roughness of the surface
Electrical methods	Sherwood and Crookall (1967), Radhakrishnan (1977)	Capacitance and inductance were used as a measure of surface roughness
Fluid methods	Moore (1965)	During measurement, time for the escape of water from the container is measured and then deduced roughness
Light scattering methods	Beckmann (1967), Griffiths et al. (1993), Marx and Vorburger (1165), Nicolau (1937),	The methods cannot be used in industries
Contact methods-stylus-based instruments	Thomas (1982), Whitehouse (1994)	The method uses a diamond stylus for traversing the test surface. The method gives accurate readings. It is considered as standard

$$H = \sum_{i=0}^{G-1} \sum_{J=0}^{G-1} \frac{P(i, j)}{1 + |i - j|} \tag{7}$$

$$MP = \max(p_{i,j}) \tag{8}$$

$$SE = - \sum_{i=0}^{2G-2} P_{x+y}(i) \log(P_{x+y}(i)) \tag{9}$$

$$DV = \sum_{i=0}^{G-1} \sum_{j=0}^{G-1} (i - \mu)^2 P(i, j) \tag{10}$$

$$DE = - \sum_{i=0}^{G-1} P_{x+y}(i) \log(P_{x+y}(i)) \tag{11}$$

$$ID - M = \sum_{i=0}^{G-1} \sum_{j=0}^{G-1} \frac{1}{1 + (i - j)^2} P(i, j) \tag{12}$$

$$ID - N = \sum_{i=0}^{G-1} \sum_{j=0}^{G-1} \frac{P_{i,j}}{\left(1 + \frac{|i-j|}{N}\right)^2} \tag{13}$$

3 Methodology

Current research work follows the methodology listed below.

1. Specimen preparation
2. Vision system setup
3. Conducting experiment.

3.1 Specimen Preparation

EDM specimens are used in the current research work. Table 2 shows the specimen details. EDM process parameters are (1) current: (2) voltage (3) pulse-on-time: (Ton) (4) pulse-off-time: (Toff). Surface roughness of different specimens is measured using a stylus instrument. These readings are later used for vision roughness calibration.

Table 2 EDM specimen details

Specimen no.	Ton (μ seconds)	I.P. (amp)
1	80	8
2	70	7
3	60	6
4	50	5
5	40	4

Fig. 1 Experimental setup

3.2 Setting up of Vision System

Figure 1 shows the experimental setup. The setup includes a vision system, specimen mounting table, illumination device, and surface plate. Vision system has a charge-coupled device (CCD) camera, advanced image processing card, a frame grabber, cables, high-resolution monitor, and a high-end server. MATLAB and MATROX image processing library have been installed in the high-end server.

3.3 Experimentation

During the experiment, a specimen is mounted on the specimen mount table. The specimen is then illuminated by suitable lighting as shown in Fig. 1. The image of the specimen is captured employing a CCD camera attached to the server. Figure 2 shows the specimen image as seen on the monitor. In this way, images are acquired for all the specimens. The images are stored in the hard disk of the server.

Fig. 2 EDM specimen image
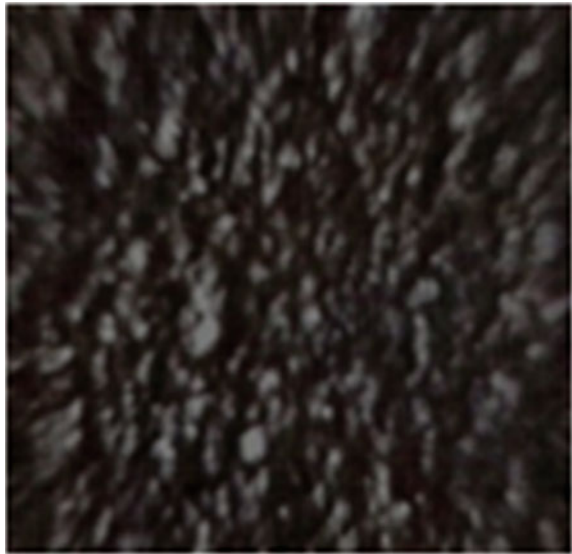
4 Results and Discussions

Table 2 shows the digital image of the EDM specimen. In Table 2, each number represents a pixel intensity value. The image shown in Fig. 2 is filtered for quality enhancement. The processed image is then used for computing the co-occurrence matrix. Table 4 shows the co-occurrence matrix for the specimen. The co-occurrence matrix is used for computing the texture features defined by Haralick (Tables 3 and 5).

It was noticed that there was a good correlation between the stylus roughness (R_a) and the contrast parameter (F1). Thus, contrast can be employed as a roughness parameter of vision method. Linear correlation was observed between 2 and 4.5 μm. The repeatability of measurement was done, and there was an error of $\pm 2\%$.

Table 3 Digital image of EDM specimen

Row/col	1	2	3	4	5	6	7
1	201	137	239	227	186	187	94
2	181	128	285	186	176	189	69
3	162	157	239	181	156	129	75
4	133	174	206	134	168	109	58
5	132	218	167	146	188	195	96
6	123	259	199	148	220	129	85
7	142	208	218	148	239	192	80

Table 4 Co-occurrence matrix for EDM specimen

1	2	3	4	5	6	7
8	10	0	0	0	0	0
10	12	2	0	8	0	0
0	15	2	0	0	7	0
7	17	2	0	0	0	8
10	21	1	0	7	6	0
8	25	1	0	0	0	0
9	20	2	0	0	0	0

Table 5 Texture features values for sample (ED1–ED10) EDM specimens

Feature no.	ED1	ED2	ED3	ED4	ED5	ED6	ED7	ED8	ED9	ED10
1	0.83	0.84	0.87	0.85	0.83	0.79	0.87	0.86	0.87	0.85
2	0.23	0.44	0.36	0.25	0.26	0.49	0.47	0.29	0.46	0.27
3	0.87	0.88	0.86	0.84	0.86	1.77	0.85	0.85	0.84	0.82
4	1.60	1.87	1.84	1.55	1.56	2.07	1.76	1.44	1.95	1.34
5	0.69	0.56	0.64	0.67	0.66	0.58	0.56	0.56	0.68	0.56
6	8.45	8.35	7.33	8.58	7.97	8.29	8.39	9.53	8.14	8.16
7	5.93	4.14	3.96	4.08	3.94	4.27	4.15	4.25	4.15	3.84
8	1.47	2.53	1.54	1.36	1.35	1.64	1.47	1.23	1.69	2.19
9	0.68	1.71	0.66	0.56	0.55	0.75	0.79	3.60	0.76	2.54
10	0.16	2.33	1.18	0.86	0.88	2.25	0.59	4.27	1.08	0.04
11	4.68	6.41	9.06	6.27	7.08	10.79	5.59	3.19	7.98	2.74
12	1.02	0.99	0.97	1.00	1.00	0.98	0.98	1.09	0.98	1.02

5 Conclusion

The method proposed in the research work uses a CCD camera connected to the vision system for acquiring EDM specimen images. The EDM specimens are prepared with different process parameters. The specimen roughness was measured by using stylus instruments. These readings are used for validating the roughness readings obtained from the vision method. The method computes the GLCM for the specimen for the processed image. GLCM is then used for computing the texture features. It was observed that contrast feature was in a good correlation with the stylus roughness values. Thus, the contrast feature can be used as a roughness parameter. The method presented here is a simple non-contact in nature. The method is quick. The method finds application in 100% inspection of surfaces.

Applications: The method proposed in this research work can be used in the surface texture inspection of molds and dies.

References

Anderson WL (1969) Surface roughness studies by optical processing methods. Proc IEEE Lett 57–95

Beckmann P (1967) II Scattering of light by rough surfaces. Wolf E (ed) Progress in optics, vol 6. Elsevier, pp 53–69

Dainty JC (1975) Laser speckle and related phenomena. Springer-Verlag, Berlin

Elmendorf A, Vaughan TW (1958) A survey methods of measuring smoothness of the wood. Opt Eng 8:275–282

Fujii, H, Asakura T (1974) Effect of surface roughness on the statistical distribution of image speckle intensity. Opt Commun 11:35–38

Griffiths BJ, Middleton RH, Wilkie BA (1993) Light scattering for the measurement of surface finish: a review. Int J Prod Res 32(11):2683–2694

Halling J (1954) A reflectometer for the assessment of surface texture. J Sci Instrum 31:318–320

Haralick RM, Shanmugam K, Dinstein I (1973) Texture features for Image classification. IEEE Trans Syst Man Cybern 3:610–621

Kayser JF (1943) Optical method for the determination of surface roughness. Foundry Trade J 70:137–138

Leger E et al (1975) Optical surface roughness determination using speckle correlation technique. Appl Opt 14:872–877

Marx E, Vorburger TV (1990) Light scattered by random rough surfaces and roughness determination. In: Proceedings of the SPIE 1165. Scatter from Optical Components

Moore DF (1965) Drainage criterion for runway surface roughness. J R Aeronaut Soc 69:337–342

Nagata K et al (1973) The determination of R.M.S. roughness, and correlation length of the rough surface by measuring the spatial coherence function. Jpn J Appl Phys 12:1693–1698

Nelson HR (1969) Taper sectioning as a means of describing the surface contour of metals. In: Proceeding conference on friction and surface finish, 2nd edition. MIT Press Cambridge, pp 217–237

Nicolau MP (1937) Application du micrometer solex a la measure de l'etat des surfaces, Mecanique, pp 80–83

Parry G (1975) The scattering of polychromatic light from rough surfaces: first-order statistics. Opt Quant Electron 7:311–318

Radhakrishnan V (1977) Application of inductive heads for non-contact measurement of surface finish. In: Proceedings on international conference of production engineering. Institution of Engineers (India), Calcutta, pp 80–89

Ribbens WB, Lazik GL (1968) Use of optical data processing techniques for surface roughness studies. Proc IEEE Lett 56:1637–1638

Shaw MC, Peklenik J (1963) A light projection technique for studying surface topology. Ann CIRP 12:93–97

Sherwood KF, Crookall JR (1967) Surface finish measurement by an electrical capacitance technique. In: Proceedings institution of mechanical engineers, part 3K, pp 344–349

Thomas TR (1982) Rough surfaces. Longman, London & New York

Thwaite EG (1979) The direct measurement of the power of the spectrum of rough surfaces by optical fourier transformation. Wear 57:71–80

Vashisht SK, Radhakrishnan V (1974) Surface studies with gloss meter. Tribology 7:70–76

Way S (1969) Description and observation of metal surfaces. In: Proceeding conference on friction and surface finish, 2nd edition. MIT Press Cambridge, Mass, pp 44–75

Westberg J (1967) Development of objective methods for judging the quality of ground and polished surfaces in production. In: Proceedings institution of mechanical engineers, part-3K, vol 182, pp 260–273

Whitehouse DJ (1994) Handbook of surface metrology. Institute of Physics Publishing, Bristol, BSI 6NX, UK

Modification and Upgradation of Semiautomated Hydraulic Extruder to Enhance Its Performance

Rushabh V. Shah and Sneh K. Soni

Abstract This paper demonstrates the deployment of some maintenance aspects, optimization and innovation measures for semiautomated hydraulic extruder. The proposed work covers the maintenance challenges faced by this continuously operated machine which reduces the work hours and cause high production loss. The first part starts from understanding challenges causing frequent disruptions in operations and covers all the changes required from induction motors to pumps and electrical system placement. Thus, mechanical, electrical, hydraulic all aspects work in an analogous way at the same time to bring in electrical efficiency, cost efficiency,and save invaluable time elapsed due to maintenance.

Keywords Modification · Upgradation · Semiautomated hydraulic extruder · Cost-effective upgrades · Electrical energy saving

1 Introduction

In a post-COVID world, most of the center theme of all the investments in projects is "Green Energy" and carbon zero policies. After the PARIS Climate treaties and various UN's referendum pace of establishing green energy projects has been increasing at a faster pace.

Primarily as we talk of green energy, we focus on solar and wind energies and as we talk of carbon zero policies, we primarily focus on EV's. Thus, it is very appropriate to relate semi-automated hydraulic extruder closely with green energy and carbon zero policies.

Whether we talk about wind energy, solar energy or EV's the non-ferrous metals that are aluminum and copper take center stage. These are the most extensively used metals in manufacturing of the aforesaid. Like in the iron and steel industry, one

R. V. Shah · S. K. Soni (✉)
Instrumentation and Controls Engineering, Nirma University, Ahmedabad, India

R. V. Shah
e-mail: 17bic047@nirmauni.ac.in

Fig. 1 Full view of extrusion press in raw condition. (spmcontrols.com)

needs rolling process to convert preforms of molds of steel into various flats, rods, etc. Likewise, here in the non-ferrous metals extrusion process takes center stage. Here to prepare rods, flats, profiles, sections, etc., the preforms are extruded by the extrusion process. As this above line suggests extruder correctly forms backbone of processing non-ferrous metals and it can be directly related to the green energy part. Solar panels itself consist of large quantities of aluminum profiles and sections. For wind energy, all the copper wire used in windmill's generator and transmission lines direct relationship. Also, if we talk about EV's, the motors which are used to provide traction to it have copper wire cores (Fig. 1).

2 Challenges Faced

As this extruder needs to generate high hydraulic pressure which ranges from 150-bar to 5000 bars depending upon the size, one can observe that these are very much power-consuming machines.

To generate such power first, one needs appropriate pumps to generate pressure which needs appropriate induction motors. Here in reference, we have taken an extruder generating about 600 bars of pressure. To generate such pressure, we need four 75 HP induction motors. So, one can guess the amount of electricity required.

Also, along with induction motors and pumps the extruder machine also has high power-consuming heater. A small compressor and oil purifying apparatus are also

Fig. 2 Motors and valves connection

directly attached to the machine. Thereafter much power is consumed in maintaining, the temperature of the fluid by small heat exchangers blower fan. The heat exchanger is attached inbuilt but has size constraints.

Now you can ascertain the size of electric motors, and all other auxiliary functions involved with the machine. Also, during a fault electric heater needs to continuously kept on as it takes a lot of time to start.

The main part starts where one can save electrical energy. One can easily predict the energy, and this machine consumes by having 4 100KW motors (75 Hp approx.) and other supporting functions. Below are the images for motors and their connection with valves. Figure 2 gives us a glimpse induction motors and network of valves. Figure 3 gives us about the glimpse of main cylinder exhorting force to extrude a billet.

3   Modification of Design to Improve Performance

For appropriate electric connection for speed control as per general convention, the motors need to be connected with drives in the circuit as such for good speed control (Mat et al. 2016). But we have devised a cost-efficient technique wherein we connect the said motors in star delta connection with contactors in a conventional way (Soheli and Hasan 2018; Krunal and Modi 2018).

The electrical panel as shown in Fig. 4 is connected to a PLC panel beside it as shown in Fig. 5. Signal flows from this panel to the PLC panel and from the PLC panel these signals are forwarded to the extruder.
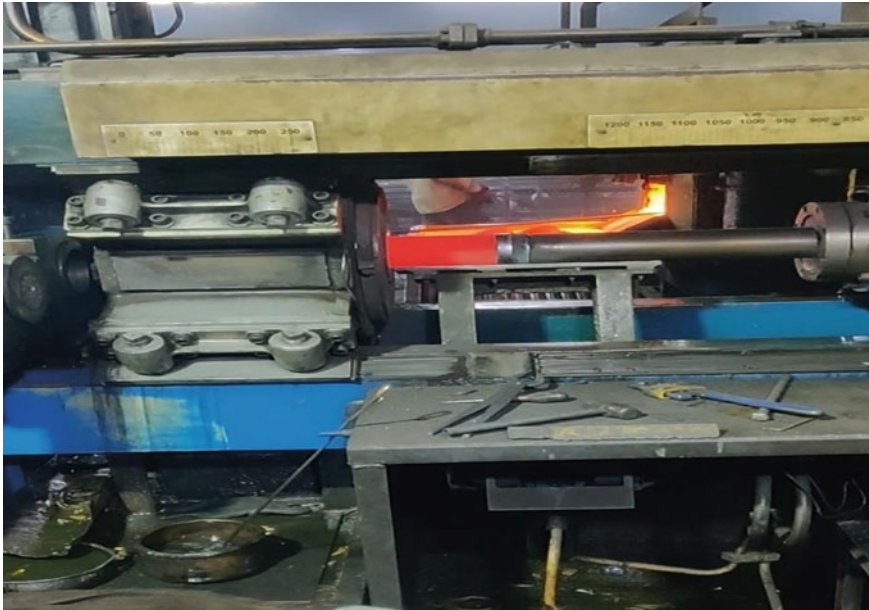
Fig. 3 Main ram of press stamping a hot billet

We know this setting is prone to spikes and surges in electric current for that perspective we can add a row of relays below the PLC (Bredhold 2009). This base idea suggests that plc and its card will have DC output, and then the relay below it will convert DC to AC. Thus, this arrangement will form an extra layer of protection. Also, in the modern era of electrical wiring in most of the factories there are tap-changer type of transformers where in automatically a surge in electric current is corrected. Most of the factories do have voltage stabilizers so the probability is low for surge to reach the circuit panel of the extruder (Nagalakshmi and Thivagar 2020). Thus, machine age, wear, component reliability, maintenance and maintainability, design and materials used in building the production machine, etc., play an important role in performance (James and Mondal 2019). Also, here we have used a single-phase preventer with contactors for surge protection (Omeje et al. 2020). This single-phase preventer save the induction motors from burnouts. It also comes to aid when there is phase imbalance and relay remains off when there is sudden phase sequence change. When the condition becomes okay it resets automatically.

4 Proposed Solutions to Save Energy

This extruder machine does not require fixed pressure. It depends upon the material composition. If the alloy has a good amount of nickel added into copper, then it

Fig. 4 Connections in star delta method with contactors and timers

will require high pressure and likewise. Pressure is directly proportional to alloying elements. For examples, if we alloy nickel element with copper, then it requires more pressure. If we alloy copper with zinc, it requires comparatively less pressure. That is completely metallurgical study. Also, pressure generation depends upon the no of holes present in die from which the material will extrude. (diameter of holes which depend on the end material required) Less the number of holes in the die more the pressure. Thus, as this machine needs variable pressure all four motors require drives to control it (Yung et al. 2002).

We have devised a cost-effective method wherein to eliminate the cost of drives we have arranged of a variable displacement pump with one of the motors. (Among 4 pumps one is variable displacement pumps) Schoenau et al. (1990). All the variable pressure can be generated with this pump. First one needs to calculate the threshold minimum pressure. The minimum will be provided by 3 fixed displacement pumps

Fig. 5 PLC panel with required protection

and the rest of variable load which depends upon material will be provided by the variable pump. If there is no variable load required, then the variable pump will be shut off for the cycle. Thus, we have achieved about 15–18% electrical energy saving on machine by these two changes.

5 Modification to Reduce Maintenance Time

Now another cost-cutting feature is that with the hydraulic machine, there is a problem that after working continuously the oil revolving inside the machine heats up to a

Fig. 6 Added metallic box-like structure with blower fan to maintain temperature

good amount of temperature. This results in hydraulic seals breaking or melting in valves and pipes. To negate this effect with a very cost-effective way is to seal the upper body of the machine in a cage-type structure where valves are situated and attached a high-power fan to that structure. So that it will continuously flush in room temperature air. This will have much positive effect on the working of an extruder.

As the breakdown will take hours to solve this will save lot of time and cost. The most basic hardship with maintaining hydraulic machines is that the hydraulic seals fail every time. Whether in valves or flanges. This way we can save cost (Fig. 6).

Before injecting the fresh air and without hood, the upper body temperature is used to reach **65–70 °C.** After all the cost-effective optimization of hood and fan, we were able to control it toward 45–50 °C range this optimization had the most effect on the extruder.

The wear and tear and maintenance time were saved as much as 7–8 h. per week as there was less breaking of seals. As the maintenance time is saved productivity got real a boost. This all is accounted for just a small cost-efficient hood and fan. Also, the heating of hydraulic seals depends upon the thickness of pipes as heating of fluid oil is directly proportional to pipe thickness (Yung et al. 2002).

6 Conclusion

First, we realized all the challenges associated to extruder machine. Be it electrical energy saving, pump's orientation or modification required in design. Then for electrical wiring, we implemented cost-saving measures wherein we saved the cost of electrical drives attached to motors by doing wiring in a more cost-effective star delta way with single-phase preventers, saving approximately 5–7% cost. Cost of 4 drives saved by using variable displacement pump. We saved cost on 4 drives and provided the same isolation level which drives provided with alternate route of relays and single-phase preventers. We also saved electrical energy by fixing 3 pumps as fixed displacement pumps after finding the threshold pressure required and made 4th pump as a variable displacement pump. By this measure, we save around 15–18% of electrical energy. Without this the 4th pump use to run parallel with the other 3 at full capacity. Also, we made changes in design and made a metallic box-like structure around main functional valves and placed a blower fan on valves to save time from breakage of seals due to heat generated in the high-temperature environment plus the heat generated from continuous rotation of oil in pipes. The blower fan would put in air at the atmospheric temperature at high velocity and try to maintain the atmospheric temperature around valves. Thus, it will reduce breakdown time caused due to frequent breakage of seals and save valuable working hours.

So, with this work we have tried to do detailed study on the present design of extruder machine. Based on our rigorous study, we have highlighted few key modifications in the present design, which cannot only improve machine's life expectancy but can also improve its efficiency in terms of less electricity consumption.

References

Niazi MA, Hayat Q, Khan B, Afaq M (2020) Speed control of three phase induction motor using variable frequency derive control system, Electrical Engineering Department, Wah Engineering College, Wah Cantt, Pakistan

Bredhold D (2009) The basics of control relays

James CD, Mondal S (2019) A review of machine efficiency in mass customization. Department of Management Studies, Indian Institute of Technology (Indian School of Mines), Dhanbad, India

Krunal J, Modi PJ (2018) Automatic star delta starter. Int J Adv Res 6(4):1160–1170

Mat A, Canavar M, Timurkutluk B, Kaplan Y (2016) Investigation of micro-tube solid oxide fuel cell fabrication using extrusion method

Nagalakshmi N, Thivagar T (2020) Automatic tap-changer with TRIAC switch for constant voltage and current measurements. Int J Recent Technol Eng (IJRTE) 9(2). ISSN: 2277-3878

Omeje CO, Ezugwu EO, Okozi SO (2020) Experimental design of a bidirectional single phasing protection for a three phase induction motor with voice notification earth mat design for 132/33Kv substation in rivers state using ETAP view project unmanned aerial devices and systems view project. Int J Sci Eng Res 10:342–351

Schoenau GJ, Burton RT, Kavanagh GP (1990) Dynamic analysis of a variable displacement pump. J Dyn Sys Meas Control 112(1):122–132. https://doi.org/10.1115/1.2894129. (11 pages)

Soheli SN, Hasan MS (2018) Phase motor by using 3 phase star delta starter voltage reducing method with iinverter. https://doi.org/10.14445/23488379/IJEEE-V5I11P104
Thompson MR, Sun J (2009) Wet granulation in a twin-screw extruder: implications of screw design
Yung KL, Xu Y, Lau KH (2002) Simulation of transient process in melting section of reciprocating extruder

Design of Pitch Controlling System for Two-Wheel Self-Balancing Vehicle Based on Arduino

Mahmmadabararkhan N. Diwan, Karan Shah, and Dhairya U. Patel

Abstract Two-wheeled self-controlling vehicle contains plethora of technology related to an energy-efficient transportation industry and renewable energy resources. It also helps in parking space management and thereby aids in traffic controlling as it is very compact, easy to control and has good manoeuvrability as compared to other compact vehicles. However, current self-balancing control system of two-wheeled vehicle is facing unstable operations, high failure rate, poor accuracy and sensitivity of the control system. Therefore, proper vertical control, low-frequency gyroscope error and improved precision of the motor are required as the technological advancement in the transportation is one of the basic necessities. Hence, this research paper focuses on the advancement in self-controlling system of the two-wheeled vehicle.

Keywords Two-wheel self-balancing control system · Balancing system · Arduino UNO · Microcontroller · Gyroscope · Accelerometer

1 Introduction

Automotive companies are working on the transportation technology which can reduce the environmental problems and other global problems (traffic and parking). Even after sufficient advancement in automotive engine, the fuel consumption in world is around 97,103,871 barrels per day and 4,433,000 barrels per day in India (Worldometer Homepage 2021). As the two-wheel self-balancing vehicle eliminates this kind of barriers, it is one of the important branches of mobile robots. This vehicle comprises of gyroscope and acceleration sensors with two servo motors each on one wheel. When gyroscope detects the change in C.G. of the human body, it calculates the advances to be made in vehicle to keep it up, and then, these signals are given to the microcontroller which will drive motors accordingly. When C.G. moves forward, i.e. vehicle leans forward, the motors will rotate in forward direction at a calculated speed in order to prevent the vehicle from falling, same for the backward direction.

M. N. Diwan (✉) · K. Shah · D. U. Patel
Department of Automobile Engineering, Knowledge Institute of Technology and Engineering, Bakrol, Anand 388315, Gujarat, India

FORWARD   CENTER   BACKWARD
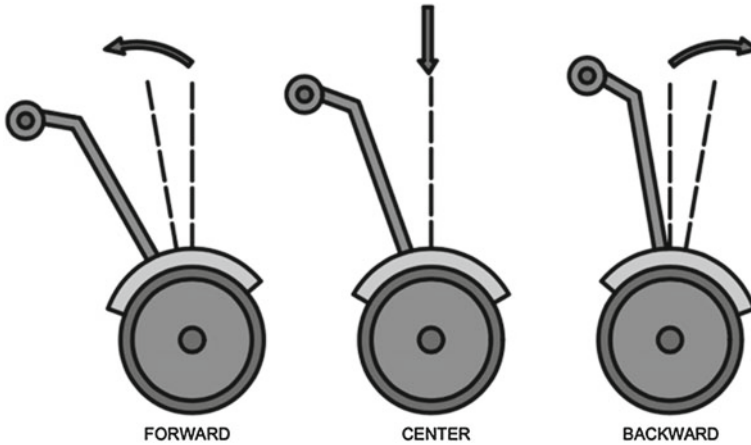
Fig. 1 Principle of Arduino microcontroller

The microcontroller is also able to detect the lateral movement of vehicle, so the turning action can be achieved without falling (Zhang 2019).

There has been a lot of advancement done in these technologies, f example by using process identifier control algorithm (PDI) (Zhang 2019), by using LQR controller based on pole placement theory (Junfeng 2011; Hellman 2015) and by using hybrids fuzzy PD controller (Zhang 2012). However, they are not effective as they are working on the same principle.

This article presents the effectiveness of controlling the motor by totally different approach using Arduino microcontroller as shown in Fig. 1.

2 Components

2.1 *Arduino Board*

The Arduino UNO is an open-source microcontroller board based on the Microchip ATmegha328P. The board is equipped with 14 digital input/output pins. It is programmed to generate the specific type of output when the vehicle tilts up to certain limit, and it is combined with accelerometer and gyroscope (as shown in Fig. 2.) (Zhang 2019).

Fig. 2 Arduino board
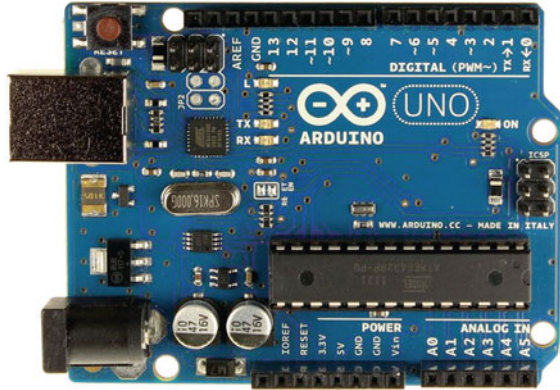
Specifications:

NAME: UNO DIP R3 ATmega328
Number memory stick: 3
Operating voltage: 5V
Input voltage: 7-12 V
Dimension of product: 15 * 14 * 3 cm.

2.2 Imu

An inertial measurement unit is an electronic device that measures and reports a body's angular rate, specific force and orientation of body using combination of gyroscope and accelerometer. (as shown in Fig. 3.)

Fig. 3 IMU
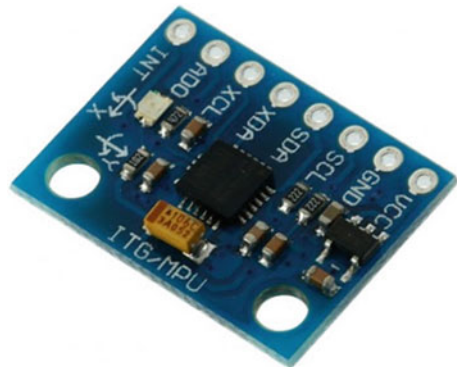
Fig. 4 PCB
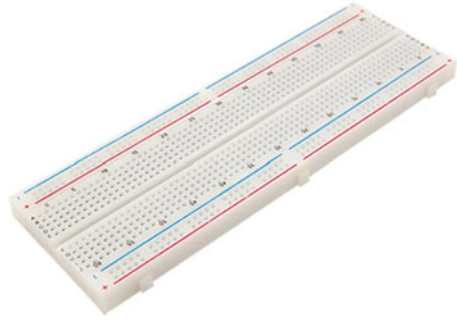
Specifications:

NAME: REES52 GY-521 Mpu6050 Module.

3 Axis Accelerometer, 3 Axis Gyroscope.

2.3 PCB Board

A breadboard is the device which is used to make the circuits by connecting electronic devices. (as shown in Fig. 4.)

Specifications:

NAME: MB102 830 Points Solderless Prototype PCB Breadboard.
Distribution holes: 200.
Terminal holes: 630.
Dimension: 16 * 7 * 2 cm.

2.4 Motor

Electric motor drives the wheel at a required speed. It also helps to turn the vehicle. (as shown in Fig. 5.)

Fig. 5 DC motor

Specifications:

NAME: MY1016 350 W 24 V 2750RPM DC.
Output power: 350 W.
Supply voltage: 24/36 V DC.
Full load current: $\leq$ 19.20A.
No load current: $\leq$ 2.5A.
Speed: 2750 RPM.
No load speed: 3300RPM.

2.5 Motor Controller

Motor controller is the device used to control motor by running it to achieve required
speed and torque. (as shown in Fig. 6.)

Fig. 6 Controller

Fig. 7 Battery

Specifications:

NAME: MAXON motor controllers (MAXPOS).

2.6 Battery

Battery is the device which is the power source of whole system. The battery (2 batteries) used is lead-acid battery. Lead-acid battery converts chemical energy to electrical energy. (as shown in Fig. 7.)

Specifications:

NAME: 12 V Sealed Lead Acid Battery.
Battery capacity: 8Ah/20 h.
Voltage: 12 V.
Voltage regulation: 13.5–13.8 V (stand-by use) and 14.7–14.7 V (cyclic use).
Initial current: 2.40 A Max.

3 Calculation

Required power of the motor:
By considering three speeds: lower speed, moderate speed and high speed.
For speed,
Low speed (V_1) = 8 km/h = 2.22 m/s

Moderate speed $(V_m) = 14\text{km/h} = 3.89$ m/s

High speed $(V_h) = 20$ km/h $= 5.5$ m/s

For force,

(Assuming that time required to reach top speed is 5 sec and gross vehicle weight is 120 kg)

$$F_l = ma_l = 120 * \frac{2.22}{5} N = 53.28 \text{ N} \tag{1}$$

$$F_m = ma_m = 120 * \frac{3.89}{5} N = 93.36 \text{ N} \tag{2}$$

$$h_m = ma_h = 120 * \frac{5.55}{5} N = 133.3 \text{ N} \tag{3}$$

Power,

(Eliminating the power required at the moderate speed in order to find the range)

$$P_{min} = 53.28 * 2.2 = 118.28 \text{ W} \tag{4}$$

$$P_{max} = 133.3 * 5.55 = 739.81 \text{ W} \tag{5}$$

The power obtained is total motor power required to drive the vehicle, but the vehicle is driven by two motors. Hence, the power is divided by 2 in order to find the power for one motor.

So, the power per motor is approximately 350 W.

4   Work Methodology

Starting with the Initial Measurement Unit (IMU) containing gyroscope and accelerometer, which is programmed to measure the initial state of vehicle in order to start the vehicle; i.e., vehicle is in balance at its rest condition, so it will not generate the signal which causes the motor rotation. When vehicle is at initial position and C.G. inclines forward, it will start rotating motor causing vehicle to move forward same for the reverse direction. But when vehicle is in running condition and C.G.
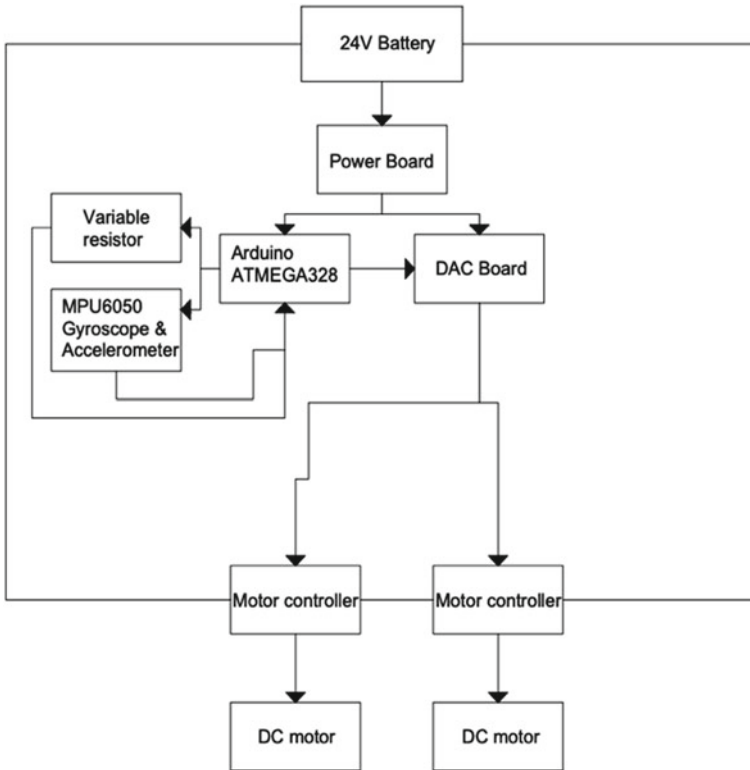
Fig. 8 Working Methodology

moves backward (from the forward direction), it will not start the motor to rotate in reverse direction directly, rather it will rotate the motor in forward direction at high rpm rate for the fraction of second just to maintain the balance and then after allows the motor to rotate in backward direction. The working of this system is shown by the prototype (Fig. 8).

5 Programming

Fraction of programming code is shown for the understanding.

```
#include "I2Cdev.h"
#include<Wire.h>
#include <PID_v1.h>
#include "MPU6050_6Axis_MotionApps20.h"
#include<SoftwareSerial.h>
#include <digitalIOPerformance.h>
//library for faster pin R/W
//#include <Ultrasonic.h>

#define d_speed 1.5
#define d_dir 3


#define IN1 11
#define IN2 10
#define IN3 9
#define IN4 3


char content = 'P';
int MotorAspeed, MotorBspeed;
float MOTORSLACK_A = 40;
// Compensate for motor slack range (low
PWM values which result in no motor
engagement)
float MOTORSLACK_B = 40;
#define BALANCE_PID_MIN -255
// Define PID limits to match PWM max in
reverse and foward
#define BALANCE_PID_MAX 255
```

Initial values to define motor speed.

```
MPU6050 mpu;

const int rxpin = 6;        //Bluetooth
serial stuff
const int txpin = 5;
SoftwareSerial blue(rxpin, txpin);
//Ultrasonic ultrasonic(A0, A1);
//int distance;



// MPU control/status vars
bool dmpReady = false;  // set true if
DMP init was successful
uint8_t mpuIntStatus;   // holds actual
interrupt status byte from MPU
uint8_t devStatus;      // return status
after each device operation (0 = success,
!0 = error)
uint16_t packetSize;    // expected DMP
packet size (default is 42 bytes)
uint16_t fifoCount;     // count of all
bytes currently in FIFO
uint8_t fifoBuffer[64]; // FIFO storage
buffer

// orientation/motion vars
Quaternion q;           // [w, x, y, z]
quaternion container
VectorFloat gravity;    // [x, y, z]
gravity vector
float ypr[3];           // [yaw, pitch,
roll]   yaw/pitch/roll container and
gravity vector
```

MCU inputs.

6 Result and Testing

By integrating the software system and the hardware system, motor controlling is obtained successfully. The motor and computers in the base maintain the balancing of vehicle during the operation. When even the external force is given to the vehicle, it comes in an equilibrium state. It becomes less jerky compared to the old methods.

Fig. 9 Working model
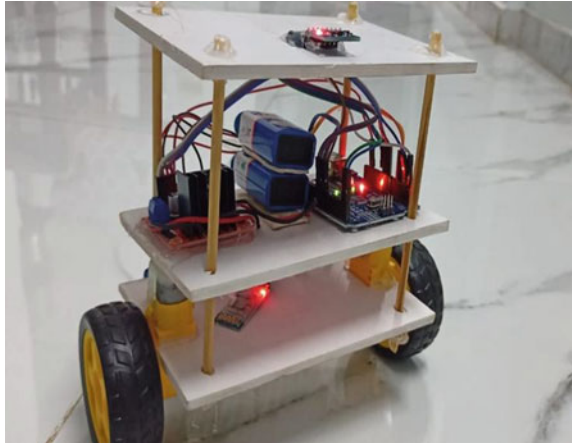
Fig. 10 Working model
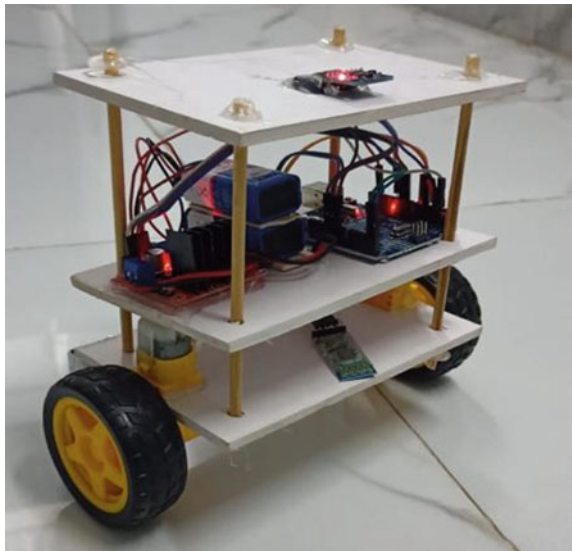
The unnecessary motor is eliminated just by reversing it I opposite direction for a moment. The system becomes most trustworthy when driver loses his balance.

The actual photographs of the prototype are shown in Figs. 9, 10 and 11.

7 Further Development

There are number of advancement which can be implemented in order to increase the performance and functionality.

Fig. 11 Working model
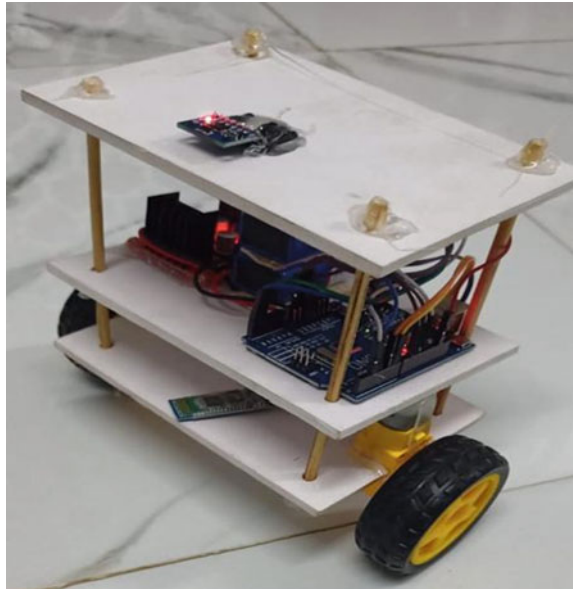
- Cost reduction by cheaper controller and cheaper motor.
- Encoder could be added to enhance the feedback control.
- Warning signals and light can be added.
- Reduction in the cost of main board by self-designing PCB which can integrate motor controller, MPU6050 and DAC.
- Smart system can be added like obstacle detector or automatic braking in order to get safe ride.

8 Conclusion

The aim of this paper was to develop the balancing system for two-wheeled self-controlling scooter which is more reliable. The overall functionality and performance of the vehicle have been evaluated thoroughly by a number of test drives. The testing was carried out at the maximum speed of 20 km/h; however, it seemed that the model is also able to perform the same task even at the speed of 25 km/h. This project has been implemented with an idea to find an effective solution to transportation problem, and it has been achieved successfully.

References

Castro A (2012) Modelling and dynamic analysis of a two-wheeled inverted-pendulum

EE312 (2010) Elextronic design lab pproject report. EE Department, IIT Bombay

Hellman (2015) Two-wheeled self-balancing robot. KTH VETENSKAP OCH KONST

Hu T (2007) Design and implementation of self-balancing coaxial two wheel robot based on HSIC. In: Proceeding of SPIE, Volume 6794, 6794H-1–9

Hughes B (2009) Ergonomics of Segway. Reaction of forces by segway on human

Junfeng W (2011) Research on control method of two-wheeled self-balancing robot. In: International conference on intelligent computation technology and automation

Li M The design of a segway AR-tactile navigation system. http://www.graphics.rwth-aachen.de/media/papers/li_2012_pervasive_021.pdf

Lin SC (2009) Nonlinear adaptive sliding-mode control design for two-wheeled human transportation vehicle. In: IEEE international conference on systems, man, and cybernetics, pp 1965–1970

Nagarajan U (2009) State transition, balancing, station keeping, and yaw control for a dynamically stable single spherical wheel mobile robot. In: IEEE international conference on robotics and automation, pp 998–1003

Nguyen HG Segway Robotic Mobility Platform. http://pharos.ece.utexas.edu/wiki/images/8/8e/Segway-spie2004.pdf

Worldometer Homepage. https://www.worldometers.info/oil/india-oil/. Last accessed 2021/06/12

Zhang W (2012) A two-wheeled self-balancing robot with the fuzzy PD control method. Hindawi Publishing Corporation, vol 2012, pp 1–13

Zhang B (2019) Design of two-wheel self-balancing vehicle based on visual identification. EURASIP J Image Video Process 34

Design and Development of the Wheelchair Components Using the Topology Optimization Method

Pratyush Srivastava and Pankaj Sahlot

Abstract A number of people on the globe have been encountering difficulties in functioning and have almost no suppleness, have been using the wheelchair, and other assistive equipment for their assistance for a very long time. It has assisted them in traveling faster and independently at all places possible. With the advent of electrically assisted systems, there are several other functions that the wheelchair can provide to the user, namely climbing the stairs with the help of a stair-climbing wheelchair or standing upright with the help of the motorized wheelchair. However, wheelchairs for a specific group of people, viz. sportsmen, require a thoroughly different kind of design to cater to their needs. It is essential to effectuate a study, which is a cause-and-effect analysis and has an ideation process followed by the feasibility analysis that can help us design parts that can be incorporated in the wheelchair. This paper discusses the feasibility of the wheelchair concerning the components already present in a wheelchair. Thus, these components can be appended or modified based on various factors, namely inefficient product design or the environmental facts and the parameters which insinuate us about the extent of modifications are repetition, force, duration, and body posture. These components have been designed and topologically optimized to reduce the weight and material requirements in the product and to allow users to reach a particular point swiftly and comfortably. This study can help in design products considering the human factors and also considering the optimization of the products. Thus, this study is an endeavor to consider all the design and engineering factors that can be used to design an efficient and safe product for the people in the scope of the study.

Keywords Product design · Product development · Topology optimization · Ergonomics · Design thinking · Human-centered innovation · Mobility

P. Srivastava · P. Sahlot (✉)
Mechanical Engineering, School of Technology, Pandit Deendayal Energy University, Gandhinagar, GJ 382426, India
e-mail: pankaj.sahlot@sot.pdpu.ac.in

P. Srivastava
e-mail: pratyush.smc17@sot.pdpu.ac.in

1 Introduction

According to the World Report on Disability 2011, in contemporary times, around 15% of the total population in the world has some kind of disability of whom 2–4% of people experience considerable impediments in executing some or the other kind of functions (Inkpen et al. 2012). Although there has been a precipitous increase in the number of wheelchair users who happen to be sportsmen and with the rising number of innovations happening in the field of mobility and adaptive/assistive equipment, they are envisaging a reassuring future to take part in numerous sports which will not only give them a sense of gratification but also a perception of autonomy which, by all means, is vital for their growth as an independent individual (Perret 2017).

A wheelchair user immensely relies on the wheelchair; thus, it is akin to a second home to them. However, analyzing the prevailing designs and taking feedback from the users make it perceptible that there are certain areas, namely climbing down a stair-like structure or taking a roundabout to avoid heavy structures, where a user would experience a considerable challenge while traversing and there is a need to revamp the design to eradicate all the problems caused by the use of the prior designs.

Researchers have worked on numerous problem areas which would elicit designs that are exceedingly efficient in terms of functionality. Wang et al. (2017) designed a wheelchair for paralyzed patients that can transmute into a sitting chair, reclining chair, or a standing chair. In the standing position, a person can reach an elevated site and perform the entailed exercise, and the user uses the reclined form for some respite. For this, they have performed kinematic analysis using the vector equation analytical method to attain kinematic behavior or physical elements through the change in posture. Mo et al. (2014) designed an electronically assisted wheelchair that has a parallelogram structure and was conceived as a wheelchair that can get attuned to the natural body posture. In the propositioned design, the springs attached to the non-adjacent apexes can accrue energy. Therefore, a small-capacity electric motor, which is economical to procure, can be used to lift the system. Chen (2011) designed an electronically assisted wheelchair that has a sliding seat. This system can expedite people's movement and give them the independence to shift from their wheelchair to an approachable chair, which was followed by the determination of the dislocation span to ensure the warrant that the wheelchair does not tumble. They conceived a CAD model and then performed the simulations on the computer and also accomplished the static and dynamic analysis of the designed system. Furthermore, they implemented design optimization techniques in the system to make the design more ergonomic and serviceable. However, the integration of the suspension system along with the frame and the base was not discussed and the predicament and the vexation of the wheelchair toppling down have not been addressed yet, and the study to keep all the wheels of the wheelchair grounded while traversing on a coarse trail is still being investigated.

There is a scope of exploring and improving the ergonomics aspect of the product, namely the back or seat rest and the side rest of the wheelchair. Moreover, the active muscles, mainly the upper body, which involved in thrusting the wheelchair ahead, is

always under constant oppression, which may lead to impairments, viz. muscle strain, repetitive strain injury, shoulder impingement, musculoskeletal disorder, etc., if there is persistent oppression on the muscle group. Van der Woude et al. (2001) studied and authenticated that the use of augmenting propulsion systems, namely lever propulsion, arm-crank propulsion, hub-crank, etc., can preclude these secondary damages in wheelchair users. Moreover, with the use of these propelling systems, the power at the output is reasonably higher than the normal systems, thus one can travel at a higher speed and for longer duration; hence, they can traverse a longer distance. Sarraj et al. (2010) carried out a study that is based on a survey that involved a questionnaire to assess the contentment level of the participants on a lever-based propulsion wheelchair that they have developed. Based on the research, it was seen that the lever-based propulsion wheelchair was preferred over the customary wheelchair in terms of the output, dexterity, safety, comfort, and the overall experience of using the wheelchair can be enhanced. Thus, this product is appropriate for the people associated with or participate in sports. However, the research does not talk about the ergonomic attributes of the product and has been avowed that this can be considered as a study to enhance the potential prototypes. Soewardi et al. (2019) designed an ergonomic wheelchair using the quality function deployment method, which facilitated the identification of the design description of the wheelchair. They surveyed to collect user's requirements and the design considerations. They also used anthropometry data to use body measurements in their study. The dimensions were considered for sitting height, back height, width, etc. Then, statistical examination was done to substantiate the proposition. The result of the study was that the conceived wheelchair was comparatively more safe, comfortable, and was swifter than the customary wheelchair. However, the research does not discusses the design and optimization of individual components to be used in the wheelchair.

Therefore, the scope of this project is to design a wheelchair for sportsmen residing in the rural parts of India. The ancillaries and other novel parts or mechanisms designed to be the part of the wheelchair can be fabricated easily, and the entire product is frugal and austere, although, has reasonable strength and litheness which can be expected by a performance wheelchair.

2 Methodology

In this section, we discuss the approach that was taken to analyze and design the wheelchair. This will include the "thinking process" and execution which will further include the cause-and-effect analysis to identify the problems, the design thinking approach used to solve the problems, the ideation process, the data collection, and the design and simulation process carried out on the software.

2.1 Thinking Process

A major part of the research was finding out the causes of the problem and the problems themselves. The causes could be related to the product or related to the environment. In the case of the causes related to the environment, there has to be a germane modification in the product's current design.

The "design thinking" method can be used to identify constituents in the wheelchair that would require a potential reformation. Moreover, to contrive ancillary components that may aid the user to use the wheelchair effectively.

The design thinking technique mainly includes five phases: empathize, define, ideation, prototype, and test. Thus, as the first step, we have attempted to understand the problems faced by the user, then we cognized and defined the problem and delineated the scope of the problem, then we ideated and thought of numerous mechanisms to solve the problem, and then we made the model on the CAD software and performed topology optimization of the part on the FEA software which was followed by validating the results for same load conditions.

According to the concept of design thinking, this method, per se, is a creative problem-solving process that offers various innovative paradigms of progressions and abilities which will facilitate the enhancements, amendments, expediting, and conceptualizing various problems not related to design and engineering but also in multidisciplinary groups in several organizations, namely working on business thinking methods, innovation consulting and management, etc. (Calouste 2012).

The result of this process in the form of a product is entirely "Human-Centered." Thus, the components proposed to be included in the wheelchair, along with being topologically optimized, must leverage the ergonomic and functional aspects of the product. Hence, the designed components must be as per the rules of ergonomics (Hand 1994) to ensure that it does not cause any hindrance while using the wheelchair, viz. discomfort in the shoulders, elbows, and other active muscle groups which are responsible for propelling the vehicle forward.

A major fragment of the research incorporated exploring a conceivable method to apply the topology optimization (TO) technique and more pertinently finding out the right causes which might have the potential to thwart the motion of a person using the wheelchair. The TO method is a mathematical tool to optimize the product inside the design space under certain load conditions, constraints, and boundary conditions. Hence, doing so can enhance a product's performance by using less material and making it lighter. However, the use of topology optimization can also facilitate enhancing the product design aspect of the product, viz. aesthetics, ergonomics, etc. Using topology optimization also increases the process efficiency and decreases the time needed to render and investigate the product (Hydro et al. 2013).

Products often designed using the topology optimization technique are often manufactured using additive manufacturing (AM) techniques. Moreover, topology optimization materializes to be one of the "Design for AM (DfAM)" techniques. Employing AM allows us to design parts and concentrate on improving the part in
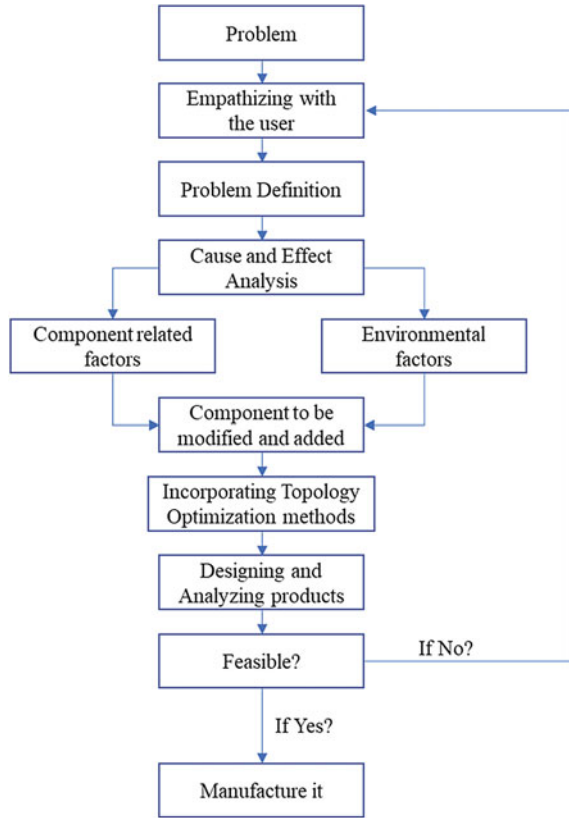
terms of the product design, consecutively. Moreover, complex parts can be manufactured with great strength, which is also anticipated by a topology optimized product (Zhu et al. 2021; Brackett et al. 2011; Liu et al. 2018; Fetisov and Maksimov 2017).

Therefore, the designed part can then be manufactured using a pertinent fabrication technique, namely casting and welding operations or additive manufacturing methods (Fig. 1).

2.2 Ideation

It is important to understand the four main spheres or parameters which can help us understand the degree of problem a wheelchair user face. Those areas are duration, posture, direction, and magnitude of force, and repetition (Kulkarni et al. 2017). Thus, it is vital to target causes in terms of the wheelchair components, and if there are environmental reasons, there has to be a germane modification in the product's current design.

The parts that are identified for optimization are the castor wheel joint and rear suspension frame base.

The castor wheel joint in the customary wheelchair is a rigid structure; hence, it has no flexibility along any axis. As a result, the wheelchair might topple when the user would wish to descend from a stair-like structure. With the introduction of a special spring-based mechanism at the castor wheel joint, there can be a certain degree of freedom associated with the wheelchair. Thus, negotiating any obstacle is reasonably easier, which might have bothered the user in the former case. Furthermore, as this design is targeted at people associated with sports in rural areas, this will indubitably help them to give their best in the game. Moreover, the designed joint is also topologically optimized; thus, it uses less material for fabrication and is lightweight.

The castor wheel mechanism is conceived to ensure that the angular separation between the two front wheels does not exceed a certain limit. Thus, whenever the wheelchair would descend a star-like structure, only one of the wheels would go down and the wheelchair would remain upwards, hence making it more stable as compared to a castor wheel structure, which does not have any degree of freedom (Fig. 2).

At the rear of the wheelchair, suspensions are added to provide a jerk-less motion to the user and to ensure that all four wheels in the wheelchair are grounded all the time. The joints connecting the suspensions to the wheelchair and the base rod are topologically optimized, and hence have all the advantages that any topologically optimized part has.

The base of the frame is also topologically optimized and is, therefore, lightweight and would require less material to fabricate it; however, the strength of the part is still intact. These components can be made from the same material as that of the wheelchair's main body.

a. CAD Model   b. Schematic diagram
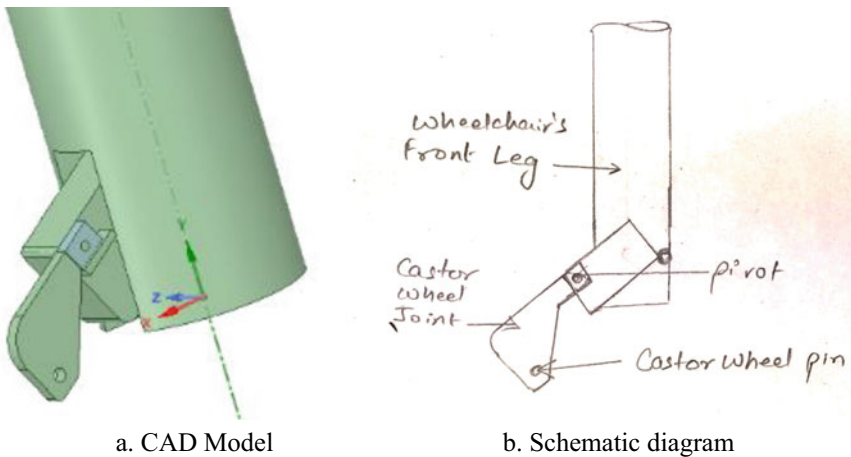
Fig. 2 Castor wheel mechanism

Table 1 Data for the wheelchair's dimensions based on anthropometry study (Kulkarni et al. 2017)

Component	Dimensions (mm) (average value)
Seat height	480
Height from the ground (absolute)	914
Back height	406
Length (along the side until the castor wheels)	1060
Seat width	457
Full width	630
Armrest height (from the chair seat)	228

There are other addendums to the wheelchair, namely the 'basket' attached to the leg to carry material, the rims of the wheelchair that succors the user to push the wheelchair ahead; itis usually attached outside, however, in the modification, it is shifted inside so that the palms of the user do not get dirty if they touch the wheels fortuitously, provision of folding the wheelchair as and when required, provision of adjusting the main wheels of the wheelchair is provided if the user wants to adjust based on the arm length. This would ensure that there is no unwanted stress on the elbows and shoulder. Moreover, brakes have been added to the wheelchair to control its motion.

2.3 Data Collection and Tools Used

The data for wheelchair dimensions were procured from the anthropometric data for Indian citizens. It consisted of the physiological information of the human body, namely the average shoulder length of a twenty-five-year-old man, the average height of the chair for the person to sit comfortably, etc. Therefore, anthropometric data can be used as a reliable source to design and fabricate ergonomic products.

For the design of the wheelchair, ANSYS SpaceClaim was used. The material selected for making the frame of the wheelchair is steel. The entire analysis was done on ANSYS's static structural tool, and the FE analysis was carried out on mechanical enterprise. We could examine the deformations and stresses on the part under a given load and boundary conditions. The solutions were linked with the topology optimization tool which would give parts that have optimized topologies.

The optimized parts can be then used in making the complete wheelchair (Table 1).

3   Results

After carrying out the design analysis, the equivalent (Von-mises) stresses and the corresponding topology optimization of the part are observed. The pictures representing the same are shown in Fig. 3.

From the equivalent stress analysis (Fig. a), it is evident that when the bearing load is applied at the hole, the stress values are higher at the cylindrical support. From the total deformation analysis (Fig. b), it is evident that the deformation is maximum at the end of the joint and is minimum at the cylindrical supports because that does not have any degree of freedom. In the topology optimization (Fig. c) of the castor wheel joint, we can observe that the mass of the optimized part is reduced. Moreover, the value of stresses while doing (the validation was satisfactory (Fig. 4).

From the above equivalent stress study (Fig. a), it is evident that when the load is applied, the stress values are higher at the cylindrical support, comparable to the castor wheel joint. From the total deformation analysis (Fig. b), it is evident that the deformation is maximum at the joint and is minimum at the fixed supports because that does not have any degree of freedom. The analysis will be accurate for the other joint as well. Topology optimization (Fig. c) of the suspension joint can substantiate that the mass of the optimized part is reduced keeping the strength intact.

Ancillaries like brakes (Fig. a), adjustments (Fig. b.), and the provision to keep the materials (Fig. c.) have been provided in the wheelchair to ensure that the wheelchair is frugal, ergonomic, and safe (Fig. 5).

a. Equivalent Stress Analysis

b. Total Deformation

c. Topology Optimized Part

Fig. 3 Castor wheel joint

a. Equivalent Stress

b. Total Deformation
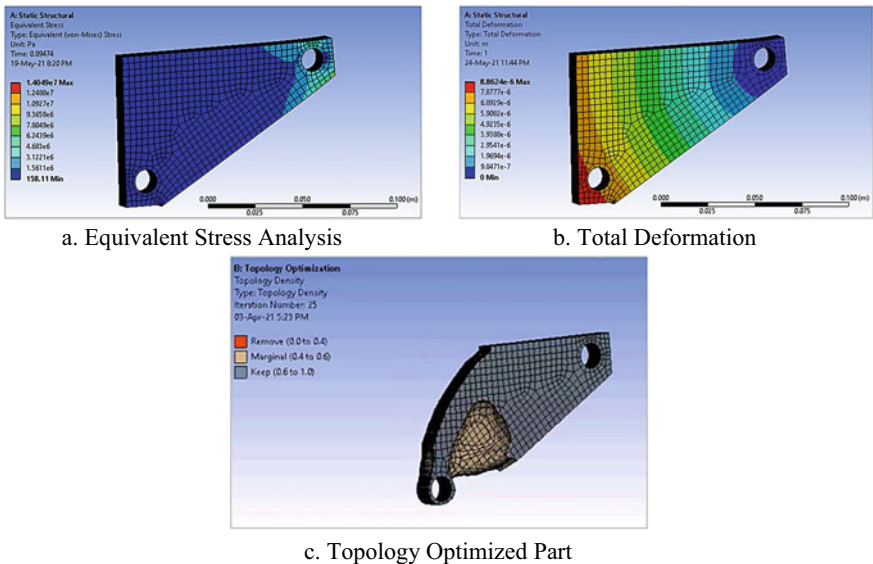
c. Topology Optimized Part
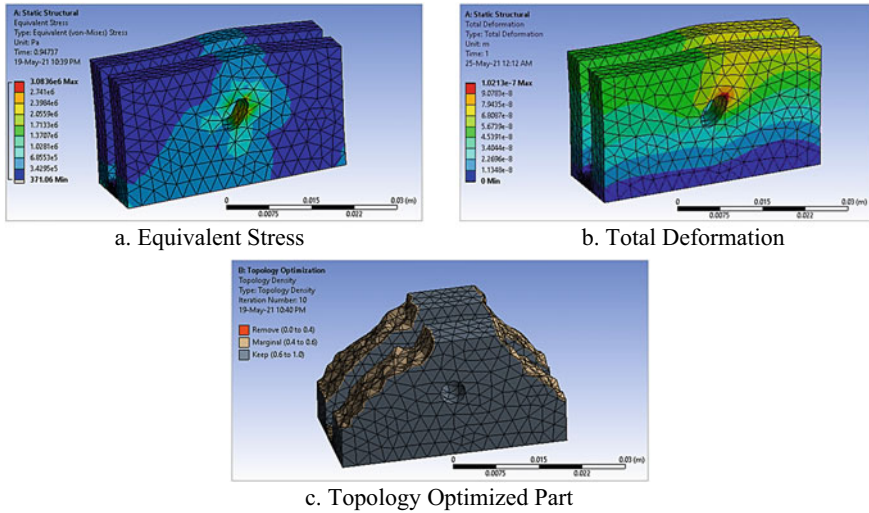
Fig. 4 Rear suspension joint

4 Conclusion and Future Work

From the study, we can say that the components that were added or modified can be incorporated into the tangible wheelchair. The application of these components would ensure that the user should feel very less jerk while using the wheelchair and one can traverse his/her path while in the game without encounter any major impediment. The components designed to be the part of the wheelchair can be fabricated easily, and the entire product is frugal and austere although has reasonable strength and litheness which can be expected by a performance wheelchair. Thus, concerning the scope that a wheelchair to be used by the sportsmen in the rural parts of India can be vindicated.

Considering the prospects of this study, we can suggest that a greater number of components can be identified based on the cause-and-effect analysis and by performing the feasibility study of the product. The product can be studied for various application areas which can consequently be made available for the masses. The design thinking methodology and topology optimization techniques can be used for further analysis; however, there is a scope of amendment in that aspect as well. As the design of the components would involve use of topology optimization technique; hence, fabrication is an arduous process; thus, using additive manufacturing technologies are effectual.

The entire research can facilitate in understanding the product design and engineering techniques in much greater detail, the application of which can serve as a modus operandi for the critical analysis, improving and designing a better product and making them safe, efficient, and prudent, which can impact and improve the quality of lives of people in an efficacious manner.

a. Addition of brakes   b. Adjustment for the main wheels

c. Provision for keeping materials and belongings in the wheelchair
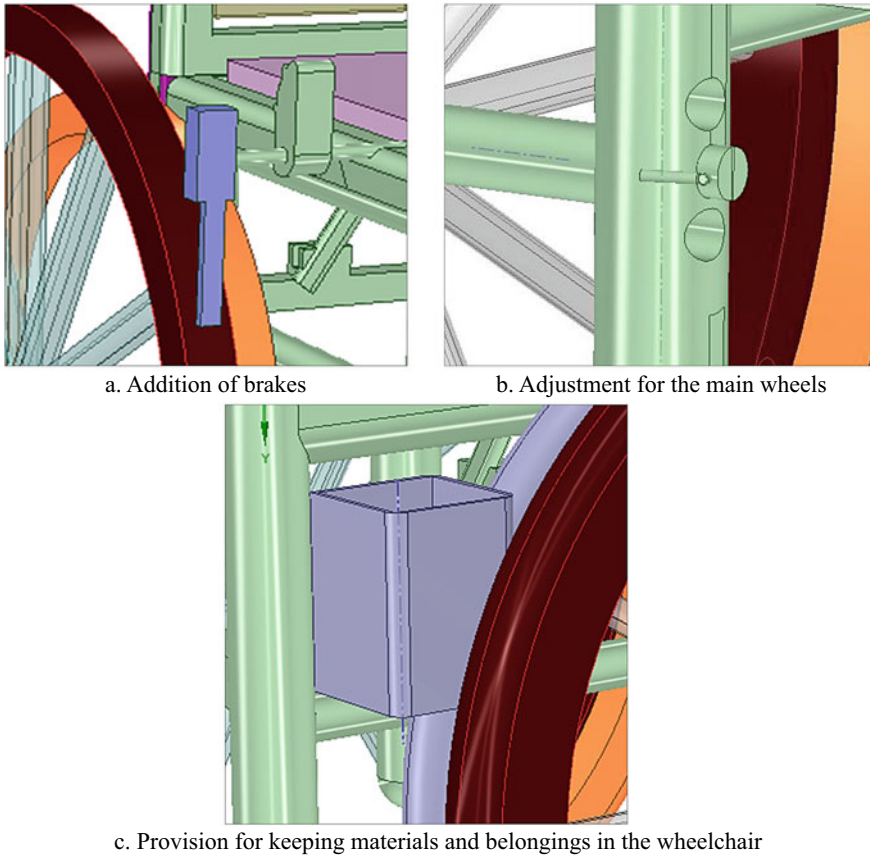
Fig. 5 Ancillaries in the wheelchair

References

Brackett D, Ashcroft I, Hague R (2011) Topology optimization for additive manufacturing, In: 22nd annual solid freeform fabrication symposium, pp 348–362

Calouste A (2012) Design thinking as an effective toolkit for innovation Katja Tschimmel. In: Proceedings XXIII ISPIM conference on action innovation: innovating from experience, p 20

Chen X, Wu Z, Deng H (2011) An optimization design for the standard manual wheelchair, Thesis, ISRN: BTH-AMT-EX—2011, Blekinge Institute of Technology, Karlskrona, Sweden

Fetisov KV, Maksimov PV (2017) A case study on topology optimized design for additive manufacturing a case study on topology optimized design for additive manufacturing, p 12. https://doi.org/10.1088/1757-899X/276/1/012026

Flanagan J, Johansson R (2002) The acting and perceiving hand, encyclopedia of the human brain, pp 399–414. https://doi.org/10.1016/B0-12-227210-2/00157-6

Kentli A (2019) Topology optimization applications on engineering structures, truss and frames—recent advances and new perspectives, IntechOpen, https://doi.org/10.5772/intechopen.90474

Inkpen P, Parker K, Kirby RL (2012) Manual wheelchair skills capacity versus performance. Arch Phys Med Rehabil 93(6):1009–1013. https://doi.org/10.1016/j.apmr.2011.11.027

Kulkarni C, Dandavate A, Chamnalli M (2017) Ethnographic and ergonomics considerations in design of wheelchair. Int J Sci Eng Res 8(2):997–1001 [Online]. Available: http://www.ijser.org

Liu J et al (2018) Current and future trends in topology optimization for additive manufacturing current and future trends in topology optimization for additive manufacturing, p 28. https://doi.org/10.1007/s00158-018-1994-3

Mo T, Sun Y, Yang Y (2014) New mechanism used in standing wheelchair, Thesis, Blekinge Institute of Technology, Karlskrona, Sweden

Perret C (2017) Elite-adapted wheelchair sports performance: a systematic review. Disabil Rehabil 39(2):164–172. https://doi.org/10.3109/09638288.2015.1095951

van der Woude LH (2001) Alternative modes of manual. Am J Phys Med Rehabil, October:765–777

Sarraj AR et al (2010) Evaluation of a wheelchair prototype with non-conventional, manual propulsion. Ann Phys Rehabil Med 53(2):105–117. https://doi.org/10.1016/j.rehab.2009.12.001

Soewardi H, Afgani MKA (2019) Innovative design of ergonomic wheelchair for disabled people. IOP Conf Ser Mater Sci Eng 598(1).: https://doi.org/10.1088/1757-899X/598/1/012033

Wang D, Yu H (2017) Mechanical design of a wheelchair with multi-posture characteristics. 86(Eame):181–185. https://doi.org/10.2991/eame-17.2017.44

Zhu J, Zhou H, Wang C, Zhou L, Yuan S (2021) A review of topology optimization for additive manufacturing: status and challenges. Chin J Aeronaut 34(1):91–110. https://doi.org/10.1016/j.cja.2020.09.020

Optimization of Process Parameters Using Response Surface Methodology to Improve Surface Finish in Face Gear Grinding

Aditya Nema, **Vivek Patel**, **and Abhishek Kumar**

Abstract Face gear is an important mechanical tool that is utilized in various aerospace and automobile applications where high-power transmission is necessary. CAD modeling has made the designing part easier but the fabrication process is a challenge as there is a lot to stress generation on the face gear due to the conventional grinding process which causes unacceptable surface roughness values that can lead to cracking and failure of the machine. This report tends to follow the work of a research based on modeling and optimization of face gear grinding and improve the surface finish. Response surface methodology was used to perform the analysis and find the optimal points using Minitab, and the data is compared with the previous work done. The confidence level of the RSM model was 91.44%. Roughness values obtained from optimized parameters using RSM were better than those values obtained by using range analysis optimal points.

Keywords Face gear grinding · Surface roughness · Optimization · Response surface methodology

1 Introduction

Transmission of high-intensity power in machines such as helicopter aircraft (as shown in Fig. 1) and heavy-duty vehicles requires face gears due to its high load-bearing capability and bigger transmission ratio. Designing of the face gear is, however, easy but the fabrication process is difficult. Many different researches have been performed on ways to fabricate face gears such as milling, shaping, planning, and grinding. Computer numerical control (CNC) with number of degrees of freedom provides effective machining of face gears.

Modeling and simulation of the design model of face gears have become efficient with the help of CAD/CAM integration. Many different techniques have also been

A. Nema (✉) · V. Patel · A. Kumar
Department of Mechanical Engineering, Pandit Deendayal Petroleum University, Gandhinagar 382007, India
e-mail: lncs@springer.com

developed. However, there is still area that is required to be checked in-order to improve the quality of the machined face gears. The concern is the surface of face gear rather than speed of material removal. In order to improve upon the surface finish, some optimization needs to be performed by controlled design of experiments and the variable parameters, Usually, optimization can be categorized into two types, i.e., (1) single objective and (2) multi-objective. In the current situation, there is need of single objective optimization. There are various conventional and non-conventional techniques for optimization. Figure 2 also shows the classification of various tools and techniques for finding optimal solutions. Design and optimization tools such as regression analysis and response surface method are effective in understanding the relationship between variables and objective function and find the optimal solution (Khuri and Mukhopadhyay 2010).

Ming et al. (2017) categorized two manufacturing methods for face gears into coarse fabrication and finishing operation. For both methods, milling, shaping, and grinding operations are suitable to provide primary geometry of face gear as well as the final finish to the face gear. Yang et al. (2014) applied plunge milling in the fabrication of spur face gear to reduce the complexity in the design of apparatus and cost. It shows the operation of plunge milling performed using CNC processing in which both the actions of grinding and milling are done at the cutting edge. Litvin et al. (2002) explained in detail about the face gear drive and its design, mathematical model of the design to generate the worm surface, FEM modeling is performed for observe the stress on the surface of face gear and improvement was done on bending stress using top edge to be curved. A patent was also passed for the design approve by US patent. Another design was also proposed by Wu et al. (2018) which showed mathematical designing and generation of face gear, stresses were also calculated using ABAQUS software. The method was found useful for other transmission gears as well with the help of more advanced calculation. Wang et al. (2017) applied disk cutter for machining face gears. Modeling and simulation were performed to investigate on the errors in computation. Lastly, experimentations were done to observe the accuracy of the process. Deng et al. (2014) presented a modified method for developing face gears using disk cutter. The method showed effectiveness in the designing and feasibility for manufacturing and application for the same. However, parameters could have been optimized in order to get higher finish. Tang et al. (2016) used a planner for face gear fabrication using a CNC planner. Mathematical equation was derived for the face gear, the machining efficiency was, however, better than the one with plunge milling, optimization was not performed. Similar type of work on finding new grinding methods was proposed by Guo et al. (2015), Zhou et al. (2019), Wang et al. (2015, 2016), Shi et al. (2019).
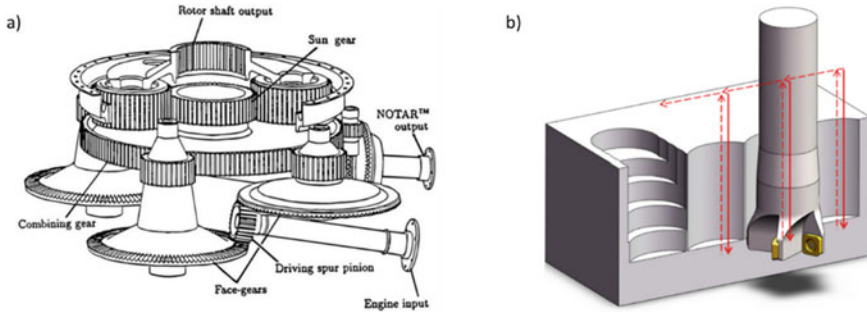
Fig. 1 **a** Application of face gear in helicopter transmission (Litvin et al. 2002) **b** Plunge Milling (Yang and Tang 2014)

2 Response Surface Methodology

It is an effective way in which relationship between the factors and objective function can be understood by analyzing the results of objective for design of experiments which be visualized in the form of polynomial equations and graphs. This model also helps in understanding the significance of the factors on the defined objectives. This methodology also predicts the values of objective at the desired levels of factors and the optimal values of the factors for desired value of objective as well (Khuri and Mukhopadhyay 2010). From the literature, it has been found that no research has been performed on the optimization of the process parameters of face gear grinding using RSM.

3 Result and Discussion

The work is carried out with reference to a study on methods to improve and reduce the surface roughness of face gears using CNC operation which was proposed by Ming et al. (2017), where L25 orthogonal design of experiments was applied, variance, and range analysis was also done. In this present investigation, response surface methodology was employed on the data and polynomial equation was generated for the results of surface roughness with the help of graph plots. Analysis of variance was performed to find the significance of each factor. Minitab software has been used to generate and evaluate the response model. Table 1 shows the three factors considered, i.e., spindle speed (rpm), feed speed (m/min), and abrasive code with five levels of factors, and the factors are coded as A, B, and C, respectively. The optimal results of surface roughness from the range analysis to be 0.293 μm.
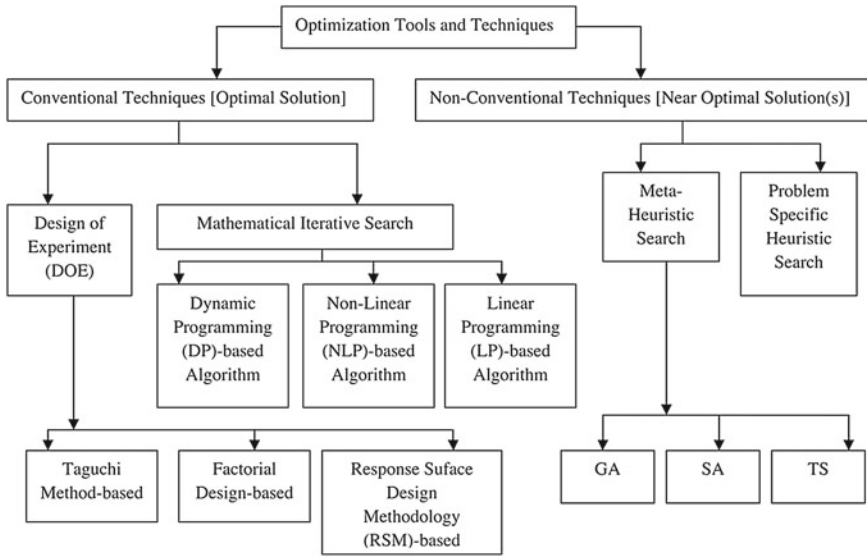
Fig. 2 Categorization of various optimization techniques (Mukherjee and Ray 2006)

Table 1 Factors of various levels and its optimum value based on range analysis with reference Ming et al. (2017)

Factors	Levels					Optimal levels	Results of Ra (μm)
	I	II	III	IV	V	A, B & C	
Disk wheel Spindle speed (rpm) A	1300	1600	2000	2500	3200	3200	0.293
Disk wheel Feed Speed (m/min) B	1.6	2.1	2.6	4	5.6	2.6	
Abrasive Code (#) C	60	80	100	120	150	150	

3.1 Analysis of Variance

ANOVA is reliable method of understanding the significance of the variables for the objectives. Fisher's value for various alpha values is compared with the f-value which needs to be more to obtain significance. From Table 2, where DF is the degree of freedom, SS is sums squares, MS is mean square, F is Fisher's value, and P is the probability. It can be observed that the disk feed speed is the most significant factor with the highest F-value (65.69), then disk spindle speed with comparatively less significance (47.75) and then abrasive code (5.64) with least significant factor. However, all the factors were significant as the f-value is more than Fisher's value (2.131) as shown in the Pareto chart in Fig. 3.

Table 2 Analysis of variance of the second order optimization

Source	DF	Adj SS	Adj MS	F-Value	P-Value
Model	9	0.593045	0.065894	17.80	0.000
Linear	3	0.532886	0.177629	47.98	0.000
A	1	0.176766	0.176766	47.75	0.000
B	1	0.243184	0.243184	65.69	0.000
C	1	0.020884	0.020884	5.64	0.031
Square	3	0.018968	0.006323	1.71	0.208
A*A	1	0.012263	0.012263	3.31	0.089
B*B	1	0.000350	0.000350	0.09	0.763
C*C	1	0.000322	0.000322	0.09	0.772
2-Way Interaction	3	0.003519	0.001173	0.32	0.813
A*B	1	0.001160	0.001160	0.31	0.584
A*C	1	0.002941	0.002941	0.79	0.387
B*C	1	0.001313	0.001313	0.35	0.560
Error	15	0.055527	0.003702		
Total	24	0.648572			

Fig. 3 Pareto chart showing effect of factors and its significance
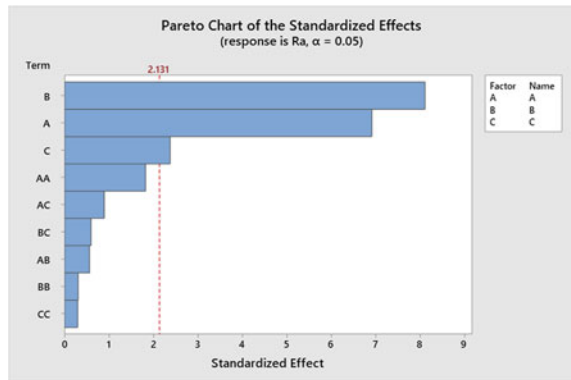
3.2 Factorial Plots and Surface Plots

To understand the effect of factors on the surface roughness, Fig. 4 shows the line and surface plots showing the effect of factors on R_a. It can be observed from the graphs that surface roughness tends to get lower at higher rpm, i.e., higher spindle speed and higher abrasive code. But with more feed, the roughness value tends to increase.
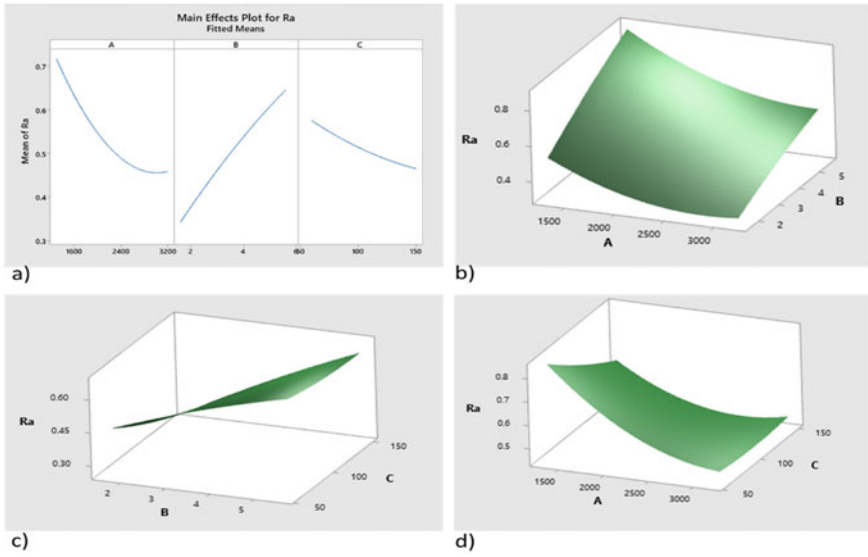
Fig. 4 **a** Factorial plots of the factors for Ra **b** Surface plots between Ra-A-B **c** Surface plot between Ra-B-C **d** Surface Plot between Ra-A-C

3.3 Regression Equation from Response Analysis and Optimal Solution

To predict the response of factors at the desired values, a second-order polynomial equation is formulated for the surface roughness with respect to the three factors disk wheel spindle speed, disk wheel feed speed, and abrasive code signified as A, B, and C, respectively. The equation is-

$$
\begin{aligned}
Ra = {} & 1.469 - 0.000616A + 0.0935B - 0.00678C + 0.000000A \times A \\
& - 0.0036B \times B + 0.000006C \times C - 0.000014A \times B \\
& + 0.000001A \times C + 0.000386B \times C
\end{aligned}
\tag{1}
$$

After analyzing the results, the response model generated for R_a shows 91.44% confidence. The optimal solutions were spindle speed at 2528.2 rpm, feed speed at 1.6 m/min, and abrasive code of 150 giving the roughness value of 0.2588 μm, which is higher than the optimal value 0.293 μm obtained from range analysis by Ming et al. (2017) as shown in Table 2.

4 Conclusion

Face gear grinding is an important process to remove any chance of mishappening to as this component is used in high-power transmission of helicopters. From the results, it can be concluded that response surface methodology is able to provide improved optimal results as compared to the simple range analysis. Prediction of surface values within the given range of the factors is also possible with this technique.

References

Deng XZ, Li GG, Wei BY, Deng J (2014) Face-milling spiral bevel gear tooth surfaces by application of 5-axis CNC machine tool. Int J Adv Manuf Technol 71:1049–1057. https://doi.org/10.1007/s00170-013-5499-3

Guo H, Peng X, Zhao N, Zhang S (2015) A CNC grinding method and envelope residual model for face gear. Int J Adv Manuf Technol 79:1689–1698. https://doi.org/10.1007/s00170-015-6915-7

Khuri AI, Mukhopadhyay S (2010) Response surface methodology. Wiley Interdiscip Rev Comput Stat 2:128–149. https://doi.org/10.1002/wics.73

Litvin FL, Fuentes A, Zanzi C et al (2002) Face-gear drive with spur involute pinion: geometry, generation by a worm, stress analysis. Comput Methods Appl Mech Eng 191:2785–2813. https://doi.org/10.1016/S0045-7825(02)00215-3

Ming X, Gao Q, Yan H et al (2017) Mathematical modeling and machining parameter optimization for the surface roughness of face gear grinding. Int J Adv Manuf Technol 90:2453–2460. https://doi.org/10.1007/s00170-016-9576-2

Mukherjee I, Ray PK (2006) A review of optimization techniques in metal cutting processes. Comput Ind Eng 50:15–34. https://doi.org/10.1016/j.cie.2005.10.001

Shi X, Zhou Y, Zhang W, Tang J (2019) A new worm grinding method of face gears based on the optimization of dressing wheel profile. Forsch Im Ingenieurwesen/Eng Res 83:751–757. https://doi.org/10.1007/s10010-019-00353-6

Tang J, Yang X (2016) Research on manufacturing method of planing for spur face-gear with 4-axis CNC planer. Int J Adv Manuf Technol 82:847–858. https://doi.org/10.1007/s00170-015-7417-3

Wu Y, Zhou Y, Zhou Z et al (2018) An advanced CAD/CAE integration method for the generative design of face gears. Adv Eng Softw 126:90–99. https://doi.org/10.1016/j.advengsoft.2018.09.009

Wang Y, Lan Z, Hou L et al (2015) A precision generating grinding method for face gear using CBN wheel. Int J Adv Manuf Technol 79:1839–1848. https://doi.org/10.1007/s00170-015-6962-0

Wang Y, Hou L, Lan Z, Zhang G (2016) Precision grinding technology for complex surface of aero face-gear. Int J Adv Manuf Technol 86:1263–1272. https://doi.org/10.1007/s00170-015-8241-5

Wang Y, Hou L, Lan Z, Zhu C (2017) Precision milling method for face-gear by disk cutter. Int J Adv Manuf Technol 89:1545–1558. https://doi.org/10.1007/s00170-016-9189-9

Yang XY, Tang JY (2014) Research on manufacturing method of CNC plunge milling for spur face-gear. J Mater Process Technol 214:3013–3019. https://doi.org/10.1016/j.jmatprotec.2014.07.010

Zhou R, Zhao N, Li W et al (2019) A grinding method of face gear mating with a conical spur involute pinion. Mech Mach Theory 141:226–244. https://doi.org/10.1016/j.mechmachtheory.2019.07.013

'2D Simulation to Study the Effect of Flaps on Various Aerofoils at Different Angles'

Vishal Kaushik, Ashwini Wandile, Vaibhav Girade, and Chetna Khadse

Abstract Opting for modifications in the existing technology comes with many challenges. The purpose of this project is to deal with one such challenge by analyzing three different aerofoils used in aviation industry and wind turbines industry. The aerofoils chosen for study are NACA 0012, NACA 0018, and S 1046. The flaps are implemented on all the three aerofoils, and values of lift and drag are recorded for angles from 0° to 10° through computational analysis with the help of ANSYS Fluent software. The variation in C_L (coefficient of lift) and C_D (coefficient of drag) is plotted for different AOAs (angle of attack). From the graphs, we can observe the changes in lift and drag. The study helped us understand the behaviors of the three aerofoils with change in angle of attack. NACA 0018 was found to be more efficient as compared to the other two aerofoils.

Keywords Aerofoil · NACA 0012 · NACA 0018 · S 1046 · AOA · C_L · C_D

1 Introduction

Lift is by far the most important characteristic and advantage of an aerofoil. It is because of this characteristic and advantage that they are used extensively in air travel and wind turbines. As air moves around an aerofoil, because of its shape, on the upper side there is high velocity and low pressure, and on the lower side, there is low velocity and high pressure. Because of this, the aerofoil is lifted up and we say that lift is produced. There are primarily two types of aerofoils put to use—i. Symmetric, ii. Asymmetric Yang et al. (2017). In this paper, we have considered three aerofoils and evaluating them by using ANSYS Fluent software package. Below is the graph plotted shown in Fig. 1 for NACA 0012, NACA0018, and S1046 airfoils between y/c versus x/c. Also in Fig. 2 is the bar graph showing the corresponding values of coefficient of lift and drag for the mentioned three aerofoils. In Fig. 2, nomenclature of an aerofoil is shown (Table 1).

V. Kaushik (✉) · A. Wandile · V. Girade · C. Khadse
Department of Aeronautical Engineering, PCE, Nagpur, MH, India
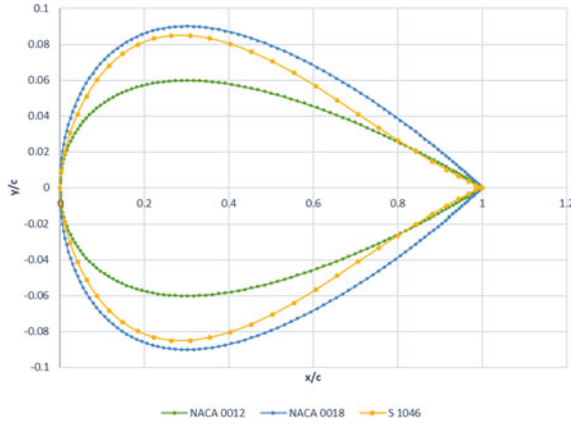
Fig. 1 Geometric profiles of the aerofoils used and reference taken from Zhang et al. (2016)
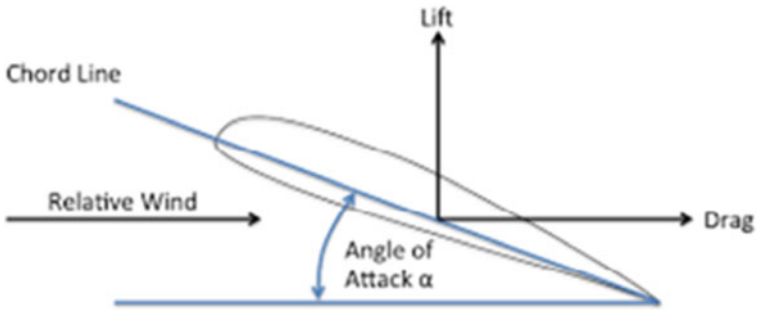
Fig. 2 Nomenclature of an aerofoil Srinivasa Rao et al. (2018)

Table 1 Maximum lift and drag for the following aerofoils at 0° angle of attack

Aerofoil	Maximum lift	Maximum drag
S 1046	2.9702e-04	1.0793e-02
NACA 0012	3.7281e-04	9.8051e-03
NACA 0018	7.9646e-04	1.0048e-02

Below is the indication of each digit in NACA and S series aerofoils is depicted Senthil Kumar et al. (2018)

A.   NACA0012—(0012-il) NACA 0012

NACA 0012 airfoil
Max thickness 12% at 30% chord.
Max camber 0% at 0% chord Ganesh Ram et al. (2014).

B.   NACA0018—(0018-il) NACA 0018

     NACA 0018 airfoil
     Max thickness 18% at 30% chord.
     Max camber 0% at 0% chord.

C.   S 1046—(s1046-il) S1046 17% (Danny Howell)

     Selig S1046 airfoil
     Max thickness 17% at 30.8% chord.
     Max camber 0% at 0% chord.

2 CFD Analysis

A.   **CFD Analysis of aerofoils without flaps**:
     The procedure followed to analyze all the three chosen aerofoils is same which is as follows:

   I.   The coordinates of the aerofoils are downloaded from airfoiltools.com
   II.   The coordinated are imported to ANSYS Design Modeler.
   III.   Surface of the aerofoil is created from these coordinates by using 'surface from edges' tool.
   IV.   A domain is created by sketching a semicircle in the front and rectangle on the rear side and then using the 'surface from sketches' tool. Center of the semicircle is taken at 0.1 m of chord, and length of the rectangle is 31 m and height is 20 m above and below x-axis Yan et al. (2019).
   V.   The aerofoil is removed from domain by using Boolean function.
   VI.   The domain is split into six faces for better meshing.
   VII. While meshing, three named selections are created for convenience—i. Aerofoil, ii. Inlet, iii. Outlet.
   VIII. A structured mesh is formed by using biasing feature.
   IX.   After meshing, solution setup is done with k-ω SST model.
   X.   Lift and drag force monitors are created.
   XI.   Initialization is hybrid (Figs. 3, 4, 5, 6 and 7; Table 2).

B.   **CFD Analysis of aerofoils with flaps**:

With the help of the same software, same mesh, and same setup, all the three airfoils are once again analyzed after implementing simple flaps on them (Figs. 8, 9, 10, 11 and 12; Tables 3 and 4).

(a)

(b)
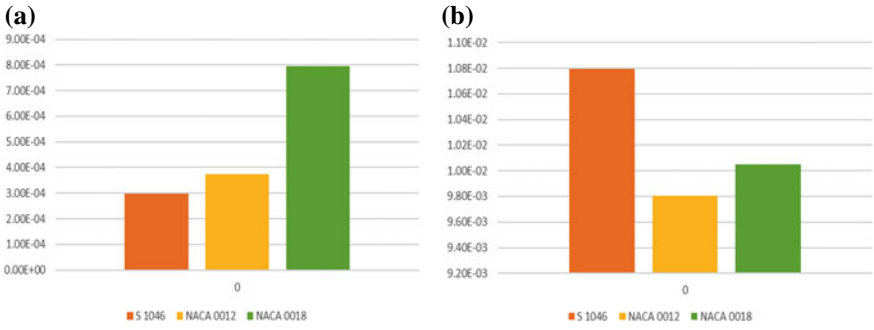
Fig. 3 **a** Lift plot at 0° **b** Drag plot at 0°
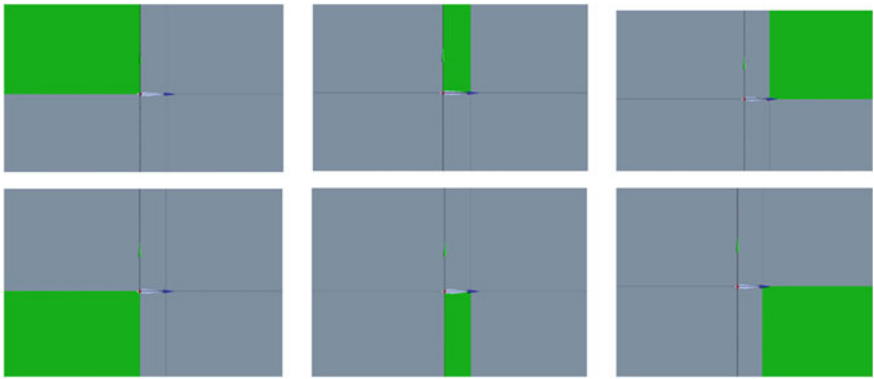
Fig. 4 Six faces after face split
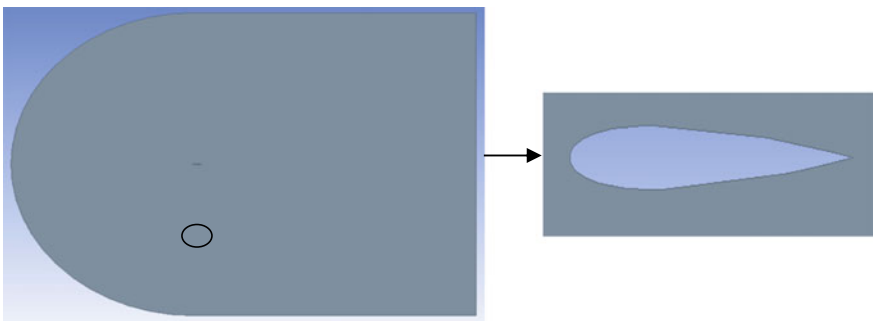
Fig. 5 Airfoil removed from domain

Fig. 6 Structured mesh
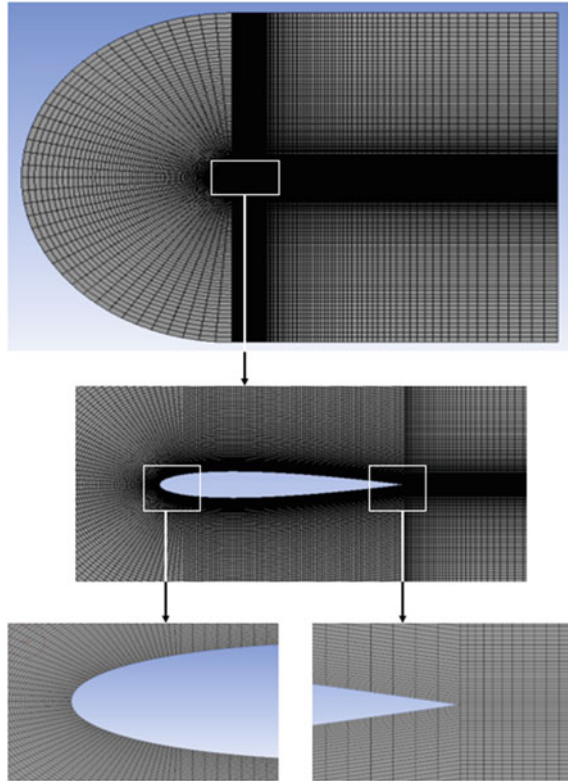
3 Results

From the above graphs, certain results are being obtained. They are as follows

1. For all the three aerofoils considered in the project—NACA 0012, NACA 0018 and S 1046—initial lift at 0° is lower than that at 10°.
2. At 2° the lift suddenly drops to a very low value for NACA 0012 and S 1046, though it is more than that at 0°. After that as we go on increasing the angle of attack of flaps, lift increases almost proportionally.
3. For NACA 0018, the highest amount of lift is obtained by 2° deflection of flap which is the highest value among all the values of lift obtained.
4. As for the drag, no such unusual behavior is observed. Drag goes on increasing with the increasing angle of attack for all the three aerofoils almost proportionally.
5. Along with higher lift, NACA 0018 also gives higher drag as compared to NACA 0012 and S 1046, as evident from the above graphs.

Airfoil	Pressure-contour	Velocity-contour
NACA 0012		
NACA 0018		
S 1046		
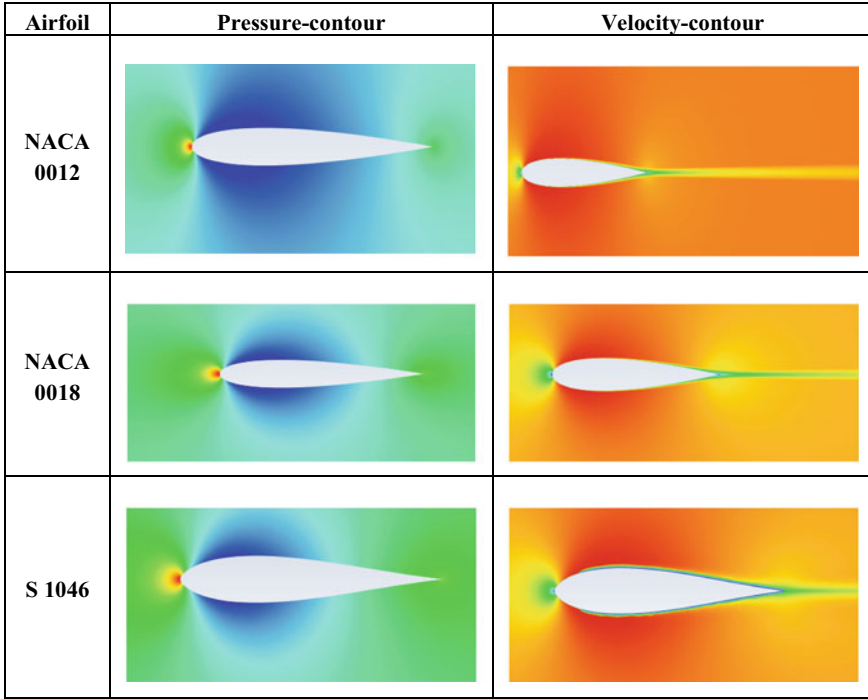
Fig. 7 Pressure and velocity contours of aerofoils without flaps

Table 2 Details of CFD analysis

Software used	ANSYS R2 2020 (student version) package
Mesh type	Structured C-mesh
Turbulence model	k-ω SST Zaheer et al. (2019)
No. of nodes	84520
Fluid	Air
Boundary conditions	Inlet velocity = 50 m/s
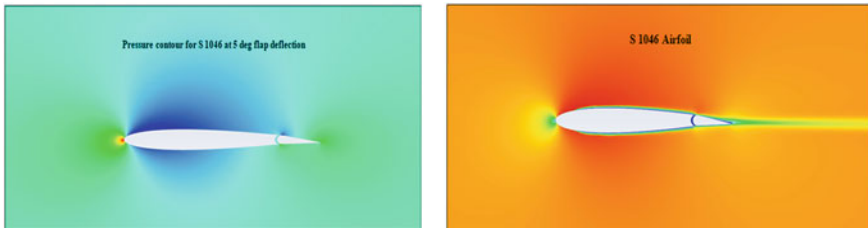
Fig. 8 S1046 aerofoil pressure and velocity contours at 5° flap deflection
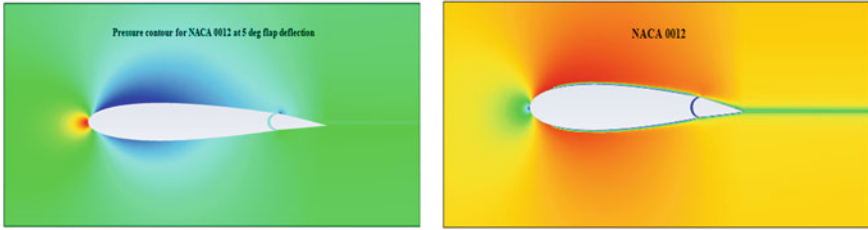
Fig. 9 NACA0012 aerofoil pressure and velocity contours at 5° flap deflection
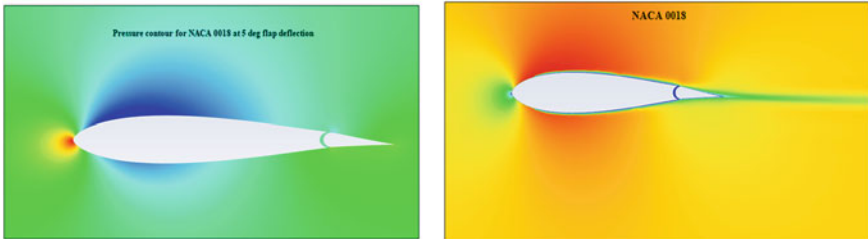
Fig. 10 NACA0018 aerofoil pressure and velocity contours at 5° flap deflection

| (a) | (b) |
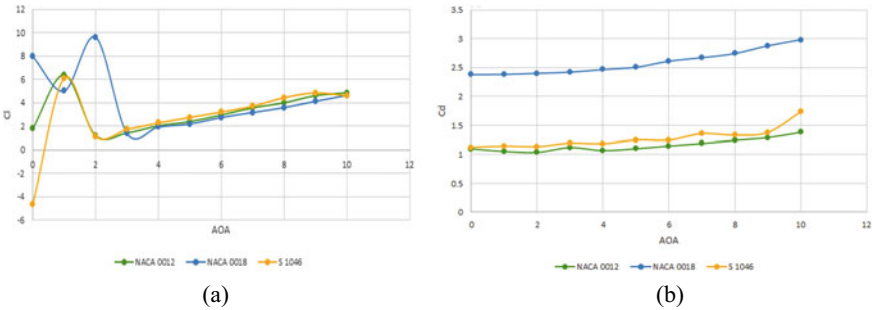
Fig. 11 a) C_L versus alpha graph **b)** C_D versus alpha graph of S1046, NACA0012, and NACA0018 aerofoils with flaps

4 Conclusions

The conclusions drawn from the above study are as follows:

1. As lift increases with increasing angle of attack for all the three aerofoils with flaps, this makes flaps a good modification to these aerofoils.
2. Out of the three aerofoils considered in this project—namely NACA 0012, NACA 0018, and S 1046 – the NACA 0018 with flap is more efficient than the other two aerofoils.
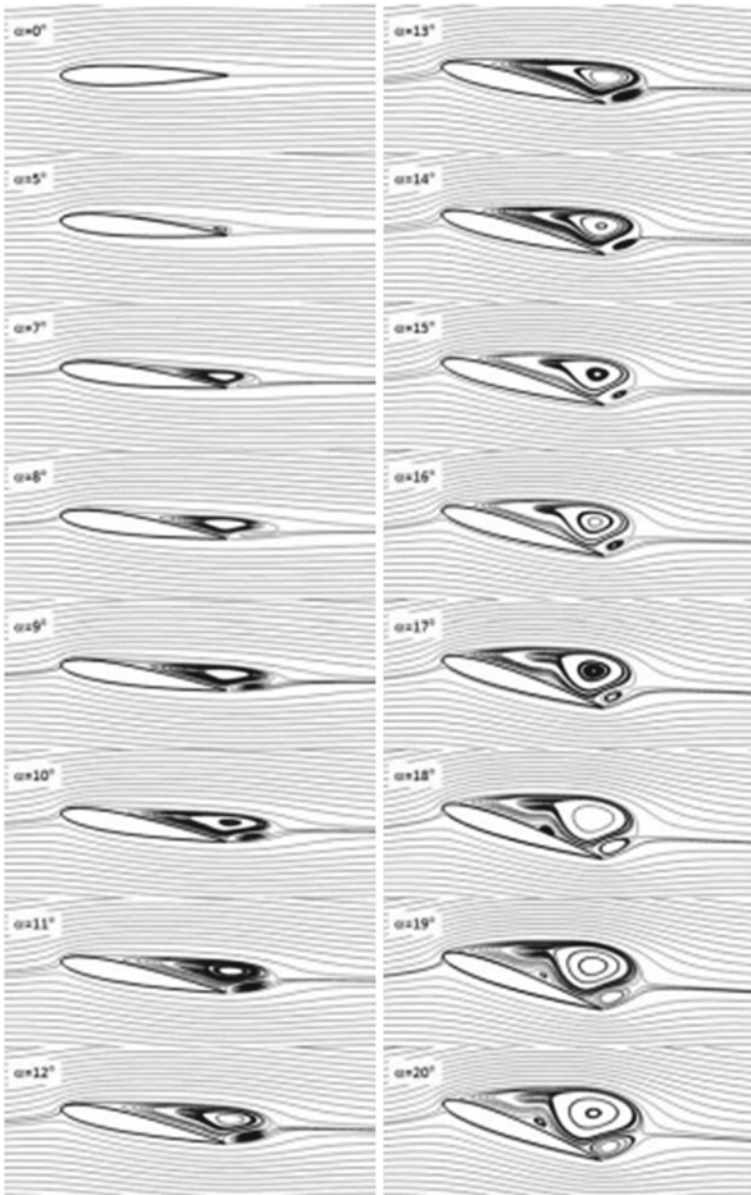
Fig. 12 Streamlines at different angles of attack (α) below 20° for NACA 0012 (2015)

Table 3 Coefficient of Lift (C_L) for flap deflection from 0° to 10°

AOA (degree)	NACA 0012	NACA 0018	S 1046
0	1.78E+00	7.96E+00	−4.65E+00
1	6.39E+00	5.00E+00	6.10E+00
2	1.20E+00	9.62E+00	1.11E+00
3	1.42E+00	1.37E+00	1.71E+00
4	2.03E+00	1.93E+00	2.27E+00
5	2.39E+00	2.19E+00	2.73E+00
6	2.95E+00	2.74E+00	3.21E+00
7	3.57E+00	3.16E+00	3.70E+00
8	4.00E+00	3.58E+00	4.43E+00
9	4.61E+00	4.13E+00	4.85E+00
10	4.85E+00	4.63E+00	4.59E+00

Table 4 Coefficient of Drag (C_d) for flap deflection from 0° to 10°

AOA (degree)	NACA 0012	NACA 0018	S 1046
0	1.10E+00	2.38E+00	1.12E+00
1	1.05E+00	2.38E+00	1.15E+00
2	1.04E+00	2.40E+00	1.14E+00
3	1.12E+00	2.42E+00	1.20E+00
4	1.07E+00	2.47E+00	1.19E+00
5	1.10E+00	2.51E+00	1.25E+00
6	1.15E+00	2.61E+00	1.25E+00
7	1.19E+00	2.67E+00	1.36E+00
8	1.24E+00	2.74E+00	1.33E+00
9	1.29E+00	2.88E+00	1.38E+00
10	1.38E+00	2.98E+00	1.73E+00

3. Though the drag of NACA 0018 is higher than NACA 0012 and S 1046 (all with flap), the lift obtained is dramatically high. This makes it best suited for implementing on a vertical axis wind turbine.
4. With more modifications to these aerofoils, their lift and drag characteristics can be improved and desired values of lift and drag can be reached so as to obtain higher lift.
5. With higher lift characteristics, these aerofoils will be able to generate more energy in wind turbines and will help reduce the load on conventional energy sources.
6. When implemented on airplane, they will provide more lift helping reduce the use of fuel and will cut the cost of aviation fuel required by a great margin.

5 Future Scope

1. The world is in dire need of improvement in non-conventional energy resources so as to meet the day-by-day increasing energy demand. Wind energy is one of the most reliable resources in this aspect. This project provides a suggestion for the improvement in the conventional designs of airfoils implemented for harnessing wind energy.

2. An airfoil is a basic shape used in any wind turbine blade. It is because of the characteristics of this shape, the way it behaves with respect to incoming wind that makes it most suitable for use in airplanes, wind turbines, etc.

3. With modification in this shape, such as leading edge and trailing edge flaps, slats, and wing tip devices, the lift and drag characteristics can be improved and ultimately the efficiency can be increased. Here we have provided computational analysis of one such modification with the results.

4. In the future, this modification can help us reach the desired configurations and to increase the energy production of wind turbines and lower the fuel consumption manifolds. Wind energy is a clean form of energy, and it does not harm our environment in any way and neither does it add on to the crisis of pollution. This project is a step forward in the direction of upliftment of the ways in which it is harnessed. This will ultimately help mankind in creating a prosperous future for coming many generations.

References

Ganesh Ram RK, Cooper YN, Bhatia V, Karthikeyan R, Periasamy C (2014) Design optimization and analysis of NACA 0012 airfoil using computational fluid dynamics and genetic algorithm. Appl Mech Mater 664:111–116. https://doi.org/10.4028/www.scientific.net/AMM.664.111.

Kurtulus DF (2015) On the unsteady behavior of the flow around NACA 0012 airfoil with steady external conditions at Re=1000. Int J Micro Air Veh 7(3):301–326. https://doi.org/10.1260/1756-8293.7.3.301

Senthil Kumar M, Naiju CD, Patruni H (2018) Experimental study and CFD analysis of an aerofoil structure for automotive body design. SAE Tech Pap 2018. https://doi.org/10.4271/2018-28-0091.

Srinivasa Rao T, Mahapatra T, Chaitanya Mangavelli S (2018) Enhancement of lift-drag characteristics of NACA 0012. Mater Today Proc 5(2): 5328–5337. https://doi.org/10.1016/j.matpr.2017.12.117

Yan Y, Avital E, Williams J, Korakianitis T (2019) CFD analysis for the performance of Gurney flap on aerofoil and vertical axis turbine. Int J Mech Eng Robot Res 8(3):385–392. https://doi.org/10.18178/ijmerr.8.3.385-392

Yang Y, Li C, Zhang W, Guo X, Yuan Q (2017) Investigation on aerodynamics and active flow control of a vertical axis wind turbine with flapped airfoil. J Mech Sci Technol 31(4):1645–1655. https://doi.org/10.1007/s12206-017-0312-0

Zaheer Z, Reby Roy KE, Nair GS, Ragipathi V, Niranjan UV (2019) CFD analysis of the performance of different airfoils in ground effect. J Phys Conf Ser 1355(1). https://doi.org/10.1088/1742-6596/1355/1/012006

Zhang T-T, Huang W, Guo Wang Z, Yan L (2016) A study of airfoil parameterization, modeling, and optimization based on the computational fluid dynamics method. J Zhejiang Univ Sci A 17(8): 632–645. https://doi.org/10.1631/jzus.A1500308

Recent Advances in Manufacturing Infrastructure

Multi-response Optimization and Effect of Alumina Mixed with Dielectric Fluid on WEDM Process of Ti6Al4V

Jay Vora, Nisarg Prajapati, Smit Patel, Shlok Sheth, Aditya Patel, Sakshum Khanna, Izaro Ayesta, L. N. López de Lacalle, and Rakesh Chaudhari

Abstract Titanium and titanium alloys (Ti6Al4V) are functional materials that have various uses in the marine, chemical, biomedical, aerospace fields because of their unique combination of mechanical and physical properties. Conventional machining of Ti6Al4V is difficult owing to its high hardness, higher chemical reactivity, and lower thermal conductivity. Non-contact operation between tool and work material such as wire electrical discharge machining (WEDM) process was found to be most effective. In the current study, the effect of different input machining parameters of the WEDM process has been studied for Ti6Al4V. Selected input WEDM process parameters based on past literature include pulse on time (T_{on}), pulse off time (T_{off}), and current while material removal rate (MRR) and surface roughness (SR) as the response variables. Grey relational analysis (GRA) technique along with Taguchi's design was used for attaining multiple objectives simultaneously. A validation study was conducted to verify obtained results from optimization. Lastly, results obtained by GRA at optimal parameter settings were compared with nano-alumina powder mixed with dielectric fluid at a concentration of 1 g/l. Improvement in the value of MRR and SR was found by 22.08% and 16.25%, respectively, for Ti6Al4V.

Keywords WEDM · TI6AL4V · ANOVA · GRA · Nano-alumina powder · Optimization

1 Introduction

Titanium and titanium alloys are functional materials that have various uses in the marine, chemical, biomedical, aerospace fields because of their unique combination of mechanical and physical properties (Chaudhari et al. 2020a, b; Khanna et al. 2020,

J. Vora · N. Prajapati · S. Patel · S. Sheth · A. Patel · S. Khanna · R. Chaudhari (✉)
Department of Mechanical Engineering, Pandit Deendayal Energy, University, Gandhinagar, Gujarat 382007, India

I. Ayesta · L. N. L. de Lacalle
Department of Mechanical Engineering, University of the Basque Country, Escuela Superior de Ingenieros Alameda de Urquijo s/n., 48013 Bilbao, Spain

2021b). These materials are highly resistant to fatigue and have a satisfactory tensile strength at higher temperatures. The high toughness of these materials allows them to be used to produce machine parts and molds. Ti6Al4V is one of the most widely used alloys of titanium. It is an α-β titanium alloy that consists of 6% of aluminum and 4% of vanadium. It has a higher strength-to-weight ratio and has great biocompatibility. It is also considered a better corrosion resistive material compared to materials such as stainless steel and various alloys based on cobalt (Arrazola 2009; Khanna 2021a). It is the most commonly preferred material in the aerospace industry due to its lower density, higher strength, and corrosion resistive properties (Gupta 2021). Titanium alloys can be used when direct contact with a bone or tissue is required because of their great biocompatibility (Haghighat 2021). Conventional machining of titanium alloys is difficult owing to their high hardness, higher chemical reactivity, and lower thermal conductivity (Chaudhari et al. 2019, 2020c, d). Furthermore, as the material is very hard, the tool wear rate is very high and the time consumed to machine it is also very high. Various types of coolants are used to decrease the amount of heat generated among the workpiece and the tool, which significantly elevates the cost of production. The incongruities during machining make it challenging to imagine outcomes. Oke et al. (2020) concluded that in traditional machining, the common procedure to date is to cut titanium at high depth, however, with a lower cutting speed. Hence, compared to traditional steel machining the rate of production is significantly reduced. Cutting apparatuses and workpieces undergo a substantial amount of damage, which has been accounted as a significant challenge while machining alloys of titanium utilizing conventional methods of machining. Hence, non-conventional techniques are used to machine this element.

Wire electrical discharge machining (WEDM) is one such unconventional method of machining that can be used to machine titanium alloys (Chaudhari 2019; Prasad et al. 2021). WEDM uses sparks that are generated between the metal workpiece and the tool to remove the material (Sheth et al. 2020; Rathi et al. 2020; Chaudhari et al. 2020e). Materials like titanium alloys are difficult to machine, and WEDM can be used to machine such materials economically and effectively. There are many input process parameters through which one can machine an element and obtain the desired output. WEDM method has numerous process variables which needed to be controlled to acquire a better surface. Along with better surface integrity, higher productivity is also a key requirement of any industry that can be obtained by increasing MRR and simultaneously decreasing SR value. Nanopowder-mixed dielectric fluid for the WEDM process is one of the ways of improving the process capabilities and achieving both objectives simultaneously. Prasad et al. (2021) concluded that T_{ON} and peak current were the most considerable factors on which R_a and MRR were dependent while machining Ti6Al4V using WEDM. Dabade and Karidkar (2016) used L8 orthogonal array (OA) for determining the influence of machining variables on MRR, Kerf width, dimensional deviation, and SR while machining Inconel 718 through WEDM. They concluded that T_{on} was the most important parameter among other parameters. Sivaprakasam et al. (2014) performed micro-WEDM on titanium alloy and with the help of ANOVA determined

that voltage, feed rate, and interaction of voltage and capacitance were the most significant parameters for MRR, kerf width, and SR. Chakraborty et al. (2020a) mixed boron carbide (B_4C) of grain size 10 µm with different dielectrics like kerosene, deionized water, and surfactant added deionized water for machining titanium alloy with WEDM. Porwal and Maurya (2019) reviewed that for determining the optimal limit of response variables like MRR, SR, Kerf width. Artificial neural network (ANN) modeling is a better approach compared to mathematical modeling. Pramanik et al. (2019) performed WEDM on titanium alloy and conveyed how the output parameters kerf width, MRR, discharge gap, and wire degradation were affected by input parameters like pulse on time, flushing pressure, and wire tension. Chakraborty et al. (2020b) conducted powder mixed wire EDM (PMWEDM) on Ti6Al4V and concluded that in order to achieve high productivity with lower energy consumption, low pulse is favored. Yi et al. (2017) used cutting fluid suspended with graphene oxide for the drilling of Ti6Al4V and determined that there was a significant improvement in SR up to 15.1% and also the cutting force reduced by 17.21% when graphene oxide was mixed with cutting fluid compared to conventional cutting fluid. A review study conducted by Gupta et al. (2020) showed that powder mixed dielectric fluid has shown better machining of titanium alloys. A comparative study between the regression model and adaptive-network-based fuzzy inference system (ANFIS) model was conducted by Kumar et al. (2019) concluded that the ANFIS model performed better than the regression model in predicting SR and MRR while machining Ti-6Al-4 V. A research experiment conducted by Gugulothu (2020) determined that drinking water was a better dielectric fluid compared to deionized water and the mixture of deionized and drinking water during the electrical discharge machining of titanium alloy. Also, applying analysis of variance (ANOVA) it was figured that T_{on} has a major impact on SR, whereas for MRR the discharge current plays a similar role.

In this paper, Taguchi's L9 orthogonal array was used to conduct the experiments of Ti6Al4V alloy. Selected input WEDM process parameters based on past the literature include pulse on time (T_{on}), pulse off time (T_{off}), and current while MRR and SR as the response variables. The adequacy and significance of machining parameters were tested by ANOVA for each response variable. Taguchi's approach has a limitation of attaining only one response variable at a time. According to the same, the GRA technique along with Taguchi's design was used for attaining multiple objectives simultaneously. A validation study was conducted to verify obtained results from optimization. Nanopowder-mixed dielectric fluid for the WEDM process can improve the process capabilities. Pursuant to the same, at optimized parameter settings obtained, alumina powder was mixed with dielectric fluid at a concentration of 1 g/l, and results were compared to understand the significance of the PMWEDM process.

2   Experimental Setup and Experimentation

Experiments of the present study were performed on concord wire-cut EDM appa-
ratus (DK7732) by using work material of titanium-based alloy Ti6Al4V having
dimensions of 10 mm diameter rod. Figure 1 shows the experimental setup of the
WEDM process used in the current study. A wire of material molybdenum having a
diameter of 0.18 mm is used as a tool electrode along with deionized water as dielec-
tric fluid. The effect of nano-alumina (Al_2O_3) powder concentration mixed dielectric
fluid on selected response variables (MRR and SR) has been studied by comparing
the results obtained between with and without the addition of nano-alumina powder
in dielectric fluid. Nano-alumina powder was mixed properly with dielectric fluid
in the main tank, and then it was sprayed through nozzles in the machined zone.
SR and MRR were considered as process variables for output, whereas discharge
current, T_{on}, and T_{off} were selected as machining variables. For the experimentation,
three levels for each of the three control parameters were selected using Taguchi's
L9 orthogonal array. All the experiments were repeated 3 times for better accuracy,
and the average value has been considered for analysis. MRR was determined by
dividing the difference between the initial mass and the final mass after machining
against the time taken to machine it. On the other hand, the measurement of SR was

Fig. 1   WEDM setup

Table 1 Taguchi's L9 array with experimental results

Sr. no	T_{on} (μs)	T_{off} (μs)	Current (A)	MRR (gram/sec)	SR (μm)
1	60	5	3	0.003217	5.55
2	60	10	4	0.003571	6.2
3	60	15	5	0.003700	7.16
4	80	5	4	0.004545	6.8
5	80	10	5	0.004774	7.5
6	80	15	3	0.003947	5.21
7	100	5	5	0.005681	7.6
8	100	10	3	0.004518	6.02
9	100	15	4	0.004838	7.13

completed using Mitutoyo make surftest SJ-410 model. The values were obtained experimentally for SR and MRR for the selected nine trials as shown in Table 1.

3 Results and Discussion

3.1 Analysis of Response Variables

MRR plays an important role in increasing productivity, and hence, higher MRR is a favorable outcome for the experiment. Table 1 represents MRR values for the preferred trials of experimentation. Minitab 14 statistical software was considered for the analysis of the experimental data. To obtain the input process variables on each of the output process variables, analysis of variance or ANOVA approach was utilized, with a confidence level of 95%. Table 2 shows the significance of input variables T_{on}, T_{off}, and discharge current on the output parameter MRR. The close relation of the R-square values signifies that the model is appropriate for MRR. As we have considered a confidence level of 95%, the value P for any input parameter should be lesser than

Table 2 ANOVA for MRR and SR

Source	DF	Adj SS	Adj MS	F Value	P Value
ANOVA for MRR					
T_{ON}	2	0.000004	0.000002	94.87	0.01
T_{OFF}	2	0	0	4.21	0.192
Current	2	0.000001	0.000001	27.59	0.035
Error	2	0	0		
Total	8	0.000005			

Table 2 (continued)

Source	DF	Adj SS	Adj MS	F Value	P Value
R-sq = 99.22%, R-sq(adj) = 96.87%					
ANOVA for SR					
T_{ON}	2	0.58702	0.29351	2.25	0.308
T_{OFF}	2	0.03376	0.01688	0.13	0.886
Current	2	5.08776	2.54388	19.49	0.049
Error	2	0.26109	0.13054		
Total	8	5.96962			
R-sq = 95.63%, R-sq(adj) = 82.51%					

0.05 to consider that parameter as significant (Chaurasia et al. 2019; Wankhede et al. 2020). The value of P for T_{off} is greater than 0.05, and hence, it can be considered as an insignificant parameter for MRR. The most important parameter for MRR is T_{on} with a contribution of 80% followed by discharge current and T_{off}. Figure 2 shows the influence of the three parameters at various levels of input on MRR. The increase in discharge current elevates the discharge energy which causes the rise in MRR. The increase in the value of T_{on} signifies a rise in the duration of a spark which causes the discharge energy to increase. The reason for this can be attributed to the fact that as T_{on} and current increase, discharge energy and spark intensity also upsurge which causes a rise in the melting and vaporization of the material from the workpiece at

Fig. 2 Main effect plot for MRR

the machining zone resulting in the escalation of MRR (Chaudhari 2019). Hence, an increase in T_{on} increases MRR. However, a continuous decrease in the value of MRR has been observed with an increase in the value of T_{off} because this is due to the absence of the spark during the machining (Chaudhari 2019).

To acquire better surface quality, the minimum value of SR is desired. Table 2 shows ANOVA for surface roughness. As per ANOVA, current plays the most dominant role on the surface roughness with 85.22% contribution. As the value of P was observed to be less than 0.5 for T_{on} and T_{off} which shows that T_{on} and T_{off} are not affecting SR. An extreme close relation between the R-squared values shows the adequacy of the model. A major impact plot for surface roughness contemplating the disparity in the level of input parameters is demonstrated in Fig. 3. Figure 3 shows that the value of SR was observed as increasing with an increase in the value of T_{on}. Because of the increase in the value of T_{on}, the discharge energy increases; this in succession raises the rate of melting and induces to inflate crater size and provides higher SR (Chaudhari et al. 2020c). The amount of SR is found to be decreasing as T_{off} increases. This is due to the decrease in discharge energy with an increase in T_{off}. With the increase in current, the SR appears to be increasing. Ionization of deionized water happens when a high current flows, which generates high discharge and thermal energy (Chaudhari et al. 2020c). Hence, it creates deeper and larger craters and elevates surface roughness.

For MRR, $A_3B_1C_3$ is achieved as an ideal combination of input parameters. From the investigations in the L9 symmetrical exhibit, run 6 delivered the finest MRR of 0.005681 g/s. Furthermore, in the case of SR, the best performing combination

Fig. 3 Main effect plot for SR

Table 3 Validation trial

	Predicted	Experimental
Levels	$A_3B_1C_1$	$A_3B_1C_1$
MRR (gram/s)	0.004768	0.004783
SR (μm)	6.01	6.04

came out to be $A_1B_3C_1$. However, it can be observed that the optimal combination of machining parameters is not the same for both the selected objectives, which shows the need for a suitable optimization technique.

3.2 Optimization

Taguchi's methodology can enhance only a single objective at a time without considering its impact on other output parameters. To fulfill such contradicting objectives at a time, an idea parameter setting is essential. Thereby with the help of GRA, the problem can be converted into a single objective problem. Implementation of the GRA technique has yielded an optimal combination of machining parameters as $A_3B_1C_1$ as shown in Table 3. A validation trial has been conducted to verify obtained results from GRA. Close relation can be seen between the predicted and measured values from Table 3. It shows that the developed model along with GRA was found to be capable of predicting and optimizing the process parameters.

3.3 Effect of Alumina Powder Concentration on Response Variables

WEDM process consists of multiple process variables which should be controlled to acquire great surface. Along with better surface integrity, higher productivity is also a key requirement of any industry that can be obtained by increasing MRR and simultaneously decreasing SR. Nanopowder-mixed dielectric fluid for the WEDM process is one of the ways of improving the process capabilities and achieving both objectives simultaneously. The effect of nano-alumina (Al_2O_3) powder concentration mixed dielectric fluid on selected response variables (MRR and SR) has been studied by comparing the results obtained between with and without the addition of nano-alumina powder in dielectric fluid. Nano-alumina powder was mixed properly with dielectric fluid in the main tank, and then it was sprayed through nozzles in the machined zone. For comparison of results, two experiments were conducted at optimal parameters settings obtained from GRA. The obtained results are shown in Table 4. The MRR and SR values with the addition of nano-alumina powder were obtained as 0.005782 g/s and 4.95 μm, respectively, at input parameters of T_{on} at 100 μs, T_{on} at 5 μs, current at 3 A, and powder concentration at 1 g/l. An increase in

Table 4 Effect of nano-alumina powder on MRR and SR

Condition	Input process parameters	Response variables
With addition of Nano-Alumina powder at 1 g/l	Pulse on time = 100 µs Pulse off time = 5 µs Current = 3 A Powder conc. = 1 g/l	MRR = 0.006241 g/sec SR = 4.55 µm
Without Nano-Alumina powder	Pulse on time = 100 µs Pulse off time = 5 µs Current = 3 A Powder conc. = 0 g/l	MRR = 0.004768 g/sec SR = 6.01 µm

nano-alumina powder concentration has increased MRR due to a higher erosion rate and simultaneously decreases SR due to uniform sparking distribution and uniform flushing of debris (Yih-Fong and Fu-Chen 2005; Chaudhari et al. 2021). It can be observed from Table 4 that MRR and SR of the Ti6Al4V were improved by 23.62% and 31.86%, respectively, with the addition of nano-alumina powder concentration with dielectric fluid at 1 g/l.

4 Conclusions

In the current study, the impact of T_{on}, T_{off}, and discharge current on resulting factors like MRR and SR are examined through the WEDM process for Ti6Al4V. The significance of input parametric quantities such as T_{on} and discharge current is dominant for MRR, whereas in the case of SR, discharge current played a major role. By analyzing the data on ANOVA for MRR, T_{on} came out to be the major affecting factor with the contribution of 80% followed by discharge current. On contrary, change in T_{off} does not show any effect on MRR. Furthermore, the key contribution of about 85.22% by discharge current followed by T_{on} with 9.83% and T_{off} with 0.56% was discovered for the output variable of SR. For both MRR and SR, a very close relationship with the least difference was observed between R-squared and Adj R-squared for SR which shows the suitability of machining parameters. Through GRA, the optimum parametric settings for maximizing MRR and minimizing SR were unveiled to be $A_3B_1C_1$ (T_{on} = 100 µs, T_{off} = 5 µs, and current = 3 A). A validation study showed a negligible difference between predicted and examined values. Lastly, results obtained by GRA at optimal parameter settings were compared with nano-alumina powder mixed with dielectric fluid at a concentration of 1 g/l. It was found that MRR and SR of the Ti6Al4V were improved by 23.62% and 31.86%, respectively, with the addition of nano-alumina powder concentration with dielectric fluid at 1 g/l.

References

Arrazola P-J et al (2009) Machinability of titanium alloys (Ti6Al4V and Ti555. 3). J Mater Process Technol 209(5):2223–2230

Chakraborty S, Mitra S, Bose D (2020a) Performance analysis on eco-friendly machining of Ti6Al4V using powder mixed with different dielectrics in WEDM. Int J Autom Mech Eng 17(3):8128–8139

Chakraborty S, Mitra S, Bose D (2020b) Experimental investigation on enhancing die corner accuracy during powder mixed wire EDM of Ti6Al4V. Mater Today Proc

Chaudhari R et al (2019a) Multi-response optimization of WEDM process parameters for machining of superelastic nitinol shape-memory alloy using a heat-transfer search algorithm. Materials 12(8):1277

Chaudhari R et al (2019b) Pareto optimization of WEDM process parameters for machining a NiTi shape memory alloy using a combined approach of RSM and heat transfer search algorithm. Adv Manuf 2019:1–17

Chaudhari R, Vora J, Parikh DM, Wankhede V, Khanna S (2020a) Multi-response optimization of WEDM parameters using an integrated approach of RSM–GRA analysis for pure titanium. J Inst Eng (India) Ser D, 1–10

Chaudhari R, Vora JJ, Parikh D (2020b) A review on applications of nitinol shape memory alloy. In: Recent advances in mechanical infrastructure: proceedings of ICRAM 2020, p 123

Chaudhari R et al (2020c) Effect of WEDM process parameters on surface morphology of nitinol shape memory alloy. Materials 13(21):4943

Chaudhari R et al (2020d) Surface analysis of wire-electrical-discharge-machining-processed shape-memory alloys. Materials 13(3):530

Chaudhari R et al (2020e) Optimization of parameters of spark erosion based processes. Spark erosion machining. CRC Press, pp 190–216

Chaudhari R, Vora J, Lacalle LN, Khanna S, Patel VK, Ayesta I (2021) Parametric optimization and effect of nano-graphene mixed dielectric fluid on performance of wire electrical discharge machining process of Ni55. 8Ti shape memory alloy. Materials 14(10):2533

Chaurasia A, Wankhede V, Chaudhari R (2019) Experimental investigation of high-speed turning of Inconel 718 using PVD-coated carbide tool under wet condition. Innovations in infrastructure. Springer, pp 367–374

Dabade U, Karidkar S (2016) Analysis of response variables in WEDM of Inconel 718 using Taguchi technique. Procedia Cirp 41:886–891

Gugulothu B (2020) Optimization of process parameters on EDM of titanium alloy. Mater Today Proc 27:257–262

Gupta V, Singh B, Mishra R (2020) Machining of titanium and titanium alloys by electric discharge machining process: a review. Int J Mach Mach Mater 22(2):99–121

Gupta MK et al (2021) Experimental characterisation of the performance of hybrid cryo-lubrication assisted turning of Ti–6Al–4V alloy. Tribol Int 153:106582

Haghighat PJ et al (2021) A simple approach to design fluorapatite glass-ceramic coatings on the surface modified Ti6Al4V substrates for biomedical applications. J Aust Ceramic Soc 2021:1–13

Khanna S, Patel R, Marathey P, Chaudari R, Vora J, Banerjee R, Ray A, Mukhopadhyay I (2020) Growth of titanium dioxide nanorod over shape memory material using chemical vapor deposition for energy conversion application. Mater Today Proc 28:475–479

Khanna S et al (2021a) Unravelling camphor mediated synthesis of TiO2 nanorods over shape memory alloy for efficient energy harvesting. Appl Surf Sci 541:148489

Khanna S, Marathey P, Paneliya S, Chaudhari R, Vora J (2021b) Fabrication of rutile–TiO2 nanowire on shape memory alloy: a potential material for energy storage application. In: Mater Today Proc

Kumar S, Dhanabalan S, Narayanan C (2019) Application of ANFIS and GRA for multi-objective optimization of optimal wire-EDM parameters while machining Ti–6Al–4V alloy. SN Appl Sci 1(4):1–12

Oke SR et al (2020) An overview of conventional and non-conventional techniques for machining of titanium alloys. Manuf Rev 7:34

Porwal R, Maurya, R (2019) A contribution concerning trends in modelling of Wire-micro EDM of Titanium alloys-a review. In: IOP conference series: materials science and engineering. IOP Publishing

Pramanik A, Basak A, Prakash C (2019) Understanding the wire electrical discharge machining of Ti6Al4V alloy. Heliyon 5(4):e01473

Prasad AR, Ramji K, Kolli M (2021) Machinability studies of lead induced Ti-6Al-4V alloy using Taguchi technique on WEDM process. Mater Today Proc

Rathi P et al (2020) Multi-response optimization of Ni55. 8Ti shape memory alloy using Taguchi–grey relational analysis approach. In: Recent advances in mechanical infrastructure. Springer, pp 13–23

Sheth M et al (2020) Multi-objective optimization of Inconel 718 using combined approach of Taguchi—grey relational analysis. Advances in mechanical engineering. Springer, pp 229–235

Sivaprakasam P, Hariharan P, Gowri S (2014) Modeling and analysis of micro-WEDM process of titanium alloy (Ti–6Al–4V) using response surface approach. Eng Sci Technol Int J 17(4):227–235

Wankhede V et al (2020) Experimental investigation of FDM process parameters using Taguchi analysis. Mater Today Proc 27:2117–2120

Yi S et al (2017) Performance and mechanisms of graphene oxide suspended cutting fluid in the drilling of titanium alloy Ti-6Al-4V. J Manuf Process 29:182–193

Yih-Fong T, Fu-Chen C (2005) Investigation into some surface characteristics of electrical discharge machined SKD-11 using powder-suspension dielectric oil. J Mater Process Technol 170(1–2):385–391

Application of Friction Stir Welding (FSW) in Automotive and Electric Vehicle

Karn Kavathia and Vishvesh Badheka

Abstract Friction stir welding (FSW) is a newly patented welding process. The recent development of FSW is improving the process and replacing other welding practices in almost all manufacturing industries. This technique is still under study for further development and to be used in various applications such as in the field of aerospace, automotive, railway, shipbuilding and offshore, and much more. In this paper, authors have studied FSW and its application in the automotive industries. FSW has replaced other welding methods and are observing benefits in technical and economical terms. The existence of this process in the automotive industries has already taken place into creation of new products. But the change in the mode of automotive industries from IC engines to electric vehicles questions the existence of the FSW process and application under electric vehicles.

Keywords Friction stir welding · Automotive · Manufacturing process · Friction welding

1 Introduction

Friction stir welding is an invented welding process by the inventors of The Welding Institute (TWI). They were the first ones to submit an original patent. It is still under the process of development at The Welding Institute and many other institutions. This process is known for the solid-state joining process, and it is considered the most important development in the field of metal bonding under green technology. Initially, this process is used in many industries to join aluminum alloys (Thomas et al. 1991; Dawes et al. 1995). The basic concept of FSW is simple as shown in Fig. 1. A uniquely designed pin and shoulder non-consumable rotary tool insert into the plates or adjacent edges of the plates to be connected and extends transversely along the parting line. The heat generated by the tool causes friction between the tools and the workpiece, resulting in plastic deformation of the workpiece. The rotational motion

K. Kavathia (✉) · V. Badheka
Pandit Deendayal Energy University, Gandhinagar, Gujarat 382426, India
e-mail: karn.kmc18@sot.pdpu.ac.in

Fig. 1 Schematic drawing of friction stir welding (FSW)
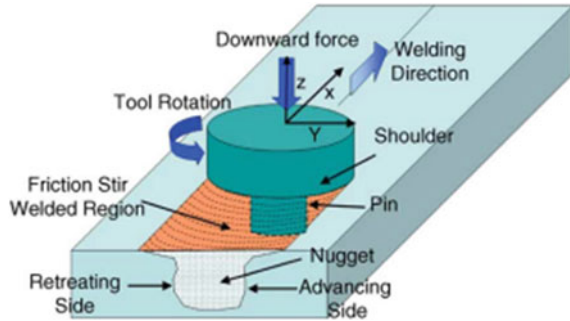
of the pin generates localized heating which causes melting of material surrounding the pin. The rotational and translation motion of the pin moves material from the front of the pin to the back of the pin. Using this process, a joint is created under a solid-state condition. In brief, the process is defined as a method of connecting two or more workpieces, in which the tool moves in a periodic rotation concerning the workpiece, enters the joint area, locally plasticizes, and then moves along the interface, thereby creating a solid bond between the workpieces' (Mishra and Ma 2005).

Conventional friction stir welding is performed by firmly fixing the plates to be joined on a welding jig. The design of the fixture is a very important consideration. The plates are fixed on the connecting line without gaps. The welding process requires the need to prevent the workpiece from spreading and lifting during the welding process. This is the reason why welding accessories are generally equipped with features that can limit the workpiece. FSW accessories are usually equipped with a removable anvil, if accidental damage to the anvil is caused by contact with the pin of the welding tool, it can be replaced. Because the anvil insert is highly coupled with the workpiece in terms of heat transfer at the welding point. When designing FSW attachments, it is mandatory to consider the quality and diffusibility of the anvil insert.

2 Technical Justification of FSW

Compared with the arc welding process, the uniqueness and good characteristics of FSW provide a variety of technical basis for using this process because FSW is a solid-state welding process which shows improved weldability. Certain forms of materials are difficult to weld and cannot be welded, resulting in the formation of cracks and brittle phases, and the ability to join two different alloys together, which increases advantage. Reduced distortion is the result of reduced peak temperature leading to reduced longitudinal and traversing distortion. This resulted in a new construction method, and by reducing assembly problems and secondary processing operations, it significantly affected the total manufacturing and assembly costs. The

use of FSW and the reduction of maximum temperature and residual stress lead to fatigue cracks, corrosion, and stress corrosion performance are improved. This allows the technology to be used in long-life applications. FSW is an autogenously welding process that eliminates the use of filler metal and wire feeding which avoids the unnecessary cost. When welding the thick materials, FSW can accomplish in a single pass that improved joint strength and ductility. FSW is a fully mechanized process that improves joint path control for more consistent quality. As mentioned above, the FSW can be held firmly in place during the welding process, so the joint will not separate under the action of the welding tool, so the workpiece will stay in place with the anvil during the welding process. This causes the need of special fixture requirement that also has a practical restriction on the size of the workpiece. In FSW, it is possible to form butt weld, corner weld, and laps weld. The keyhole welding process is essential in figuring out how the weld joint begins and ends to form a repairable assembly. A retractable pin was manufactured to allow variable penetration of the weld, allowing the pin to gradually retract throughout the welding process, thus eliminating critical holes. The welding process produces nearly flawless welds for many heavy industries at a relatively low cost (Jones and Adams 1999; Lohwasser 2005).

3 Economic Justification of FSW

Since each application has a unique process, the economic rationale for FSW has been proposed in a few studies. FSW helps reduce processing time and direct labor. Compared to other welding methods, FSW can be completed in a single pass, with no cooling time, cleaning, inspection, and maintenance between passes. FSW is a fully mechanized process that is limited by the capabilities of the equipment used, which includes rotating the welding system and traversing the joint and the weld fixture used to restrain the workpiece during welding. High forces are used in this process, and the equipment and accessories have a certain cost. On the other hand, under the FSW economic reasons, the license fee to use the basic process is included. (Mononen 2001; Kallee and Mistry 1999; Midling et al. 1999; Thomas et al. 1993).

4 Comparison of FSW and Other Welding Parameters

Mishra and Ma (2005) have mentioned some of the benefits of using FSW. In terms of metallurgical benefits: solid-phase process, low single-piece deformation, good dimensional stability and repeatability, no loss of alloying elements, excellent metallurgical properties in the joint area, fine microstructure, no cracking, and replace connection done by fasteners of multiple parts. In terms of environmental benefits, no protective gas is required, surface cleaning is not required, grinding residues are removed, solvents required for degreasing are removed, and consumable materials

such as carpets, wires, or any other gas are saved. In terms of energy efficiency, the use of improved materials can reduce weight, reducing only 2.5% of the energy required for laser welding and reducing fuel consumption in light aircraft, automotive, and marine applications.

5 Friction Stir Welding in Automobile Industry

As people pay more and more attention to environmental pollution and the global fossil energy shortage, the auto industry has been trying to improve fuel efficiency by reducing the weight of vehicles. A possible solution to reduce the weight of the car is to introduce lightweight aluminum alloys to replace the structural steel parts. However, there is a problem of difficulty in joining aluminum. All aluminum car parts can be friction welded: bumper beam, rear spoiler, crash box, alloy wheels, air suspension system, rear axle, driveshaft, intake manifold, booster, water cooling for whichever is more suitable for FSW, the structure may need to be modified slightly, but should not be insurmountable. Due to the high electrical/thermal conductivity and a low melting point of aluminum alloys, burns and splashes are very common. Also, when combining aluminum alloy and steel, it is more difficult to obtain a good weld quality due to the difference in their physical properties that result in deformation and low strength. Although some people have successfully welded steel and aluminum, people have always believed that it is impossible to reliably and continuously weld directly between two dissimilar metals. In the automotive industry, rivets, bolts, and nuts are generally used for gluing and mechanical joining to join steel and aluminum alloys.

5.1 Friction Stir Welding of Steel and Aluminum Alloy

Aluminum alloy is a useful alternative to steel and can be used to make products in many advanced industrial applications. Aluminum alloy is considered a non-weldable material. It is difficult and uneconomical to weld aluminum alloys with fusion welding (tungsten inert gas and metal inert gas) and resistance welding techniques. FSW is solid-state welding that uses non-consumable rotating tools to weld aluminum alloys using friction energy. FSW does not require the preparation of solder joints, fusion, and remelting of materials to be joined. The FSW process can eliminate weld defects. Basic knowledge of FSW is required to perform it effectively. Choosing the appropriate process welding parameters and the temperature distribution during welding are important parameters that affect the quality and performance of the weld. FSW can be used to weld similar and different aluminum alloys. FSW can also be used to join aluminum alloys with high-strength steel and other lightweight materials. The progress of various types of FSW processes was discussed, such as friction stir tracing technology (FSS), fixed shoulder FSW process (SSFSW), friction

Table 1 Various alloys and its major alloying elements (Shah and Badheka 2019)

Alloy Series	Major alloy element
1XXX	Pure Aluminum
2XX	Copper (1.9–6.8%)
3XXX	Manganese (0.3–1.5%)
4XXX	Silicon (3.6–13.5%)
5XXX	Magnesium (0.5–5.5%)
6XXX	Magnesium and silicon (Mg 0.4–1.5%, Si 0.2–1.7%)
7XXX	Zinc (1–8.2%)
8XXX	Others

stir spot welding (FSSW), for welding alloys similar and different aluminum. From the current research, it is mentioned that FSW is very suitable for the mass production process, producing a large number of parts with high productivity (Rudrapati 2019) (Table 1).

Mahto et al. (2015) had an experiment on rolled AA 6061-T6 and AISI 304 stainless steel each having thickness of 1 mm. Place aluminum plates on top of steel plates to create overlapping joints between them. Use a high-speed tool HS10-4–3-10 with a hardness of 58 HRC. A tool with a shoulder diameter of 20 mm, a cylindrical pin diameter of 4 mm, and a pin height of 1 mm. Experiment with changing v and the PD tool, while maintaining the speed and rake angle (α) at 1800 rpm and 1°, respectively. When the tool is inserted into the top plate (Al), the shoulders and pins generate heat, which plasticizes the metal, and the applied pressure helps the aluminum atoms to diffuse into the steel plate, forming an IMC layer., which makes the connection between aluminum and steel. The results showed that an increase in v and PD showed a gradual increase in ultimate tensile shear stress. The maximum UTSS observed under a v of 125 mm/min and a tool PD of 0.3 mm is 220.73 MPa. This welding condition leads to a thermomechanical lock and an iron-rich IMC layer between the aluminum and the steel plate. At a higher value of v, due to the reduction of the heat-affected zone (HAZ), the heat input to the weld zone decreases. As welding speed increases, the base metal failure area moves to the RS side, which can lead to a higher USS. An increase in PD increased pressure strengthening the weld region. The percent elongation increases as v, and PD tools increase. Fe_2Al_5 is inherently brittle, and the thickness of the IMC must be at least 10 μm to obtain a good welding effect. The microhardness value of the welding surface from AISI 304 steel to AA6061-T6 sheet is measured at a distance of 2.2 mm from the welding center and AS and RS along the vertical direction within 0.2 mm. The hardness gradually increases along with the thickness of the steel, then suddenly increases to the maximum value at the Al/steel interface and then gradually decreases in the Al matrix. This sudden increase in hardness is due to the existence of IMC (Mahto et al. 2015; Movahedi et al. 2011; Bozzi et al. 2010) (Fig. 2).
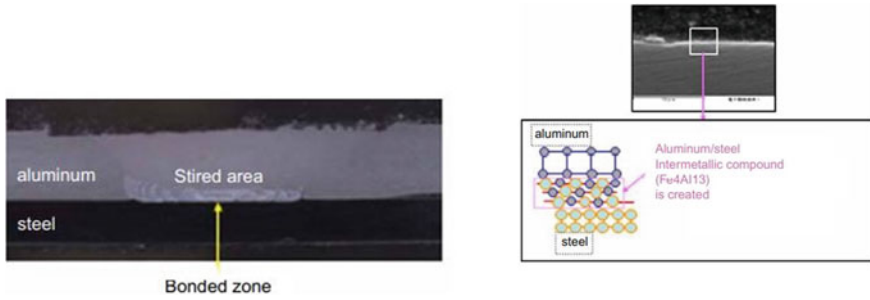
Fig. 2 **a**, **b** Bonding of steel and aluminum

5.2 Application

Honda has discovered a new technology that continuously joins steel and aluminum alloys using FSW to reduce vehicle weight and improve fuel economy. They used this welding method to fabricate the front subframe of the new "Accord 2013". This is the world's first application of FSW technology to mass-produced vehicles. As described above, the pin moves down and dives to reach the steel surface, the contact of the pin with the steel surface is detected, and the FSW tool stops moving down and stays there while the top of the pin is in contact with the steel surface. Then, the surface of the steel transforms into a plastic flow state and forms an intermetallic compound (Fe4Al13) to establish a strong metal bond between aluminum and steel. The FSW tool cuts the weld while maintaining a constant depth, while plasticizing adjacent aluminum areas along the direction of travel. Before sending the steel for FSW should be coated with a sealant on its surface. The sealant creates a gap between two different metals and spontaneously protects them from galvanic corrosion (Figs. 3 and 4).

Fig. 3 Subframe of Honda Accord 2013 model
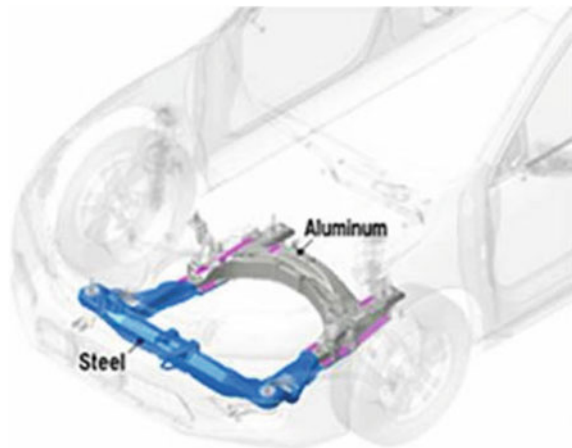
Fig.4 Sealing
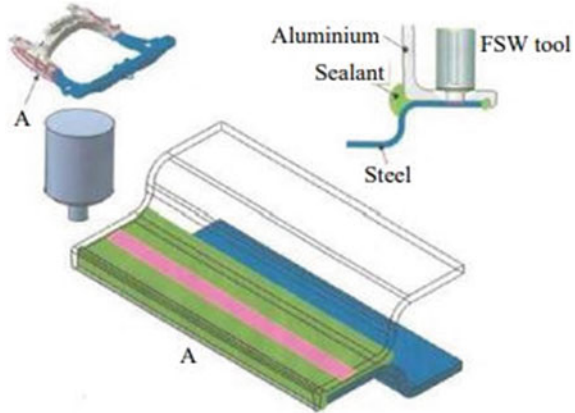
There are multiple positions to weld. Initially, there are four types of welding positions, as shown below.

Well, the main types of welds are (a) Fillet Weld (F): In this weld, two pieces of metal are fused at an approximate right angle to each other. (b) Grove Weld (G): A grove weld is formed when a filler metal is deposited in grove between two pieces of metal. In addition to this, some most common joints are also used as (a) Butt joint: Two pieces of metal are in the same plane joined by edges meeting. (b) Lap joint: Two pieces of metal partially overlap one another. (c) Corner joint: Two pieces are fused at a 90-degree angle. (d) T-joint: Two pieces are joined at a right angle. (e) Edge joint: Flat sides of two pieces of metal are welded together (Buel 2020). Getting back to welding the chassis of a vehicle will be a difficult task with respect to four deformation types of automotive chassis, namely vertical bending, lateral bending, horizontal lozenge, and longitudinal torsion Kamini Gupta (n.d.). The welded studs and shoulders have been processed in different positions to obtain a high-quality surface finish. Mentioning the position of the shoulder and the welding pin will be a tedious task, with different structures and sizes, but mainly focused on the manufacturing company and the model that made it. The results after applying this technique are surprising. The built-in steel/aluminum subframe is 25% lighter than the previous model that fastened two metal bolts together. The weight reduction of vehicles affects the improvement of fuel economy. This process allows the structure of the subframe to be changed so that the suspension mounting points can be repositioned, thereby increasing the rigidity of the mounting points by 20%, which should be translated into improving the dynamic performance of the car (Kusuda 2016) (Fig. 5).

Kallee (n.d.) listed a few applications. Ford of Detroit, USA, used FSW process for the center tunnel of Ford GT sports car. The center channel is a structural component that increases the rigidity of the chassis and also serves as a hermetic fuel tank. The location of the fuel tank provides good weight distribution and crash resistance. First
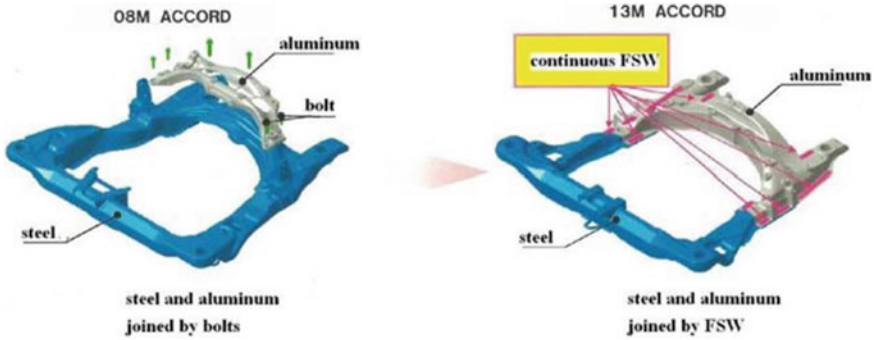
Fig. 5 Comparison between Honda Accord 2008 and Honda Accord 2013 respectively

install the mechanical components (including the fuel pump, liquid level sensor, and vapor control valve) on the rail. The one-piece fuel tank is then blow molded around the track. This "ship in a bottle" design concept maximizes the amount of fuel and reduces the number of connections to the fuel system (Fig. 6).

Mazda of Japan used friction stir spot welding on the rear door and engine cover of the Mazda RX-8. The hood of the sports car has an impact-absorbing structure designed to improve pedestrian protection. Compared to resistance spot welding, they use this process to prevent spatter and significantly reduce energy consumption (Fig. 7 and 8).

Pierburg, located in Dusseldorf, Germany, developed the concept of exhaust gas recirculation (EGR) cooler FSW. This product reduces the nitrogen oxides (NOx) of diesel engines by sending cooled exhaust gas into the combustion chamber. The cooler present here is made of die-cast aluminum which provides a layered rib structure. All the internal interfaces are FSW welded instead of using heat-resistant fasteners and seals.

Fig. 6 Friction Stir Welding for center tunnel of Ford GT
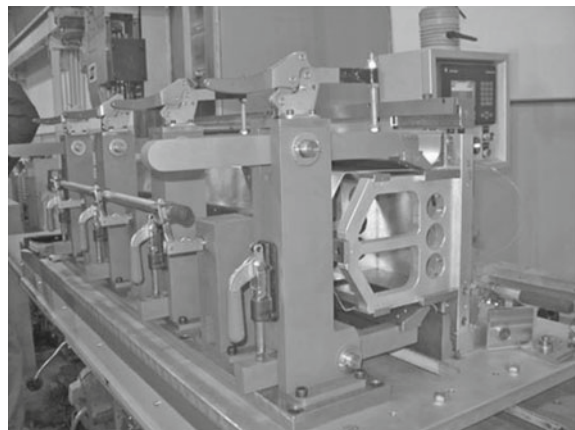
Fig. 7 Robotic friction stir welding arm for rear door of Mazda RX-8
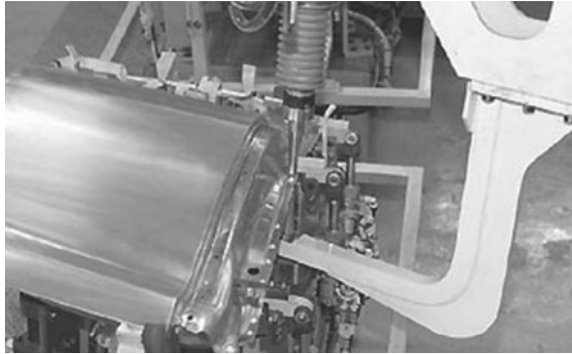
Fig. 8 Rear door outer panel of Mazda RX-8

The Tower Motor Company of Grand Rapids present in Michigan, USA, produces aluminum suspension linkages for Lincoln City Motors, which are designated as stretch luxury sedans. They are fitted with a heavy-duty rear axle, whereas the other rear suspension remains unchanged. The suspension connecting rod is comprised of two identical extrusions, and FSW is carried out at once with two screws on both sides. This gives out an excellent fatigue performance.

The Fontaine Trailer in Jasper, Alabama, USA, produced a 1.22 m high aluminum flatbed trailer. It weighs 3.5 tons, yet the maximum payload that can be carried is 27 tons. It has an FSW aluminum main beam, and an FSW floor with integrated side rails that uses FSW to improve floor strength, which can provide a higher payload and reduce fuel consumption.

New technology was discovered to connect two parts of a wheel, in which a cast or forged intermediate piece was FSW to a rim made from a forged alloy. This concept was industrialized by DanStir in Copenhagen and TWI. FSW allows for an inner cavity, reducing wheel weight by 20–25%.

6 Friction Stir Welding for Electric Vehicles

Driven by global issues including environmental policies, technological progress, economics, demographics, and changing consumer preferences, the world is ready to make a huge shift to electric and hybrid vehicles. Concepts such as driving with green energy have a direct impact on the use of aluminum. As a result, the automotive industry's demand for casting welding has soared. An example is the manufacture of battery trays and heat exchangers. This is where green energy and green technology meet-friction stir welding. Different kinds of cars are produced in the market, namely battery-powered cars and hybrid cars, as well as plug-in hybrid cars (Dragan 2014).

6.1 Bonding Technology Requirements in the Automotive Industry

Problems that come along with electric vehicles are characterized in that they are heavier than internal combustion engine vehicles, and energy storage devices account for most of the weight and costs involved. Another aspect of electric vehicle design is the unfavorable temperature behavior of storage devices. Large-capacity and heavy-duty battery systems should be installed with a low center of gravity, and the passenger compartment and trunk should be restricted as much as possible. These systems must be firmly installed and able to support the specific load of the vehicle during their service life. In addition, the system must not impair collision behavior and must take into account other hazards, such as fire and environmental pollution in dangerous situations.

For plug-in hybrid vehicles such as Volvo V60 Hybrid, the energy storage device is usually located in the rear axle area under the rear seats. The housing of the storage system of a hybrid vehicle is usually die-cast aluminum. To ensure temperature control, some manufacturers have integrated a cooling system on the floor and installed battery modules with low heat transfer resistance on the floor. The main difficulty lies in manufacturing the storage box to create a closed, pressure-tight cooling circuit that can withstand the stress caused by alternating pressure, resulting in small thermal deformation of the mounting surface and allowing permanent bonding of different aluminum alloys. In some plug-in hybrid vehicles, the cast housing is sealed with an extruded plate in a cooling circuit that can be integrated. In an all-electric vehicle, the housing for the storage devices occupies the majority of the vehicle's chassis area and is located primarily between the wheel axles. The power housing is installed separately, but some concepts indicate that the longitudinal beam has been integrated into the storage housing of the vehicle. To ensure the required stiffness of the storage box, these components are produced from a frame part with a beam welded to an aluminum base plate, or by using a double-walled extruded part welded together to form the base. The complex connection of the front and rear of the vehicle and the possible tightness and low component grade requirements due

to heat input during welding lead to high requirements for the storage box joining technology. When the battery box is manufactured, the seam must be sealed to seal the cooling circuit and to be able to reliably withstand the alternating pressure load for the life of the vehicle.

6.2 Battery Housing for Plug-In Hybrid Vehicles with Integrated Cooling Using FSW

Battery housings for plug-in hybrid vehicles are usually manufactured as die-cast parts. If the cooling circuit is integrated directly into the housing, the area must then be closed by welding on aluminum foil. Usually, the welding area is milled during the machining of the casting body, which causes irregularities in the skin and contact surface of the casting. The task is to design a component with the smallest cross-section in the welding area of the cast body to produce a wider rigidity in the area where the cooling water is connected. The flatness of the module mounting surface is critical to the optimal cooling of the battery pack. The weak point in the pressure component is the process-related exit hole at the end of each weld, which is caused by the angle of inclination and displaced material, so it is necessary to place the end of the seam outside the area pressure, and if the pressure surface is to be minimized, then the seam should be welded along the circumference "closing" the probe exit hole.

6.3 Battery Housing for Electric Vehicles Using FSW

The storage housing consists of an extruded profile, which is welded by arc welding to form a frame structure. After machining the seams in the base weld area, these frames are welded to a bottom plate or bottom plate made up of several double-walled extruded profiles to form a liquid-tight housing using a friction stir welding process. When using a double-walled substrate, it comes from both sides of a single compression piece in the preliminary operation. If the longitudinal edges cannot be used due to standard tolerances, the profile must be machined before welding. The amount of clearance has a great influence on the interface at the bottom of the seam, which must be taken into account when designing the component. The base plate is machined in the connection area, and the hollow profile is welded to the outer strip on which the cooling channel is integrated into the base plate. Machining steps are required to be able to weld the profile reliably and pressure-tightly. The energy storage shell concept is a part of the frame with additional support rods, which are sealed by the base plate. The friction stir welding process is used to weld the substrate around to seal the liquid. The struts are welded to the base plate to absorb the weight of the battery. For the concept of the base and the bottom, it is necessary

to ensure the process compatible design of the frame outline in the welding area. The stiffness of the profile is the main factor. For most manufacturers, the frame part of the side member is a part of the vehicle structure and must be designed to meet the requirements of a side impact. The wall thickness of the welding area must be defined as suitable for the process because the material surrounding the welding pin is plastic and does not contribute to the stiffness of the structure. The beginning and end of the seam will deform the contour and increase the wall thickness. These deformations can cause surface compaction defects.

7 Friction Stir Welding Defects and Causes

Incorrect selection of process parameters leads to insufficient/excessive heating during the process, which in turn leads to insufficient/excessive material flow at the joint. Welding defects are generated in friction stir welding (Leon and Bharathiraja 2020). Various common welding defects and their causes are as follows (Table 2).

Table 2 FSW defects and causes

Defect	Location	Causes	References
Tunnel	Between stirring zone (SZ) and thermomechanically affected zone (TMAZ) in advancing side	– High feed rate – Low tool rotational speed – Improper pin offset – Insufficient plunge depth	Tongne et al. (2015)
Void	Under weld surface or the advancing and retreating sides of the weld	– Inadequate forging pressure – High tool transverse velocity	Xavier and Jayabalan (2015)
Excess Flash	Outer edges of weld joint	– High tool rotation speed – Low weld speed – High vertical force	Soni et al. (2017)
Kissing bond	Advancing side of Stirring Zone (SZ)	– Insufficient material flow – Improper removal of oxide layer form faying surface	Zhou et al. (2018)
Hooking	Both retreating and advancing sides of thermomechanically affected zone (TMAZ)	– Improper tool design – Inappropriate tool tilt angle	Gharavi et al. (2016)

8   Application of Friction Stir Welding in Defects

As mentioned above, the author briefly described the role of FSW in solid-state joining technology, which is applicable to aluminum, copper, titanium, and steel in manufacturing. FSW also plays a role in the technology of repairing cast products, welded joints, worn, and corroded surfaces to change the microstructure or eliminate defects. Repair welding is a timeless process in the fabrication of structures. The repaired structure produces the same static strength, ductility, fracture toughness, and fatigue strength as the base structure. Previously, the welding process followed a series of sequences to avoid poor workmanship, part failure, resulting in a large number of warranty claims and customer dissatisfaction. Repairs are usually made for welding defects, defective parts, and worn parts (Fig. 9).

FSW can be used to repair gaps and defects and cracked parts. The method for repairing circular cavities in welds, longitudinal cavities on the surface and subsurface, and exit holes in processing include the step of making a plug-like filling material with the same composition as the original material or compatible with the original material. Place in a vacuum, place the vacuum and FSW through the plug (Fig. 10).

Welding Procedure
- The welding procedure is necessary and the welder must be able to use it. This serves as a user manual and includes process and specific information about welding technology.

Welding Equipment
- All materials such as welding torches, arches, pipes, brackets, grinders, and wire feeders should be easily accessible and stored in the welding cart.

Materials
- Sufficient materials must be properly stored for maintenance. Some common materials are inserts and fuels for preheating and interpass temperature, and shielding gas.

Alignment markers
- The alignment mark is the center punch mark, which is made by joints in different positions.

Welding Sequences

Safety
- Make sure the welder complies with all safety rules.

Weld Quality
- The welding quality must be checked. The final weld must be smooth, without gaps, and without reinforcements.

Fig.9 Logical sequence of successful repair welding (Salami and Khandani 2014)

Fig.10 Schematic
illustrating a method for
repairing a void (Rosen et al.
1998)
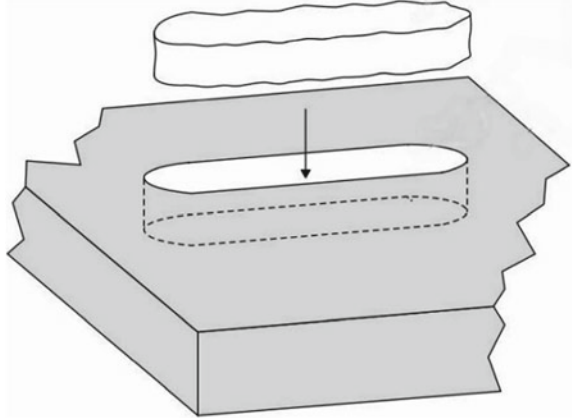
For the first time, Boeing announced a method to repair cracks in components using FSW. The cited method includes preparing the surrounding surface of the crack to repair and weld the first part of the component on the first side of the crack and the second part of the component on the second side of the crack to form a fusion crack area. The logical flow diagram for this method is shown below. To increase strength, the method can also include patches in the area of the fusion crack (Fig. 11).

9 Conclusions

In the end, FSW is discovered and has been into use from many years ago. Its discovery made many industrial changes in terms of technical and economical activities. Studies on FSW are playing a vital role in increasing application and replacing other harmful welding processes. This process has improved the weight and quality of the vehicle. A gradual shift from IC engine type vehicles to electric vehicles has increased the usage of this process in reducing weight and further expanding its application to electronic closure, inverter housing, and mounting brackets.
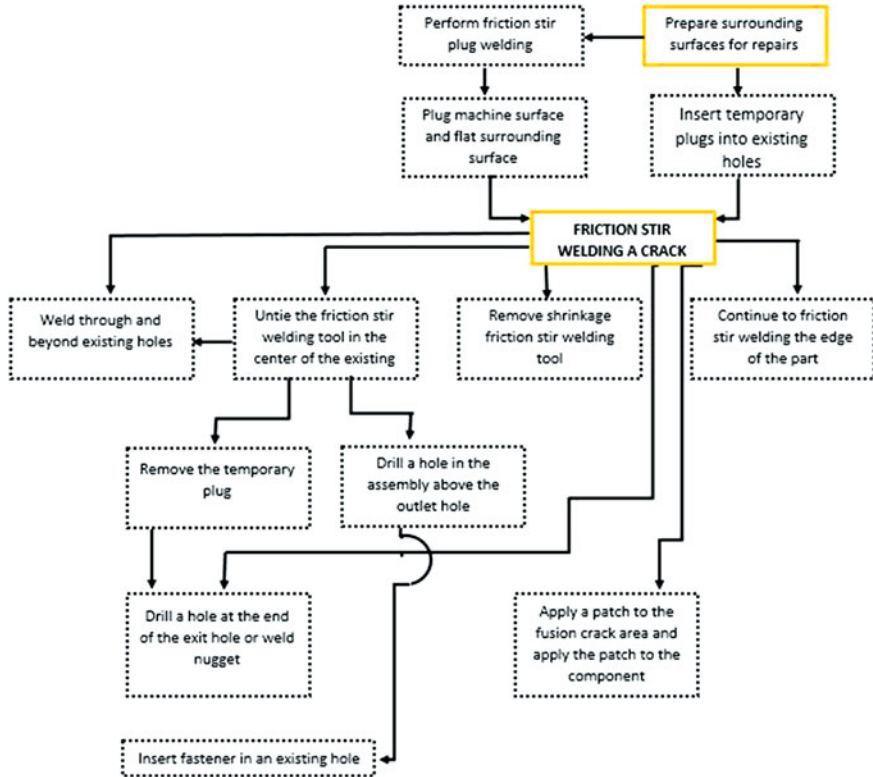
Fig.11 Logic flow diagram representing methods of repairing the crack (Talwar and Perez 2006)

References

Bozzi S, Helbert-Etter AL, Baudin T, Criqui B, Kerbiguet JG (2010) Intermetallic compounds in Al 6016/IF-steel friction stir spot welds. Mater Sci Eng A 527:4505–4509

Buel Z (2020) What are the different welding positions? Retrieved from Tulsa Welding School. https://www.tws.edu/blog/welding/what-are-the-different-welding-positions/. (13 Aug 2020)

Dawes C, Thomas W (1995) TWI bulletin 6, November/December 1995, p 124

Dragan M (2014). Bulletin of the institute of welding. Biuletyn Instytutu Spawalnictwa, no 5, pp 103–110

Gharavi F, Fadaeifard F, Matori KA, Yunus R, Othman NK (2016) Mechanical and structural evaluation of friction stir welded 6061 aluminium alloy lap joints at different welding speeds. Kov Mater 54(5):351–361

Jones C, Adams G (1999) Assembly of a full scale external tank barrel section using friction stir welding. 1st international symposium on friction stir welding, Thousand Oaks, CA, USA, 14–16 Jun 1999

Kallee SW (n.d.). Industrial applications of friction stirwelding. Friction stir welding, pp 118–163

Kallee SW, Mistry A (1999) Friction stir welding in the automotive body in white production. In: 1st international symposium on friction stir welding, Thousand Oaks, CA, USA, 14–16 June 1999

Kamini Gupta RS (n.d.) Design of golf cart frame for friction stir welding. Mater Design 2008

Kusuda Y (2016) Honda develops robotized FSW technology to weld steel and aluminum and applied it to a mass-production vehicle. Ind Robot Int J 40(3):208–212

Leon JS, Bharathiraja J (2020) A review on friction stir welding in aluminium alloys. Mater Sci Eng 954

Lohwasser D (2005) Friction stir welding in A350. In: EADS research workshop, AIRBUS, (Nov 2005)

Mahto RP, Bhoje R, Pal SK, Joshi HS, Das S (2015) A study on mechanical properties in friction stir lap welding of AA 6061-T6 and AISI 304. Mater Sci Eng A

Midling OT, Kvale JS, Dahl O (1999) Industrialization of friction stir welding technology in panels production for the maritime sector. In: 1st international symposium on friction stir welding, Thousand Oaks, CA, USA, 14–16 June 1999

Mishra RS, Ma ZY (2005) Friction stir welding and processing. Mater Sci Eng R 50:1–78

Mononen JT (2001) Cost comparison of PSW and MIG welded aluminum panels. In: 3rd international FSW symposium, Kobe, Japan, 27–28 Sept 2001

Movahedi M, Kokabi AH, Seyed Reihani SM, Najafi H (2011) Mechanical and microstructural characterization of A1–5083/St-12 lap joints made by friction stir welding. Procedia Eng 10:3297–3303

Rosen CD, Litwinski E, Valdez JM (1998) Friction stir welding process to repair voids in aluminum alloys. The Boeing Company, Seal Beach

Rudrapati R (2019) Recent advances in joining of aluminum alloys by using friction stir welding. Mass Production Processes

Salami P, Khandani T (2014) Friction stir welding/processing as a repair welding. In: Advances in friction stir welding and processing, pp 427–457

Shah PH, Badheka VJ (2019) Friction stir welding of aluminium alloys: an overview of experimental findings–process, variables, development and applications. Proc Inst Mech Eng Part L J Mater Design Appl 1191–1226

Soni N, Chandrashekhar S, Kumar A, Chary VR (2017) Defects formation during friction stir welding: a review. Int J Eng Manag Res 7(3):121–125

Talwar R, Perez R (2006) Method of repairing a crack in a component utilizing friction stir welding. In: Grant, TB. Company Editor

Thomas WM, Nicholas ED, Needham JC, Murch MG, Templesmith P, Dawes CJ (1991) Patent application no. 9125978.8 (Dec 1991)

Thomas WM, Nicholas ED, Needham JC, Murch MG, Temple-Smith P, Dawes CJ (1993) Improvements related to friction welding. PCT patent application no. PCT/GB92/02230, 10 June 1993

Tongne A, Jahazi M, Feulvarch E, Desrayaud C (2015) Banded structures in friction stir welded Al alloys. J Mater Process Technol 221:269–278

Xavier MF, Jayabalan V (2015) Journal of Materials Processing Technology Tool travel speed effects on the microstructure of friction stir welded aluminum–copper joints. J Mater Process Tech 217:105–113

Zhou N, Song D, Qi W, Li X, Zou J, Attallah MM (2018) Influence of the kissing bond on the mechanical properties and fracture behaviour of AA5083-H112 friction stir welds. Mater Sci Eng A 719:12–20

A Review on Cloud Manufacturing Technologies of Industry 4.0

Vrund Shah, Jay Vora, Smit Patel, and Rakesh Chaudhari

Abstract The concept of cloud manufacturing was introduced in 2010; however, its significance is getting noticed in recent years. It is being looked at as a new manufacturing paradigm that would help in shifting the approach of the manufacturing industry from being production-oriented to being service-oriented. Although research has been carried out in this field still, there is a lack of understanding of basic concepts, key characteristics, and their relationship with other technologies. In the current study, an attempt has been made to clarify the understanding of the people regarding the aforementioned issues. Also, because its implementation in the industry will be challenging, the key issues and factors influencing its implementation have been discussed in depth.

Keywords Industry 4.0 · Technology · Cloud manufacturing · Cloud computing · User models

1 Introduction

Today's manufacturing enterprises worldwide are getting reshaped and collaboration, innovation, service, and sustainability play a censorious role in that (Li et al. 2011). The manufacturing industry is undergoing a major transformation as it is shifting its approach from being production-oriented to service-oriented (Li et al. 2012). To face the new challenges which are faced due to manufacturing transformation number of information technologies are developing rapidly, such technologies include cloud computing (Armbrust et al. 2010) and the Internet of things (IoT) (Wolf 2009). Owing to the convergence of cloud computing and current manufacturing requirements a new notion of cloud manufacturing is introduced (Li et al. 2010; Ren et al. 2012). It is a new manufacturing paradigm that encourages the growth of a service-oriented, extremely synergistic, and inventive manufacturing base. Cloud manufacturing is a sophisticated, structured manufacturing method aimed at fulfilling growing

V. Shah · J. Vora · S. Patel · R. Chaudhari (✉)
Department of Mechanical Engineering, Pandit Deendayal Energy, University, Gandhinagar, Gujarat 382007, India

demands for enhanced product personalization, skilled innovations, greater market reaction adaptability, and global collaboration. The capacity to supply consumers with services that support the whole life cycle of a product is cloud manufacturing's biggest strength. This is achieved by giving access to a shared pool in which all manufacturing resources are virtualized. Cloud manufacturing is a convergence of cloud computing, the Internet of things, artificial intelligence, manufacturing technologies, and service computing from a technical standpoint (Li et al. 2011). Although the notion of cloud manufacturing was first suggested in 2010, its importance has just lately been recognized, and rapid progress is being made in both academic study and industrial implementation (Liu et al. 2018; Wu et al. 2012). Even though many researchers from various fields have presented their understanding of cloud manufacturing, there is still a lot of confusion regarding the basic concepts, key characteristics, and their relationship with some related concepts. There is also a need to discuss the key issues related to cloud manufacturing and its future perspective.

The purpose of this study is to address the aforementioned difficulties, and the rest of the paper is organized as follows. The role of cloud computing and other enabling technologies in creating the cloud manufacturing concept was investigated first, followed by the basic concepts of cloud manufacturing. After having determined the user model's basic characteristics, the factors that influence it were investigated. The challenges of putting cloud manufacturing into practice have been researched and documented. Finally, cloud manufacturing's future potential has been discussed.

2 Key Technologies of Cloud Manufacturing

2.1 Fundamental Concepts of Cloud Manufacturing

It is critical to first grasp the essential concepts of cloud manufacturing as a foundation for further discussion.

Manufacturing resource: A manufacturing resource is a unit that supports multiple operations or activities during a product's life cycle. It can be further divided into **hard resources** and **soft resources.** Manufacturing cell or IT hardware can be considered as a hard resource, whereas software, knowledge, data, or other intellectual elements as soft resources (Ren et al. 2013).

Manufacturing capability: It is a metric that is used to assess professional competence. Manufacturing capability can be defined as any manufacturing resources that are required to complete a job during the product life cycle (Ren et al. 2013).

Cloud manufacturing platform or Cloud platform: It manages a networked pool of manufacturing resources as well as capabilities, and an IT-based infrastructure.

Cloud manufacturing service or cloud service: It is a manufacturing capability-based function that aids in the achievement of a goal in a product life cycle activity.

In terms of technology, cloud services are divided into two categories: **On-cloud** and **Off-cloud**. In an On-cloud service, the operator has complete control over the cloud platform, but in an Off-cloud service, the operator must perform additional tasks (Ren et al. 2013).

Cloud user: A person participating in cloud manufacturing can be considered a cloud user (Wu et al. 2012).

Resource visualization: It is a method for mapping a physical manufacturing resource to a logical process.

Capability servitization: It's a method for encapsulating a manufacturing capability into a common cloud service utilizing an abstract description.

Cloud manufacturing system: It is an amalgamation of cloud users, manufacturing resources and capabilities, cloud platform, and certain manufacturing applications (Ren et al. 2013).

2.2 Role of Cloud Computing in Cloud Manufacturing

Cloud computing is defined as a shared computing architecture that meets the needs of external clients by supplying a pool of virtualized, dynamically expandable, managed computing power, storage, platforms, and services through the Internet (Foster et al. 2008). The three basic service modes in cloud computing are infrastructure as a service (IaaS), platform as a service (PaaS), and software as a service (SaaS) (SaaS) (Buyya et al. 2009). Hardware resources such as computers, networks, virtual machines (VM) which allow the users to modify their own IT infrastructure are provided by IaaS. PaaS provides a platform that allows developers to design, test, and execute their applications. The platforms comprise a programmed execution environment, database, and operating system. Cloud users are given access to and allowed to utilize the application software published on the cloud by SaaS. As users have self-services that are available on-demand cover IT infrastructure, platform, and software using any tablets or smartphones, there is a noteworthy reduction in the investment cost for developing and managing IT systems. This helps fulfill the users' demand for a dynamic computing and storage scale. Key characteristics of cloud computing that contribute to developing the cloud manufacturing concepts are service-centric perspective, virtualization and shared virtual pool of resources, scalability and elasticity, pay-as-you-use scheme, and on-demand customization and user experience.

Fig. 1 IoT industrial resource furnace (Gubbi et al. 2013)
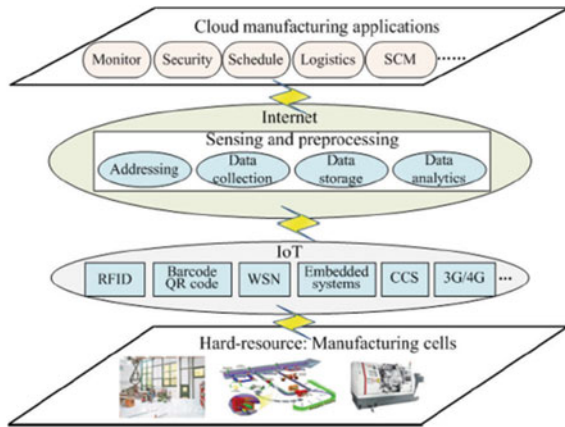
2.3 Key Characteristics of Cloud Manufacturing

2.3.1 Manufacturing Resources on the Internet of Things and Ever-Present Sensing

Smart communication and sense of production resources are two significant features given by cloud manufacturing. The recent advances of IoT technology which is transforming the Internet play an important role in this (Gubbi et al. 2013). As previously said, manufacturing resources are divided into two categories: hard resources and soft resources. The establishment of integrated Internet of soft resources was easy as compared to hard resources until recent developments in IoT technology. Figure 1 shows a typical IoT industrial resource framework. The invention of technologies like radio frequency identification(RFID) (Buckley 2006), the barcode and quick response (QR) code, and wireless sensor network (WSN) (Akyildiz et al. 2002) which supports the IoT has made the development of a smart network of analogous manufacturing resources specifically the hard resources. To identify the connected resources in the cloud manufacturing environment, each resource has a uniform resource name (URN) (Atzori et al. 2010) and users via looking at the URN-URL (uniform resource locator) table access the URL on the Internet. The smart Internet of industrial "things" will generate a significant amount of "Big Data," necessitating the usage of cloud-based storage technologies (White 2010).

2.3.2 Virtual Manufacturing Society and Demand-Driven Manufacturing System

The research on VM originated the term virtualization (Figueiredo et al. 2005). Virtualization is the process of mapping a genuine physical manufacturing resource to a virtual resource in cloud manufacturing (Ren et al. 2013). It enables the utilization
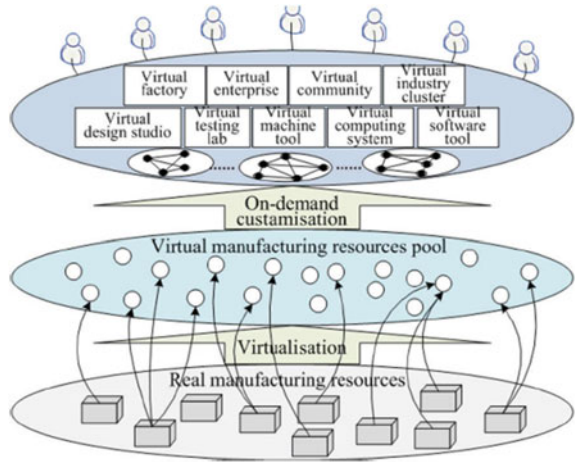
and sharing of resources by more users in an optimized manner. Furthermore, because of the flexibility, it possesses it can adapt easily without causing any effect to the service quality. Figure 2 shows a virtual manufacturing society in cloud manufacturing. In manufacturing resource, virtualization mapping plays an important role. Typically there are three types of mapping: one-to-one, one-to-many, and many-to-one (Xu 2012). The real manufacturing resources after virtualization forms a virtual manufacturing resource pool, and according to the demand, there will be various customization such as virtual factory, VE, VM tool, etc. Hence, it can be concluded that cloud manufacturing might lead to virtual manufacturing civilization.

2.3.3   Manufacturing as a Service and Providing of Capability Over the Entire Life Cycle

Cloud manufacturing supports a new business model that aids in the transformation of manufacturing industries from production to service-oriented manufacturing. The manufacturing services cover all stages of the life cycle of a product (Wu et al. 2013) as shown in Figure 3. Therefore, it concludes that cloud manufacturing service can be considered as "manufacturing as a service." As there is a large number of cloud manufacturing services when any user has any innovative idea, it can be converted into a physical product by using all the required manufacturing services and delivered to the user. This proves to be a great help to small enterprises which are having limited manufacturing resources that are so costly that they cannot afford them.
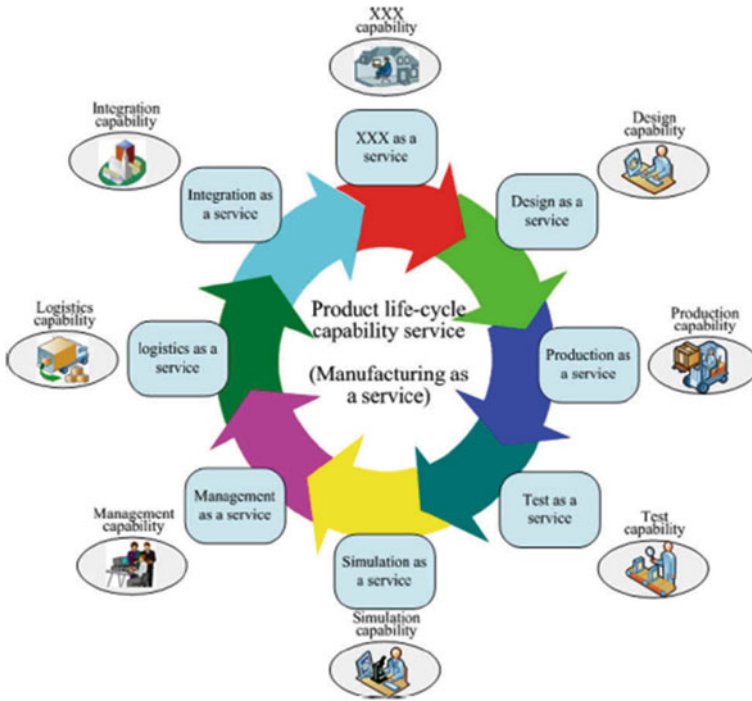
Fig. 3 Capability service (Wu et al. 2013)

2.3.4 Efficient Collaboration and Seamless Integration

Interconnection of shared manufacturing resources is made possible by the cloud which provides a shared platform helping in cooperation. A cyber business environment is created by the cloud manufacturing platform from where any supplier or demander can find the partner which meets their requirements. Also, a fundamental framework is provided by the cloud platform which manages the material and capital flow that occurs during an interaction between members. As shown in Figure 4, a shared service pool is formed where a large range of services gather, and based on requirements, various subtasks can be accomplished by integrating the interoperable services.

2.3.5 Manufacturing with a High Level of Knowledge and Collective Invention

Since one of the most essential variables in business rivalry is innovation, cloud manufacturing places a premium on knowledge reuse and innovative manufacturing. The manufacturing cloud can be considered a pool of multidisciplinary knowledge.

Fig. 4 Collaboration and integration (Wu et al. 2013)
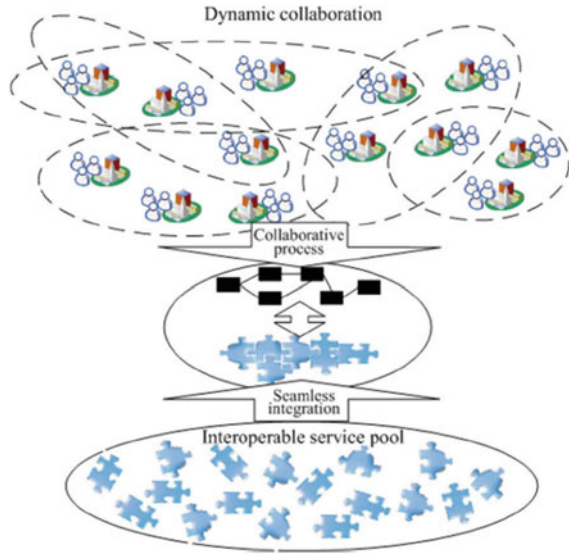
Apart from knowledge, AI technologies are also required to make necessary decisions. As shown in Figure 5 both knowledge and AI technologies support product and service life cycles (Ren et al. 2017). In the product, life cycle knowledge and AI help in innovation and improving the efficiency of various stages such as design, production, simulation, whereas they support various stages in the cloud service life cycle including service description, scheduling, and other phases. It is quite evident from the figure that knowledge can come from any user may it be craftsmen or any expert. Thus, a social platform is offered by the cloud through which ideas can be shared and talents can communicate.

Fig. 5 Knowledge-intensive manufacturing (Ren et al. 2017)
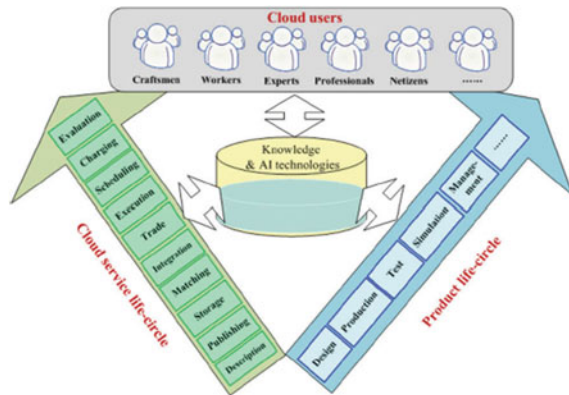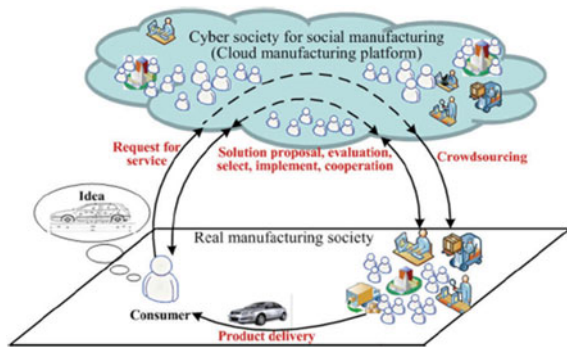
2.3.6   In the Direction of Future Social Manufacturing

Social manufacturing is a phenomenon in which everyone may completely engage
in all stages of a product's life cycle, thanks to cloud technologies (Wu et al. 2013). It
will play a major role in enabling a highly personalized product from imagination to
reality at a lower cost, enhanced quality, and increased agility. Figure 6 shows how
crowdsourcing can be done in social manufacturing. When a customer has a hazy
concept about a product, he or she can upload it to the cloud and submit a service
request. Various experts with appropriate knowledge can submit their solutions on
the cloud platform, which are then accepted and integrated to coordinate the required
resources after being evaluated by the customer. Finally, after the product is produced
it will be delivered to the customer via a logistic network that too would be available
on the cloud platform.

2.4   User Model in Cloud Manufacturing

Figure 7 displays the various types of cloud manufacturing users and their relation-
ships. The key participants in cloud manufacturing are the cloud provider, cloud
customer, and cloud operator.

Cloud provider: The entity which provides manufacturing resources, as well as capa-
bilities in form of service, is known as cloud providers. They also acquire customized
jobs as well as comprehensive benefits via a cloud manufacturing platform.

Cloud customer or consumer: A demand for any application in the product life cycle
is made by the cloud customer. The on-demand service is offered through a cloud
manufacturing platform, which ensures that the services provided are competitive in
terms of cost, innovation, business agility, and productivity.

Cloud operator: The entity which operates the cloud manufacturing platform is
known as the cloud operator. All the technical processes and business strategies are

Fig. 7 Users in cloud manufacturing (Ren et al. 2017)
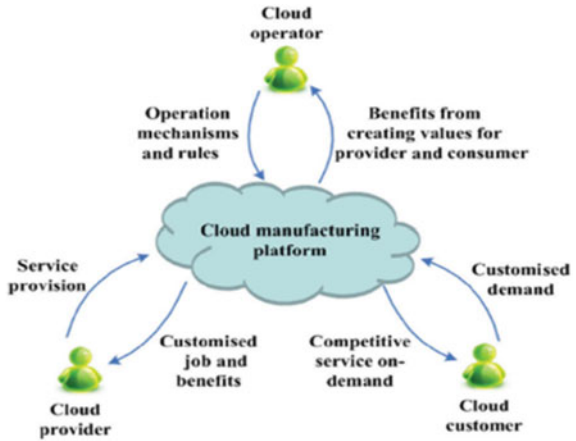
set up by cloud operators. Along with it all the business transactions, supply, and demand of services, as well as social networks of the cloud provider and operator, are managed by the cloud operator (Ren et al. 2017).

2.5 Factors Driving Cloud Manufacturing Implementation

The elements that drive cloud manufacturing implementation have been classified into four parts: scope, enterprise, industry, and technology.

Scope: Cloud manufacturing can be disposed of as a private cloud, a community cloud, a public cloud, or a hybrid cloud across an organization, a country, or even the entire globe. A private cloud is less complicated to set up than a communal cloud or another type of cloud (Low et al. 2011).

Enterprise: When cloud manufacturing is implemented in any enterprise its success depends on the adoption and participation of the whole enterprise. The factors which affect the enterprise to adoption and participation are understanding of top management and their support, enterprises objectives and business requirements, enterprise size, and adequate knowledge and information to the employees and their cooperation (Low et al. 2011).

Industry: The manufacturing sector consists of numerous industries, and each industry has its process and characteristics and is also at different stages of development which eventually leads to a different degree of requirements, difficulties, and complexities for the implementation of cloud manufacturing (Low et al. 2011).

Technology: In the cloud manufacturing process, each technology, for example, has a specific purpose. Building cloud platforms necessitates the use of IoT, while

managing and operating cloud manufacturing necessitates the use of other technologies, and some technologies have an impact on an organization's desire to embrace (Low et al. 2011).

2.6 Problems Faced by the Implementation of Cloud Manufacturing

The term "cloud manufacturing" is still a bit of a misnomer. The current definition of cloud manufacturing perplexes individuals as to what it is, how it may be done, and what its benefits and cons are. To address this, the notion of cloud manufacturing should be broken down into simpler components and a simplified definition provided.

Owing to the naked truth that cloud manufacturing is an almost new idea, most businesses are unfamiliar with it (Zang et al. 2016). In addition, cloud manufacturing's success is contingent on enterprise adoption and engagement. As a result, it will take time for businesses to grasp the concept and put it into practice. There are various conditions for cloud manufacturing implementation that the company lacks, as well as an analysis of the cost of implementation, risks, and advantages that must be completed.

Cloud manufacturing is an amalgamation of many technologies (Li et al. 2011) a hierarchy needs to be developed as to which technologies to be used at which stage of implementation of cloud manufacturing and also clarification needs to be done regarding the core technologies and the supporting technologies.

2.7 Future Perspectives

Hierarchy and classification of technologies in cloud manufacturing need to be discussed, i.e., which technology will be needed at what level of implementation and which should be developed up to what maturity level (Wang et al. 2012).

The degree of enterprise involvement is determined by the degree of cloud manufacturing deployment. For example, at a junior level, a business would deploy cloud manufacturing to a lesser extent, so what amount of involvement would be necessary from the company, and what changes would be required if the degree of cloud manufacturing implementation was increased in the future.

Prerequisites and changes in the architecture of enterprise for implementing cloud manufacturing (Liu et al. 2017). As the majority of the resources would be virtualized some changes in the architecture of the enterprise at management as well as operation level are evident so what changes need to be done should be studied and presented.

Development of evaluation index helps in determining the maturity of the cloud manufacturing system. As the utilization of cloud manufacturing is a slow and progressive process evaluation index is needed to keep track of the progress of its implementation.

3   Conclusions

As cloud manufacturing is a relatively new idea, its goal, scope, boundaries, and capabilities are currently unknown. A comprehensive review of cloud manufacturing technologies for Industry 4.0 was conducted in this paper. In the current study, numerous technologies which contribute to the development of the notion of cloud manufacturing, as well as the interrelationships between them, were outlined in detail as follows:

- Cloud computing, in particular, is the most essential enabling technology since it lays the groundwork for the development of the cloud manufacturing idea.
- The elements that drive cloud manufacturing implementation have been divided into four categories: scope, enterprise, industry, and technology. Also, the issues faced by industrial implementation have been discussed and presented.
- Although research has been going on in this field for a long time, still there are some future perspectives that are yet to be researched and analyzed like there is a need to develop a hierarchy of technologies, changes in the architecture of industry for implementing cloud manufacturing, and also an evaluation index which would help to understand the level of maturity of cloud manufacturing have been listed.

References

Akyildiz IF, Su W, Sankarasubramaniam Y, Cayirci E (2002) Wireless sensor networks: a survey. Comput Netw 38:393–422

Armbrust M, Fox A, Griffith R, Joseph A, Datz R, Konwinski A, Lee G (2010) Above the clouds: a view of cloud computing. Commun ACM 53(4):50–58

Atzori L, Iera A, Morabito G (2010) The internet of things: a survey. Comput Netw 54:2787–2805. https://doi.org/10.1016/j.comnet.2010.05.010

Buckley J (2006) The internet of things: from RFID to the next-generation pervasive networked systems. Auerbach, New York

Buyya R, Yeo CS, Venugopal S, Broberg J, Brandic I (2009) Cloud computing and emerging it platforms: vision, hype, and reality for delivering computing as the 5th utility. Futur Gener Comput Syst 25(6):599–616

Figueiredo R, Dinda P, Fortes J (2005) Guest editors introduction: resource virtualization renaissance. IEEE Comput 38(5):28–31

Foster I, Zhao Y, Raicu I, Lu S (2008) Cloud computing and grid computing 360-degree compared. In: Proceedings of grid computing environments workshop, Austin, TX, 1–10. Piscataway, NJ. IEEE Society Press

Gubbi J, Buyya R, Marusi S, Palaniswami M (2013) Internet of things (IoT): a vision, architectural elements, and future directions. Futur Gener Comput Syst 29(7):1645–1660

Li BH, Zhang L, Wang S, Tao F, Cao J, Jiang X, Song X et al (2010) Cloud manufacturing: a new service-oriented networked manufacturing model. Comput Integr Manuf Syst CIMS 16(1):1–7

Li BH, Zhang L, Ren L, Chai X, Tao F, Luo Y, Wang Y et al (2011) Further discussion on cloud manufacturing. Comput Integ Manuf Syst CIMS 17(3):449–457

Li BH, Zhang L, Ren L, Chai X, Tao F, Wang Y, Yin C et al (2012) Typical characteristics, technologies and applications of cloud manufacturing. Comput Integr Manuf Syst CIMS 18(7):1345–1356

Liu Y, Xu X, Srinivasan A, Zhang L (2017) Enterprises in cloud manufacturing: a preliminary exploration. In: American society of mechanical engineers, 2017 12th international manufacturing science and engineering conference collocated with the JSME/ASME 2017

Liu Y, Wang L, Wang XV (2018) Cloud manufacturing: latest advancements and future trends. Proc Manuf 25:62–73

Low C, Chen Y, Wu M (2011) Understanding the determinants of cloud computing adoption. Ind Manag Data Syst 111(7):1006–1023

Ren L, Zhang L, Tao F, Zhang X, Luo Y, Zhang Y (2012) A methodology toward virtualization-based high performance simulation platform supporting multidisciplinary design of complex products. Enterp Inf Syst 6(3):267–290

Ren L, Zhang L, Tao F, Zhao C, Chai X, Zhao X (2013) Cloud manufacturing: from concept to practice. Enterp Inf Syst. https://doi.org/10.1080/17517575.2013.839055

Ren L, Zhang L, Wang L, Tao F, Chai X (2017) Cloud manufacturing: key characteristics and applications. Int J Comput Integr Manuf 30(6):501–515

Wang SL, Guo L, Kang L, Li Q, Song WY, Chen GS (2012) Cloud manufacturing application mode and program analysis. Comput Integr Manuf Syst 18(7):1637–1643

White T (2010) Hadoop: the definitive guide. 2nd ed. O'Reilly Media, Sebastopol, CA

Wolf W (2009) Cyber physical systems. Computer 42(3):88–89

Wu D, Thames JL, Rosen DW, Schaefer D (2012) Towards a cloud-based design and manufacturing paradigm: looking backward, looking forward. In: Proceedings of the ASME 2012 international design engineering technical conference & computers and information in engineering conference (IDETC/CIE12), Paper number DETC2012–70780, Chicago, IL, August 12–15

Wu D, Thames JL, Rosen DW, Schaefer D (2013) Enhancing the product realization process with cloud-based design and manufacturing systems. Trans ASME J Comput Inf Sci Eng 13(4): 041004-1–041004-14

Xu X (2012) From cloud computing to cloud manufacturing. Robot Comput Integr Manuf 28(1):75–86

Zang T, Liu Y, Xu X (2016) Cloud manufacturing: an industry survey. In: American society of mechanical engineers 2016 11th international manufacturing science and engineering conference, vol 2 materials; biomanufacturing; properties, applications and systems; sustainable manufacturing, Blacksburg, Virginia, USA, June 27–July 1. https://doi.org/10.1115/MSEC2016-8752

Effect of Different Tool Electrodes (Wire) of WEDM Process of Inconel 718

Rakesh Chaudhari, Het Patel, Manav Sheth, Nisarg Prajapati, Kishan Fuse, Kumar Abhishek, and Jay Vora

Abstract In the present era of industrialization, the use of materials like Inconel 718 which is nickel–chromium superalloy is increased due to the use in various areas like the aerospace industry, automobile industry, medical industry, and chemical industry. Inconel 718 is a worn and corrosion-resistant, high strength superalloy that exhibits temperature-resistant properties even at very high/elevated temperatures. In this present study, we have adopted wire electrical discharge machining (WEDM) for machining Inconel 718. As it is high strength material, conventional machining finds it difficult to machine due to which we have adopted a non-conventional machining method. For our investigation in the present study, molybdenum and brass as two different wire electrodes have been selected based on their advantages to observe their effect in WEDM for surface analysis. For the study, L9 orthogonal array was employed, which took into account three parameters at three levels for both wire electrodes. To notice the outcome and significance of input factors like discharge current, pulse-on time (T_{on}), and pulse-off time (T_{off}) on the output parameters like material removal rate (MRR) and surface roughness (SR), analysis of variance (ANOVA) has been used for analysis. Whereas the Taguchi optimization method is limited to optimize a single objective at a time, the TOPSIS method was used to consider both criteria together.

Keywords WEDM · Inconel 718 · Taguchi · TOPSIS · Molybdenum wire · Brass wire

R. Chaudhari · H. Patel · M. Sheth · N. Prajapati · K. Fuse · J. Vora (✉)
Department of Mechanical Engineering, Pandit Deendayal Energy, University, Gandhinagar, Gujarat 382007, India
e-mail: Jay.vora@sot.pdpu.ac.in

K. Abhishek
Department of Mechanical and Aero-Space Engineering, Institute of Infrastructure Technology Research and Management (IITRAM), Ahmedabad, Gujarat 380026, India

1   Introduction

The superalloy Inconel 718 material remains highly corrosion and wear-resistant, high tensile strength nickel-based superalloy and possesses high creep strength at an elevated temperature ranging from −423 to 1300F. It has some extensive applications in various fields such as aerospace engine applications including the heat treating industry, nuclear engineering, chemical and medical industries, automobiles, gas turbine components, etc. (Aggarwal et al. 2015a). In aerospace and automobile applications for proper dimensional accuracy, it requires a good surface finish of the components. Due to which there is a great importance of good SR and a rich production rate of components. Whereas due to the low thermal conductivity of nickel-based alloys, it exhibits poor machinability by machining with conventional methods. In addition to this, traditional/conventional machining exhibits poor surface finish/profile of final product due to unwanted tool wear which consists of carbide and hard abrasives particles (Aggarwal et al. 2015a; Yang et al. 2017; Chaurasia et al. 2019). Non-conventional machining methods are extensively utilized for nickel-based alloys to remove all of these effects (Chaudhari et al. 2019,2020a; Khanna et al. 2021; Sheth et al. 2021).

Due to its numerous advantages, the WEDM process is widely recognized. It is based on the thermoelectric concept, in which the heat energy of a spark is employed to remove material from a workpiece. This method is generally used to generate challenging and complicated shapes with good surface roughness and great material removal rate very accurately and precisely (Khanna et al. 2020, 2021; Chaudhari et al. 2020b, c). In this method, different wire electrodes of various diameters ranging from 0.050–0.35 mm are used such as copper, brass, coated, molybdenum wires considering the tensile strength, fracture resistance, conductivity, and melting point of the wire for different workpiece materials. Here the wires are guided by diamond guides and are kept straight under high tension, and a wire spool is used to draw the wire. In this process, high frequency, DC pulses are transferred from wire to workpiece resulting in spark generation in the narrow gap. In past, various researchers have studied the significance of wire electrode on machining aspects of WEDM process. Rajeev Kumar et al. (Kumar et al. 2015) studied the effect of different wire electrodes for titanium by using three different wire electrodes, namely brass, zinc-coated, and HCS wire having steel core and concluded that HCS wire gives the highest MRR among all three, and an excellent surface finish is obtained with a brass electrode. Mohanty et al. (2014) analyzed the effect of brass, copper, and graphite wire on the machining characteristics of the Inconel 718. They observed that the selection of wire electrodes plays a major role in improved machining results. Yadav and Yadav (2020) compared bare and galvanized electrodes in EDM. They concluded that MRR, tool wear, and SR were mostly affected by coated tool electrodes. Unplated copper tools have poor processing performance. Compared with coated tools with the same processing parameters, it has a higher SR and largest TWR. For the same machining variables, coated tools require less processing time. Mahapatra and Patnaik (2006) utilized a covered wire anode to research WEDM machining

execution. Covered metal wire results in high MRR in comparison with the brass wire electrode. Covered brass wire can likewise obtain a remarkable surface finish. Rajesha et al. (2011) arranged the analyses according to Taguchi's L18 symmetrical exhibit and preliminaries were completed in a CNC-EDM machine with copper wire electrode. The significance of machining variables was studied on MRR during the machining of Inconel 718. Discharge current was observed to be the most significant machining variable. Aggarwal et al. (2015b) had experimented on Inconel 718 using brass wire electrodes in WEDM. It was observed that, for MRR and SR, T_{on} to the most significant factor. Han et al. (2007) noticed the consequence of input constraints on the output process parameter SR and concluded that good SR is obtained with low pulse duration and discharge current. The increased discharge current resulted in a more undesirable workpiece surface roughness, Williams and Rajurkar (1991) concluded. It can be observed from past studies that the performance of the WEDM process highly depends on the type of wire electrode used. Different electrodes like brass wire, copper wire, molybdenum wire, and zinc-coated wires have been used for several applications (Kapoor et al. 2012; Rathi et al. 2020; Chaudhari 2019).

The foremost objective of this work is to generate and evaluate the performance of the WEDM process during the machining of Inconel 718 using different wire electrodes. Two different wire electrodes, namely brass and molybdenum wires, were used in the current study. For experimentation, the L_{18} orthogonal array of Taguchi was selected with four machining variables. Current, T_{on}, and T_{off} were the three factors at three levels for both wire electrodes simultaneously. MRR and SR were nominated as output process variables. The influence and contribution of each process parameter on the individual output response variable were investigated using ANOVA. Optimization is done by the TOPSIS method which is a multi-decision analysis technique that optimizes more than one criteria at a time.

2 Experimental Setup and Experimentation

For this current study, a tube-shaped Inconel 718 rod of 15 mm diameter having a density of 8.19 g/cm^3 has been considered as a work material (anode) to be machined using accord WEDM (DK7732) with 0.18 mm reusable molybdenum and brass wire electrodes (cathode). Figure 1 shows the experimental setup of the WEDM process used in the current study. Four machining variables (current, T_{on}, and T_{off} at three levels and wire electrode at 2 levels) were are selected to observe the effect on MRR and SR. Taguchi's L_{18} design was implemented for experimentation. Considering the impediments of the WEDM apparatus available and different parameters, input parameters chosen for research are shown in Table 1. The calculation of MRR was carried out as shown in Eq. 1:

$$MRR = \frac{Mass\ of\ the\ machined\ sample\ (W)\ [g]}{Time\ taken\ for\ machining\ (t)\ [sec]} \tag{1}$$

Table 1 Taguchi's L18 array with experimental results

Sr. no	Electrode type	T_{on} (μs)	T_{off} (μs)	Current (A)	MRR (gram/s)	SR (μm)
1	Molybdenum	30	10	2	0.012048	3.35
2	Molybdenum	30	20	4	0.008598	4.52
3	Molybdenum	30	30	6	0.007326	5.4
4	Molybdenum	60	10	2	0.012578	5.01
5	Molybdenum	60	20	4	0.010695	5.62
6	Molybdenum	60	30	6	0.008163	5.01
7	Molybdenum	90	10	4	0.014705	6.75
8	Molybdenum	90	20	6	0.011560	5.74
9	Molybdenum	90	30	2	0.004385	5.12
10	Brass	30	10	6	0.013698	5.6
11	Brass	30	20	2	0.005555	5.2
12	Brass	30	30	4	0.008196	5.6
13	Brass	60	10	4	0.012165	6.02
14	Brass	60	20	6	0.009970	6.44
15	Brass	60	30	2	0.005263	5.7
16	Brass	90	10	6	0.014084	7.02
17	Brass	90	20	2	0.005698	5.5
18	Brass	90	30	4	0.004761	5.66

SR measurement was completed using Mitutoyo make Surftest SJ-410 model. The values were obtained experimentally for SR and MRR for the selected eighteen trials as displayed in Table 1.

3   Results and Discussion

ANOVA has been instigated to study the influence of machining variables going on MRR and SR. Mean values have been taken into consideration for analysis. The graphs depicting the mean values of various parameters for different output parameters have been explained in the subsequent discussion.

3.1   Influence of Machining Variables on MRR

To assess the influence of input parameters on each output response variable, the statistical software Minitab 14 with ANOVA was used on the experimental data collected using Taguchi experimental design with a 95 percent significant level to

assess the influence of input parameters on each output response variable, as shown in Table 2 below for MRR. As seen in Table 2, T_{off} is considered the most significant parameter for MRR. Further, current, wire electrode, and T_{on} are comparatively less significant for MRR. For a 95% level of confidence, the P-value of the particular control factor should be less than or equal to 0.05 to be significant for the machining process (Wankhede et al. 2020). P-value of wire electrode, T_{off}, and current which is less than 0.05 shows the significance of these machining variables for MRR. Figure 1 shows the impact of machining variables on MRR. From Fig. 2, it is clear to see that MRR for the molybdenum wire tool is more as compared to the brass electrode. In the current study, the mean values for MRR for molybdenum wire electrode are above 0.01 g/s, whereas that of brass wire electrode is nearly around 0.0085 g/s. Due to the ability to resist very high pulling forces of molybdenum

Table 2 Analysis of variance for MRR

Source	DF	SS	MS	F	P
Wire electrode	1	0.000006	0.000006	4.66	0.050
T_{on}	2	0.000001	0.000001	0.51	0.615
T_{off}	2	0.000146	0.000073	53.86	0.000
Current	2	0.000033	0.000016	12.04	0.002
Error	10	0.000014	0.000001		
Total	17	0.000200			

Fig. 1 WEDM setup

Main Effects Plot for MRR

Data Means
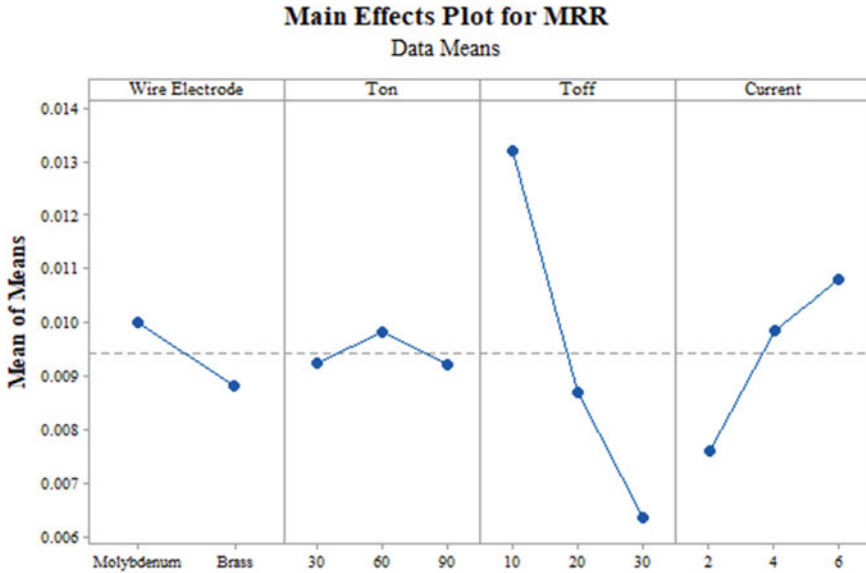
Fig. 2 Influence of machining variables on MRR

wire, the MRR obtained is greater than the brass electrode. And also because of the very high melting temperature moly wire in WEDM can handle very high working temperature resistance for almost all materials due to which MRR is high for moly as compared to the brass electrode. From Fig. 2, it can be observed that the effect of T_{on} on MRR is nearly constant and varying between 0.0095 and 0.010 g/s mean of means values, which indicates that T_{on} is independent of MRR because it nearly remains constant for all the values in the range. Therefore, T_{on} has no significant result on cutting speed in the range of 30–90 µs. The outcome of T_{off} on MRR shows a decreasing trend with a rise in T_{off} because of reduced spark ejection time and less amount of MRR (Chaudhari et al. 2020d). Thus with an increase in T_{off}, MRR is decreasing. Also, the slope indicates that it has a great effect on MRR; a slight increase in T_{off} leads to a decrease in MRR. Thus, the lowest $T_{off,}$ i.e., 10 µs, is optimum for high MRR. With an increase in current value, the influence of clearance form on MRR exhibits an increasing tendency (Chaudhari et al. 2021). Thus, a rise in current value leads to a rise in MRR. Figure 2 indicates that it has a great effect on MRR; a slight escalation in current leads to a surge in MRR. Therefore, the highest current, i.e., 6A, is optimum for high MRR.

3.2 *Influence of Machining Variables on SR*

To evaluate the effect of machining variables for SR, the statistical programmed Minitab 14 with ANOVA was used on the experimental data obtained through Taguchi experimental design with a 95 percent significant level. The ANOVA analysis for SR is shown in Table 3. The most important parameters for SR were found to be Ton, current, and wire electrode. Further, T_{off} is comparatively less significant for SR. However, the P-value of wire electrode, T_{on}, and current which is less than 0.05 shows the significance of these machining variables for SR. Figure 2 shows the impact of machining variables on SR. Figure 3 shows that SR for the brass wire electrode is more as compared to that of the molybdenum wire electrode. This means that by machining with a molybdenum wire electrode, a fine surface finish

Table 3 Analysis of variance for SR

Source	DF	SS	MS	F	P
Wire electrode	1	2.1494	2.14936	6.52	0.029
T_{on}	2	3.2484	1.62421	4.93	0.032
T_{off}	2	0.1334	0.06671	0.20	0.820
Current	2	2.6608	1.33041	4.04	0.050
Error	10	3.2963	0.32963		
Total	17	11.4882			
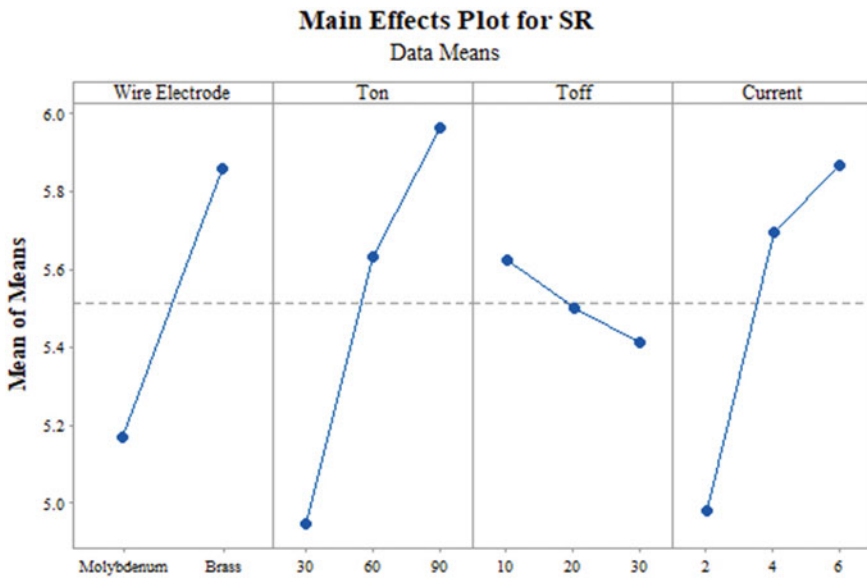
Fig. 3 Influence of machining variables on SR

can be obtained relative to the brass wire electrode. A significant difference can be observed in SR values by both these electrodes in Fig. 3. The mean value for SR for the molybdenum wire electrode is below 5.2 μm, whereas that of for brass wire electrode is around 5.9 μm. Because of molybdenum's high hardness, molybdenum wire maintains excellent wall straightness, which is in contrast to brass electrodes. Due to the ability to resist very high pulling forces of molybdenum wire, straighter cuts are obtained that resist much better the side forces and other movements. This allows cutting very fine and with a good surface finish.

The effect of T_{on} is directly proportional to SR and obtains a constantly increasing trend because the higher the T_{on}, the higher will be the energy of discharge and spark intensity results in poor surface texture and vice versa. This indicates that the increase in T_{on}, SR value also increases. The effect of T_{off} on SR shows a reducing trend with growth in T_{off} (inversely proportional). Thus with the increase in T_{off}, SR is decreasing as discharge energy falls with the rise in T_{off} leading to the plunging of the crater dimensions and hence reducing SR (Chaudhari et al. 2020d). The effect of current on SR shows a growing tendency with a rise in current value and vice versa. Higher current causes ionization of the deionized water which also contributes to the inflation of crater size (Chaudhari et al. 2021). Thus with an increase in current value, SR is increasing.

3.3 Multi-objective Optimization Using TOPSIS

Taguchi optimization technique is limited to optimize a single objective at a time we only can get optimize the combination of output parameters differently as already discussed above. So to consider both criteria together, the TOPSIS method was used for optimization. This method has been adopted due to various advantages like it simple, rational, comprehensible, and it possesses high efficiency as compared to other multi-objective optimization methods. Thus for optimization of two response parameters at a time for this study by TOPSIS method, the following steps were performed:

Step 1: A decision matrix has been generated and obtained the weight of the criteria.

Step 2: The decision matrix was calculated as a normalized decision matrix.

Step 3: This became possible to have a weighted normalized matrix.

Step 4: Positive and negative perfect results were obtained.

Step 5: Based on positive and negative ideal solutions, calculate Euclidian distances, separation measures.

Step 6: Using separation measures compute the closeness coefficient index to the positive perfect result.

Table 4 TOPSIS analysis

Run	MRR	SR	Closeness Coefficient Index (CCI)	Rank
1	0.012048	3.35	0.799	1
2	0.008598	4.52	0.499	9
3	0.007326	5.4	0.341	13
4	0.012578	5.01	0.699	2
5	0.010695	5.62	0.533	8
6	0.008163	5.01	0.429	10
7	0.014705	6.75	0.604	4
8	0.011560	5.74	0.572	6
9	0.004385	5.12	0.258	15
10	0.013698	5.6	0.679	3
11	0.005555	5.2	0.279	14
12	0.008196	5.6	0.375	12
13	0.012165	6.02	0.577	5
14	0.009970	6.44	0.423	11
15	0.005263	5.7	0.208	17
16	0.014084	7.02	0.569	7
17	0.005698	5.5	0.249	16
18	0.004761	5.66	0.200	18

Step 7: The priority order should be rated in decreasing order based on the closeness coefficient index.

After performing the above TOPSIS analysis step by step by performing mathematical calculations, the results have been obtained as shown in Table 4. As per step 7, the final matrix was ranked. Rank 1 was considered as the optimized value after TOPSIS analysis from all 18 trials considering both molybdenum and brass wire electrodes. The optimized result rank 1 gives the optimal combination of WEDM parameters corresponding to the molybdenum wire electrode, T_{on} of 30 µs, T_{off} of 10 µs, and current of 2A.

4   Conclusions

In the current study, WEDM machining of Inconel 718 was carried out to investigate the importance of the input constraints on the performance factors and observe the consequence of various wire tools. The input parameters considered were wire electrode, T_{on}, T_{off}, and discharge current for performance factor of MRR and SR. TOPSIS was applied to improve both response parameters concurrently. While

considering the parameters and their factors employed in the current study and accordance with the above outcomes and discussions, the subsequent decisions can be made:

- Using Taguchi analysis with ANOVA, it can be concluded that wire electrode, T_{off}, and discharge current considerably affect the MRR. It was found that T_{off} was the most influential parameter in determining MRR. Molybdenum wire electrode was found to be best suited for high MRR in contrast to brass wire electrode.
- For SR, wire electrode, T_{on}, and release current was observed to be the noteworthy machining variables. Molybdenum wire electrode was found to be best suited for obtaining lower SR value in contrast to brass wire electrode.
- According to TOPSIS analysis based on ranking, molybdenum wire electrode gives an optimum combination of process parameters among all 18 combinations. The best optimal combination of process constraints for MRR and SR was a molybdenum electrode, T_{on} of 30 μs, T_{off} 10 μs, and released current of 2 A.

References

Aggarwal V, Khangura SS, Garg R (2015a) Parametric modeling and optimization for wire electrical discharge machining of Inconel 718 using response surface methodology. Int J Adv Manuf Technol 79(1–4):31–47

Aggarwal V, Khangura SS, Garg R (2015b) Parametric modeling and optimization for wire electrical discharge machining of Inconel 718 using response surface methodology. Int J Adv Manuf Technol 79(1):31–47

Chaudhari R, Vora JJ, Mani Prabu SS, Palani IA, Patel VK, Parikh DM, de Lacalle LNL (2019) Multi-response optimization of WEDM process parameters for machining of superelastic nitinol shape-memory alloy using a heat-transfer search algorithm. Materials 12(8):1277

Chaudhari R et al (2019) Pareto optimization of WEDM process parameters for machining a NiTi shape memory alloy using a combined approach of RSM and heat transfer search algorithm. In: Advances in manufacturing, pp 1–17

Chaudhari R, Vora JJ, Patel V, Lacalle LN, Parikh DM (2020a) Effect of WEDM process parameters on surface morphology of nitinol shape memory alloy. Materials 13(21):4943

Chaudhari R, Vora JJ, Parikh D (2020) A review on applications of nitinol shape memory alloy. In: Recent advances in mechanical infrastructure: proceedings of ICRAM

Chaudhari R, Vora JJ, Patel V, López de Lacalle LN, Parikh DM (2020c) Surface analysis of wire-electrical-discharge-machining-processed shape-memory alloys Materials 13(3):530

Chaudhari R et al (2020d) Optimization of parameters of spark erosion based processes. Spark Erosion Machining. CRC Press, pp 190–216

Chaudhari R, Vora J, Lacalle LN, Khanna S, Patel VK, Ayesta I (2021) Parametric optimization and effect of nano-graphene mixed dielectric fluid on performance of wire electrical discharge machining process of Ni55. 8Ti shape memory alloy. Materials 14(10):2533

Chaurasia A, Wankhede V, Chaudhari R (2019) Experimental investigation of high-speed turning of INCONEL 718 using PVD-coated carbide tool under wet condition. In: Innovations in infrastructure. Springer, Singapore, pp 367–374

Han F, Jiang J, Yu D (2007) Influence of machining parameters on surface roughness in finish cut of wedm. Int J Adv Manuf Technol 34:538–546

Kapoor J, Singh S, Khamba JS (2012) High-performance wire electrodes for wire electrical-discharge machining–a review. Proc Inst Mech Eng Part B J Eng Manuf 226(11):1757–1773

Khanna S, Patel R, Marathey P, Chaudari R, Vora J, Banerjee R, Ray A, Mukhopadhyay I (2020) Growth of titanium dioxide nanorod over shape memory material using chemical vapor deposition for energy conversion application. Mater Today Proc 28:475–479

Khanna S, Marathey P, Paneliya S, Chaudhari R, Vora J (2021) Fabrication of rutile–TiO2 nanowire on shape memory alloy: a potential material for energy storage application. Mater Today Proc

Khanna S, Marathey P, Patel R, Paneliya S, Chaudhari R, Vora J, Ray A, Banerjee R, Mukhopadhyay I (2021) Unravelling camphor mediated synthesis of TiO2 nanorods over shape memory alloy for efficient energy harvesting. Appl Surf Sci 541:148489

Kumar R, Aggarwal V, Goyal A (2015) Effect of different wire electrode's material on the performance of wire electrode discharge machining

Mahapatra SS, Patnaik A (2006) Parametric optimization of wire electrical discharge machining (WEDM) process using Taguchi method. J Braz Soc Mech Sci Eng 28(4):422–429

Mohanty CP, Mahapatra SS, Singh MR (2014) A particle swarm approach for multi-objective optimization of electrical discharge machining process. J Intell Manuf 27(6):1171–1190

Rajesha S, Sharma AK, Kumar P (2011) An approach to optimisation of process parameters while EDMing Inconel 718 using Taguchi's orthogonal array. Int J Prod Quality Eng 2(1):19–26

Rathi P, Ghiya R, Shah H, Srivastava P, Patel S, Chaudhari R, Vora J (2020) Multi-response optimization of Ni55. 8Ti shape memory alloy using taguchi–grey relational analysis approach. In: Recent advances in mechanical infrastructure. Springer, Singapore, pp 13–23

Sheth M, Gajjar K, Jain A, Shah V, Patel H, Chaudhari R, Vora J (2021) Multi-objective optimization of inconel 718 using Combined approach of Taguchi—Grey relational analysis. In: Advances in mechanical engineering. Springer, Singapore, pp 229–235

Wankhede V, Jagetiya D, Joshi A, Chaudhari R (2020) Experimental investigation of FDM process parameters using Taguchi analysis. Mater Today Proc 27:2117–2120

Williams RE, Rajurkar KP (1991) Study of wire electrical discharge machined surface characteristics. J Mater Process Technol 28:127–138

Yadav AK, Yadav SKS (2020) Experimental study of Zinc coated and bare electrode machining of Ni-alloy for EDM-a comparative study

Yang C-B et al (2017) Single and multiobjective optimization of Inconel 718 nickel-based superalloy in the wire electrical discharge machining. Int J Adv Manuf Technol 93(9–12):3075–3084

Effect of Speed and Temperature on the Tribological Behaviour of ADI

Rajendra M. Galagali, **M. H. Ashok**, **Vishwanath M. Khadakbhavi**, **J. Shivakumar**, **Suprit Malagi**, and **Chiranjivi Patil**

Abstract The investigations were done on the sliding wear (Dry) of austempered ductile iron against temperature and sliding speed by using the pin-on-disc machine. The performance of wear, coefficient of friction and temperature were observed with regard to the sliding contact. The wear mechanism predominant was investigated by metallographic observations on worn surfaces. The wear rate was high up to 2 m/s sliding speed and drastically decreased above 2 m/s speeds. At room temperatures, the increase in wear rate is due to the work hardening effect which was observed because of conversion of remained austenite into martensite. As in the case of elevated temperatures, a steady wear rate is observed with a dry sliding condition which increased drastically with speed. The temperature in hands with the sliding speed influences wear rate to a greater extent. But a lower value is observed with the coefficient of friction with the sliding speed in both the conditions, that is room temperature and elevated temperature. Even there is increase in the temperature level as the speed increases and became near to constant at about 2.5 m/s. Burnt spots are being seen on the worn surface at various locations subjecting the material to severe plastic deformation.

Keywords Austempered ductile iron · Wear · Elevated temperature · Coefficient of friction · Dry sliding wear

1   Introduction

Metals play a very important role in the human engineering life. Last few decades out of metals, iron with a ductile nature is having a superior blend of toughness and strength in comparison with grey cast iron. They are widely used in dry as well as

R. M. Galagali · M. H. Ashok · V. M. Khadakbhavi (✉) · S. Malagi · C. Patil
S. G. Balekundri Institute of Technology, Belagavi, Karnataka, India
e-mail: vishwanathk@sgbit.edu.in

J. Shivakumar
Hyderabad Institute of Technology and Management, Hyderabad, Telangana, India

lubricated conditions. Commonly used applications include gears, cylinder levers, piston rings, disc brakes, etc. As it is noticed in the microstructure, it contains nodular graphite which is responsible for good strength, fair fracture toughness and resistance to fatigue (Zavaras et al. 1990; Handbook 1990). The mechanical properties of ductile iron are improved by subjecting it to heat treatment, such as austempering (Handbook 1990; Hayrynen 1995). The austempered ductile iron heat treatment involves austenising the ductile iron at a temperature of about 800–950 °C. Later, it is quenched at a temperature of 200–400 °C to obtain the austempering temperature (Gowri 2013). For enough time, the material is maintained at the same temperature to stabilise to austenite stage. In the final stage, it is cooled to the atmospheric temperature. By changing the austempering temperature, a variety in the grades of austempered ductile iron shall be obtained. The microstructure obtained is ausferrite which is designated by the existence of bainitic ferrite and carbon stabilised austenite (Darwish and Elliott 1993; Daber and Rao 2008).

In the last few years, several investigations were carried out on the behaviour of austempered ductile iron in view of sliding wear (dry) to favour their use in engineering applications. During the test, the surfaces were subjected to shear stress at plastic stage during dry sliding. Due to rigorous stresses, the conversion of remained austenite takes place to martensite (Daber and Rao 2008), hence undergoing strain hardening of the material. Thus, the material becomes eligible to with stand high load and wear conditions (Owahdi et al. 1998; Lu and Zhang 1990). Haseeb et al. (2000) suggested that the wear of the oxidised surface in ADI is mainly contributed by strain-induced conversion of remained austenite and strain hardening process of bainitic ferrite. Kumari and Rao et al. (2009) showed the importance of ausferritic microstructure for improved wear resistance of ADI.

Not a long ago, a lot of investigations were carried out on the tribological behaviour of the ADI material. Luo et al. (1995) did the comparison investigation on the ductile iron with different martensitic and various austenitic conditions. Even Velez (2001) has proved the ADI material having fine ausferrite has higher resistance to wear properties as compared to different irons of similar hardness. It was also showed by Mohan et al. (2002) for fine ausferrite a higher wear resistance was observed in comparison with the tempered martensite with same hardness.

In the current study, the investigation is done to understand the behaviour of the ADI with regard to the dry slides. The conditions were chosen as per the literature survey. The interest is shown on the combined effect of temperature and sliding speed on the coefficient of friction and the wear properties.

2 Material and Experimental Procedures

In this paper, the experimentation is done on the iron which is ductile in nature with the chemical composition: 2.5% Si, 0.161 Mn, 0.014% S, 0.027% Cr, 0.151% Ni, 0.421% Mo, 3.52% C, 0.78% Cu, 0.037% P. The material was treated to austenite phase for 120 mins. at 870 °C. Later, it was treated to the austemper phase for 180 mins. at around 380 °C.

The pin-on-disc instrument is setup to perform the wear test without lubrication (dry) at different temperatures with humid environment of about 285 and 37%. The ADI material is used for the pin of 10 mm diameter with a combination of EN32 steel disc with 65 HRC. Initially, the rubbing surface have a roughness of Ra = 0.5μm and the speed is maintained at a range of 1.5 and 6 m/s. Tests were conducted at room temperature (RT) and an elevated temperature (ET) of 150 °C with a 34.335 N load applied at a distance of 2000 mm. The material loss was measured at an accuracy of 0.1 mg.

The values were acquired and transformed to the wear volumes by taking care of 7.1 g/cm3 density. The total experiments were repeated for 3 times to minimise any errors in the setup.

For every test conducted, the coefficient of friction and the temperature is noted. The temperature is measured with the help of thermocouple made up of chromel–alumel which was fixed in a small pit (Diameter—0.8 mm). The gap of 8 mm is maintained between the pit and the pin. The linear heat flow was considered, and the average temperature of the surface is noted by following the perspective of Ashby et al. (1990) and also by Zhang and Alpas (1997). The scanning electron microscopy is used to examine the obtained wear surfaces. Apart from this the surfaces were even examined by microhardness profiles by utilising Vickers hardness test at 50 kg load.

3   Results and Discussions

The wear loss reached its steady state after running through a small sliding distance of less than 250 m. In Fig. 1, experimental steady-state wear rates are reported as a function of sliding speed. In review with the papers (Fordyce and Allen 1990; Straffelini et al. 2011), it was found that the wear rate decreases with the increase in the speed of the slider for room temperature operating conditions. However, reverse trend is observed when the operating conditions changed, i.e., when the experimental work is carried out with the same processing parameters at ET. For the room temperature conditions at the sliding speed of 1.5 m/s, the wear rate is at its top and slowly decreases as the sliding speed increases. The remaining sliding speeds from 2 to 6 m/s the wear rate has become almost steady. The wear rate observed at ET is steady for sliding speeds from 1.5 to 2.5 m/s. It increased for a sliding speed of 4 m/s but reached its peak value at a sliding distance of 6 m/s. The wear rate observed for a small sliding speed, temperature does not have any role on wear rate. However, its role is predominant at higher sliding speeds. The wear rate is highly influenced by the variations in the sliding speed and temperature. The specific wear rate is defined as the wear mass loss per unit sliding distance per unit load vary between 0.0029 × 10-12 and 0.0461 × 10-12 m2/N at room temperature and 0.023 × 10-12 to 0.1969 × 10-12 m2/N at 150 °C. The results obtained are model of a little oxidative wear at room temperature (Stott 1998; Lim and Ashby 1987) (Table 1).
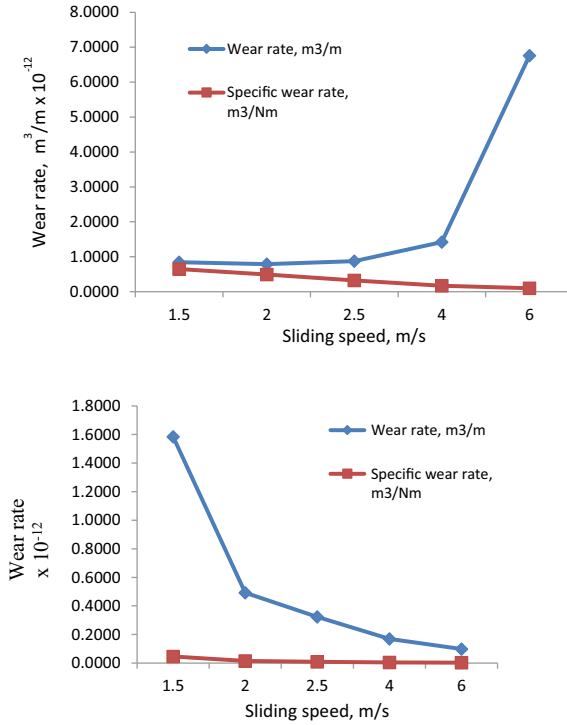
Fig. 1 a. Graph indicating the changes in the wear rate against the sliding speed elevated temperatures. **b**. Graph indicating the changes in wear rate and specific wear rate against the sliding speed at room temperature

Table 1 Table indicating the changes in the wear rate, Coefficient of friction, temperature and microhardness against the sliding speed elevated temperatures

Sl. no	Sliding speed	WR $\times 10^{-12}$ m3/m	COF	Temp	Microhardness, HV
S1 ET	1.5	0.8451	0.5068	194	414
S2 ET	2	0.7887	0.4631	204	396
S3 ET	2.5	0.8732	0.4107	210	352
S4 ET	4	1.4225	0.3262	215	350
S5 ET	6	6.7606	0.2942	220	284
S6 RT	1.5	0.6479	0.6087	75	502
S7 RT	2	0.4930	0.5068	96	513
S8 RT	2.5	0.3239	0.4340	103	521
S9 RT	4	0.1690	0.3903	108	528
S10 RT	6	0.0986	0.3553	111	533

Fig. 2 Graph indicating the changes in the coefficient of friction against the sliding speed at room temperature and elevated temperatures

Figure 2 highlights the changes in the coefficient of friction against the sliding speed at room temperature and elevated temperatures. On an average, it took sliding distance around 500 m to attain the steady state. Figure 3 highlights the changes in the frictional force against the time. It is observed that the coefficient of friction decreases as the sliding speed increases in both cases that is at room temperature and elevated temperature. As observed the wear rate has decreased with the increase in the sliding speed at room temperature is in line with the decrease in the value of coefficient of friction with increase in the sliding speed. However, reverse is observed at elevated temperature though the friction coefficient decreases.

Figure 4 highlights the changes in the surface temperature level against the sliding speed for the room temperature and elevated temperature. It was observed that there is an increase in the surface temperature as the sliding speed increases. Thus, sliding speed has a role in increasing the surface temperature due to local heating.
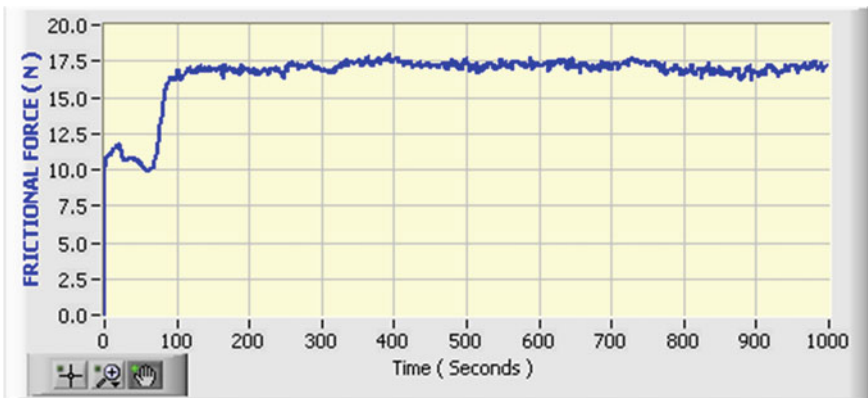
Fig. 3 Graph indicating the changes in the frictional force against the time

Fig. 4 Graph indicating the
changes in the surface
temperature against the
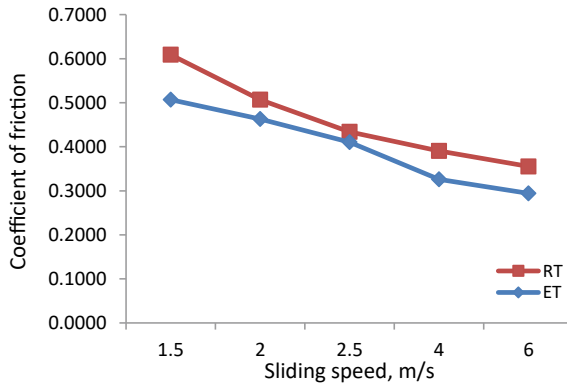sliding speed at room
temperature and elevated
temperatures
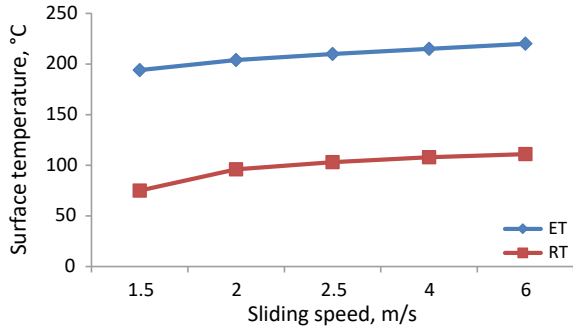
Fig. 5 Graph indicating the
changes in the microhardness
against the sliding speed at
room temperature and
elevated temperature
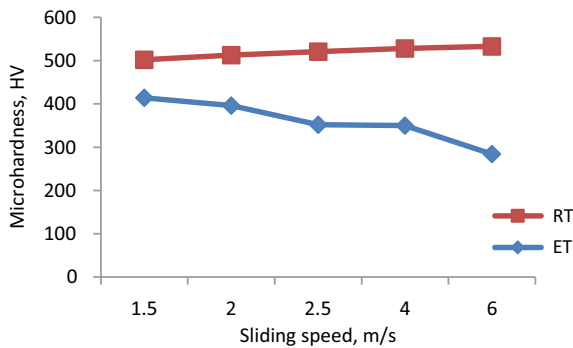
Figure 5 highlights the changes in the microhardness level against the sliding speed for the room temperature and elevated temperature. It is observed that as the sliding speed increases to 2.5 m/s there is considerable increase in the microhardness and further decreases in small amounts with speed. The increase in hardness is an indication of work hardening effects due to the conversion of the remained austenite (formed during asutempering) into complete martensite. The agreement can be seen with the report by Daber and Rao (1998). However, reverse trend is being observed at elevated temperatures indicating no process of conversion of the remained austenite. Thus, supporting the increase in wear rate which is observed for elevated temperature operating conditions.

To know the type of wear a microscopic inspection of worn-out surfaces for the test samples at RT and ET was conducted. The images generated of SEM for the worn-out surface of RT sample is given in Fig. 6a and b.

Some additions of graphite were worn and scattered on the wear track giving rise to a dry lubrication. As a part of evidence, we can observe wear grooves, pits and scratch marks along the movement on the. As evidenced from the morphologies, there is permanent deformation and formation of tongue. This clearly shows that wear has occurred due to the adhesion and the process of delamination.

As evidenced from the worn surfaces of test sample at ET shown in Fig. 7a and b, there are burn out spots being seen at various locations on the surface. The surface

Fig. 6 **a** and **b** SEM image of worn-out surface for the highest speed at RT
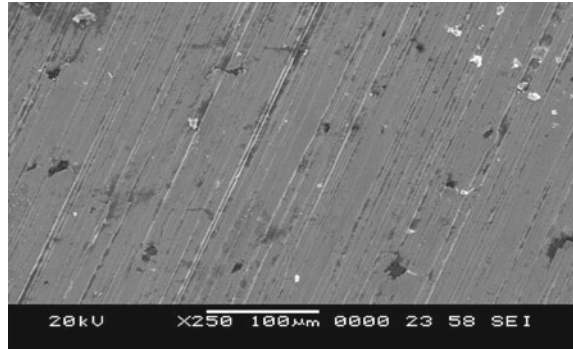
(a)
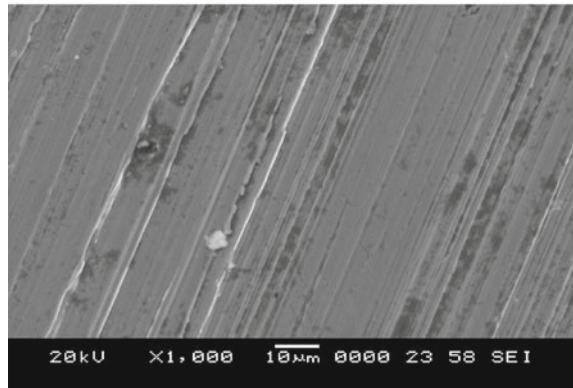
(b)

peels off at those weak surfaces by delamination and groves are formed. This process of wear predominates at ET. Hence, the material is subjected to severe wear at ET.

From wear debris collected shown in Fig. 8, by observation, it is clear that small portion of surface was oxidised. Brown colour powder was formed due to wear as per the given experimental conditions which indicates oxidation wear.

4   Conclusions

In the present investigation the dry sliding wear of ADI was investigated as a function of speed and temperature. The following conclusions can be drawn based on the experimental results and analysis.

As the sliding speed increases to 6 m/sec the wear rate decreases to 0.0986×10^{-12} m^3/min. The hardness measured at this point is 533 which is maximum, and this happens due to the work hardening effects of transformation of retained austenite into martensite at room temperature. But surprised to observe the wear rate 6.7606

Fig. 7 **a** and **b** SEM image of worn surface for highest speed at ET
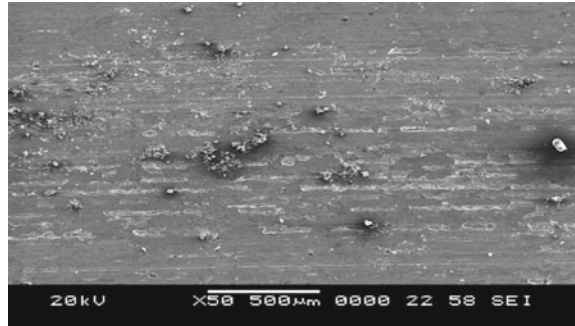
(a)
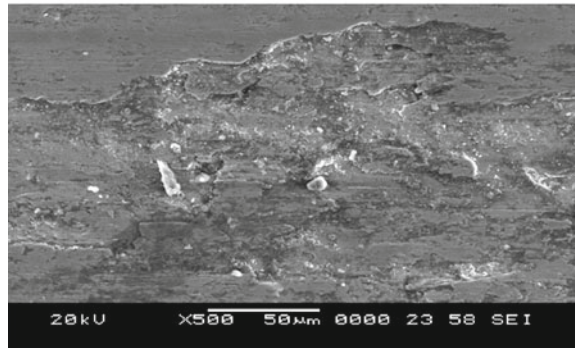
(b)

Fig. 8 Wear debris
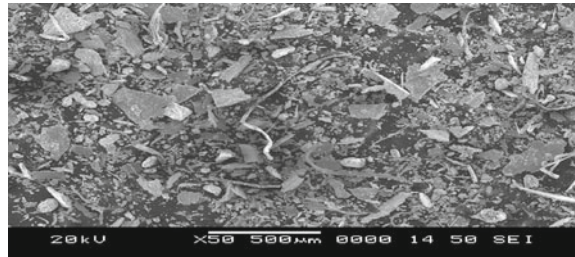
$\times\ 10^{-12}$ m^3/min with sliding speed 6 m/sec at an elevated temperature of 150°C the hardness measured is 284 and is reduced, and this happens due to the prohibition of formation of martensite. The wear is severe for higher sliding speeds of 6 m/s and above. Thus, we can conclude that the material usage at higher sliding speeds at higher working temperatures to be avoided (Daber and Rao 2008).

There is a decrease in the coefficient of friction to 0.3553 at room temperature and at elevated temperature the coefficient of friction of 0.2942 with the sliding speed of 6 m/s. As the waviness or the roughness on the surface is smoothened by the sliding motion of the other material, the movement will be smooth and slips on the surface, hence reducing the coefficient of friction.

There is increase in the surface temperature up to 111 °C at room temperature and up to 220 °C at elevated temperature at higher speeds 6 m/sec. The gap between wear rate and specific wear rate is least at a sliding speed of 6 m/s at room temperature. Worn surfaces of samples at ET test conditions have shown burnt spots subjected to severe plastic deformation. The material gets eroded from these spots by adhesion. Also, the work hardening effects are prohibited making the material weak towards wear resistance resulting in severe wear, especially at higher sliding speeds. This forbidden the material for being used at elevated temperature applications (Ahmadabad et al. 1999).

References

Ahmadabad MN, Ghasemi HM, Osia M (1999) Wear 231:293

Ashby MF, Abulawi J, Kong HS (1990) On surface temperatures at dry sliding surfaces. Cambridge University Press, Cambridge

Daber S, Rao PP (2008) Formation of stress-induced martensite in austempered ductile iron. J Mater Sci 43:357–367

Darwish N, Elliott R (1993) Austempering of low manganese ductile iron, part I processing window. Mater Sci Technol 9:572–585

Fordyce EP, Allen C (1990) The dry sliding wear behavior of an austempered spheroidal cast iron. Wear 135:265–278

Gowri S (2013) Understanding austempered ductile iron process, production, properties and applications–part II. Indian Foundry J 59(2)

Handbook (1990) ASM handbook, properties and selection: irons, steels and high performance alloys, vol 1, ASM International, Materials Park, Ohio

Haseeb ASMA, Islam MdA, Bepari MdMA (2000) Tribological behavior of quenched and tempered, and austempered ductile iron at the same hardness level. Wear 244:15–19

Hayrynen KL (1995) ADI: another avenue for ductile iron foundries. Mod Casting 8:35–38

Kumari UR, Rao PP (2009) Study of wear behaviour of austempered ductile iron. J Mater Sci 44:1082–1093

Lim SC, Ashby MF (1987) Wear mechanism maps. Acta Mater 35:1–24

Lu GX, Zhang H (1990) Sliding wear characteristics of austempered ductile iron with and without laser hardening. Wear 138:1–12

Luo Q, Xie J, Song Y (1995) Wear 184:1–10

Mohan S, Prakash V, Pathak JP (2002) Wear 252:16

Owahdi A, Hedjazi J, Davami P (1998) Wear behavior of 1.5Mn asutempered ductile iron. Mater Sci Technol 14:245–250 (1998).

Stott FH (1998) The role of oxidation in the wear of metals. Tribol Int 31:61–71

Straffelini G, Pellizzari M, Maines L (2011) Effect of sliding speed and contact pressure on the oxidative wear of austempered ductile iron. Wear 270:714–719

Tikotkar RG, Kabadi VR, Ganechari SM (2008) Effect of wear rate and specific wear rate on hard steel. Int J Mech Automob Eng 1(1):2009

Velez JM (2001) Wear 251:1315

Zavaras AA, Broady HD (1990) US Government Research Announcement Index, PB-126647/xab, National Center for Manufacturing Science

Zhang J, Alpas AT (1997) Transition between mild and severe wear in aluminum alloys, Acta Mater 45:513–528. LNCS Homepage. http://www.springer.com/lncs. Accessed 21 Nov 2016

Investigation on Effect of Reinforcing Fillers and Matrix on Polymer Bio-composites—A Review

Sumit Das Lala, Payel Deb, Emon Barua, Ashish Deoghare, and Chiranjib Bhowmik

Abstract Inherent properties of polymer matrix composites (PMCs) like light in weight, resistance to corrosion, and high strength-to-weight ratio make it a promising candidate to substitute the conventional materials and alloys in structural, aerospace, and biomedical applications. Bio-composites are fabricated by reinforcing natural fibers/fillers in the matrix. Matrix and reinforcements are the two major components of the composite material. These constituents have a significant role in improving the composite properties. In the present study, an attempt has been made to investigate the effect of various natural fibers/fillers and matrix components on the properties of the composite. It is observed from the study that content of fiber/filler and surface modification of both matrix and reinforcement can significantly improve the bio-composite properties. The review will explore immense potentiality of the bio-composites toward widespread applications.

Keywords Polymer matrix bio-composites · Reinforcement and matrix · Natural fibers and fillers

S. Das Lala (✉) · C. Bhowmik
Department of Mechanical Engineering, Parul Institute of Engineering and Technology, Parul University, Vadodara, Gujarat 391760, India
e-mail: lncs@springer.com

P. Deb
Department of Mechanical Engineering, The ICFAI University, Agartala, Tripura 799210, India

E. Barua
Department of Mechanical Engineering, Golaghat Engineering College, Bogorijeng, Golaghat, Assam 785621, India

A. Deoghare
National Institute of Technology Silchar, Silchar, Cachar, Assam 788010, India

1 Introduction

Composites are materials synthesized by the combination of two different materials that retain their individual properties in the mixture. The composite shows improved mechanical properties compared to the constituent parent materials. They can be broadly classified as MMCs, CMCs, and PMCs. In the past few years, PMCs have earned a lot of interest from the researchers, scientist, and industrialist owing to their superior properties like high tensile and flexural strength, lightweight can be easily molded to form complicated structures, etc. Literatures reveal that there is a reduction of the total weight of the product to nearly 40–50% by the use of PMCs (Tavakkolizadeh and Saadatmanesh 2003). Bio-composites are mostly fabricated from natural fibers/fillers reinforced in the polymer matrix. Both the components play a significant role in enhancing the composite properties. The present review article provides an overview on the effect of different natural fibers/fillers and matrix on the properties of PMCs. The review emphasizes upon the effect on the properties of composites such as tensile, flexural and impact strength, creep behavior, elongation at break, and biodegradability due to the incorporation of natural fibers/fillers in different weight proportions in the composite. The effect of fiber–matrix treatment, adding of coupling agents, silane agents and blending or hydrophobic coating of matrix in PMCs for improving the fiber–matrix interaction are also been explored in the present work.

2 Polymer Matrix Composites (PMCs)

PMCs are synthesized from either continuous or short fibers reinforced in the polymer matrix. The main purpose of reinforcing polymers is to improve their mechanical properties. The enhanced properties of fiber-reinforced PMCs serve as suitable candidates for repair and retrofit of structures (Tavakkolizadeh and Saadatmanesh 2003). The composites generally consist of two main components—reinforcement and matrix. The composite properties can be considerably enhanced by improving the individual properties of matrix and reinforcement.

2.1 Natural Fibers or Fillers as Reinforcements in Composites

Reinforcement is one of the major components of composite material which plays a significant role in improving their mechanical properties. Literature emphasizes on the various natural fibers like banana, sugar palm, bagasse, jute, henequen, abaca, sisal, hemp, Curaua, *Sterculia urens,* date palm, flax fibers, rice straw as reinforcements in the PMCs. Polymer bio-composites have gained a lot of interest and wider

application in the past few years due to their inherent properties (Wang et al. 2006). They find promising application as reinforcements in PMCs. Sapuan et al. (2006) fabricated a composite using woven banana fiber as reinforcements in epoxy matrix and reported that the strength and Young's modulus in x- and y-directions are 14.14 MN/m^2, 3.398 MN/m^2, and 0.976 GN/m^2, 0.863 GN/m^2, respectively. In addition, when the maximum load of 36.25 N is applied in a three-point bending test, the maximum stress and modulus in x-direction were found to be 26.181 MN/m^2 and 2.685 GN/m^2, respectively. The reason for the enhanced properties of the composites is mostly subjected to the fiber length of banana. Similar approach was adopted by Liu et al. (2009) by reinforcing banana fibers (BaF) in high-density polyethylene (HDPE)/Nylon-6 blends. In order to improve the interaction between the resin and banana fiber, maleic anhydride grafted styrene/ethylene–butylene/styrene triblock polymer (SEBS-g-MA) and maleic anhydride grafted polyethylene (PE-g-MA) were used. The moduli and flexural strength were found to be maximum at 1.7 wt.% SEBS-g-MA concentration, whereas the optimum tensile strength with SEBS-g-MA concentration of 3.3 wt.%. The reason for this is better interfacial bonding of fiber and matrix which improved due to the addition of SEBS-g-MA. There is an increase in the tensile strength initially with BaF content from 29.3 to 38.8 wt.%. It is because of the higher content of cellulose and comparatively lower microfibrillar angle of banana fiber providing better mechanical properties. The value, however, decreases beyond 38.8 wt.% of BaF which is because of the poor wettability of the fiber by the matrix. The modulus and flexural strength, however, increase with increase in fiber content. Mechanical and water absorption tests were carried out by Venkateshwaran et al. (2011) on the banana/epoxy composite material. Sisal fibers were hybridized with banana fiber to improve the properties of the composite. Banana fiber showed high content of ash, carbon, and cellulose along with high strength and hardness which can be further increased by the addition of sisal fibers. The investigator observed that addition of sisal fibers up to 50% enhances the tensile, flexural, and impact strength of the composite by 16%, 4%, and 35%, respectively. The reason is high tensile strength of sisal fibers. But SEM images reveal formation of voids that are attributed to poor wettability of the fiber by the matrix. The main purpose of carrying out the water absorption test is to measure the composite degradation properties. Leman et al. (2008) investigated the Fickian diffusivity constant, amount of moisture present, and factor of correction for the natural fiber composites developed from sugar palm fibers and epoxy composite. Samples were fabricated using 10 and 20% wt. fiber content and oven-dried for 60 h. The maximum value of Fickian diffusivity constant is 3.76 $\times 10^{-7}$ mm^2/s for 20% fiber loading. The specimen with 20% fiber content absorbs the maximum water compared to other specimens. The reason for such behavior is short fibers getting deposited onto the composite floor surface resulting in moisture absorption by the fiber and epoxy resin. Xu et al. (2010) investigated the creep behavior of bagasse fiber-reinforced virgin and recycled polyvinyl chloride (B/PVC), high-density polyethylene (B/HDPE) and wood/HDPE composite. The bagasse/PVC composites exhibited higher value of stiffness compared to bagasse/HDPE composites. But wood/HDPE composite has better stiffness than bagasse/HDPE composites. The effect of temperature on the creep behavior is significant for all the developed

composites. Bagasse/ recycled polyvinyl chloride composite show higher sensitivity than bagasse/ virgin polyvinyl chloride composite which is due to differences of the two matrices or possibly thermal degradation of the recycled PVC. Herrera-Franco and Valadez-Gonzlez (2005) reinforced short henequen fibers in polyethylene matrix and investigated the degree of fiber–matrix adhesion and its effect on the mechanical properties of the composite. Surface treatment process improves the properties of the HDPE/xylene solution. The tensile strength increases by 11% and 19%, respectively, for pre-impregnation process and addition of silane coupling agent. The combination of alkali treatment and silane coupling increases the tensile strength by 30%. An increase of flexural strength by 3% and 13% was stated for alkali treatment of fibers and addition of coupling agent, respectively. The enhancement is due to the chemical interaction of both the coupling agents and alkali treatment on the fibers. Punyamurthy and Sampathkumar (2014) developed treated abaca fiber composites and claimed that composites after treatment show enhancement in impact strength in comparison with untreated abaca fiber-reinforced epoxy composites. Benzene diazonium-treated fibers show the highest impact strength 7.68 mJ/mm^2. Acrylic acid treatment, permanganate treatment, and alkali treatment of fibers show impact strength 7.12 mJ/mm^2, 6.8 mJ/mm^2, and 6.5 mJ/mm^2, respectively. Fiber weight of 30%, 40%, and 50% show impact strengths of 4.1 mJ/mm^2, 6.5 mJ/mm^2, and 4.58 mJ/mm^2 for alkali treated fibers, 4.3 mJ/mm^2, 6.8 mJ/mm^2, and 4.8 mJ/mm^2 for permanganate treated abaca/epoxy composites, 4.46 mJ/mm^2, 7.12 mJ/mm^2, and 5.02 mJ/mm^2 for acrylated abaca-epoxy composites and 4.82 mJ/mm^2, 7.68 mJ/mm^2, and 5.38 mJ/mm^2 for benzene diazonium chloride treated abaca-epoxy composites, respectively. The researchers concluded that upto 40% fiber addition the impact strength increases which are due to the good wettability of fiber with the matrix. However above 40%, the interaction between fiber and matrix decreases resulting in poor mechanical properties of the composite. Oksman et al. (2002) investigated the longitudinal stiffness, strength, and morphology of unidirectional sisal–epoxy composites. The researchers observed that the fibers when included in the composite show a higher effective modulus of 40 GPa as compared to fiber alone which is 24 GPa. However, the tensile strength of fiber in the composite and fiber only are 400 MPa and 550 MPa respectively. It is because of misalignment of fibers in the matrix. The composite shows an elastic modulus 20 GPa and tensile strength 210 MPa with 20% sisal content. Manila hemp fiber reinforced with starch resin was developed by Ochi (2006). The researchers found that up to 70% fiber, the tensile and flexural strengths of the composites were 365 MPa and 223 MPa, respectively. Reduction of pores and fiber wt.% were observed because of the utilization of biodegradable resins. Curaua fibers after alkali treatment were incorporated in biodegradable resin by Gomes et al. (2007) to improve the mechanical properties of green composites. Tensile test shows improved properties of composites after treatment of fibers to about 2–3 times higher than untreated fiber composites, without substantial decrease in strength. The reason is ascribed to better bonding of fibers in the matrix due to the alkali treatment of fibers which removes lignin and other materials improving fiber–matrix adhesion. The tensile strengths were 276 MPa and 334 MPa, respectively, for PF and PS methods. The fracture strain for treated fiber composites was

2.78% which is higher than for untreated fibers (1.24%). S*terculia urens* short fibers (SUSF) incorporated cellulose matrix composites were developed by Jayaramudu et al. (2013). The composites reveal comparable tensile properties than conventional packaging materials, such as polypropylene. The fact being thin fibers arranged in uniaxial directions which provide good tensile strength. But the tensile strength and modulus for the cellulose matrix were 85.1 MPa and 6223 MPa, respectively, that is more in comparison with the developed composite. The composite having quick degradability shows utilization in packing and health science. Date palm fibers and date palm along with flax fibers was incorporated in corn starch by Ibrahim et al. (2014) to develop the composite. Their study shows strong fiber–matrix interaction. However, smaller void fractions were observed up to fiber content of 50% wt. The strength and modulus of date palm/TPS composite increase about three times and two times up to 31 MPa and 2.8 GPa with 20–50% increase in fiber content. The properties decline with 60–80% increase in fiber content. The decrease of property at higher fiber weight is due to the poor wetting of the fibers by the matrix. The flexural strength and modulus increase for 20–50 fiber wt.% composite from 35 MPa and 2.5 GPa, respectively, to 73.6 MPa and 5 GPa, respectively. Moreover, the hybrid composite shows tensile strength of 42.2 MPa and served as a useful composite for different applications. Rouison et al. (2004) fabricated hemp/kenaf fiber-reinforced unsaturated polyester composites after drying the fibers to a moisture content of 1–2%. The researchers observed a decrease in the injection time of resin at high fiber content. The properties of the specimens were examined by tensile and flexural strength. The tensile strength of the composite as compared to pure resin was increased from 13.1 to 44.3 MPa at 20.6% fiber content. The composite reveals high flexural strength of 71.4 MPa for 20.6% fiber content. The motive behind is to achieve better bonding of fiber and the matrix phase which occurred due to the drying of fibers. This resulted in a better wetting of the fibers by the matrix with the removal of gas bubbles creation. Rice straw (RS) along with corn-based adhesives (CA) composite was fabricated by Liu et al. (2012). RS treated utilizing NaOH and hot water reveals better interaction and highest flexural strength at 10% starch content with composite density as 700 kg/m^3. But untreated fillers and matrix reveal greater moisture absorption that increases with increase in starch content upto 14%. There is also reduction in density upto 500 kg/m^3. This is due to the presence of SiO_2 and wax on straw surface in the untreated rice straw and cornstarch. The composite finds promising applications in the manufacturing of ceiling panels and bulletin board. Andersons et al. (2016) incorporated flax fiber in starch acetate for investigating the interfacial shear strength (IFSS) of the composite. IFSS value was found to be 5.5–20.5 MPa for the composite. Increase in fiber content increases IFSS that further decreases with increment in the content of plasticizer. It is due to better mechanical properties obtained by a suitable combination of the high crystalline cellulose content and the low microfibril angle with fiber axis. It is interesting to note that for neat polymer, IFSS equals to or higher as compared to yield strength portraying good interaction within the components.

Natural fillers such as corn stalk, reed stalk, oilseed stalk, and wood flour along with agro-waste materials such as argan, almond, walnut, peanut, peach nut, and rubber seed shell have also marked their contribution as suitable reinforcements in

PMCs. Liu et al. (2010) developed a novel wood floor (WF) reinforced high-density polyethylene (HDPE) and Nylon-6 co-blend composite which consists of both nylon fiber and wood floor as reinforcing materials. The tensile and flexural strengths of pre-dried extruded samples with 30% fiber weight at 190 °C were increased by 16% and 23%, respectively, and tensile and flexural moduli by 32% and 29%, respectively, with respect to the HDPE-based composite. The addition of Nylon-6 microfibrils enhanced the creep behavior of the HDPE/WF composite, but the value was lowered compared to pure HDPE. The reason behind this is low Nylon-6 microfibrils as compared to WF and fractional loss of anisotropic Nylon-6 microfibrillar morphologies during the post-processing. Investigation was carried out by Nourbakhsh and Ashori (2010) by reinforcing corn stalk, reed stalk, and oilseed stalk in thermoplastics such as polypropylene which will act as an alternative to wood fibers. The effect of addition of reinforcement and calcium carbonate on the mechanical properties of the composite was also studied. The researchers observed that elastic and flexural moduli of neat PP samples were 1252 MPa and 1130 MPa, whereas maximum tensile modulus ranges from 2.54 to 2.40 GPa for oilseed stalk and corn stalk filled composites and 2.21 GPa for reed stalk, respectively. The flexural modulus of pure PP is improved twice with the addition of oilseed fiber. The findings are accredited to fiber aspect ratio, improved fiber–matrix adhesion, transfer of stress at the interface, and mixing temperatures. Moreover, high aspect ratio of the oilseed fibers permits better transfer of stress between the matrix and the fibers resulting significant improvement in properties. Essabir et al. (2016) synthesized araun nut shell (ANS) reinforced polypropylene bio-composite and observed an increase tensile strength by 30% and Young's modulus by 62% with the incorporation of ANS particle upto 10% wt. content. In a work reported by Zahra et al. (2015), the authors reported that incorporation of alkali-treated almond shell (AS) particles increases Young's modulus by 14% compared to untreated ones. Moreover, there is also an increase in the thermal stability of the treated composite compared to the neat polymer. Xu et al. (2016) incorporated high temperature modified rubber seed shell in high-density polyethylene and observed an improvement in thermal properties, water absorption properties, and interfacial bonding of the composite developed using 220 °C modified rubber seed shell particles. The filler content is restricted to 50% wt. A work reported by Zaaba et al. (2016) shows high tensile strength, elongation at break, and elastic modulus for treated recycled polypropylene/peanut shell composite at lower filler content of 5–10% wt. However, lower water resistance is observed for the recycled polypropylene/peanut shell composite. Talikoti et al. (2015) reported that incorporation of walnut shell powder in epoxy resin enhances the tensile, flexural, and compression strength by 10.4%, 17.6%, and 42%, respectively. A decrease in the strength of the composite is observed beyond 10% wt. of filler content.

The study reveals that incorporation of natural fibers can improve the properties of the polymer composite. It is also observed that most of the natural fiber composite show improvement in the composite properties with a fiber loading not exceeding 50% wt. except for manila hemp fibers which show improvement of properties upto 70% wt. of filler content. Hence, the fiber content can be restricted within 50% wt. of filler for polymer bio-composites for better properties. Natural fibers contain

elements such as lignin, cellulose, hemicellulose, wax and certain moisture absorbing material which hampers the interfacial adhesion between the matrix and the natural fibers. Thus, various pre-treatment processes such as alkali treatment and saline treatment are to be carried out on the natural fillers to improve their adhesion with the matrix. Hence, there is a mandatory requirement of pre-treatment of natural fibers/fillers before incorporating them in the matrix.

2.2 Biopolymer Matrix in Composites

The matrix is one of the major components of the composite material in which the reinforcements are incorporated. It plays a major role in improving the composite properties. The matrix when grafted or blended with compatibilizers and coupling agents improves fiber–matrix interaction leading to enhanced properties of the composite. The interfacial adhesion between reinforcements and matrix is improved by addition of coupling agents (DiBenedetto 2001). Composites developed with polytrimethylene terephthalate (PTT)/ seam husk (SH) after grafting with glycidyl methacrylate are found to have enhanced mechanical properties compared to PTT/SH composites as reported by Wu et al. (2013). The grafting of composite increases its water resisting capacity compared to ungrafted composite. But biodegradability of both the composites was fairly accurate and is found to be improving with increasing SH content. It is accredited to better filler–matrix interaction obtained as a result of grafting of the PTT. However, ungrafted composite performed better compared to the grafted in a time-dependent course as shown from the results of FB proliferation. Starch- and cellulose-based biopolymers have emerged as an important material for composite production. Wu (2003) fabricated composite with starch as reinforcement and polycaprolactone, maleic anhydride (MAH) grafted PCL as matrix using mixing process. Introduction of PCL shows adverse effect on the composite properties. The reason behind this is poor compatibility issues of PCL and starch. But grafting of PCL improves water resistivity of the composite compared to ungrafted ones. The amount of water absorption for starch/ PCL increases to about 0.9–2% from starch/ PCL-g-MAH. However, fusion heat (Hf) decreases with increase in content of starch in ungrafted composite while it increases for the grafted ones. It is due to the improvement in bonding between PCL and starch due to the addition of MAH. Both the grafted and ungrafted composite show poor mechanical properties. Investigation was carried out on four different composites with grafted PCL by Singh et al. (2003). SEM investigation shows improvement in the biodegradability of the polymer. It was concluded by the authors that this biodegradability was not dependent on the concentration of starch rather it is dependent upon the compatibilization efficiency. The hydrophobic coating of starch particle increases the strength from 16.1 to 17.1 MPa and the elongation at break from 40 to 50 times, respectively. However, reduction in elastic modulus from 256 to 216 MPa was observed. Two composites with thermoplastic pea starch as reinforcement and carboxymethyl cellulose (CMC) and microcrystalline cellulose (MC) as matrix were fabricated by

Ma et al. (2008) utilizing a screw extruder. CMC or MC insertion in the composites enhances bonding with Starch. Tensile strength increases upon increase of both the matrices which is because of the outstanding intrinsic bonding of the filler–matrix interface caused by the chemical similarity (polysaccharide structure) of starch and cellulose derivatives. But MC introduction increased thermal stability, whereas CMC decreased it. It is due to the fact that the thermal stability of CMC is poor leading to lower thermal stability of CMC/TPS composite. Further, TPS/MC shows better water resistance than TPS/CMC composites. Galindo-Rosales et al. (2015) developed cork sheets/shear thickening fluid (STF) composites. It was concluded that mechanical properties of the composite depend on the cork sheets and the shear thickening response of the fluid. Thus, the composites can show better properties with cork sheets despite having network of microchannels and random concentration of the corn starch solution.

Thus, it is seen that matrix plays a significant role in enhancing the composite properties. The properties of the composite may get hampered if the binding between the matrix and the reinforcement is not uniform. It is further observed from the aforesaid study that modification of matrix component is more essential rather than its content in the composite to significantly improve the overall properties of the developed composite. Thus, coupling agents and compatibilizers are grafted with the matrix which improves the fiber–matrix interaction resulting in enhanced properties of the composite.

3 Conclusions

The review provides the current scenario of research in the domain of polymer bio-composites. The major advantage of using polymer as a matrix material develops composites with lightweight, water resistance and significant mechanical properties such as high tensile, flexural, and impact strength. Bio-composites are fabricated by reinforcing natural fibers/fillers in the polymer matrix. It is observed that almost all the bio-composites with filler content not exceeding 50% wt. show improved composite properties. The exception is observed for Manila hemp fiber composite which shows enhancement in composite properties even at 70% wt. of filler loading. The natural fibers are hydrophilic in nature which limits their binding with the hydrophobic polymer matrix. Thus, the composite shows poor mechanical properties. Pre-treatment processes such as silane treatment and alkali treatment are employed to enhance the interaction between the fiber and the matrix and improve their interfacial bonding. It is further noted that improvement on composite properties also depends on the surface modification of matrix through grafting rather than its overall content in the composite. This review will direct the researchers to fabricate bio-composites that can be a replacement to commercially available synthetic composites and suitable for different industrial and household applications.

References

Andersons J, Modniks J, Joffe R, Madsen B, Nättinen K (2016) Apparent interfacial shear strength of short-flax-fiber/starch acetate composites. Int J Adhes Adhes 64(XX):78–85

DiBenedetto AT (2001) Tailoring of interfaces in glass fiber reinforced polymer composites: a review. Mater Sci Eng A 302(1):74–82

Essabir H, Bensalah M.O, Rodrigue D, Bouhfid R, Qaiss AEK (2016) Biocomposites based on Argan nut shell and a polymer matrix: effect of filler content and coupling agent. Carbohydr Polym 143(XX):70–83

Galindo-Rosales FJ, Martínez-Aranda S, Campo-Deaño L (2015) CorkSTFµfluidics-a novel concept for the development of eco-friendly light-weight energy absorbing composites. Mater Des 82(XX):326–334

Gomes A, Matsuo T, Goda K, Ohgi J (2007) Development and effect of alkali treatment on tensile properties of curaua fiber green composites. Compos Part A Appl Sci Manuf 38(8):1811–1820

Herrera-Franco PJ, Valadez-Gonzlez A (2005) A study of the mechanical properties of short natural-fiber reinforced composites. Compos Part B Eng 36(8):597–608

Ibrahim H, Farag M, Megahed H, Mehanny S (2014) Characteristics of starch-based biodegradable composites reinforced with date palm and flax fibers. Carbohydr Polym 101(1):11–19

Jayaramudu J, Reddy GSM, Varaprasad K, Sadiku ER, Sinha Ray S, Varada RA (2013) Preparation and properties of biodegradable films from Sterculia urens short fiber/cellulose green composites. Carbohydr Polym 93(2):622–627

Leman Z, Sapuan SM, Saifol AM, Maleque MA, Ahmad MMHM (2008) Moisture absorption behavior of sugar palm fiber reinforced epoxy composites. Mater Des 29(8):1666–1670

Liu H, Wu Q, Zhang Q (2009) Preparation and properties of banana fiber-reinforced composites based on high density polyethylene (HDPE)/Nylon-6 blends. Bioresour Technol 100(23):6088–6097

Liu H, Yao F, Xu Y, Wu Q (2010) A novel wood flour-filled composite based on microfibrillar high-density polyethylene (HDPE)/Nylon-6 blends. Bioresour Technol 101(9):3295–3297

Liu J, Jia C, He C (2012) Rice straw and cornstarch biodegradable composites. AASRI Procedia 3(1):83–88

Ma X, Chang PR, Yu J (2008) Properties of biodegradable thermoplastic pea starch/carboxymethyl cellulose and pea starch/microcrystalline cellulose composites. Carbohydr Polym 72(3):369–375

Nourbakhsh A, Ashori A (2010) Wood plastic composites from agro-waste materials: analysis of mechanical properties. Bioresour Technol 101(7):2525–2528

Ochi S (2006) Development of high strength biodegradable composites using Manila hemp fiber and starch-based biodegradable resin. Compos Part A Appl Sci Manuf 37(11):1879–1883

Oksman K, Wallström L, Berglund LA, Toledo Filho RD (2002) Morphology and mechanical properties of unidirectional sisal-epoxy composites. J Appl Polym Sci 84(13):2358–2365

Punyamurthy R, Sampathkumar D (2014) Abaca fiber reinforced epoxy composites: evaluation of impact strength. Int J Sci Bas Appl Res 18(2):305–317

Rouison D, Sain M, Couturier M (2004) Resin transfer molding of natural fiber reinforced composites: cure simulation. Compos Sci Technol 64(5):629–644

Sapuan SM, Leenie A, Harimi M, Beng YK (2006) Mechanical properties of woven banana fibre reinforced epoxy composites. Mater Des 27(8):689–693

Singh RP, Pandey JK, Rutot D, Dege P, Dubois P (2003) Biodegradation of poly(caprolactone)/starch blends and composites in composting and culture environments: the effect of compatibilization on the inherent biodegradability of the host polymer. Carbohydr Res 338(17):1759–1769

Talikoti CB, Hawal TT, Kakkamari PP, Patil MS (2015) Preparation and characterization of epoxy composite reinforced with walnut shell powder. Int Res J Eng Technol 2(5):721–725

Tavakkolizadeh M, Saadatmanesh H (2003) Fatigue strength of steel girders strengthened with carbon fiber reinforced polymer patch. J Struct Eng 129(2):186–196

Venkateshwaran N, ElayaPerumal A, Alavudeen A, Thiruchitrambalam M (2011) Mechanical and water absorption behaviour of banana/sisal reinforced hybrid composites. Mater Des 32(7):4017–4021

Wang W, Sain M, Cooper PA (2006) Study of moisture absorption in natural fiber plastic composites. Compos Sci Technol 66(3–4):379–386

Wu CS (2003) Physical properties and biodegradability of maleated-polycaprolactone/starch composite. Polym Degrad Stab 80(1):127–134

Wu CS, Hsu YC, Yeh JT, Liao HT, Jhang JJ, Sie YY (2013) Biocompatibility and characterization of renewable agricultural residues and polyester composites. Carbohydr Polym 94(1):584–593

Xu Y, Wu Q, Lei Y, Yao F (2010) Creep behavior of bagasse fiber reinforced polymer composites. Bioresour Technol 101(9):3280–3286

Xu K, Tu D, Chen T, Zhong T, Lu J (2016) Effects of environmental-friendly modified rubber seed shell on the comprehensive properties of high density polyethylene/rubber seed shell composites. Ind Crops Prod 91(XX):132–141

Zaaba NF, Ismail H, Mariatti M (2016) Utilization of polyvinyl alcohol on properties of recycled polypropylene/peanut shell powder composites. Proc Chem 19(XX):763–769

Zahra F, Mechtali E, Essabir H, Nekhlaoui S, Bensalah MO (2015) Mechanical and thermal properties of polypropylene reinforced with almond shells particles: Impact of chemical treatments. J Bionic Eng 12(XX):483–494

Experimental Investigations and Optimization of WEDM Parameters Using Taguchi Analysis of Pure Titanium

Rakesh Chaudhari, Hem Shah, Izaro Ayesta, L. N. López de Lacalle, and Jay Vora

Abstract Titanium along with its alloys has found vast applications in the areas of aerospace engineering, automobile engineering, biomedical implants, petrochemical, pharmaceutical, and marine industry on the account of their vital properties like greater strength-to-density ratio, outstanding corrosion resistance, maintenance of high strength even at elevated temperatures, excellent bio-compatibility, high fatigue strength, and fracture-resistant characteristics. On the account of their extensive applications, there is a crucial need for accurate and precise machining of pure titanium. Traditional machining of titanium and its alloys is strenuous on the account of their properties like low thermal conductivity, high chemical reactivity, and low elastic modulus. Wire electric discharge machining (WEDM) is a non-conventional manufacturing process that can be utilized for machining titanium and its alloys by overcoming these limitations. In the current work, multi-response optimization of three machining parameters for machining of pure titanium by utilizing the WEDM process has been implemented. Taguchi's robust L_9 orthogonal array (OA) has been employed for generating nine sets of experimental trials, while ANOVA has been used to test the significance of pulse-on time (T_{on}), pulse-off time (T_{off}), and current on two machining responses, namely material removal rate (MRR) and surface roughness (SR). For simultaneous optimization of MRR and SR, the Grey–Taguchi hybrid optimization approach is utilized.

Keywords WEDM · Pure titanium · Taguchi · GRA

R. Chaudhari · H. Shah · J. Vora (✉)
Department of Mechanical Engineering, Pandit Deendayal Energy University, Gandhinagar, Gujarat 382007, India

I. Ayesta · L. N. L. de Lacalle
Department of Mechanical Engineering, University of the Basque Country, Escuela Superior de Ingenieros Alameda de Urquijo s/n., 48013 Bilbao, Spain

1   Introduction

Titanium and alloys of titanium hold a greater strength-to-density ratio and that is retained even at increased temperatures. They have outstanding corrosion resistance and erosion resistance owing to which there are vast applications of these metals in the domain of aerospace engineering, chemical and petrochemical industries, pharmaceutical and food processing sector, offshore and marine engineering (Veiga et al. 2012; Johny and Thiagarajan 2020). They have excellent bio-compatibility, and as a consequence, they have been broadly utilized in biomedical applications and surgical implants. Due to the high fatigue strength and fracture-resistant characteristics of titanium and its alloys, they have found wide applications in nuclear waste storage, water desalination, and production of automotive components, pressure vessels, and process equipment (Johny and Thiagarajan 2020). However, titanium has a very poor thermal conductivity which leads to localization of heat at the point of contact of the tool with the chip resulting in high thermal gradients within the machining zone. This in turn leads to increased tool wear rate and eventually tool failure. Also, titanium is chemically reactive at elevated temperatures which may cause the tool to weld with the metal leading to its premature failure. Titanium has a low elastic modulus which is responsible for deflection of job, chatter, and vibration while machining (Sarkar et al. 2008). Owing to these limitations of conventional machining of titanium, there is a crucial need to explore the machinability of titanium with non-traditional processes. WEDM is one of the processes which can be effectively used to machine titanium. WEDM is a thermo-electric machining technique in which the tool does not have any contact with the work material directly. A high-intensity spark is produced between the continuously fed wire (electrode) and the electrically conductive workpiece causing the metal to melt at the machining zone leading to the removal of material (Sharma et al. 2017; Ho et al. 2004; Majumder and Maity 2018). WEDM process is widely used for difficult-to-machine materials like titanium alloys, shape memory alloys, and some of the super-alloys like Inconel (Manjaiah et al. 2015, 2014; Bharti et al. 2010; Guo et al. 2013; Al-Amin et al. 2021).

Kumar et al. (2015) conducted a study to optimize MRR and overcut for machining of pure titanium with input variables such as T_{on}, T_{off}, current, servo voltage (SV), wire feed rate (WFR), and wire tension (WT) by applying response surface methodology (RSM). Results showed that overcut was highly influenced by T_{on} (30%), followed by T_{off} (28%). The influence of current is only 14%. However, the influence of T_{on} and T_{off} on MRR was observed to be 53% and 23%, respectively. Mouralova et al. (2018) analysed the surface integrity of heat-treated Ti-6-Al-4 V alloy machined with the WEDM process. They concluded that experimental specimens had the lowest SR compared to other non-heat-treated specimens. X-ray analysis showed that several fine micro-fissures and flaws were observed on the material which was stuck on the machined surface. Veiga et al. (2012) investigated the effects of T_{on}, T_{off}, and current on MRR and SR for WEDM machining of pure titanium. The optimized set of machining parameters was obtained as $T_{on} = 6 \, \mu s$,

$T_{off} = 4\,\mu s$, and current $= 6$ A. The predicted set of parameters was in good conformance with the validation trial. Rouniyar and Shandilya (2018) used Taguchi's L_{27} OA for designing experimental runs for powder mixed electric discharge machining (PMEDM) of Ti6Al4V alloy with T_{on}, T_{off}, current, and graphite powder concentration as input parameters which were optimized by using grey relational analysis (GRA) approach for optimizing MRR and SR. The current was the most influential parameter followed by powder concentration. Chalisgaonkar and Kumar (2016) analysed the surface morphology of pure titanium for finish-cut operation of WEDM using zinc-coated and un-coated brass wire considering cutting speed and SR as output parameters and wire type, T_{on}, T_{off}, current, WFR, SV, and wire offset (W_{off}) as input process parameters. Low T_{on} and W_{off} yielded the best surface finish with an un-coated wire electrode after a trim-cut operation. The thickness of the recast layer produced during the rough-cut operation was more than that of the trim cut. Use of lower W_{off} and low T_{on} and current is reported for restraining recast layer denseness. Kumar et al. (2013) conducted the study on multi-objective optimization for WEDM of pure titanium in which Box–Behnken design was utilized for generating experiment matrix with six input parameters, viz. T_{on}, T_{off}, current, spark gap voltage, WFR, and WT, while MRR, dimensional deviation, wire wear ratio (WWR), and SR were considered as output responses that were modelled using RSM and optimized by desirability approach. The importance of input process parameters on response variables was analysed using ANOVA which showed that T_{on}, T_{off}, current, and SGV were the dominating parameters for all the four responses, while WFR and WT did not influence the output parameters. Chalisgaonkar et al. (2020) optimized MRR and SR for machining of pure titanium considering six input parameters using feed-forward back propagation neural network (BPNN). They concluded that with the increase in sparking energy, more depressions are produced and the size of debris also increases. Chalisgaonkar and Kumar (2013) conducted a study on pure titanium for optimizing MRR and SR simultaneously using Taguchi's design of experiments (DOE) methodology and utility concept with T_{on}, T_{off}, current, WFR, SV, and WT as input process variables. Results showed that T_{on}, $T_{off,}$ and SV were dominating factors for MRR alteration, while SR was significantly affected by T_{on}. Ghodsiyeh et al. (2014) used RSM for obtaining an optimal set of parameters with control factors such as T_{on}, T_{off}, current, and SV for optimizing multiple responses, viz. SR, WWR, wire lag (LAG), SG, and white layer thickness for WEDM of Ti-6Al-4 V alloy using zinc-coated brass wire. ANOVA results depicted that the most significant parameters influencing the process are T_{on}, current, and SV. The contribution of T_{on} on SR was 57.16%, while that of SV on SG and LAG was 38.71% and 63.45%, respectively. The influence of current on WWR was found to be 40.45%, while that on white layer thickness was 29.26%. T_{off} was reported to be an insignificant parameter. Rathi et al. (2020) conducted multi-objective optimization for WEDM of nitinol shape memory alloy (SMA) in which T_{on}, $T_{off,}$ and current were used as machining variables for generating Taguchi's L_9 OA. GRA was applied to optimize two machining response parameters, namely MRR and SR. ANOVA results showed that all three process variables were statistically found substantial for machining. The current was the most substantial factor for MRR as well as SR with 81.10%

and 81.02% contribution, respectively. For MRR, T_{on} and T_{off} contributed 2.55% and 16.32%, respectively, while for SR, T_{on} and T_{off} contributed 16.20% and 2.68%, respectively. The optimum set of input parameters was obtained using GRA, and the confirmation experiment revealed a concordance with the projected results.

Taguchi's L_9 OA has been used in the current study to conduct the experiments of pure titanium in the present study. Selected input WEDM process parameters based on past literature include T_{on}, T_{off}, and current while MRR and SR as the response variables. The adequacy and significance of machining parameters were tested by ANOVA for each response variable. Taguchi's approach has a limitation of attaining only one response variable at a time. Pursuant to the same, the GRA technique along with Taguchi's design was used for attaining multiple objectives simultaneously. A validation study was conducted to verify obtained results from optimization.

2 Materials and Methods

In the current research, a rectangular block of pure titanium metal having a thickness of 10 mm was considered for conducting experimental trials with CONCORD make DK-7732 Computer Numeric Control (CNC) WEDM machine. Machining specimens (anode) of dimensions 6 mm × 3 mm × 10 mm were cut using a molybdenum tool electrode wire (cathode) having a diameter equal to 0.18 mm. Three significant process parameters, i.e. T_{on}, $T_{off,}$ and current, were selected for analysis, and their levels were determined based on peer literature survey and practical considerations. In this research, machining trials were conducted by implementing Taguchi's highly sophisticated DOE methodology with the L_9 approach to obtain nine pre-defined sets of experimental parameters. The three control factors were examined at three levels using a 3-level Taguchi design. The significance and effects of the input process parameters on two machining responses, namely MRR and SR, were examined by employing ANOVA. The calculation of MRR was carried out as shown in Eq. 1:

$$\text{MRR} = \frac{\text{Mass of the machined sample}(W)[\text{g}]}{\text{Time taken for machining}(t)[\text{s}]} \tag{1}$$

SR measurement was completed using Mitutoyo make Surftest SJ-410 model. The cut-off length (λ_c) was selected as 0.8 mm with the evaluation length of 8 mm.

3 Results and Discussion

The values were obtained experimentally for SR and MRR for the selected nine trials as displayed in Table 1.

Table 1 Taguchi's L9 array with experimental results

Sr. no	T_{on} (µs)	T_{off} (µs)	Current (A)	MRR (g/s)	SR (µm)
1	40	7	3	0.001674	13.3
2	40	14	4	0.003657	16.5
3	40	21	5	0.000954	14.1
4	60	7	4	0.001689	18.5
5	60	14	5	0.001269	16.6
6	60	21	3	0.000737	15.6
7	80	7	5	0.001968	16.8
8	80	14	3	0.001013	17.2
9	80	21	4	0.000876	17.9

3.1 Influence of Machining Variables on MRR

The analysis of experimental results was conducted using Minitab statistical software. ANOVA was conducted at a 95% level of confidence to test the significance of control factors on each of the machining responses as summarized in Table 2. For a 95% level of confidence, the P-value of the particular control factor should be less than or equal to 0.05 to be significant for the machining process (Rathi et al. 2020). From Table 2, it can be seen that the P-value for T_{on} is greater than 0.05 while the P-value for T_{off} and current is less than 0.05. Hence, it can be inferred that T_{on} is an insignificant parameter, while T_{off} and current both are significant parameters for the machining process. Along with that, the current has the maximum influence on MRR with 80% contribution, while T_{off} has very less influence on MRR with only 20% contribution. The predicted R-squared values and the adjusted R-squared values insinuate that the presented regression model can explain the variation adequately for the selected response. The main effects plot for MRR variation with each of the three control factors is depicted in Fig. 1. From Fig. 1, it is inferred that with the rise in T_{on} and current, the MRR also increases. The reason for this can be attributed to the fact that as T_{on} and current increase, discharge energy and spark intensity also upsurge which causes a rise in the melting and vaporization of the material from the workpiece at

Table 2 ANOVA for MRR

Source	DF	Adj. SS	Adj. MS	F-value	P-value
T_{on}	2	0.000000	0.000000	5.43	0.156
T_{off}	2	0.000001	0.000000	29.67	0.033
Current	2	0.000004	0.000002	166.5	0.006
Error	2	0.000000	0.000000	–	–
Total	8	0.000005	–	–	–

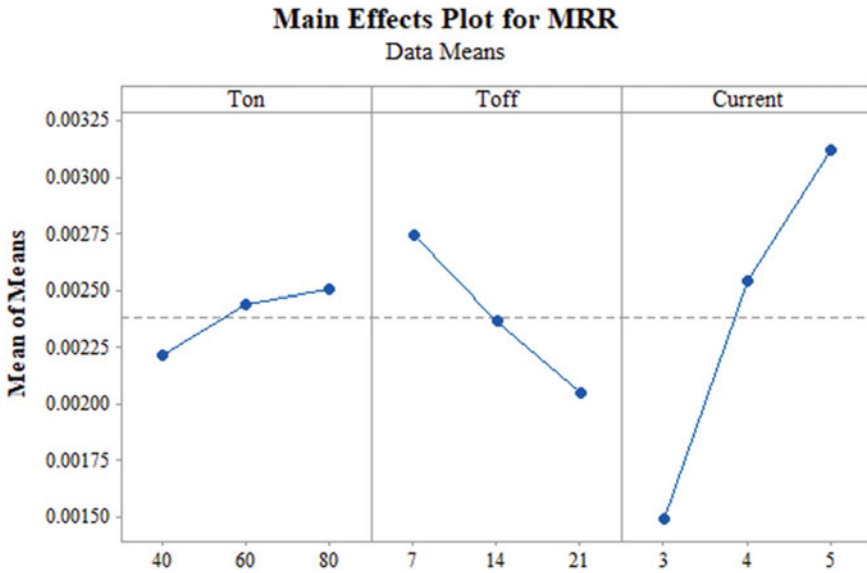R-square = 99.51%, R-square (adj) = 98.03%, R-square (pred) = 90.01%

Fig. 1 Impact of machining variables on MRR

the machining zone resulting in escalation of MRR (Majumder and Maity 2018). Along with this, it can be seen that with the increase in T_{off}, MRR decreases. This is because, as T_{off} increases, discharge energy and spark intensity decline, and as MRR is unswervingly proportional to the discharge energy, it also decreases. As T_{on} is increased, the time for which the pulse will take place in a single duty cycle will increase leading to a boost in discharge energy. As T_{off} is increased, the period for which the pulse will remain off in a single duty cycle will increase leading to a fall in discharge energy (Chaudhari et al. 2021).

3.2 Influence of Machining Variables on SR

Table 3 shows ANOVA for SR. From Table 3, it can be inferred that T_{on} and current are significant parameters for the machining process whereas T_{off} is an insignificant parameter. Furthermore, current proves to be the most influential parameter for SR with 86.49% contribution followed by T_{on} with 9.86% contribution and T_{off} contributed least with only 3.14% contribution. The predicted R-squared values and the adjusted R-squared values insinuate that the presented regression model can explain the variation adequately for the selected response. The main effects plot for SR variation with each of the three control parameters is depicted in Fig. 2.

Table 3 ANOVA for SR

Source	DF	Adj. SS	Adj. MS	F-value	P-value
T_{ON}	2	1.7553	0.87764	19.06	0.050
T_{OFF}	2	0.5585	0.27924	6.06	0.142
Current	2	15.4044	7.70218	167.2	0.006
Error	2	0.0921	0.04604	–	–
Total	8	17.8102	–	–	–

R-square = 99.48%, R-square (adj) = 97.93%, R-square (pred) = 89.53%

Fig. 2 Impact of machining variables on SR

From the main effects plot of SR given in Fig. 2, it is found that SR proliferates with an increase in T_{on} and current. The reason for this is that as T_{on} increases, the discharge energy of the process increases due to which there is an ascent in the melting rate of the metal (Chaudhari et al. 2020). This upswing in the melting rate induces crater proliferations of larger size. Hence, the SR of the machined surface increases. The surge of SR with the increase in current can be attributed to the fact that greater currents cause ionization of the deionized water which also contributes to the inflation of crater size. The SR is found to decrease with the rise in T_{off} as discharge energy decreases with the increase in T_{off} leading to the plunging of the crater dimensions and hence reducing SR (Chaudhari et al. 2020).

From the main effects plot of MRR, the optimal combination of machining parameters is obtained as $A_3B_1C_3$. This is the same as the combination of parameters used

in run 7 of Taguchi's L_9 OA which provides the best MRR of 0.0019685 g/s. Moreover, the optimal combination of machining parameters of SR is $A_1B_3C_1$. Hence, a conflict of optimality was found between the two quality characteristics. Thus, there is a concrete need for multi-objective optimization of the two quality characteristics (QCH) for arriving at an optimal solution.

3.3 Optimization

Taguchi method can only be utilized to optimize single-objective optimization problems. But in practice, there is more than one dependent variable so the Taguchi method cannot be applied directly. Hence, grey relational analysis (GRA) combined with the Taguchi approach is employed to transform the multiple output optimization model to a single-objective optimization model using grey relational grade (GRG). MRR is a QCH that has to be maximized, hence, the Larger-the-better type Signal-to-Noise (S/N) ratio is considered for MRR while SR is a QCH which has to be minimized, so the Smaller-the-better type S/N ratio is preferred. The GRA optimization is carried out, and the grey relational coefficients (GRC) and their respective GRG are generated. Based on the GRG generated, the factor response table has been constructed as given in Table 4. For each of the control factors, the level having the highest factor response value corresponds to the optimal level value for that particular parameter.

From Table 4, the optimal set of machining parameters acquired is $A_2B_1C_3$. The predicted and experimental values of MRR and SR are given in Table 5. The experimental values are in virtuous conformance with the experimental values which corroborates the legitimacy of the investigation.

Table 4 Factor response table

Parameters	Level 1	Level 2	Level 3
T_{on}	0.5453	**0.6165**	0.5553
T_{off}	**0.6088**	0.5523	0.5559
Current	0.5739	0.5609	**0.5822**

Table 5 Validation trial

	Predicted	Experimental
Levels	$A_2B_1C_3$	$A_2B_1C_3$
MRR (g/s)	0.003528	0.003644
SR (μm)	14.53	14.28

4   Conclusions

In this research work, an investigation on pure titanium was carried out to optimize MRR and SR simultaneously for WEDM machining using Grey–Taguchi combined approach. Taguchi's robust L_9 OA was used as DOE, while ANOVA was used to test the significance of the control factors. The key findings of the investigation are as follows:

1. T_{off} and current were found to be significant parameters for MRR, whereas for SR, current and T_{on} were obtained as significant parameters.
2. ANOVA results proved that that current was the most significant parameter for MRR as well as SR with 80% and 86.49% contribution, respectively. Followed by current, the second most influential parameter was T_{off} for MRR with 20% contribution and T_{on} for SR with 9.86% contribution.
3. The predicted R-squared values and the adjusted R-squared values insinuate that the presented regression model can explain the variation adequately for the selected responses.
4. The optimum set of input parameters obtained using the Grey–Taguchi hybrid approach is $A_2B_1C_3$. The corresponding values of T_{on}, T_{off}, and current are 60 µs, 7 µs, and 5 A, respectively.
5. To examine the legitimacy of the predicted optimum set of parameters, a confirmatory experimental trial was conducted and the results of the same were in good conformance with the predicted results which proves that the methodology and results of the experimental investigation are legitimate.
6. The confirmation experiment indicated an improvement of 3.28% overpredicted value for MRR while 1.72% overpredicted value for SR.

References

Al-Amin M, Abdul-Rani AM, Ahmed R, Shahid MU, Zohura FT, Abd Rani MD (2021) Multi-objective optimization of process variables for MWCNT-added electro-discharge machining of 316L steel. Intl J Adv Manuf Technol, 1–20

Bharti PS, Maheshwari S, Sharma C (2010) Experimental investigation of Inconel 718 during die-sinking electric discharge machining. Int J Eng Sci Technol 2(11):6464–6473

Chalisgaonkar R, Kumar J (2013) Optimization of WEDM process of pure titanium with multiple performance characteristics using Taguchi's DOE approach and utility concept. Front Mech Eng 8(2):201–214

Chalisgaonkar R, Kumar J (2016) Investigation of the machining parameters and integrity of the work and wire surfaces after finish cut WEDM of commercially pure titanium. J Braz Soc Mech Sci Eng 38(3):883–911

Chalisgaonkar R, Kumar J, Pant P (2020) Prediction of machining characteristics of finish cut WEDM process for pure titanium using feed forward back propagation neural network. Mater Today Proc 25:592–601

Chaudhari R et al (2020) Optimization of parameters of spark erosion based processes, in spark erosion machining. CRC Press, pp 190–216

Chaudhari R, Vora J, Lacalle LN, Khanna S, Patel VK, Ayesta I (2021) Parametric optimization and effect of nano-graphene mixed dielectric fluid on performance of wire electrical discharge machining process of Ni55. 8Ti shape memory alloy. Materials 14(10): 2533

Ghodsiyeh D, Golshan A, Izman S (2014) Multi-objective process optimization of wire electrical discharge machining based on response surface methodology. J Braz Soc Mech Sci Eng 36(2):301–313

Guo Y, Klink A, Fu C, Snyder J (2013) Machinability and surface integrity of Nitinol shape memory alloy. CIRP Ann Manuf Technol 62(1):83–86

Ho KH, Newman ST, Rahimifard S, Allen RD (2004) State of the art in wire electrical discharge machining (WEDM). Int J Mach Tools Manuf 44(12–13):1247–1259

Johny A, Thiagarajan C (2020) Investigation of surface integrity and it's optimization on pure titanium using molybdenum wire by reciprocated travelling WEDM–a review. Mater Today Proc 33:2581–2584

Kumar A, Kumar V, Kumar J (2013) Multi-response optimization of process parameters based on response surface methodology for pure titanium using WEDM process. Intl J Adv Manuf Technol 68(9):2645–2668

Kumar A, Kumar V, Kumar J (2015) Semi-empirical model on MRR and overcut in WEDM process of pure titanium using multi-objective desirability approach. J Braz Soc Mech Sci Eng 37(2):689–721

Majumder H, Maity K (2018) Application of GRNN and multivariate hybrid approach to predict and optimize WEDM responses for Ni-Ti shape memory alloy. Appl Soft Comput 70:665–679

Manjaiah M, Narendranath S, Basavarajappa S (2014) Review on non-conventional machining of shape memory alloys. Trans Nonferr Met Soc China 24(1):12–21

Manjaiah M et al (2015) Effect of electrode material in wire electro discharge machining characteristics of Ti50Ni50−xCux shape memory alloy. Precis Eng 41:68–77

Mouralova K, Kovar J, Klakurkova L, Blazik P, Kalivoda M, Kousal P (2018) Analysis of surface and subsurface layers after WEDM for Ti-6Al-4V with heat treatment. Measurement 116:556–564

Rathi P, Ghiya R, Shah H, Srivastava P, Patel S, Chaudhari R, Vora J (2020) Multi-response optimization of Ni55. 8Ti shape memory alloy using taguchi–grey relational analysis approach. In: Recent advances in mechanical infrastructure. Springer, Singapore, pp 13–23

Rouniyar AK, Shandilya P (2018) Multi-Objective optimization using Taguchi and grey relational analysis on machining of Ti-6Al-4V alloy by powder mixed EDM process. Mater Today Proc 5(11):23779–23788

Sarkar S, Sekh M, Mitra S, Bhattacharyya B (2008) Modeling and optimization of wire electrical discharge machining of γ-TiAl in trim cutting operation. J Mater Process Technol 205(1–3):376–387

Sharma N, Raj T, Jangra KK (2017) Parameter optimization and experimental study on wire electrical discharge machining of porous Ni40Ti60 alloy. Proc Inst Mech Eng Part B J Eng Manuf 231(6):956–970

Veiga C, Davim JP, Loureiro AJ (2012) Properties and applications of titanium alloys: a brief review. Rev Adv Mater Sci 32(2):133–148

Multi-response Optimization of Alumina Powder-Mixed WEDM Process Using Taguchi-TOPSIS Approach of Nitinol SMA

Rakesh Chaudhari, Manav Sheth, Het Patel, Kishan Fuse, Izaro Ayesta, L. N. López de Lacalle, and Jay Vora

Abstract Shape memory alloys are used in a variety of industries, including aircraft, medicine, automobiles, tubing, petroleum industry, and many more. Nitinol which primarily contains varying concentrations of nickel and titanium is one of the most extensively used SMAs. WEDM process is a well-known technique for the production of intrinsic and complicated shapes for materials that are hard to machine. In the present work, three different concentrations of aluminum oxide powder (Al_2O_3) were considered to mix with the dielectric fluid of WEDM. Powder-mixed-wire electrical discharge machining (PM-WEDM) is a promising development in WEDM performance. The experimental design is developed using Taguchi L9 orthogonal array. Three levels of four control variables were taken into consideration. The key objective of this paper is to observe improvement in material removal rate (MRR) and surface roughness (SR) from a powder-mixed configuration. The output response is affected by different input variables like pulse-on time (T_{on}), pulse-off time (T_{off}), current, and powder concentrations. Technique for order preference by similarity to ideal solution (TOPSIS) was used as an optimization method to determine the most appropriate combination based on the different process parameters.

Keywords Alumina powder · PM-WEDM · Shape memory alloys · Nitinol · TOPSIS · Optimization

R. Chaudhari · M. Sheth · H. Patel · K. Fuse · J. Vora (✉)
Department of Mechanical Engineering, Pandit Deendayal Energy University, Gandhinagar 382007, Gujarat, India
e-mail: jay.vora@sot.pdpu.ac.in

I. Ayesta · L. N. L. de Lacalle
Department of Mechanical Engineering, University of the Basque Country, Escuela Superior de Ingenieros Alameda de Urquijo s/n., 48013 Bilbao, Spain

1 Introduction

Alloys that remember or memorize the initial form and once deformed revert to same shape while being heated upto a specified temperature is known as Shape memory alloy (SMA). The material was first recognized by Ölander (1932). This material memorizes the shape over its distortion at higher temperatures. The material which is deformed in its martensite phase returns to its prior memorized shape when it is heated up to a temperature well above its austenitic finish temperature (Rathi et al. 2020). This phenomenon of memorizing only the high-temperature phase is known as the one-way shape memory effect. Another form of shape memory effect (SME) is a two-way SME that takes place when the alloy memorizes various shapes at two temperatures. The material here returns to its low-temperature shape when it is transformed into martensite upon cooling. This property of the alloy has made it popular in the field of biomedical as well as orthopedic domain owing to its notable characteristics such as pseudo-elasticity and shape memory effect (Chaudhari et al. 2020a). The alloys find its application in various fields such as robotics, automotive, sensors, manufacturing industries, and actuators (Khanna et al. 2020, 2021; Chaudhari et al. 2019). Nitinol is one of the widely recognized binary alloys which has nearly similar proportions of nickel titanium. Nitinol alloy is also known for its surprising property such as super-elasticity and biocompatibility. The nickel-based alloys possess an austenitic matrix owing to which they harden rapidly at the time of machining (Weinert and Petzoldt 2004). Larger amount of time needed for operation, tool wear increase, inferior surface quality, etc., are some of the reasons which obstruct the conventional machining of these alloys (Chaudhari et al. 2020b; Lin et al. 2000). Other factors such as ductility, higher hardness, and chemical reactivity worsen its aspect of machining with traditional methods (Khanna et al. 2021; Chaudhari et al. 2020c; Chaudhari 2019). Thus, non-traditional techniques are more preferred for processing of SMAs. In addition, the end application of these alloys requires excellent dimensional precision, fair surface integrity, and acceptable surface roughness (SR).

Wire electrical discharge machining is one such machining process that has efficient performance in processing different components with greater accuracy along with varying hardness and complex shapes, which is otherwise near to impossible for operation using traditional machining methods (Sheth et al. 2021). Various process variables are needed to be controlled to achieve better surface finish and better surface integrity (Chaudhari et al. 2020d). One of the ways to improve the performance along with productivity is addition of nanopowder to EDM electrolyte. The inclusion of these particles improves ignition mechanism and henceforth improves spark discharge (Jeswani 1981). This enables efficient machining performance (Chaudhari et al. 2021; Sivaprakasam et al. 2019).

Kumar et al. (2019) analyzed to compare the machining of Inconel 825 based on nanopowder-mixed EDM and conventional EDM processes. Here, Al_2O_3 nanopowder was mixed with the dielectric fluid. As compared to the conventional dielectric, the Al_2O_3 mixed dielectric fluid had a superior surface condition and an

improved rate of material removal. MRR raised from 32.75 to 47 mg/min, while SR value lowered from 2.245 to 1.487 μm. Ranjan et al. (2019) researched the effects of the various variables of the process and powder concentration on MRR and SR. The two abrasive powders analyzed were aluminum oxide and silicon carbide. The highest value of MRR at 6.1 mm^3/min has been observed with the use of aluminum oxide powder. The increment in the powder concentration for both powders has shown a decrease in the SR values. A review study conducted by Shard et al. (2018) showed that powder-mixed dielectric fluid has shown better machining of titanium alloys. Yi et al. (2017) used cutting fluid suspended with graphene oxide for the drilling of Ti6Al4V and determined that there was a significant improvement in SR up to 15.1% and also the cutting force was reduced by 17.21% when graphene oxide was mixed with cutting fluid compared to conventional cutting fluid. Patel et al. (2016) investigated the effect of the incorporation of aluminum powder. The experimental findings showed that increasing peak current and T_{on} increases MRR. MRR continues to increase as slurry concentrations increased from 0.5 to 1.5 g/L. And optimum slurry concentration was found to be 1 g/L.

According to the existing literature, a limited amount of study has been performed to analyze the machining of SMAs using the PM-WEDM technique. In the current study, four input parameters were selected: T_{on}, T_{off}, current, and powder concentration, with MRR and SR as the two most important response variables. TOPSIS as an optimization technique was used in combination with Taguchi for designing the experimentation.

2　Experimental Setup and Experimentation

To machine the samples, a nitinol cylindrical bar with a diameter of 6 mm was used on a concord wire-cut EDM machine DK7732. As the electrode, 0.18-mm diameter molybdenum wire had been utilized. Figure 1 shows the PM-WEDM setup used during experimentation. For the machining results of MRR and SR, four process parameters, T_{on}, T_{off}, current, and powder concentration, were considered. Input parameters along with their range were selected based on the past literature and preliminary experimental trials. Taguchi's L9 orthogonal array was considered for experiments with four input variables, each of three levels. For calculating MRR value, the weight of the work material was determined along with the time taken for machining. Mitutoyo's Surftest SJ410 model was utilized to determine surface roughness. Table 1 presents the experimentally obtained MRR and SR values for 9 different experimental runs.

Fig. 1 PM-WEDM setup used during experimentation

Table 1 Experimental results

Trial run	T_{on} (μs)	T_{off} (μs)	Current (A)	Powder conc (g/L)	MRR (g/s)	SR (μm)
1	25	5	2	0	0.00134	5.55
2	25	10	4	0.5	0.00208	4.55
3	25	15	6	1	0.00289	3.32
4	50	5	4	1	0.00340	5.22
5	50	10	6	0	0.00300	6.43
6	50	15	2	0.5	0.00122	5.21
7	75	5	6	0.5	0.00453	5.43
8	75	10	2	1	0.00168	4.88
9	75	15	4	0	0.00204	7.13

3   Results and Discussion

3.1   *Effect of Input Process Parameter on MRR*

Figure 2 depicts variations in MRR as input parameters change. It has been found that as current and T_{on} rise, so does MRR. The discharge energy of the spark rises as T_{on}
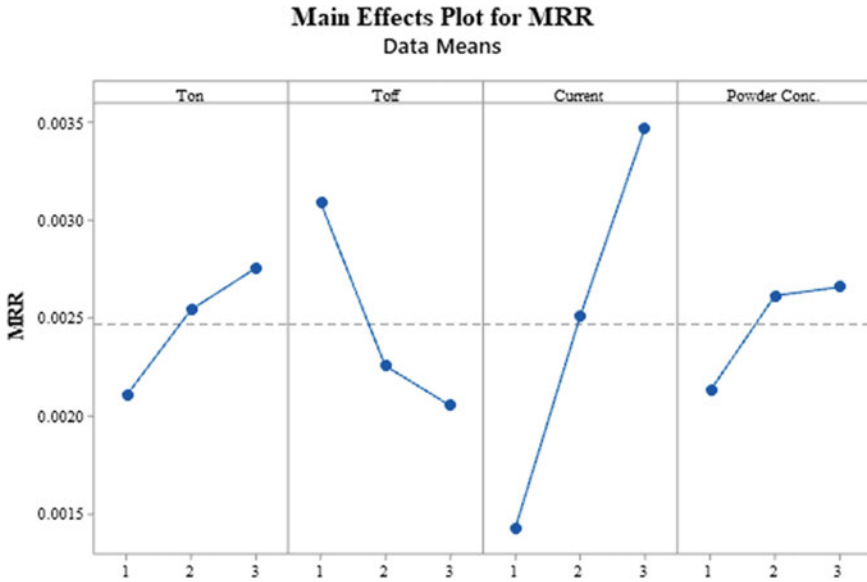
Fig. 2 Main effects plot for MRR

increases (Chaudhari et al. 2019). The work material is then melted and vaporized as an effect of the thermal energy. An increase in the value of T_{on} also increases the discharge energy. This leads to obtaining a higher MRR value. Also, MRR decreases as T_{off} value rises due to decrement in spark which is a result of lowered discharge energy (Chaudhari 2019). MRR value has been shown in Fig. 2 which indicates that it is increased in tandem with the rise in powder concentration. Sparking frequency and thermal conductivity increases due to addition of Nano-powders which in turn leads to an enhancement in the erosion rate from surface of work (Chaudhari et al. 2021). Thus due to the higher erosion rate, an improvement in the MRR is observed.

3.2 Effect of Input Process Parameter on SR

Figure 3 illustrates the main effect plot of SR that presents how SR varies with the change in input variables. It can be seen that T_{on} and current have an adverse influence on the machined surface quality. Increased T_{on} also implies more discharge energy (Chaudhari et al. 2020c). As a result, the SR rises as T_{on} increases. Figure 3 also indicates a reduction in SR as T_{off} increases. Higher T_{off} reduces the number of active sparks, lowering the discharge energy (Sheth et al. 2021). Small craters are created as a result of less discharge, which significantly lowers the SR of the work surface. After incorporating powder to dielectric liquid, the strength of fluid insulation drops, which expands the difference between the electrodes. Due to expansion of these gaps,

Fig. 3 Main effects plot for SR

an increase in powder concentration occurs which leads to the formation of small craters due to decrease in the electrical intensity over the machining spot. This in turn enhances performance by achieving a better surface quality (Chaudhari et al. 2021). On increasing the powder's concentration, there is a decrease in SR values significantly, which shows a favorable response. It was also observed that the powder concentration plays a significant role in MRR and SR.

3.3 Multi-objective Optimization Using TOPSIS

Taguchi's method is limited to optimize a single objective at a time we only can get optimize the combination of output parameters differently (Wankhede et al. 2020). TOPSIS is a method for determining order choice based on how closely it resembles the optimal solution. In 1981, Hwang and Yoon introduced the TOPSIS hypothesis (Gadakh 2012). The TOPSIS's objective is to achieve the right alternative that is the shortest length to positive and the furthest away to the negative optimal solution (Shivakoti et al. 2017). Mathematical calculations involved in the TOPSIS method are comparatively easier, and the obtained results are much reliable in comparison with other MCDM techniques (Gadakh 2012; Shivakoti et al. 2017). Thus, to optimize two response parameters by TOPSIS method, the following procedures were followed:

Step 1: Initially, the decision matrix was generated and obtained the normalized decision matrix.

Table 2 TOPSIS analysis with closeness coefficient index

Exp. no.	T_{on} (μs)	T_{off} (μs)	Current (A)	Powder conc. (g/L)	MRR (g/s)	SR (μm)	CCi	Rank
1	25	5	2	0	0.00134	5.55	0.190	9
2	25	10	4	0.5	0.00208	4.55	0.378	5
3	25	15	6	1	0.00289	3.32	0.604	3
4	50	5	4	1	0.0034	5.22	0.617	2
5	50	10	6	0	0.003	6.43	0.454	4
6	50	15	2	0.5	0.0012	5.21	0.217	7
7	**75**	**5**	**6**	**0.5**	**0.00453**	**5.43**	**0.766**	**1**
8	75	10	2	1	0.00169	4.88	0.290	6
9	75	15	4	0	0.00205	7.13	0.207	8

Step 2: Based on the weight defined for the criteria, the weighted normalized matrix was calculated. By considering the importance of both the objectives, an equal weight of 0.5 for MRR and SR has been considered.

Step 3: From the weighted normalized matrix, positive and negative optimal solutions were obtained.

Step 4: Based on positive and negative optimal solutions, separation of each alternative was calculated.

Step 5: Finally, the relative closeness coefficient index (CC_i) was obtained.

Step 6: From the closeness coefficient index, the ranks were determined in descending order of their value.

After conducting the method step by step, the final results are shown in Table 2.

Thus, the highest value of CC_i is the final alternative with the highest ranking which here was found to be the 7th run of the experiment. T_{on} of 75 μs, T_{off} of 5 μs, discharge current 6 A, and 0.5 g/L Al_2O_3 powder concentration were determined to be the optimum input parameter conditions utilizing TOPSIS to achieve maximum MRR and minimize SR.

4 Conclusions

The influence of processing parameters on performance responses was investigated using WEDM machining of 6 mm nitinol cylindrical bar in this study. The input variables considered were T_{on}, T_{off}, current, and Al_2O_3 powder with different concentrations, while the performance responses were SR and MRR. To determine the importance of process parameters, 9 experiments were performed using the Taguchi L9 orthogonal array. Using TOPSIS, process parameters were successfully optimized for multiple machining characteristics with an optimal combination of input variables

as T_{on} of 75 µs, T_{off} of 5 µs, discharge current 6 A, and 0.5 g/L Al_2O_3 powder concentration. It was clear from the results of the experimental tests that usage of Al_2O_3 powder with 0.5 g/L concentration was significantly favorable for MRR as well as SR, in comparison with conventional WEDM process (without powder addition).

References

Chaudhari R et al (2019) Pareto optimization of WEDM process parameters for machining a NiTi shape memory alloy using a combined approach of RSM and heat transfer search algorithm. Adv Manuf, 1–17

Chaudhari R, Vora JJ, Patel V, Lacalle LN, Parikh DM (2020c) Effect of WEDM process parameters on surface morphology of nitinol shape memory alloy. Materials 13(21):4943

Chaudhari R, Vora JJ, Mani Prabu SS, Palani IA, Patel VK, Parikh DM, de Lacalle LNL (2019) Multi-response optimization of WEDM process parameters for machining of superelastic nitinol shape-memory alloy using a heat-transfer search algorithm. Materials 12(8):1277

Chaudhari R, Vora JJ, Parikh D (2020). A review on applications of nitinol shape memory alloy. In: Recent advances in mechanical infrastructure: proceedings of ICRAM 2020

Chaudhari R, Vora JJ, Patel V, López de Lacalle LN, Parikh DM (2020) Surface analysis of wire-electrical-discharge-machining-processed shape-memory alloys. Materials 13(3):530

Chaudhari R et al (2020) Optimization of parameters of spark erosion based processes, in spark erosion machining. CRC Press, pp 190–216

Chaudhari R, Vora J, Lacalle LN, Khanna S, Patel VK, Ayesta I (2021) Parametric optimization and effect of nano-graphene mixed dielectric fluid on performance of wire electrical discharge machining process of Ni55. 8Ti shape memory alloy. Materials 14(10):2533

Chaudhari R, Khanna S, Vora J, Patel VK, Paneliya S, Pimenov DY, Giasin K, Wojciechowski S (2021) Experimental investigations and optimization of MWCNTs-mixed WEDM process parameters of nitinol shape memory alloy. J Mater Res Technol

Gadakh VS (2012) Parametric optimization of wire electrical discharge machining using TOPSIS method. Adv Prod Eng Manag 7(3):157

Jeswani M (1981) Effect of the addition of graphite powder to kerosene used as the dielectric fluid in electrical discharge machining. Wear 70(2):133–139

Khanna S, Patel R, Marathey P, Chaudari R, Vora J, Banerjee R, Ray A, Mukhopadhyay I (2020) Growth of titanium dioxide nanorod over shape memory material using chemical vapor deposition for energy conversion application. Mater Today Proc 28:475–479

Khanna S, Marathey P, Paneliya S, Chaudhari R, Vora J (2021) Fabrication of rutile–TiO2 nanowire on shape memory alloy: a potential material for energy storage application. Mater Today Proc

Khanna S, Marathey P, Patel R, Paneliya S, Chaudhari R, Vora J, Ray A, Banerjee R, Mukhopadhyay I (2021) Unravelling camphor mediated synthesis of TiO₂ nanorods over shape memory alloy for efficient energy harvesting. Appl Surf Sci 541:148489

Kumar A, Mandal A, Dixit AR, Das AK, Kumar S, Ranjan R (2019) Comparison in the performance of EDM and NPMEDM using Al 2 O 3 nanopowder as an impurity in DI water dielectric. Intl J Adv Manuf Technol 100(5):1327–1339

Lin H, Lin K, Chen Y (2000) A study on the machining characteristics of TiNi shape memory alloys. J Mater Process Technol 105(3):327–332

Ölander A (1932) An electrochemical investigation of solid cadmium-gold alloys. J Am Chem Soc 54(10):3819–3833

Patel S, Thesiya D, Rajurkar A (2016) Effect of aluminium powder concentration on powder mixed electric discharge machining (PMEDM) of inconel-718. J Mach Forming Technol 8(1/2):29

Ranjan A, Chakraborty S, Kumar D, Bose D (2019) Multi-objective optimization of a hybrid machining process abrasive powder mixed WEDM of inconel 718 using particle swarm optimization technique. Mater Today Proc 18:3606–3616

Rathi P, Ghiya R, Shah H, Srivastava P, Patel S, Chaudhari R, Vora J (2020) Multi-response optimization of Ni55. 8Ti shape memory alloy using Taguchi–grey relational analysis approach. In: Recent advances in mechanical infrastructure. Springer, Singapore, pp 13–23

Shard A, Shikha D, Gupta V, Garg MP (2018) Effect of B 4 C abrasive mixed into dielectric fluid on electrical discharge machining. J Braz Soc Mech Sci Eng 40(12):1–11

Sheth M, Gajjar K, Jain A, Shah V, Patel H, Chaudhari R, Vora J (2021) Multi-objective optimization of inconel 718 using combined approach of Taguchi—grey relational analysis. In: Advances in mechanical engineering. Springer, Singapore, pp 229–235

Shivakoti I, Pradhan BB, Diyaley S, Ghadai RK, Kalita K (2017) Fuzzy TOPSIS-based selection of laser beam micro-marking process parameters. Arab J Sci Eng 42(11):4825–4831

Sivaprakasam P, Hariharan P, Gowri S (2019) Experimental investigations on nano powder mixed Micro-Wire EDM process of inconel-718 alloy. Measurement 147:106844

Wankhede V, Jagetiya D, Joshi A, Chaudhari R (2020) Experimental investigation of FDM process parameters using Taguchi analysis. Mater Today Proc 27:2117–2120

Weinert K, Petzoldt V (2004) Machining of NiTi based shape memory alloys. Mater Sci Eng A 378(1–2):180–184

Yi S, Li G, Ding S, Mo J (2017) Performance and mechanisms of graphene oxide suspended cutting fluid in the drilling of titanium alloy Ti-6Al-4V. J Manuf Process 29:182–193

Rail Welding Technology: Processes and Welding Quality

Trushil Alpeshkumar Patel and Vishvesh Badheka

Abstract In developing countries like India, the transportation system plays an important role in overall economic development. The major transportation system in India is Indian Railways which has a vast transportation network to carters to the needs of 1.38 billion people. Also, the development of the country's first 508.17-km-long bullet train corridor is under process for economic prosperity. To run and maintain this, rail welding plays an important role. The paper reviews on different types of rail welding techniques as they are important for heavy load trains and high-speed rail network, i.e., flash butt welding, gas pressure welding, thermite welding, and enclosed arc welding with the weld quality, and also highlights the different welding techniques that are been used in developed countries and futuristic weld techniques that can be utilized for better weld quality of the rail.

Keywords Welding in rail · Flash butt welding · Gas pressure welding · Thermite welding · Enclosed arc welding · Welding quality

1 Introduction

India is an emerging nation and developing in all the sector; to cope with this development, the Indian Railways plays an important role as a major transportation system in India, and it is one of the highest contributors in Indian GDP. The rail network of India lies more than 123,000 km with total of 22,000 trains (https://indianrailways.gov.in/railwayboard/view_section.jsp%3Flang=0%26id=0,1, 2021). The Indian Railway System (IRS) comprises 18 divisions of railway network which are developing and growing constantly to meet the demand and provide service to the nation. This IRS is country's biggest job recruiting system due to vast range of field and size. The demand of railway network in India has been growing since the globalization for export and import of goods as it plays an important role. The advantages of this rail

T. A. Patel (✉) · V. Badheka

Department of Mechanical Engineering, Pandit Deendayal Energy University, Gandhinagar 382007, India

e-mail: trushil.pmc18@sot.pdpu.ac.in

network are high safety in the operation and 8–10% reduction in fuel consumption. The welding in rail is one of the most important and complicated jobs due to rail cross section and the material of the rail that is used which has high carbon content material and has high damage resistance as they are suitable for this application. The rail is made up of JIS E1101 with carbon content 0.72–0.82 wt.% and HB321-388 (Saita et al. 2013). As the rail network in India rises, the quality of the rail should be maintained at optimum levels and the introduction of bullet train which is high-speed train would require better weld quality of rail than that are in the current usage due to heavy load stress on the weld region.

2 Welding in Rail

In rail industries, welding plays a major role as the connection of track is been done using welding technologies. The rail is usually been welded in section of 200 m mostly carried out in the industries (indoor welding process) which are then later welded on site with the help of different welding techniques (Saita et al. 2013). The rail was joined using rivets in past which has been developed to welding processes due to its better weld quality and high safety factor. The total welding portion in the rail network is 2% of the total rail, which is approximately 2000 km of only weld portion in the railway network (Saita et al. 2013). The common methods that are used in this process are flash butt welding, gas pressure welding, thermite welding, and arc welding.

2.1 Different Types of Welding in Rail

The different type of welding in rail has been done are been explained in the paper. The most common welding methods that are used in Indian Railways are thermite method and SKV thermite welding which is short-term preheating welding method (Indian Railways 1996).

2.2 Thermite Welding Process

It is one of the cheap methods which is used to weld the rails (Indian Railways 1996). In this method, an external filler metal is used to create the weld; hence, there is no loss of the rail length and the process is much more relaxing and can be performed easily. Figure 1 represents the thermite welding process.

In this, the welding takes place due to exothermic reaction caused between the aluminum and oxidized iron. In this process, a mold is created around the rail which
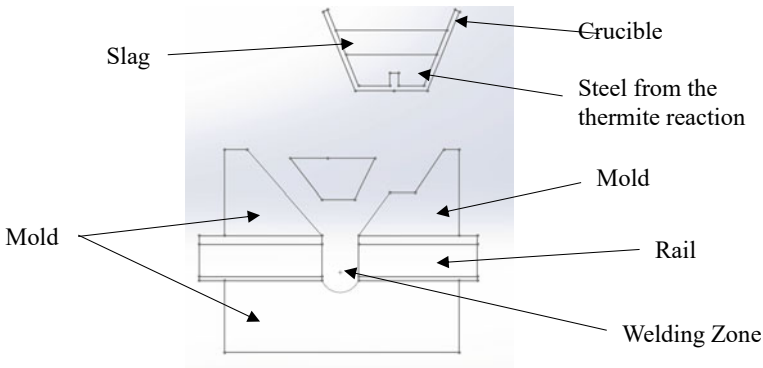
Fig. 1 Thermite welding

is preheated with oxygen or propane to prevent air bubble during the solidification process.

In this process, the thermite powder consists of oxide iron and aluminum which reacts within 15–20 s with the help of ignition agent resulting in 2000 °C of temperature which cause molten state of iron; this process takes place in crucible (Saita et al. 2013). After the melting of the material, the molten iron is poured into the mold and solidification takes place which takes up to 5 min (Saita et al. 2013).

After completion of solidification, the trimming of the extra portion of the weld is done with the help of the hydraulic trimmer.

In this process, the use of filler material results in decreasing the mechanical properties of the joint as the addition of filler material which has different compositions than that of the rail.

2.3 Enclosed Arc Welding Process

Figure 2 shows the enclosed arc welding process. The process takes place between the rails which consist of gap of 12–16 mm and also 8–22 mm depending upon the condition (Kuzmenko 2006). The total timing required for the welding process is more than 60 min which comprise both pretreatment and posttreatment processes (Okumura 1995). In this process, an electrode is used to form a web-like structure from the base to the head of the rail when the electric current is passed through the system and then the electrode melts and forms the bond between the welds; a special type of electrode is made so that the carbon content of the weld is high to achieve the desired properties (Karimine 1996).
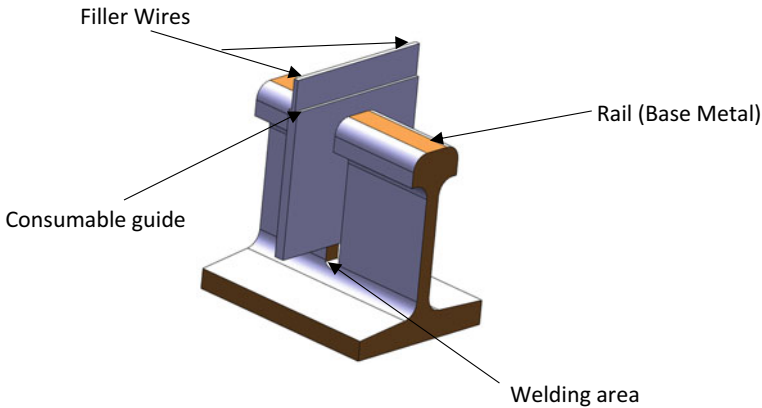
Fig. 2 Enclosed arc welding

2.4 Flash Butt Welding Process

The total process takes place in for major steps that are preheating process, flashing process, upsetting process, and trimming process. This technique has high productivity and high-quality weld (Saita et al. 2013). In this process, a large hydraulic press is needed with high voltage transformer. In mobile-type field welding, the alternative current is mainly used with approximate time of 2–4 min, whereas for shop welding direct current is used with high power source and a preheating system is used which reduces the time to 1.5–2 min for the process (Mitsuru 2015).

Preheating: In this process, the rail is been heated using electric short-circuiting method in which a large current is flown through the rail faces which result in spark formation and this process helps in reducing the time for the melting of the rail in the upcoming process. This step can be carried out to reduce the time of weld.

Flashing: In this process, the electric sparks are continuously produced which result in melting of the faces of rail as this starts to take place; the rail is been moved toward each other at a rate of 0.1–2 mm/s; as a result, in this the rail length is reduced to 10–20 mm of the total length of the rail (Saita et al. 2013).

Upsetting: When the rail is joined, an external pressure/load is applied because plastic deformation is seen at the molten part of the rail which result in bulge formation at the weld formation which can be seen in Fig. 3.

Stripping: Before the cooling of the weld, the bulge that is present at the joint is removed and the profile of the rail is obtained.

This process is mainly used to join short rail to form 200-m-long rail which is done in industries (indoor welding plant); some of the welding plants for the process are shown in Table 1.
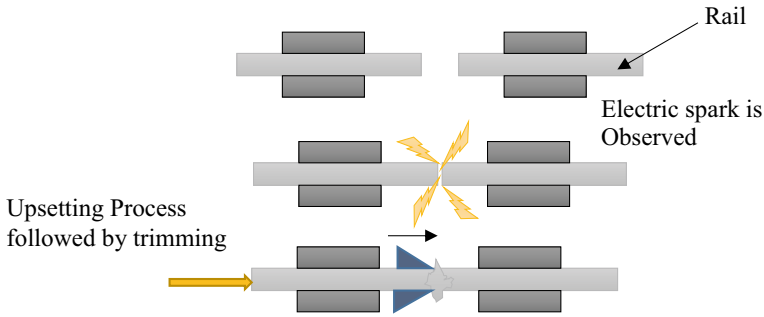
Fig. 3 Flash butt welding

Table 1 Flash butt welding at different locations in India (Civil-Railway Airport Harbour Engineering-Railway Engineering-Rail Joints and Welding of Rails 2009)

Sr. no.	Railway division	Location of industries where flash butt is performed (in plant)
1	Central Railway	Chalisgaon and Kalyan
2	Eastern Railway	Bandel and Mughalsarai
3	Northern Railway	Meerut
4	Southern Railway	Arakkonam
5	Western Railway	Sabarmati
6	South Eastern Railway	Jharsuguda
7	West Central Railway	Itarsi
8	South Central Railway	Maulali
9	North Eastern Railway	Gonda

2.5 Gas Pressure Welding Process

In gas welding, an oxygen acetylene torch is used to heat the rail ends. This task is performed by a skilled worker, and the rail is heated up to the temperature of 1000–1200 °C (Saita et al. 2013). A high pressure is applied to both ends which result in the formation of this weld joint due to plastic deformation of the rail. As the rail cools down, a bulge formation can be seen which results in decreasing the rail length to 20–40 mm of the total length (Saita et al. 2013). Figure 4 shows the gas welding process. After the rail cools down, the trimming process is taken place to remove the bulge for better surface finish. The trimming process takes place with the help of trimmers and cutters. The overall time required for this process is 6–7 min (Saita et al. 2013). Countries like Japan use this type of techniques, about 31% of the total welding in the rail system (Kuzmenko and Bajić 2010).
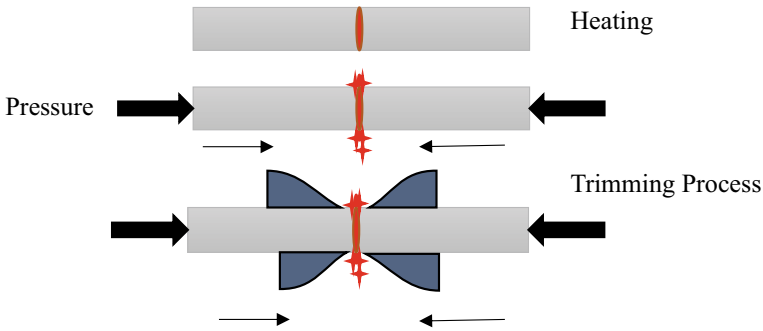
Fig. 4 Gas pressure welding

3 Different Parameters in Welding

Different parameters such as weld quality, drawbacks of weld, improvement in weld quality, and the comparison between the welds based on costing, time, type of labor, mobility, and many more are discussed.

3.1 Weld Quality

The weld quality depends upon the heat-affected zone (HAZ), hardness number, microstructure, working parameters, and many more. With the help of HAZ and hardness number, the material strength can be determined. The higher the HAZ, the higher the change in microstructure of the weld resulting in decreasing the strength. The higher the hardness number, better the strength of the weld joint. Table 2 compares the different weld technologies based on HAV and Hardness number the result shows that the least have that is seen is in thermite welding whereas the maximum was obtained in gas pressure welding as the heating in this is done using torch which result in heat conduction in rail and increasing the HAZ. The maximum hardness that can be achieved in the weld is by thermite welding and the minimum in flash butt welding process.

Table 2 Weld quality based on HAZ and hardness number

Properties	Gas pressure welding	Enclosed arc welding	Flash butt welding	Thermite welding
Heat-affected zone (HAZ) (Saita et al. 2013)	100 mm	50 mm	30–45 mm	40 mm
Hardness number	280–320HB (Yamamoto et al. 2014)	280–320 (V. D. 2010)	320–340HB (Bauri et al. 2020)	340-360HB (Mutton and Alvarez 2004)

The failure at the joint is 60% of the total failure in the rail; hence, the weld quality plays a major role in maintenance of the track as reducing this failure will decrease maintenance and cost of repair for the rail system (Dearden 1968). Offereins and Mutton (2001) proved that the ductile property of the weld using thermite welding process can be increased by 1.7 times just by increasing the cooling time, and the fracture failure of the weld is increased from 60 to 450 MPa.

3.2 Drawback in Welding Process

The common welding problems that are faced by different welding methods are explained in Table 3 with the effect of weld quality.

Figure 5 shows the failure of thermite weld with respect to the days; it has been seen that the maximum failure is observed in first 60 days. The major defect that was observed was due to skink age of central line at the foot of the weld, and the major reason behind is lack of preheating before the welding process (Mutton and Alvarez 2004). The main types of failure which are seen in this type of welding are straight break or vertical fracture at the central line or at the edge web corners (Offereins 2001).

Table 3 Common welding problems

| Welding process	Conditions	Outcome due to the conditions
Thermite welding	For winter conditions, the cooling rate is increased	As the cooling rate increases, the crystallization of the weld pool results in crack formation in weld and creation of pores in the slag (Kozyrev et al. 2017)
Flash butt welding	For curvature rail lines	Due to curvature in the rail, huge shock is exerted by the wheels on the rail which result in damaging of weld zone due to heavy stress on the weld part (Baracaldo and Santos 2018)
Gas pressure welding	Lack of contact during heating and forging process	Causing weld defects like inclusion of oxides which decreases the weld quality (Saita et al. 2013)
Enclosed arc welding	Lack of preheating	In HAZ, the cold cracking can be observed and elimination of this is not possible (Saita et al. 2013)
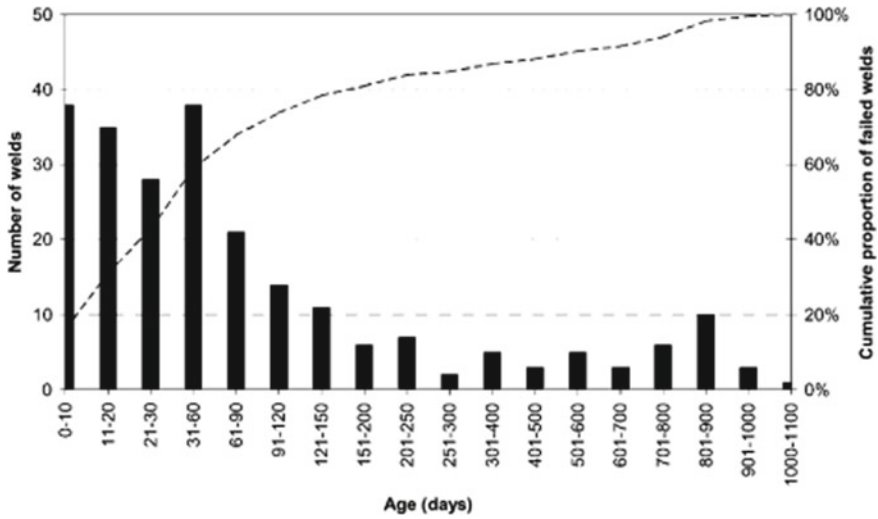
Fig. 5 Total welding failure with respect to number of weld and days (Mutton and Alvarez 2004)

3.3 Increased Weld Quality

Figure 6 represents the effect of heat treatment on the thermite weld. The thermite weld has microstructure that is coarse in nature and is sensitive to stress change which may result in less resistance to fatigue failure. To increase the weld quality of thermite weld, a post-heat treatment can be done so that the ductility and toughness can be increased. The heat treatment replaces coarse to finer structure of ferritic–pearlitic structure and fine ferrite networks (Ilić et al. 1999).

Figure 7 shows the FBW for different processes based on machine type, i.e., the use of stationary FBW (indoor) and mobile FBW (outdoor mostly carried in rail track assembly area). It is found that the use of stationary FBW machine is preferred as the
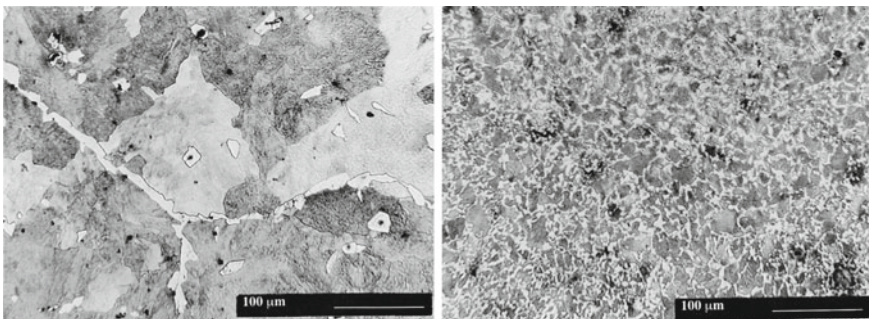

Fig. 6 Microstructure of weld before heat treatment (left image) and after heat treatment (right image) (Ilić et al. 1999)
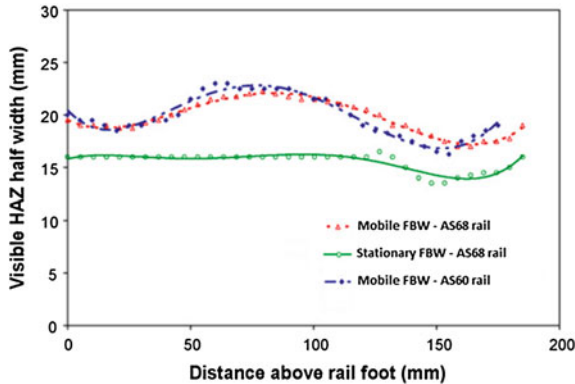
Fig. 7 HAZ for different FBW processes (Tawfik et al. 2008)

HAZ of this is much narrower due to lesser heating period and high material removal rate during upsetting process (Tawfik et al. 2008). The mobile FBW machine requires high heat input which results in high HAZ and lowers the weld quality (Tawfik et al. 2008).

In flash butt welding process to avoid and eliminate the crack formation and reduce the undesirable microstructure such as martensite and bainite, a post-heat treatment can be performed by applying blue flames on weld within 2 min after the upsetting process and that should be maintained for at least for 10 min till the temperature s to 400–450 °C (Indian Railways 1996).

In gas pressure welding, the reduction in CO_2 emission by one-third with the same properties of weld as shown in Fig. 8 can be achieved just by changing the gas which is acetylene to mixture of hydrogen and ethylene gas with similar HAZ of conventional process (Yamamoto et al. 2014).

3.4 Parameter Comparison of Welding Process

The cost of welding also plays a major role in deciding the type of weld that has to be performed the most to least expensive process of weld are as follows gas pressure welding > Flash butt welding (400–600/weld) > Thermite welding (700–1200/weld) > Enclosed arc welding (Saita et al. 2013). Table 4 shows different types of welding and its comparison on different parameters.
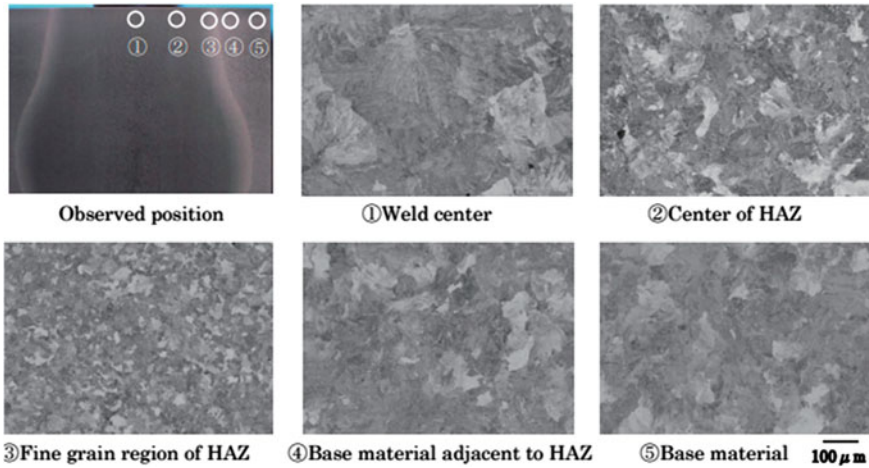
Fig. 8 Microstructure of weld performed using mixture of hydrogen and ethylene gas (Yamamoto et al. 2014)

Table 4 Parameter comparison of welding process (Saita et al. 2013; Indian Railways 1996)

Parameters	Gas pressure welding	Enclosed arc welding	Flash butt welding	Thermite welding
Cost of welding	Low cost	Low cost	High cost (400–600 Rs/weld)	Expensive (700–1200 Rs/weld)
Cost of equipment	High	Low	High	Low
Quality of weld	Excellent	Good	Excellent	Good
Mobility	Medium	High	Low	High
Time for welding	5–7 min	60 min	2–4 min	60 min
Skilled and unskilled workers	Skilled worker	Skilled worker	Unskilled worker	Unskilled worker
Special operation	Use of torch to heat the rail	High current is required to perform the weld	Hydraulic press and voltage transformer	Crucible is required for the reaction process

4 Welding in Developed Countries and Future Scope

For gas pressure welding, an automated system was developed to reduce the time and to minimize the trimming process, which can be easily operated by unskilled worker (Saita et al. 2013). In this technique, one of the workpieces is oscillated at particular amplitude and frequency which result in friction pressure; as a result, plastic deformation is seen, the oscillation is stopped, and force is applied to the joint which result in welding (Bhamji et al. 2011). Japan uses gas welding to weld its rail which contributes to 30% of the total weld in rail, the gas welding is done

using mixture hydrogen, and ethylene gas as hydrogen can be stabilized with the help of hydrocarbons (Yamamoto et al. 2008). Russia uses electro-contact method to weld its rail which comprises 600 thousand by rail welding train and 50 thousand by moving rail (Kalashnikov 2017).

Country like Australia uses thermite welding for installation and repair purposes as the baring axial load of the system is up to 37.5 tones, where the small section is welded using flash butt weld up to 400 m; then, this section is welded using thermite welding (Mutton and Alvarez 2004). Use of single crucible improves the weld quality as well as the process can be much easier and more attractive toward the crew welds (Offereins and Mutton 2001). For enclosed arc welding process, a semi-operated mechanical machine has been manufactured to decrease the weld timing to reach 30 min (Tatsumi 2008). To remove the reheating process in thermite reaction, an alternative thermite mixture is used to achieve the hardness of the rail, which also result in decreasing the time of welding process (Fukada 2001). The use of high manganese steel crossing for the cross section of the rail with flash butt welding as the weld process which results in wear resistance and improving the performance of the rail (Zhang et al. 2007).

Linear friction welding is one of the new technologies which are been experimented for the repair of rail; this is most commonly used in aero engines (Li et al. 2016) as this technique gives better weld quality, is environmental-friendly, and requires lesser energy. The development of APT 1500RT which is a rail bonding vehicle, which can perform flash butt welding the machine performed flash butt welding at an altitude of 2,230 m in Mexico efficiently (Plasser Theurer Railway-News 2018).

Hybrid welding process combines laser beam with an electric plasma, the laser helps in increasing the productivity rate of the weld, and this system can be used to weld the rail as an alternative method for better weld quality in the future (Mathieu et al. 2020). Narrow gap arc welding is a technique that can be used to weld thick section using cored and flux cored wire; this is much more economical method with lesser weld time (Mathieu et al. 2020).

5 Conclusion

- In installation of rail, welding plays an important role and the selection of the welding techniques is a major part depending upon the conditions.
- In the present work, review of four common techniques which are flash butt welding, gas pressure welding, thermite welding, and enclosed arc welding is reported.
- In India, the techniques that are currently used in welding are thermite welding and flash butt welding processes. As the development of the rail network the adoption of new techniques to increase the weld quality and reduce the environmental hazard such as using of alternative mixture of gas in gas pressure welding and use of enclosed arc welding process.

- To decrease the weld failure in thermite and flash butt welding process, a post-heat treatment can be performed which will decrease the chance of crack formation and maintain high weld quality.
- For high-speed rail, the gas pressure and enclosed arc welding can be used as high-quality weld and high strength of the weld.

References

https://indianrailways.gov.in/railwayboard/view_section.jsp%3Flang=0%26id=0,1 (2021)

Baracaldo RR, Santos MC, Echeverría MA (2018) Effect of flash butt welding parameters on mechanical properties of wheel rims Ingeniería mecánica, Universidad Nacional de Colombia, Sede Bogotá, Bogotá, Colombia

Bauri L, Alves L, Pereira H, Tschiptschin A, Goldenstein H (2020) The role of welding parameters on the control of the microstructure and mechanical properties of rails welded using FBW. J Market Res 9(4):8058–8073. https://doi.org/10.1016/j.jmrt.2020.05.030

Bhamji I, Preuss M, Threadgill PL, Addison AC (2011) Solid state joining of metals by linear friction welding: a literature review. Mater Sci Technol 27(1):2–12. https://doi.org/10.1179/026708310x520510

Civil-Railway Airport Harbour Engineering-Railway Engineering-Rail Joints and Welding of Rails (2009)

Dearden J (1968) Continuous welded rails. Br Weld J 4:158–169

Fujii M, Nakanowatari H, Nariai K (March 2015) Rail flash-butt welding technology JFE technical report no 20

Fukada Y (2001) RTRI Rep 15(4):5

Ilić N, Jovanović MT, Todorović M, Trtanj M, Šaponjić P (1999) Microstructural and mechanical characterization of postweld heat-treated thermite weld in rails. Mater Charact 43(4):243–250. https://doi.org/10.1016/s1044-5803(99)00006-6

Indian Railways (1996) Manual for flash butt welding of rails, Government of Indian ministry of railways, Research Designs and Standards Organisation, Lucknow, 226011

Kalashnikov EA (2017) Techniques of welding rails: trends in Russia and abroad E.A

Karimine K (1996) Q J Jpn Weld Soc 14(3):578

Kozyrev NA, Kozyreva OA, Usoltsev AA, Kryukov RE (2017) Modern methods of rail welding. In: IOP conference series: materials science and engineering, vol 253, p 012002

Kuzmenko GV, Bajić D (2010) Elektrolučno zavarivanje popunjavajućom elektrodom, Međunarodno savetovanje. ZAVARIVANJE 2010. Tara (CG), 14–19

Kuzmenko GV (2006) Single-pass arc welding of thick metal using embedded electrode. Paton Weld J 6:35–40

Li W, Vairis A, Preuss M, Ma T (2016) Linear and rotary friction welding review. Int Mater Rev 61(2):71–100. https://doi.org/10.1080/09506608.2015.1109214

Mathieu A, Tkachenko I, Tomashchuk I, Cicala E, Bolot R (2020) Laser-assisted narrow gap arc welding of an 18MND5 steel thick plate. Procedia CIRP 94:551–556. https://doi.org/10.1016/j.procir.2020.09.181

Mutton P, Alvarez E (2004) Failure modes in aluminothermic rail welds under high axle load conditions. Eng Fail Anal 11(2):151–166. https://doi.org/10.1016/j.engfailanal.2003.05.003

Offereins G (2001) BHP reacts quickly to a spate of weld failures. Intl Railw J 41:15–16

Offereins GA, Mutton PJ (2001) Recent experience with the performance of aluminothermic rail welds under high axle loads

Okumura M (1995) Nippon steel technical report 65:41–49

Plasser & Theurer Railway-News (8 March 2018) New rail welding technology proves successful worldwide. https://railway-news.com/new-rail-welding-technology-proves-successful-worldwide/

Poznyakov VD (2010) Properties of welded joints of rail steel in electric arc welding. Paton Weld J 8:16–21

Saita K, Karimine K, Ueda M, Iwano K, Yamamoto T, Hiroguchi K (December 2013) Trends in rail welding technologies and our future approach. Hiroguchi Nippon Steel & Sumitomo Metal Technical Report No. 105. UDC 625.143.48:621.791.5/.7

Tatsumi M (2008) Tetsudosoken Getsurei Happyokai Koenyoushi (Abstract of Collection of Articles of Monthly Presentation Meeting, Railway Technical Research Institute) (3)

Tawfik D, Mutton PJ, Chiu WK (2008) Experimental and numerical investigations: Alleviating tensile residual stresses in flash-butt welds by localised rapid post-weld heat treatment. J Mater Process Technol 196(1–3):279–291. https://doi.org/10.1016/j.jmatprotec.2007.05.055

Yamamoto RI, Tatsumi M, Itoh H, Terashita Y, Yoshida Y (2014) Gas pressure welding method of rails by mixed gas of hydrogen and ethylene gas. Q Rep RTRI 55(1):39–45. https://doi.org/10.2219/rtriqr.55.39

Yamamoto R, Tatsumi M, Terashita Y (2008) Development of Gas pressure welding method applying Hydrogen Gas. RTRI Report, vol 22, no 8, pp 45–50

Zhang F, Lv B, Hu B, Li Y (2007) Flash butt welding of high manganese steel crossing and carbon steel rail. Mater Sci Eng A 454–455:288–292. https://doi.org/10.1016/j.msea.2006.11.018

Evaluation of Mechanical and Thermal Properties of Banana/Aramid/E-Glass Powder Hybrid Composite Plate

D. R. Rajkumar , **S. Karthik** , and **K. Santhy**

Abstract The current study focuses on the production of epoxy composites reinforced with aramid, banana fiber, and E-glass powder, as well as the evolution of their mechanical and thermal properties. The composite specimens are composed of 15:30:5:50 volume fractions of unidirectional aramid fiber, unidirectional banana fiber, E-glass powder, and epoxy resin. Three specimens with different orientations such as 0º, 45º, and 90º of aramid and banana fibers were fabricated using hand lay-up method. The entire fabricated composite has four layers of the order of banana–aramid–aramid–banana fiber. The tensile and flexural properties are carried out experimentally based on ASTM D638 and ASTM D790 standard. From the tensile test, it is observed that 90º orientation of hybrid composite has better tensile strength than other two orientations. However, the 45º orientation of the hybrid composite outperforms the other two orientations in terms of flexural strength. According to TGA study, thermal stability of the composite was improved and in bar with epoxy resin even though natural fiber was present.

Keywords Banana fiber · Aramid fiber · E-glass powder · Fiber orientations · Thermogravimetric analysis

1   Introduction

In recent times, scientist and design engineers are working on hybrid composites which include natural fiber and synthetic fibers for various applications in different fields (Velmurgan and Manikandan 2005; Boopalan et al. 2013; Ramesh et al. 2013). The natural fibers are renewable, non-abrasive, low density, biodegradable, possess a good calorific value, exhibit excellent mechanical properties, and are inexpensive (Ramesh et al. 2014). The amalgamation of natural fibers with glass fiber increases

D. R. Rajkumar (✉) · S. Karthik
CARE College of Engineering, Tiruchirappalli 620 009, India

K. Santhy
Indus University, Ahemadabad 382 115, India

the tensile and flexural strength which can be used for medium strength applications. Jassala et al. (2002) reviewed aramid fibers and reported that its application is limited due to low compressive strength and moisture absorption. It was mainly used in military helmets, aerospace, brake pads, gaskets due to their inherent resistance to organic solvents, fuels, lubricants, and exposure to flame. In 2018, Prasad and Talupula (2018) done a detailed review on the history, synthesis, polycondensation, fiber formation, dope structure, aramid spinning, aramid fiber heat treatment, and structure and property relationship of aramid fiber. In addition, discussed the chemical, physical, thermal, and mechanical properties of aramid fiber.

Corbière-Nicollier et al. (2001) reported the lifetime assessment cycle study to decide the environmental performance of biofiber as a substitute for E-glass fiber. From the study, biofiber was compared with other usages of biomass, and biomaterials are three to ten times efficient than E-glass fiber. Joseph et al. (2002) compared the mechanical properties of banana fibers- and glass fibers-reinforced phenol formaldehyde composites and mentioned the interfacial shear strength of banana fiber-reinforced phenol formaldehyde composite higher than glass fiber. In plastic industry, cellulosic fibers like banana fibers obtained from pseudo-stem of banana plant have been used as cost-cutting fillers. This is exactly attained by surface modification of the resin or the filler materials. Pothan et al. (2003) studied the effect of fiber surface treatments on the fibber–matrix interaction in banana–polyester composites. In his work, the fiber surface was modified perfectly by various silanes and alkali treatment which provides better interfacial interaction between fiber and resin. This was achieved by 1% alkali treatment. The surface modification of the fiber was characterized by scanning electron microscope and Fourier transform infrared spectroscopy. Maleque et al. (2007) reported mechanical properties of pseudo-stem banana fiber-reinforced epoxy composite on the tensile, flexural, and impact strength. The analysis showed that tensile strength on the pseudo-stem banana epoxy composite was increased by 90% compared to virgin epoxy. Banana epoxy composite depicted better result in flexural and impact strength also.

Samal et al. (2009) aimed to evaluate the influence of the fiber volume fraction, fiber length, and alkaline treatment on the mechanical and thermal properties of short random banana fiber-reinforced polyurethane derived from castor oil. From the results, treated banana fiber composites showed better tensile strength and Young's modulus than untreated banana fiber. Another result also produced from the test states that there was increase of fiber volume fraction and length decides the mechanical properties. Merlini et al. (2011) used randomly oriented banana fiber-reinforced composite with volume fraction varying as 5, 10, 15, 17.5 and 20% were fabricated and characterization revealed that the thickness as 5 and 3 mm composite plate. The mechanical test results showed that the 5-mm thickness plate showed better performance in tensile, flexural, and impact strength. In 2017, Ebrahimnezhad-Khaljiri et al. (2017) reported a review on mechanical properties of banana fiber-reinforced composites and manufacturing techniques. It gave very detailed insight on physical, chemical, mechanical properties of banana fiber and shares about filament winding and compression molding method of manufacturing of banana fiber-reinforced composites. Out of these two, compression molding was best

and less expensive method. Dhakal and Gowda (2017) prepared two sets of biocomposites made of banana fiber with epoxy resin with 0, 5, 10, 15, and 20% volume fraction of fiber with 10-mm and 20-mm length. Tensile, flexural, and impact tests were conducted, and the results revealed that above 15% fiber with 20-mm length, mechanical properties were not increased. Thermogravimetric report gave that fiber has the temperature stability up to 220 °C.

Pagnoncelli et al. (2017) evaluated fabrication and performance on hybrid composites made of banana and E-glass fiber composite reinforced with polypropylene. Haake twin screw extruder followed by compression molding method was used to fabricate short banana/glass fiber composite with and without the presence maleic anhydride-grafted polypropylene as a coupling agent. Dilleswara Rao et al. (2017) used an interlayer/layer-by-layer form composites with aramid, and semi-carbon fibers were fabricated by hand lay-up method characterized by thermal and mechanical testing. The mechanical test revealed that more semi-carbon fibers to aramid fiber decrease the tensile and flexural modulus. By thermal test results, for more semi-carbon fibers mass loss will be reduced. Santosh et al. 2018) got improved results on the mechanical properties of the composites by using higher fiber content proved by mechanical and ballistic analysis of aramid/vinyl ester composites. Anidha et al. (2019) fabricated composites using various volume fractions (0.112, 0.166, 0.213, 0.274, and 0.346) of banana and pineapple leaf fibers as reinforcement in polyester resin to study the thermal conductivity of composites on different fiber loadings. Based on the measurement by using scanning electron micrometer, the thermal conductivity and specific heat capacity were decreased with increase in fiber content.

Balaji et al. (2020) carried out an investigation on the dynamic mechanical and tailored morphological behavior of aramid fiber (AF) treated with bagasse/epoxy resin, a biodegradable composite, and found that treated fiber composites have enhanced dynamic mechanical properties compared to those of untreated fiber-based composites. Because of numerous failure problems with conventional bumper material, Sunder Selwyn (2021) fabricated a bumper made of multiple aramid layers of different interior angles to determine the mechanical properties. The tensile and flexural test aramid composites depicted tensile strength of 147 MPa and high flexural strength of 86.8 Mpa which proved aramid composite plates were extremely suitable material for automobile bumper application.

However, to the best of author's knowledge, the combination of unidirectional aramid and banana fibers with E-glass powder has not been reported yet. Hence in this pilot study, these materials are selected along with epoxy resin. Hand lay-up method is adopted to fabricate hybrid composite plate in three different fiber orientations (0°, 45°, and 90°). The hybrid composite plate is cut as per ASTM standards for experiment to determine tensile, flexural, and thermal properties. The observed results are plotted and tabled.

2 Experimental

2.1 Materials

Aramid fiber, banana fiber, and E-glass powder were purchased from Go Green Products Pvt. Ltd., Chennai, India. Epoxy resin (LY556) and hardener (HY 951) were purchased from Herenba Instruments & Engineers Pvt. Ltd., Chennai, India. The physical and mechanical properties of the banana, aramid, E-glass powder, and epoxy resin materials are shown in Table 1.

2.2 Composite Fabrication

In this research work, a four-layered hybrid composite was fabricated using hand lay-up method. First for a dimension of $300 \times 300 \times 3$ mm^3, stainless steel mold is prepared. For easy removal of composite plate after curing, a mosaic wax was applied inside the mold. Then, 5% wt. of E-glass powder was mixed with 50% wt. of epoxy resin (LY556) along with hardener (HY951) in the ratio of 10:1 stirred properly. Then, the unidirectional banana fiber was arranged at 0° direction; after that, E-glass powder, resin, and hardener mixer were poured on the spread banana fiber inside the steel mold. A hand-operated roller was used to distribute the resin mixer uniformly inside the mold. Then, unidirectional aramid fiber is spread over the banana fiber. The procedure is repeated to fabricate the four-layered composite plate with stacking sequence as shown in Fig. 1. Finally after 48 h of curing, the 0°, 45°, and 90° hybrid composite plates were removed from the mold. The composite here after called as ABGE-FRP (A-Aramid; B-Banana; G-E-glass powder; E-Epoxy resin; Fiber Reinforced Polymer) composite. Test samples are cut as per ASTM standards. To maintain uniformity and homogeneity in the fabrication from the beginning to the end, supreme care was taken.

Table 1 Physical and mechanical properties of banana, aramid, E-glass powder, and epoxy resin (Samal et al. 2009; Bhattacharyya and Fakirov 2012; Migliaresi and Pegoretti 2002)

Materials	Density (g/cm^3)	Diameter (mm)	Tensile strength (GPa)	Young's modulus (GPa)	Elongation at break (%)	Moisture absorption (%)
Banana fiber	0.712	40–60	500	12	5.9	9
Aramid fiber	1.44	–	2.8	65	4.0	–
E-glass powder	2.56	5–25	3.4	72	4.7	–
Epoxy resin	1.2–1.3	–	55–130	3.1–3.3	1–5	0.10–0.15

0° Fiber Orientation

45° Fiber Orientation

90° Fiber Orientation

Banana Fiber   Aramid Fiber   E-glass powder +Epoxy resin
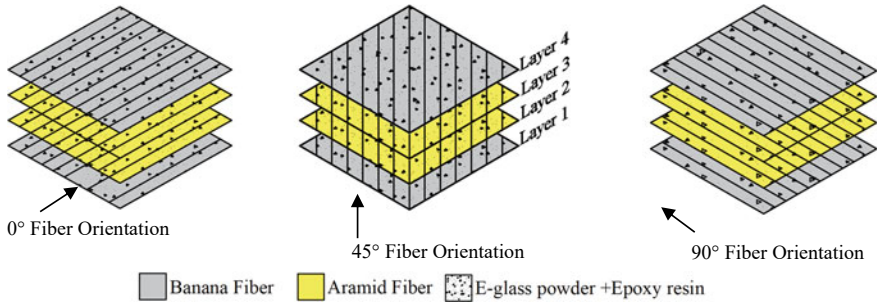
Fig. 1 Isometric view of ABGE-FRP hybrid composite with stacking sequence

(a) Tensile-Test Specimen   (b) Tensile-Test Set up

Fig. 2 Tensile test specimens and UTM test setup

2.3 Tensile Test

Three tensile test specimens of ABGE-FRP composite on 0º, 45º, and 90º were prepared according to ASTM D638 standard. The test specimen of the dimension 165 mm × 19 mm × 3 mm was mounted in the grips of the Tinius Olsen Universal Testing Machine (UTM) with 10-mm gauge length. The test specimens and UTM setup are shown in Fig. 2a, b, respectively. The corresponding stress–strain plot is shown in Fig. 3, from which tensile strength and elastic modulus can be determined for the hybrid composite. For each orientation, 3 specimens are involved, and the average value is taken for final calculation.

2.4 Flexural Test

Influence of 0º, 45º, and 90º fiber arrangement ABGE-FRP hybrid composite on the flexural properties was investigated by using 3-point bending test. The test specimens
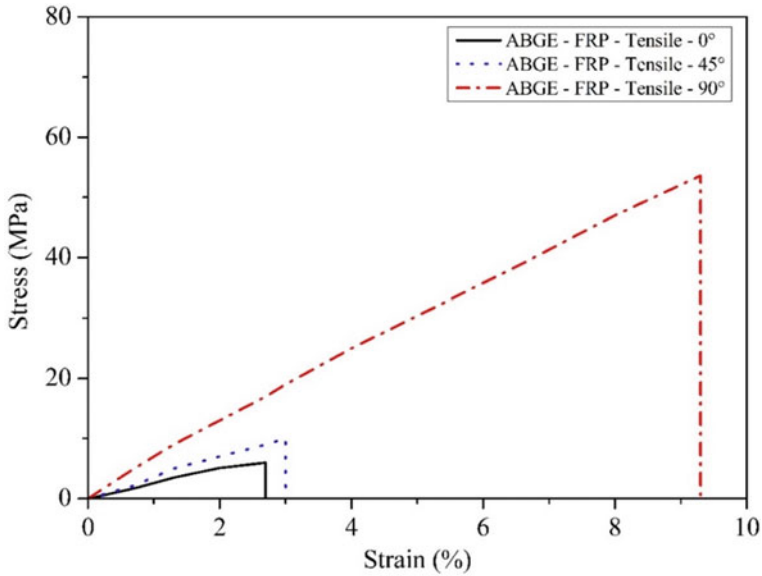
Fig. 3 Stress–strain curve of ABGE-FRP hybrid composites of 0°, 45°, and 90º orientation using tensile test

and test setup are shown in Fig. 4a, b, respectively. Flexural tests were conducted on 3 replicate test specimens having dimension of 127 mm × 12.7 mm × 3 mm on 0°, 45º, and 90º orientation of each as per ASTM D790 standard. The crosshead speed and gauge length were set to 1.27 mm/min and 50 mm, respectively. The corresponding stress–strain diagram of 3-point bend test is shown in Fig. 5. For each orientation, 3 specimens involved, the average value is taken for final calculation.

(a) Flexural-Test Specimens

(b) Flexural-Test Setup

Fig. 4 Flexural test specimens of ABGE-FRP hybrid composites of 0°, 45°, and 90º orientations and 3-point bending test setup
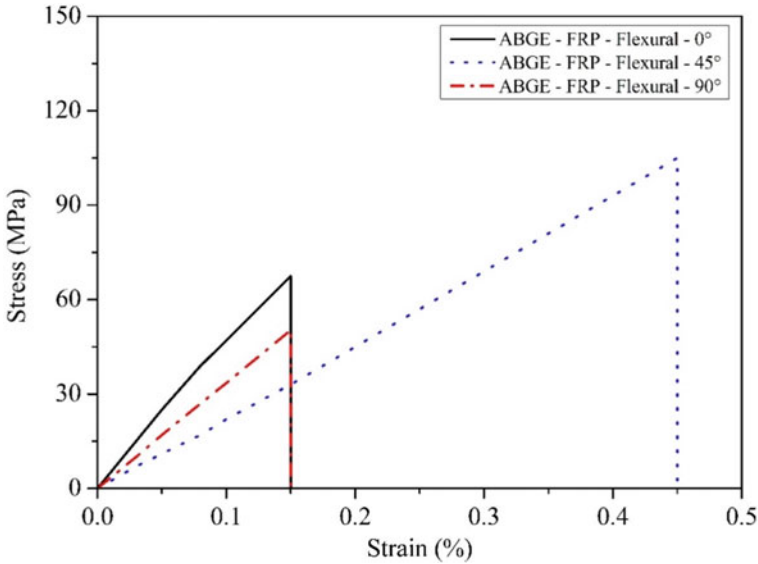
Fig. 5 Stress–strain curve of ABGE-FRP composites using 3-point bending test

2.5 Thermogravimetric Analysis (TGA)

Figure 6 shows the thermogravimetric analysis of ABGE-FRP composite. For this analysis, PerkinElmer STA 6000 instrument is used to conduct the thermal stability and thermal degradation test. TGA detects the mass loss with a resolution of 0.1 µg as a function of temperature. From ABGE-FRP composite, 8 ± 1 mg sample is filled evenly and loosely in an alumina crucible of 6.4-mm diameter and 3.2-mm depth. The temperature range is between room temperature (25 ± 3 °C) and 800 °C at heating rate of 10 °C/min under nitrogen environment. For each run, inert environment is ensured by using nitrogen to avoid any undesirable oxidative incident. The TGA curves of ABGE-FRP composites are analyzed by Pyris™ software version 5.0 and shown in Fig. 6. For comparison, the TGA curves of aramid, treated banana, E-glass powder, and resin are plotted along with ABGE-FRP composite in Fig. 7.

3 Results and Discussion

Tensile Test

Figure 4 shows the stress–strain curve of ABGE-FRP hybrid composites. The tensile test provides the tensile strength, Young's modulus, maximum strain, and load to be withstood by the composite. The observed tensile properties of the composites are listed in Table 2.
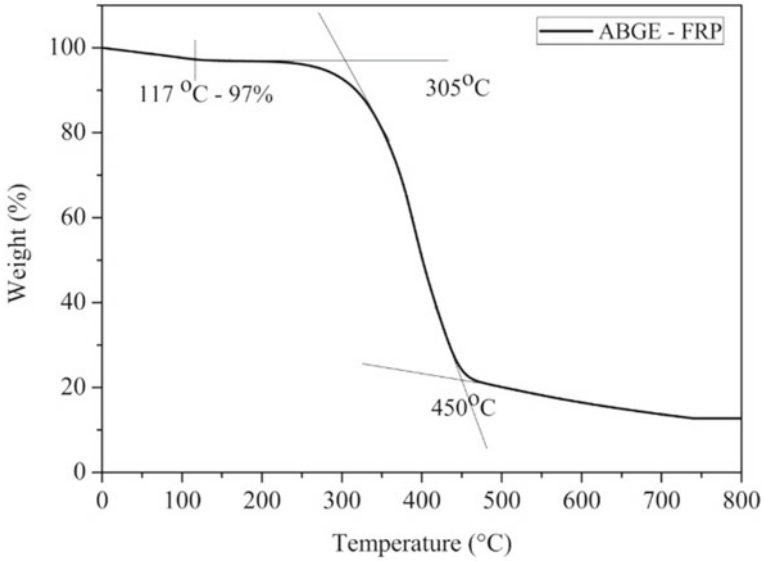
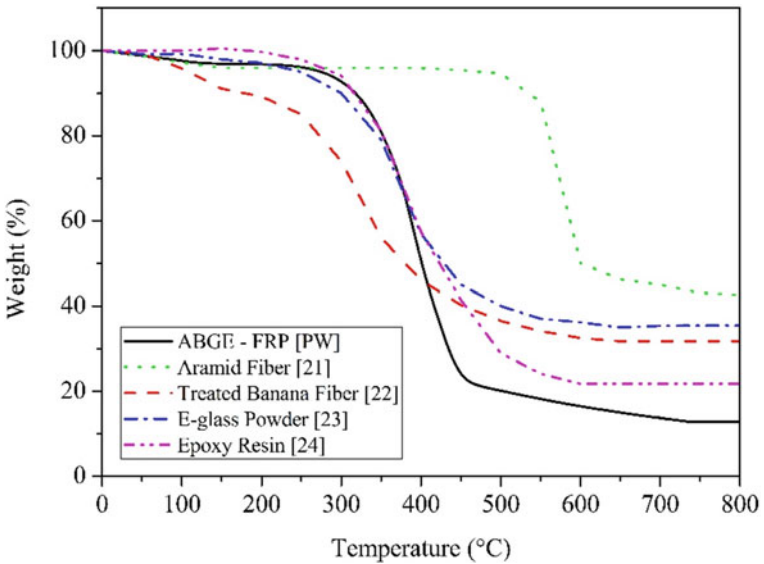**Fig. 6** Thermogravimetric curve of ABGE-FRP (aramid/banana/E-glass powder/epoxy resin) hybrid composite plate

Fig. 7 Thermogravimetric curves of ABGE-FRP composite, aramid, treated banana fiber, E-glass powder, and epoxy resin [PW—present work]

Table 2 Tensile test results of ABGE-FRP composite

Tensile properties	0° fiber orientation	45° fiber orientation	90° fiber orientation
Tensile strength (MPa)	6	10	53.6
Young's modulus (GPa)	0.0022	0.0033	0.058
Max. strain	2.7	3	9.3
Load (N)	225	375	1849

The variation in tensile properties with respect to orientation arises only from fiber even though E-glass powder is also present as reinforcement material. The E-glass powder is uniformly mixed with resin which contributes only to isotropic changes in the properties.

The ABGE-FRP hybrid composites at 0° and 90° orientation are perpendicular and parallel to the applied load, respectively. Hence, tensile strength is higher for 90° orientation and lower for 0° orientation of fibers. As expected, the tensile strength of hybrid composite with 45° orientation lies between the tensile strength 90° and 0° orientation of hybrid composites. The similar pattern is observed in Young's modulus. On controversy, the aramid fiber Young's modulus is higher than banana fiber and vice versa in tensile strength. The tensile test result indicates fiber orientation plays an important role even in the presence of E-glass particulate reinforcement material.

Flexural Test

Figure 5 shows the stress–strain curve derived from the flexural test of 0°, 45°, and 90° fiber orientation of ABGE-FRP hybrid composites. Flexural test is conducted to determine flexural strength, flexural modulus, and the maximum bending load withstood by the composite materials using three-point bending test.

Flexural strength (σ_f) and flexural modulus (E_f) can be calculated using the below formulae (Hodgkinson 2000)

$$\sigma_f = \frac{3\,PL}{2\,bh^2}$$

$$E_f = \frac{L^3 m}{4\,bh^3}$$

where L is the span length, P is applied force, m is the slope of the load/deflection curve, and b and h are the breadth and thickness of the beam, respectively.

Table 3 presents the calculated flexural properties from the flexural curve by 3-point bending test. From the results, it is clearly observed that 45° fiber orientation of ABGE-FRP composites holds good flexural properties than 0° and 90° fiber orientations. Aramid fiber envelops an inclination of breakup gradually that appears to

Table 3 Flexural test results of ABGE-FRP hybrid composite

Flexural properties	0° fiber orientation	45° fiber orientation	90° fiber orientation
Flexural strength (MPa)	67.5	105	50.25
Flexural modulus (GPa)	0.451	0.233	0.335
Strain	0.15	0.45	0.15
Load (N)	2531	3937	1884

assimilate expansive vitality and way better elongation properties (Sunder Selwyn 2021). When bending load is applied to the composite which has fibers at 45° orientation, the load will be distributed in x and y directions. It is evident that from Fig. 5, the load displacement bearing capacity is more in 45° fibers. Hence, 45° orientation of fiber composites bears better flexural property than other orientations.

Thermo Gravimetric Analysis (TGA)

TGA was performed to determine the thermal stability of ABGE-FRP hybrid composite. Figure 7 shows the comparison of TGA between ABGE-FRP composite and aramid fiber (Li 2018), treated banana fiber (Parre et al. 2020), E-glass powder (Srinivasa Reddy et al. 2018), and epoxy resin (Chen 2017). In general, TGA confirmed three parameters, thermodynamic reactions, decomposition, and to the extent of thermal stability of the composite. From the curve in Fig. 6, at the beginning 3 wt.% of mass loss is at 117 °C. This loss is because of moisture content in the composite. Later, a moderate weight loss at 305 °C due to decomposition of cellulose, hemicellulose, and lignin is present in the banana fiber. From the literature (Li 2018; Parre et al. 2020; Srinivasa Reddy et al. 2018; Chen 2017) in Fig. 7, aramid has high thermal stability than banana fiber, E-glass powder, and epoxy resin. The major weight loss happens at 450 °C for ABGE-FRP composite.

4   Conclusions

As a pilot study, aramid and banana fibers are used as a reinforcing material and E-glass powder as filler with epoxy matrix, and the ABGE-FRP hybrid composites have been fabricated by hand lay-up method by taking utmost care for 0°, 45°, and 90° fiber orientations. Tensile and flexural properties are obtained experimentally as per ASTM standards. Then, TGA is carried out to determine the thermal stability of the ABGE-FRP hybrid composites. Based on the results, the following conclusions are derived and given below

- Among the three different orientations of the composites, 90° fiber orientation composites obtained the highest tensile strength and Young's modulus of 53.6 MPa and 58 MPa, respectively.
- The maximum flexural strength obtained by 45° fiber orientations is 105 MPa. However, 0° fiber orientations achieved the highest flexural modulus of 451 MPa.
- TGA of ABGE-FRP hybrid composite shows that thermal stability of the composite is in bar for epoxy resin even in the presence of natural banana fiber.

Further study is required in terms of moisture observation and failure mechanism.

References

Anidha S, Latha N, Muthukkumar M (2019) Reinforcement of Aramid fiber with bagasse epoxy bio-degradable composite: investigations on mechanical properties and surface morphology. J Mater Res Technol 8(3):3198–3212

Balaji A, Purushothaman R, Udhayasankar R et al (2020) Study on mechanical, thermal and morphological properties of banana fiber-reinforced epoxy composites. J Bio TriboCorros 6:60

Bhattacharyya D, Fakirov S (2012) Synthetic polymer-polymer composites. University of Auckland, Hanser, New Zealand

Boopalan M, Niranjanaa M, Umapathy MJ (2013) Study on the mechanical properties and thermal properties of jute and banana fiber reinforced epoxy hybrid composites. Compos B Eng 51:54–57

Chen G, Feng J, Qiu W, Zhao Y (2017) Eugenol-modified polysiloxanes as effective anticorrosion additives for epoxy resin coatings. RSC Adv 7:55967–55976

Corbière-Nicollier T, Gfeller Laban B, Lundquist L, Leterrier Y, Månson JA, Jolliet O (2001) Life cycle assessment of biofibres replacing glass fibres as reinforcement in plastics. Resour Conserv Recycl 33(4):267–287

Dhakal S, Gowda BSK (2017) An experimental study on mechanical properties of banana polyester composite. Mater Today Proc 4:7592–7598

Dilleswara Rao P, Venkata Rao D, Lakshumu Naidu A, RajuBahubalendruni MVA (2017) Mechanical properties of banana fiber reinforced composites and manufacturing techniques: a review. Intl J Res Dev Technol 9(5):39–46

Ebrahimnezhad-Khaljiri H, Eslami-Farsani R, Banaie KA (2017) The evaluation of the thermal and mechanical properties of aramid/semi-carbon fibers hybrid composites. Fibers Polym 18(2):296–302

Hodgkinson JM (2000) Mechanical testing of advanced fibre composites. CRC Press Cambridge, England

Jassala M et al (2002) Aramid fibres-An overview. Indian J Fiber Text Res 27(3):290–306

Joseph S, Sreekala MS, Oommen Z, Koshy P, Thomas S (2002) A comparison of the mechanical properties of phenol formaldehyde composites reinforced with banana fibres and glass fibres. Compos Sci Technol 62(14):1857–1868

Li Z, Liu B, Kong H, Yu M, Qin M, Teng C (2018) Layer-by-layer self-assembly strategy for surface modification of aramid fibers to enhance interfacial adhesion to epoxy resin. Polymers (Basel), 10(8):820

Maleque MA, Belal FY, Sapuan SM (2007) Mechanical properties study of pseudo- stem banana fiber reinforced epoxy composite. Arab J Sci Eng 32:359–364

Merlini C, Soldi V, Barra GMO (2011) Influence of fiber surface treatment and length on physico-chemical properties of short random banana fiber-reinforced castor oil polyurethane composites. Polym Testing 30(8):833–840

Migliaresi C, Pegoretti A (2002) Fundamentals of polymeric composite materials, integrated biomaterials science, edited by R. Barbucci. Kluwer Academic/Plenum Publishers, New York

Pagnoncelli M, Piroli V, Romanzini D, Pereira IM, Rodrigues Dias R, Amico SC, Zattera AJ (2017) Mechanical and ballistic analysis of aramid/vinyl ester composites. J Compos Mater, 1–11

Parre A, Karthikeyan B, Balaji A, Udhayasankar R (2020) Investigation of chemical, thermal and morphological properties of untreated and NaOH treated banana fiber. Mater Today Proc 22(3):347–352

Pothan LA, Oommen Z, Thomas S (2003) Dynamic mechanical analysis of banana fiber reinforced polyester composites. Compos Sci Technol 63(2):283–293

Prasad VV, Talupula S (2018) A review on reinforcement of basalt and aramid (Kevlar 129) fiber. Mater Today Proc 5:5993–5998

Ramesh M, Palanikumar K, Hemachandra Reddy K (2013) Comparative evaluation on properties of hybrid glass fiber-sisal/jute reinforced epoxy composites. Procedia Eng 51:745–750

Ramesh M, Sri AnandaAtreya T, Aswin US, Eashwar H, Deepa C (2014) Processing and mechanical property evaluation of banana fiber reinforced polymer composites. Procedia Eng 97:563–572

Samal SK, Mohanty S, Nayak SK (2009) Banana/glass fiber-reinforced polypropylene hybrid composites: fabrication and performance evaluation. Polym Plast Technol Eng 48:397–414

Santosh PVCRK, Gowda ASSS, Manikanth V (2018) Effect of fiber loading on thermal properties of banana and pineapple leaf fiber reinforced polyester composites. Mater Today Proc 5:5631–5635

Srinivasa Reddy P, Victor Babu T, Kumar S (2018) Dynamic mechanical analysis and thermo-gravimetric analysis on chopped strand mat reinforced with polyester resin and graphite powder. Adv Mater Res 1148:48–60

Sunder Selwyn T (2021) Formation, characterization and suitability analysis of polymer matrix composite materials for automotive bumper. Mater Today Proc 43(2):1197–1203

Velmurgan R, Manikandan V (2005) Mechanical properties of glass/palmyra fiber waste sandwich composites. Indian J Eng Mater Sci 12:563–570

Enhancing Productivity of a Manufacturing Company Using Value Stream Mapping—A Case Study

M. B. Kiran

Abstract With the success of Toyota, post Second World War, many companies' world-over wanted to embrace lean philosophy. Lean philosophy is people-centric. Lean tools can help a company in being flexible in terms of volume and variety. It would also reduce the response time. This has made the customer very happy, as he would be getting the required quality product on time. Though lean tools have all these advantages, companies implementing lean tools will have to face multiple challenges for becoming successful. Many companies in fact have failed in lean transformation. Bearing manufacturing is no exception. In the current research, an attempt is made to implement lean tools for improving productivity in a bearing manufacturing company. Lean implementation has resulted in reduced setup time. It was also observed that work in process, changeover time and waiting time got reduced. Enhancement in machine uptime and product quality improvement are also noticed.

Keywords Value stream mapping · Lean system · VSM · Productivity improvement

1 Introduction

Modern-day manufacturing needs both flexibility and responsiveness for meeting the demands of customers. Both these objectives can be achieved by lean manufacturing. Lean manufacturing is improving production processes for ensuring maximum customer value by reducing waste. Transforming from conventional manufacturing to lean manufacturing is very challenging. The case study considered in this research work demonstrates the different steps involved in this transformation process. Though many researchers have used many lean tools like −5S, Single Minute Exchange of

M. B. Kiran (✉)
Department of Mechanical Engineering, School of Technology, Pandit Deendayal Energy University, Gandhinagar, Gujarat, India
e-mail: MB.Kiran@sot.pdpu.ac.in

Dies (SMED), VSM, etc. in the analysis of systems, not many have reported implementing these lean tools in a bearing manufacturing company. In this context, the present research work assumes special significance. Present research work mainly focuses on lean tool implementation in a bearing manufacturing company to eliminate all types of wastes (Fig. 1).

2 Literature Survey

Lean manufacturing was first introduced by Toyota Motor Company in Japan (Adler 1993; Sobek and Liker 1998). After the Second World War, Japanese automobile companies have realized the importance of tackling challenges from customers—product variety and quality. This has also made Toyota Motor company study the best practices followed by FORD motors of the U.S.A., especially concerning improving productivity, improving quality, and flexibility (Ohno 1998). Toyota Production System (TPS) or lean manufacturing tools (Krafcik 1998) help in identifying different types of waste in the manufacturing/service industry. Jidoka (automation with a human touch) and just in time (JIT) are the two pillars of TPS. Waste (Russell and Taylor 1999) is any activity that is not contributing to product creation. Also, the customer is not paying for these non-value adding (NVA) activities. To identify these NVA (waste), the lean system provides a different set of tools like 5S, Single-piece flow, Kaizen, Visual control, Poka-yoke, Value Stream Map (VSM) and standardization of work (Kaynak 2003; Womack et al. 1990; Mohanty et al. 2007; Rother and Shook 1999). It was observed that the main intent of TPS is to eliminate NVA, and it achieves this objective by using tools like JIT and automation with human involvement. Several researchers have been working on understanding the reasons behind the success of TPS (Liker 1999; Womack and Jones 1994). They have studied on principles, tools, and best practices of TPS. The uniqueness of TPS philosophy is that it places a strong emphasis on people. Employee participation is the basis for the effectiveness of TPS. Lean production strives to achieve the benefits of both mass and craft production. Researchers (Womack and Jones 2010; Serrano et al. 2008) have explored in detail using VSM as a redesigned tool in manufacturing companies utilizing case studies. Sahoo et al. (2008) have conducted an extensive study of the application of lean tools implementation in the forging industry. They identified the different types of water by using the value stream mapping tool and subsequently eliminate the different types of wastes. They have also claimed to have achieved not only a significant reduction in setup time but also reported very less WIP.

Research Objectives:

(1)   To study and observe tapered roller bearing manufacturing company. This study includes both manufacturing and assembly lines of the company.
(2)   To explore possibility of using current state VSM for identifying all forms of waste.

Fig. 1 Manufacturing process sequence in the fabrication shop

(3)   To construct future state VSM after eliminating all types of wastes in a Bearing manufacturing company for enhancing productivity.

(4)   Provide recommendations regarding steps to be followed for elimination of wastes and to achieve productivity.

3   Methodology

3.1   Selecting a Product Line of the Company

In this case study, a taper roller bearing manufacturing line is considered for implementing lean tools. Roller bearings consist of outer ring (OR), inner ring (IR), roller and cage components. Outer and inner rings are made from steel bars. The roller is made from steel wire, and the cage is made from closed rolled annealed sheets. The steel used here is SAE-52100 (high carbon and high chromium steel).

3.2   Creating Current VSM

The organization considered in this case study completes the assembly of tapered roller bearings. The organization gets the parts inner ring (IR), outer ring (OR), roller (R), and cage (C) from three different suppliers. Supplier A: supplies inner ring; Supplier B: supplies outer ring; Supplier C: supplies both roller and cage components. Both inner ring and outer ring are received in semi-finished condition from the suppliers. They will be processed further in the fabrication shop before they are sent to the assembly line.

The process of assembling tapered roller bearing involves the following steps.

- Demagnetizing and cleaning of outer and inner rings—The main objective of this process is to remove residual magnetism in bearing components. Residual magnetism may cause undesired effects—adhesion of particles, heat build-up, energy loss, vibration, wear and tear, etc.
- Inspection is done to ensure everything is in order
- Cone assembly process is done for assembling all the four components of tapered roller bearings—cage, inner ring, roller, and outer ring.
- Demagnetization—This process ensures removing any residual magnetism in the assembled bearing.
- Inspection of assembled bearing is done to ensure demagnetization of the assembled bearing is done properly or not.
- Vibration and noise testing-machining imperfections, viz. waviness of inner and outer rings results in noise and vibration of the assembled bearing. Every assembled bearing is subjected to vibration and noise testing for adhering to standards and to enhance product quality.

- Conservation of oil spraying and collection—This process ensures adequate lubrication for the bearing. Also, this makes roller bearing assembly corrosion resistant.
- Packaging process ensures the assembled and tested tapered roller bearings are in proper shape for their delivery to customers. That is, to ensure that each pack contains the required number of bearings.

The points (different machines constituting the product line, cycle time of each machine, communications between machines, work standards followed, the production rate of each machine, capacity of different machines, material flow, information flow, waiting time at each workstation, machine uptime/downtime, unnecessary movements of materials, people, defect rates at each workstation) were considered and completely understood before going on to create the current value stream map. Figure 2a, b shows the current VSM for the product line under consideration.

Value stream map shows the suppliers, assembly line consisting of the number of work stations, and the customer. In this case study, there are three suppliers one each for inner ring, outer ring, roller, and cage. All four components are assembled in the assembly line. While drawing the value stream map, all the data about the assembly line (viz. cycle time, change over time, machine availability, and defect information) is captured and indicated in the respective boxes representing workstations. Here, cycle time means the actual time required for processing. The setup time is the time required for loading or unloading of the part for processing. Work in process details are also shown between the two workstations. Work in process shows the amount of inventory that is kept between any two work stations. The VSM also shows the material movement from one workstation to another. In addition to material flow, VSM also shows the information flow happening between different entities. Information flow is essential for exercising proper production control. The current state VSM also shows the production lead time and the total processing time. VSM also shows the timeline which shows both processing time and leads time. VSM shows the bottlenecks and the area for improvements.

$$\text{Machine Uptime} = \frac{\text{Actual operating time}}{\text{Available time}} \tag{1}$$

With a monthly demand of 50,000 bearings, Takt time was about 25 s. While reviewing this VSM with a possibility of constructing a future state map, for eliminating all types of wastes including the ones listed below—changeover time, number of defects, machine down-time, unnecessary movements of workers, and work in process.
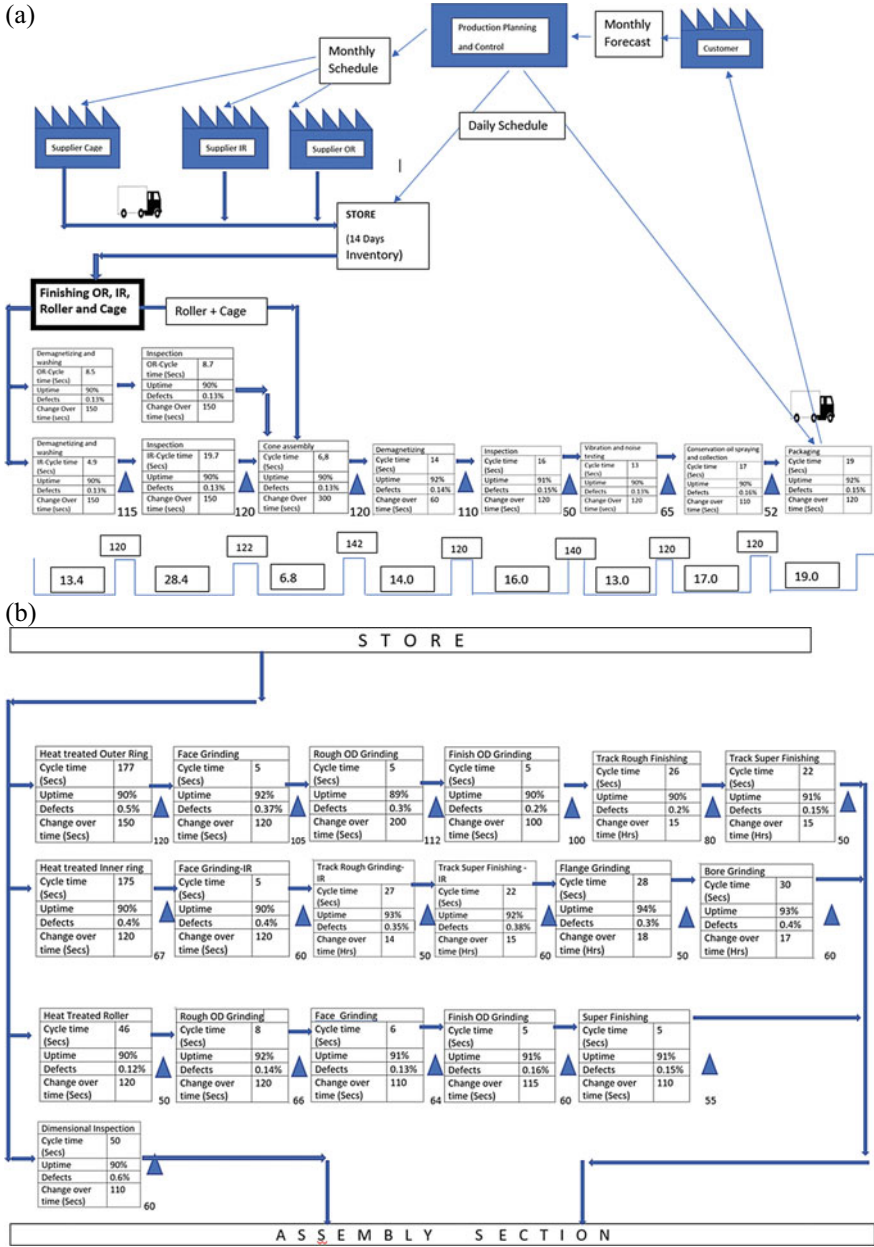
Fig. 2 a Current State VSM of Assembly Section. b Current State VSM of Fabrication Section

3.3　Creating Future State VSM

Creating a future value stream map requires a complete understanding of the customer's requirement/or demand. Especially, the variation in the product demand with time. Figure 3a, b shows the future stream map for the product line under consideration.

To start with milk run concept was implemented for the supply of raw materials—inner ring, outer ring, and cage to the company under consideration. So, initially, the company shares the daily requirement of raw materials with all three suppliers.

A single truck collects all the three raw materials (daily requirement) from three different suppliers and delivers raw materials to the company. Earlier, the company used to keep 14 days of stock of raw materials. Now, after implementing the milk run, this was reduced to 2.0 Days of stock.

4　Results and Discussions

Value stream mapping helps in identifying the bottleneck in the manufacturing process. In Fig. 2a, b, work in process maintained between any two work stations is large. For example, in Fig. 2a, the WIP kept between demagnetizing (IR) and inspection processes is 115 nos. When WIP is large, there is a huge investment tied-up. Also, a lot of space is wasted in storing WIP. There will be a huge waiting time and inventory carrying cost associated with large WIP. Thus, having a large WIP is a type of waste.

In the current study, an effort has been made to reduce WIP inventory by implementing the supermarket concept. Figure 3a shows the VSM of the tapered roller bearing assembly line with the supermarket. With a supermarket, the supplier will do the replenishment of parts only after receiving a Kanban. Thus, supermarket works on pull concept. The quantity of semi-finished products is controlled by the number of Kanban cards in the supermarket. The organization considered in this case study implemented Kanban and visualized Kanban by using a Kanban board.

The Cone assembly process, Fig. 2a, had the maximum changeover time of 300 s. Changeover time is a non-value adding time. Hence, an effort was made to bring down as much as possible. The procedure followed—(i). Observing time for clean-up, (ii). Observing time for setup, (iii). Observing time for start-up, (iv). Interviews were conducted with the operators and experts, and (v). Establishing standard work procedure

By following the above process, the changeover time could be reduced from 300 s to 90 s. This is a significant contribution. The number of defects was also brought down from 0.13% to 0% defects. This was achieved mainly because of clarity in understanding work procedure because of standardized work. Every worker had to follow the standard work procedure. That is the standard way of performing the assembly operation. Also, the training is given to the operators helped in achieving
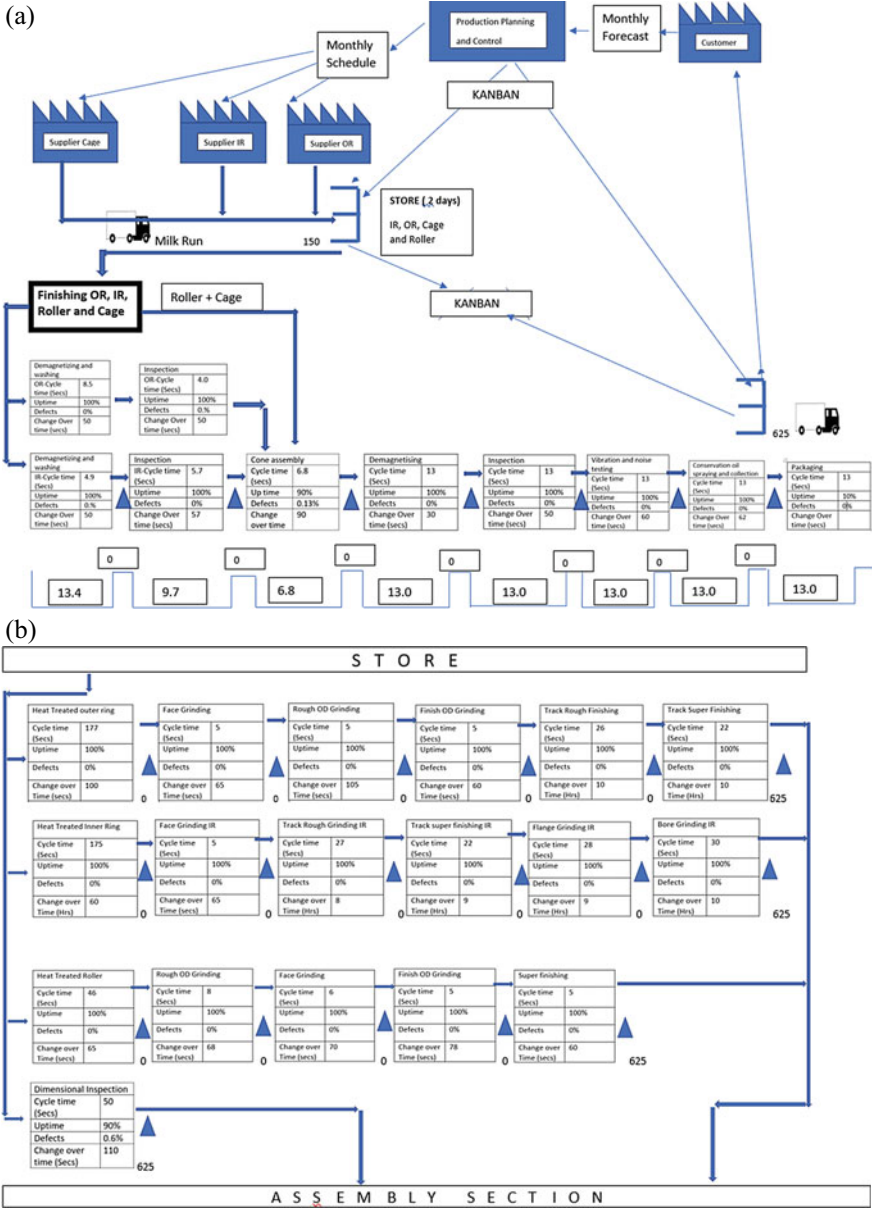
Fig. 3 a Future State VSM of Assembly Section. b Future State VSM of Fabrication Section

this improvement in quality. Quality improvement is also because of load leveling. Because of this, the operators are not unduly overloaded. The machine uptime was increased from 90% to 100%. This was achieved by proposing preventive maintenance. Also, the operator was made responsible for both assembly and maintenance operations. Thus, the number of people required was also brought down.

In demagnetizing and washing operation had a changeover time 150 s. After defining and implementing standard work procedure, the changeover time is reduced from 150 s to 50 s. This was tested for both inner and outer ring components.

5 Conclusion

An attempt has been made in this research work for analyzing the manufacturing and assembly line of a tapered roller bearing manufacturing company, by using a value stream mapping tool. After collecting necessary data from manufacturing and assembly lines, current state VSM is drawn. Current state map showed different forms of wastes. Future state value stream is constructed after eliminating/minimizing all forms of waste.

Waste includes transportation, inventory, movement, work in process, over-processing, over-production, and delay. Each and every workstation of the manufacturing and assembly lines are studied and appropriate methods are suggested for the elimination/minimization of wastes. Certain types of wastes, for example, setup time, is essential non-value adding activity. Hence, it cannot be eliminated. It can only be minimized. Same is true with changeover time. Table 1 shows the summary of productivity improvements possible by following suggested methods.

Table 1 Summary of productivity improvements

Item	Improvement
Work in process (WIP)	50–80% reduction
Changeover time	70–90% reduction
Machine uptime	100–113%
Defects %	0%
Movements of operators	60–80%
Setup time	80–90% reduction

References

Adler PS (1993) Time-and-motion regained Harvard business review 71(1):97–108

Barot RS, Raval K, Berawala HS, Patel A (2020) Implementation of lean practices in water heater manufacturing industry. Mater Today: Proc. ISSN 2214-7853

Kaynak H (2003) The relationship between total quality management practices and their effects on firm performance. J Oper Manag 21(4):405–415

Krafcik JF (1998) Triumph of the lean production system. MIT Sloan Manag Rev 30(1):41

Liker JK (19997) Becoming lean: Inside stories of US manufacturers. Productivity Press, Portland, OR

Mohanty R, Yadav O, Jain R (2007) Implementation of lean manufacturing principles in auto industry Vilakshan–XIMB. J Manag 1(1):1–32

Ohno T (1998) Toyota production system: beyond large-scale production Portland. CRC Press, OR

Rother M, Shook J (1999) Learning to see: value stream mapping to create value and eliminate Muda. Lean Enterprise Institute, Cambridge, MA

Russell RS, Taylor BW (1999) Operations management 2nd ed., Prentice-Hall, Upper Saddle River, NJ

Sahoo AK, Singh NK, Shankar R, Tiwari MK (2008) Lean philosophy: implementation in a forging company. Int J Adv Manuf Technol 36(5/6):451–62

Serrano I, Ochoa C, de Castro R (2008) Evaluation of value stream mapping in manufacturing system redesign. Int J Product Res 46(16):4409–30

Sobek DK, Liker JK (1998) Another look at how Toyota integrate product development. Harvard Bus Rev 76(4):36–47

Womack J, Jones DT, Roos D (1990) The machine that changed the world. Macmillan, New York, NY

Womack JP, Jones DT (1994) From lean production to lean enterprise. Harvard Bus Rev 72(2):93–103

Womack JP, Jones DT (2010) Lean thinking: banish waste and create wealth in your corporation. Simon and Schuster, New York

Classical Lean Manufacturing Philosophy–A Review

M. B. Kiran

Abstract After the Second World War, with the success of Toyota Company, many manufacturing organizations over the world have started embracing lean philosophy. Only a few companies were able to successfully manage the challenges during lean implementation and could become successful. Even the companies who became successful have not reaped full dividends. This clearly shows that not only complete understanding of lean philosophy is essential but also companies should be capable of managing the challenges during lean implementation. In this research work, an effort is made to study the different lean implementations and challenges faced, and provide the future directions for the benefits of interested academicians and practitioners.

Keywords Lean manufacturing · Green manufacturing · Lean system · TPS · 5S · Kanban · PDCA

1 Introduction

Today's customer not only demands product variety but also expects quick response time. To survive in today's world, companies will have to transform into lean for meeting customer's expectations. While performing the lean transformation process, companies will have to overcome multiple challenges, to become successful. It was reported that many companies could not succeed in the lean transformation process (Singh et al. 2010). Thus, there is a huge need for a comprehensive understanding of the lean implementation done across domains. In this context, the present research work assumes special significance. The current research work not only an attempt is made to study the existing lean implementations but also to identify challenges, research gaps, and future directions.

M. B. Kiran (✉)
Department of Mechanical Engineering, School of Technology, Pandit Deendayal Energy University, Gandhinagar, Gujarat, India
e-mail: MB.Kiran@sot.pdpu.ac.in

2   Literature Survey

Manufacturing companies of today will have to overcome the challenges, *viz.* volume flexibility, variety flexibility, and quick response time, for sustaining in business. The traditional manufacturing techniques use large batch sizes. This is good as long as there is a huge demand for a product and less product variety. Today, the customer expectations are different. That is, there is a demand for huge product variety. In this context, large batch sizes are not possible. This has made companies look for newer approaches for dealing with smaller batch sizes.

Toyota Company from Japan is the first to conceive and implement the lean philosophy (Womack et al. 1990). Lean philosophy is focused on waste elimination. Waste is defined as any activity which is not adding any value to the product. Value is defined by the customer. Also, the value varies from customer to customer. In lean philosophy, the focus was on waste elimination, whereas in traditional systems, the focus was on cost reduction. Also, the lean philosophy is customer-driven. That is, product manufacturing will happen only when there is a customer order. This forms what is known as the pull system. In a pull system, whenever there is a demand for the product, the required raw material is pulled into the manufacturing system, for manufacturing a product as per the customer's expectations, whereas in a traditional manufacturing company, the manufacturing will happen even when there is no order from the customer. This is how lean manufacturing was different from traditional manufacturing.

Lean philosophy achieves waste reduction by eliminating variation in product quality. In a lean system, product quality variation is reduced by designing manufacturing processes having consistent process capability. Consistent process capability is achieved by defining standard methods and procedures. By defining standard procedures, it becomes clear to the production manager, whether the operator is following standard procedure or not, while manufacturing a product. Appropriate action may be taken by the manager by looking into abnormality identified through visual controls. Thus, abnormal conditions can be corrected and the operator may be advised to follow the standard method.

Many researchers have started working on lean philosophy (Ohno 1988; Ketchum and Trist 1992; Krafcik 1988; Kim 1993; Liker 1997; Spear and Bowen 1999). While studying many lean implementations in product and process-based companies, researchers have observed variation in lean project implementations (Nepal et al. 2011; Panwar et al. 2015; Abdulmalek et al. 2006). It was also observed by many researchers that lean project success also depends on organization culture (Stone 2012). Researchers have observed that lean implementation is organization specific.

Different organizations have different cultures. It is very much essential to understand the organization's culture before going for lean project implementation. Lean philosophy is largely people-centric. Active involvement of people is very much essential for the success of lean projects. People from all departments and at all levels will have to participate in the success of lean projects. Lean philosophy (Fig. 1)
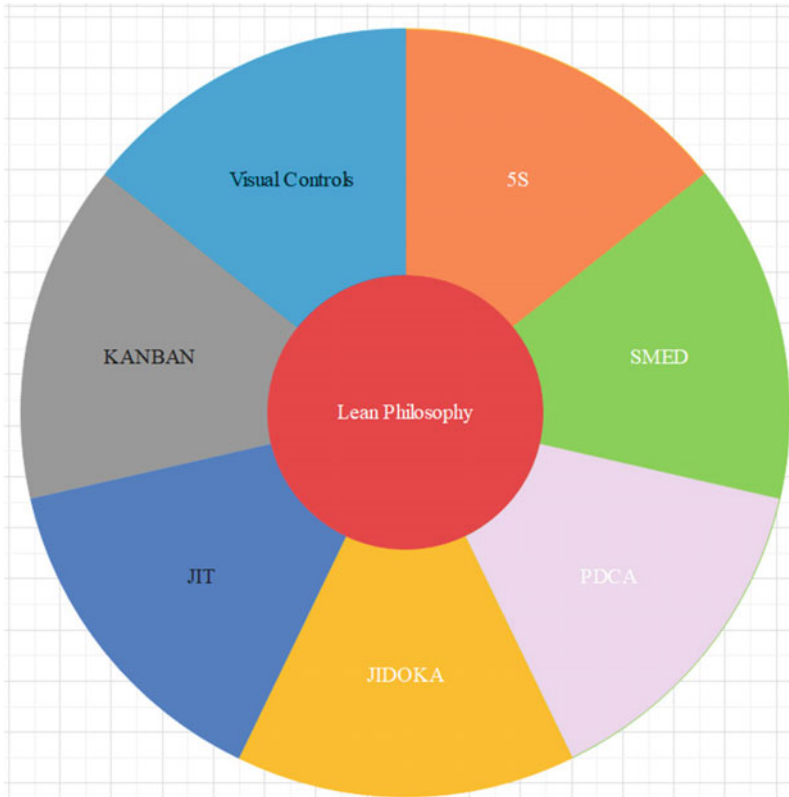
Fig. 1 Lean philosophy and lean tools

offers tools such as 5S, for improving the working condition for workers. 5S includes (Fig. 2) sort, set in order, shine, standardize, and sustain (Stone 2012).

Employee commitment to change is determined by the employer's long-term commitment toward employees (Trist 1981). Work standardization is an important part of lean philosophy and forms the foundation for continuous improvement (Benton and Shin 1998). Work standardization would help a manufacturing line in delivering consistent product quality. Work standardization makes all operators use a standard method for manufacturing. Implementing work standardization would also help in knowing whether the operator follows the right method or not. In a lean organization, the production manager will spend much of his work time on the shop floor, where the value is being created. Thus, by Gemba walk, the production manager will come to know whether an operator is using a standard process or not. Then, he is going to take appropriate actions.

Toyota's production system (TPS) or lean system strongly believes that employee job satisfaction, job safety, and employee involvement can only make a manufacturing company more flexible and responsive to customer expectations. The main
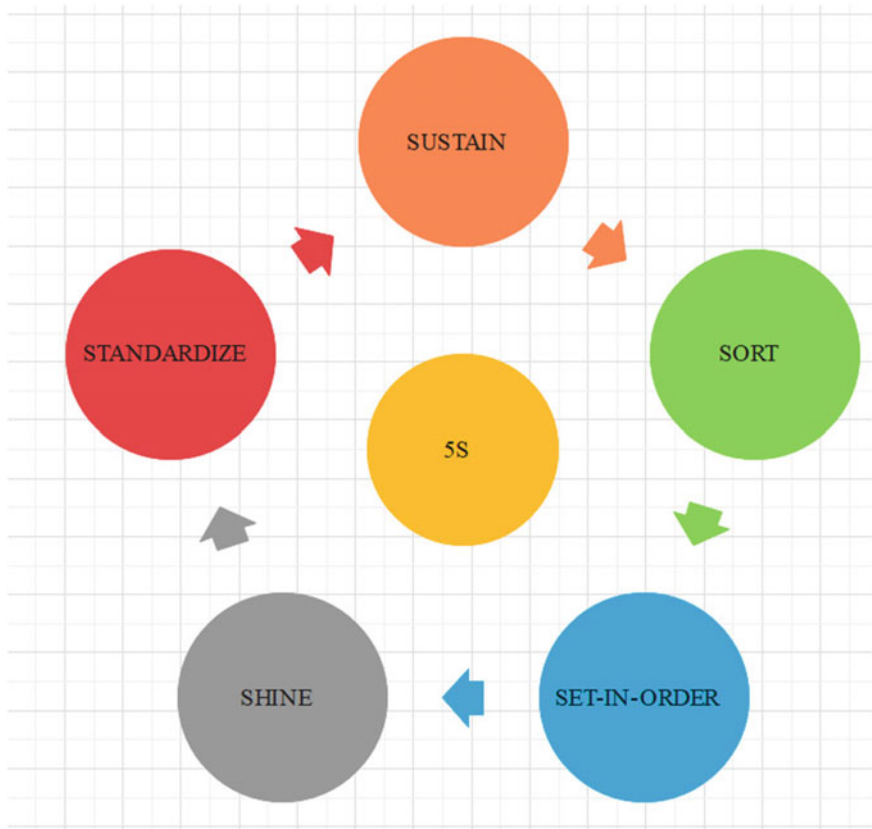
Fig. 2 Components of 5S—sort, set in order, shine, standardize, and sustain

reason behind many companies using TPS is that it will make the companies adaptable and highly responsive. One of the characteristics of TPS is that all machines are highly connected and at the same time are also flexible in product manufacturing (Sobek and Liker 1998). Connectedness means that the machines will have well-defined agreements between them. Womack and Jones (2010) have studied the different dimensions of TPS.

TPS offers a set of tools, Kanban, value stream map, PDCA, SMED, etc., and can be used by companies for transforming to lean. These lean tools may be used for waste identification for subsequent elimination. There can be different forms of waste such as unnecessary transportation of materials, inventory of materials, unnecessary movement of workers, work in process, over-processing of raw materials, overproduction of products, and delay in subsequent processing. It was demonstrated in one research work (Bhasin and Burcher 2006) that the lean transformation projects are going to fail by the improper selection of lean tools. They have also cited that lack of proper lean project monitoring and control is the important reason for the failure

of lean projects. Grewal and Sareen (2006) have used a value stream map for the identification of waste in the production industry. Abdulmalek and Rajgopal (2007) has used a value stream map in the processing industry; the authors have claimed a significant reduction in non-value-added activities. Kasul and Motwani (1997) have studied the implementation of TPS in a manufacturing line. Mayr et al. (2018) have concluded that standardization of work, waste elimination, and customer focus are essential before the introduction of Industry 4.0. Just in time is the process of buying raw materials in time. This will bring down the inventory-related waste. Internet of things would help in tracking the status of components in real time, and status reporting to managers is possible (Mao et al. 2018; Müller et al. 2018; Sanders et al. 2017). The simulation technique was used by certain authors for ensuring continuous flow and to detect the bottlenecks in the manufacturing system (Lu and Yue 2011). The authors have also recommended employment of simulation in the training of employees. Al-Ahmari et al. (2016) have proposed how to reach an optimized level while training employees by using the augmented reality. By using the monitoring capability of the Internet of things, such as product tracking, unnecessary movement and unnecessary transportation can be minimized (Brintrup et al. 2010; Bonci et al. 2016). Cao et al. (2017) have used RFID-based data-driven monitoring for identifying waste related to the transportation of materials. Big data analytics are widely used for analyzing the vast amounts of data that are generated through heterogeneous sensors.

The efficiency of visual management (Andon) can be enhanced by using digital technologies. Internet of things can make the real-time availability of status of a different production equipment (Zhong et al. 2015). This would help all the concerned operators and managers know the status of the different manufacturing lines.

Jidoka is (Fig. 3) one of the pillars of TPS. The objective of Jidoka is to enhance the quality of product by detecting anomalies in the manufacturing process (Boersch et al. 2018). Human-based Jidoka system permits operators to stop the manufacturing line in case of any issue. This can be done with the help of a visual control. The visual control shows the status of the production line at a given point in time. The main objective of Jidoka is to make the human–machine interface more human centric. The researchers (Boersch et al. 2018) have studied how by using big data, anomalies in the manufacturing process can be studied, thereby improving the product quality. Many researchers (Mao et al. 2018; Wagner et al. 2017) have started working on integrating Industry 4.0 with lean tools such as SMED for achieving operational excellence. Many researchers (Kumar et al. 2018; Tao et al. 2017; Kiran 2021) have explored using robotics, cloud, and big data for detecting anomalies in the manufacturing system. Whenever a defect is identified in a production line, all the machines in the line would be stopped. A root cause analysis is done, and the defect is fixed; only then, all the machines in production line start. Thus, Jidoka ensures defect-free production of products.

Single-Minute Exchange of Dies (SMED) is a lean tool used for minimizing the setup and changeover time. SMED is also called as quick changeover of tools. SMED is the minimum time necessary for shifting from one batch to the next batch. Both setup and changeover are essential but non-value-adding activities. Hence, the
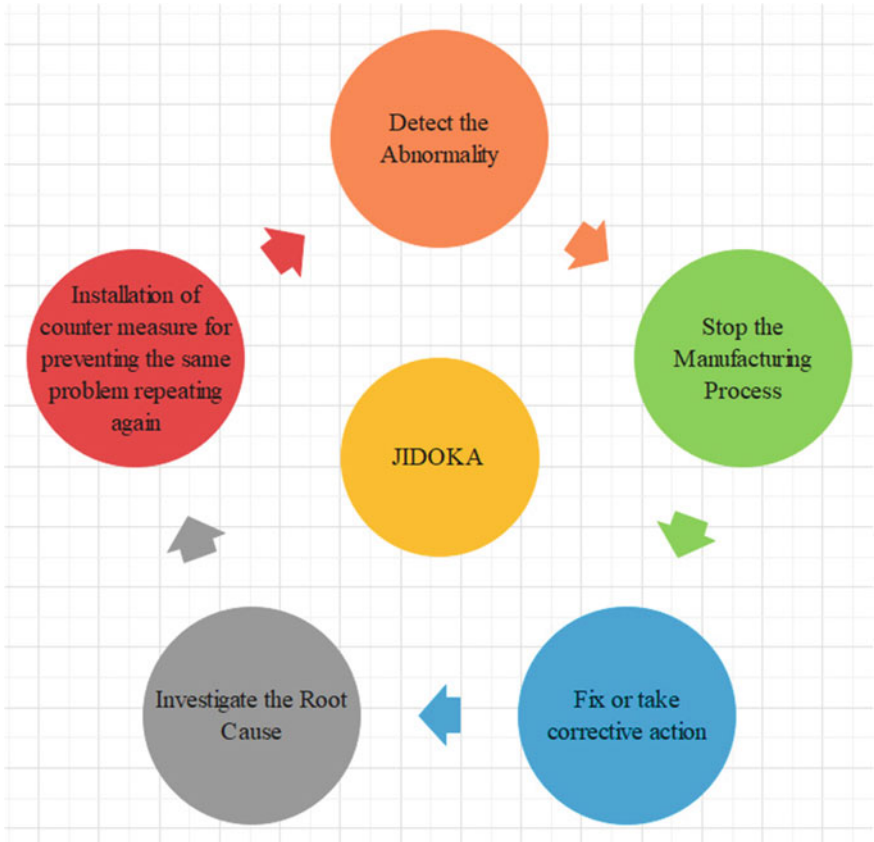
Fig. 3 Steps in Jidoka process

objective must be to reduce the time taken for performing these activities. During analysis, the internal setup time is converted into external setup time for reducing the setup time.

In conventional manufacturing setups, setup time was considered as very expensive. Hence, they used to manufacture products with large batch sizes (Shingo 1985). The problem with the production with large lots is that there will be waste-related large inventory. Nowadays, companies will have to meet several objectives such as competitive pricing, quick response time, flexibility, and product quality. In order to meet all these objectives, it is very much essential to understand the production process in detail, that is, which of the activities in manufacturing are really adding value and which of the activities are not adding value. Companies will have to produce variety of products, with small batch sizes and subsequently with more tool changes. Thus, to be competitive at the market place, the only possibility is to eliminate/or reduce the non-value-adding activities, by reducing setup times. Many researchers

have provided schemes for reducing setup time in different domains (Holweg 2006; Johansen and McGuire 1986; Noaker 1991; Gilmore and Smith 1990).

The problem of minimizing setup time can be achieved by implementing SMED methodology. Before implementing SMED, it is very much essential to implement standardization, for the manufacturing process. Standardization makes all workers follow standard way of manufacturing components. The main objective of SMED is to separate setup time into external and internal setups, as for as possible to convert internal setup time into external setup time. Researcher (Holweg 2006) has proposed the following procedure for performing the SMED (Fig. 4).

Plan–Do–Check–Act (PDCA) cycle is also called Shewhart cycle or Deming cycle and provides a systematic progression from one level to another level. This is also known as continuous improvement process. PDCA would enable companies to move from current level to reach desired level. In 'Plan' phase, problem identification is done. In 'Do' phase, implementation of the procedure is done for solving the problem defined in the first stage. In 'Check' phase, close examination of the process is done
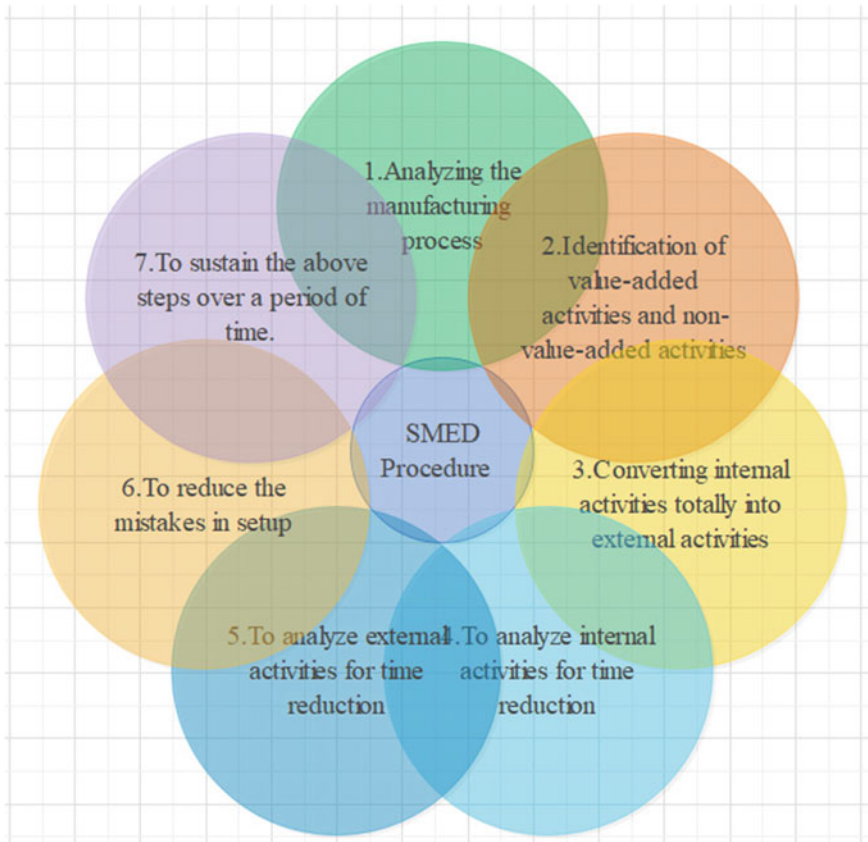

Fig. 4 Procedure of single-minute exchange of dies (SMED)

Fig. 5 PDCA cycle—its stages

to see if the pre-defined objectives are achieved or not. In 'Act' phase, proper actions will be initiated if the desired objectives are not met by the process implementation.

Dr. W. Edwards Deming was credited for introducing the PDCA cycle in Japan in the year 1950. Figure 5 shows the PDCA cycle, scientific method for improvement.

Machine maintenance is very much required for keeping the machines up and running. To implement lean, a manufacturing company should ensure the machines are available at all times. With the availability of the Industry Internet of Things, the remaining useful life of the machine can be determined by using data obtained from sensors, and hence, condition-based monitoring systems are possible. This would also help in selecting the appropriate maintenance policy for a given machine tool.

3 Conclusion

Traditional manufacturing systems require large batch sizes and hence cannot be used for meeting the expectations of the modern-day customer, *viz*. product variety, product volume flexibility, and high response time. This has made companies embrace lean

Table 1 Directions for future research work

Area of manufacturing	Problems to be addressed
Procurement of raw materials	1. Increasing the effectiveness of supply chain using Industry 4.0 2. Vendor assessment rating by machine learning and big data analytics
Manufacturing	1. Making use of cyber-physical systems for data exchange and independent decision making, without human intervention 2. Increasing the security for cyber-physical system 3. Real-time tracking of components 4. Machine-to-machine data exchange using cloud computing 5. Intelligent decision making using data warehousing and data mining 6. Product inspection using machine learning techniques and neural networks 7. Use of robotics for automated loading and unloading 8. Designing effective production schedule 9. Number of trip reduction in automated guided vehicles
Machine maintenance	1. Condition monitoring of machine tools, using machine learning 2. Developing maintenance policies using Industry 4.0 3. Maintenance for reliability
Logistics	1. Enhancement of productivity in logistics using Industry 4.0 2. Real-time data processing using cloud computing

philosophy. Lean philosophy provides required flexibility. Lean philosophy is people-centric. Lean philosophy focuses on waste elimination. A traditional system on the other hand was focused on reducing the manufacturing cost. This is how the lean system is different from the traditional system. The lean system offers different tools—5S, TPM, Jidoka, visual management, value stream map, etc. The tools would help in identifying the different forms of waste for subsequently waste removal (Table 1).

It was also noticed that many companies could not become successful in lean implementation because of continuous top management support, lack of effective leadership, lack of communication between managers and workers, lack of active participation of employees, unreliable suppliers, lack of logistic support, improper plant layout, quality variation in incoming raw materials. Thus, the above challenges will have to be managed by companies for becoming successful in lean implementation.

With the introduction of Industry 4.0 technologies, companies have started using Industry 4.0 for enhancing the effectiveness of lean tools. Many researchers have proposed different schemes for addressing manufacturing-related problems such as anomaly detection using big data analytics, product tracking using RFID, and machine maintenance by using sensors. Still, many production-related problems—vendor selection, supplier evaluation, intruder detection, defect identification and classification, robust inspection system, consistent quality of incoming materials, getting materials on time in right quantities in consistent fashion, production

scheduling, selecting right maintenance policies for machine tools, use of Big data for defect prediction, classifications and disposal, cloud based reverse logistics, cloud-based inspection, protecting cyber physical systems by providing necessary security infrastructure, lack of proper coordination among different elements of supply chain, need addressing for achieving operational excellence.

References

Abdulmalek FA, Rajgopal J (2007) Application of VSM to process industry. Int J Product Econ 107(1):223–36

Abdulmalek FA, Rajgopal J, Needy KL (2006) A classification scheme for the process industry to guide the implementation of lean. Eng Manag J 18(2):15–25

Al-Ahmari AM, Abidi MH, Ahmad A, Darmoul S (2016) Development of a virtual manufacturing assembly simulation system. Adv Mech Eng 8 (3):1–13. https://doi.org/10.1177/168781401663 9824

Benton WC, Shin H (1998) Manufacturing planning and control: the evolution of MRP and JIT integration. Europ J Oper Res 110(3):411–440

Bhasin S, Burcher P (2006) Lean viewed as a philosophy. J Manuf Technol Manag 17(1):56–72

Boersch I, Füssel U, Gresch C, Großmann C, Hoffmann B (2018) Data mining in resistance spot welding: A NonDestructive method to predict the welding spot diameter by monitoring process parameters. Int J Adv Manuf Technol 99(5–8): 085–1099. https://doi.org/10.1007/s00170-016-9847-y

Bonci A, Pirani M, Longhi S (2016) A database-centric approach for the modeling, simulation, and control of cyber-physical systems in the factory of the future. IFAC-Papers on line 49(12):249–254

Brintrup A, Ranasinghe D, McFarlane D (2010) RFID opportunity analysis for leaner manufacturing. Int J Product Res 48 (9):2745–2764. https://doi.org/10.1080/00207540903156517

Cao W, Jiang P, Lu P, Liu B, Jiang K (2017) Real-time data-driven monitoring in job-shop floor based on radio frequency identification. Int J Adv Manuf Technol 92(5–8):2099–2120. https://doi.org/10.1007/s00170-017-0248-7

Gilmore M, Smith D (1990) Setup reduction in pharmaceutical manufacturing: an action research study. Int J Product Res 16(3):4–17

Grewal CS, Sareen KK (2006) Development of a model for lean implementation: a case study automobile industry. Industr Eng J 5:24–7

Holweg M (2006) The genealogy of lean production. J Oper Manag 25:420–437

Johansen P, McGuire KJ (1986) A lesson in SMED with Shigeo Shingo. Industr Eng 18:26–33

Kasul RA, Motwani JG (1997) Successful implementation of TPS in a manufacturing setting: a case study. Industr Manag Data Syst 97:274–279

Ketchum L, Trist E (1992) All teams are not created equal: how employee empowerment works. Sage Publications, London

Kim DH (1993) The link between individual and organizational learning. MIT Sloan Manag Rev 35:37–50

Kiran MB (2021) conference on advances in thermal-fluids engineering, (ATFE 2021), held at Pandit Deendayal energy University, 25–26 March, 2021, ISBN: 978-93-5457-145-9

Krafcik JF (1988) Triumph of the lean production system. MIT Sloan Manag Rev 30(1):41

Kumar M, VaishyaR, Parag P (2018) Real-time monitoring system to lean manufacturing. Procedia Manuf 20:135–140

Liker JK (1997) Becoming lean: Inside stories of US manufacturers. Productivity Press, Portland, OR

Lu S, Yue H (2011) Real-time data-driven visual simulation of process manufacturing: a case study. Proceedings of the 2011 Chinese control and decision conference, CCDC 2011, pp. 1806–1809. https://doi.org/10.1109/ccdc.2011.5968491

Mao J, Xing H, Zhang X (2018) Design of intelligent warehouse management system. Wirel Personal Commun 102(2):1355–1367

Mao J, Xing H, Zhang X (2018) Design of intelligent warehouse management system. Wirel Personal Commun 102 (2):1355–1367. https://doi.org/10.1007/s11277-017-5199-7

Mayr A, Weigelt M, Kuhl A, Grimm S, Erll A, Potzel M, Franke J (2018) Lean 4.0—a conceptual conjunction of lean management and industry 4.0. 51st CIRP conference on manufacturing systems, Procedia CIRP 72: 622–628

Müller R, Vette-Steinkamp M, Hörauf L, Speicher C, Burkhard D (2018) Development of an intelligent material shuttle to digitize and connect production areas with the production process planning department. Procedia CIRP 72:967–972

Nepal BP, Yadav OP, Solanki R (2011) Improving the NPD process by applying lean principles: a case study. Eng Manag J 23(1):52–68

Noaker P (1991) Pressed to reduce setup? Manuf Eng 107:45–49

Ohno T (1988) Toyota production system: beyond large-scale production. CRC Press, Portland, OR

Panwar A, Nepal BP, Jain R, Rathore APS (2015) On the adoption of lean manufacturing principles in process industries. Product Plann Control 26(7):564–587

Sanders A, Subramanian KRK, Redlich T, Wulfsberg JP (2017) Industry 4.0 and lean management—synergy or contradiction? In: Lödding H, Riedel R, Thoben KD, von Cieminski G, Kiritsis D (eds) Advances in production management systems. the path to intelligent, collaborative and sustainable manufacturing. APMS 2017. IFIP Advances in Information and Communication Technology, 514, pp. 341–349. https://doi.org/10.1007/978-3-319-66926-7_39

Shingo S (1985) A revolution in manufacturing: the SMED system. Productivity Press, Cambridge, MA

Singh B, Garg SK, Sharma SK (2010) Scope for lean implementation: a survey of 127 Indian industries. Int J Rapid Manuf 1(3):323–333

Sobek DK, Liker JK (1998) Another look at how Toyota integrates product development. Harvard Bus Rev 76(4):36–47

Spear S, Bowen HK (1999) Decoding the DNA of the toyota production system. Harvard Bus Rev 77:96–108

Stone KB (2012) Lean transformation: Organizational performance factors that influence firms' leanness. J Enterprise Transf 2(4):229–249

Tao F, Cheng J, Cheng Y, Gu S, Zheng T, Yang H (2017) SDMSim: a manufacturing service supply-demand matching simulator under cloud environment. Robot Comput Integr Manuf 45:34–46

Trist E (1981) The evolution of sociotechnical systems as a conceptual framework and as an action research program. In: Van de Ven AH, Joyce WF (eds), Perspectives on organization design and behavior (pp 19–75). John Wiley, New York, NY

Wagner T, Herrmann C, Thiede S (2017) Industry 4.0 impacts on lean production systems. Procedia CIRP 63:125–131

Womack JP, Jones DT (2010) Lean thinking: Banish waste and create wealth in your corporation. Simon and Schuster, New York

Womack JP, Jones DT, Roos D (1990) The machine that changed the world. Simon and Schuster, New York

Zhong RY, Lan S, Xu C, Dai Q, Huang GQ (2015) Visualization of RFID-enabled Shopfloor logistics big data in cloud manufacturing. Int J Adv Manuf Technol 84 (1–4):5–16. https://doi.org/10.1007/s00170-015-7702-1

A Review on Key Technologies of Industry 4.0 in Manufacturing Sectors

Rakesh Chaudhari, Vrund Shah, Sakshum Khanna, Kumar Abhishek, and Jay Vora

Abstract As the world faced recession in the past few years, it helped change the perspective of people towards the industrial sector, and real value-adding activities started to get more importance. In the coming time, everything will be digitized starting from business model to products and services including machines and operators, i.e. digitalization era. Industry 4.0 has been presented to face the latest challenges of any company/organization about connectivity and ingress to real-time data and thus leading to the digitization era. Owing to the obliviousness in the concept of industry 4.0 and its key technologies, this paper lays its emphasis on clarifying the concepts, key technologies, and potential benefits as well as limitations of each technology. In the current study, different technologies of Industry 4.0 have been studied in detail in the manufacturing sectors.

Keywords Industry 4.0 · IIOT · Cloud computing · Big data

1 Introduction

The global recession faced by the world in the past few years has changed people's perspectives towards the industrial sector, i.e. more importance is given to real value-adding activities. The companies in the past used to relocate the activities for lowering their labour cost, but now, they are trying to regain their diligence in the market. Although every company/organization works differently, they all face the challenge of connectivity and ingress to real-time data across various processes, products, partners, and people. The word Industry 4.0 has been presented to face the latest challenges in any company/organization (Hofmann and Rüsch 2017). Industry 4.0 can be referred to as a new phase in an Industrial Revolution where the main emphasis

R. Chaudhari · V. Shah · S. Khanna · J. Vora (✉)
Department of Mechanical Engineering, Pandit Deendayal Energy University, Gandhinagar 382007, Gujarat, India
e-mail: jay.vora@sot.pdpu.ac.in

K. Abhishek
Department of Mechanical Engineering, IITRAM, Ahmedabad 380026, Gujarat, India

is on interconnectivity, ingress to real-time data, automation, and machine learning. It emphasizes achieving an elite level of operational productivity and efficiency by connecting the physical world to the virtual world (Lu 2017; Peruzzini et al. 2017). For the production approaches, Peruzzini et al. (2017) defined it as an intelligent flow of workpiece machine by machine in a factory on real-time communication between machines which helps in making manufacturing smart as well as adaptive. It also focuses on establishing intelligent and communicative systems.

A misconception about industry 4.0 is that it is just about ploughing money into technologies and tools which help to upgrade manufacturing efficiency, but rather, it is about transforming the way not only the entire business works but expands as well. It changes the lifestyle, helps in fabricating new business models, and changing the course of manufacturing hands, hence, re-establishing the industry for digital transformation. It brings a healthy development in the industrial framework by pivoting on creating smart products, smart processes, and smart procedures.

Since the Industry 4.0 boom, because there is an obliviousness in this area, there arises a need for elucidation of Industry 4.0 concepts and their key technologies. The further paper emphasizes clarifying its key technologies and also benefits of adapting each technology. In the present work, a comprehensive review of recent work on applications of Industry 4.0 in different fields has been discussed.

2 Key Technologies of Industry 4.0

Electronics and IT are the main characteristics of Industry 4.0 for manufacturing and services extremely developed automation and digitalization processes (Lu 2017). Several authors have described the nine key technologies (also called the nine pillars) of the Industry 4.0 framework which are as follows (Leyh et al. 2017; Motyl et al. 2017; Saucedo-Martinez et al. 2017; Gilchrist 2016).

2.1 Industrial Internet of Things (IIoT)

Before understanding the industrial Internet of things (IIoT), it is important to define the Internet of things (IoT). Madakam et al. (2015) has defined Internet of things as an amalgamation of two words "internet" and "things", where Internet is a network of network, and things can be any object or even a person. Today, IoT has found many applications in the manufacturing industry, transportation, healthcare, aerospace and aviation industry, agriculture and breeding, and recycling (Sezer et al. 2018; Choi and Chung 2017; Bandyopadhyay and Sen 2011). Bandyopadhyay and Sen (2011) have presented its potential applications in the manufacturing industry; with the help of IoT, production process can be optimized, the life cycle of a product can be monitored as well. It is also possible to develop self-organizing and intelligent manufacturing solutions. However, they have also pointed out the key challenges that
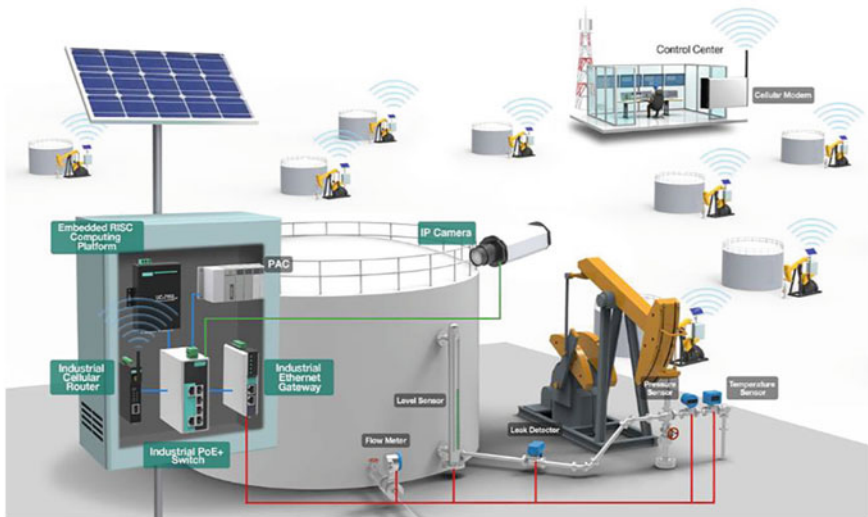
Fig. 1 Typical IIoT network (Medium Corporation, nd)

exist owing to limited ICT support which are (1) network foundation, (2) security, privacy, and trust, (3) managing heterogeneity and a large amount of information, (4) sensor data mining, communication, data stream processing mechanism. The conceptualization of IIoT was introduced to show a particular application of IoT in industries. Andulkar et al. (2018) has defined IIoT as the interrelation of industrial products which includes components and/or machines to the Internet. Linking the collected data through sensors in a factory with an IoT platform can be considered as IIoT. K. Choi and Chung (2017) found that IIoT escalates production efficiency but with big data analysis. Figure 1 shows a typical IIoT network.

2.2   Big Data (BD)

Big data (BD) can be defined as an abundant amount of structured, unstructured, and semi-structured data which can be obtained from different types of interconnected heterogeneous objects (Bortolini et al. 2017). According to Babiceanu and Seker (2016), the core characteristic of BD is data analysis. Tao et al. (2018) in their paper has claimed that in the manufacturing field, systematic guidance for production activities within the entire product life cycle can be provided by BD. Fault-free and cost-efficient running of processes can also be made possible with help of BD (Yin and Kaynak 2015). Cheng et al. (2018) have shown that BD analysis can also be used for decision-making and/or to figure out the solution of problems related to the operation. Tao et al. (2018) have shown how BD offers a tremendous transfiguration opportunity from the current manufacturing paradigm to smart manufacturing.

However, major limitations to be considered are current data collection techniques and limit of applicability in low latency and real-time applications owing to network unavailability, overfull bandwidth.

2.3 Simulation

Simulation can be stated precisely as a replica of the operation of a system or a real-world process. Lachenmaier et al. (2017) have shown how various challenges of the manufacturing industry related to the complexity of the system can be approached with this technology. Zuniga et al. (2017) have discussed the advantage of simulation is exceptional and apparent in a customized product manufacturing environment and how simulation modelling helps in reducing cost, decreasing development cycles, and also increasing product quality. Rodic (2017) in his study has concluded that although simulation is adopted in big companies and SMEs, there are substantial differences in the problem faced and methodologies used to overcome it depending on company size.

2.4 Augmented Reality (AR)

Objectives of the augmented reality (AR) are the capability of combining real and virtual objects in a real environment, the capability to line up the real and virtual objects, and the capability of running collectively in 3D and real-time (Syberfeldt et al. 2016). They have also investigated how AR helps in increasing operator's knowledge by utilizing artificial information available about the environment where it is to be used. As far as the manufacturing process is concerned, Rentzos et al. (2013) have shown how AR can be used for simulation, assistance, and guidance, and it has demonstrated to be streamlined technology in closing some gaps like the one that exists between product development and manufacturing operations. Palmarini et al. (2018) have claimed that maintenance is one of the most propitious fields of Dini and Mura (2015) have shown that major technical challenges faced by current AR technologies are usability and portability of hardware, system delays, and delays in preparation, programming, and setup time of the system.

2.5 Additive Manufacturing (AM)

Additive manufacturing (AM) is a qualifying technology that helps in advancing new products, new business models as well as new supply chains. Hannibal and Knight (2018) have defined AM as a collection of technology that sanctions the "3D

printing" of physical objects. According to Tofail et al. (2018), the potential bene-fits of AM in the manufacturing field includes manufacturing of parts directly from CAD model, considerable customization without added cost or tooling, manufac-turing of complex geometries, hollow parts. They have also shown how AM makes utmost material utilization with a "zero waste" approach and on-demand manufac-turing is possible and that too with excellent stability. However, the main challenge is to convert the shapes and objects produced by AM to functional objects. Jiang et al. (2017) have shown that AM has the potential to replace many conventional manufacturing processes.

2.6 Horizontal and Vertical Integration

Horizontal integration is described as an intercompany integration, and it is consid-ered as a foundation for an elite-level alliance between companies (Suri et al. 2017). In horizontal integration, an interconnected ecosystem within a similar value creation network is created. Salkin et al. (2018) have shown that product lifecycle can be enriched by using information systems created in horizontal integration. Suri et al. (2017) have described vertical integration as an intracompany integration and networked manufacturing. They have also considered it as a substructure for trading information and partnership among different levels of the organization. They have studied how it "digitizes" all the processes taking place in an organization taking account of all data from the manufacturing process. According to several authors (Salkin et al. 2018; Posada 2015), the model of I4.0 has another level of integra-tion that considers the whole product life cycle which is end-to-end integration. The scope of end-to-end integration closes the gap between design, manufacturing, and customer (Wang et al. 2016).

2.7 Autonomous Robot

Robots are considered to be the most crucial to hold out the flexibility in demand level (Pedersen et al. 2016). Salkin et al. (2018) have shown how robots with AI can consequently reduce the production cost as they are compatible and flexible and can ease manufacturing of non-identical products, and autonomous robots can manage various processes such as product development, manufacturing, and assem-bling phases in manufacturing systems. According to Hassan and Liu (2017), with numerous autonomous industrial robots (AIR) employed together as a team, it is possible to have a broad spectrum in manufacturing applications. The main problem associated with the use of industrial robots is their interaction with humans. However, Koch et al. (2017) have introduced a concept of collaborative robots also known as

cobots. They work near humans. Makrini (2018) have studied that with the introduction of cobots, the human–robot barrier breaks down, hence, offering substantial affordability and flexibility in operations.

2.8   Cyber Security

As new devices are getting linked to the World Wide Web, the Internet is on an exponential trend. It can be expected that in time to come, the leading source of data will be from defunct objects (Sergey et al. 2017). He (2016) have stated about the increasing vulnerability that can lead to compromised particulars for people and enterprises as it creates new opportunities for attack. So cybersecurity becomes a very important enabling technology in the I4.0. Kannus and Ilvonen (2018) described cybersecurity (CS) as a recently developed term in a distinguished level of information security, and with word "cyber" it also applies to the industrial environment and IoT; hence, CS can be defined as a technology attributed to protect, detect, and respond to attacks. According to Tsuchiya et al. (2018), not only manufacturing systems can cease operating by cyber-attack but also the safety of operators is also a stack. Elhabashy et al. (2018) have discussed how cyber-attacks that can manipulate the product design, process, machine parameters can cause a delay in a product's launch, ruin customer trust, and increase the warranty cost. Thus, making cybersecurity a very important enabling technology.

2.9   Cloud Computing (CC)

Cloud computing (CC) refers to using a network of remote servers which are hosted on the Internet to stockpile, manage, and process data. It works as a substitute technology for the companies who are planning to put money in IT subcontracting resources. The use of CC has many advantages linked to cost reduction as it reduces direct and overhead expenses on the removal of IT framework and giving portability, hence, allowing the use of any sort of device linked to the Internet across any world location. Wang et al. (2017) described cloud manufacturing (CMfg) as a notion that was put forward to improve the current manufacturing system using the CC technology. Liu et al. (2019) have discussed the problems faced by the implementation of cloud manufacturing and how to overcome them. The main problems include the concept of CMfg not being clear which includes its extension, intension, boundary, and capabilities, enterprise-wide adoption and participation, and as cloud manufacturing is an amalgamation of various technologies to have the knowledge about which technology to be applied at what phase in cloud manufacturing. To overcome the problems, it is important to decompose the concept of cloud manufacturing into smaller components to ensure enterprise-wide adoption, and participation work has to be done on certain prerequisites and basic requirements for implementing CMfg,
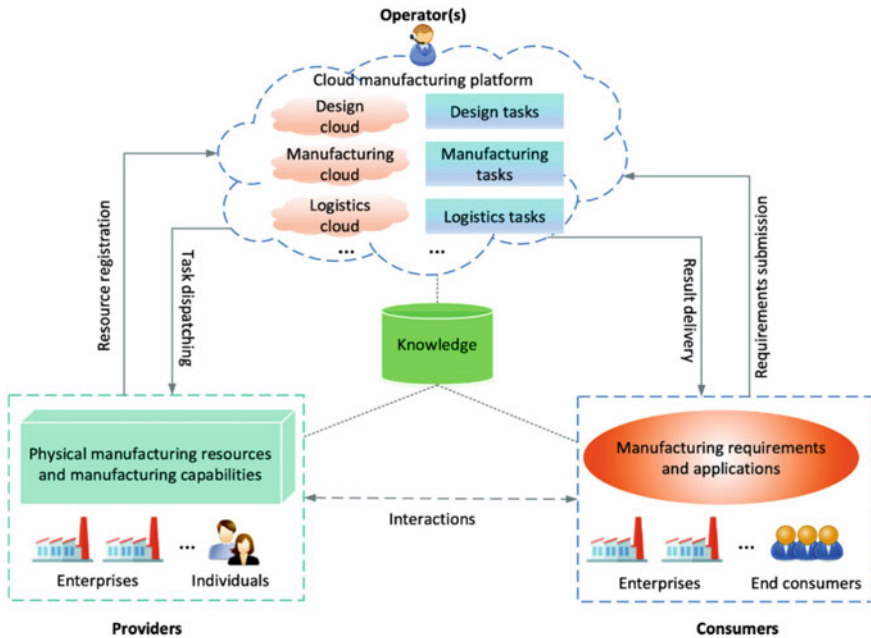
Fig. 2 CMfg model (Liu et al. 2018)

and a hierarchy of technologies have to be prepared. The two main characteristics of CMfg which make it most important enabling technology is its amalgamation of various technologies like IoT, CC, AR, BD, AI, etc., and it has a service-oriented approach. Hence, shifts the manufacturing approach from production-oriented to service-oriented (Xu 2012). It mainly consists of three categories as shown in Fig. 2.

3 Conclusions

In the present study, a detailed review was carried out on key technologies of Industry 4.0 in the manufacturing sectors. As mentioned before, the enabling technologies lay the foundation for Industry 4.0. Industry 4.0 helps in making the manufacturing system more flexible and collaborative. As far as the manufacturing systems are concerned, the adoption of each technology individually will have a lesser impact. Contrast if they are implemented together will have a larger impact. The IIoT is the concept that shows the application of IoT in industries. On adopting IoT/IIoT, everything in the industry can be interconnected with each other. Also, with the implementation of IoT/IIoT, enormous amounts of data will be generated. This data needs to be stored, processed, and analysed as well and that is when BD analysis comes into play. BD analysis helps in taking decisions faster as it helps in getting a

conclusion from the enormous amount of data that is generated. To face the problem of complexity in the manufacturing industry, simulation becomes a handy technology as it helps in reducing cost, developments cycle time, and increased product quality. To close the gap that exists between product development and manufacturing operations, AR plays a major role. AM makes utmost material utilization with its "zero waste" approach and has the potential to replace many conventional manufacturing processes. To hold out the flexibility in demand level, autonomous robots are inevitable and with the introduction of cobots, the human–robot barriers also break. As the integration of the system is necessary for I4.0 both at the intercompany and intracompany level, making horizontal and vertical integrations is necessary. On the grounds of new devices getting connected to the Internet every day, the opportunities of cyber-attacks increase and the information of individuals as well as any organization is at stack, hence, making cybersecurity an unavoidable technology in I4.0. The adoption of CC in manufacturing, i.e. CMfg has a larger impact on a manufacturing system compared to other technologies applied individually as CMfg itself is an amalgamation of various technologies like IoT, CC, AR, BD, AI, etc., and it also helps in shifting the manufacturing approach to being service-oriented.

References

Andulkar M, Le DT, Berger U (2018) A multi-case study on Industry 4.0 for SME's in Brandenburg, Germany. Proceedings of the 51st Hawaii international conference on system sciences

Babiceanu RF, Seker R (2016) Big Data and virtualization for manufacturing cyberphysical systems: a survey on the current status and future outlook. Comput Ind 81:128–137

Bandyopadhyay D, Sen J (2011) Internet of things: applications and challenges in technology and standardization. Wirel Personal Commun 58(1):49–69

Bortolini M, Ferrari E, Gamberi M, Pilati F, Faccio M (2017) Assembly system design in the Industry 4.0 era: a general framework. IFAC-PapersOnLine 50(1):5700–5705

Cheng B, Zhang J, Hancke GP, Karnouskos S, Colombo AW (2018) Industrial Cyberphysical systems: realizing cloud-based big data infrastructures. IEEE Ind Electron Mag 12(1):25–35

Choi K, Chung S-H (2017) Enhanced time-slotted channel hopping scheduling with quick setup time for industrial Internet of things networks. Int J Distrib Sens Netw 13:(6)

Dini G, Mura MD (2015) Application of augmented reality techniques in Throughlife engineering services. Procedia CIRP 38:14–23

Elhabashy AE, Wells LJ, Camelio JA, Woodall WH (2018) A cyber-physical attack taxonomy for production systems: a quality control perspective. J Intel Manuf, 1–16

Gilchrist A (2016) Introducing Industry 4.0, in: Industry 4.0, Apress, Berkeley, CA, pp 195–215

Hannibal M, Knight G (2018) Additive manufacturing and the global factory: disruptive technologies and the location of the international business. Int Bus Rev 27(6):1116–1127

Hassan M, Liu D (2017) Simultaneous area partitioning and allocation for complete coverage by multiple autonomous industrial robots. Auton Robot 41(8):1609–1628

He H et al (2016) The security challenges in the IoT enabled cyber-physical systems and opportunities for evolutionary computing & other computational intelligence. 2016 IEEE congress on evolutionary computation (CEC), 1015–1021

Hofmann E, Rüsch M (2017) Industry 4.0 and the current status as well as future prospects on logistics. Comput Indus 89:23–34

Jiang R, Kleer R, Piller FT (2017) Predicting the future of additive manufacturing: a Delphi study on economic and societal implications of 3D printing for 2030. Technol Forecast Soc Chang 117:84–97

Kannus K, Ilvonen I (2018) Future prospects of cyber security in Manufacturing: findings from a Delphi study. Proceedings of the 51st Hawaii international conference on system sciences

Koch PJ, van Amstel MK, Dębska P, Thormann MA, Tetzlaff AJ, Bøgh S, Chrysostomou D (2017) A skill-based robot co-worker for industrial maintenance tasks. Procedia Manuf 11:83–90

Lachenmaier JF, Lasi H, Kemper H-G (2017) Simulation of production processes involving cyber-physical systems. Procedia CIRP 62:577–582

Leyh C, Martin S, Schäffer T (2017) Industry 4.0 and lean production—a matching relationship? an analysis of selected industry 4.0 models. 2017 federal conference on computer science and informatics systems (FedCSIS) Prague 11, 989–993

Liu Y, Wang L, Wang XV, Xu X, Zhang L (2018) Scheduling in cloud manufacturing: state-of-the-art and research challenges. Int J Prod Res

Liu Y, Wang L, Wang XV, Xu X, Jiang P (2019) Cloud manufacturing: key issues and future perspectives. Int J Comput Integrated Manuf 32(9):858–874

Lu Y (2017) Industry 4.0: a survey on technologies, applications and open research issues. J Ind Inform Integr 6:1–10

Madakam S, Ramaswamy R, Tripathi S (2015) Internet of things (IoT): a literature review. J Comput Commun 3:164–173

Makrini IE et al (2018) Working with walt: how a cobot was developed and inserted on an auto assembly line. IEEE Robot Autom 25(2):51–58

Medium Corporation (n.d.) Industrial Internet of Things. Available from: https://medium.com/@jaydev_21091/industrial-internet-of-things-74a4ffb44679

Motyl B, Baronio G, Uberti S, Speranza D, Filippi S (2017) How will change the future engineer's skills in the industry 4.0 framework? a questionnaire Survey. Procedia Manuf 11:1501–1509

Palmarini R, Erkoyuncu JA, Roy R, Torabmostaedi H (2018) A systematic review of augmented reality application in maintenance. Rob Comput Integr Manuf 49:215–228

Pedersen MR, Nalpantidis L, Andersen RS, Schou C, Bøgh S, Krüger V, Madsen O (2016) Robot skills for manufacturing: from concept to industrial deployment. Rob Comput Integr Manuf 37:282–291

Peruzzini M, Grandi F, Pellicciari M (2017) Benchmarking of tools for user experience analysis in industry 4.0. Procedia Manuf 11:806–813

Posada J et al (2015) visual computing as a key enabling technology for industry 4.0 and industrial internet. IEEE Comput Graph Appl 35(2):26–40

Rentzos L, Papanastasiou S, Papakostas N, Chryssolouris G (2013) Augmented reality for human-based assembly: using product and process semantics. IFAC Proc 46(15):98–101

Rodič̌ B (2017) Industry 4.0 and the new simulation modelling paradigm. Organizacija 50(3):193–207

Salkin C, Oner M, Ustundag A, Cevikcan E (2018) a conceptual framework for industry 4.0, in industry 4.0: managing the digital transformation, Springer Series in Advanced Manufacturing, Springer, Cham, pp 3–23

Saucedo-Martinez JA, Pérez-Lara M, Marmolejo-Saucedo JA (2017) Industry 4.0 framework for management and operations: a review. J Ambient Intell Human Comput 9(3):789–801

Sergey M, Nikolay S, Sergey E (2017) Cyber security concept for Internet of Everything (IoE), systems of signal synchronization, generating and processing in telecommunications (SINKHROINFO), Kazan 2017, pp 1–4

Sezer OB, Dogdu E, Ozbayoglu AM (2018) Context-aware computing learning, and big data in internet of things: a survey. IEEE Int Things J 5(1):1–27

Suri K, Cuccuru A, Cadavid J, Gérard S, Gaaloul W, Tata S (2017) Model-based development of modular complex systems for accomplishing system integration for industry 4.0. 5th international conference on model-driven engineering and software development (MODELSWARD 2017)

Syberfeldt A, Holm M, Danielsson O, Wang L, Brewster RL (2016) Support systems on the industrial shop-floor of the future – operator's perspective on augmented reality. Procedia CIRP 44:108–113

Tao F, Cheng J, Qi Q, Zhang M, Zhang H, Sui F (2018) Digital Twin-driven product design, manufacturing and service with big data. Int J Adv Manuf Technol 94(9–12):3563–3576

Tao F, Qi Q, Liu A, Kusiak A (2018), Data-driven smart manufacturing. J Manuf Syst. in press

Tofail SAM, Koumoulos EP, Bandyopadhyay A, Bose S, O'Donoghue L, Charitidis C (2018) Additive manufacturing: scientific and technological challenges, market update and opportunities. Mater. Today 21(1):22–37

Tsuchiya A, Fraile F, Koshijima I, Ortiz A, Poler R (2018) Software defined networking firewall for industry 4.0 manufacturing systems. J Ind Eng Manage 11(2):318–333

Wang S, Wan J, Li D, Zhang C (2016) Implementing smart factory of industry 4.0: an outlook. Int J Distrib Sens Netw 12(1)

Wang XV, Givehchi M, Wang L (2017) Manufacturing system on the cloud: a case study on the cloud-based process planning. Procedia CIRP 63:39–45

Xu X (2012) From cloud computing to cloud manufacturing. Rob Comput Integr Manuf 28(1):75–86

Yin S, Kaynak O (2015) Big data for modern industry: challenges and trends [Point of View]. In: Proceedings of the IEEE 103(2):143–146

ZúñigaER, Moris MU, Syberfeldt A (2017) Integrating simulation-based optimization, lean, and the concepts of industry 4.0, 2017 Winter simulation conference (WSC), Las Vegas, NV 2017, pp 3828–3839

A Review on Improving the Surface Characteristics of Aluminum Alloy via Friction Stir Processing

Aaditya Trivedi, Niral Jhaveri, Meet Gor, and Pankaj Sahlot

Abstract This study presents the impact of friction stir processing (FSP) on the surface characteristics such as hardness and wear of aluminum alloys. Aluminum alloys (Al) have the potential to be applied in various engineering applications. However, it does not have the required surface properties. Researchers have been working on improving the material properties of Al alloys for the past many years. FSP has gained attention in the last decade because of its ability to modify the material's characteristics. In the recent times, FSP has gained interest among the researchers. FSP results in an intense plastic deformation and amalgamation of materials which result in a refined and uniform microstructure, leading to better hardness values and improved wear resistance. Moreover, defects like porosity, voids, thermal cracks could be minimized in the stir zone at optimal tool parameters. This study reviews the influence of various process parameters like tool geometry, tool rotational speed, number of passes, processing regions, reinforcement particles, and volume percentage of these particles on Al alloys.

Keywords Friction stir processing · Aluminum alloys · Reinforcement particles · Hardness · Wear

A. Trivedi · N. Jhaveri · M. Gor · P. Sahlot (✉)
Mechanical Department, School of Technology, Pandit Deendayal Energy University,
Gandhinagar 382426, Gujarat, India
e-mail: Pankaj.Sahlot@sot.pdpu.ac.in

A. Trivedi
e-mail: Aaditya.tmc17@sot.pdpu.ac.in

N. Jhaveri
e-mail: Niral.jmc17@sot.pdpu.ac.in

M. Gor
e-mail: Meet.gmtmm19@sot.pdpu.ac.in

1　Introduction

Friction stir processing (FSP) is a solid-state novel practice stemmed from friction stir welding (FSW) which is used to modify the local microstructure of the base alloy to accomplish the desired properties. The non-consumable tool while rotating at very high speeds plunges into the specimen until the pin shoulder touches its surface (Mishra and Ma 2005). The tool is then made to traverse relative to the workpiece along the processing direction. Due to high tool RPM, friction is generated, which, in turn, generates heat. This heat generated will result in solid metal modification. There are four different processed regions in a FSPed specimen: base material (BM), heat affected zone (HAZ), thermomechanical affected zone (TMAZ), and stir zone (SZ). FSP offers numerous advantages such as improving a material's fatigue, corrosion resistance, microstructural, and mechanical properties along with diminishing defects such as porosity, voids, thermal cracks effectively (Sahlot et al. 2018a). However, FSP also brings with it few disadvantages such as requirement of heavy-duty clamping, high initial machine cost. Being a pioneering technology, it has a potential to gain importance due to its multipurpose applications. With the use of suitable reinforcement particles, the effects of FSP on the surface composite can be amplified. Aluminum alloys being lightweighted and inflammable in nature in addition with their excellent surface characteristics have a myriad number of applications in aerospace engineering, automobile manufacturing, electronic technology, etc. Researchers by employing FSP on Al alloys have noticed an improvement.

2　Hardness

Hardness defines a material's ability to resist plastic deformation, penetration, indentation, etc. Several methods have been developed over time for hardness testing like Brinell, Rockwell, Vickers. From an engineering point of view, hardness is an important aspect to comprehend as the resistance to wear generally rises with hardness (Sahlot et al. 2018b). The effects of tool processing parameters, viz. number of passes, tool RPM, tool design, reinforcement particles, and volume of reinforcement particles on the hardness of the Al alloy have been discussed comprehensively.

The size and shape of the non-consumable tool utilized in the FSP process have a large effect on the surface characteristics of the base alloy. García-Bernal et al. (2016) through their experiment established a relation between the tool shoulder diameter and the maximum temperature achieved in the processing region. Generally, larger the tool shoulder diameter, larger is the shoulder area, more is the heat input, and, thus, higher is the temperature of the processed region. Additionally, the ratio of a tool's shoulder diameter to its pin diameter should be approximately 1:2 to obtain a thermally stable and uniform microstructure. Mahmoud et al. (2009) studied the effect of tool probe geometries on the Al/SiC surface composite (SC) (Fig. 1). A
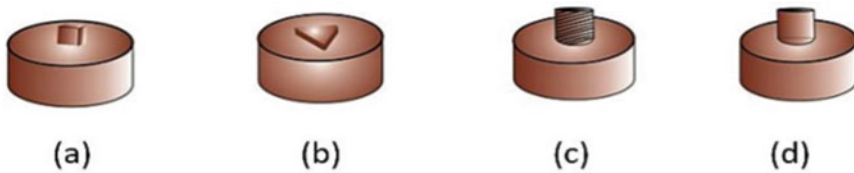
Fig. 1 Different tool probe shapes **a** Square; **b** Triangular; **c** Circular with thread; **d** Circular (Sharma et al. 2015)

square probe homogeneously spreads the reinforcing particles in the SZ. A finer-grain size was achieved (~1 μm) using the square probe when compared to the other shapes. As a result, the micro-hardness value increased to 60 HV from 23 HV of the base alloy. However, the weight loss due to wear of the flat faces' probes, viz. triangular and square, was greater than the circular probe. The worn-out material of these flat probes is mixed with the matrix, thereby creating an impure mixture. Moreover, the tool material selection is also a crucial parameter to determine the quality of the final product. It depends highly on the temperature involved, wear resistance, toughness, etc. Soft materials can be easily processed using H13 and stainless steel tools, while the hard materials need to be processed using harder tools like WC and PCBN.

Formation of SC allows the amalgamation of all variants of reinforcing particles. The consumable particles can be applied through grooves, drilled holes, or by using cover plate. These particles can help avoid defects like porosity, voids and also, perhaps, improve the material properties of the specimen. In an experiment, Prabhu et al. (2019) found the micro-hardness values to increase from 64 HV for the as-built AA6082 alloy to 87 HV for FSPed AA6082/$CaCO_3$ SC. The increased hardness of the SC is mainly because of the presence of reinforcing particles which lead to significant grain size reduction during FSP, thereby causing a reduction in dislocation mobility. In addition, Narimani et al. (2016) found the micro-hardness values as 65 HV for the as-received AA6063 alloy and 140 HV for AA6063-TiB_2 SC. Furthermore, due to the variation of distribution of TiB_2 particles in the SC, a higher variation in micro-hardness values from the center of stir zone was observed. Moreover, Kumar et al. (2020) found the highest hardness values for FSPed A356/SiC SC (89.1 HV) when compared to the as-built A356 (54 HV) and FSPed A356 alloy (66.3 HV) mainly because of the removal of cast micro-porosity, refined grain structure of SC, and uniform dispersal of fine Si particles in the matrix. Different reinforcement particles have different effects on the properties of the specimen. Sharma et al. (2019) concluded that Al-SiC-GNP SC had the highest micro-hardness value of ~75–80 HV when contrasted to Al-SiC-CNT SC, Al-SiC-Graphite SC, and as-received Al. This is ascribed to the mechanical exfoliation and uniform distribution of GNP (which contributes to resist the dislocation movement and, hence, resists the composite failure), hardness of abrasive SiC particles, and large coefficient of thermal expansion among GNP, SiC, and aluminum matrix. Rao and Simhadri (2021) found that AA5083 alloy along with 100% TiB_2 + 0% B_4C reinforcing particles

resulted in a 120.5 HV hardness which was 27% higher than that of base metal. Grain growth, thermal expansion, and pinning effect led to dislocation of grain boundaries and, hence, a higher hardness value. In addition, varying the wt. percentage of the reinforcing particles resulted in different hardness values.

The essential tool processing parameters include the tool RPM, tool travel speed, number of passes. One of the useful techniques to produce structurally sound specimens is to carry out multipass techniques. Khodabakhshi et al. (2017) incorporated multipass FSP to manufacture ultra-fine-grained (UFG) Al–Mg-SiC nanocomposite. It was discovered that the grain size was refined from 6.3 μm of the base alloy to about 1.4 μm of the SZ due to dynamic recrystallization. With an increase in the number of passes, homogenization of SiC nanoparticles is gradually improved and the distance between the reinforcement particles is decreased, leading to the creation of dislocations, which increased the hardness from 51.5 HV to 123 HV. The tool rotational speed is also one of the important parameters as it can monitor the heat input and material flow during FSP. Hence, tool RPM is significant for determining the material properties. Yang et al. (2018) concluded that a high tool rotational speed results in a better distribution of Al_2O_3 reinforcements in the AA2024 SZ, causing the pinning effect to improve. Additionally, at 1500 RPM, the hardness values were found out to be ~140–155 HV, which decreased to ~140–147 HV at 1200 RPM and further decreased in value at 900 RPM. Moreover, Qin et al. (2020) found that the hardness values of Al-Mg_2Si weld nuggets (WN) were the highest for the tool rotational speeds of R700 followed by R900, R500, R1200 and the least for R300. At the rotational speeds of R1200 and R300, detectable cavities and defects were observed, whereas at the speeds of R700 and R900, the matrix was strengthened by the inclusion of broken eutectic phase and the debris of the primary Mg_2Si phase. Butola et al. (2019) using Taguchi technique found that the micro-hardness value increased from 700–1000 rpm and decreased from 1000–1300 rpm for AA7075 SC.

It is important to understand the characteristics of different processing zones of the specimen, viz. stir zone (SZ), TMAZ, HAZ, and the base metal zone (BM). Vinothkumar et al. (2020) performed an experiment on Al2024 with Si_3N_4 and AlN composite. It was found that the hardness value in SZ (58.1 HV) was higher than that in HAZ (55.2 HV) and BM (54.1 HV). It is very important to understand the effect of different reinforcements on different Al alloys. Hence, it is very important to carefully select these foreign particles in order to improvise the surface properties. In an experiment performed by Kumar et al. (2020), the maximum value of average micro-hardness was found when AA6016 alloy was reinforced with 50% Al_2O_3 and 50% AlN. This equal composition (50% Al_2O_3 + 50% AlN), perhaps, resulted in a maximum increase in nucleation sites which leads to a significant reduction in the size of Al matrix. Moreover, the average hardness value was higher in SZ than BM as shown in Fig. 2 because of dissolution of precipitates. As evident from Fig. 2, with varying % of reinforcement particles, the hardness values tend to alter. On the contrary, Vázquez et al. (2016) while performing FSP on heat treated Al7075-T651/TiC SC found that the hardness value of the BM was higher than that of SZ. The FSP thermal treatments affected the T651 early treatment, thereby reducing the hardness in the SZ. The average hardness is decreased in the SZ of specimen from
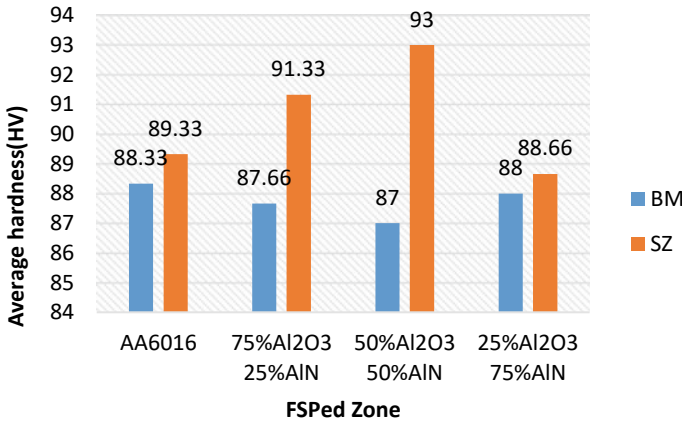
Fig. 2 Comparison of the average hardness values obtained in BM and SZ (Kumar et al. 2020)

~195 HVN to ~150 HVN due to plastic deformation of the material. Moustafa and Mosleh (2020) studied the impact of FSP on different regions of the specimen. With respect to the processing centerline, the micro-hardness curves were irregular because of non-uniform plastic flow field on the retreating and advancing sides. In another research, Yang et al. (2019) found that FSP triggered a reduction in the dislocation substructure and weakened the dislocation strengthening phenomena. On careful scrutinization, it was observed that HAZ and TMAZ had greater micro-hardness values than SZ. This is due to the size of Si particles and the spacing between Si particles are smaller in TMAZ than in the SZ. Whereas, HAZ has Si particles of cellular structure and pinning effect on dislocation movement.

In summary, the strength of Al alloy generally increases with the FS process. Researchers generally preferred a range of 900–1200 RPM for tool RPM. Addition of appropriate reinforcement particles and incorporation of multiple passes are highly recommended so as to form a finished material with the greatest strength.

3 Wear

Wear is deforming or gradual removal of the material from the specimen, done either chemically or mechanically (Sahlot et al. 2017). The effect of parameters like amount of load, number of passes, reinforcement particles, volume of reinforcement particles is discussed in detail.

Reinforcing particle plays major part in increasing the wear resistance of the as-formed SC. In a research by Kumar et al. (2020), weight loss is revealed as 17 mg for the as-built A356 alloy, 9 mg for the FSPed specimen, and 3 mg for FSPed SC. When compared to as-built alloy, FSPed specimen and FSPed SC have significantly higher wear resistance. This is because of reinforcements, which reduce the area of

contact between the pin and disk. The load is carried by the particles interacting with the disk, thereby reducing the coefficient of friction of the processed SC. One other reason is the higher hardness of the pin, which resists the asperities from penetrating the surface. Adetunla and Akinlabi (2018) concluded that by adding Ti-6Al-4 V to 1100 Al Alloy, wear rate of base alloy can be significantly reduced. It is also important to understand the effect of volume and type of reinforcement particles on the wear rate. In an experiment performed by Prabhu et al. (2019), Al alloy is reinforced with $CaCO_3$. Due to the addition of $CaCO_3$ particles, the wear rate is reduced to one-third the amount of wear resistance for as-built Al alloy and two-third the amount of wear resistance for the FSPed Al alloy. A tribo mixed layer is formed at the sliding surface due to the presence of $CaCO_3$. In the experiment done by Bharti et al. (2020), Al alloy was reinforced with ZrO_2 particles. A reduction in weight loss is witnessed when this SC underdoes FSP. However, the reduction in weight loss is less when FSP is carried out in the absence of reinforcement particles. Weight loss is witnessed to be the highest in a sample where no reinforcements were added and no FSP was conducted. This is observed because of ZrO_2 reinforcement particles, which forms a layer that takes the normal reaction load. This load is generated because of an interaction with the disk. In another experiment performed by Ali et al. (2021), AA7075-T6 was fabricated by performing FSP with reinforced WC nanoparticles at 0 wt.%, 3 wt.%, 6 wt.%, and 9 wt.%. The specimen with 0 wt.% WC particles caused the highest wear rate, and the specimen with 9 wt.% WC resulted in the lowest wear rate. This is attributed to strengthening mechanism and homogeneous distribution of reinforcement particles. Kishan et al. (2016) observed that wear rate decreased with an increase in the percentage of foreign particles. Due to the improved hardness, the dispersion of TiB_2 particles (which act as load-bearing elements) is improved. However, the wear rate increases even with higher percentage of reinforcements. It is because foreign particles are pulled out from the composite pin during the wear test. Adhesive wear is converted into abrasive wear due to the presence of these particles which acts as barriers. Hence, extra material is worn from the composite pin. The least wear rate as visible from Fig. 3 was obtained at the optimum tool processing conditions, i.e., tool rotational speed set at 1120 RPM; vol.% of reinforcement (TiB_2) is set at 4 vol.%. In this era, where the global warming has reached an alarming stage, it is important to consider and implement the use of renewable resources in every way possible. One commonly used renewable reinforcement is rice husk ash (RHA). It is a renewable agricultural by-product formed from rice mill. Marini et al. (2020a) in an experiment found the wear resistance of the AA6061 alloy increases due to incorporation of RHA particles and performing FSP. The wear rate is reduced because of the presence of hard reinforced RHA particles. The contact area between the rubbing probe and rotating disk is reduced due to the presence of RHA particles. Moreover, the bonding between the alloy and RHA particles also resulted in lower wear rate. In an experiment, Marini et al. (2020b) after performing wear test on AA6061 alloy, FSPed AA6061 alloy, and FSPed AA6061/6 vol.% RHA SC found that wear performance of the composite material was improved. This is mainly ascribed to the significant microstructural refinement achieved due to the presence
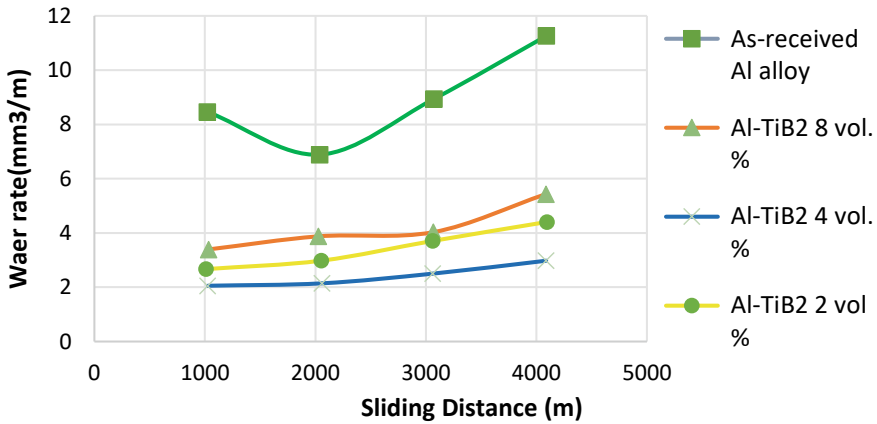
Fig. 3 Wear rate of Al-TiB$_2$ SC and as-received Al alloy (Kishan et al. 2016)

of reinforcing particles, which thereby increased hardness and wear performance of the composite.

Wear resistance is vulnerable to small changes in process parameters. Therefore, it is crucial to select optimal parameters to improve the wear resistance of the specimen. The amount of load applied is one of the important parameters which determine the wear characteristics. In an experiment performed by Sert and Celik (2014), it was found that as the load increases, wear rate also increases. Both abrasive and adhesive wear take place; however, the wear effects can majorly be attributed to abrasive wear since the applied load increases and the broken particles from the wear area arise in between the ball and the material. Tool rotational speed is another important processing parameter which helps developing the wear resistance. Sharma et al. (2021) found that AA7075 SC was fabricated by incorporating B$_4$C particles. With the presence of B$_4$C particles, an increase in rotational speed increased the wear resistance, but an opposite trend is observed when these particles are absent. Best results are attained at optimal conditions, i.e., 1600 RPM and 30 mm/min feed rate. Vijayavel et al. (2021) analyzed the impact of tool design on the wear rate. They concluded that for a tapered tool, as the ratio of tool shoulder diameter to pin diameter increases, the wear rate decreases till it reaches three and then starts increasing. High wear rate of a normal tool is due to a lesser hardness value, coarser acicular SiCps particles, non-uniform spread along the main Al boundaries, wettability at the contact of two substances, imperfect bonding between the Al matrix and SiCps, materials porosity, and chemical reactions at the consumable particles/matrix boundary. In a research by Ande et al. (2019), researchers concluded that higher the frictional force, greater will be the power requirement to remove the material, and, hence, a lower wear rate. In an experiment performed by Moharrami et al. (2020), it was found that multiple FSP passes on in situ Al-25% Mg$_2$Si composite reduce wear rate significantly. This is attributed to an increase in capacity of the composite to bear load and to homogeneous distribution of Mg$_2$Si particle. Mohammed and Subhi (2021)

in an experiment found that as the plunge depth increases, the wear rate decreases due to the load-bearing capacity of SiC particles. But on increasing tool RPM, wear rate increases. This is due to separation of SiC particles at the time of wear testing. According to researchers, to obtain a low wear rate, a 1460 tool RPM and 0.3 mm plunge depth are preferred. In addition to load, the number of passes also determines wear rate.

In summary, the wear and friction characteristics of the composite surface obtained by the FSP method are improved when compared with the BM. The wear characteristics of the alloy are altered depending on the load applied. The rate of wear is increased with an increase in the load. To achieve a high wear resistance and low wear rate for an Al alloy, it becomes indispensable to incorporate appropriate reinforcing particles. Additionally, an optimal tool RPM around the range of 1400–1500 RPM would be preferred.

4 Conclusion

A thorough review on the impact of several FSP parameters on the Al alloy has been presented. The strength of the lightweight Al alloy can be increased manifold which makes them durable and usable in various applications. The changes occurring entirely depend upon the type of SC formed alongside with the processing parameters and reinforcing particles being utilized. Optimal tool processing parameters which vary with varying base alloys should be carefully selected as they can play a major role in determining the surface characteristics. The practicality of FSP has been successfully validated through numerous experiments, but the existing process is still immature. With further research in the field, FSP can lay a pathway to many more new applications for fabrication, processing of materials. Although facing a lot of challenges, FSP brings attractive opportunities among researchers. Being a green technology, FSP can compete with the conventional processing techniques.

References

Adetunla A, Akinlabi E (2018) Mechanical characterization of Al/Ti-6Al-4V surface composite fabricated via FSP: a comparison of tool geometry and number of passes. Mater Res Express 5(11). https://doi.org/10.1088/2053-1591/aadce5

Ande R, Gulati P, Shukla DK, Dhingra H (2019) Microstructural and wear characteristics of friction stir processed Al-7075/SiC reinforced aluminium composite. Mater Today Proc 18:4092–4101. https://doi.org/10.1016/j.matpr.2019.07.353

Bharti S, Ghetiya ND, Dutta V (2020) Investigating microhardness and wear behavior of Al5052/ZrO2 surface composite produced by friction stir processing. Mater Today Proc xxxx: 2–7. https://doi.org/10.1016/j.matpr.2020.06.318

Butola R, Ranganath MS, Murtaza Q (2019) Fabrication and optimization of AA7075 matrix surface composites using Taguchi technique via friction stir processing (FSP). Eng Res Express 1(2). https://doi.org/10.1088/2631-8695/ab4b00

Feroz Ali L, Soundararajan R, Kovarthanam M, Mohamed Aniq A (2021) Wear and friction properties of AA 7075-T6 with × wt% of WC surface composite fabricated by FSP technique. Mater Today Proc xxxx. https://doi.org/10.1016/j.matpr.2020.11.368

García-Bernal MA, Mishra RS, Verma R, Hernández-Silva D (2016) Influence of friction stir processing tool design on microstructure and superplastic behavior of Al-Mg alloys. Mater Sci Eng A 670:9–16. https://doi.org/10.1016/j.msea.2016.05.115

García-Vázquez F, Vargas-Arista B, Muñiz R, Ortiz JC, García HH, Acevedo J (2016) Efeito dos parâmetros do proceso de fricção agitação para reforçar uma placa de aluminio Al7075-T651 com TiC. Soldag. e Insp. 21(4):508–516. https://doi.org/10.1590/0104-9224/SI2104.10

Khodabakhshi F, Gerlich AP, Švec P (2017) Fabrication of a high strength ultra-fine grained Al-Mg-SiC nanocomposite by multi-step friction-stir processing. Mater Sci Eng A 698:313–325. https://doi.org/10.1016/j.msea.2017.05.065

Kishan V, Devaraju A, Prasanna Lakshmi K (2016) Tribological Properties of nano TiB2 particle reinforced 6061-T6 aluminum alloy surface composites via friction stir processing

Kumar H, Prasad R, Kumar P, Tewari SP, Singh JK (2020) Mechanical and tribological characterization of industrial wastes reinforced aluminum alloy composites fabricated via friction stir processing. J Alloys Compd 831:154832. https://doi.org/10.1016/j.jallcom.2020.154832

Mahmoud ERI, Takahashi M, Shibayanagi T, Ikeuchi K (2009) Effect of friction stir processing tool probe on fabrication of SiC particle reinforced composite on aluminium surface. Sci Technol Weld Join 14(5):413–425. https://doi.org/10.1179/136217109X406974

Marini CD, Fatchurrohman N, Zulkfli Z (2020a) Investigation of wear performance of friction stir processed aluminium metal matrix composites. Mater Today Proc xxxx. https://doi.org/10.1016/j.matpr.2020.07.568

Marini CD, Fatchurrohman N, Zulkfli Z (2020b) Morphological study of friction stir processed aluminium metal matrix composites. Mater Today Proc xxxx. https://doi.org/10.1016/j.matpr.2020.07.569

Mohammed MH, Subhi AD (2021) Exploring the influence of process parameters on the properties of SiC/A380 Al alloy surface composite fabricated by friction stir processing. Eng Sci Technol Int J xxxx. https://doi.org/10.1016/j.jestch.2021.02.013

Moharrami A, Razaghian A, Paidar M, Šlapáková M, Ojo OO, Taghiabadi R (2020) Enhancing the mechanical and tribological properties of Mg2Si-rich aluminum alloys by multi-pass friction stir processing. Mater Chem Phys 250. https://doi.org/10.1016/j.matchemphys.2020.123066

Moustafa EB, Mosleh AO (2020) Effect of (Ti–B) modifier elements and FSP on 5052 aluminum alloy. J Alloys Compd 823. https://doi.org/10.1016/j.jallcom.2020.153745

Mishra RS, Ma ZY (2005) Friction stir welding and processing. Mater Sci Eng Rep 50(1–2):1–78. https://doi.org/10.1016/j.mser.2005.07.001

Narimani M, Lotfi B, Sadeghian Z (2016) Investigating the microstructure and mechanical properties of Al-TiB2 composite fabricated by Friction Stir Processing (FSP). Mater Sci Eng A 673:436–442. https://doi.org/10.1016/j.msea.2016.07.086

Nirmal Kumar K, Aravindkumar N, Eswaramoorthi K (2020) Fabrication of AA6016/(Al2O3+AlN) hybrid surface composite using friction stir processing. Mater Today Proc 33(xxxx):315–319. https://doi.org/10.1016/j.matpr.2020.04.107

Qin QD, Zhao HL, Li J, Zhang YZ, Su XD (2020) Microstructure and mechanical properties of friction stir processed Al−Mg2Si alloys. Trans Nonferrous Met Soc China 30(9): 2355–2368. https://doi.org/10.1016/S1003-6326(20)65384-5

Sahlot P, Jha K, Dey GK, Arora A (2017) Quantitative wear analysis of H13 steel tool during friction stir welding of Cu-0.8%Cr-0.1%Zr alloy. Wear 378–379:82–89

Sahlot P, Nene SS, Frank M, Mishra RS, Arora A (2018a) Towards attaining dissimilar lap joint of CuCrZr alloy and 316L stainless steel using friction stir welding. Sci Technol Weld Join 23(8):715–720. https://doi.org/10.1080/13621718.2018.1499186

Sahlot P, Jha K, Dey GK, Arora A (2018b) Wear-induced changes in FSW tool pin profile: Effect of process parameters. Metal Mater Trans A 1–12. https://doi.org/10.1007/s11661-018-4580-9.

Santha Rao D, Shashank Simhadri T (2021) Improvements in mechanical properties of aluminium alloy-titanium di boride and boron carbide hybrid composite produced through friction stir processing route. Mater Today Proc xxxx. https://doi.org/10.1016/j.matpr.2021.01.774

Sharma V, Prakash U, Kumar BVM (2015) Surface composites by friction stir processing: a review. J Mater Process Technol 224(June):117–134. https://doi.org/10.1016/j.jmatprotec.2015.04.019

Sharma A, Narsimhachary D, Sharma VM, Sahoo B, Paul J (2019) Surface modification of Al6061-SiC surface composite through impregnation of graphene, graphite & carbon nanotubes via FSP: A tribological study. Surf Coat Technol 368(January):175–191. https://doi.org/10.1016/j.surfcoat.2019.04.001

Sharma H, Kumar Tiwari S, Singh Chauhan V, Kumar R, Gulati P (2021) Wear analysis of friction stir processed aluminum composite reinforced by boroncarbide. Mater Today Proc xxxx. https://doi.org/10.1016/j.matpr.2021.02.468

Sert A, Celik ON (2014) Wear behavior of SiC-reinforced surface composite Al7075-T651 aluminum alloy produced using friction stir processing. Indian J Eng Mater Sci 21(1):35–43

Sivanesh Prabhu M, Elaya Perumal A, Arulvel S, Franklin Issac R (2019) Friction and wear measurements of friction stir processed aluminium alloy 6082/CaCO3 composite. Meas J Int Meas Confed 142:10–20. https://doi.org/10.1016/j.measurement.2019.04.061

Vijayavel P, Sundararajan T, Rajkumar I, Ananthakumar K (2021) Effect of tool diameter ratio of tapered cylindrical profile pin on wear characteristics of friction stir processing of Al-Si alloy reinforced with SiC ceramic particles. Met Powderrep 76(2):75–89. https://doi.org/10.1016/j.mprp.2020.04.005

Vinothkumar H, Saravanakumar S, Ramesh C, Prakash P, Ragul Vignesh A, Naveen S (2020) Investigation on Al2024 with Si3N4 and AlN composites using friction stir processing. Mater Today Proc 33(xxxx):3089–3092. https://doi.org/10.1016/j.matpr.2020.03.683

Yang K, Li W, Huang C, Yang X, Xu Y (2018) Optimization of cold-sprayed AA2024/Al2O3 metal matrix composites via friction stir processing: Effect of rotation speeds. J Mater Sci Technol 34(11):2167–2177. https://doi.org/10.1016/j.jmst.2018.03.016

Yang T et al (2019) Effect of Friction Stir Processing on Microstructure and Mechanical Properties of AlSi10Mg Aluminum Alloy Produced by Selective Laser Melting. Jom 71(5):1737–1747. https://doi.org/10.1007/s11837-019-03343-9

Influence of Machining Parameters of Fiber Laser Cutting on Al6061-T6

Jay Vora, Chintan Patel, Kumar Abhishek, and Rakesh Chaudhari

Abstract Low-density high-strength alloys are a more useable material in recent development in the manufacturing industries, automotive industries, and aircraft industries. Among all materials, Al6061-T6 material is a very common material for these industries. Fiber laser cutting of this material gives more benefits as compared to other conventional laser cutting. In the current study, machining process parameters such as laser output power, cutting speed, and assist gas pressure were used for fiber laser cutting of Al6061-T6. Taguchi's L9 OA was selected to perform the experiments by varying laser power from 1600 W to 2000 W, cutting speed from 2500 to 4500 mm/min, gas pressure from 10 to 14 bar. The main aim of the current study is to identify the correspondence between the input major control process parameters and output response variables for Al6061-T6. Surface roughness, dross at bottom of the cut edge, kerf width of the cut surface, and taperness of cut edge were selected as output parameters. Lower SR was observed at higher cutting speed and lower power and gas pressure. Lower kerf width was obtained at the lowest machining speed, highest gas pressure, and lower power. Dross height was firstly found to be decreasing and then increases as power and cutting speed increases. At higher gas pressure, cutting speed has no more impact on the dross height. Tapper angle was found to be the least at the higher heat input and gas pressure.

Keywords Fiber laser cutting · Al6061-T6 · Surface roughness · Kerf width · Dross height · Taperness

J. Vora · C. Patel · R. Chaudhari (✉)
Department of Mechanical Engineering, Pandit Deendayal Energy University, Gandhinagar 382007, Gujarat, India

K. Abhishek
Department of Mechanical and Aerospace Engineering, Institute of Infrastructure, Technology, Research and Management (IITRAM), Ahmedabad 380026, Gujarat, India

1   Introduction

Recent advancements in automobiles, aircraft, and other industries make ample use of low weight and high-strength material having a higher strength-to-weight ratio. A newer development in the automobile (Hirsch 2011) and aircraft industries needs material that gives higher fuel-efficient performance (Saito et al. 2000). Other industries need to develop a product with higher strength without getting the bulky product. Hence, in the recent years, demand for low-density high-strength alloys is increasing like aluminum alloys, magnesium alloys, titanium alloys (Patel et al. 2016; Chaudhari et al. 2020; Rathi et al. 2020). Among all alloys, aluminum alloys are more likely to use in many industries. Lightweight alloys like aluminum alloys are preferred at any application where weight reduction is required. As fuel price increases tremendously and same time awareness of the environment also increases in people, researchers give more attention to produce sustainable products. For producing sustainable products so that they will perform their function without affecting the environment, lightweight alloys like aluminum alloys are most preferable. The lightweight alloys are good candidates to develop sustainable products (Chaudhari et al. 2020; Mayyas et al. 2012). It will also give functional benefits to the vehicle and the structure's weight reduction. Low-density high strength material provides higher strength-to-weight ratio, so this material is well-suited for the application where weight reduction is essential which reduces the functioning cost. This material is used in the case of aircraft, automotive, spaceflight, and shipbuilding sectors.

There are different manufacturing processes for aluminum alloys such as machining-conventional and non-conventional machining processes (Chaudhari 2019). Among all machining processes, beam-based machining processes are more famous for cutting complex parts. In particular, laser beam cutting can produce intricate two-dimensional parts with high productivity and effectiveness compared to other beam-based processes like the EBM because it requires a vacuum in the machining zone. Laser cutting is considered a beam-based contactless machining process where tool wear is not present, yet there are potential complications regarding aluminum's thermophysical and optical properties. This low-density high-strength aluminum alloys affect the laser cutting performance due to thermophysical and optical properties and the chemical composition. Properties like (i) the high reflectivity of laser beams causes high requirements in laser power for cutting operation due to more amount of laser energy get reflected and back-reflected beams may chance to fail the laser cutting lens system; (ii) higher thermal conductive nature of aluminum alloy creates more heat affected zone due to radial transfer of heat in the material; (iii) at higher temperature, molten metal reacts with the assist gas and it will lead to the formation of oxides of aluminum which alters the base material property; and (iv) molten aluminum material has a higher viscosity which creates difficulties in the removal of molten material from machining zone, and it may affect the cutting quality.

Laser beam cutting is the most preferable way of cutting or trimming process for sheet metal cutting of complex-shape geometries (Dubey 2008). The laser cutting process is a more powerful and effective method for sheet metal trimming in the automobile industry because it is not suffering from any tool breakage as harden parts of the press tool may suffer from wear and tear during functioning as it works in the higher stress and higher temperature. Sometimes, it may suffer from sudden failure also. These all increase maintenance as well as machining costs in the operations like the piercing and trimming process. Hence, beam-based cutting has been applied in almost all automotive industries. The laser cutting process facilitates minimum wastage of base material, negligible thermal distortion of the specimen, and almost no tool wear and tear. As laser cutting is beam-based machining process which did machining without making any contact, hence, it does not have direct tool contact, so tool wear and tear is absent as other conventional machining processes suffering from wear and tear issues. Laser cutting with fiber laser source is allowing the automation with a higher degree of freedom; hence, it nearly cuts or trims any complex shape of the parts. Many different ways can produce laser; according to that, it is classified into many categories. Among all types of laser, CO_2 and Nd-Yag laser machines were the first choice for cutting the metals. Majorly, research work is done with the continuous-mode CO_2 laser and pulsed-mode Nd-Yag laser for the low-density high-strength alloys. In the recent years, mature and efficient high-power fiber lasers are evolving, and fiber laser application is also increasing in almost all industries. High-power lasers have good laser properties due to their advantageous characteristics; conventional laser, like CO_2 and Nd-Yag laser cutting are replaced by fiber laser cutting (Kratky et al. 2008). Fiber laser has characteristics like Sorter wavelength (around 1 μm), good focus ability, superior beam product parameter, smaller focused diameter, high output power with good beam quality, high operating efficiency, minimal floor equipment (Wandera 2010). Fiber laser is the solid-state laser in which laser is generated by a laser generator (laser generator is equipped with the optical fiber doped with rare earth elements), and it will irradiate at the specimen. High-power-focused laser is the primary source of heating causes rapid heating, melting, evaporation, and ablation of material. Since, laser cutting performance is measured based on machining time as well as how effectively cuts the material. Fiber laser ($\lambda = 1$ μm) can cut material faster and with acceptable cut quality than that of the conventional CO_2 laser ($\lambda = 10$ μm) for the material thickness less than 5 mm (Powell and Kaplan 2012). In the area of sheet metal trimming, CO_2 laser and Yag laser are replaced with the high-power fiber laser due to characteristics as mentioned earlier. Hence, fiber laser cutting machine has become a research topic for advanced materials like low-density high-strength alloys. Riveiro et al. (2010) examined the effect of the different assist gas on the cut quality of aluminum alloy while cutting with a CO_2 laser source. In this study, the author used non-identical assist gases, including Ar, N_2, O_2, and compressed air gas, to evaluate its effect. In another study, Riveiro et al. (2010) experimented with the continuous mode and pulsed mode of the laser. He found that CW power gives the higher cutting speed and MRR at the same time with good cut quality. Akhtar et al. (2014) performed experiments and did a simulation in the Abaqus final element analysis and examined the effect of size of

cutting on thermal stress or distortion. Search et al. (2013) performed experiments on Al7075-TiB$_2$ for analyzing and optimizing the parameter's effect on the surface roughness, volumetric MMR, dimensional accuracy. Jiang et al. (Jiang et al. 2020) performed experiments on the material of Al6061-T6 by varying the parameter like power, stand of distance (SOD), sample thickness to observe the temperature at the cutting zone. Riveiro et al. (2008) used an off-axis supersonic nozzle for fiber laser cutting. He used two argon gas flows to perform experiments, one with the subsonic nozzle, coaxial with laser, and other gas flow with supersonic nozzle. Scintilla and Tricarico (2013) focused on identifying the influence of cutting speed and assist gas pressure for low-density high-strength alloys like aluminum, titanium, and magnesium by doing different experiments by varying both parameters. Scintilla (2014) used response surface methodology to investigate the influence of the cutting speed, focal position, and assist gas pressure on dross height, kerf width, and roughness. Chen et al. (2016) performed numerous experiments establishing the relationship of temperature at cut front edge T$_{ce}$ with surface quality. They manipulate the different parameters to vary the cut edge temperature to examine outputs. In another study by Chen et al. (2016), they performed various experiments by varying the laser power cutting speed and gas pressure, and he observed the effect of those parameters on the striation pattern.

From the existing studies, it has been noticed that limited work has been done to investigate the cutting/trimming of Al6061-T6 using fiber laser cutting. In the present work, laser power, cutting speed, and gas pressure are considered as machining variables while SR, kerf width, dross, and taperness as the response variables. Taguchi's 3-level L9 orthogonal array has been used for conducting the experiments. Investigation of machining variables on output variables has been studied with the help of the main effect plot.

2   Experimental Setup and Experimentation

In the present study, experiments were carried out on the Al6061-T6 material having a 2.5 mm thickness plate. Table 1 shows the mechanical properties of the Al6061-T6 alloy used in the current study. All experiments were carried out with continuous-mode high-density fiber laser by using a laser cutting machine. All the experiments

Table 1 Properties of AL6061-T6 material

Hardness (HRB)	95 HB
Density (g/cm^3)	2.70
Modulus E (GPa)	70
Melting point (°C)	650
Tensile strength (MPa)	260
Thermal conductivity (W/mK)	166

Table 2 Machining variables with three different levels

Control factor	Levels		
	1	2	3
Laser power (W)	1600	1800	2000
Cutting speed(mm/min)	2500	3500	4500
Gas pressure (bar)	10	12	14

were repeated three times for better accuracy, and the average value has been considered for analysis. The fiber laser cutting machine is attached with a CW-mode fiber laser generator manufactured by the RAYCUS model name is RFL-C3000. It is a single-mode laser generator having a maximum of 3 kW output power.

All parameters were identified based on trial runs and past literature. Experiments were performed on the AL6061-T6 material having 2.5 mm thickness. Experiments were performed by varying three parameters at three-level, namely fiber laser power (1600 to 2000 W), cutting speed (2500–3500 mm/min), and gas pressure (10–14 bar). Table 2 shows the values of input process parameters at different levels. For supplying the assist gas (nitrogen as assist gas), converging nozzle having a 2 mm outlet diameter is used. The SOD was set at 0.5 mm. Laser-cut focus and focal were set 3 mm and 150 mm above the specimen surface, respectively. Table 3 shows Taguchi's 3-level L9 OA design used along with the values of input process parameters. Figure 1 shows the measurement process of SR, kerf, and dross measurements.

Table 3 Taguchi's L9 OA with measured values of output responses

Run	Laser power (W)	Cutting speed (mm/min)	Gas pressure (bar)	SR (μm)	Kerf width (μm)	Dross (mm)	Kerf width at bottom (μm)
1	1600	2500	10	6.3435	227.27	0.29	178.64
2	1600	3500	12	6.0715	223.91	0.13	187.44
3	1600	4500	14	4.734	224.75	0.14	181.99
4	1800	2500	12	6.3595	228.96	0.12	180.73
5	1800	3500	14	6.712	227.27	0.19	189.96
6	1800	4500	10	5.2985	215.49	0.19	190.80
7	2000	2500	14	7.1795	234.01	0.2	190.38
8	2000	3500	10	6.1245	222.22	0.17	187.45
9	2000	4500	12	5.4485	225.59	0.27	203.38
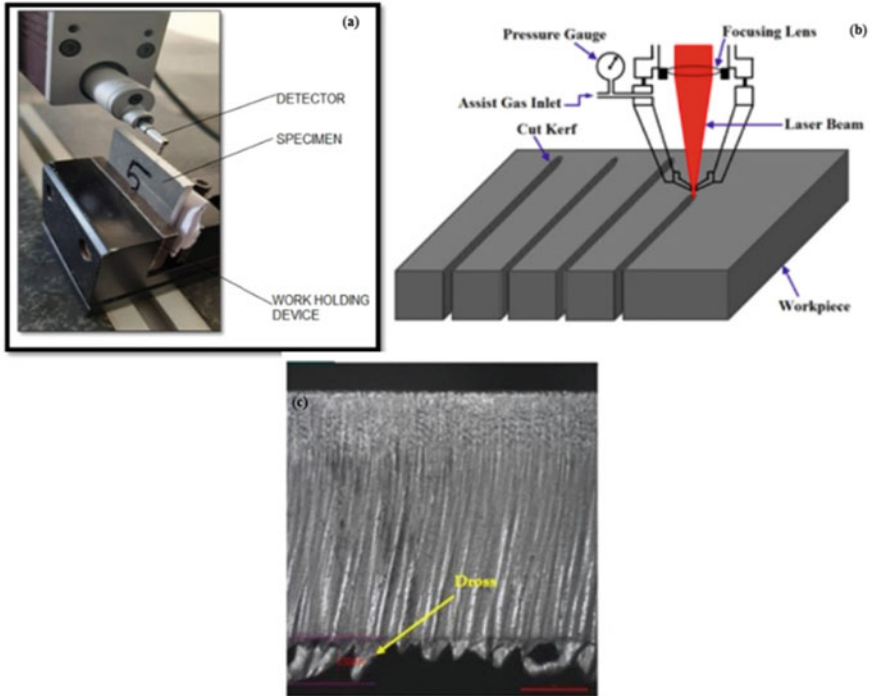
Fig. 1 **a** SR measurement, **b** Kerf measurement, **c** Dross measurement

3 Results and Discussion

3.1 Surface Roughness

Table 3 shows the measured values of SR for all the experiments. SR is analyzed at the middle of the cut edge by taking average values of three measurements. The cutoff length (λ_c) was selected as 0.8 mm with the evaluation length of 15 mm. Surface roughness is characterized by the arithmetic mean of peaks and valleys of the cut edge known as the Ra value. Ra value of the cut edge surface concerning laser power, cutting speed, and gas pressure is mentioned in Fig. 2. As shown in the graphs, SR increases as power increases, decreases as cutting speed increases and increases as gas pressure increase. As laser power increases, heat input at the machining zone increases; hence, more heat will generate more amount of molten material that will lead to poor surface finish. Cutting speed is also a higher influence parameter; at lower cutting speed value, it creates more peaks and valleys. Due to this reason, the obtained value of SR is not smooth. SR was observed to increase slightly with an increase in the gas pressure. This is due to the unstable machining at
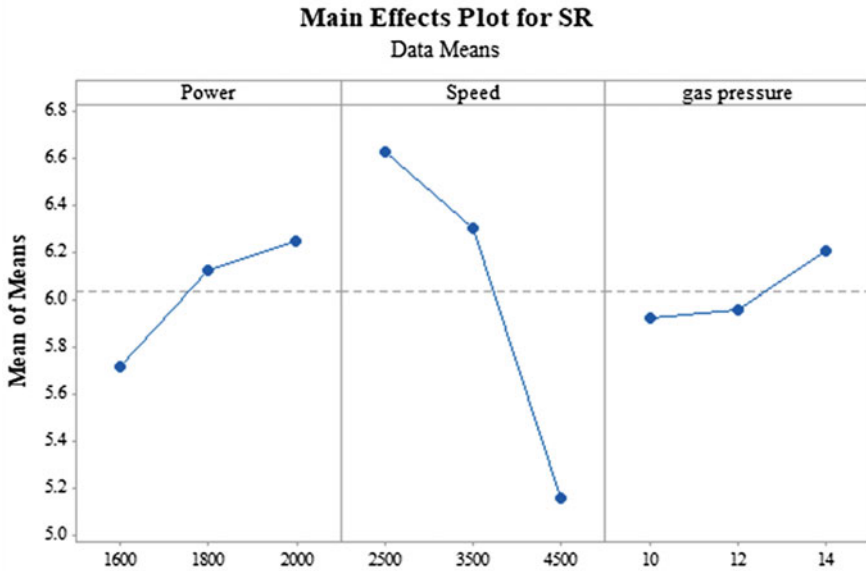
Fig. 2 Main effect plot for SR

higher gas pressure which in turn produces worsen cutting edge. It is recommended to have process parameters of 1600 W laser power, 4500 mm/min cutting speed, and 10 bar gas pressure for obtaining the least SR.

3.2 Kerf Width Measurement

Kerf is the width of material removed from the machining zone via gas pressure during the cutting operation. Table 3 shows the measured values of kerf width. Minimum kerf width is desirable to reduce the wastage of material. Figure 3 shows the variation of kerf width value of cut edge surface against input process parameters of laser power, cutting speed, and gas pressure. The main effect plot of kerf shows a direct relation of kerf width for the gas pressure and indirect relation with cutting speed, but for power, it was observed that it first decreases and then increases as laser power increases. Kerf width largely depends on the supplied heat and gas pressure. As gas pressure increases, more amount of material is removed from the machining zone that leads to higher kerf width. Power and cutting speed both control the supplied heat; higher heat creates more amount of molten material, hence creates wider kerf. Smaller kerf width is achieved at the 1800 W power, 4500 mm/min cutting velocity, and 14 bar assist gas pressure.
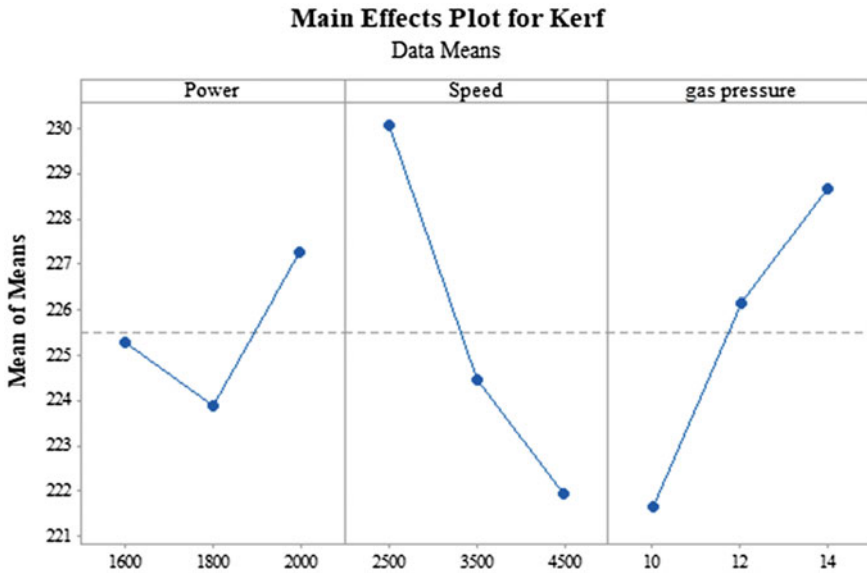
Fig. 3 Main effect plot for kerf

3.3 Dross Measurement

Dross is an extra material that is not excluded from the machining zone and re-solidified at the bottom of the kerf. Dross is also a quality parameter because it decreases the functionality of a part or product. The measured values of dross are shown in Table 3. Relation between dross and selected range of parameters like laser power, cutting speed, and gas pressure can be seen as per the main effect plot in Fig. 3. It has been observed that dross value decreases as laser power and cutting speed increase, and a further increase in power dross value again increases. This is due to heat supply in the machining zone as power and cutting velocity manipulate the heat supply. At the lower heat value, molten material has a higher viscosity, and it does not easily allow to exclude the material, and at higher heat input, the molten material quantity is more which is also difficult to remove. Higher gas pressure assists in removing the material more easily. It is recommended to have process parameters of 1800 W laser power, 3500 mm/min cutting speed, and 12 bar or higher gas pressure for obtaining the least dross value (Fig. 4).

3.4 Taperness

The converging nature of the irradiating beam results in taperness of the cut edge, and it further decreases the machining quality. Taperness in the cutting changes the

Main Effects Plot for Dross
Data Means
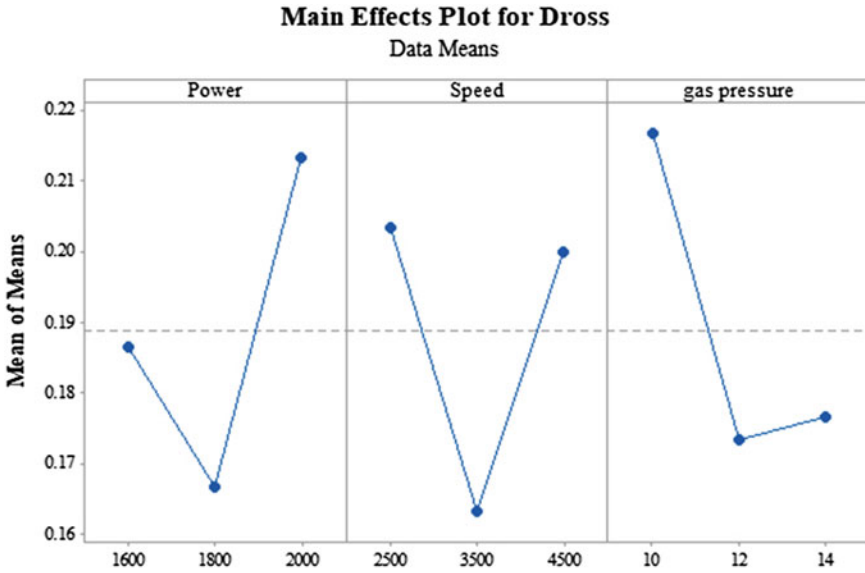
Fig. 4 Main effect plot for dross

dimensional accuracy of the cut edge of the specimen. Figure 5 shows the variation of top and bottom edge values for all the performed experiments. It can be observed that a large difference is in the upper and bottom kerf for the first experiments as it is executed at the lower power and lower gas pressure, while the smallest difference
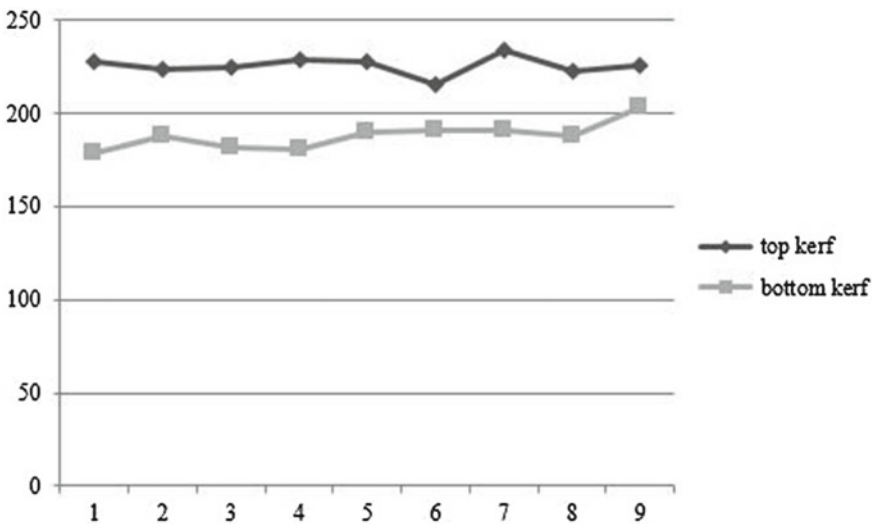

Fig. 5 Variation of taperness for nine experiments

occurs for the ninth experiment as it is performed at maximum power and the highest gas pressure. Due to fact that the more heat melts material and has lower viscosity as heat is more, higher pressure gas excludes the molten material more easily; hence, taperness in the cut edge would be lower. The tapper angle percentage for the first experiment is around 2%, and the taper angle percentage for the ninth experiment is 0.884%. So, it is recommended to have maximum power and higher gas pressure to reduce the taperness.

4 Conclusions

In the current study, the influence of machining parameters of fiber laser cutting with 50 μm output core diameters was carried out on SR, kerf width, dross measurement, and taperness for Al6061-T6. Following conclusions can be drawn from obtained results:

- The fiber laser cutting method for Al6061-T6 material shown better characteristics for selected responses as fiber laser cutting has good characteristics which help in the effective cutting of reflective materials.
- SR was observed to be the most influenced response for input process parameters. Minimum surface roughness value is achieved at the 1600 W laser power, 4500 mm/in cutting speed, 10 bar gas pressure.
- Kerf width was most influenced by the laser cutting speed. The least kerf width was achieved at the 1800 W laser power, 4500 mm/in cutting speed, 10 bar gas pressure.
- Dross height was found to be the most significant for the gas pressure. Minimum dross height was achieved at the 1800 W laser power, 3500 mm/in cutting speed, 12 bar or more than 12 bar gas pressure. Taper angle of the cut edge depends on the heat supplied and the assist gas pressure. Optimized heat supplied and higher gas pressure help in the straight cutting. Minimum taper angle was achieved at the 2000 laser power and 12 or more gas pressure.

References

Akhtar S, Kardas OO, Keles O, Yilbas BS (2014) Laser cutting of rectangular geometry into aluminum alloy: Effect of cut sizes on thermal stress field. Opt Lasers Eng 61:57–66

Chaudhari R et al (2019) Multi-response optimization of WEDM process parameters for machining of superelastic nitinol shape-memory alloy using a heat-transfer search algorithm. Materials 12(8):1277

Chaudhari R, Vora J, Parikh DM, Wankhede V, Khanna S (2020) Multi-response optimization of WEDM parameters using an integrated approach of RSM–GRA analysis for pure titanium. J Inst Eng (India): Series D 101(1):117–126

Chaudhari R, Vora JJ, Parikh D (2020) A review on applications of nitinol shape memory alloy. Recent advances in mechanical infrastructure: proceedings of ICRAM 2020, p 123

Chen C, Gao M, Zeng X (2016) Author ' s accepted manuscript aluminium alloy. Int J Mach Tools Manuf

Chen C, Gao M, Jiang M, ZengX (2016) Surface morphological features of fiber laser cutting of AA2219 aluminum alloy. Int J Adv Manuf Technol, 1219–1226

Dubey AK, VYÃ (2008) Laser beam machining— a review, 48:609–628

Hirsch J (2011) Aluminium in innovative light-weight car design. Mater Trans 52(5):818–824. https://doi.org/10.2320/matertrans.l-mz201132

Jiang D, Panjehpour A, Niazi S, Akbari M (2020) Laser cutting of Al 6061-T6 aluminium alloy sheet: Effect of cutting condition and sheet thickness on the temperature and edge cut quality. Lasers Eng 45(4–6):293–308

Kratky A, Schuöcker D, Liedl G (2008) Processing with kW fibre lasers: advantages and limits. XVII Int Symp Gas Flow Chem Lasers High-Power Lasers 7131: 71311X

Mayyas A, Qattawi A, Omar M, Shan D (2012) Design for sustainability in automotive industry: a comprehensive review. Renew Sustain Energy Rev 16(4):1845–1862

Patel VV, Sejani DJ, Patel NJ, Vora JJ, Gadhvi BJ, Padodara NR, Vamja CD (2016) Effect of tool rotation speed on friction stir spot welded AA5052-H32 and AA6082-T6 dissimilar aluminum alloys. Metallogr Microstr Anal 5(2):142–148

Powell J, Kaplan AFH (2012) A technical and commercial comparison of fiber laser and CO_2 laser cutting. ICALEO 2012–31st Int Congr Appl Lasers Electro-Opt 277:277–281

Rathi P, Ghiya R, Shah H, Srivastava P, Patel S, Chaudhari R, Vora J (2020) Multi-response optimization of Ni55. 8Ti shape memory alloy using taguchi–grey relational analysis approach. In: Recent advances in mechanical infrastructure (pp 13–23). Springer, Singapore

Riveiro A, QuinteroF, Lusquiños F, Pou J, Salminen A, Kujanpaa V (2008) Influence of assist gas in fibre laser cutting of aluminum-copper alloy. ICALEO 2008–27th international congress application lasers electro-optics, congress proceeding, vol 2004, no 2008, pp 688–694

Riveiro A, Quintero F, Lusquiños F, Comesaña R, Pou J (2010) Influence of assist gas nature on the surfaces obtained by laser cutting of Al-Cu alloys. Surf Coatings Technol 205(7):1878–1885

Riveiro A, Quintero F, Lusquiños F, Comesaña R, Pou J (2010) Parametric investigation of CO_2 laser cutting of 2024-T3 alloy. J Mater Process Technol 210(9):1138–1152

Saito M, Iwatsuki S, Yasunaga K, Andoh K (2000) Development of aluminum body for the most fuel e $ cient vehicle. vol 21, pp 511–516

Scintilla LD (2014) Experimental investigation on fiber laser cutting of aluminium thin sheets. High-power laser mater. process. lasers, beam Deliv. diagnostics, Appl. III, vol 8963, no Dmmm, p. 89630X

Scintilla LD, Tricarico L (2013) Fusion cutting of aluminum, magnesium, and titanium alloys using high-power fiber laser. Opt Eng 52(7):076115

Search H, Journals C, Contact A, Iopscience M, Conf IOP, Address IP (2013) Optimization and analysis of laser beam machining parameters, 1

Wandera C (2010) Performance of high power fibre laser cutting of thick-section steel and medium-section aluminium

A Review on Machining Aspects of Shape Memory Alloys

Jay Vora, Aryan Jain, Manav Sheth, Kunj Gajjar, Kumar Abhishek, and Rakesh Chaudhari

Abstract Shape memory alloys (SMA) are emerging Modern Age smart materials which can memorize and regain their original shape. Other unique and versatile properties of SMAs include biocompatibility, pseudoelasticity, high corrosion, wear resistance, and many more. Due to such fascinating characteristics, SMAs have gained a lot of attraction and interest over the last few years in the wide range of applications. Major applications have been in the field of aerospace, biomedical and automotive. Conventional machining of SMA is relatively challenging due to severe strain hardening, high toughness, and high cutting forces. Whereas, non-conventional machining significantly improved the surface morphology and dimensional accuracy as well as lowered the machining time. Machining of SMAs has always been critical due to their smart nature. In the current study, different machining aspects of shape memory alloys have been studied in detail for conventional and non-conventional machining processes.

1 Introduction

Shape memory alloys (SMAs) are a new generation of smart materials which, when heated after being deformed under load, revert to their original shape. Some of the few remarkable properties of SMAs include pseudoelasticity, shape memory effect (SME), superelasticity and microstructure transition temperature based on the application (Hargovind et al. 2019). SMAs have numerous applications in the biomedical and engineering industry. These smart alloys were first examined by

J. Vora · A. Jain · M. Sheth · K. Gajjar · R. Chaudhari (✉)
Department of Mechanical Engineering, Pandit Deendayal Energy University, Gandhinagar 382007, Gujarat, India

K. Abhishek
Department of Mechanical and Aero-Space Engineering, Institute of Infrastructure, Technology, Research and Management (IITRAM), Ahmedabad 380026, Gujarat, India

Ölander (1932); in 1932, he observed pseudoelastic behavior in Au–Cd alloy. The expression shape memory alloys were coined by Vernon and Vernon (1941), based on his polymeric dental material. Khandros and Kurdjumov in 1949 and Read and Chang in 1951 reported the memory effect (Jani 2014). Buehler along with his colleagues, in 1962 observed SME in a nickel–titanium equiatomic alloy, and it was named as nitinol as it was discovered in the Naval Ordnance Laboratory (Jani 2014). Nitinol is the most widely used SMAs in the field of biomedical as it is biocompatible and has high corrosion and wear resistance; it is also used in actuators in aerospace and robotics applications (Chaudhari et al. 2019a, 2020a, b, c). Nowadays, there has been tremendous growth in the applications of SMAs in the different fields of science and engineering.

Since the invention of SMAs, many types of alloys were found since then which exhibit shape memory effects, including NiTi, AuCd, CuZnAl, CuAlNi, and many others (Jani 2014). Nitinol is the most important shape memory alloy in terms of the application in the Biomedical field; there is a study going on to add a third element in the nitinol alloy by substituting Co in place of Ni in some proportion, it was found that by adding Co in different percentage (Machado and Savi 2003). It was found that it exhibits dual-stage phase transition as well as better ductility. As a result of the reformation of martensite structure during ambient temperature deformation. Its application is found in the aerospace field, in which wings morphing is done to increase its speed, reduce power consumption, etc. However, it has its disadvantage of having surface discontinuity added weight so the study has been done to use SMA to tackle those disadvantages. Among several SMA, nickel–titanium alloys are prevalent in medical (sunglass frames, orthopedic implants, orthodontic clips, guide wires, blood filters, surgical instrumentation, cardiovascular stents, etc.) and industrial (micro-electromechanical systems (MEMS), cellular phone antennas, fasteners, sensors, actuators, coupling, helicopter rotor, etc. (Chaudhari 2019b; Khanna 2021a, b, 2020; Kaya and Kaya 2019).

SMA belongs to the group of alloys which regains their primary form, undergoing a temperature base memorization process with the link with two transformation phases. Such phenomenon is identified as shape memory effect (Chaudhari et al. 2021). This behavior of SMA can be seen in different actuation systems in many engineering fields. Basically, two transformation phases play an important role: (i) Austenite (stable at high temperature), (ii) Martensite (stable low temperatures) (Markopoulos et al. 2015). There are three distinct crystal structures, austenite, twinned, and detwinned martensite, along with two phases, bringing the total number of feasible transformations to six. When SMAs are heated, the phase transition of martensite into austenite occurs, with the austenite start temperature (A_s) as the beginning point and austenite finish temperature (A_f) as the finishing point. After A_s point, regaining the original form starts. The transition starts to return to martensite during the cooling process, initiates at a martensite start temperature (M_s), and finishes at a martensite finish temperature (M_f) (Otsuka and Ren 1999). Pseudoelasticity (PE) or superelasticity (SE) where applying mechanical loading above the

A_f temperature, the SMA reverts to its initial form. The other known shape memory characteristics are one-way SME, in which the deformed shape is regained when the external load is released and afterward, heating would help in retrieving the initial form (Petrini and Migliavacca 2011).

In this paper, different machining aspects of shape memory alloys have been discussed in detail. Machining is among the most extensively utilized manufacturing methods across many industrial sectors for achieving the finished product's required output. It also helps in providing specific surface properties such as, but is not limited to, residual stress, microstructure, and dimension. The surface end of a product, which is most well-liked by the product's useful results, will determine its consistency. Since improvements to a product's surface result in modifications to its mechanical and physical properties. The heat generated during the machining process leads to plastically distorted layers which affect the machined surface (Jawahir 2011; Chaurasia et al. 2019). Because of its high strength, strain hardening, substantial heat generation, high durability, machining of Modern Age smart materials like nitinol is critical. As SMAs are more susceptible to temperature, phase transition, and high rate of strain, it becomes arduous to machine such alloys. The phase transition of SMA is impacted due to the generation of heat while machining, which is considered one of the most complicated aspects of the machining of SMAs (Kheirikhah et al. 2010). As a result, discovering the problems during SMA machining is crucial, as only a few studies have been conducted. Therefore, the next step is to improve machinability by lowering the complexities in SMA machining (Weinert et al. 2004; Velmurugan et al. 2018; Hassan et al. 2014). There are two types of machining, with conventional methods and one with non-conventional methods.

2 Shape Memory Alloys Using Conventional Machining Processes

A conventional machining process is a sub-category of subtractive manufacturing where removal of material takes place using a sharp machine tool to obtain the desired accuracy. This kind of machining includes techniques like lathe, milling, drilling, etc. There has been so much research done regarding different conventional machining processes on SMAs.

2.1 High-Speed Milling

It is a modified version of normal milling; in this process, lighter milling is combined with high rotational speed and feed rates to increase MRR as well as to decrease tool wear (TW) resulting in higher tool life, as well as lower cutting forces generated by the fast passage (Abele and Fröhlich 2008). A different study was conducted by

Huang (2004) on a detailed study on nitinol alloys by HSM. For cutting speeds less than 200 m/min, they discovered that elevated levels of cutting velocities contributed to lower cutting forces, improved surface quality in addition to lower TW; however, for speeds greater than 200 m/min, cutting speed had no impact on cutting, surface hardness, or surface finish; however, higher speed generated considerable TW. In one independent study done by Wang (2020) where they applied electrochemical polishing as a surface finish process on nitinol alloys after milling, it was discovered that the current density value was 1.5 A/cm^2, a 7 cm distance between cathode and anode, and 20 s of polishing duration resulted in better surface roughness (SR) and surface finish, as well as increased grain size. They concluded that by adjusting the processing parameters, the SR could be significantly lowered to one-tenth of the initial value.

2.2 Turning

It is a technique used to remove material from a cylindrical component by removing excess material while holding the tool stationary and rotating the workpiece. Weinert et al. (2004) studied the impact of different tool materials on nitinol alloys, including uncoated cemented carbide, polycrystalline diamond (PCD), and cubic boron nitride (CBN), were studied. It was observed that uncoated cemented carbides were not suitable for machining purposes due to excessive TW. They found that the best result can be obtained if there is a multi-layered coating applied. Their coating method consists of 8 layers of TiAlN and TiCN in an alternating pattern; first layer and last layer of TiN were made, and they compared the result with high hardness TiB$_2$ and observed that TiB$_2$ shows high flank wear and also because of tribo-chemical dissolving of TiB$_2$, it resulted in high cratering on the rake face. Now for the PCD tool, it was observed that after turning operation, high notch wear occurs and as higher cutting forces involved in machining NiTi alloys are high, so in combination with low ductility of PCD notch, wear can occur and eventually lead to unexpected breakage of the tool. While in CBN notch, wear cannot be noticed, but TW was high as compared to coated cemented carbides in the same operating conditions and thus coated cemented carbides are preferred. Weinert and Petzoldt (2004) performed a separate study on the impact of operational parameters for machining of NiTi alloys and found that when cutting speeds were less than 20 m/min, cutting forces were exceptionally high and because of its high tool and notch wear was observed. In one another study by Kaynak (2013) where they examined the impact of cryogenic machining on TW with cryogenic cooling, that resulted in a significant reduction of notch wear at the depth of the cut line and progressive flank wear at the nose area at the lower values of cutting velocity, and TW is lowered at a higher value of cutting velocities as compared to the standard lubrication.

2.3 Drilling

The drilling technique finds its applications for SMAs mostly in the medical sector including spinal vertebral spacers, spinal rods, etc. In a study conducted by Weinert (2004) the effect of different operational parameters of drilling on two different types of NiTi alloys namely α-NiTi and β-NiTi has been reported. It was observed that α-NiTi possess more energy for the same cutting speed than β-NiTi and other than that, there is no significant observation but it is worth noting that the cutting velocities from 80 to 120 m/min generate the minimum cutting energy, so it is considered optimal and it can also be backed by the fact SR is also minimum. It was also investigated that SR varies from 0.7 μm to 2.4 μm but for α-NiTi, there is no such relation between SR and cutting speed but for β-NiTi, it was found that for low cutting speed, there is high SR (2.4 μm) but it drops to 1 μm for speeds around 100 m/min and then starts increasing again.

Due to its exceptional characteristics such as biocompatibility, superelasticity, corrosion strength, mechanical strength, and self-healing tribological surfaces, SMAs are commonly used in the medical sector to fabricate micro-devices (Hosseini et al. 2009). Because of its adherent characteristics of phase transformation, SE, and SME, the machining of SMAs faces several challenges. Apart from that, when machined NiTi is used in medical, aerospace, or automotive applications, higher precision and accuracy are demanded. As a consequence of extremely high cutting forces, traditional processing of shape memory alloy is difficult, resulting in low surface morphology, increased TW, and effects on the material property caused by the heat (Mohammed and Al-Ahmari 2020). Furthermore, during conventional machining of nitinol SMA alloy, it is observed to have a low thermal conductivity that impacts its machinability and leads to the conclusion as non-conventional machining is more relevant for SMAs as compared to conventional techniques (Sheth 2020).

3 Shape Memory Alloys Using Non-conventional Machining Processes

Non-conventional machining is defined as the process which removes the material based on various energies such as mechanical, chemical, electrical, thermal, or combinations of these energies without making contact of the tool with the workpiece (Chaudhari 2020d). It is primarily utilized for materials that are extremely hard and brittle, including superalloys and SMAs. Traditional machining methods are observed as less effective than non-traditional techniques which include wire electro-discharge machining (WEDM), spark erosion machining, abrasive water jet machining (AWJM), and laser beam machining (LBM), etc.

3.1 Wire Electrical Discharge Machining (WEDM)

WEDM is a contactless material removal technique that utilizes high-frequency sparks generated between tool and work material (Chaudhari 2020d). It can cut any intricate shapes of high-strength material while ensuring that it is electrically conductive (Sheth 2020; Wankhede 2020). The study of Chaudhari (2019) observed the influence of process parameters which are pulse on time (T_{on}), pulse off time (T_{off}), and current on output response, i.e., MRR, SR, and microhardness (MH). The results of single objective optimization show that maximum MRR is obtained at 10-T_{on}, 5-T_{off}, 5-current values while maximum hardness at 63 of T_{on}, 32 of T_{off}, and 6-current values and minimum SR at 65 of T_{on}, 32 of T_{off}, and 6-current values. The above results show that T_{off} and current are most significantly influencing SR and MH while T_{off} is significantly influencing MRR. It has been observed that the shape memory effect was retained even after machining. Liu (2018) carried out a study on the impact of WEDM on nitinol SMA fatigue. It was discovered that the surface integrity of machined cut samples can be increased by subsequent trim cuts and that trim cuts have a 48% longer fatigue life than machined cut samples. Hsieh et al. (2009) studied the tendency to regain its original form and performance variations of TiNiZr/Cr SMA in WEDM and concluded that as wire electrode feed rate increases, T_{on} increases and the shape recovery degrades slightly due to recast layer defoliation. In an independent study investigated by Rathi et al. (2020) of machining Ni55.8Ti by WEDM machining process using Taguchi GRA combined approach. Here, they considered three input process parameters: T_{on}, $T_{off,}$ and discharge current with response variables such as MRR and SR. After experimentation and optimization, it was concluded that using GRA, the optimized process parameters were obtained at T_{on} as 100 µs, T_{off} 20 µs, and discharge current 6A and corresponding values of output parameters MRR and SR had been determined as 0.7193 mm^3/s and 10.553, respectively.

3.2 Spark Erosion Discharge Machining

In this technique, the material is removed by vaporization and melting caused by repeated electric discharge in between the tool and work material in presence of dielectric fluid. Saeed et al. (2013) analyzed the effects of the rotational tool in EDM input parameters include T_{on}, T_{off}, pulse current, and voltage on output responses; MRR, SR, and TW, and tool electrode revolution is carried out at 200 RPM. MRR in the rotational EDM is less than the traditional EDM because the rotational spark reduces the dielectric resistance and also increases the machining gap which decreases the MRR. While the SR of the rotational tool is less than the traditional spark due to fewer electrical discharge craters because of continuous movement of spark. Tool rotation can also improve the TW rate due to the transform

of heat from outside to the space between the workpiece and electrode. Thus, the rotational tool at 200 RPM decreases the MRR but improves the SR and TW rate than the traditional EDM method.

3.3 Abrasive Water Jet Machining (AWJM)

A technique that employs a combination of abrasive particles and a high-pressure water jet to cut difficult, temperature-sensitive materials. When a high-pressure water jet is transformed into a high-velocity jet, the material gets extracted by plowing, micro-cutting, crack initiation, and propagation. Since no thermal or electrical energy is used in this method, material defects are avoided. The stand-off distance, jet pressure, traverse speed, and abrasive flow rate are all considerable variable factors in AWJM. Kong (2013) investigated the surface characteristics and geometrical accuracy in multimode AWJM of nitinol SMAs alloys and the geometrical accuracy is generated by three modes, i.e., cutting, countersinking, milling. The result shows that thicker workpieces have greater kerf straightness than thinner ones because cutting straight kerf geometry is difficult due to high ductility and twinned martensite transformation of nitinol. Multimode AWJM produces standard quality surfaces. There is no deformed shape, cracks, and white layer formation in the workpiece during machining. The most effective technique was to countersink holes using a conic rotation of the jet with a pinpoint above the workpiece. Quality of surfaces can be obtained by machining nitinol by AWJM and possible to make highly intricate geometrical parts. From the study of Kong et al. (2011) on challenges faced by using water jet machining (WJM) on nitinol SMAs by controlled depth milling. From the crystal structure perspective, the AWJM process is considered better than simple WJM due to depth controlled during milling operations. Material elimination is achieved by microabrasion, which includes grooving and plowing, which is expanded further by water droplet impingement, as determined by debris and grit progression. It results in a lower depth of penetration than AWJ milling due to which surface integrity may be reduced. Thus, AWJM is considered better machining than plain water jet for nitinol SMAs alloys (Kong et al. 2011).

3.4 Laser Beam Machining (LBM)

It is a thermal-based technique that utilizes laser as the heat source to produce heat and removes material by melting and vaporization. The laser machining process has been considerably used for fabrication because of its excellent quality, flexibility, and at different velocities for various applications (Thawari 2005). Ultrashort pulse laser which one of which is femtosecond lasers which is probably used for machining

nitinol because of its distinct beam material interaction and beam characteristics. This short pulse produces a high power density that results in instant vaporization at the region of beam–material interaction and also has a short time for heat diffusion, thus results in a minimal heat-affected zone at the processed region. This short pulse laser results in a reduction of thermal influence on nitinol (Huang et al. 2004). Huang et al. (2004) investigated surface characteristics of nitinol SMA using femtosecond LBM. The SR is influenced by two variables, i.e., beam power and beam spacing. As the beam power increases, the deeper the cuts become for given beam spacing because that beam overlaps and the surface becomes rough. At particular beam power, the SR is high at very low and high values of beam spacing so an optimal beam spacing should be taken to minimize SR during the machining process. In this study, the femtosecond laser produces SR of around 0.2 µm on nitinol that is comparable to precision milling. From the study of (Pfiefer et al. 2010) on effects of input parameters of pulsed Nd; YAG laser cutting of NiTi SMAs. 1 mm thick SMA sheet was cut using pulsed Nd; YAG laser with high average power. Then, results are compared with ultrashort pulse laser which has a high cutting velocity (v-2-12 mm/s) and decent cut characteristics (Rz-10-30 µm) so a lower surface roughness is achieved. However, it has a higher thermal effect than an ultrashort pulse laser, culminating in a HAZ (size 6–30 µm) that influences mechanical characteristics which cuts with less accuracy.

4 Conclusions

In the present study, a detailed review was carried out on machining aspects of nitinol shape memory alloys. Shape memory alloys (SMAs) are a new generation of smart materials which, when heated after being deformed under load, revert back to their original shape. Several SMAs were developed over the years. However, nitinol became a famous shape memory alloy owing to low production cost as compared to other SMAs, safer and easier handling, and superior mechanical properties. The phase transition of SMA is impacted due to the generation of heat while machining, which is considered one of the most complicated aspects of the machining of SMAs. As a consequence of extremely high cutting forces, traditional processing of shape memory alloy is difficult, resulting in low surface morphology, increased TW, and effects on the material property caused by the heat. The non-contact nature of non-traditional machining was observed to be more suitable for these SMAs. WEDM, EDM, AWJM, LBM were among these non-traditional machining processes which were observed to be more favorable from machining aspects, as well as the retention of shape memory properties.

References

Abele E, Fröhlich B (2008) High speed milling of titanium alloys. Adv Product Eng Manag 3(3):131–140

Chaudhari R et al (2019a) Pareto optimization of WEDM process parameters for machining a NiTi shape memory alloy using a combined approach of RSM and heat transfer search algorithm. Adv Manuf, 1–17

Chaudhari R et al (2019b) Multi-response optimization of WEDM process parameters for machining of superelastic nitinol shape-memory alloy using a heat-transfer search algorithm. Materials 12(8):1277

Chaudhari R et al (2020a) Surface analysis of wire-electrical-discharge-machining-processed shape-memory alloys. Materials 13(3):530

Chaudhari R et al (2020b) Effect of WEDM process parameters on surface morphology of nitinol shape memory alloy. Materials 13(21):4943

Chaudhari R et al (2020c) Optimization of parameters of spark erosion based processes. In: Spark erosion machining. 2020, CRC Press, pp 190–216

Chaudhari R et al (2020d) Multi-response optimization of WEDM parameters using an integrated approach of RSM–GRA analysis for pure titanium. J Inst Eng (India): Series D, 1–10

Chaudhari R, Vora JJ, Parikh D (2020) A review on applications of nitinol shape memory alloy. Recent advances in mechanical infrastructure: proceedings of ICRAM 2020, p 123

Chaudhari R, Vora J, Lacalle LN, Khanna S, Patel VK, Ayesta I (2021) Parametric optimization and effect of nano-graphene mixed dielectric fluid on performance of wire electrical discharge machining process of Ni55. 8Ti Shape Memory Alloy. Materials 14(10):2533

Chaurasia A, Wankhede V, Chaudhari R (2019) Experimental investigation of high-speed turning of INCONEL 718 using PVD-coated carbide tool under wet condition. In Innovations in infrastructure. Springer, pp 367–374

Daneshmand S et al (2013) Experimental investigations into electro discharge machining of NiTi shape memory alloys using rotational tool. Int J Electrochem Sci 8:7484–7497

Hargovind S, Narendranath S, Ramesh MR (2019) Advanced machining of TiNiCo shape memory alloys for biomedical applications. Emerg Mater Res 8(1):14–21

Hassan MR, Mehrpouya M, Dawood S. Review of the machining difficulties of nickel-titanium based shape memory alloys. In: Applied mechanics and materials 2014 (Vol 564, pp 533–537). Trans Tech Publications Ltd

Hosseini S, adrnezhaad S, Ekrami A (2009) Phase transformation behavior of porous NiTi alloy fabricated by powder metallurgical method. Mater Sci Eng C 29(7):2203–2207

Hsieh S et al (2009) The machining characteristics and shape recovery ability of Ti–Ni–X (X = Zr, Cr) ternary shape memory alloys using the wire electro-discharge machining. Int J Mach Tools Manuf 49(6):509–514

Huang H (2004) A study of high-speed milling characteristics of nitinol. Mater Manuf Process 19(2):159–175

Huang H, ZhengH, Lim G (2004) Femtosecond laser machining characteristics of Nitinol. Appl Surface Sci 228(1–4):201–206

Jani JM et al (2014) A review of shape memory alloy research, applications and opportunities. Mater Design (1980–2015) 56:1078–1113

Jawahir I et al (2011) Surface integrity in material removal processes: recent advances. CIRP Annals 60(2):603–626

Kaya E, Kaya İ (2019) A review on machining of NiTi shape memory alloys: The process and post process perspective. Int J Adv Manuf Technol 100(5):2045–2087

Kaynak Y et al (2013) Tool-wear analysis in cryogenic machining of NiTi shape memory alloys: a comparison of tool-wear performance with dry and MQL machining. Wear 306(1–2):51–63

Khanna S et al (2020) Growth of titanium dioxide nanorod over shape memory material using chemical vapor deposition for energy conversion application. Mater Today: Proc 28:475–479

Khanna S et al (2021a) Fabrication of rutile–TiO_2 nanowire on shape memory alloy: a potential material for energy storage application. Mater Today: Proc

Khanna S et al (2021b) Unravelling camphor mediated synthesis of TiO_2 nanorods over shape memory alloy for efficient energy harvesting. Appl Surface Sci 541:148489

Kheirikhah MM, Rabiee S, Edalat ME (2010) A review of shape memory alloy actuators in robotics. In Robot soccer world cup. Springer

Kong MC et al (2013) On geometrical accuracy and integrity of surfaces in multi-mode abrasive waterjet machining of NiTi shape memory alloys. CIRP Annals 62(1):555–558

Kong M, Axinte D, Voice W (2011) Challenges in using waterjet machining of NiTi shape memory alloys: an analysis of controlled-depth milling. J Mater Proc Technol 211(6):959–971

Liu J et al (2018) Effect of wire-EDM on fatigue of nitinol shape memory alloy. Mater Manuf Process 33(16):1809–1814

Machado L, Savi M (2003) Medical applications of shape memory alloys. Brazilian J Med Biolog Res 36(6):683–691

Markopoulos A, Pressas I, Manolakos D (2015) A review on the machining of nickel-titanium shape memory alloys. Rev Adv Mater Sci 42:28–35

Mohammed MK, Al-Ahmari A (2020) Laser-Machining of Microchannels in NiTi-based shape-memory alloys: experimental analysis and process optimization. Materials 13(13):2945

Ölander A (1932) An electrochemical investigation of solid cadmium-gold alloys. J Amer Chem Soc 54(10):3819–3833

Otsuka K, Ren X (1999) Recent developments in the research of shape memory alloys. Intermetallics 7(5):511–528

Petrini, L. and F. Migliavacca, Biomedical applications of shape memory alloys. Journal of Metallurgy, 2011. 2011

Pfeifer R et al (2010) Pulsed Nd: YAG laser cutting of NiTi shape memory alloys—Influence of process parameters. J Mater Proc Technol 210(14):1918–1925

Rathi P et al (2020) Multi-response optimization of Ni55. 8Ti shape memory alloy using taguchi–grey relational analysis approach. In: Recent advances in mechanical infrastructure. Springer. pp 13–23

Sheth M et al (2020) Multi-objective optimization of Inconel 718 using combined approach of taguchi—grey relational analysis. In: Advances in mechanical engineering. 2020, Springer, pp 229–235

Thawari G et al (2005) Influence of process parameters during pulsed Nd: YAG laser cutting of nickel-base superalloys. J Mater Proc Technol 170(1–2):229–239

Velmurugan C, Senthilkumar V, Dinesh S, Arulkirubakaran D (2018) Machining of NiTi-shape memory alloys-a review. Mach Sci Technol 4:22(3):355–401

Vernon LB, Vernon HM (1941) Process of manufacturing articles of thermoplastic synthetic resins. Google Patents

Wang G et al (2020) Effect of electrochemical polishing on surface quality of nickel-titanium shape memory alloy after milling. J Mater Res Technol 9(1):253–262

Wankhede V et al (2020) Experimental investigation of FDM process parameters using Taguchi analysis. Mater Today: Proc 27:2117–2120

Weinert K et al (2004) Drilling of NiTi shape memory alloys. Materialwissenschaft und Werkstofftechnik: Entwicklung, Fertigung, Prüfung, Eigenschaften und Anwendungen technischer Werkstoffe 35(5):338–341

Weinert K, Petzoldt V (2004) Machining of NiTi based shape memory alloys. Materials science and engineering: a 378(1–2):180–184

Weinert K, Petzoldt V, Kötter D (2004) Turning and drilling of NiTi shape memory alloys. CIRP Annals 53(1):65–68

Author Index